

# ISOTOPE METHODS FOR DATING OLD GROUNDWATER



**IAEA**

International Atomic Energy Agency

ISOTOPE METHODS  
FOR DATING OLD GROUNDWATER

The following States are Members of the International Atomic Energy Agency:

AFGHANISTAN	GUATEMALA	PANAMA
ALBANIA	HAITI	PAPUA NEW GUINEA
ALGERIA	HOLY SEE	PARAGUAY
ANGOLA	HONDURAS	PERU
ARGENTINA	HUNGARY	PHILIPPINES
ARMENIA	ICELAND	POLAND
AUSTRALIA	INDIA	PORTUGAL
AUSTRIA	INDONESIA	QATAR
AZERBAIJAN	IRAN, ISLAMIC REPUBLIC OF	REPUBLIC OF MOLDOVA
BAHRAIN	IRAQ	ROMANIA
BANGLADESH	IRELAND	RUSSIAN FEDERATION
BELARUS	ISRAEL	RWANDA
BELGIUM	ITALY	SAUDI ARABIA
BELIZE	JAMAICA	SENEGAL
BENIN	JAPAN	SERBIA
BOLIVIA	JORDAN	SEYCHELLES
BOSNIA AND HERZEGOVINA	KAZAKHSTAN	SIERRA LEONE
BOTSWANA	KENYA	SINGAPORE
BRAZIL	KOREA, REPUBLIC OF	SLOVAKIA
BULGARIA	KUWAIT	SLOVENIA
BURKINA FASO	KYRGYZSTAN	SOUTH AFRICA
BURUNDI	LAO PEOPLE'S DEMOCRATIC REPUBLIC	SPAIN
CAMBODIA	LATVIA	SRI LANKA
CAMEROON	LEBANON	SUDAN
CANADA	LESOTHO	SWAZILAND
CENTRAL AFRICAN REPUBLIC	LIBERIA	SWEDEN
CHAD	LIBYA	SWITZERLAND
CHILE	LIECHTENSTEIN	SYRIAN ARAB REPUBLIC
CHINA	LITHUANIA	TAJIKISTAN
COLOMBIA	LUXEMBOURG	THAILAND
CONGO	MADAGASCAR	THE FORMER YUGOSLAV REPUBLIC OF MACEDONIA
COSTA RICA	MALAWI	TOGO
CÔTE D'IVOIRE	MALAYSIA	TRINIDAD AND TOBAGO
CROATIA	MALI	TUNISIA
CUBA	MALTA	TURKEY
CYPRUS	MARSHALL ISLANDS	UGANDA
CZECH REPUBLIC	MAURITANIA	UKRAINE
DEMOCRATIC REPUBLIC OF THE CONGO	MAURITIUS	UNITED ARAB EMIRATES
DENMARK	MEXICO	UNITED KINGDOM OF GREAT BRITAIN AND NORTHERN IRELAND
DOMINICA	MONACO	UNITED REPUBLIC OF TANZANIA
DOMINICAN REPUBLIC	MONGOLIA	UNITED STATES OF AMERICA
ECUADOR	MONTENEGRO	URUGUAY
EGYPT	MOROCCO	UZBEKISTAN
EL SALVADOR	MOZAMBIQUE	VENEZUELA
ERITREA	MYANMAR	VIETNAM
ESTONIA	NAMIBIA	YEMEN
ETHIOPIA	NEPAL	ZAMBIA
FIJI	NETHERLANDS	ZIMBABWE
FINLAND	NEW ZEALAND	
FRANCE	NICARAGUA	
GABON	NIGER	
GEORGIA	NIGERIA	
GERMANY	NORWAY	
GHANA	OMAN	
GREECE	PAKISTAN	
	PALAU	

The Agency's Statute was approved on 23 October 1956 by the Conference on the Statute of the IAEA held at United Nations Headquarters, New York; it entered into force on 29 July 1957. The Headquarters of the Agency are situated in Vienna. Its principal objective is "to accelerate and enlarge the contribution of atomic energy to peace, health and prosperity throughout the world".

# ISOTOPE METHODS FOR DATING OLD GROUNDWATER

INTERNATIONAL ATOMIC ENERGY AGENCY  
VIENNA, 2013

## COPYRIGHT NOTICE

All IAEA scientific and technical publications are protected by the terms of the Universal Copyright Convention as adopted in 1952 (Berne) and as revised in 1972 (Paris). The copyright has since been extended by the World Intellectual Property Organization (Geneva) to include electronic and virtual intellectual property. Permission to use whole or parts of texts contained in IAEA publications in printed or electronic form must be obtained and is usually subject to royalty agreements. Proposals for non-commercial reproductions and translations are welcomed and considered on a case-by-case basis. Enquiries should be addressed to the IAEA Publishing Section at:

Marketing and Sales Unit, Publishing Section  
International Atomic Energy Agency  
Vienna International Centre  
PO Box 100  
1400 Vienna, Austria  
fax: +43 1 2600 29302  
tel.: +43 1 2600 22417  
email: [sales.publications@iaea.org](mailto:sales.publications@iaea.org)  
<http://www.iaea.org/books>

© IAEA, 2013

Printed by the IAEA in Austria

April 2013

STI/PUB/1587

### IAEA Library Cataloguing in Publication Data

Isotope methods for dating old groundwater : — Vienna : International Atomic Energy Agency, 2013.

p. ; 30 cm.

STI/PUB/1587

ISBN 978-92-0-137210-9

Includes bibliographical references.

1. Groundwater flow — Measurement. 2. Radioactive tracers in hydrogeology. 3. Groundwater recharge — Mathematical models. I. International Atomic Energy Agency.

IAEAL

13-00793

# FOREWORD

In many parts of the world, groundwater constitutes a major source of water for agricultural, energy, industrial and urban use, and it is expected to play an even greater role in the next decades on a global scale. The rising importance of groundwater is a result of increasing water demands deriving from population growth and concerns about the impact of predicted climate change on the hydrological cycle. Unfortunately, in many cases, water officials and managers lack the knowledge of the local groundwater resources required to ensure adequate and long term access to available water resources. In order to adopt adequate policies and to share resources with limited accessibility, sound and comprehensive information on the amount and condition of existing water resources is required.

New scientific, technical, social and legal questions and a growing number of conflicts and issues regarding water usage require a better understanding of the movement, origin and age of groundwater. Isotope hydrology methods have great potential to provide the hydrogeological information required to rapidly and effectively assess and map groundwater resources. For several decades, one of the major tools for obtaining information about groundwater origin, and its properties and movement has been the use of isotopes, which has often provided insights not available using other techniques. Information on groundwater age is required to address aspects such as recharge rates and mechanisms, resource renewability, flow rate estimation in aquifers and vulnerability to pollution, especially when dealing with shared water resources. Age information, mainly provided by radionuclides and modelling, is considered highly relevant for validating conceptual flow models of groundwater systems, calibrating numerical flow models and predicting the fate of pollutants in aquifers. Isotope tracers are now used to study groundwater age and movement, covering time spans from a few months up to a million years.

The understanding of groundwater occurrence and movement in large continental basins has been a matter of debate among experts. Despite the large number of studies which have been carried out in the past, many open questions remain, and ideas and concepts are often revised based on new conceptual models, isotope and tracer analyses or water flow models. The book's 14 chapters explain what is currently understood about the use and application of radionuclides and related geochemical tracers and tools to assess groundwater age and movement over time spans beyond a few thousand years.

The IAEA officers responsible for this publication were A. Suckow, P.K. Aggarwal and L. Araguas-Araguas of the Division of Physical and Chemical Sciences.

### *EDITORIAL NOTE*

*Although great care has been taken to maintain the accuracy of information contained in this publication, neither the IAEA nor its Member States assume any responsibility for consequences which may arise from its use.*

*The use of particular designations of countries or territories does not imply any judgement by the publisher, the IAEA, as to the legal status of such countries or territories, of their authorities and institutions or of the delimitation of their boundaries.*

*The mention of names of specific companies or products (whether or not indicated as registered) does not imply any intention to infringe proprietary rights, nor should it be construed as an endorsement or recommendation on the part of the IAEA.*

*The IAEA has no responsibility for the persistence or accuracy of URLs for external or third party Internet web sites referred to in this book and does not guarantee that any content on such web sites is, or will remain, accurate or appropriate.*

# CONTENTS

CHAPTER 1. INTRODUCTION.....	1
1.1. BACKGROUND.....	1
1.2. OBJECTIVES.....	2
1.3. SCOPE.....	2
1.4. STRUCTURE.....	3
CHAPTER 2. CHARACTERIZATION AND CONCEPTUALIZATION OF GROUNDWATER FLOW SYSTEMS.....	5
2.1. INTRODUCTION.....	5
2.2. THE GROUNDWATER FLOW SYSTEM.....	5
2.2.1. Hydrological cycle.....	6
2.2.2. Timescales for recharge and discharge.....	7
2.3. CHARACTERIZATION OF GROUNDWATER FLOW SYSTEMS.....	8
2.3.1. Geological framework.....	8
2.3.2. Hydrological framework.....	9
2.3.3. Hydrochemical framework.....	12
2.4. DEVELOPMENT OF A NUMERICAL GROUNDWATER FLOW MODEL.....	16
2.5. SUMMARY GUIDELINES FOR THE CHARACTERIZATION OF GROUNDWATER SYSTEMS AND THEIR FREQUENCY DISTRIBUTIONS OF AGE.....	17
CHAPTER 3. DEFINING GROUNDWATER AGE.....	21
3.1. INTRODUCTION: WHY SHOULD GROUNDWATER BE DATED?.....	21
3.2. WHAT DOES 'GROUNDWATER AGE' MEAN?.....	21
3.3. GROUNDWATER AGE DISTRIBUTION.....	24
3.3.1. Examples of groundwater age distribution.....	26
3.4. CHARACTERISTICS OF IDEAL TRACERS.....	28
3.5. ADDITIONAL LIMITATIONS ON TRACER MODEL AGES.....	29
3.6. TRACERS IN THIS BOOK.....	30
APPENDIX TO CHAPTER 3.....	32
CHAPTER 4. RADIOCARBON DATING IN GROUNDWATER SYSTEMS.....	33
4.1. INTRODUCTION.....	33

4.2.	INTERPRETATION OF RADIOCARBON AGE OF DISSOLVED INORGANIC CARBON IN GROUNDWATER.....	35
4.2.1.	Determination of initial $^{14}\text{C}$ in recharge water, $A_0$ .....	36
4.3.	SUMMARY OF PREDOMINANT GEOCHEMICAL REACTIONS IN GROUNDWATER SYSTEMS AFFECTING INTERPRETATION OF RADIOCARBON AGE.....	49
4.4.	GENERALIZED GEOCHEMICAL ADJUSTMENT MODELS.....	52
4.5.	TOTAL DISSOLVED CARBON.....	54
4.6.	GEOCHEMICAL MASS TRANSFER MODELS.....	55
4.6.1.	Some practical precautions and special cases in geochemical mass balance modelling.....	57
4.7.	EXAMPLES USING NETPATH.....	58
4.7.1.	Alliston Aquifer System, Ontario, Canada.....	59
4.7.2.	Floridan Aquifer System, FL, USA.....	61
4.8.	RADIOCARBON DATING OF DISSOLVED ORGANIC CARBON.....	63
4.9.	HYDRODYNAMIC AND AQUIFER MATRIX EFFECTS ON RADIOCARBON AGES.....	66
4.9.1.	Mixing processes.....	66
4.9.2.	Subsurface production.....	66
4.9.3.	Diffusive exchange with confining layers.....	66
4.9.4.	Transport models.....	67
4.9.5.	Analytical solutions.....	67
4.9.6.	Matrix diffusion in unsaturated zones.....	70
4.9.7.	General conclusions regarding the effects of hydrodynamics and heterogeneity on $^{14}\text{C}$ model ages in groundwater.....	70
4.10.	GUIDELINES FOR RADIOCARBON DATING OF DISSOLVED CARBON IN GROUNDWATER SYSTEMS.....	71
	APPENDIX TO CHAPTER 4.....	74
	CHAPTER 5. KRYPTON-81 DATING OF OLD GROUNDWATER.....	91
5.1.	INTRODUCTION.....	91
5.1.1.	Krypton in the environment.....	91
5.1.2.	Krypton in hydrology.....	92
5.2.	LARGE VOLUME GAS SAMPLING TECHNIQUES.....	98
5.2.1.	Sampling requirements.....	98
5.2.2.	Physical principles of gas extraction.....	99
5.2.3.	Gas extraction system designs.....	100
5.2.4.	Specific parameters, remarks and extraction efficiencies.....	101
5.2.5.	Optimal design of gas extraction units.....	102

5.3.	GAS PREPARATION AND PURIFICATION.....	102
5.3.1.	Introduction.....	102
5.3.2.	Purification system at the University of Bern .....	105
5.3.3.	Purification system at the University of Illinois, Chicago .....	106
5.4.	DETECTION METHODS OF NOBLE GAS RADIONUCLIDES.....	107
5.4.1.	Low level counting.....	108
5.4.2.	Accelerator mass spectrometry .....	109
5.4.3.	Atom trap trace analysis.....	110
5.4.4.	Resonance ionization mass spectrometry.....	112
5.5.	FIRST ATTEMPTS AT <sup>81</sup> Kr DATING: THE MULTITRACER COMPARISON IN THE SOUTH-WESTERN GREAT ARTESIAN BASIN.....	112
5.5.1.	Introduction.....	112
5.5.2.	Study area.....	114
5.5.3.	Krypton-81 groundwater ages.....	114
5.5.4.	Comparison with helium data .....	115
5.5.5.	Comparison with chlorine-36 data .....	116
5.5.6.	Additional evidence for the correctness of krypton-81 ages.....	120
5.5.7.	Summary .....	121
5.6.	ADDENDUM: SIGNAL ATTENUATION DUE TO HYDRODYNAMIC DISPERSION.....	123
CHAPTER 6. CHLORINE-36 DATING OF OLD GROUNDWATER.....		125
6.1.	BASIC PRINCIPLES OF CHLORINE-36 .....	125
6.1.1.	Chlorine-36 in the hydrological cycle.....	125
6.2.	SAMPLING TECHNIQUES FOR CHLORINE-36 .....	127
6.3.	CHLORINE-36 SAMPLE PREPARATION AND MEASUREMENT .....	127
6.4.	CHLORINE-36 RESEARCH GROUPS AND LABORATORIES.....	130
6.5.	SPECIFICS OF THE <sup>36</sup> Cl METHOD .....	131
6.5.1.	Meteoric sources of <sup>36</sup> Cl.....	132
6.5.2.	Secular variation in the atmospheric deposition of <sup>36</sup> Cl.....	134
6.5.3.	Chlorine-36 from nuclear weapons fallout .....	134
6.5.4.	Processes affecting <sup>36</sup> Cl during recharge.....	136
6.5.5.	Subsurface processes influencing <sup>36</sup> Cl concentrations and <sup>36</sup> Cl/Cl .....	138
6.5.6.	Use of other environmental tracers to interpret chloride systematics .....	146
6.6.	COMPARISON OF <sup>36</sup> Cl WITH OTHER METHODS OF DATING.....	148
6.6.1.	Comparison with radiocarbon .....	148
6.6.2.	Comparison with <sup>4</sup> He .....	149
6.6.3.	Comparison with <sup>81</sup> Kr .....	150
6.6.4.	Comparison without a well defined flow path.....	151
6.6.5.	Summary .....	152

CHAPTER 7. DATING OF OLD GROUNDWATER USING URANIUM ISOTOPES — PRINCIPLES AND APPLICATIONS .....	153
7.1. INTRODUCTION .....	153
7.1.1. History.....	153
7.1.2. Scope and objective.....	154
7.2. NATURAL ABUNDANCE OF URANIUM ISOTOPES .....	154
7.3. URANIUM GEOCHEMISTRY .....	156
7.4. URANIUM ISOTOPE MEASUREMENTS .....	158
7.5. URANIUM ISOTOPE DATING METHOD.....	159
7.5.1. Introduction.....	159
7.5.2. Mathematical formulation of the model.....	160
7.5.3. Identification of model parameters.....	164
7.6. CASE STUDIES .....	170
7.6.1. Carrizo sandstone aquifer, South Texas, USA .....	170
7.6.2. Continental Intercalaire aquifer, north-west Sahara.....	173
7.7. SUMMARY.....	176
CHAPTER 8. HELIUM (AND OTHER NOBLE GASES) AS A TOOL FOR UNDERSTANDING LONG TIMESCALE GROUNDWATER TRANSPORT .....	179
8.1. INTRODUCTION .....	179
8.2. THE GEOCHEMICAL CONSTRUCT FOR APPARENT $^4\text{He}$ TRACER AGES .....	179
8.3. SAMPLING AND ANALYSIS .....	181
8.3.1. Sampling methods.....	181
8.3.2. Laboratory processing methods .....	182
8.3.3. Mass spectrometry .....	182
8.4. IDENTIFYING MULTIPLE $^4\text{He}$ COMPONENTS FROM MEASUREMENTS .....	183
8.4.1. Equilibrium with air, $^4\text{He}_{\text{eq}}$ .....	183
8.4.2. Excess ‘air’ components, $^4\text{He}_{\text{exc}}$ .....	185
8.4.3. Radiogenic production, $^4\text{He}_{\text{rad}}$ .....	186
8.4.4. Summary .....	204
8.5. CASE STUDIES .....	204
8.5.1. Setting the stage .....	204
8.5.2. Simple open system aquifer models.....	205
8.5.3. Helium-4 as a component in groundwater flow models evolves .....	206
8.5.4. Summary .....	209
8.6. CONCEPTUAL $^4\text{He}$ TRACER AGES AS A CONSTRAINT ON GROUNDWATER AGE.....	209
8.6.1. Helium-4 fluxes determined by vertical borehole variation in $^3\text{He}/^4\text{He}$ .....	210
8.6.2. Cajon Pass .....	211
8.6.3. South African ultra-deep mine waters.....	212

8.6.4.	Deep borehole sampling.....	212
8.6.5.	Summary .....	215
CHAPTER 9.	SYSTEM ANALYSIS USING MULTITRACER APPROACHES.....	217
9.1.	VERTICAL PROFILES .....	218
9.1.1.	Unconfined homogeneous aquifer.....	218
9.1.2.	Homogeneous aquifer with different recharge and discharge zones.....	225
9.1.3.	Aquifer systems — confined or partly confined .....	230
9.1.4.	Summary .....	232
9.2.	HORIZONTAL TRANSECTS .....	233
9.2.1.	Transect along an assumed flowline.....	233
9.2.2.	Horizontal transects intersecting different flowlines.....	234
9.2.3.	Summary .....	236
9.3.	IMPORTANT PATTERNS OF TRACER VERSUS TRACER .....	236
9.3.1.	Combination of tracers for different timescales.....	237
9.3.2.	Combination of tracers with similar decay timescales.....	240
9.3.3.	Linear accumulating tracer versus exponential decay tracer .....	241
9.3.4.	Noble gas patterns .....	243
CHAPTER 10.	NUMERICAL FLOW MODELS AND THEIR CALIBRATION USING TRACER BASED AGES.....	245
10.1.	INTRODUCTION .....	245
10.2.	EQUATIONS AND NUMERICAL METHODS .....	246
10.3.	AQUIFER GEOMETRY AND GRID DESIGN .....	247
10.4.	BOUNDARY CONDITIONS .....	248
10.5.	TRANSIENT SIMULATIONS .....	249
10.6.	MODEL CALIBRATION .....	250
10.7.	CALCULATION OF FLOW MODEL AGES .....	251
10.8.	SIMULATION OF DISPERSION AND APPARENT GROUNDWATER AGE.....	253
10.9.	MODEL CALIBRATION USING TRACER BASED AGES .....	256
CHAPTER 11.	MILK RIVER AQUIFER, ALBERTA, CANADA — A CASE STUDY .....	259
11.1.	INTRODUCTION .....	259
11.2.	GEOLOGICAL AND HYDROLOGICAL BACKGROUND .....	259
11.3.	THE ROLE OF GEOCHEMISTRY IN CONSTRAINING WATER AND SOLUTE TRANSPORT MODELS — THE MILK RIVER AQUIFER EXPERIENCE .....	260
11.4.	ISOTOPIC STUDIES OF THE MILK RIVER AQUIFER.....	264

11.4.1.	Radiocarbon and stable isotopes .....	264
11.4.2.	Dissolved gases .....	265
11.4.3.	Chlorine-36 and chloride.....	267
11.4.4.	Uranium isotopes .....	269
11.5.	CONCLUSIONS .....	272
CHAPTER 12. CASE STUDY MIDDLE RIO GRANDE BASIN, NEW MEXICO, USA.....		273
12.1.	INTRODUCTION .....	273
12.2.	BACKGROUND: HYDROGEOLOGICAL SETTING .....	273
12.3.	THE UNITED STATES GEOLOGICAL SURVEY MIDDLE RIO GRANDE BASIN STUDY .....	276
12.4.	STABLE ISOTOPES, <sup>4</sup> He, RADIOCARBON AGES AND HYDROCHEMICAL ZONES .....	276
12.4.1.	Stable isotopes.....	276
12.4.2.	Carbon-14 model age.....	278
12.4.3.	Helium-4 .....	280
12.4.4.	Hydrochemical zones.....	283
12.4.5.	Pre-development water levels.....	284
12.4.6.	Variations in <sup>14</sup> C model age with depth.....	286
12.4.7.	Stable isotopes, deuterium excess and radiocarbon age .....	286
12.4.8.	Carbon-14 model age profiles and recharge rates .....	287
12.5.	SUMMARY OF CHEMICAL AND ENVIRONMENTAL TRACER CONSTRAINTS ON THE FLOW SYSTEM.....	288
12.6.	GROUNDWATER MODEL DEVELOPMENT .....	289
12.7.	REFINING CONCEPTUALIZATION OF GROUNDWATER FLOW IN THE BASIN.....	293
12.8.	PALAEORECHARGE RATES .....	294
12.9.	CONCLUDING REMARKS .....	295
CHAPTER 13. METHODS FOR DATING VERY OLD GROUNDWATER: EASTERN AND CENTRAL GREAT ARTESIAN BASIN CASE STUDY .....		297
13.1.	INTRODUCTION .....	297
13.2.	DEPOSITION, STRUCTURE AND HYDROGEOLOGY OF THE EASTERN GREAT ARTESIAN BASIN.....	299
13.3.	SETTING THE STAGE .....	300
13.4.	STABLE ISOTOPE AND <sup>14</sup> C MEASUREMENTS.....	301
13.5.	THE 1982 FIELDWORK: STANNUM TO INNAMINCKA AND BONNA VISTA TO THARGOMINDAH.....	302

13.6.	THE 1985 FIELDWORK: FAIRLIGHT TRUST TO CLAYTON, ATHOL TO MUTTI MUTTI AND MT. CRISPE TO CURDIMURKA.....	308
13.7.	MODELLING <sup>36</sup> Cl AND <sup>4</sup> He.....	309
13.8.	GEOCHEMICAL MODELLING OF GROUNDWATER REACTION PATHS.....	312
13.9.	THE 2000 BENCHMARK AND SYNTHESIS.....	314
13.10.	CONTINUING WORK IN THE GREAT ARTESIAN BASIN.....	316
	CHAPTER 14. KRYPTON-81 CASE STUDY: THE NUBIAN AQUIFER, EGYPT .....	319
14.1.	NUBIAN AQUIFER .....	319
14.2.	METHODS.....	319
14.3.	KRYPTON-81 DATA.....	320
14.4.	CHLORINE-36 DATA .....	321
14.5.	CORRELATION OF <sup>36</sup> Cl AND <sup>81</sup> Kr DATA.....	322
14.6.	HELIUM-4 DATA.....	323
14.7.	CARBON-14 DATA.....	323
14.8.	HYDROGEOLOGICAL AND PALAEOCLIMATIC IMPLICATIONS OF GROUNDWATER AGE DATA.....	324
	REFERENCES .....	325
	CONTRIBUTORS TO DRAFTING AND REVIEW.....	357



# Chapter 1

## INTRODUCTION

P.K. AGGARWAL

International Atomic Energy Agency

### 1.1. BACKGROUND

Groundwater is the largest component of fresh water accessible for human use. While two thirds of the surface area of planet Earth is covered with water, most of it is sea water or saline and only 2.5% is fresh water (Shiklomanov and Rodda (2004) [1]). A large portion of this fresh water — nearly 69% — is bound in ice and permanent snow cover in the Antarctic and Arctic, and in continental mountains. About 30% of fresh water, or 0.75% of all water on Earth, is present as fresh groundwater. Only 0.26% of the total amount of fresh water on Earth is in lakes, rivers and reservoirs that are most easily accessible for human use (the remaining 1% is estimated to occur as soil moisture, swamp water and permafrost). Groundwater, in both renewable and non-renewable aquifers, accounts for about 95% of accessible fresh water or 0.7% of all water on Earth, and provides more than half of all domestic and irrigation water used around the world (Fig. 1.1). In semi-arid and arid regions, and in domestic supplies for rural areas, 80–100% of all fresh water may be derived from groundwater.

In many parts of the world, groundwater levels are rapidly declining as groundwater withdrawal far exceeds natural recharge. Irrigated agriculture, particularly from groundwater, has been responsible for many of the strides made in self-sufficient food production in parts of Asia and has contributed to the ‘green revolution’ of the 1960s, resulting in greater food security. It is now estimated that more than half of the world’s food production is derived from irrigated agriculture. Owing to the extent that fossil or non-renewable groundwater is being used to increase food production, both the water supply and food production may potentially become unsustainable in the future. The United Nations’ Millennium Development Goals, adopted in 1999 by the governments of nearly 180 countries, and subsequent commitments, include the goal “to stop the unsustainable exploitation of water resources by developing water management strategies at the regional, national and local levels...”

Sustainable use and management of aquifers necessitates an understanding of aquifer hydrogeology and its dynamics. This understanding can be gained over a period of decades by observations and measurements of precipitation, river flows, groundwater levels, etc. Early developments in groundwater hydrology focused on means to estimate aquifer storativity and hydraulic conductivity, which led to the establishment of the theory of transient groundwater flow (Anderson (2008) [2]). Isotope techniques

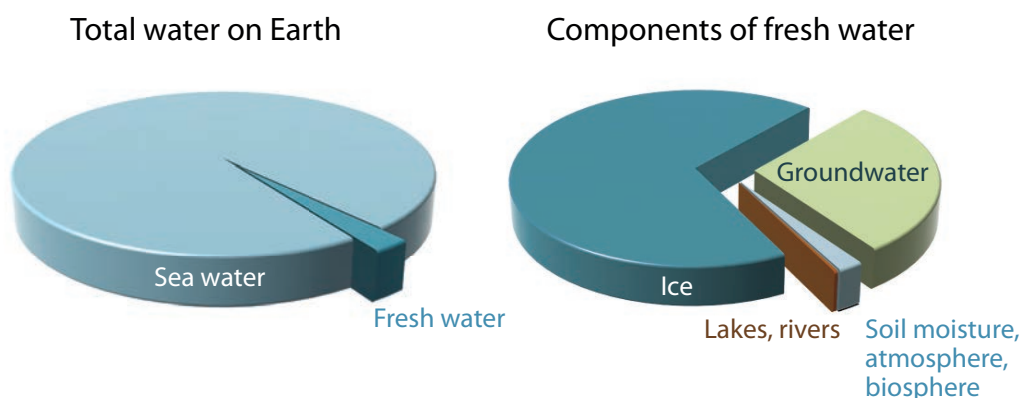


FIG. 1.1. Occurrence of water on Earth (based on data from Shiklomanov and Rodda (2004) [1]).

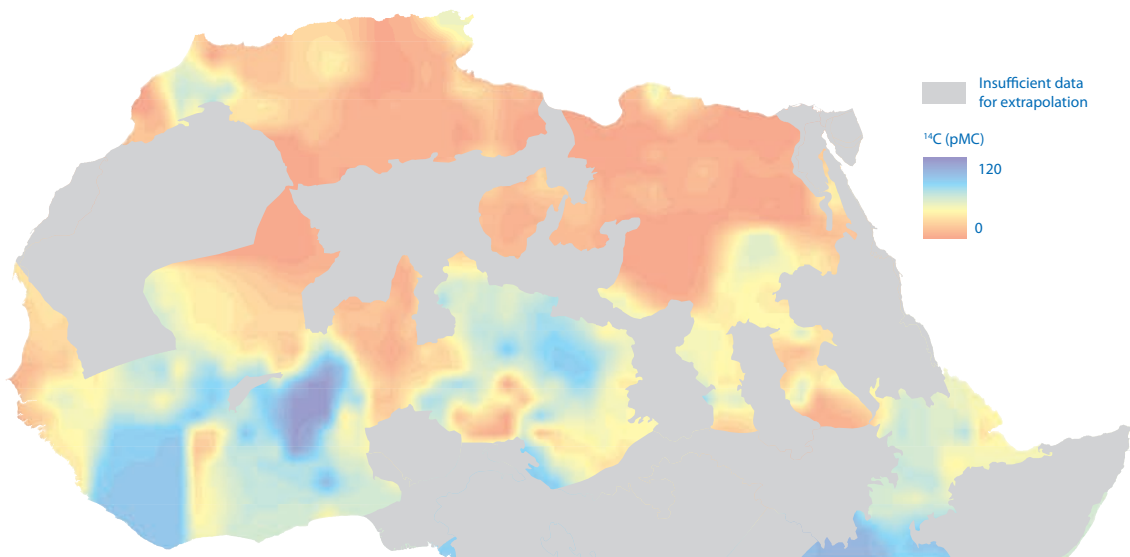


FIG. 1.2. Distribution of  $^{14}\text{C}$  in groundwater in northern Africa.

— and particularly those that can be applied to estimate the age of groundwater — help to cost effectively build a conceptual framework of aquifer hydrogeology and flow system. The use of groundwater age for estimating aquifer storage, the rate of groundwater renewal and flow velocity was conceived as early as the natural radioactivity of tritium and  $^{14}\text{C}$  was discovered more than sixty years ago (Aggarwal et al. (2012) [3]). Groundwater age also provides unmatched advantages for improving numerical models of groundwater flow in large, regional aquifers where water level data are normally scarce.

The age of groundwater ranges from less than a month to a million years, or perhaps more. Old groundwater — defined in this book as groundwater with estimated ages greater than about one thousand years — occurs in many African, Asian and Latin American aquifers as indicated by measured  $^{14}\text{C}$  activities (IAEA (2007) [4]). The Nubian Aquifer in northern Africa, for example, is estimated to contain groundwater that was recharged at various times over the past million years (Sturchio et al. (2004) [5]). Figure 1.2 shows the distribution of groundwater  $^{14}\text{C}$  in northern and central Africa. This groundwater is presently used for drinking and irrigation. With an increasing population and potential changes in the current climate, it will become an even more important resource for meeting the fresh water demands of the region. It is crucial to understand the nature of recharge and groundwater flow in past climates in order to better characterize the changes that may be induced under new climate regimes.

## 1.2. OBJECTIVES

This book aims to provide the reader with a comprehensive understanding of why groundwater age is an important parameter for characterizing aquifer hydrogeology, how to estimate groundwater ages using different isotopes and how best to use age data for the analysis of groundwater flow.

## 1.3. SCOPE

A number of isotopes can be used to interpret groundwater ages over a wide range of timescales. (Fig. 1.3). A need was identified to create a synthesis of various isotope methods to date old groundwater and to critically evaluate their advantages and disadvantages for use in hydrology. This book is intended to provide hydrogeologists with a guideline describing existing sampling and measurement methods, and to provide tools to ensure reliability of the resulting interpretation of isotope data. A ‘critical’ evaluation is intended to assess sampling efforts required in the field and to select possible cooperation partners

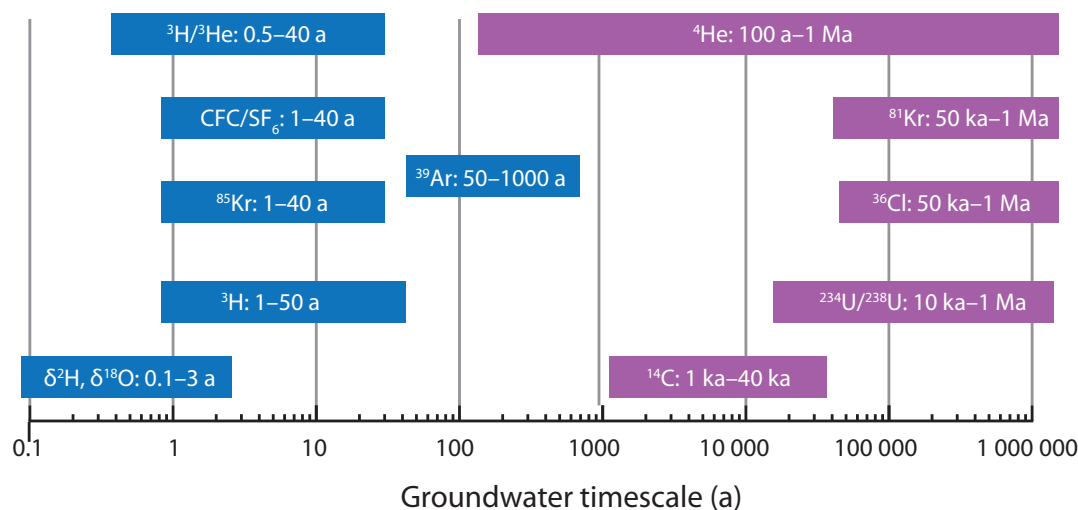


FIG. 1.3. Isotope and chemical tracers use for estimating groundwater age.

and assess the problems inherent to each method, as well as model assumptions which lead to water age results of 20 000 to 1 million years.

It is hoped that sufficient detail and examples have been provided to convey to the reader that obtaining meaningful hydrological information from groundwater age data requires careful planning and sampling, skilled measurements and a significant number of cross checks to evaluate various assumptions. It is to be cautioned that an age estimate based on a single isotope or tracer at a single location may not be very informative. Multiple estimates, based on more than one tracer and at multiple locations, particularly when combined with a numerical model sufficient to represent the flow regime of the groundwater system of interest, are necessary to meaningfully use groundwater age data.

#### 1.4. STRUCTURE

Chapter 2 describes fundamental concepts, data needs, and approaches that aid in developing a general understanding of groundwater systems. Chapter 3 discusses in detail the meaning of groundwater age in a physical hydrological system along with pitfalls to be avoided by misinterpreting or over-interpreting age data. The subsequent five chapters describe the basis for and use of various isotope methods for dating of old groundwater:  $^{14}\text{C}$ ,  $^{81}\text{Kr}$ ,  $^{36}\text{Cl}$ , uranium isotopes and  $^4\text{He}$ .

The use of multiple isotope tracers and its potential advantages over single tracers are discussed in Chapter 9. Chapter 10 outlines the methods for combining results of groundwater age determination with quantitative numerical models of groundwater flow and transport processes within an aquifer. Finally, a series of case studies on the use of groundwater ages to characterize large, regional aquifer systems is presented. These include the Milk River aquifer in Canada (Fröhlich), the Santa Fe Group aquifer system of the Middle Rio Grande Basin in the United States of America (Plummer et al.), the Eastern Great Artesian Basin in Australia (Torgersen) and the Nubian aquifer system in northern Africa (Sturchio and Purtschert).

A wide variety of readers involved in groundwater research or in the exploration, management, planning and utilization of groundwater resources may find this book useful. Those interested in the use of multiple tracers to determine and use groundwater age data may gain a better understanding of the subject by reading all of the chapters in the order they are presented. A reader new to the concepts of groundwater dating who wants a general overview of the topic may wish to first read Chapter 2 (characterization and conceptualization), a definition of the concepts of groundwater age used in this book (Chapter 3) followed by case studies (Chapters 11–14). Readers who are familiar with isotope

techniques in general and are in need of information related to a specific isotope may wish to go directly to Chapters 4–8. Hydrologists and modellers who may not be interested in the details of the tracer techniques but in the application of groundwater tracers may wish to begin with Chapters 2 and 3, followed by Chapters 9 and 10 (system analysis using multitracer approaches and groundwater models, respectively).

## Chapter 2

# CHARACTERIZATION AND CONCEPTUALIZATION OF GROUNDWATER FLOW SYSTEMS

L.N. PLUMMER, W.E. SANFORD, P.D. GLYNN  
United States Geological Survey,  
Reston, Virginia,  
United States of America

### 2.1. INTRODUCTION

This chapter discusses some of the fundamental concepts, data needs and approaches that aid in developing a general understanding of a groundwater system. Principles of the hydrological cycle are reviewed; the processes of recharge and discharge in aquifer systems; types of geological, hydrological and hydraulic data needed to describe the hydrogeological framework of an aquifer system; factors affecting the distribution of recharge to aquifers; and uses of groundwater chemistry, geochemical modelling, environmental tracers and age interpretations in groundwater studies. Together, these concepts and observations aid in developing a conceptualization of groundwater flow systems and provide input to the development of numerical models of a flow system. Conceptualization of the geology, hydrology, geochemistry, and hydrogeological and hydrochemical framework can be quite useful in planning, study design, guiding sampling campaigns, acquisition of new data and, ultimately, developing numerical models capable of assessing a wide variety of societal issues — for example, sustainability of groundwater resources in response to real or planned withdrawals from the system, CO<sub>2</sub> sequestration or other waste isolation issues (such as nuclear waste disposal).

Tracer model ages can often help improve understanding of groundwater flow. Once developed, numerical models of groundwater flow can be used to test derived age information for consistency with geologic, hydrological and geochemical data, and to estimate the modern and palaeorecharge rates of an aquifer.

As the topic of conceptualization and characterization of groundwater systems is broad and complex, the reader is referred to some of the many useful references in the hydrological literature where additional information can be found (see, for example, texts by Bear (1979) [6]; de Marsily (1986) [7]; Domenico and Schwartz (1998) [8]; Driscoll (1986) [9]; Fetter (2000) [10]; Freeze and Cherry (1979) [11]; Mazor (2004) [12]; Todd and Mays (2005) [13]). Other examples can be found in some of the reports of hydrological investigations in the literature (see, for example, Back et al. (1988) [14]; Glynn and Plummer (2005) [15]; Glynn and Voss (1999) [16]; Heath (1984) [17]; Miller (2000) [18]; Reilly et al. (2008) [19]; Sanford et al. (2006) [20]; Thorn et al. (1993) [21]), or in training documents and other general references of the United States Geological Survey (USGS) (Franke et al. (1993) [22]; Franke et al. (1990) [23]; Heath (1983) [24]; Reilly et al. (1987) [25]).

### 2.2. THE GROUNDWATER FLOW SYSTEM

Groundwater is an important water resource that is critical for survival in many parts of the world. Environmental and isotopic tracers have become an important tool in the evaluation of that resource. Groundwater is, however, also part of the Earth's hydrological cycle. Thus, to understand a groundwater system and what tracers can reveal about it, it is important to first have an understanding of the entire hydrological cycle and how groundwater interacts with other parts of the cycle.

### 2.2.1. Hydrological cycle

Water on Earth is stored mainly as salt water in the oceans, but the fresh water that is required for life is present in atmospheric water vapour, as ice, mainly in the polar regions, and as liquid water in lakes, rivers, the soil, in unconsolidated geological materials, and in the cracks and pore spaces in rocks underground (Table 2.1).

Water cycles through these reservoirs by falling as precipitation on the land surface, partially running off into lakes and streams, partially evaporating and transpiring from the soil back into the atmosphere, and partially infiltrating through the soil and recharging groundwater reservoirs (Fig. 2.1). Water percolates downwards through the soil zone, where the pore spaces are still partially air-filled, and eventually reaches the water table (defined as where water pressure equals atmospheric pressure), where the pore spaces are completely saturated with water. The groundwater system consists of the entire thickness of water filled unconsolidated sediment and/or rock beneath the water table; however, the degree to which water is stored and transmitted in different geological materials varies dramatically. Groundwater will migrate from areas of high elevation to discharge into streams at lower elevations. These streams carry the water back to the oceans, where it can evaporate and fall again as precipitation. Groundwater near the coast can discharge directly into the oceans in submarine springs or seeps. Water levels observed in wells reflect the energy of the groundwater that feeds them.

The availability of groundwater for use as a resource depends not only on the quantity and quality of water in residence at any given time, but also on the rate that water replenishes a groundwater aquifer (Healy et al. (2007) [27]). Dating of groundwater using environmental or isotopic tracers helps in estimating groundwater age and can help evaluate the rate at which the groundwater is replenished. Physical measurements of water fluxes in the hydrological cycle also provide direct estimates of groundwater replenishment or recharge rates.

Evapotranspiration, the combination of direct evaporation and transpiration by plants, consumes much water of the total precipitation that falls upon the land surface. In cold regions, this can be less than half of the total precipitation, but in temperate climates, it is usually about two thirds of the precipitation, and in arid climates evapotranspiration can account for all but a small percentage of precipitation. Evapotranspiration can be measured at the land surface, usually by means of an energy budget, but in many temperate watersheds it can also be estimated as the difference between

TABLE 2.1. GLOBAL WATER DISTRIBUTIONS ON EARTH (*after Mook (2000) [26]*)

Water source	Volume (10 <sup>3</sup> km <sup>3</sup> )	Per cent of total fresh water
<b>Salt water</b>		
Oceans	1 350 000	
<b>Fresh water</b>		
Ice	27 800	69.3
Groundwater	8000	29.9
Lakes	220	0.55
Soil moisture	70	0.18
Atmosphere	15.5	0.038
Reservoirs	5	0.013
Rivers	2	0.005
Biomass	2	0.005

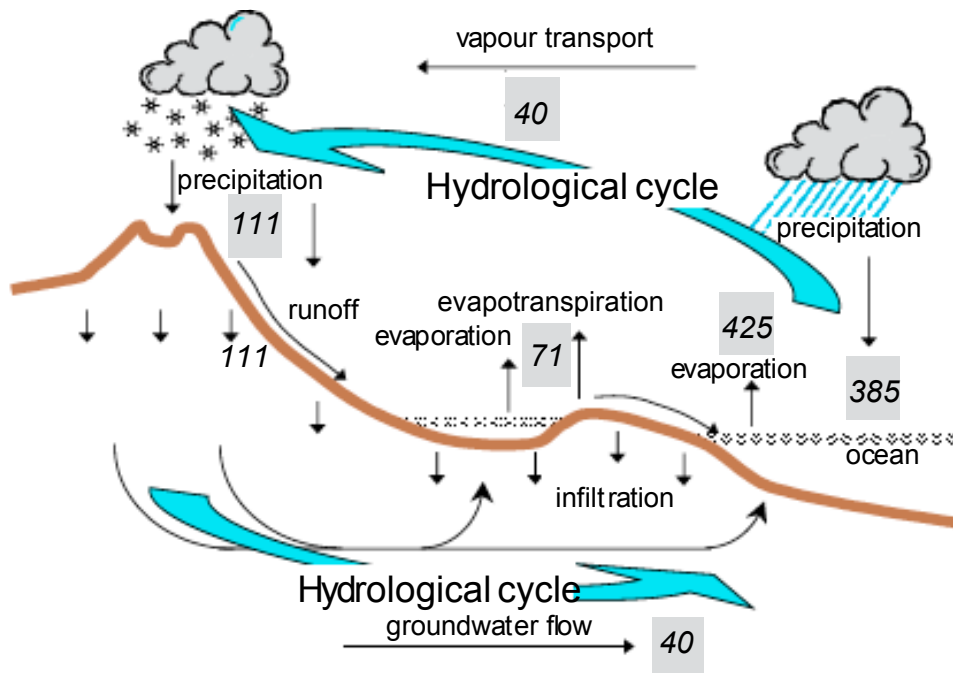


FIG. 2.1. The hydrological cycle. Numbers are annual water fluxes in  $10^3 \text{ km}^3$  per year (Mook (2000) [26]; see also: <http://ga.water.usgs.gov/edu/watercycle.html>).

the average amount of precipitation falling on the watershed and the average discharge into streams from that watershed. The average discharge from a stream represents the water that has either run off during rain events or seeped into the stream as baseflow. This approach works best when inflow and outflow of groundwater as underflow directly from or to an adjoining watershed can be assumed to be small. Baseflow measurement within a stream and the exchange of groundwater and surface water are an important and frequently used method for estimating fluxes within a groundwater system.

The porosity, or storage capacity, of rocks and unconsolidated sediments can vary from less than 1% for fractured rocks to greater than 50% for fine grained sediments. The permeability, or hydraulic conductivity, of rocks or unconsolidated sediment is a measurement of how easily they can transmit water, and this can vary between geological materials by many orders of magnitude (Freeze and Cherry (1979) [11]; Heath (1983) [24]). Rock types and/or unconsolidated sediments within the groundwater system of interest, therefore, have an enormous impact on its storage capacity, replenishment rate and capability to yield water to wells in substantial quantities. Thus, it is essential that a hydrogeological study be performed as thoroughly as resources permit to determine the nature and distribution of the rocks and/or unconsolidated sediments, and to estimate their hydraulic properties.

### 2.2.2. Timescales for recharge and discharge

Even within a groundwater system of a uniform rock type, the length of a flow path and the time of travel for water along that path can vary greatly. Rolling topography will itself create flow path variability within a system (Tóth (1963) [28]). Water that recharges near streams will stay within local, shallow flow systems and discharge within a few years to tens of years after recharge. Water that recharges further from streams will follow intermediate flow systems of moderate depth, and discharge hundreds to thousands of years after recharge. Water that recharges near topographic divides furthest from streams can take deep flow paths in regional flow systems that discharge after tens of thousands of years or longer after recharge (Fig. 2.2). Such recharge may have occurred during different climatic

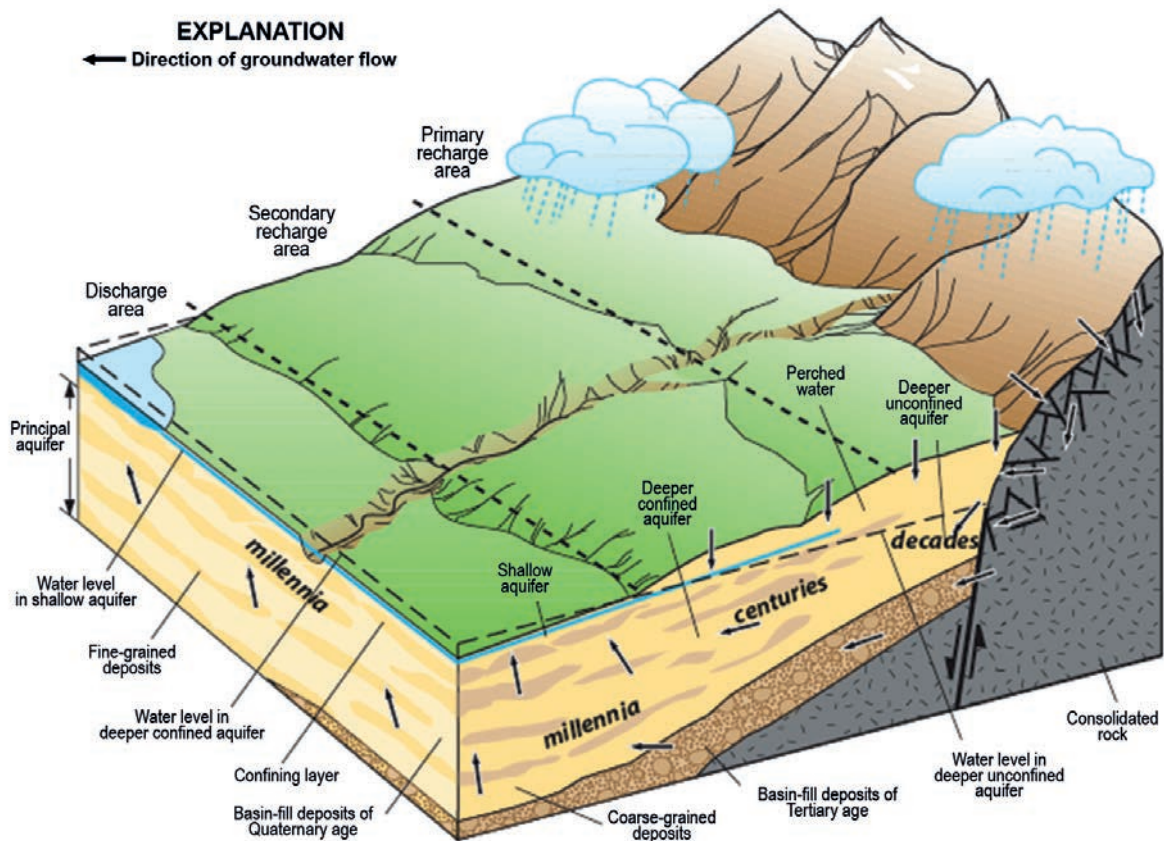


FIG. 2.2. Generalized block diagram showing conceptualization of groundwater recharge, discharge and groundwater age in a basin fill groundwater flow system (modified from Hely et al. (1971) [29]; Thiros (2000) [30]; not to scale).

conditions, such as during the most recent glacial cycle when precipitation and recharge rates were frequently higher than observed today in many locations.

## 2.3. CHARACTERIZATION OF GROUNDWATER FLOW SYSTEMS

In characterizing a groundwater flow system and developing a conceptualization of groundwater flow, three general classes of data are needed: geological, hydrological and geochemical.

### 2.3.1. Geological framework

One way of developing a geological framework of a groundwater flow system is to develop a three dimensional visualization describing its physical features. Basic features of a three dimensional geological description include characterization of thickness and lithology of rocks/sediment that compose the various geological units of the groundwater flow system and a description of geological structures. Some lithologic properties that need to be considered include effective porosity, permeability, mineralogy and their spatial and depth variations.

Mapping of faults, fracture systems, folds in rock and the orientation of these structures in relation to the direction of groundwater flow is critical in assessing the geological framework and controls on groundwater flow. Depending on their physical properties, geological structures, such as faults, can either enhance or retard groundwater flow. Regional variations in lithologic properties contribute to

aquifer heterogeneity. From the standpoint of interpreting environmental tracer data, it is important to have a good understanding of aquifer heterogeneity, such as low permeability zones, confining layers or highly fractured domains, because they can act as sources or sinks for some of the environmental tracers used for age estimation.

The environmental tracers considered in this book can be affected variously by interactions with confining layers, diffusion into or from low permeability zones, convergence/divergence of flow paths, in situ production through nuclear reactions and, in some cases, geochemical interaction with the minerals of the aquifer matrix or those in low permeability zones. Therefore, information on aquifer heterogeneity is essential when interpreting environmental tracer data in 'old' (as used in this book, 'old' is defined as generally greater than 1000 a) groundwater.

There are a number of geophysical techniques that can be used to characterize aquifer heterogeneity (see, for example, <http://water.usgs.gov/ogw/bgas/g2t.html>). However, there is never enough geophysical information from boreholes, well logs, cores or cuttings to completely describe aquifer heterogeneity throughout a system. Surface geophysical techniques (such as seismic surveys) and even remote sensing techniques (such as InSAR: <http://quake.usgs.gov/research/deformation/modelling/InSAR/index.html>) are also very useful in constructing a conceptual description of the hydrogeological framework.

Geological mapping and construction of geological cross-sections of a groundwater flow system improve understanding of the spatial distribution of structural features, lithologic facies changes and, generally, the consequent spatial variations in hydraulic conductivity and mineralogy, as well as their heterogeneous distribution through the groundwater system being studied. Sedimentary basin modelling, stratigraphic modelling and structural modelling are some of the types of geological evolution simulation modelling now being used more frequently by hydrogeologists to describe the evolution of aquifer units after development by the oil and gas industry. Sedimentary basin modelling has also been used to understand the transport and fate of pore fluids and the palaeohydrology of sedimentary basins (Bethke (1985) [31]).

### **2.3.2. Hydrological framework**

Essential information in construction of a hydrological framework includes land–surface elevation, locations of rivers and other drainage, areal distribution of precipitation, delineation of recharge and discharge areas, determination of a water balance for the groundwater flow system, mapping of the altitude of the potentiometric surfaces of the aquifers, and characterization of regional variability in the hydraulic properties of a groundwater flow system. The hydrological framework of a groundwater flow system can be visualized in maps of the potentiometric surface of aquifers, in cross-sections showing the relation of groundwater flow to the geological framework, and ultimately through a numerical model capable of simulating groundwater flow.

#### *2.3.2.1. Water levels*

Darcy's law states that groundwater flux is directly proportional to the gradient in the hydraulic head, or water level, and the hydraulic conductivity of the porous media (rock or sediment). Hydraulic gradients can be determined from contours drawn on maps defining lines of equal head depicting historical (pre-development, i.e. pre-pumping) water levels in unconfined aquifers or from water levels in piezometers in confined aquifers (see, for example, Bexfield (2002) [32]). Groundwater generally flows down the hydraulic gradient in directions normal to the lines of equal head. In confined aquifers, the hydraulic gradient is determined by mapping water levels in wells open to the aquifer of interest. Given the nature of aquifer heterogeneity and the fact that different wells can be open to different depths and different screened intervals within an aquifer, the mapped potentiometric surface is usually more

appropriately applied to regional flow characteristics than to local scale flow conditions. Information on well construction is critical in identifying wells that are only open to the aquifer of interest when mapping the potentiometric surface of a specific aquifer.

Thus, if the water levels are measured in a large number of wells in a groundwater system, it is possible to get an indication of the direction of water movement and the relative hydraulic conductivities of different parts of a geological framework. By combining water level measurements with estimated recharge rates, groundwater fluxes within a system can be calculated. As water takes the path of least resistance, it will preferentially follow more permeable layers or fracture zones. For this reason, it is often useful to have clusters, or nests, of wells at the same location that have screens open at different depths. In discharge areas, the water levels in deeper wells will be above the levels existing in shallower wells. Where layers or regions of low permeability exist, steep head gradients may also exist. In layered systems of alternating high and low permeability, flow in the former tends to be mostly horizontal, whereas flow in the latter tends to be mostly vertical. Water levels at and near points of groundwater extraction will decrease in proportion to the amount of water extracted.

A network of wells for the purpose of measuring water levels and collecting samples for analysis of environmental tracers is a basic and essential part of any groundwater investigation. Usually, such a network is assembled from existing wells open to the aquifer of interest. Essential data include well location and total depth, depth and length of the interval open to the aquifer, land surface elevation, and recognition of wells that may be open to multiple aquifers or to multiple depths within the aquifer of interest. Well construction information should be examined in relation to the geological framework to determine whether the water is derived from the aquifer of interest.

The drilling of additional wells can be very beneficial if the new wells are located where information is needed. A retrospective compilation of hydraulic data for existing wells and springs can help identify areas that should be targeted for further study. Attention should also be paid to the length of the well screen or open interval. Often, wells in fractured rock terrain or wells that are used for water extraction are open over relatively large aquifer thicknesses to maximize well yield. This reduces the usefulness of a well in interpreting water levels and environmental tracers as both types of observations are integrated vertically and, thus, cannot provide information on vertical segregation of water in the system.

A better choice for observation wells is to have a short screened interval, and to have multiple such wells at a single location; this applies to both water level and tracer measurements. In shallow water table aquifers, transient changes in water levels often occur seasonally for wells screened near the water table, with higher water levels occurring in the winter and spring when evapotranspiration is low and recharge high. It may be necessary to monitor such water levels for several seasons in order to obtain an average water level that is useful for conceptualizing a regional average flow system.

#### 2.3.2.2. *Hydraulic properties*

As mentioned previously, the type and distribution of rocks and unconsolidated sediments within a groundwater system can be a major factor affecting the rate and movement direction of water. The hydraulic conductivity of rocks and sediment can vary by more than 12 orders of magnitude. This can lead to differences of several orders of magnitude in fluxes and hydraulic gradients that are established within natural flow systems. Rock types with the highest hydraulic conductivity include karstified limestones and some volcanic rocks. Rock types with the lowest hydraulic conductivity include crystalline rocks, some fractured rocks and well-lithified sedimentary rocks, especially shales and other argillaceous lithologies. However, local zones or fractures within such rocks can be relatively permeable. Unconsolidated sediments can vary widely in their permeability, which usually correlates with sediment grain size, grain sorting and depth of burial. Gravels are extremely permeable, whereas clays typically have low permeability. Well sorted sediments will be more permeable than their poorly sorted equivalents, and burial tends to compact the sediments, decreasing both their porosity and their permeability.

The hydraulic properties of rocks or sediment can often be measured in situ. Measurements of hydraulic conductivity can also be made on core samples in the laboratory, but these small scale measurements usually have a low bias because they do not incorporate the larger scale features such as fractures or bedding. The hydraulic conductivity or transmissivity of an aquifer (its hydraulic conductivity multiplied by its thickness) is frequently measured using an aquifer test. The simplest form of these is a slug test, where a known volume of water is added or withdrawn quickly, and the water level is measured over time as it returns to its original level (Ferris et al. (1962) [33]; Kruseman and de Ridder (1990) [34]; Shuter and Teasdale (1989) [35]). Although slug tests are easy to perform, they often do not work well in highly permeable material (the water level equilibrates very quickly), and the measurement is only influenced by a limited volume of rock or sediment very near the well. A frequent alternative to simple slug tests is more complete aquifer tests, where water is extracted from a well at a constant rate over a period of time, usually at least 1–2 days. Water levels are observed throughout such a test, preferably at a well that is located some distance from an extraction well. This type of test is influenced by a much larger volume of the aquifer than a slug test, so may provide a value that is more reflective of a regional average.

Aquifer storage is also obtainable through an aquifer test, although with a little less accuracy than the transmissivity. In unconfined aquifers, a specific yield represents the volume of water released from storage from a unit area of the studied aquifer per unit decline in the water table. In bedrock aquifers, the storage term is related to compressibility of the rock matrix, which releases water as it undergoes a drop in fluid pressure. This causes a reduction in porosity as the matrix is compressed under the weight of the overburden.

#### 2.3.2.3. *Recharge amount and distribution*

In spite of the wide range of hydraulic properties associated with various rock types, the recharge rate frequently controls how quickly groundwater is replenished. This is especially true in areas of either moderate to high topographic relief and/or areas that are semi-arid to arid. In arid regions, groundwater recharge is one of the most critical water balance components because of the difficulties in its measurement. Much research has been performed to develop various techniques for measuring recharge directly in the field (de Vries and Simmers (2002) [36]; Scanlon et al. (2002) [37]), but many of these techniques are limited by the fact that they make measurements only over small areas or small time periods, or both. Conventional techniques for estimating recharge rate are based on water balance equations that include hydrometeorological (precipitation–evapotranspiration) and geohydrological (groundwater level changes) parameters. In these equations, recharge is determined as the difference between other balance quantities that are directly measurable. The uncertainty in the measurement of these quantities determines the uncertainty of the recharge rate. If recharge is high, such as in humid regions (10 to more than 100 cm/a), its uncertainty is relatively low. However, in semi-arid and arid areas with recharge rates from virtually 0 to less than 100 mm/a, the uncertainties of measured balance parameters cause very high uncertainty in the estimated recharge rate. Thus, the very approximate nature of these groundwater balance estimations prompts chemical and isotopic studies to independently assess recharge rates. Especially for drier regions, geochemical and isotopic profiling in the unsaturated and shallow groundwater zone is more reliable and accurate than water balance methods and, thus, is practically indispensable for groundwater resource assessments. Geochemical and isotopic tools for recharge rate determination include Cl, chlorofluorocarbons (CFCs),  $^3\text{H}$ ,  $^3\text{H}/^3\text{He}$  and  $^{14}\text{C}$ . For groundwater systems with low or even negligible present day recharge,  $^{14}\text{C}$  is one of the most suitable tools.

It is usually not known to what extent modern recharge rates can be applied in estimating palaeorecharge rates. Still, it is important to determine modern recharge rates to provide a benchmark for comparison to palaeorecharge rates once they are derived from groundwater age information and the application of models to the flow system. For a regional groundwater assessment, long term and

spatially averaged recharge rates are usually needed. Local measurements must either be scaled up, or other methods used that integrate larger spatial and timescales. Measurement of baseflow in streams was mentioned earlier as one such approach that can work fairly well in temperate or humid climates, where recharge is often fairly evenly distributed with precipitation.

In semi-arid to arid regions, the distribution of recharge is usually quite heterogeneous, occurring mainly in the mountains or along mountain fronts or ephemeral streams during intermittent runoff events. Local measurement techniques can be useful in areas of focused recharge. In broad areas between mountain ranges or away from streams, recharge can be nearly zero or essentially zero, as can be determined by the accumulation of solute tracers within the unsaturated zone which occurs through continued conditions where evaporation removes the water but not the solutes. The chloride-mass balance technique (Wood and Sanford (1995) [38]) is one method that has proven useful under such conditions.

In humid regions, shallow flow systems usually contain young groundwater. If 'old' groundwater exists today in humid regions, it usually is at sufficient depth or beneath sufficient hydraulic confinement that it is isolated from the active flow system. If of meteoric origin, 'old' groundwater was initially recharged at the land surface, perhaps in outcrop areas along basin margins, or along outcrops at mountain fronts or in outcrops of coastal, wedge shaped aquifers. Subsequent flow has permitted a fraction of this water to reach depths where it is sufficiently isolated from the active flow system on timescales of thousands to more than millions of years. Most aquifers are 'leaky' to some extent and eventually flow to an area of discharge. 'Old' groundwater is found in deep sedimentary basins, usually beneath sequences of confining layers (see, for example, Phillips et al. (1989) [39]), in coastal aquifers beneath confining layers (Aeschbach-Hertig et al. (2002) [40]; Castro et al. (2007) [41]; Stute et al. (1992) [42]), or in arid regions where modern recharge is insufficient to replace the 'old' water or does so only very slowly (Patterson et al. (2005) [43]; Sturchio et al. (2004) [5]).

Aquifers in arid regions today may have been recharged predominantly during pluvial (wet) climatic periods in the past, and today, 'old' water persists due to low recharge rates that are insufficient to flush the groundwater flow system. In some cases, a temporal understanding of changes in areal recharge conditions may be gained from information on the past distribution of vegetation in an area or from other information on the relative pluviosity/aridity in an area. Palaeobotanical studies of pollen or relict vegetation distribution in soils and lake sediment might be useful in this context. Examples of other measures of pluviosity/aridity include tree ring reconstructions; determination of sedimentation rates in varve sequences; radiocarbon dating of palaeolake levels; records of chloride, nitrate and other atmospherically derived solutes in unsaturated zones (Walvoord et al. (2002) [44]) and archaeological evidence of past population migrations in water stressed regions.

In spite of the techniques that are available to directly measure recharge at the land surface, environmental tracers often prove to be the best tools for constraining estimates of long term and spatially averaged recharge rates.

### **2.3.3. Hydrochemical framework**

Data on the concentrations of dissolved solutes, gases and isotopes can provide information about the local area from which they were recharged and can be used to trace groundwater flow on the timescale of the groundwater flow system. Geochemical data can be used to delineate zones of leakage through confining layers, interpret flow in relation to faults and other geological or hydraulic properties of an aquifer, and estimate travel times in groundwater systems. Dissolved gases and stable isotope data ( $^2\text{H}$  and  $^{18}\text{O}$  of groundwater) can be used to recognize palaeowaters and interpret palaeoclimatic recharge conditions. Owing to their different timescales for introduction into aquifers, some environmental tracers can be used to help recognize recharge and discharge areas. Estimates of tracer model age can help to quantify recharge rates.

As part of the well and spring inventory process, all available chemical and isotopic data on water from the aquifer should be compiled, plotted on maps and contoured with respect to a known depth interval. Where available, chemical and environmental tracer data should be plotted as a function of depth in an aquifer. For example, areas of recharge or upward leakage can sometimes be recognized on maps of  $\text{Cl}^-$  concentration in groundwater or from plots of  $\text{Cl}^-$  as a function of depth. In unconfined aquifers, data are typically plotted at mid-depth below the water table of the open interval of a well (see Chapter 12). In some cases, gradients in environmental tracer concentration (and tracer model age) can be used to estimate recharge rate. This analysis will aid in recognition of recharge and discharge areas, defining directions of groundwater flow (see below), identifying areas that should be targeted for additional investigation, and may also provide an assessment of past climatic and environmental changes and palaeorecharge information.

### 2.3.3.1. *Hydrochemical facies — relation of chemistry to groundwater flow*

Although the shape of the pre-development potentiometric surface can define recent groundwater flow direction, maps of the potentiometric surface are not available on timescales of interest, such as during the last glacial maximum (LGM). Consequently, maps of the pre-development potentiometric surface may not exactly apply to interpreting palaeogroundwater flow conditions. Still, the shape of the pre-development potentiometric surface usually represents the predominant features of the palaeoflow system. An alternative approach to interpreting palaeoflow directions is to map spatial patterns in water chemistry and isotopic composition that can indicate past directions of groundwater flow.

Geochemical reactions along groundwater flow paths can lead to regional variations in water composition that evolve in the direction of flow. Iso-concentration contours of reacting dissolved constituents drawn on maps of water composition tend to align to the direction of groundwater flow. Glynn and Plummer (2005) [15], Back (1960) [45] and Back (1966) [46] defined the hydrochemical facies concept, placing geochemical observations in the context of groundwater flow in aquifers of relatively homogeneous hydrological and mineralogical properties.

In contrast, it is sometimes possible to distinguish different sources of water to the groundwater flow system on the basis of inert chemical or isotopic constituents (such as  $\text{Cl}^-$ ;  $\text{Br}^-$ ; dissolved noble gases and dissolved  $\text{N}_2$ ;  $^{18}\text{O}$  and  $^2\text{H}$  in water; and sometimes  $\text{Na}^+$ ,  $\text{Li}^+$  and other chemical and isotopic constituents). In cases where inert tracer concentrations vary spatially along the groundwater recharge area, the path followed by a tracer delineates flow direction (Glynn and Plummer (2005) [15]). In this case, hydrochemical facies (sometimes referred to as ‘hydrochemical zones’) will align parallel to the flow direction. In more complex cases, the concentration of reactive constituents may vary spatially and temporally along a recharge area, and may also evolve along the direction of flow.

Non-reactive constituents, salinity and reactive constituents that reflect the minerals and geochemical conditions encountered at the time of recharge and in the later geochemical evolution of the groundwater can also provide information on the geological area of recharge and on the geological units traversed by groundwater to their point of sampling. Knowledge of the source and geochemical evolution of the groundwater will be essential in interpreting and adjusting tracer model ages obtained through various dating techniques discussed in this book (such as  $^{14}\text{C}$  and  $^4\text{He}$ ). Together with improved/adjusted estimates of groundwater ages, characterization of different groundwater geochemical facies in the groundwater system may also be used, as is done, for example, by Sanford et al. (2004) [47] and Sanford et al. (2004) [48] for the Middle Rio Grande Basin to calibrate groundwater flow models (and/or eventually fully coupled reactive transport models).

Extracting flow and hydrological information from geochemical observations requires understanding the aqueous reactivity of aquifer materials and the spatial and temporal distribution of recharge compositions. Many of the geochemical patterns observed in groundwater systems can also be

related to heterogeneities in either reactive mineral abundances or in hydrological properties, and may be difficult to resolve, given the limited information typically available.

Flow patterns in regional aquifers, deduced from mapping hydrochemical facies and zones, can indicate flow directions that have occurred over timescales considerably greater than the timescale over which present day or even pre-development water levels were established. Differences between regional flow directions deduced from hydrochemical patterns and those indicated by a modern (pre-development) potentiometric surface can indicate changes in hydraulic conditions (such as recharge rate) on a shorter, more recent timescale than those responsible for hydrochemical observations (Plummer et al. (2004) [49]; Plummer et al. (2004) [50]; Plummer et al. (2004) [51]; Sanford et al. (2004) [47]; Sanford et al. (2004) [48]).

Especially in arid areas, groundwater within a regional groundwater flow system may have a number of possible source areas that include various nearby streams, mountain fronts or inflow from other basins. The solute or isotopic character of the water can give clues as to the source area. The study in the Middle Rio Grande Basin of New Mexico, USA (Chapter 12), is an example of how solutes can be used to determine the source of the water, and in turn help elucidate flow paths and the nature of a groundwater flow system.

### 2.3.3.2. *Environmental tracers, hydrochemistry and timescales*

Many different solutes and isotopes that recharge with water into a groundwater system provide information on the time since recharge, either because they decay at a known rate, accumulate in an aquifer from in situ processes, or because their concentration in precipitation has changed at a known rate over time (Clark and Fritz (1997) [52]; Cook and Herczeg (1999) [53]). The range in groundwater ages that is reflected in the tracers can vary from a few years to tens or hundreds of thousands of years, to millions of years (Chapter 1). The latter is the focus of this book, with examples given of the various tracers and various field examples. A tracer model age (see Chapter 3) of a sample of water from a well can be combined with the known hydraulic properties of the hydrogeological framework to back-calculate the recharge rate that would be required to yield the interpreted tracer model age. For ‘old’ groundwater, this may yield recharge rates that are not consistent with modern estimated rates, but that may be consistent with rates that would be expected during earlier and different climatic conditions. In this sense, some tracers can serve as a repository of information on past climatic conditions. The combined measurement of tracer model ages along presumed hydrological flow paths and in vertical profiles in aquifers can be even more useful in estimating travel times and palaeorecharge rates in aquifers.

There are a few chemical and isotopic indicators that can be used in recognizing ‘old’ groundwater — at least, it may be possible to recognize water from the LGM, about 22 ka calendar years before present (BP). Dissolved gases and the  $^{18}\text{O}$  and  $^2\text{H}$  isotopic composition of water may be used to estimate elevation and temperature at the time of recharge, and the intensity of recharge (by determining excess air entrapment) for given water samples. The relationship between  $^{18}\text{O}$  and  $^2\text{H}$  is also useful in determining recharge characteristics, including the extent to which infiltrating groundwater may have been exposed to evaporation. Examples of using noble gas recharge temperatures or recharge temperatures determined from measurements of dissolved nitrogen and argon in groundwater in identifying waters recharged during colder climatic conditions are found in Stute and Schlosser (1993) [54], Aeschbach-Hertig et al. (2000) [55] and Heaton et al. (1983) [56]. Consistently, an average cooling of about  $5^\circ\text{C}$  is observed at the LGM globally, though Aeschbach-Hertig et al. (2002) [40] found cooling of nearly  $9^\circ\text{C}$  in New Jersey, USA near the last glacial ice margin. Shifts in the stable isotopic composition of groundwater at the LGM to more depleted values are often observed and attributed to lower condensation temperatures (Dansgaard (1964) [57]; Rozanski et al. (1993) [58]; Straaten and Mook (1983) [59]) and changes in moisture source. However, in some coastal aquifers, the isotopic shift is towards enrichment at

the LGM, due in part to enrichment of the stable isotopic composition of ocean water (ice-volume effect) and changes in moisture source (Plummer (1993) [60]).

Groundwater recharged during the last glacial period is generally regarded as non-renewable on human civilization timescales. That is, once withdrawn from aquifers, natural recharge processes are not sufficient to replace the water on timescales of thousands of years. Recognizing non-renewable groundwater resources is critical to managing water supplies for future generations. Similarly, very 'old' groundwater, water recharged on the hundred thousand to million year timescale, is fossil water and equally non-renewable. Its identification is equally critical in guiding future management decisions and the need to locate other water resources, including those that may provide sustainable water supplies for the future (Alley et al. (1999) [61]) or act as waste containment barriers.

### 2.3.3.3. *Obtaining representative samples from wells*

One of the most difficult problems in groundwater hydrochemistry is obtaining samples that are representative of unaltered formation water. Part of the problem is that due to well construction or the physical properties of spring sources, almost all samples are mixtures, combining all of the flowlines reaching a well screen or discharge point. In some cases, water reaching the open interval of a well or discharging at a spring may be nearly uniform in age, but, in general, it is usually necessary to assume that discharge from wells and springs consists of different components with varying ages, i.e. consists of a frequency distribution of age (see Chapter 3). Such mixtures can occur naturally in an aquifer as a result of aquifer heterogeneity, but are also created through the sampling process. In the case of wells with large open intervals to an aquifer, the discharge is a mixture of all of the flowlines drawn into the open interval of a well. In the case of springs, the discharge also typically represents a frequency distribution of age. In both cases, the tracer model age is a mixed age and needs to be evaluated in terms of the frequency distribution of age in discharge from a well or spring (see Chapter 3).

Another problem in obtaining representative samples from wells is caused by the introduction of tracers of interest into a formation during the well construction process. All drilling operations potentially introduce atmospheric components into an aquifer. Well development procedures may not adequately remove these components and, without special precautions in the drilling process, there is normally not any way to determine whether formation water contains trace contamination from drilling processes. When sampling water from wells with the intent of estimating the tracer based model age of 'old' groundwater from measurements of environmental tracer concentrations, as discussed in this book, additional samples should be collected for analysis of components that can be indicators of the introduction of contamination from drilling processes. Some useful indicators of contamination from young sources include tritium,  $^{85}\text{Kr}$  and CFCs. Owing to their extremely low detection limit, CFCs can be ideal tracers of drilling contamination (Plummer et al. (2004) [49]). In some cases, the driller may have imported treated water from municipal supplies for use in drilling and well development. Chlorinated water from municipal supplies may contain chloroform, which can be detected at extremely low concentrations using purge and trap gas chromatography with an electron capture detector (Plummer et al. (2008) [62]). If new wells are constructed, it is recommended that gas tracers be introduced into the drilling mud, such as halon-1211, sulphur hexafluoride or CFCs. Air rotary drilling procedures are not recommended because they introduce atmospheric gases into an aquifer. If jetting is used in well development, which consists of injecting high pressure air into the casing, the air injection should be far enough above the open interval of the well so as not to inject air into the formation.

Springs probably are the least desirable sources for sampling 'old' groundwater because their discharge can represent a mixture of many waters of generally unknown origin (and age). Though the discharge of some springs may contain predominantly 'old' water, it is common to find fractions of tritium or CFCs, indicating a mixture. Not knowing the frequency distribution of age in a mixture or water source limits the usefulness of springs for groundwater dating purposes. Flowing wells that are open to a narrow interval of confined aquifers at a known depth are probably the most useful for

sampling 'old' groundwater, particularly if a well has been in use for many years. An example of this is provided by the sampling of the Nubian sandstone aquifer in Egypt (Patterson et al. (2005) [43]) for  $^{81}\text{Kr}$  (see Chapter 14). Production wells with turbine pumps or pumps with impellers may promote cavitation and gas phase separation, leading to uncertainty in tracer model age interpretation based on gaseous environmental tracers. One technique that has been used successfully is to place a relatively low capacity piston sampling pump at depth within or just above the well opening and a second higher capacity pump at a relatively shallow depth to maintain a fresh supply of formation water entering the well bore in the vicinity of the sampling pump.

## 2.4. DEVELOPMENT OF A NUMERICAL GROUNDWATER FLOW MODEL

There are a number of approaches hydrologists have taken in developing numerical models of groundwater flow, including relatively simple analytical solutions (see, for example, Genuchten and Alves (1982) [63]); lumped parameter models (see, for example, Małoszewski et al. (1983) [64]; Małoszewski and Zuber (1996) [65]); and finite difference and finite element models that can solve the partial differential equations of groundwater flow and solute transport in three dimensions (see, for example, Huyakorn and Pinder (1983) [66]; Konikow and Glynn (2005) [67]; Wang and Anderson (1982) [68]).

In many studies of groundwater systems, a numerical model is constructed that represents the hydrogeological framework. Although many simplifying assumptions are ultimately made when constructing such a model, it is usually best to combine all of the information and data gathered on a system in a fashion that forces interpretation to follow the principles and observations of solute chemistry and the physics of groundwater flow. A model can often yield results that are not conceptually intuitive, or various versions of the framework can be tested to eliminate certain hypotheses. Once constructed and calibrated to the hydrologist's satisfaction, a model can also be used to predict system behaviour when there are changes in outside stresses (increased pumping or reduced recharge, for example).

Models are constructed using computer software which solves the groundwater flow equation and allows users to assign hydraulic parameters to a hydrogeological framework (see Chapter 10). The framework can be recreated numerically to follow the degree of accuracy with which a system can be described in the field. Boundary conditions must also be assigned; these usually represent impermeable boundaries at the base of a model and the amount and distribution of land surface recharge. Equations are solved to provide a three dimensional distribution of hydraulic head (water levels) within a groundwater system. From these head maps, three dimensional velocity distributions can be calculated. The hydraulic parameters assigned can be adjusted to better fit simulated water levels in a system with those which are observed. From the velocity fields, the equation for advection and dispersion of a solute can be solved. Tracer model age can be substituted as a solute in the transport equation to provide the flow model age throughout the system (Goode (1996) [69]). Flowlines can be tracked throughout a model to determine source areas for water within various parts of a system. The simulated flow model ages and water sources can then be compared with observed tracer model ages and the model can be adjusted or calibrated, to better agree with observed data. As water level and environmental tracer data are independent, the use of both types of information creates the opportunity to obtain a model that more closely reflects the real system under study.

The MODFLOW code (Harbaugh et al. (2000) [70]; McDonald and Harbaugh (1988) [71]; Reilly (2001) [72]) is one of the most widely used computer codes for development of groundwater models of groundwater flow systems. Particle tracking calculations derived from the pathline programme, MODPATH (Pollock (1989) [73]), provide a means of simulating travel times in groundwater systems and of estimating the frequency distribution of age in discharge from wells. Inverse modelling capabilities, such as those obtained from the application of UCODE (Poeter and Hill (1998) [74]) to MODFLOW–MODPATH calculations, permit refinement of the groundwater model utilizing

environmental tracer data. MODFLOW and an integrated family of compatible codes is freely available from the USGS (<http://water.usgs.gov/nrp/gwsoftware/modflow.html>). Sanford (Chapter 10) discusses construction of groundwater models and applications of groundwater models in interpreting environmental tracer data.

Development of a numerical simulation model of groundwater flow in an aquifer system is an evolving process that utilizes the hydrogeological framework established for a groundwater system and can be refined as new hydrological, geological and environmental-tracer concentration data become available.

## 2.5. SUMMARY GUIDELINES FOR THE CHARACTERIZATION OF GROUNDWATER SYSTEMS AND THEIR FREQUENCY DISTRIBUTIONS OF AGE

Dating old water in a groundwater system requires a contextual understanding of the system, its geological structure, past and present hydrological conditions, and the geochemistry and geochemical evolution of its waters. Funding limitations, temporal constraints, aquifer heterogeneity and limits on describing that heterogeneity will determine the extent of contextual understanding that can be reached. There will always be a threshold beyond which uncertainties in model age and frequency distribution in age cannot be reduced. A water resources manager or scientist trying to describe a groundwater system and understand its frequency distribution of age has the responsibility to incorporate as much information as possible, from a wide variety of sources, into a conceptual framework.

In a first step, a methodical approach might seek to obtain the following information needed to characterize a groundwater system:

- (a) Characterize the geological framework, the geological structure and geological properties of the groundwater system:
  - (i) Determine the spatial distribution of strata or other geological units;
  - (ii) Determine the distribution of faults, fractures, folds and their geophysical properties;
  - (iii) Determine the porosity and mineralogy of the various geological units, and their boundaries (faults, soil and bedrock);
  - (iv) Determine the spatial extent of aquifer heterogeneity, locating areas in which variations in lithologic properties would affect the hydraulic properties of porosity, permeability, transmissivity and storage in aquifers;
  - (v) Construct visualizations (geological maps, geological cross-sections, three dimensional descriptions of stratigraphy and lithology) of the geological framework.
- (b) Characterize the hydrological framework, and the distribution of past and present hydrological conditions:
  - (i) Determine the distribution of water levels in wells, including their distribution in space and changes over time that reflect seasonal fluctuations and drawdowns from nearby extraction wells;
  - (ii) Determine the position of perennial and intermittent streams across the system, and long term average flows or baseflows in those streams;
  - (iii) Determine the distribution of areal recharge into the system or, more specifically, the distribution of precipitation, and develop an understanding of the evapotranspiration processes, surficial geology and geomorphology limiting or focusing groundwater infiltration;
  - (iv) Assess the spatial distribution of hydraulic permeabilities and storativities associated with various geological units in the system;
  - (v) Assess the potential for groundwater leakage into aquifers of interest and assess lateral flows into, or out of, the groundwater system.
- (c) Characterize the hydrochemical framework, geochemical patterns, environmental tracers, and geochemical evolution of the waters in time and space:

- (i) Determine the spatial (vertical and horizontal) distribution of, usually, non-reactive constituents (or of constituents unlikely to leave the water phase through precipitation, sorption or degassing), to infer directions of groundwater flow;
  - (ii) Determine the spatial (vertical and horizontal) distribution of selected environmental tracers to delineate hydraulic properties of the groundwater flow system: recharge areas, discharge areas, groundwater flow paths, leakage and/or cross-formational flow, groundwater/surface water interaction, mixing and frequency distribution of age in discharge from wells and springs, and extent of evaporation (evapotranspiration);
  - (iii) Determine the spatial (vertical and horizontal) distribution of concentrations of environmental tracers, stable isotopes and dissolved gases to delineate temporal aspects of the groundwater flow system: tracer model ages, travel times, recharge rates, recharge temperatures, excess air entrapment, climatic variations in the stable isotope composition of groundwater; Determine the spatial (vertical and horizontal) distribution of both reactive and non-reactive constituents to determine through inverse and forward geochemical modelling: the extent of various water–rock reactions, the extent of mixing and other hydrochemical processes affecting solute composition and geochemical adjustments of  $^{14}\text{C}$  model ages.
- (d) Develop a conceptual description of the groundwater flow system utilizing all geological, hydrological and geochemical data. Where is the aquifer recharged? Where does the aquifer discharge? Is leakage to/from other aquifers important? How do aquitards affect groundwater storage, flow and solute transport? How does flow vary with depth? What is the spatial distribution of tracer model ages? What are the relevant timescales of the groundwater flow system?
- (e) Develop numerical models of the groundwater flow system utilizing all of the geological, hydrological and geochemical data to test the conceptual description of the groundwater flow system, eliminate hypotheses and identify additional data requirements.

Following characterization of the geology, hydrology and geochemistry of the groundwater flow system and development of a conceptual description for groundwater flow in the system, numerical

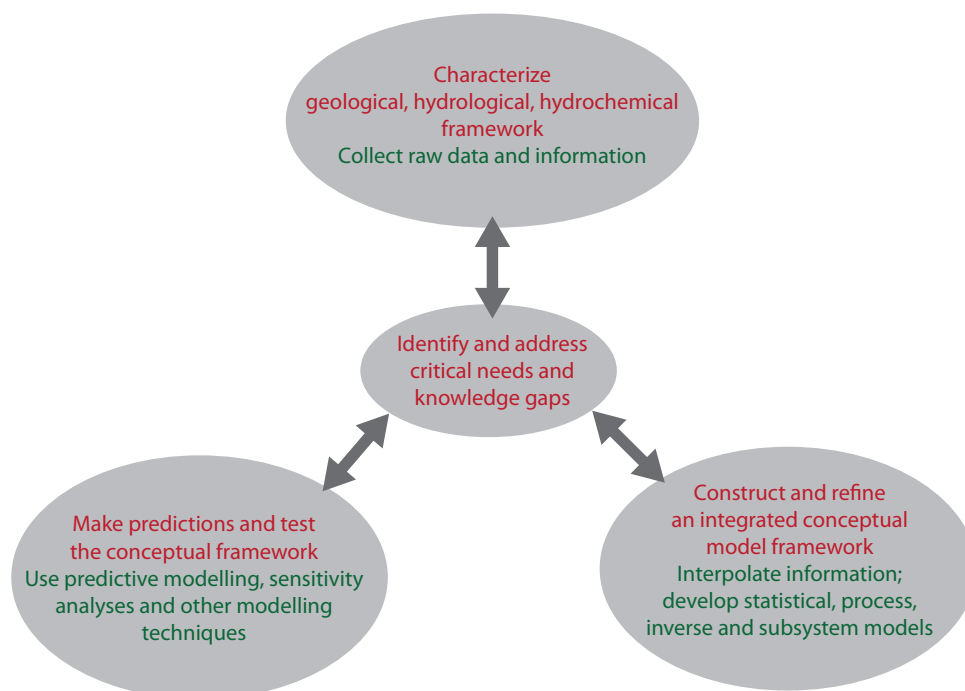


FIG. 2.3. Building a conceptual understanding: the iteration between information gathering and modelling steps needed to characterize groundwater systems and their frequency distribution of age.

modelling is a logical follow-up that can augment understanding of the groundwater system, its frequency distribution of age and identify knowledge gaps. Numerical modelling may also be a source of the estimations and assessments needed to best characterize the groundwater system. Various types of numerical modelling may be used for this purpose: deterministic hydrological and geochemical modelling to simulate given processes; statistical modelling, data modelling or geospatial modelling to simulate spatial and/or temporal distributions of information; and stochastic modelling, stratigraphic basin modelling or other types of modelling that can combine deterministic process information with statistical distributions and statistical inferences, and help create reasonable realizations to characterize and describe a groundwater system.

Inverse geochemical modelling, or inverse hydrological modelling, will be an integral part in creating a conceptual framework for a groundwater system. Inverse modelling uses the available information and measurements and seeks to determine from that information the values and spatial distribution of geological, hydrological and geochemical properties of a system. Inverse hydrological modelling, for example, is often used to determine the hydraulic conductivity of various geological units. In contrast, inverse geochemical modelling seeks to explain the observed geochemical evolution of groundwater by determining the possible sets of reactions that could be responsible for that evolution. More complex inverse modelling can be conducted to assess the possible spatial distribution of given properties. In addition to providing a better understanding of a groundwater system and its geochemical and hydrological processes, inverse modelling can help determine the most important data collection needs for a system, for example, the critical data gaps that if filled could provide a substantially better understanding and conceptual framework.

Finally, predictive modelling or forward numerical modelling can be used to simulate the hydrological and geochemical processes operating in the context of the geological structure and boundary conditions of a groundwater system. Forward modelling uses the information and data gathered, and statistical modelling and inverse modelling can be conducted to further refine that information and determine key operative processes. Through sensitivity analyses, forward modelling will provide further information regarding possible critical data gaps that need to be addressed. Forward modelling can be used to explain and predict the frequency distribution of ages in a groundwater system, thereby contributing to a conceptual understanding of that system.

The cycle of: (i) information and data gathering, (ii) inverse modelling and (iii) predictive modelling can be repeated as time and financial resources allow, or until a water resources manager or scientist feels that a sufficient understanding of the groundwater system under review and its frequency distribution of ages has been reached (Fig. 2.3).

## **ACKNOWLEDGEMENTS**

This chapter was improved through technical reviews by A. Suckow, K. Fröhlich and T.E. Reilly (United States Geological Survey). Any use of trade, product or firm names is for descriptive purposes only and does not imply endorsement by the US Government.



## Chapter 3

### DEFINING GROUNDWATER AGE

T. TORGERSEN  
Department of Marine Sciences,  
University of Connecticut,  
Groton, Connecticut,  
United States of America

R. PURTSCHERT  
Physics Institute,  
University of Bern,  
Bern, Switzerland

F.M. PHILLIPS  
Department of Earth and Environmental Science,  
New Mexico Tech,  
Socorro, New Mexico,  
United States of America

L.N. PLUMMER, W.E. SANFORD  
United States Geological Survey,  
Reston, Virginia,  
United States of America

A. SUCKOW  
Leibniz Institute of Applied Geophysics,  
Hannover, Germany

#### 3.1. INTRODUCTION: WHY SHOULD GROUNDWATER BE DATED?

This book investigates applications of selected chemical and isotopic substances that can be used to recognize and interpret age information pertaining to ‘old’ groundwater (defined as water that was recharged on a timescale from approximately 1000 to more than 1 000 000 a). However, as discussed below, only estimates of the ‘age’ of water extracted from wells can be inferred. These groundwater age estimates are interpreted from measured concentrations of chemical and isotopic substances in the groundwater. Even then, there are many complicating factors, as discussed in this book. In spite of these limitations, much can be learned about the physics of groundwater flow and about the temporal aspects of groundwater systems from age interpretations of measured concentrations of environmental tracers in groundwater systems. This chapter puts the concept of ‘age’ into context, including its meaning and interpretation, and attempts to provide a unifying usage for the rest of the book.

#### 3.2. WHAT DOES ‘GROUNDWATER AGE’ MEAN?

The concept of an ‘idealized groundwater age’ ( $\Delta t$ ) implies the time elapsed between when water entered the saturated zone (in other words, when it entered the groundwater) and when the water was sampled at a specific location ( $x, y, z$ ), presumably at a specific distance ( $\Delta s$ ) downstream in

the groundwater system (Fig. 3.1(a)). The idea of radiometric ‘dating’ of groundwater was proposed as an extension of radiocarbon dating as applied to solid materials that contain carbon (such as wood, shells, charcoal, travertine) (Münnich (1957) [75]). Radiocarbon dating of solids usually applies to materials with a (presumably) well defined initiation time (e.g. the year a tree ring was laid down or a band of travertine precipitated). The difference between this initiation time and current time is the age of the sample. The atoms of carbon within the object are presumed to have remained fixed in place, with no new carbon added or old carbon lost, until the sample is analysed for its radiocarbon content. The object is then ‘dated’ by applying the radioactive decay equation using the current measured radiocarbon content and assumed initial radiocarbon content. The interval of time calculated in this fashion is called the ‘ $^{14}\text{C}$  model age’. Provided that the basic assumptions (the initial radiocarbon content amount and the presumption that atoms of carbon have been neither gained nor lost) are correct, the ‘ $^{14}\text{C}$  model age’ should equal the actual age. However, in many cases, the basic assumptions are not valid and the  $^{14}\text{C}$  model age of the solid may significantly differ from its ‘true’ age.

Groundwater literature has not always adequately distinguished the fundamental conceptual differences between the age of solid material and the age of groundwater that result from the mobile and mixable nature of water. As a result, much groundwater dating literature refers to an idealized concept of groundwater age (see above) which has a conceptual origin in what has been referred to as a ‘hydraulic age’ (Davis and Bentley (1982) [76]). From Darcy’s law, it is known that given the permeability of a porous medium and the hydraulic gradient across it, one can calculate the specific discharge, and if the effective porosity is also known, the average interstitial velocity of the water can be calculated. By extrapolation, if the exact permeability distribution within an entire groundwater system and its distribution of hydraulic gradients are known, one can calculate velocity distributions and travel time from the water table to any given point within the system. The physics of groundwater movement, thus, dictates that any groundwater has travelled to its current location under a given set of physical conditions within a time frame determined by those conditions. This simple concept of groundwater movement has often been referred to as ‘piston’ flow. The difficulty of adequately characterizing the permeability distribution of subsurface materials has led to the measurement of environmental tracers as a means to estimate this ‘idealized groundwater age’. However, because solutes and tracers disperse (mix) in groundwater and because piston flow neglects many aspects of this dispersion and mixing, the information hypothetically contained within an estimate of such an ‘idealized groundwater age’ would still need to be interpreted within a process context. Consider, for example, the flow system depicted in Fig. 3.1, where the direction  $s$  is along the flow path and  $s\perp 1$  and  $s\perp 2$  represent orthogonal directions to  $s$ . In Fig. 3.1, (a) equals an ‘idealized groundwater age’;  $(\Delta t)$  would imply an elapsed time between the time water entered the saturated zone (when it entered the groundwater) and the time at which it was sampled at a specific position  $(x, y, z, t)$  at a specific distance  $(\Delta s)$  downstream in the groundwater basin. Figure 3.1(b) shows, however, that even for 1-D systems, groundwater (even at the most minute sampling scale) represents a collection of water molecules that have individually undergone transport and mixing reactions along multiple transport paths as a result of, for example, longitudinal dispersive processes, creating water samples that alter any ‘idealized groundwater age’ to a frequency distribution. Figure 3.1(c) shows that for more realistic 2-D and 3-D systems, additional transverse dispersion and finite sampling volumes may mix pathways of different lengths (possibly different recharge entryways) with the same velocity; or pathways with identical path lengths but different velocities. The net impact of 2-D and 3-D transverse dispersion is to create mixtures that affect the standard deviation about the mean of the frequency distribution of groundwater ages. Figure 3.1(d) indicates that transverse dispersion will also ultimately mix (very, very old) aquitard groundwater with (old) aquifer groundwater. As aquitard groundwater is characterized by a distinctly older groundwater age, it will induce a long asymmetric tail on the old side of the sample frequency distribution of groundwater ages. Figure 3.1(e) shows that the process of convergent mixing of different groundwater flows creates a mixture of component waters that is characterized by a bimodal probability distribution.

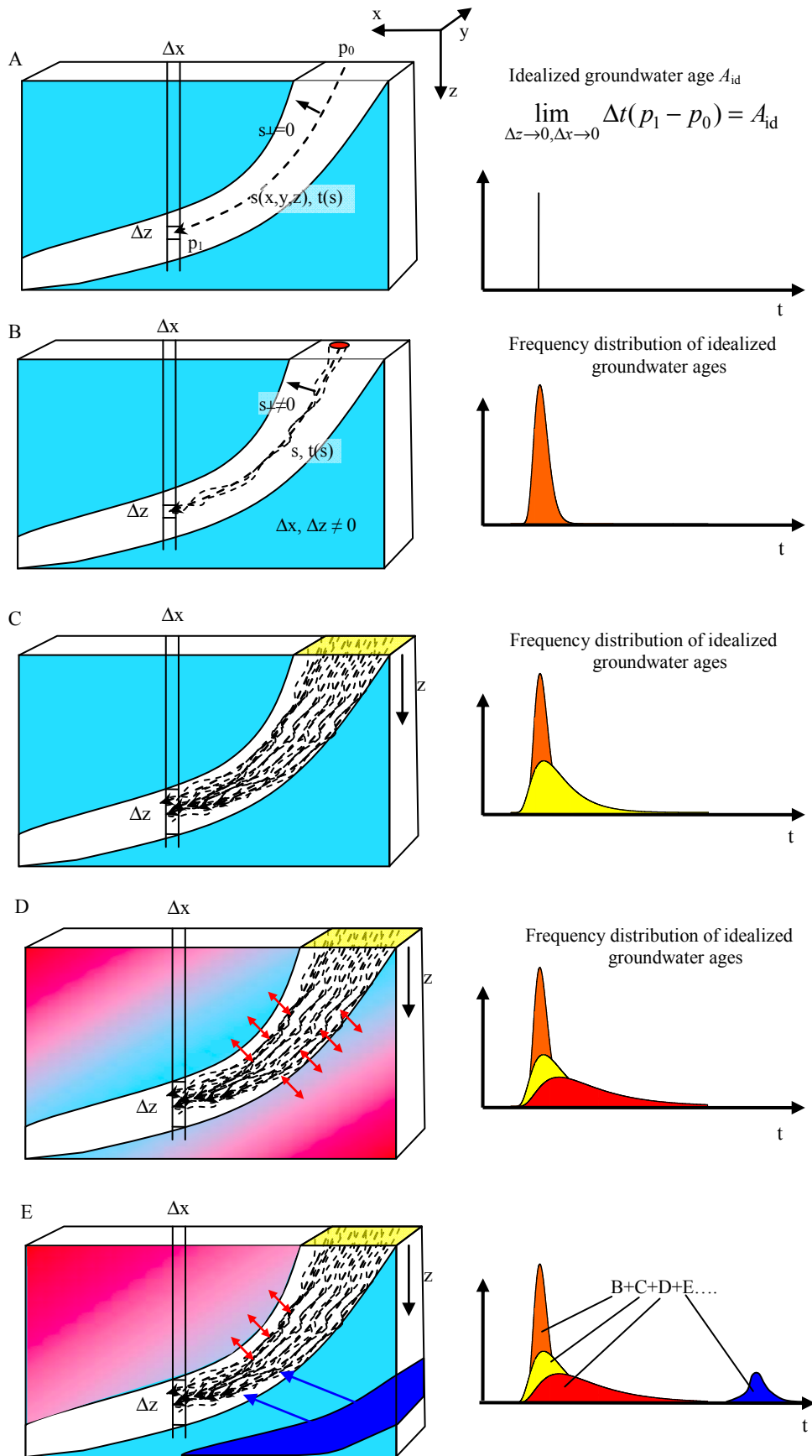


FIG. 3.1. The concept of groundwater dating represents levels of complexity. This is explained in the text below.

The following questions can be posed:

- What if the groundwater arrived at position  $(x, y, z)$  mostly by flow in the  $s$  direction, but was additionally under the influence of specific dispersive mixing parallel to the flow direction ( $D_s$ ) as well as perpendicular to the flow direction ( $D_{s\perp 1}, D_{s\perp 2}$ )? How does simple flow and simple mixing influence the interpretation of an ‘idealized groundwater age’?
- What if the groundwater arrived at position  $(x, y, z)$  via flow from two (or more) similar but not identical entryway sources (Figs 3.1(b) and 3.2)?
- How does multicomponent mixing from distinctly different source regions under convergent flow impact the meaning and interpretation of an ‘idealized groundwater age’ (Fig. 3.1(e))?
- What if the groundwater system has not operated at a steady state, e.g.  $v_s = f(t)$ ? How does (would) the observed ‘idealized groundwater age’ at position  $x, y, z$  vary as a function of time ( $\Delta t = f(x, y, z, t)$ )? When hydraulic heads may have varied significantly over the timescale of groundwater age, what if the groundwater arrived at position  $(x, y, z)$  via flow in a direction that is not equivalent to the currently defined flow direction? Within the concept of this ‘idealized groundwater age’, a calculation of groundwater velocity in the  $s$  direction ( $v_s$ ) is possible but not meaningful in this context.

These examples illustrate that even within the simple definition of an ‘idealized groundwater age’, its interpretation in terms of the processes that control ‘idealized groundwater age’ remains complex. Additionally, this illustrates an important concept:

- It is the net impact of all processes by which groundwater reaches the position  $(x, y, z, t)$  that determines groundwater age.

The corollary is:

- The understanding of groundwater age at a specific location  $(x, y, z, t)$  requires knowledge of all processes by which groundwater flows to that specific location.

These considerations demonstrate that a more physically based definition of groundwater age is needed.

### 3.3. GROUNDWATER AGE DISTRIBUTION

‘Idealized groundwater age’ has been defined above as the elapsed time since water entered the saturated zone. However, samples of groundwater are finite in volume and contain very large numbers of molecules. In a bulk fashion, groundwater moves in response to spatial gradients in fluid potential. In addition to this, inasmuch as water is a fluid and the relative positions of molecules are not fixed, those molecules move in random paths as well as through bulk flow (Fig. 3.2). These potential driven and entropy driven transport processes interact in a complex fashion to produce transport processes variously described as ‘advection’, ‘diffusion’, ‘hydrodynamic dispersion’ and so on (see Phillips and Castro (2003) [77] for a discussion of the influence of various transport processes on groundwater age tracers). One implication of groundwater transport is that the transport path of any individual molecule of water may (and almost certainly does) differ from the mean path obtained by averaging many molecules (Fig. 3.1). (It is acknowledged that water molecules have a specific identity of the order of picoseconds; for this discussion, this concept is ignored.) The result is that any finite sized sample of groundwater contains water molecules that have resided in the system for differing periods of time. This being the case, a groundwater sample at a specific location cannot be adequately characterized by any single value of ‘age’; rather, it is characterized by a frequency distribution of ages (Fig. 3.1(b), etc.).

The concept of fluid age defined by a frequency distribution of ages was introduced by Danckwerts (1953) [78]. Since then, it has been widely applied in fluid dynamics, chemical engineering, atmospheric science, oceanography and hydrology (Hooper (2003) [79]; Loaiciga (2004) [80]; McGuire and McDonnell (2006) [81]). In the chemical engineering literature, the concept is generally referred to as

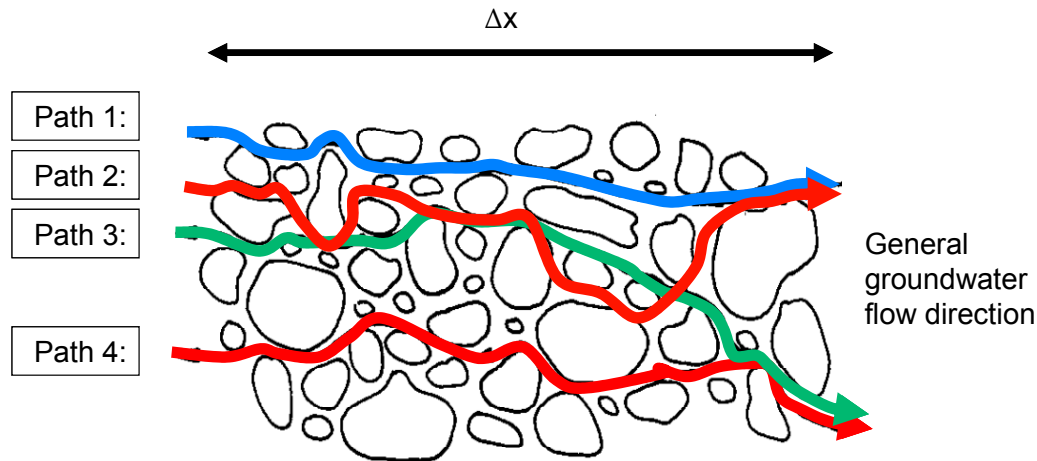


FIG. 3.2. A depiction of the role of dispersion in creating multipath routes from recharge to discharge in a 3-D groundwater system. Flow down the hydraulic head gradient produces decision points upon each encounter with the host grains of an aquifer. This probabilistic process creates dispersion in groundwater age arriving at position ( $\Delta x$ ) downstream (Fig. 3.1(b)).

the ‘residence time distribution function’. The residence time distribution is a mathematically rigorous and practically useful function (see references above for examples).

In this book, ‘frequency distribution of age’ will generally be used rather than ‘residence-time distribution’. This is simply to avoid confusion since ‘residence-time distribution’ has been traditionally used in the chemical engineering literature to refer to distribution in the discharge of a system, whereas distribution in a finite sample from within the system is generally being referred to. The mathematics of these two cases differs. Małoszewski and Zuber (1982) [82] have provided mathematical formulations applicable to frequency distribution of age in groundwater systems and Małoszewski et al. (1983) [64] show examples of their application. McGuire and McDonnell (2006) [81] reviewed analogous mathematical approaches for the outputs of drainage basins. Goode (1996) [69] pioneered a flexible numerical approach to simulating age distributions in complex groundwater systems and Varni and Carrera (1998) [83] estimated the frequency distribution of age at a single point.

An extreme example of frequency distribution for groundwater age would arise from an extensive, hydraulically uniform aquifer with a high recharge rate that is spatially localized (e.g. at a small outcrop area of the formation). This system will be advection dominated because the spatially uniform aquifer minimizes the effects of dispersive mixing relative to advective transport and the high recharge rate produces small gradients of groundwater age with flow distance. In the absence of convergent flowlines, the distribution of groundwater ages within a small sample of groundwater in this case will have a prominent mode with a relatively narrow distribution around that mode. As the ratio of dispersion to advection increases, the frequency distribution of ages (spread around the mode) increases.

Although it is tempting to characterize the ‘age’ of a water sample by calculating some central tendency, unless the system is strongly advection dominated, this can yield quite misleading results. For example, imagine a small, rapidly recharged aquifer that is bounded by thick shale of extremely low permeability. The shale is still diffusing connate water (which was present when it was deposited in the Cretaceous) into the aquifer. If 99.9% of the water discharged from the aquifer was recharged 5 years before the sampling date, and 0.1% is water from the shale (with an age of, for example, 65 million years), the average age of the discharge is 65 ka. This number conveys no useful information about the system and is, in fact, quite misleading if taken at face value. However, when a system is

strongly advection dominated, an estimate of the mode of the frequency distribution of groundwater age can still provide useful information.

To summarize, the ‘age’ of a groundwater sample is a function of the frequency distribution of the elapsed time since each of the individual water molecules crossed the water table (Figs 3.1(b)–(d)). Unfortunately, this frequency distribution is difficult (to impossible) to determine for groundwater systems, even in a coarse sense. For estimating groundwater ages, one must rely on either inferences from the concentration of chemical or isotopic tracers measured in a water sample, or on calculations based on the physics of fluid mass transport. If the age estimate is obtained from a chemical tracer measurement, then a conceptual/mathematical model must be employed to convert tracer concentrations into an age; the single age value that results is called the ‘tracer based model age’. For example, a groundwater age obtained using  $^{14}\text{C}$ -tracer data and the radioactive decay equation would be called a ‘tracer based model age’ or more specifically a ‘ $^{14}\text{C}$  based model age’. This terminology reinforces the principle that calculated age is inseparable from the conceptual/mathematical model employed and the assumptions that model includes. It is, therefore, a useful measure of age only to the extent that the model corresponds to the characteristics of a system. Following a not uncommon practice, the expression will be simplified (in a specific case) to ‘ $^{14}\text{C}$  model age’ or (in a general case) ‘tracer model age’.

In the majority of cases, the mathematical models and assumptions employed to interpret tracer data do not include mixing processes and yield single values of tracer model ages (errors cited are typically associated with tracer measurement error and do not contain information about the frequency distribution of age). These single values of tracer model ages may correspond to the mean ages of age distributions, but in most cases probably do not. Multiple tracers, combined with knowledge of the hydrogeology, can often aid in understanding (at least in a qualitative fashion) the relation between a single value of a tracer model age at a location and the frequency distribution of groundwater ages at that location.

### 3.3.1. Examples of groundwater age distribution

The examples given above illustrate possible forms of the frequency distribution of groundwater age in some simple hypothetical groundwater systems. Several examples of frequency distributions in more realistic systems have been provided by numerical modelling.

As mentioned above, if an age estimate is obtained from application of the physics of fluid mass transport, it is called the ‘hydraulic age’, which represents one type of ‘flow model age’. In many cases, such calculations include only advective transport. In more complete models, additional processes may be included and in both cases a spatial distribution of ‘hydraulic ages’ may be calculated. An excellent example of this approach is provided by Goode (1996) [69], who illustrated the role of dispersion with a simple numerical groundwater flow model for a layered system (0–30 m, hydraulic conductivity is  $10^{-5}$  m/s; 30–70 m, hydraulic conductivity is  $10^{-6}$  m/s). Figure 3.3(a) shows the hydraulic head contours (0.2 m contours) of a simple flow system, which determine the streamlines shown in Fig. 3.3(b). For a case involving only advection and no dispersion (Fig. 3.3(c)), the groundwater age structure (10 a intervals) is noticeably different from a case of advection with dispersion (Fig. 3.3(d);  $D_m = 1.16 \times 10^{-8}$  m<sup>2</sup>/s;  $\alpha_L = 6$  m,  $\alpha_T = 0.6$  m), especially at the boundary of the slow flow region in the zone of upflowing streamlines. The younger ages in the upflowing streamline region under the advection with dispersion case (Fig. 3.3(d)) are the result of dispersive mixing between slow moving streamlines and fast moving streamlines. The no-dispersion case (Fig. 3.3(c)) results in a more isolated pocket of flow and older groundwater ages.

Goode (1996) [69] and Bethke and Johnson (2008) [84] generalized these dispersion mixing and convergent mixing issues that impact the transport and mixing processes in groundwater flow systems and that influence groundwater age distribution. For 1-D groundwater flow without dispersion (piston flow, Fig. 3.1(a)), groundwater at a specific location should result in a single idealized groundwater

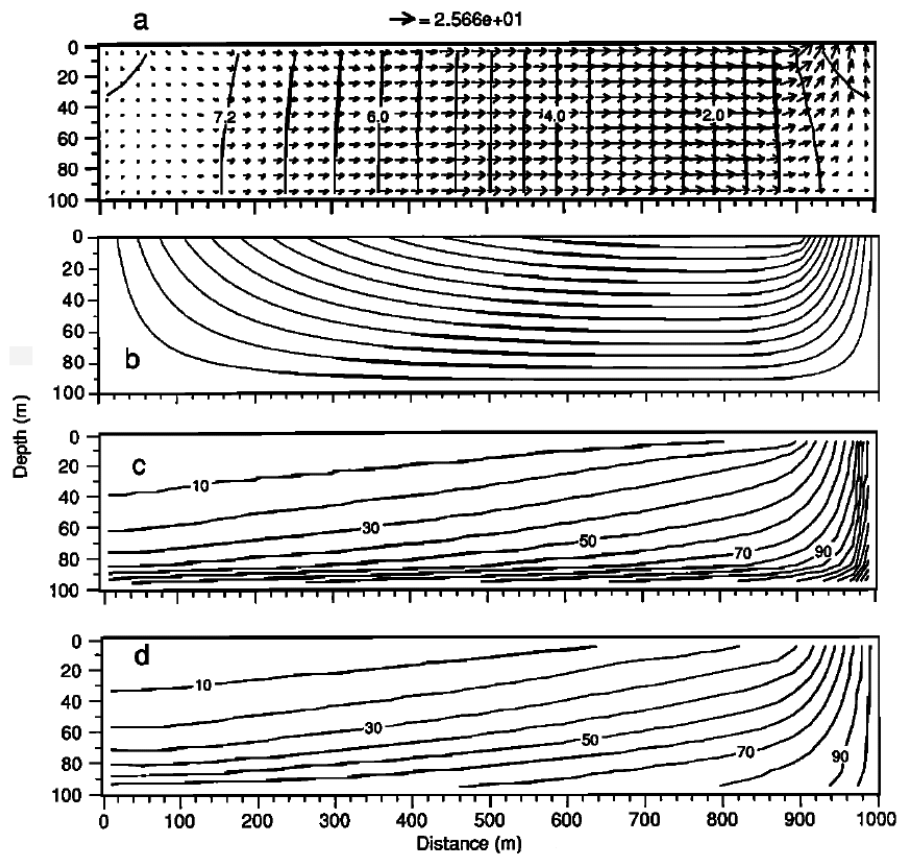


FIG. 3.3. The results of Goode (1996) [69] showing a direct simulation of groundwater ages within a very simple aquifer where the upper 30 m of the aquifer has a hydraulic conductivity of  $10^{-5}$  m/s and the lower 70 m has  $10^{-6}$  m/s. (a) shows the hydraulic head contours (0.2 m contours) and the velocity vectors; (b) shows the streamlines from recharge to discharge; (c) shows simulated age contours for the advection only condition (no dispersion) with a 10 a contour interval; (d) shows simulated age contours with dispersion (see Goode (1996) [69] for a complete description of the simulation; from Goode 1996 [69], reproduced with permission of the American Geophysical Union).

age. However, for groundwater flow with even 1-D longitudinal dispersion (in the same direction as the flow velocity), multiple microscale pathways produce a frequency distribution of groundwater ages. When 2-D and 3-D flow are included (Fig. 3.2), transverse dispersion may mix: (i) pathways of different lengths (and possibly different recharge entryways) with the same velocity; or (ii) pathways with identical path lengths but different velocities. The net impact of 2-D and 3-D transverse dispersion is to create mixtures and increase the width of groundwater age distribution (Fig. 3.1(c)).

For the longest timescale of flow, molecular diffusion may ultimately mix aquitard groundwater with the aquifer groundwater (Fig. 3.1(d)). As aquitard groundwater is usually characterized by distinctly older ages, the mixing of aquitard water with aquifer water (noting the Cretaceous shale example above) will induce a long asymmetric tail on the old side of age frequency distribution (Fig. 3.1(d)). The frequency distribution of groundwater age is, thus, dependent upon how much aquitard water was incorporated and the frequency distribution of ages within the aquitard groundwater.

In addition to simple dispersion induced mixing, groundwater flow paths may also converge to cause mixing; or an aquifer structure may induce mixing of groundwaters from layered aquifer systems. As illustrated in Fig. 3.1(e), the process of convergent mixing of different groundwater flows creates a mixture of component waters that is characterized by a bimodal age distribution. Samples collected from pumping wells or springs are susceptible to even further turbulent mixing in the discharge conduit where the sample is collected.

### 3.4. CHARACTERISTICS OF IDEAL TRACERS

An ideal groundwater age tracer should exactly replicate the transport and mixing of the groundwater with which it flows. As such, an ideal tracer: (i) should not be subject to chemical retardation with respect to the water flow; (ii) should undergo mechanical dispersion identical to that of the water molecules (and, thus, duplicate the frequency distribution of groundwater age); and (iii) should undergo molecular diffusion identical to that of the water molecules. An ideal groundwater tracer suitable for dating must then also change its concentration as a known and defined function of time from a defined initial condition to the location at which it can be sampled. The initial conditions for a tracer model age should be obtainable and should be established in the same location where the idealized groundwater age is zero. All of these attributes should result in the tracer, at the sampling location, having an age distribution that follows from the groundwater age distribution (e.g. for a radioactive tracer, this would correspond to the groundwater age distribution multiplied by the appropriate amount of decay for each age). In this context, the available choices of geochemical tracers suitable to dating needs are narrowed considerably; they are characterized by simple solubility controls, limited reactivity and known radioactive reaction rates for either ingrowth or decay (or in the case of stable tracers such as CFCs (IAEA (2006) [85]), known variability in the initial condition, simple geochemistry and ‘no’ loss terms). With a known initial condition and a known reaction (such as radioactive decay or known production), the measured concentration of a tracer in a groundwater sample at location  $x, y, z, t$  can be converted into a tracer model age through a defined mathematical formula with specific assumptions.

However, the tracer model age is subject to interpretation (and potential complication) as a result of both dispersion controlled mixing and convergence controlled mixing. The interpretation of tracer

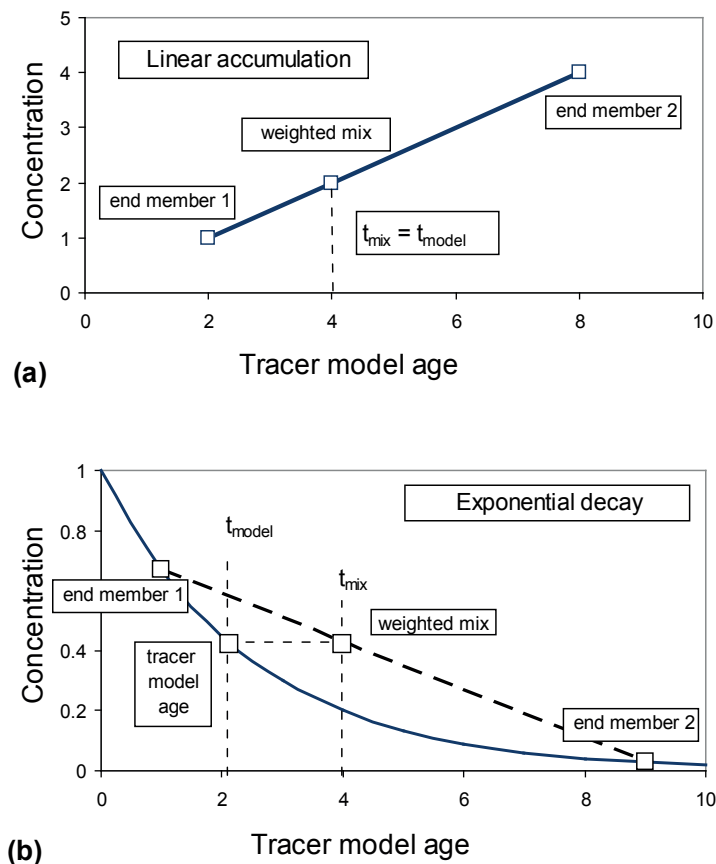


FIG. 3.4. The groundwater age of a water sample can be represented by some central measure of frequency distribution of ages (Figs 3.1(b) and (c)).

model age is functionally dependent upon whether the reaction term is linear, concave or convex versus distance/time and the timescale of the tracer.

For the case of a linearly changing (under ideal conditions, possibly  $^4\text{He}$ ) tracer concentration with time (see Fig. 3.4(a)), a mixture of young and old waters will create a mixture whose combined frequency distribution of groundwater ages accurately reflects the mixing and relative weighting of the old and the young water. However, for a tracer with exponential decay (such as  $^{14}\text{C}$  or  $^{36}\text{Cl}$ ), the mixing of old and a young groundwater will create a tracer mixture that is interpreted as younger than the weighted mean of the separate tracer ages of young and old water would imply (see Fig. 3.4(b)). In an ideal world, the tracer model age (determined by some geochemical method) would be a true reflection of the frequency distribution of groundwater age. Figure 3.4(a) shows that when a tracer increases (or decreases) linearly with time (e.g. possibly  $^4\text{He}$  or a tracer the input of which is linearly changing as a function of time), a mixture of groundwaters with different ages would produce a mixed water whose tracer model age would be in agreement with the weighted mix of groundwater ages. However, Fig. 3.4(b) shows that for a tracer whose variability with time is non-linear (typically exponential with time:  $^{14}\text{C}$ ,  $^{36}\text{Cl}$ , etc.), the effect of mixing (in this specific case) groundwaters with different ages would produce a tracer model age that does not agree with the weighted mix of groundwater ages. Without independent knowledge of what was mixed and in what proportions, it is not possible to interpret a tracer model age unequivocally as a measure of the central tendency of the frequency distribution of groundwater age.

Dispersion controlled mixing for tracers with concave functions such as radioactive decay will, therefore, always create conditions under which the tracer model age is an underestimate of the mean groundwater age; the degree of underestimation being a function of the degree of mixing and the decay constant. For convergence controlled mixing, the component end members are likely more widely disparate in their groundwater age distributions and the impact of convergent mixing on the tracer will result in a greater difference between the mean (or mode) of groundwater age distribution and the tracer model age, again with the tracer model age being younger than the correctly interpreted mixture of component end member ages. Tracer reaction rates and mixing end members must, therefore, be considered in the interpretation of tracer model ages. For cases in which the mean of the age distribution is not equal to the mode for the age distribution (e.g. Fig. 3.1(d)), or where the age distribution is bimodal (Fig. 3.1(e)), the interpretation of tracer model age and its relation to the mean or mode of age distribution becomes more complex.

### 3.5. ADDITIONAL LIMITATIONS ON TRACER MODEL AGES

Under favourable circumstances, groundwater age can be characterized by some central measure (mean, median, mode) of the frequency distribution of groundwater ages within a groundwater sample (e.g. Fig. 3.1(b)–(e)). However, because a groundwater sample has been aggregated (naturally or by some bias in the sampling protocol) via distinct and separate processes, interpreting some central tendency of distribution requires information on the nature of the distribution function. Such information is difficult to obtain for real world (as opposed to simulated, mathematically modelled) groundwater systems, and this greatly limits the ability to interpret single values of tracer model ages. To some extent, one can obtain information on the nature of age distribution via methods such as classical input–output analysis (Kirchner et al. (2000) [86]; McGuire and McDonnell [81] (2006); McGuire et al. (2005) [87]), interpretation of multiple tracers, especially radionuclides with a wide range of half-lives (Castro et al. (2000) [88]), or numerical simulation of the system (Castro and Goblet (2003) [89]; Park et al. (2002) [90]; Weissmann et al. (2002) [91]) and use these to help interpret individual tracer model ages, but even so the interpretations will have significant uncertainty associated with them.

It must be appreciated in groundwater dating that a single tracer model age is in fact a calculation that has a specific location/time associated with it ( $x, y, z, t$ ), a specific initial condition and a specific  $\Delta s$  and  $\Delta t$  that delimit interpretation constraints. This means that only bulk properties between two flow

connected sampling points can be quantified unless additional information is available from well tests, additional sampling, other tracers, other dating methods, etc. This implies that multiple measures along a flow path will provide more and better information if interpreted together rather than individually. It has been noted (Bethke and Johnson (2008) [84]) that plots of tracer model age versus distance yield slopes in units of inverse velocity. Such plots can be used to support the existence of a continuous flowline as well as discontinuities in flow velocity.

Even when the conditions for appropriate application of a geochemical tracer for the calculation of a tracer model age can be confirmed and appropriate samples can be obtained, the calculation of a tracer model age must still be interpreted with caution. A tracer model age is an interpretation and an approximation that acknowledges all of the assumptions, idealizations and limitations of a tracer, as well as comparability of a tracer to the processes that determine groundwater age. Due to aquifer heterogeneity, dispersive mixing, and other physical and chemical processes, macroscale groundwater age distribution cannot be defined by tracer model age. Still, tracer model ages provide information that helps constrain age distribution and the generalities of flow in groundwater systems.

### 3.6. TRACERS IN THIS BOOK

The tracers available for application and interpretation in terms of tracer model ages are limited for timescales greater than 1000 a. Tracer model analysis of  $^4\text{He}$ ,  $^{14}\text{C}$ ,  $^{36}\text{Cl}$ ,  $^{81}\text{Kr}$  and  $^{234}\text{U}/^{238}\text{U}$  provides valuable information and is discussed in the chapters that follow. However, the value of a tracer model age increases when two or more methodologies can be compared and contrasted in order to understand the relation between generally simplified assumptions inherent in tracer models and a more complex real system (see Chapter 9).

The geochemical groundwater tracers discussed in this book ( $^4\text{He}$ ,  $^{36}\text{Cl}$ ,  $^{14}\text{C}$ ,  $^{81}\text{Kr}$ ,  $^{234}\text{U}/^{238}\text{U}$ ) have been used to calculate tracer model ages in multiple groundwater systems with sufficient cross checks to ensure at least a minimal level of confidence in the results. In the following chapters, tracer specific processes will be defined and discussed which contribute to the calculation of tracer model ages, as well as how various processes affect the interpretation of these tracer model ages. The ‘tracer model age’ will be referred to as a generality and in specific cases will refer to, for example, the ‘ $^{14}\text{C}$  model age’ or the ‘ $^4\text{He}$  model age’ to differentiate which specific tracer has been used and what specific model has been used to calculate the tracer model age.

The case studies discussed in the following chapters reinforce the principle that multiple sampling points with multiple tracers including temperature, water chemistry, hydraulic head, stable isotopes and well borehole tests will provide information that is generally necessary for adequately characterizing groundwater basins. These can then be interpreted with the aid of detailed mathematical reaction and transport models (‘flow model ages’). Additional constraints can often be imposed on the interpretation by optimizing hydraulic models to best simulate tracer transport data (Berger (2008) [92]). Yet, even for the best tracers and the simplest groundwater systems, the system of equations describing reaction and transport in a groundwater system will be under-constrained. In order to solve equations that describe flow in a groundwater basin, assumptions and simplifications must be made with regard to basin structure, the heterogeneity of basin properties and the evolution of a basin as a steady state or unsteady state flow system subject to temporally controlled uplift and erosion. Given this complexity, simple physics based flow models (see Castro et al. (2000) [88]; Torgersen and Ivey (1985) [93]) that include transport and mixing of groundwater as well as the source and sink functions that control tracer distribution (Bethke and Johnson (2008) [84]; Bethke et al. (2000) [94]; Bethke et al. (1999) [95]; Castro and Goblet (2003) [89]; Castro et al. (1998) [96]; Castro et al. (1998) [97]; Zhao et al. (1998) [98]) are useful in evaluating the controls on groundwater movement and flow times.

Flow in groundwater systems is typically dependent on a complex spatial distribution of hydraulic properties. Data to constrain this distribution are generally sparse. The spatial distribution of hydraulic head is relatively insensitive to the distribution of hydraulic properties unless materials of differing

properties are arrayed in continuous layers of strongly contrasting values (Gomez-Hernandez and Gorelick (1989) [99]). It is within this context that estimates of groundwater age via tracer model ages can provide significant constraints on the structure of a system. However, even with this additional information, groundwater systems are always under-constrained with regard to data requirements and the resulting models are always non-unique. To some extent, this limitation can be overcome by employing geostatistically based multiple conditional simulations, but even this computationally intensive approach provides only an indication of the possible range of behaviour of a system. It benefits the conclusions of a study when groundwater scientists maintain an appropriate sense of complexity that exists in the natural systems they study.

## APPENDIX TO CHAPTER 3

### AGE TERMINOLOGY

**old groundwater.** Water that was recharged on a timescale of greater than 1000 to several million years; a practical timescale defined by the tracers discussed in this book.

**idealized groundwater age.** The elapsed time between the time water entered the saturated zone (when it entered the groundwater) and the time the same water was sampled in a specific position downstream in the groundwater system.

**frequency distribution of age.** The distribution of all idealized groundwater ages of all individual water molecules in a groundwater sample

**tracer based model age or tracer model age.** The single age value that is obtained from the application of a conceptual/mathematical model to a measurement of the concentration of a chemical tracer in a groundwater sample; in the case of a specific tracer, for example,  $^{14}\text{C}$  model age

**flow model age.** A hydraulic age calculated within a flow model

**hydraulic age.** The single valued age estimate obtained from the application of physics of fluid mass transport in the groundwater system

**mean age or average age.** The mean age is the average age of all individual water molecules in a system or sample. In terms of the mass age concept, mean age is the sum of the product of fraction of water and age of that fraction for all water fractions/ages recognized in a system

## Chapter 4

### RADIOCARBON DATING IN GROUNDWATER SYSTEMS

L.N. PLUMMER, P.D. GLYNN  
United States Geological Survey,  
Reston, Virginia,  
United States of America

“Radiocarbon dating of groundwater, which started with the original work of the Heidelberg Radiocarbon Laboratory back in the late 1950s, is certainly one of the most — if not the most — complicated and often questionable application of radiocarbon dating. The reason for this is to be found in the aqueous geochemistry of carbon in the unsaturated and saturated zones. Part of the carbon and radiocarbon content of dissolved carbon in groundwater is of inorganic and part is of organic origin.” (Mook (1992) [100]).

#### 4.1. INTRODUCTION

The radioactive isotope of carbon, radiocarbon ( $^{14}\text{C}$ ), was first produced artificially in 1940 by Martin Kamen and Sam Ruben, who bombarded graphite in a cyclotron at the Radiation Laboratory at Berkeley, CA, in an attempt to produce a radioactive isotope of carbon that could be used as a tracer in biological systems (Kamen (1963) [101]; Ruben and Kamen (1941) [102]). Carbon-14 of cosmogenic origin was discovered in atmospheric  $\text{CO}_2$  in 1946 by Willard F. Libby, who determined a half-life of 5568 a. Libby and his co-workers (Anderson et al. (1947) [103]; Libby et al. (1949) [104]) developed radiocarbon dating of organic carbon of biological origin, which revolutionized research in a number of fields, including archaeology and quaternary geology/climatology, by establishing ages and chronologies of events that have occurred over the past approximately 45 ka.

Cosmogenic  $^{14}\text{C}$  is produced in the upper atmosphere by the nuclear reaction (Mackay (1961) [105]; Mak et al. (1999) [106]):



where  $^{14}\text{C}$  oxidizes to  $^{14}\text{CO}$  and then  $^{14}\text{CO}_2$ , and mixes with the atmosphere.  $^{14}\text{CO}_2$  is absorbed by plants during photosynthesis and becomes incorporated into the Earth’s biological and hydrological cycles. The atmospheric mixing ratio of  $^{14}\text{CO}_2$  is balanced by the rate of cosmogenic production, uptake by the various carbon reservoirs on Earth (atmosphere, oceans, marine organisms, plants) and radioactive decay. Carbon-14 decays according to:



with a generally accepted (consensus) half-life of  $5730 \pm 40$  a (Godwin (1962) [107]). Chiu et al. (2007) [108] review the various measurements of  $^{14}\text{C}$  half-life and suggest that the modern half-life may be underestimated by approximately 300 a.

The conventional radiocarbon age,  $t$ , in years is, by definition:

$$t = \tau \ln \frac{A_o}{A} \quad (4.3)$$

where

- $\tau$  is the Libby mean-life ( $5568 \text{ a}/\ln 2$ , where 5568 is the Libby half-life);  
 $A_o$  is the initial  $^{14}\text{C}$  specific activity (in Bq/kg or mBq/g; 1 Bq = 1 disintegration per second);  
 $A$  is the measured  $^{14}\text{C}$  specific activity.

By international convention, specific activities are compared to a standard activity,  $A_{\text{ox}}$ , where  $A_{\text{ox}} = 0.95$  times the specific activity of NBS oxalic acid ( $0.95 \times 13.56$  disintegrations per minute per gram of carbon (dpm/g C) in the year 1950 A.D.). The initial  $^{14}\text{C}$  specific activity,  $A_o$ , and the measured  $^{14}\text{C}$  specific activity of a sample,  $A$ , can be expressed as a percentage of this standard activity in per cent modern carbon (pmc) where  $\text{pmc} = (A/A_{\text{ox}}) \times 100$  (Mook (1980) [109]). The modern, pre-nuclear-detonation atmospheric  $^{14}\text{C}$  content is, by convention, 100 pmc, corresponding to 13.56 dpm/g C in the year 1950 A.D. (Stuiver and Polach (1977) [110]). Conventional radiocarbon ages continue to be reported based on the Libby half-life, so as not to conflict with earlier studies, and  $^{14}\text{C}$  model ages are then defined in 'radiocarbon years'. A further complication in radiocarbon dating was the discovery that the amount of  $^{14}\text{CO}_2$  in the atmosphere has not been constant over time. Past variations in the solar wind and the geomagnetic fields of the sun and Earth have caused variations in the flux of cosmic rays reaching the Earth, resulting in variations in the atmospheric concentration of  $^{14}\text{CO}_2$  (Kalin (1999) [111]). It is likely that the atmospheric  $^{14}\text{C}$  content has also changed in response to changes in the residence time of the major global reservoirs (terrestrial, biosphere and ocean). The discovery of past variations in the amount of atmospheric  $^{14}\text{C}$  has led to another major field of radiocarbon investigations in determining and refining radiocarbon calibration scales to convert radiocarbon years to calendar years. For example, the last glacial maximum (LGM) occurred about 18 ka radiocarbon years ago, which corresponds to about 21 ka calendar years (Bard et al. (1990) [112]). However, recent analysis of the Barbados sea level record places the LGM at about 26 ka calendar years (Peltier and Fairbanks (2006) [113]).

Münnich was the first to extend radiocarbon dating to dissolved inorganic carbon (DIC) in groundwater (Münnich (1957) [75]; Münnich (1968) [114]). Over the past 50 years, an extensive literature of investigations and applications of radiocarbon in hydrological systems has followed. Many advances in collection and analysis of  $^{14}\text{C}$  have also followed and now  $^{14}\text{C}$  content is almost routinely determined on carbon samples as small as 1 mg by using accelerator mass spectrometry (AMS). Many of the original studies were reported in proceedings of symposia sponsored by the Isotope Hydrology Section of the IAEA. A number of reviews summarize some of the advances, principles and problems in radiocarbon dating of DIC in groundwater (Fontes (1983) [115]; Fontes and Garnier (1979) [116]; Fontes (1992) [117]; Geyh (2005) [118]; Kalin (2000) [111]; Mook (1980) [109]; Mook (2005) [119]). Numerous studies have applied radiocarbon dating to establish chronologies of the (approximately) 0–40 ka timescale in hydrological systems, to estimate modern and palaeorecharge rates to aquifers, to recognize non-renewable palaeowaters, to extract palaeoclimatic information from the groundwater archive, to calibrate groundwater flow models, and to investigate the availability and sustainability of groundwater resources in areas of rapid population growth. It is beyond the scope of this chapter to review these many studies.

In spite of the many advances in collection, analysis and application of radiocarbon in the hydrological sciences, interpretation of the radiocarbon model age of dissolved carbon in groundwater is still limited by many uncertainties in determining the initial  $^{14}\text{C}$  content of dissolved carbon in recharge areas to aquifers and in accounting for the many chemical and physical processes that alter the  $^{14}\text{C}$  content along flow paths in aquifers. The purpose here is to summarize the current state of methods used to interpret  $^{14}\text{C}$  model age from measurements of  $^{14}\text{C}$  in DIC and dissolved organic carbon (DOC) in groundwater.

Historically, hydrologists and geochemists have resorted to simplifying assumptions regarding geochemical adjustments of radiocarbon in groundwater systems, often without sufficient data to know whether additional processes are needed to accurately date the DIC in groundwater systems. As many

geochemical interactions and hydrological processes in groundwater systems can affect radiocarbon content in aquifers, modern approaches to radiocarbon dating in groundwater systems are often treated within the context of geochemical modelling; that is, the study of geochemical evolution of water–rock systems. Relatively large uncertainties in the  $^{14}\text{C}$  model age of DIC in groundwater systems remain, however, and as a result, although radiocarbon calibration is commonly applied to dating of biological carbon, such calibration is rarely warranted in radiocarbon dating of DIC in groundwater due to the many unknown geochemical and physical processes affecting the  $^{14}\text{C}$  content of DIC.

Bethke and Johnson (2008) [84] recently distinguished between (i) sample age calculated according to a geochemical age-dating technique, as commonly applied in ‘traditional’ radiocarbon adjustment models; and (ii) piston flow age, the time required to traverse a flowline from the recharge point to a location in the subsurface. Furthermore, they recognized that because of hydrodynamic processes occurring in aquifers, a groundwater sample is a collection of water molecules, each of which has its own age. Similarly, Fontes (1983) [115] wrote:

“Owing to dispersion, the ‘age’ of a groundwater sample corresponds generally to a time distribution of many elementary flows. Thus, except in the theoretical case of a pure piston flow system, or of stationary waters entrapped in a geological formation, the concept of groundwater age has little significance.”

These age concepts are discussed in Chapter 3 in the context of this book.

Although hydrodynamic processes can cause difficulties in the interpretation of tracer model age, many hydrogeological settings have been investigated where radiocarbon dating has provided useful information on flow and recharge rates, and  $^{14}\text{C}$  model ages have been partially corroborated by concordance with other isotopic and environmental tracers on the 0–40 ka timescale. The interpretation of the  $^{14}\text{C}$  model age is provided below, where the model age is the  $^{14}\text{C}$  piston flow age calculated by a ‘traditional’ geochemical adjustment method that is applied to DIC. Then, some of the more advanced geochemical modelling techniques that can help refine a  $^{14}\text{C}$  model age and quantify hydrodynamic mixing on the basis of solution chemistry and isotopic compositions will be discussed. A discussion of advances in radiocarbon dating of DOC follows. Finally, the complexities of assessing the effects of diffusive processes and leakage from or through confining units will be examined.

This chapter reviews some of the past radiocarbon adjustment models, the conditions under which they apply, and summarizes the geochemical modelling approach to radiocarbon dating as implemented in the inverse geochemical modelling code NETPATH (Plummer et al. (1994) [120]) which applies radiocarbon dating to the total dissolved carbon (TDC) system (DIC + DOC +  $\text{CH}_4$ ). In an effort not to obscure the presentation with too many equations and details, these have been placed in the Appendix to Chapter 4, along with some example calculations. Units used in reporting radiocarbon measurements and conventional radiocarbon age are defined in the Appendix to Chapter 4. Equations describing isotopic fractionation in the carbonate system are summarized in the Appendix to Chapter 4, where they are generalized to systems of TDC (DIC + DOC +  $\text{CH}_4$ ). The Appendix to Chapter 4 also provides some guidance on radiocarbon calibration to calendar years. Details pertaining to field sampling are provided as well as reference to available software used in radiocarbon dating of DIC in groundwater. Finally, the Appendix to Chapter 4 supplies a reference to selected AMS facilities providing radiocarbon determinations.

## 4.2. INTERPRETATION OF RADIOCARBON AGE OF DISSOLVED INORGANIC CARBON IN GROUNDWATER

Carbon-14 of cosmogenic origin is incorporated in groundwater during recharge by interaction of infiltrating water with soil  $\text{CO}_2$  from plant root respiration and microbial degradation of soil organic matter (see, for example, Kalin (1999) [111]). Following recharge, DIC becomes isolated

from the modern  $^{14}\text{C}$  plant–soil gas–air reservoir and decays with time. Many physical and chemical processes can affect the  $^{14}\text{C}$  content of DIC in groundwater, beyond that of radioactive decay, and must be considered to interpret radiocarbon model ages and their uncertainties. The most important considerations in radiocarbon dating of DIC in groundwater can be grouped under four general topics:

- (a) Determination of the initial  $^{14}\text{C}$  content,  $A_0$ , of DIC in groundwater recharge, at the point where infiltrating water is isolated from the unsaturated zone  $^{14}\text{C}$  reservoir;
- (b) Determination of the extent of geochemical reactions that occur within the aquifer following isolation from the unsaturated zone and the effect of geochemical reactions on  $^{14}\text{C}$  content;
- (c) Evaluation of the extent to which physical processes alter the  $^{14}\text{C}$  content (such as mixing of old and young water in samples pumped from wells; hydrodynamic dispersion along hydrological flow paths; matrix diffusion and/or diffusive exchange with confining layers, leakage from other aquifers or surficial waters, in situ production);
- (d) When warranted, correction for historical variations in atmospheric  $^{14}\text{C}$  content, through application of radiocarbon calibration scales.

These four topics are discussed below.

#### 4.2.1. Determination of initial $^{14}\text{C}$ in recharge water, $A_0$

In the unsaturated zone,  $\text{CO}_2$  partial pressure is typically substantially higher than that in the atmosphere (about  $10^{-3.5}$ ) as a result of biological activity, soil moisture and, often, higher temperature (Brook et al. (1983) [121]). As infiltrating water moves through the unsaturated zone, the  $\text{CO}_2$  in infiltrating water is augmented by soil zone  $\text{CO}_2$ . The dissolved  $\text{CO}_2$  reacts with carbonate and silicate minerals in the soil and sediment of the recharge area, resulting in increased concentrations of dissolved carbon (DIC and DOC) in the infiltrating water.

The term  $A_0$  refers to the initial  $^{14}\text{C}$  content of DIC in groundwater that occurs following recharge and isolation of the water from the modern  $^{14}\text{C}$  reservoir of unsaturated zone  $\text{CO}_2$ .  $A_0$  must be known or estimated to date the  $^{14}\text{C}$  of dissolved carbon in groundwater in hydrological systems. In the following, the term ‘pmc’ is used to express the  $^{14}\text{C}$  content as a per cent of the modern standard (see above).

##### 4.2.1.1. Estimation of $A_0$ from measurements in recharge areas

Ideally, measurements of the radiocarbon content of DIC and DOC in groundwater from the recharge areas of aquifers can be used to define  $A_0$ , but this approach has two complications. First, many of the waters in recharge areas of aquifers today contain tritium and/or CFCs, which are indications of potential contamination of  $^{14}\text{C}$  from post-nuclear detonation (post-1950s) water. Water from the post-1950s bomb era has  $^{14}\text{C}$  amounts that are greater than the historic values that existed in pre-1950s recharge areas, and, if these observed values from recharge areas are used in dating, radiocarbon model ages will be biased old. Waters from recharge areas of aquifers can also be mixtures of pre- and post-bomb era waters, again leading to an old bias in the  $^{14}\text{C}$  model age. The issue here is not so much that of contamination, but rather of insufficient knowledge of the contamination to adequately calculate the effective  $A_0$  value that would incorporate only natural, pre-bomb,  $^{14}\text{C}$  dilution processes, and would have applied at the time of recharge of the old groundwater under investigation.

Secondly, even if pre-bomb waters can be identified in the recharge area today, consideration needs to be given to the palaeoclimatic conditions corresponding to the time an old, geochemically evolved water sample was recharged. As shown below using some of the well known adjustment models, modelled values of  $A_0$  can be sensitive to the  $\delta^{13}\text{C}$  of soil gas  $\text{CO}_2$ . Further, the  $\delta^{13}\text{C}$  of soil gas  $\text{CO}_2$  can change significantly over time in recharge areas in response to climatic variations that cause changes in the relative proportions of plants utilizing the  $\text{C}_3$  and  $\text{C}_4$  photosynthetic pathways. In addition, the extent to which recharge waters evolve in isotopic equilibrium with soil gas (open system

evolution) or react with carbonates following recharge (closed system evolution) (Clark and Fritz (1997) [52]; Deines et al. (1974) [122]) can lead to uncertainties in  $^{14}\text{C}$  model age of old groundwater as much as a full  $^{14}\text{C}$  half-life. Isotopic fractionation in open and closed systems is discussed in the Appendix to Chapter 4. Even if it can be determined whether recharge waters presently evolve under open or closed system conditions, it is not known whether modern conditions prevailed when the old groundwater was recharged.

Another assumption that is commonly made, and which is applicable in most but perhaps not all cases, is that the ‘recharge area’ of old groundwater was the same as that observed today. In some cases, differences in regional climate may have caused differences in the relative amounts of recharge from different areas over time. Furthermore, modern water resource management activities can also affect the distribution of modern recharge. Changes in aridity and other climatic factors in a recharge area over the timescale of an aquifer can cause changes in the distribution of  $\text{C}_4$  to  $\text{C}_3$  in plants, which can result in changes in the value of  $\delta^{13}\text{C}$  of soil gas  $\text{CO}_2$ . Some of the models used to estimate values of  $A_0$  in recharge areas (see below) are quite sensitive to the value of  $\delta^{13}\text{C}$  of soil gas  $\text{CO}_2$ . Finally, although geological and tectonic processes often have not had enough time to significantly alter the landscape of groundwater recharge over the  $^{14}\text{C}$  timescale, exceptions do occur.

Still, if a set of groundwater samples can be obtained from the modern recharge area, or along a flow path, examination of the  $^{14}\text{C}$  content of DIC in relation to tritium (Geyh (2005) [118]; Kalin (1999) [111]; Verhagen (1984) [123]; Verhagen et al. (1974) [124]) or other anthropogenic environmental tracers, such as tritium and CFCs (IAEA (2006) [85]; Plummer et al. (2004) [49]; Plummer et al. (2004) [50]; Plummer and Busenberg (2000) [125]), or in relation to distance of flow in aquifers (Geyh (2000) [126]; Vogel (1970) [127]) can be used to estimate the modern, pre-bomb content of  $^{14}\text{C}$ .

Figure 4.1 compares  $^{14}\text{C}$  specific activities of DIC, expressed as pmc, as a function of CFC-12 and  $^3\text{H}$  concentrations for waters from recharge areas of the Middle Rio Grande Basin aquifer system of New Mexico, USA (Plummer et al. (2004) [50]). The data suggest that the pre-nuclear detonation content of  $^{14}\text{C}$  of DIC in recharge areas to the groundwater system was near 100 pmc. Carbon-14 values  $>100$  pmc have CFC-12 piston flow ages from the mid-1960s for groundwater that infiltrated

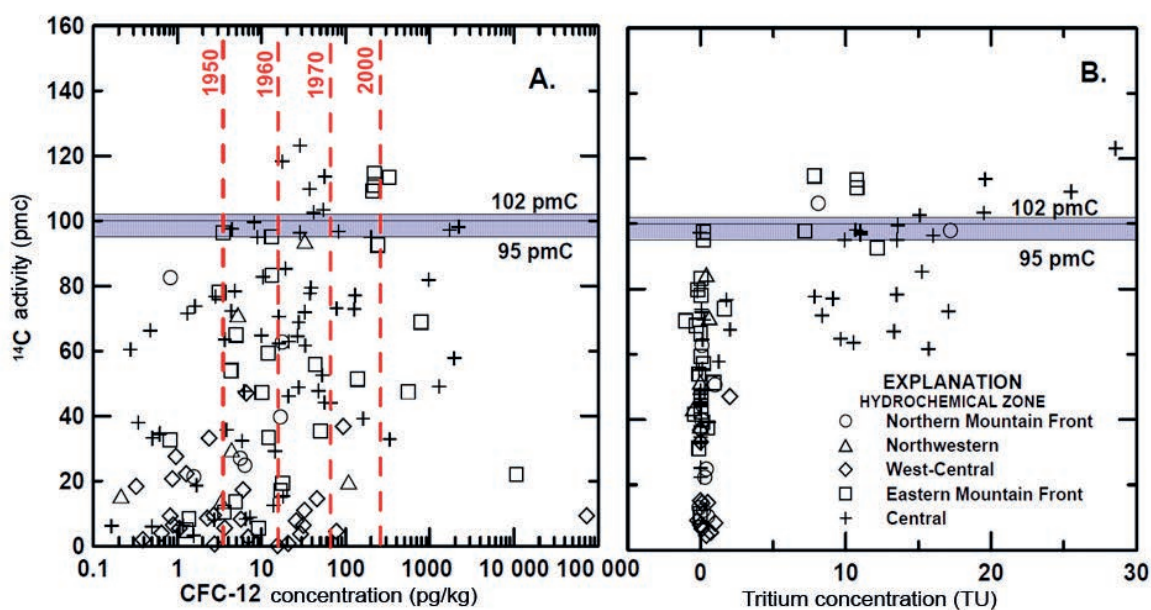


FIG. 4.1. Carbon-14 content, expressed as pmc (per cent of the modern standard) of DIC in groundwater from the Middle Rio Grande Basin, NM, USA, as a function of (a) CFC-12 concentration (see graph in (b) for explanation of symbols) and (b) tritium.

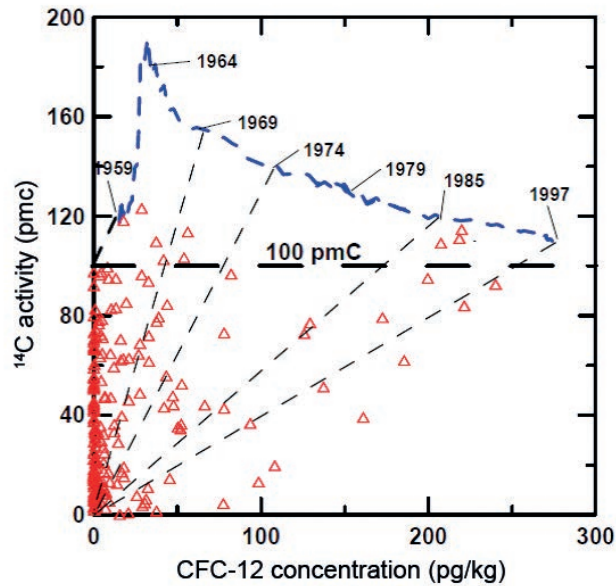


FIG. 4.2. Concentrations of  $^{14}\text{C}$  and CFC-12 measured in groundwater from the Middle Rio Grande Basin, NM, USA (red triangles), in relation to concentrations expected for water containing modern DIC, not diluted with old DIC. The blue line represents the atmospheric input of radiocarbon (Levin and Kromer (1997) [128]; Levin et al. (1994) [129]) and CFC-12 (<http://water.usgs.gov/lab>) (unmixed, piston flow). The light dashed lines represent hypothetical mixing of old water with water from 1969, 1974, 1985 and 1997 (modified from Plummer et al. (2004) [49]).

from the Rio Grande (central zone) and post-1995 ages for waters which infiltrated along the eastern mountain front; the latter comprised mixtures or samples containing a fraction of non-atmospheric CFC-12 (Fig. 4.1(a)). The highest  $^{14}\text{C}$  value in samples low in tritium and CFC-12 is near 100 pmc (Figs 4.1(a) and (b)), consistent with open system evolution from this semi-arid region of the southwest USA (modified from Plummer et al. (2004) [49]).

Waters in the northern mountain front, north-western and eastern mountain front hydrochemical zones were recharged along mountain fronts that border the basin to the north and east. Water from the west-central zone is thought to have recharged in high elevation areas north of the basin (Plummer et al. (2004) [49]; Plummer et al. (2004) [50]). Water from the central zone originated as seepage from the Rio Grande, which flows north to south through the centre of the basin. Many of the groundwater samples have low  $^{14}\text{C}$  values and are likely tens of thousands of years old, especially those of the central zone (Fig. 4.1).  $A_0$  can be inferred, however, as the maximum  $^{14}\text{C}$  value in samples with the lowest CFC-12 and/or lowest  $^3\text{H}$  content, as these samples were likely the youngest samples that recharged prior to the bomb era (pre-1950s). The maximum pmc value of  $^{14}\text{C}$  in groundwater low in CFC-12 (<20 pg/kg) and low in  $^3\text{H}$  (<0.5 TU) is near 100 pmc in the Middle Rio Grande Basin samples, and probably within the range of 95–102 pmc (Fig. 4.1), suggesting a predominantly open system evolution (Appendix to Chapter 4).

During the past approximately 20 years, the  $^{14}\text{C}$  content of atmospheric  $\text{CO}_2$  has averaged  $120 \pm 10$  pmc in the northern hemisphere (Fig. 4.2). Most of the observed  $^{14}\text{C}$  values in samples that contain  $^3\text{H}$  or CFCs are in the range of 95–120 pmc, which is again consistent with the assumption of open system evolution (Fig. 4.1). As no samples with  $^{14}\text{C}$  values higher than 123 pmc were observed, it is assumed that waters recharged during the mid-1960s and early 1970s (Fig. 4.2) were not sampled in recharge areas or, if present, were mixed and diluted with fractions of older, pre-bomb water. The distribution of  $^{14}\text{C}$  values (Fig. 4.1) in both mountain front areas and in recent seepage from the Rio Grande suggests that  $A_0$  is likely in the range of 95–102 pmc. In the Middle Rio Grande Basin study

(Plummer et al. (2004) [49]; Plummer et al. (2004) [50]), a value of  $A_o$  equal to 100 pmc was assumed for all waters. The unadjusted  $^{14}\text{C}$  model ages would decrease by 400 a if a value of  $A_o$  of 95 pmc were used instead of 100 pmc, and increase by 150 a if a value of  $A_o$  of 102 pmc were used instead of 100 pmc. These  $^{14}\text{C}$  model age differences are quite minor in comparison to uncertainties in age due to geochemical reactions.

#### 4.2.1.2. Estimation of $A_o$ using ‘traditional’ geochemical adjustment models

If geochemical reactions occur that affect the DIC, these reactions usually result in a lowering of the  $^{14}\text{C}$  content of DIC, independent of the radioactive decay of  $^{14}\text{C}$ . Applied to the initial  $^{14}\text{C}$  value, the carbonate reactions will lower the adjusted value of  $A_o$  (termed  $A_{nd}$ , where the subscript refers to ‘no decay’), resulting in adjusted  $^{14}\text{C}$  model ages that are younger than the unadjusted (or conventional)  $^{14}\text{C}$  model age. It is, therefore, important to recognize and quantify the effects of any geochemical reactions occurring that can affect the  $^{14}\text{C}$  content of DIC.

Traditionally, hydrologists have applied models that account for some of the more important carbonate reactions that occur in groundwater systems (Eichinger (1983) [130]; Evans et al. (1979) [131]; Fontes (1983) [115]; Fontes and Garnier (1979) [116]; Fontes (1992) [117]; Ingerson and Pearson Jr. (1964) [132]; Kalin (1999) [111]; Mook (1972) [133]; Tamers (1975) [134]) to the DIC of water from a single well to estimate adjusted  $^{14}\text{C}$  model ages (Fig. 4.3). Each traditional adjustment model is based on a set of assumptions regarding chemical and isotopic fractionation reactions that may affect the DIC  $^{14}\text{C}$  content of a water sample, without radioactive decay of the  $^{14}\text{C}$ . The models produce an initial  $^{14}\text{C}$  value,  $A_o$ , that has been adjusted for geochemical reactions without accounting for radioactive decay (also denoted  $A_{nd}$ ). An effort is made in this publication to retain original notation; therefore, there is some redundancy in terminology. In the traditional approach to radiocarbon dating, values  $A_o$  or  $A_{nd}$ , are compared to the measured  $^{14}\text{C}$  value in the decay equation to estimate  $^{14}\text{C}$  model age (Fig. 4.3).

This approach is best suited for geochemical systems undergoing relatively simple water–rock reactions, such as usually occurs in shallow recharge areas, but, depending on the choice of model, can be applied to radiocarbon dating of DIC in groundwater systems undergoing carbonate mineral dissolution, gypsum dissolution, Ca/Na ion exchange,  $\text{CO}_2$  gas dissolution and isotope exchange

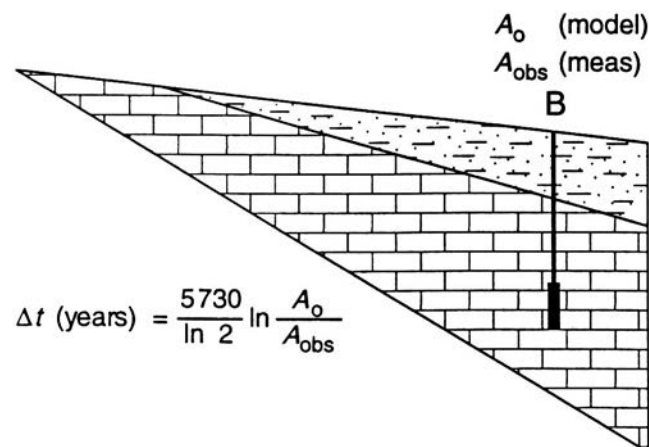


FIG. 4.3. Conceptualization of the application of ‘traditional’ adjustment models in radiocarbon dating of DIC in groundwater. The models, such as those of Tamers, Fontes and Garnier, Mook, Ingerson and Pearson, Eichinger and others, are applied to a single water analysis in the system (Plummer and Sprinkle (2001) [135]).

between soil CO<sub>2</sub>, calcite and DIC during recharge. Some of the well known traditional adjustment models are described below.

The geochemical aspects of radiocarbon dating can be divided into two parts: (i) definition of the <sup>14</sup>C content at an initial point in the system ( $A_o$ ), such as in the recharge zone where water becomes isolated from the modern <sup>14</sup>C reservoir and (ii) adjustment of this initial <sup>14</sup>C value for chemical reactions occurring along the flow path to the final well where <sup>14</sup>C content ( $A$ ) has been measured (Wigley et al. (1978) [136]). Traditionally, radiocarbon dating of groundwater has combined these two problems to develop an adjustment model that can be applied to a single water analysis at some point in the flow system. In this case, water chemistry,  $\delta^{13}\text{C}$ , and the <sup>14</sup>C value of DIC are measured for a single water sample. An adjustment model accounting for inorganic reactions affecting the inorganic carbon reservoir is applied to the single water analysis to define the <sup>14</sup>C pmc value expected in the observed water if there were no radioactive decay of <sup>14</sup>C. The adjusted <sup>14</sup>C pmc value is compared to the measured <sup>14</sup>C value through the radioactive decay equation to estimate the <sup>14</sup>C model age of DIC in the water sample. Time elapsed since recharge,  $t$ , is:

$$t = \frac{5730}{\ln 2} \ln \left( \frac{A_{\text{nd}}}{A} \right) \quad (4.4)$$

where

5730 is the modern half-life of <sup>14</sup>C;

$A_{\text{nd}}$  is the initial <sup>14</sup>C content (pmc value) after adjustment for geochemical reactions without radioactive decay, often referred to as  $A_o$  in traditional adjustment models;

$A$  is the measured <sup>14</sup>C content (pmc value) in the sample.

The above decay equation differs from the conventional radiocarbon age in that  $A_o$  (and  $A_{\text{nd}}$ ) is no longer defined to be 100 pmc and the modern <sup>14</sup>C half-life is used. To apply radiocarbon calibration scales, the Libby half-life (5568 a) is used or age is converted to the Libby half-life (Appendix to Chapter 4). A series of adjustment models that have been used to estimate values of the adjusted initial <sup>14</sup>C value in groundwater are summarized below. Most of these models were discussed by Fontes (1983) [115], Fontes and Garnier (1979) [116], Fontes (1992) [117] and Kalin (1999) [111].

#### ***Vogel model***

Vogel (1967) [137] and Vogel (1970) [138] assigned an estimate of  $85 \pm 5$  pmc for  $A_o$  based on approximately one hundred <sup>14</sup>C measurements of dissolved carbon in groundwater from north-western Europe (Fontes and Garnier (1979) [116]), and isotope mass balance calculations that included isotope dilution and isotope exchange processes during recharge (Vogel and Ehhalt (1963) [139]).

#### ***Tamers model***

Tamers (1967) [140] assumed that the initial quantity of soil zone CO<sub>2</sub> containing <sup>14</sup>CO<sub>2</sub> was diluted by dissolution of radiocarbon-‘dead’ calcite in recharge areas. If the reactions take place at approximately neutral to somewhat alkaline pH, where HCO<sub>3</sub><sup>-</sup> (and CO<sub>2(aq)</sub>) are the predominant species, the reaction is:



To a first approximation, half of the HCO<sub>3</sub><sup>-</sup> is derived from soil gas CO<sub>2</sub> (‘g’) and half from calcite (‘c’). Tamers assumed that CO<sub>2(aq)</sub> (‘a’) was derived from soil gas CO<sub>2</sub>. A carbon and <sup>14</sup>C mass balance assuming  $C_T = a + b$  (where ‘b’ is HCO<sub>3</sub><sup>-</sup>) is, following the notation of Kalin (1999) [111]:

$$A_{\text{oTamers}} C_T = (a + 0.5b)A_g + 0.5bA_c \quad (4.6)$$

or

$$A_{o\text{Tamers}} = [(a + 0.5b)A_g + 0.5bA_c]/(a + b) \quad (4.7)$$

where  $A$  denotes the  $^{14}\text{C}$  pmc value.

Owing to chemical equilibria in the carbonate solution, it is not exactly correct to assume that the quantity ‘a’ ( $\text{CO}_{2(\text{aq})}$ ) is all from soil  $\text{CO}_2$ . A more general approach is to perform a carbon mass balance, assuming DIC was derived from soil  $\text{CO}_2$ , and carbonate minerals. This avoids the need to make assumptions about predominant species in the carbonate system.

The Tamers model can be derived by using simple chemical and carbon isotope mass balance relations. The chemical evolution of precipitation (rain) in the calcite– $\text{CO}_2$  water system is as follows:



and the chemical mass balance relations are:

$$\Delta C_{\text{DIC}} = \Delta \text{CO}_2 + \Delta \text{calcite} \quad (4.9)$$

and

$$\Delta \text{Ca} = \Delta \text{calcite} \quad (4.10)$$

where  $\Delta$  represents the change in moles, final (groundwater) minus initial (rain).

The  $^{14}\text{C}$  isotope mass balance is then:

$$A_o \Delta C_T = A_{\text{calcite}} \Delta_{\text{calcite}} + A_{\text{CO}_2} \Delta \text{CO}_2 \quad (4.11)$$

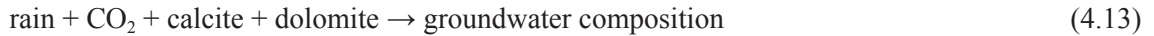
and

$$A_o = (A_{\text{calcite}} \Delta_{\text{calcite}} + A_{\text{CO}_2} \Delta \text{CO}_2) / \Delta C_T \equiv A_{o\text{Tamers}} \quad (4.12)$$

The Tamers model is extended in NETPATH (Plummer et al. (1994) [120]) to the  $\text{CO}_2$ –calcite–dolomite water system and to the  $\text{CO}_2$ –calcite–dolomite–gypsum water system. These are described below.

#### ***Tamers model in the $\text{CO}_2$ –calcite–dolomite–water system***

Here, the carbonate minerals are assumed to be calcite and dolomite, and are referred to as the ‘Tamers model’, as implemented in NETPATH (denoted ‘Tamers, NP’). The geochemical reaction is:



and the chemical mass balance relations are:

$$\Delta C_T = \Delta \text{CO}_2 + \Delta_{\text{calcite}} + 2\Delta_{\text{dolomite}} \quad (4.14)$$

$$\Delta \text{Ca} = \Delta_{\text{calcite}} + \Delta_{\text{dolomite}} \quad (4.15)$$

$$\Delta \text{Mg} = \Delta_{\text{dolomite}} \quad (4.16)$$

$$A_o \Delta C_T = A_{\text{calcite}} \Delta_{\text{calcite}} + A_{\text{CO}_2} \Delta \text{CO}_2 + 2A_{\text{dolomite}} \Delta_{\text{dolomite}} \quad (4.17)$$

The solutions to these equations are as follows:

$$\Delta_{\text{dolomite}} = \Delta\text{Mg} \quad (4.18)$$

$$\Delta_{\text{calcite}} = \Delta\text{Ca} - \Delta_{\text{dolomite}} = \Delta\text{Ca} - \Delta\text{Mg} \quad (4.19)$$

$$\Delta\text{CO}_2 = \Delta\text{C}_T - \Delta_{\text{calcite}} - 2\Delta_{\text{dolomite}} = \Delta\text{C}_T - \Delta\text{Ca} - \Delta\text{Mg} \quad (4.20)$$

$$A_{\text{oTamers, NP}} = [A_{\text{calcite}}(\Delta\text{Ca} - \Delta\text{Mg}) + A_{\text{CO}_2}(\Delta\text{C}_T - \Delta\text{Ca} - \Delta\text{Mg}) + 2A_{\text{dolomite}} \Delta\text{Mg}] / \Delta\text{C}_T \quad (4.21)$$

The term ‘ $\Delta$ ’ represents the change in mass (moles) taken as final minus initial.

#### ***Tamers model in the CO<sub>2</sub>–calcite–dolomite–gypsum water system***

This model is another mass balance model implemented in NETPATH that is similar to the previous modified Tamers model, but with the addition of a mass balance on SO<sub>4</sub>, assumed from gypsum dissolution in the recharge area or soil, referred to as the ‘mass balance’ model in NETPATH (Plummer et al. (1994) [120]) (denoted ‘Tamers, MB’).

$$A_{\text{oTamers, MB}} = [A_{\text{calcite}}(\Delta\text{Ca} - \Delta\text{Mg} - \Delta\text{SO}_4) + A_{\text{CO}_2}(\Delta\text{C}_T - \Delta\text{Ca} - \Delta\text{Mg} + \Delta\text{SO}_4) + 2A_{\text{dolomite}} \Delta\text{Mg}] / \Delta\text{C}_T \quad (4.22)$$

Both modified forms of the Tamers model default to the Tamers model if there is no dissolution of dolomite or gypsum.

#### ***Pearson model***

Ingerson and Pearson Jr. (1964) [132] solved the Tamers model for the dilution of soil zone CO<sub>2</sub> by dissolution of carbonate minerals by using isotope mass balance relations for <sup>13</sup>C and <sup>14</sup>C (denoted ‘Pearson’):

$$\delta_T \Delta_{\text{DIC}} = \delta_g \Delta_g + \delta_c \Delta_c \quad ({}^{13}\text{C isotope mass balance}) \quad (4.23)$$

$$A_T \Delta_{\text{DIC}} = A_g \Delta_g + A_c \Delta_c \quad ({}^{14}\text{C isotope mass balance}) \quad (4.24)$$

$$\Delta_{\text{DIC}} = \Delta_g + \Delta_c \quad (\text{inorganic carbon mass balance}) \quad (4.25)$$

$$A_{\text{oPearson}} = \frac{A_g (\delta_c - \delta_T) + A_c (\delta_T - \delta_g)}{(\delta_c - \delta_g)} \quad (4.26)$$

or

$$A_{\text{oPearson}} = \frac{(A_g - A_c)(\delta_T - \delta_c)}{(\delta_g - \delta_c)} + A_c \quad (4.27)$$

where

$A$  is <sup>14</sup>C pmc value;

$\delta$  is <sup>13</sup>C;

and the subscripts T, g and c refer to total DIC, soil gas CO<sub>2</sub> and carbonate mineral(s), respectively, following the notation of Fontes (1992) [117].

Therefore, the Tamers model and the Pearson model account for the same processes; the Tamers model finds a solution on the basis of chemical and <sup>14</sup>C mass balance relations, and the Pearson model uses only isotopic mass balance relations for <sup>13</sup>C and <sup>14</sup>C.

The Tamers, mass balance and Pearson models assume a simple mixing between CO<sub>2</sub> dissolved in soil water and carbon derived from the dissolution of carbonate minerals, with no other sources or sinks of carbon in the system. These assumptions imply that the groundwater evolves chemically and isotopically through dissolution of carbonate minerals under closed (to CO<sub>2</sub> gas exchange) conditions; that is, CO<sub>2</sub> enters the water in the unsaturated zone (open to CO<sub>2</sub> gas exchange) and carbonate minerals react in the saturated zone (closed to CO<sub>2</sub> gas exchange). Although none of the mass balance models specifically incorporate isotope exchange, it would be appropriate to use values of δ<sup>13</sup>C and the <sup>14</sup>C content of soil gas CO<sub>2</sub> as those in water in isotopic equilibrium with the soil gas, thus accounting for isotopic fractionation in dissolution of soil gas CO<sub>2</sub>. Examples of chemical and isotopic evolution of recharge waters in open conditions are provided in the Appendix to Chapter 4. The remaining models (below) consider isotopic exchange.

### ***Eichinger model***

Eichinger (1983) [130] modified the Pearson model (Eq. (4.26)) to include cases of partial isotopic exchange. The model is as follows, again following the notation of Kalin (1999) [111]<sup>1</sup>:

$$A_{\text{oEichinger}} = A_{\text{oPearson}} \times B \quad (4.28)$$

where

$$B = (\delta_T - \delta_c) / (\delta_i - \delta_c) \quad (4.29)$$

and

$$\delta_i = [a\delta_a + 0.5b(\delta_a + \delta_c)] / (a + b) \quad (4.30)$$

and

$$\delta_c = [a(\delta_c - \varepsilon_{cb} + \varepsilon_{gb} + \varepsilon_{ag}) + b(\delta_c - \varepsilon_{cb})] / (a + b) \quad (4.31)$$

In Eichinger's model, the term  $A_{\text{oPearson}}$  is the Pearson model (Eq. (4.26)), which accounts for the same geochemical processes as the Tamers model, but is solved using <sup>13</sup>C isotope mass balance relations, and δ<sub>T</sub> is the measured value of δ<sup>13</sup>C of total DIC in the groundwater. The term δ<sub>i</sub> estimates the value of δ<sup>13</sup>C of the total DIC after dissolution of the carbonate phase, but without any isotope exchange with carbonates. The term δ<sub>c</sub> estimates the value of δ<sup>13</sup>C of the DIC if the groundwater is in isotopic equilibrium with the solid phase, where δ<sub>c</sub> is δ<sup>13</sup>C of calcite, ε<sub>cb</sub> is the additive fractionation factor between calcite and HCO<sub>3</sub><sup>-</sup>, ε<sub>gb</sub> is the additive fractionation factor between CO<sub>2(gas)</sub> and HCO<sub>3</sub><sup>-</sup>, and ε<sub>ag</sub> is the additive fractionation factor between CO<sub>2(aq)</sub> and HCO<sub>3</sub><sup>-</sup> (see the Appendix to Chapter 4). The Eichinger model only includes isotope exchange with the solid phase.

### ***IAEA model***

In an IAEA study, Salem et al. (1980) [141] proposed that the Pearson model could be considered as a two step process: (i) equilibrium of the HCO<sub>3</sub><sup>-</sup> with the gas phase followed by (ii) dissolution of solid carbonate. The equation is (Fontes (1992) [117]):

$$A_{\text{oIAEA}} = \frac{(\delta_T - \delta_c)(A_g - A_c) + (\delta_g - \varepsilon_{gb} - \delta_c)A_c}{(\delta_g - \varepsilon_{gb} - \delta_c)} \quad (4.32)$$

<sup>1</sup> There is a typographical error in Eq. (10) of Kalin (1999) [111] where the term δ<sub>c</sub> should be replaced with δ<sub>e</sub>, as above. Further confusion regarding Eichinger's equation was noted in Plummer et al. (1994) [120] and Fontes (1992) [117], correcting a typographical error in Eichinger (1983) [130]. Finally, although mathematically correct and programmed correctly in NETPATH, Plummer et al. (1994) [120] add to the confusion by erroneously defining the term δ<sub>e</sub>.

As with Pearson's model, this model implies that all chemical reactions can be accounted for by the  $^{13}\text{C}$  isotopic composition of the end members (pure mixing), with one of them completely isotopically exchanged with the gas phase. The IAEA model can be solved in NETPATH by choosing the Pearson model and selecting the isotope mass balance model ('mass balance with fractionation') for definition of  $\delta^{13}\text{C}$  of soil gas  $\text{CO}_2$ . As pointed out by Fontes (1992) [117], the IAEA model gives higher  $A_o$  values than the Pearson model. In one numerical example,  $A_o$  from Pearson's model was approximately 58.2 pmc, but the IAEA model gave 96.2 pmc (Fontes (1992) [117]).

### ***Evans model***

Evans et al. (1979) [131] developed a model to account for isotopic fractionation during recrystallization (dissolution–precipitation) of calcium carbonate in groundwater. It is assumed that calcite is in isotopic equilibrium with dissolved  $\text{HCO}_3^-$ . Their equation, as modified by Fontes (1992) [117] reduces to:

$$A_{o\text{Evans}} \approx (A_g - A_c) \left( \frac{(\delta_T + \varepsilon_{cb} - \delta_c)}{(\delta_g + \varepsilon_{cb} - \delta_c)} \right) + A_c \quad (4.33)$$

As pointed out by Fontes (1992) [117], the modified model (Evans et al. (1979) [131]) is similar to Pearson's model and produces  $A_o$  values similar to Pearson's model despite the fact that the two models have quite different conceptualizations and derivations.

### ***The Mook model***

The Mook model (Mook (1972) [133]; Mook (1976) [142]; Mook (1980) [109]) estimates  $A_o$  in a step by step approach, considering partial or complete isotopic equilibration in the soil zone between  $\text{CO}_2$  gas and all aqueous carbon bearing species, including part of the dissolving carbonate mineral (Fontes (1992) [117]). The Mook model is more appropriate in systems in which reactions with carbonate minerals are not dominant (Fontes (1992) [117]; Mook (1976) [142]). The Mook model can be expressed as the Tamers model plus a correction term (Fontes (1992) [117]). Here, the Mook model is provided using the notation of Plummer et al. (1994) [120], which is mathematically equivalent to the form given by Fontes and Garnier (1979) [116]).

$$\begin{aligned} A_{o\text{Mook}} = & N_{\text{CO}_2\text{aq}} A_{\text{CO}_2\text{aq}(o)} + 0.5(1 - N_{\text{CO}_2\text{aq}})(A_{\text{CO}_2\text{aq}(o)} + A_{\text{ls}(o)}) \\ & + (A_{\text{CO}_2\text{g}(o)}(1 - 2 \times 10^{-3} \varepsilon_{\text{gb}}) - 0.5(A_{\text{CO}_2\text{aq}(o)} + A_{\text{ls}(o)})) \\ & \times \frac{\delta^{13}\text{C} - N_{\text{CO}_2\text{aq}} \delta^{13}\text{C}_{\text{CO}_2\text{aq}(o)} - 0.5(1 - N_{\text{CO}_2\text{aq}})(\delta^{13}\text{C}_{\text{CO}_2\text{aq}(o)} + \delta^{13}\text{C}_{\text{ls}(o)})}{\delta^{13}\text{C}_{\text{CO}_2\text{g}(o)} - \varepsilon_{\text{gb}}(1 + 10^{-3} \delta^{13}\text{C}_{\text{CO}_2\text{g}(o)}) - 0.5(\delta^{13}\text{C}_{\text{CO}_2\text{aq}(o)} + \delta^{13}\text{C}_{\text{ls}(o)})} \end{aligned} \quad (4.34)$$

where

$N$  refers to the fraction of DIC represented by the subscripted species;  
the subscript o refers to the initial condition before isotope exchange;  
the subscript ls refers to limestone;  
and the subscript g refers to  $\text{CO}_2$  gas.

Values of the additive fractionation factors (isotopic enrichment factor),  $\varepsilon_{ij}$  are provided in the Appendix to Chapter 4.

### ***The Fontes and Garnier model***

Fontes and Garnier (1979) [116] (see also Fontes (1983) [115]; Fontes (1992) [117]) present the 'global exchange–mixing model in closed system' for estimation of  $A_o$ . This model considers the mixing of two end members, soil gas  $\text{CO}_2$  and solid carbonate mineral, which is accompanied by a partial

isotopic exchange in a closed system during the mixing. The isotopic exchange is assumed to occur between a part of the CO<sub>2</sub> gas and calcite solid in the system (Fig. 4.4), where  $q$  and  $q'$  are the moles of calcite and CO<sub>2(gas)</sub> that undergo complete isotopic exchange (with an isotopic enrichment factor,  $\epsilon$ , between CO<sub>2</sub> gas and calcite). The partial isotope exchange in <sup>13</sup>C (Fontes and Garnier (1979) [116]) is described by the following carbon isotope mass balance relations:

$$\delta_T C_T = (C_M - q)\delta_M + (C_T - C_M)\delta_g + q(\delta_g - \epsilon) \quad (4.35)$$

and

$$\delta_T C_T = C_M \delta_M + (C_T - C_M - q')\delta_g + q'(\delta_M + \epsilon) \quad (4.36)$$

where (retaining the notation of Fontes and Garnier (1979) [116])

$\delta$  is <sup>13</sup>C content in ‰;

$C$  refers to carbon;

$T, M, g$  refer to total, solid carbonate and gas, respectively;

$q$  is the moles of solid carbonate in isotopic equilibrium with a part of the soil gas CO<sub>2</sub>;

$q'$  is the moles of soil gas CO<sub>2</sub> in isotopic equilibrium with the solid carbonate;

$\epsilon$  is the isotopic enrichment factor (additive fractionation factor) between CO<sub>2</sub> gas and solid carbonate ( $\epsilon_{gc} = \delta_g - \delta_c$ ).

As  $q = -q'$ , the isotope exchange is shown by:

$$q = -q' = \frac{\delta_T C_T - C_M \delta_M - \delta_g (C_T - C_M)}{\delta_g - \epsilon - \delta_M} \quad (4.37)$$

where the sign of  $q$  indicates the direction of the exchange.

If  $q$  is positive, the isotopic exchange is dominated by gaseous CO<sub>2</sub>, as might apply to infiltration water in contact with sediment that is low in carbonate mineral content in the soil zone, unsaturated zone or near the water table. Calculated values of  $q$  that are less than zero imply that the isotopic exchange is dominated by solid carbonate mineral, as might be more common in the saturated zone. Both processes occur and the sign of  $q$  indicates which process predominates during the isotopic evolution.

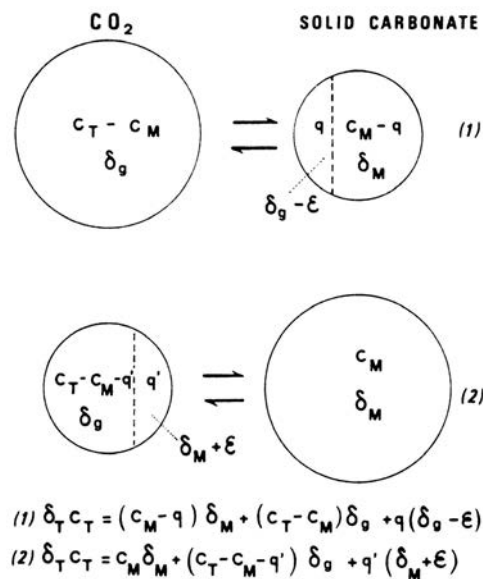


FIG. 4.4. The global exchange-mixing model in a closed system (Fontes (1983) [115]; Fontes and Garnier (1979) [116]).

In Fig. 4.4, cases 1 and 2 refer to exchange controlled by gaseous CO<sub>2</sub> of isotopic composition  $\delta_g$ , and solid carbonate (calcite) of isotopic composition  $\delta_M$ , respectively. The variables  $q$  and  $q'$  are the molalities of calcite and CO<sub>2(gas)</sub> that undergo complete isotopic exchange (with an enrichment factor  $\varepsilon$  between CO<sub>2</sub> and calcite).  $C_T$  and  $C_M$  are the molalities of DIC and DIC of mineral origin, respectively; this is taken from Fontes and Garnier (1979) [116].

The carbon isotope mass balance relations of Fig. 4.4 can be written for <sup>14</sup>C, prior to radioactive decay, so that  $A_o$  is:

$$A_o C_T = C_M A_M + (C_T - C_M) A_g + q(A_g - 0.2\varepsilon - A_M) \quad (4.38)$$

where

$A$  is the <sup>14</sup>C pmc value;

$\varepsilon^{14}\text{C}(\%) \cong 0.2 \varepsilon^{13}\text{C}(\text{‰})$  (see Craig (1954) [143] and the Appendix to Chapter 4).

In developing their model, Fontes and Garnier (1979) [116] apply a chemical mass balance similar to that of the Tamers model, with provision for base exchange (Ca/Na cation exchange) and gypsum dissolution to estimate the mass of carbon dissolved from inorganic sources,  $C_M$ . Fontes (1992) [117] shows that the Fontes and Garnier (1979) [116] model reduces to the Tamers model if there is no isotopic exchange ( $k = 0$ ):

$$A_{oF-G} = A_{oTamers} + k \quad (4.39)$$

or

$$A_{oF-G} = \left(1 - \frac{C_M}{C_{DIC}}\right) A_{CO_2g} + \frac{C_M}{C_{DIC}} A_M + k \quad (4.40)$$

where

$C_M$  is the moles of carbon from carbonate mineral dissolution;

$C_{DIC}$  is the moles of total DIC in the groundwater sample;

$A_{CO_2g}$  is the <sup>14</sup>C value of CO<sub>2</sub> gas;

$A_M$  is the average <sup>14</sup>C pmc value of the carbonate minerals dissolving;

and

$$k = \left( A_{CO_2g} - 0.2\varepsilon_{i-j} - A_M \right) \left( \frac{\delta^{13}C_{DIC} - \frac{C_M}{C_{DIC}} \delta^{13}C_M - \left(1 - \frac{C_M}{C_{DIC}}\right) \delta^{13}C_{CO_2g}}{\delta^{13}C_{CO_2g} - \varepsilon_{i-j} - \delta^{13}C_M} \right) \quad (4.41)$$

where  $\varepsilon_{i-j}$  refers to the additive fractionation factor (also referred to as the isotopic enrichment factor; see Appendix to Chapter 4) between species  $i$  and  $j$ .

In using the model of Fontes and Garnier (1979) [116],  $k$  is first solved by using the additive fractionation factor,  $\varepsilon_{CO_2g-HCO_3^-}$  ( $\cong \delta^{13}C_{CO_2g} - \delta^{13}C_{HCO_3^-}$  at isotopic equilibrium). If  $k$  is positive, then the exchange is primarily between CO<sub>2(gas)</sub> and HCO<sub>3</sub><sup>-</sup>, and  $A_o$  is calculated by using the value of  $k$  based on  $\varepsilon_{CO_2g-HCO_3^-}$ . If  $k$  is negative, the reaction is dominated by isotopic exchange between calcite and bicarbonate, and the additive fractionation factor is replaced with the value of  $\varepsilon_{calcite-HCO_3^-}$  (Appendix to Chapter 4), ( $\cong \delta^{13}C_{calcite} - \delta^{13}C_{HCO_3^-}$  at isotopic equilibrium).

In application to recharge waters, the model of (Fontes and Garnier (1979) [116]) often yields quite reasonable estimates of  $A_o$ , but it is sensitive to values of  $\delta^{13}C$  of soil gas CO<sub>2</sub>, which are often not

available. Therefore, several models are available in NETPATH to estimate the  $\delta^{13}\text{C}$  of soil gas  $\text{CO}_2$ , as described below.

#### 4.2.1.3. Models to estimate the $\delta^{13}\text{C}$ of soil gas $\text{CO}_2$

The models of Ingerson and Pearson, Evans, IAEA, Mook, Fontes and Garnier, and Eichinger all require a definition of  $\delta^{13}\text{C}$  of soil gas  $\text{CO}_2$ . In the absence of measurement, several models were implemented in NETPATH (Plummer et al. (1994) [120]) to estimate values of  $\delta^{13}\text{C}$  of soil gas  $\text{CO}_2$ . These are: (i) user defined; (ii) closed system mass balance without fractionation; (iii) a two-step process in which the mass balance is solved by assuming that  $\text{CO}_2$  gas dissolved into the initial water maintaining isotopic equilibrium with the dissolved  $\text{CO}_2$  (aq) (open system), followed by carbonate dissolution in a closed system; and (iv) a complete open system in which the  $\delta^{13}\text{C}$  of soil gas  $\text{CO}_2$  is calculated corresponding to isotopic equilibrium with the chemical and isotopic composition of the initial solution.

##### **Model 1**

Model 1, ‘user defined’, is used if  $\delta^{13}\text{C}$  measurements of soil gas  $\text{CO}_2$  are available or if there is climatic evidence that the palaeo- $\delta^{13}\text{C}$  of soil gas  $\text{CO}_2$ , at the time the water sample was recharged, differed from today.

##### **Model 2**

Model 2 solves a carbon isotope mass balance without isotopic fractionation for the case of dissolution of  $\text{CO}_2$  gas, calcite, dolomite and gypsum:

$$\delta^{13}\text{C}_{\text{CO}_2, \text{aq}(o)} = \frac{\delta^{13}\text{C}_{\text{DIC}} C_{\text{DIC}} - \Delta_{\text{calcite}} \delta^{13}\text{C}_{\text{calcite}} - 2\Delta_{\text{dolomite}} \delta^{13}\text{C}_{\text{dolomite}}}{\Delta_{\text{CO}_2\text{g}}} \quad (4.42)$$

and

$$\delta^{13}\text{C}_{\text{CO}_2, \text{g}(o)} \equiv \delta^{13}\text{C}_{\text{CO}_2, \text{aq}(o)} \quad (4.43)$$

##### **Model 3**

Model 3 solves the same carbon isotope mass balance as in model 2, but assumes that the dissolved  $\text{CO}_2$  is in isotopic equilibrium with the soil gas:

$$\delta^{13}\text{C}_{\text{CO}_2, \text{g}(o)} \equiv \delta^{13}\text{C}_{\text{CO}_2, \text{aq}(o)} + \varepsilon_{\text{CO}_2\text{g}-\text{CO}_2, \text{aq}} \quad (4.44)$$

Model 3 applies to recharge through an unsaturated zone devoid of carbonate minerals, followed by subsequent carbonate mineral dissolution in the saturated zone (closed system dissolution).

##### **Model 4**

Model 4 assumes that the recharge water evolved under open system conditions:

$$\delta^{13}\text{C}_{\text{CO}_2, \text{g}(o)} \equiv \delta^{13}\text{C}_{\text{DIC}} + \varepsilon_{\text{CO}_2\text{g}-\text{s}} \quad (4.45)$$

where  $\varepsilon_{\text{CO}_2\text{g}-\text{s}}$  is the pH dependent isotopic enrichment factor between  $\text{CO}_2$  gas and the DIC of the aqueous solution (see Wigley et al. (1978) [136] and the Appendix to Chapter 4). Models 3 and 4 tend to be the most realistic. Model 4 can apply, among other scenarios, to semi-arid regions with low recharge rates through carbonate bearing unsaturated zones.

#### 4.2.1.4. Summary of traditional adjustment models

Table 4.1 lists geochemical processes included in the better known traditional adjustment models.

Several studies have carefully documented differences between the various traditional adjustment models by using examples (Fontes (1992) [117]; Plummer and Sprinkle (2001) [135]). Fontes (1992) [117] compared calculated and measured  $^{14}\text{C}$  content in DIC for a series of unsaturated zone waters that recharge a chalk aquifer. Model calculations of  $A_0$  from Tamers (1975) [134], Evans et al. (1979) [131], Fontes and Garnier (1979) [116], the IAEA (Salem et al. (1980) [141]), Ingerson and Pearson Jr. (1964) [132], Eichinger (1983) [130] and Mook (1972) [133] were compared to the measured  $^{14}\text{C}$  profile. The measured  $^{14}\text{C}$  content of DIC decreased from 117.5 pmc at a 2 m depth through the unsaturated zone to 67.1 pmc at a 20 m depth. The models most successful at estimating the initial  $^{14}\text{C}$  value at a 20 m depth and, thus, most representative of recharge waters, were those of Eichinger (71.5 pmc), Evans (75.5 pmc), Fontes and Garnier (77.1 pmc), and Ingerson and Pearson (77.2 pmc).

Plummer and Sprinkle (2001) [135] compared adjusted  $^{14}\text{C}$  model ages of DIC in 25 water samples from the Floridan aquifer, FL, USA, based on the models of Tamers (1975) [134], Ingerson and Pearson Jr. (1964) [132], Mook (1972) [133], Eichinger (1983) [130], and Fontes and Garnier (1979) [116], with the unadjusted  $^{14}\text{C}$  model age (Eq. (4.3), where  $A_{\text{nd}} \equiv 100$  pmc). As expected, the adjusted  $^{14}\text{C}$  model ages were always younger than the unadjusted  $^{14}\text{C}$  model age. Relatively small differences (typically less than 10%) in adjusted  $^{14}\text{C}$  model age based on these traditional adjustment models were found when applied to the waters of the Floridan aquifer. However, Plummer and Sprinkle (2001) [135] demonstrated that the traditional adjustment models did not account for the observed enrichment in  $\delta^{13}\text{C}$  of DIC in many of the more geochemically evolved groundwater samples. As a result, more complex adjustment models that included redox reactions, mixing with saline water, and carbonate mineral recrystallization were constructed by using NETPATH (see examples in Section 4.7.2).

TABLE 4.1. SUMMARY OF GEOCHEMICAL REACTIONS INCLUDED IN SELECTED TRADITIONAL  $A_0$  ADJUSTMENT MODELS

Process	$A_0$ model <sup>a</sup>									
	Conventional $^{14}\text{C}$ age:	Vogel	Tamers	Mass balance	Pearson	IAEA	Mook	Evans	Eich- inger	Fontes and Garnier
Carbonate dissolution			×	×	×	×	×	×	×	×
Soil gas $\text{CO}_2$ dissolution			×	×	×	×	×	×	×	×
$\text{CO}_2$ gas– aqueous exchange						×	×			×
Calcite– $\text{HCO}_3^-$ exchange								×	×	×
Gypsum dissolution				×						×
Ca/Na cation exchange										×

<sup>a</sup> See above text for references and discussion of each model.

Selection of the most appropriate adjustment model depends on which models most completely account for the geochemical processes affecting the chemical and isotopic composition of the waters. The model of Fontes and Garnier (1979) [116] is the most geochemically complete of the traditional adjustment models and often yields estimates of  $A_0$  that are reasonable in aquifers undergoing relatively common inorganic geochemical reactions (Table 4.1). However, the model of Fontes and Garnier (1979) [116], as well as several other traditional adjustment models, depends on knowing the  $\delta^{13}\text{C}$  value of unsaturated zone  $\text{CO}_2$  in the recharge area. This can be estimated from the observed or postulated value of DIC  $\delta^{13}\text{C}$  in the recharge area by using soil gas  $\text{CO}_2$  models 3 or 4 (see Section 4.2.1.3), which usually bound the range of soil gas  $\text{CO}_2$   $\delta^{13}\text{C}$  values. Alternatively, attention should be paid to palaeoclimatic conditions in the recharge area and possible changes in  $\text{C}_3$  abundance relative to  $\text{C}_4$  plants.

As a general rule, it is best to apply the traditional adjustment models only to waters in recharge areas to estimate the pre-bomb value of  $A_0$  in a recharge zone. Waters in recharge areas tend to be the least geochemically evolved and most suitable for estimation of  $A_0$  using the traditional adjustment models. More sophisticated geochemical corrections, such as those provided by NETPATH, discussed below, can clarify the evolution of recharge water into observed palaeowater. This process leads to the further geochemical adjustment of  $A_0$ , accounting for more complex geochemical reactions occurring in the aquifer that are not accounted for in traditional adjustment models. It leads to the final adjusted value of  $A_0$ , denoted  $A_{\text{nd}}$  (Eq. (4.3)), and often to improved estimates of the adjusted  $^{14}\text{C}$  model age.

#### 4.3. SUMMARY OF PREDOMINANT GEOCHEMICAL REACTIONS IN GROUNDWATER SYSTEMS AFFECTING INTERPRETATION OF RADIOCARBON AGE

Many more geochemical and isotopic reactions occur in groundwater systems that are not considered by any of the traditional adjustment models. The most important of these pertain to the presence of organic carbon, either as  $^{14}\text{C}$ -bearing DOC in recharge waters and/or as a reactant in redox reactions that are driven by the oxidation of (usually  $^{14}\text{C}$ -‘dead’) organic carbon buried in aquifer sediment. In the first case, DOC in recharge waters is usually oxidized microbially to bicarbonate in the aquifer, adding to the initial  $^{14}\text{C}$  concentration; failure to include initial DOC (and its  $^{14}\text{C}$  content) leads to adjusted radiocarbon ages that are too young. In the second case, old organic carbon is oxidized in the aquifer, which dilutes the  $^{14}\text{C}$  reservoir, and if not accounted for, the adjusted age is too old. Commonly occurring redox reactions involving organic carbon in aquifers include oxygen reduction, nitrate reduction, manganese reduction, iron reduction, sulphate reduction and methanogenesis (see, for example, McMahon and Chapelle (2008) [144]). Each of these redox reactions adds carbon to the DIC concentration derived from organic sources.

Other common reactions, such as de-dolomitization (Plummer et al. (1990) [145]) or weathering of feldspars cause precipitation of calcium carbonate, which involves an isotopic fractionation affecting both  $^{13}\text{C}$  and  $^{14}\text{C}$ . Although the Fontes and Garnier model includes Ca/Na cation exchange, there are many other types of cation exchange that occur in groundwater. The most important of these involve the uptake of magnesium for sodium (Plummer et al. (1990) [145]) or the release of protons from organic matter in exchange for sodium (proton exchange) (Appelo (1994) [146]; Plummer et al. (1994) [120]). Uptake of magnesium and/or calcium on exchangers, such as clay minerals, permits additional dissolution of carbonate minerals (calcite and/or dolomite), which dilutes the  $^{14}\text{C}$  reservoir. If not corrected for cation exchange, the ‘adjusted’  $^{14}\text{C}$  model age is too old. In the case of proton exchange, calcium and magnesium are taken up on organic matter, presumably releasing both protons and sodium ions. The released protons react with old carbonates, if present, diluting the  $^{14}\text{C}$  reservoir and, again, if not accounted for, the ‘adjusted’  $^{14}\text{C}$  model age is too old. A list of important geochemical reactions and processes that can affect interpretation of  $^{14}\text{C}$  model age, but are not entirely accounted for by the application of ‘traditional’ adjustment models, is provided in Table 4.2. An even deeper appreciation for the complexity of radiocarbon dating in groundwater systems is gained when one realizes that

TABLE 4.2. SUMMARY OF SELECTED CHEMICAL AND PHYSICAL PROCESSES IN GROUNDWATER SYSTEMS AFFECTING INTERPRETATION OF RADIOCARBON AGE (in addition to those listed in Table 4.1)

Process/reaction	Resulting water type	Effect on $\delta^{13}\text{C}$	Effect on $^{14}\text{C}$	Effect on unadjusted age
Dissolution of calcite and dolomite (marine carbonates)	Ca-Mg-HCO <sub>3</sub>	Increase in $\delta^{13}\text{C}$ ; isotope dilution	Decrease in $^{14}\text{C}$ ; isotope dilution	Old bias
CaSO <sub>4</sub> dissolution (not a carbon source), calcite precipitation	Ca-SO <sub>4</sub> -HCO <sub>3</sub>	Small decrease in $\delta^{13}\text{C}$ as $^{13}\text{C}$ is enriched in calcite cement; isotope fractionation	Small decrease in $^{14}\text{C}$ of DIC as $^{14}\text{C}$ is enriched in calcite cement; isotope fractionation	Old bias
CaSO <sub>4</sub> dissolution (not a carbon source), dolomite dissolution and calcite precipitation; de-dolomitization	Ca-Mg-SO <sub>4</sub> -HCO <sub>3</sub>	Increase in $\delta^{13}\text{C}$ if dolomite enriched in $^{13}\text{C}$ , also slightly opposite trend from calcite cement formation; isotope fractionation	Decrease in $^{14}\text{C}$ ; isotope dilution; isotope fractionation	Old bias
Ca/Na exchange, Mg/Na exchange, proton exchange (carbonate dissolution)	Na-HCO <sub>3</sub>	Increase in $\delta^{13}\text{C}$ ; isotope dilution	Decrease in $^{14}\text{C}$ ; isotope dilution	Old bias
Recrystallization of calcite (aragonite, Mg-calcites); isotopic exchange (calcite)	No change (increase in Sr, Mg from aragonite and Mg calcite)	Increase in $\delta^{13}\text{C}$ ; isotope exchange	Decrease in $^{14}\text{C}$ ; isotope exchange	Old bias
Oxidation of organic matter: Fe reduction (FeOOH)	Increase in Fe <sup>2+</sup> and HCO <sub>3</sub>	Decrease in $\delta^{13}\text{C}$ ; isotope dilution	Decrease in $^{14}\text{C}$ ; isotope dilution	Old bias
Oxidation of organic matter; sulphate reduction (pyritization)	Decrease in SO <sub>4</sub> , possible increase in H <sub>2</sub> S, decrease in Fe <sup>2+</sup>	Decrease in $\delta^{13}\text{C}$ ; isotope dilution	Decrease in $^{14}\text{C}$ ; isotope dilution	Old bias
Fermentation of organic matter; methanogenesis	Increase in CH <sub>4</sub> and CO <sub>2</sub>	Increase in $\delta^{13}\text{C}$ of CO <sub>2</sub> , depleted CH <sub>4</sub> ; isotope dilution	Decrease in $^{14}\text{C}$ ; isotope dilution	Old bias
Dissolution of plagioclase feldspar; dissolution of other primary silicates (calcite precipitation)	Na-Ca-HCO <sub>3</sub>	Small decrease in $\delta^{13}\text{C}$ as $^{13}\text{C}$ is enriched in calcite cement; isotope fractionation	Small decrease in $^{14}\text{C}$ as $^{14}\text{C}$ is enriched in calcite cement; isotope fractionation	Minor or none

Leakage of saline waters (may cause carbonate dissolution)	Na-Cl	Small increase in $\delta^{13}\text{C}$ ; isotope dilution	Small decrease in $^{14}\text{C}$ ; isotope dilution	Old bias
Leakage or exchange with aquitards; diffusion, matrix diffusion	Multiple	Variable	Decrease in $^{14}\text{C}$ ; isotope dilution	Old bias
Addition of $\text{CO}_2$ of magmatic origin (geogenic $\text{CO}_2$ )	Multiple	Generally enriched in $\delta^{13}\text{C}$ , range from $-2$ to $-6\text{‰}$	Decrease in $^{14}\text{C}$ ; isotope dilution	Old bias
Warming along a geothermal gradient; calcite dissolution (closed system)	Small increase in $\text{Ca}^{2+}$ and $\text{HCO}_3^-$	Small increase in $\delta^{13}\text{C}$ ; isotope dilution	Small decrease in $^{14}\text{C}$ ; isotope dilution	Old bias
Increase in hydrostatic pressure with depth; calcite dissolution	Small increase in $\text{Ca}^{2+}$ and $\text{HCO}_3^-$	Small increase in $\delta^{13}\text{C}$ ; isotope dilution	Small decrease in $^{14}\text{C}$ ; isotope dilution	Old bias
Evapotranspiration	Increase in all solutes in proportion to original water	None	None	None

multiple reactions and processes, such as those listed in Table 4.2, often occur together or in sequence along flow paths in aquifers.

#### 4.4. GENERALIZED GEOCHEMICAL ADJUSTMENT MODELS

Wigley et al. (1978) [136] and Wigley et al. (1979) [147] describe the chemical and isotopic evolution of inorganic carbon in groundwater by the differential equations:

**Carbon mass balance**

$$d(m_{\text{DIC}}) = \sum_{i=1}^N dI_i - \sum_{i=1}^M dO_i \quad (4.46)$$

**Carbon isotope mass balance**

$$d(Rm_{\text{DIC}}) = \sum_{i=1}^N R^* dI_i - \sum_{i=1}^M R\alpha_{i-s} dO_i \quad (4.47)$$

where

- $R$  is the isotope ratio;
- $m_{\text{DIC}}$  is the molality of DIC;
- $I$  and  $O$  refer to incoming and outgoing moles of carbon, such as through dissolution and precipitation, respectively;
- $N$  and  $M$  are the total number of incoming and outgoing phases;
- $i$  refers to the  $i$ th carbon-bearing phase;
- superscript \* refers to the incoming phases;
- $\alpha_{i-s}$  is the fractionation factor between the  $i$ th phase and the aqueous solution (adjusted for pH effects on the distribution of inorganic carbon species in solution; see Appendix to Chapter 4).

Analytical solutions to the two differential equations, in the form of Rayleigh distillation processes, were derived by Wigley et al. (1978) [136] and Wigley et al. (1979) [147] for the cases shown in Table 4.3.

The analytical solutions to the isotope evolution problem assume constant relative rates of reaction along the evolutionary flow path from the initial to the final condition. Thus, the ratio of incoming to outgoing moles of carbon is assumed to be constant along the flow path and, in its implementation

TABLE 4.3. SUMMARY OF ANALYTICAL SOLUTIONS TO RAYLEIGH DISTILLATION MODELS<sup>a</sup>

		Number of fractionating outputs			
		0	1	2	M
Number of inputs	0		×	×	
	1	×	×	×	
	2	×			
	N				NETPATH

<sup>a</sup> X: analytical solution in Wigley et al. (1978) [136] and Wigley et al. (1979) [147]. N and M refer to the total number of incoming and outgoing carbon-bearing phases, respectively.

in NETPATH, equal to that calculated from the net mass transfer for any particular model solved in the mass balance problem. Although the net mass transfer is determined by using inverse modelling techniques, as in NETPATH, the relative rates of reaction may vary along flow paths in groundwater systems. In application of the Wigley et al. equations to groundwater systems, it is also assumed that fractionation factors,  $\alpha_{i-s}$ , are constant over the path of the reaction, and that a single value applies for each, even though pH can vary on the path. Although not exhaustive, Wigley et al. (1978) [136] and Plummer et al. (1983) [148] have shown that for some common geochemical reactions in groundwater systems, the modelled isotopic composition is not particularly sensitive to uncertainties in relative rates of reaction and variations in  $\alpha_{i-s}$  along the reaction path.

NETPATH (Plummer et al. (1994) [120]) uses equations of chemical mass balance, electron balance and isotope mass balance to define all possible net geochemical reactions between the analysed initial and final water compositions along a flow path. As pairs of samples that occur along a specific flow path in an aquifer cannot always be identified, representative initial water compositions can be constructed through the simulation of geochemical reactions by using computer codes such as PHREEQC (Parkhurst and Appelo (1999) [149]); alternatively, waters in the recharge zone that apply to other flow paths can be selected if they can be assumed to be representative of initial conditions. The geochemical reactions are constrained to occur among reactant and product minerals and gases for the system, and to be consistent with the observed mineralogy, chemical and isotopic data of the aquifer and groundwater system.

Having found all of the possible geochemical reactions that can account for the chemical and isotopic constraints, NETPATH (Plummer et al. (1994) [120]) solves the chemical reaction as a forward isotope evolution model, using the general case of N non-fractionating inputs (dissolving carbonate phases) and M fractionating outputs (precipitation carbonate phases) (Wigley et al. (1978) [136]; Wigley et al. (1979) [147]). For each simulation, NETPATH calculates the  $^{14}\text{C}$  pmc value of TDC (TDC = DIC + DOC +  $\text{CH}_4$ ), in the final water. NETPATH can be used to construct  $^{14}\text{C}$  adjustment models for a wide range of geochemical systems, including those considered in the ‘traditional’ adjustment models and many more systems that cannot be treated by previous DIC adjustment models. The approach is diagrammed in Fig. 4.5.

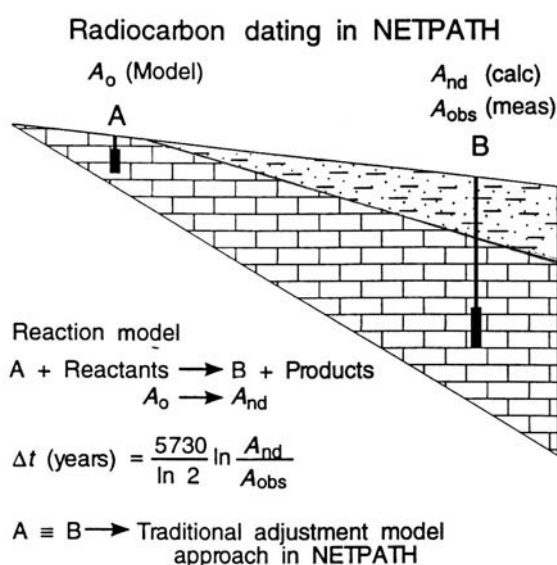


FIG. 4.5. Conceptualization of radiocarbon dating of dissolved inorganic carbon (or total dissolved carbon, TDC) in NETPATH (from Plummer and Sprinkle (2001) [135]).

By combining carbon mass balance equations with Rayleigh distillation equations for all incoming carbon sources and all isotopically fractionating outgoing carbon phases, the initial  $^{14}\text{C}$  ( $A_o$ ) is adjusted for the modelled geochemical reactions (Fig. 4.5). Two evolutionary waters are selected in Fig. 4.5: the initial, A, and final, B. A and B are typically on a flow path but are only required to be representative of evolutionary pairs.  $A_o$  is modelled, measured or estimated in water from the initial well. NETPATH constructs geochemical adjustment models to estimate the  $^{14}\text{C}$  content of TDC in water from well B, without radioactive decay,  $A_{\text{nd}}$ . The piston flow travel time between A and B is calculated from the decay equation (Eq. (4.4)).

NETPATH includes most of the well known adjustment models described above, which can be applied to the initial water to obtain estimates of  $A_o$ . In radiocarbon dating of DIC in groundwater using NETPATH, the ‘traditional’ adjustment models are usually applied to the initial water only; in the recharge portions of aquifers, the geochemical reactions may be less complex than those further down gradient. Application of models to the initial water is useful in defining  $A_o$  in recharge areas where the  $^{14}\text{C}$  content of DIC has not been measured or is contaminated with fractions of post-nuclear detonation  $^{14}\text{C}$ .

Alternatively, NETPATH can be used to reconstruct the isotopic composition of the initial water by considering a reaction path beginning with precipitation that is in equilibrium with atmospheric  $\text{CO}_2$ , which subsequently reacts in open (or closed) systems with soil gas  $\text{CO}_2$  and reactive minerals in the recharge zone. In this case, the initial water chemical composition is solved by using forward simulation models such as PHREEQC.

In general use, the initial and final waters are defined separately in NETPATH. NETPATH is then used to describe the geochemical reactions that reproduce the chemical and  $\delta^{13}\text{C}$  isotopic composition of DIC in the final water. This approach develops a separate adjustment model for each water analysis. The adjustment is applied to the initial  $^{14}\text{C}$  to compute the  $^{14}\text{C}$  expected in DIC (or TDC) at the final well in the absence of radioactive decay,  $A_{\text{nd}}$  (Fig. 4.5). The adjusted ‘no decay’  $^{14}\text{C}$  pmc value is then used with the measured  $^{14}\text{C}$  pmc value to compute the apparent piston-flow travel time from the initial to the final point. Further details of radiocarbon dating applications in NETPATH are provided in Plummer et al. (1994) [120].

#### 4.5. TOTAL DISSOLVED CARBON

Radiocarbon dating is usually only applied to the DIC of a system. None of the ‘traditional’ adjustment models described above allow for the presence of DOC. All carbon isotopic calculations in NETPATH are made in terms of TDC ( $\text{TDC} = \text{DIC} + \text{DOC} + \text{CH}_4$ ). For consistency with this definition of TDC, it is necessary to change the values of  $A_o$  calculated from the above inorganic models to the following:

$$A_{o\text{TDC}} = \frac{A_{o\text{DIC}}m_{\text{DIC}} + {}^{14}\text{C}_{\text{DOC}}m_{\text{DOC}} + {}^{14}\text{C}_{\text{CH}_4}m_{\text{CH}_4}}{m_{\text{TDC}}} \quad (4.48)$$

where

DOC is dissolved organic carbon;  
and  $m$  is molality.

If the concentrations of DOC and  $\text{CH}_4$  are zero in the initial solution, then  $A_o$  is defined identically to the above described inorganic carbon  $A_o$  models. If DOC and/or  $\text{CH}_4$  are present in the water to be  $^{14}\text{C}$  dated, their concentrations and  $^{13}\text{C}$  and  $^{14}\text{C}$  isotopic composition must be defined.

Special treatment is needed in NETPATH in defining the  $^{13}\text{C}$  and  $^{14}\text{C}$  composition of TDC. First, the carbon isotope fractionation factors, which are defined for inorganic carbon species, are calculated relative to TDC by using measured or defined values of the carbon isotopic composition of DOC and

CH<sub>4</sub> (Plummer et al. (1994) [120]) (see the Appendix to Chapter 4). If DOC and/or CH<sub>4</sub> are present, NETPATH computes the average <sup>14</sup>C model age of TDC. In NETPATH, DOC represents the sum of the moles of carbon (expressed in millimoles of carbon per kilogram of H<sub>2</sub>O) of all of the dissolved organic species.

It is usually not possible to identify all of the individual DOC species that make up DOC. Similarly, it is difficult to determine the <sup>13</sup>C and <sup>14</sup>C content and oxidation state of carbon in individual organic species in solution. Considering these uncertainties, NETPATH accepts an average <sup>13</sup>C and <sup>14</sup>C content, and average oxidation state of carbon for the total DOC. If it is known, for example, from laboratory experiments that one or several of the dissolved organic species that make up the total DOC are reactive, more realistic models would be obtained by using data specific to the reactive species.

#### 4.6. GEOCHEMICAL MASS TRANSFER MODELS

By using charge balance constraints and mass balance constraints on chemical, redox and isotopic constituents, inverse geochemical modelling helps eliminate reaction hypotheses that are inconsistent with chemical and isotopic observations, and can point to additional data needs that are critical to resolution of the problem. Typically, inverse geochemical modelling leads to multiple hypotheses, also known as reaction model solutions or sets of reactions, that may explain the observations and hopefully improve the conceptualization of groundwater flow and geochemical evolution in the system (Parkhurst and Plummer (1993) [150]; Plummer et al. (1983) [148]). When applied to radiocarbon dating of DIC in groundwater, the modelling, though non-unique, can place constraints on the calculated tracer model age of the waters. Several approaches have been taken to address geochemical model uncertainty.

Pearson (1992) [151] combined geochemical mass balance modelling with radiocarbon dating to generate a distribution of possible <sup>14</sup>C model ages considering the non-unique nature of the modelling process. Parkhurst developed an inverse modelling capability in PHREEQC that considers the uncertainty in chemical data (Parkhurst (1995) [152]; Parkhurst (1997) [153]; Parkhurst and Appelo (1999) [149]). This uncertainty can be related to the analytical uncertainty of a particular sample or to the variability of analyses for a series of samples that should represent a particular water. Although PHREEQC does not treat radiocarbon dating in a general way, it can adjust an initial <sup>14</sup>C content for all of the possible geochemical reactions in the system, and, in principle, lead to an estimation of the range of <sup>14</sup>C model ages consistent with all of the chemical and isotopic data. As the generally available version of PHREEQC does not calculate fractionation factors as a function of solution composition, average isotopic compositions of precipitating or exsolving phases need to be calculated and entered manually. PHREEQC also produces what are called ‘minimal models’ within the inverse modelling mode. Minimal models are geochemical mass balance reaction models that include only reactants and products that, within the uncertainty in the chemical and isotopic data, must be included to account for the observed chemical and isotopic data.

Glynn and Brown (2012) [154] propose the combined use of inverse geochemical modelling using codes such as NETPATH or PHREEQC (in inverse modelling mode) and forward modelling (e.g. using PHREEQC or other codes) as an efficient way to conceptualize the geochemical evolution of groundwater systems. Inverse geochemical modelling helps identify the key geochemical reaction possibilities that can explain observed field data. The possibilities considered by inverse geochemical modelling include the possible ‘mixing’ or contributions of water and solutes converging (or diffusing) from various confining and transmissive zones (or surface water bodies) to form the ‘final’ groundwater sample collected for analysis. NETPATH and PHREEQC require that specific ‘initial’ water compositions be defined, as opposed to having a continuum of solution compositions, to represent this mixing process. Following inverse geochemical modelling and the determination of possible reaction and ‘mixing’ processes, forward ‘predictive’ modelling can be used: (i) to estimate the relative movements of reaction fronts, water and solutes; (ii) to assess the degree to which the groundwater system can be considered to be at a chemical steady state for the purpose of inverse modelling and radiocarbon

dating with NETPATH; and (iii) to determine whether the mass transfers and  $^{14}\text{C}$  model ages calculated through inverse modelling are reasonable given the hydrogeochemist's knowledge of hydrological processes (flow rates as well as dispersive and diffusive mixing), reaction kinetics, mineral abundances, and the availability of surfaces and exchange capacities for sorption. Generally, the combined use of inverse and forward geochemical modelling will result in a better understanding of the essential data requirements; additional data and field observations are needed to improve the understanding of a groundwater system (Glynn and Plummer (2005) [15]). An iterative, progressively more informed process of data collection based on inverse and forward geochemical modelling, although not always practical, can provide an efficient framework for investigating groundwater systems.

NETPATH and PHREEQC (in inverse modelling mode) have many complementary capabilities, which may often argue for both codes being used together in trying to estimate a  $^{14}\text{C}$  model age. PHREEQC has the advantage of being able to consider uncertainties in 'initial' and 'final' solution compositions, as well as some additional mass and charge balance constraints (such as balances on individual valence states for various elements, water mole balance, individual solution charge balances, alkalinity balance) beyond those considered by NETPATH. NETPATH has the major advantage of solving the Wigley et al. (1978) [136] and Wigley et al. (1979) [147] isotope evolution equations, automatically (or manually if desired), calculating the relevant isotopic compositions of exsolving or precipitating phases, and allowing the straightforward calculation of  $^{14}\text{C}$  geochemical dilution adjustments (and  $A_0$  estimates following classical adjustment models). PHREEQC does not currently (2010) have these capabilities. Thorstenson and Parkhurst (2004) [155], however, calculated thermodynamically rigorous individual isotope equilibrium constants for common geochemical reactions and isotopes, and PHREEQC may eventually allow some automatic calculation of isotopic composition of exsolving phases in its forward modelling mode. PHREEQC forces mass balance constraints on all of the elements and redox states represented by given mineral reactions; in contrast, NETPATH allows one to use a subset of elemental and isotopic constraints. For a given set of aqueous solutions and chemical reactions postulated by the modeller and given uncertainty limits provided for various chemical and isotopic constituents (and pH) for each solution, PHREEQC will adjust 'initial' and 'final' solution compositions to satisfy individual solution charge imbalances, while minimizing the adjustments made. Similar to NETPATH, PHREEQC will also calculate all of the possible sets of reaction mass transfers and solution mixtures that can explain the evolution of the 'initial' waters into a 'final' water composition.

The modeller could combine the advantages of both codes through an iterative inverse modelling process: (i) using PHREEQC to calculate adjusted 'initial' and 'final' solution compositions; (ii) entering the adjusted solutions (and postulated reactions) in NETPATH; (iii) running NETPATH to calculate the isotopic compositions of exsolving or precipitating phases; (iv) entering those isotopic phase constraints back into PHREEQC; and (v) calculating new adjusted solutions in PHREEQC and iterating in this fashion until a suitable set of NETPATH reaction models is obtained with a reasonable  $^{14}\text{C}$  model age calculation. A new version of NETPATH, NetpathXL (Parkhurst and Charlton (2008) [156]) allows for the efficient combined use of a spreadsheet input data file for both codes, with minimal adjustment required to use either code. When developing inverse models in PHREEQC, there is an option to write all of the solution data as defined into a .lon file that can be read by NetpathXL. In addition, there is an option to write one .pat file and multiple .mod files (one for each model), which can be read by NetpathXL. The .pat file contains the solution compositions as adjusted by the inverse model, so it should be possible to run the exact PHREEQC model in NetpathXL to explore isotope compositions and  $^{14}\text{C}$  model ages. Recently, the IAEA developed a Windows based version of NETPATH (NETPATH-WIN and DB-WIN) that also permits spreadsheet input of data (El-Kadi et al. (2011) [157]).

Some of the modelling efforts and concepts described above were the focus of previous research efforts. Pearson (1992) [151] considered early on the possible effects of analytical uncertainties on the radiocarbon dating of groundwaters. In his approach to the issue, Pearson used a spreadsheet version of BALANCE (Parkhurst et al. (1982) [158]), a precursor code to NETPATH and a commercial

software code to automatically run a Monte Carlo distribution of a spectrum of inverse model simulations (with changing input solution compositions), and thereby obtain a range of  $^{14}\text{C}$  model ages. Cheng and Long (1984) [159] programmed a carbon isotope subroutine for the forward modelling code, PHREEQE (Parkhurst et al. (1980) [160]), that allowed for the simulation of chemical and carbon isotopic compositions along a postulated reaction path. Phillips et al. (1989) [39] used this capability in their investigation of radiocarbon dating for groundwater in the San Juan Basin of New Mexico. It is anticipated that many new numerical simulation tools will be developed in the future for the investigation of tracer model ages, following on these early starts and building on our current capabilities.

#### **4.6.1. Some practical precautions and special cases in geochemical mass balance modelling**

Inverse models (mass balance models) such as those produced in NETPATH and PHREEQC are combinations of masses of minerals and gases that must enter and/or leave (dissolve or precipitate) the initial water as it evolves chemically (and isotopically) to the final water. Each combination of phases and associated masses is a model, and exactly accounts for the change in moles of each element or isotope (selected as constraints) in the model between initial and final water. The model may include mixing with multiple waters in addition to calculated mass transfer and evaporation. As electrical neutrality is assumed, errors result if mass balance models are constructed between initial and final waters that do not balance in charge. This is particularly critical in radiocarbon dating in systems in which oxidation of organic carbon is considered. As phases are electrically neutral combinations of cations and anions, charge imbalance in the mass balance is (mathematically) left to the phases in the model that are not combinations of cations and anions, such as  $\text{CO}_2$ ,  $\text{CH}_2\text{O}$  (a simplified formula for organic carbon of oxidation state zero) and  $\text{CH}_4$ . NETPATH has an option that, prior to solving the mass balance models, distributes the charge imbalance in proportion to the equivalents of cations and anions in initial and final waters. PHREEQC attains electrical neutrality through the adjustment of pH or the concentration of a selected ion. In general, it is best to construct geochemical models with complete chemical analyses.

Inverse geochemical models are not constrained by thermodynamics. Some models may be found that indicate dissolution of one or more phases for which thermodynamic analysis indicates the waters are oversaturated with the phase(s). Other models may require precipitation of a phase from undersaturated waters. Neither situation is possible and can be eliminated on the basis of thermodynamic infeasibility (Plummer (1985) [161]; Plummer et al. (1983) [148]). More common are mineral–water reactions in partial equilibrium systems (Helgeson (1968) [162]) in which one or more phases dissolve and one or more phases precipitate, some of which remain near thermodynamic equilibrium. Examples of partial-equilibrium chemical systems are provided in Plummer (1985) [161].

Individual inverse geochemical models may be found to be unreasonable for a wide variety of reasons, in addition to a lack of thermodynamic feasibility. Some models may indicate reaction mass transfers that are unrealistic given what is known regarding: (i) the kinetics of the reaction, (ii) the availability or concentration of a particular reactant, or (iii) the limited presence or absence of a particular reaction product. In addition, the ages calculated through inverse geochemical modelling may be unreasonable given the hydrological knowledge of a system, and could point to needed improvements in either the set of geochemical reactions considered to explain the observed evolution of the waters, or the possibility of additional hydrodynamic (and geochemical) processes. The calculation of a negative age for a groundwater sample is an obvious instance of such a discrepancy.

Any linear combination of ‘end member’ reaction models calculated by inverse modelling codes such as NETPATH or PHREEQC can potentially supply a mathematically consistent explanation of observed geochemical evolution in a groundwater system (Plummer et al. (1983) [148]). The possibility that a linear combination of unreasonable models, or of a mix of unreasonable and reasonable models, may be mathematically consistent with the observations is a troubling possibility that should

nevertheless be kept in mind when analysing reaction and inverse model possibilities for the purpose of radiocarbon dating in groundwater systems. The best way to avoid this conundrum is to obtain sufficient data regarding the chemical and isotopic composition of groundwater along a flow path, and to apply a sufficient number of constraints in inverse modelling to algebraically constrain the number of inverse models that can be calculated.

Recrystallization of carbonates is another important reaction that can greatly affect calculated  $^{14}\text{C}$  model age (Buddemeier et al. (1972) [163]; Garnier (1985) [164]; Mozeto et al. (1984) [165]). Recrystallization of calcite can be driven by small differences in Gibbs free energy between primary and secondary solids. The differences can result from trace impurities in the original calcite, such as Na and  $\text{SO}_4$  in calcites of marine origin, that are released as the calcite recrystallizes into a more pure calcite in fresh water aquifers. Recrystallization can also be driven by differences in the surface free energy of physically damaged calcite in aquifers undergoing tectonic stress or in carbonate minerals crushed by the scouring of glaciers. In NETPATH, it is possible to specify the moles of a carbonate mineral that exchange isotopically with a kilogram of water. An indication that calcite recrystallization may be occurring in carbonate groundwater systems is the observation that  $\delta^{13}\text{C}_{\text{DIC}}$  (measured)  $>$   $\delta^{13}\text{C}_{\text{DIC}}$  (modelled). Unfortunately, other uncertainties in the model can lead to the same observation, such as uncertainty in the isotopic composition of reactants or failure to consider all possible reactants.

#### 4.7. EXAMPLES USING NETPATH

In many aquifers, reliable radiocarbon ages have been interpreted by using the traditional adjustment models described above. These tend to be aquifers where the processes of carbonate mineral dissolution and isotopic exchange processes of  $\text{CO}_2$  and calcite dominate the recharge process and evolution in the system. Similar results can be obtained by using NETPATH in these systems. For

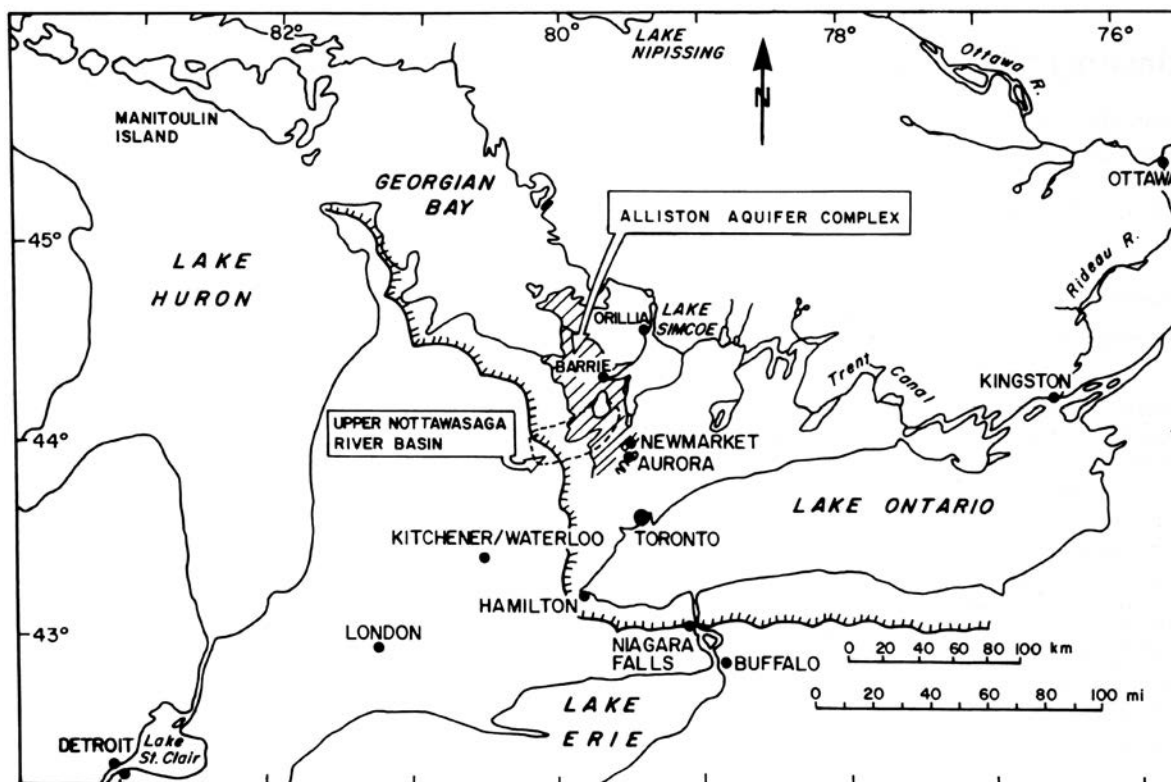


FIG. 4.6. Location of the regional confined Alliston aquifer, southern Ontario, Canada (from Aravena et al. (1995) [166]).

example, the initial water could be chosen as precipitation and the final water as a groundwater sample from the recharge zone.

Here, two examples are considered where geochemical modelling was essential in interpreting  $^{14}\text{C}$  model age. The first example involves the Alliston aquifer of Ontario, Canada, where palaeorecharge in glacial drift has undergone extensive interaction with buried organic matter in the methanogenic sediment (Aravena et al. (1995) [166]). In the second case, radiocarbon dating of water in the Floridan aquifer, FL, USA, undergoing de-dolomitization (dolomite and gypsum dissolution with calcite precipitation), oxidation of organic carbon (with iron reduction, sulphate reduction, pyrite formation), mixing with old saline water and recrystallization of marine calcite is considered (Plummer and Sprinkle (2001) [135]).

#### 4.7.1. Alliston Aquifer System, Ontario, Canada

Aravena et al. (1995) [166] present chemical and isotopic data from groundwater in the Alliston aquifer (Fig. 4.6), a regional confined aquifer in southern Ontario, Canada, composed of sand and gravel lenses. The aquifer is confined above by a thick glacial till and below by Palaeozoic bedrock or by early Wisconsin glacial till. The water chemistry was predominantly  $\text{Ca-Mg-HCO}_3^-$  type in the recharge

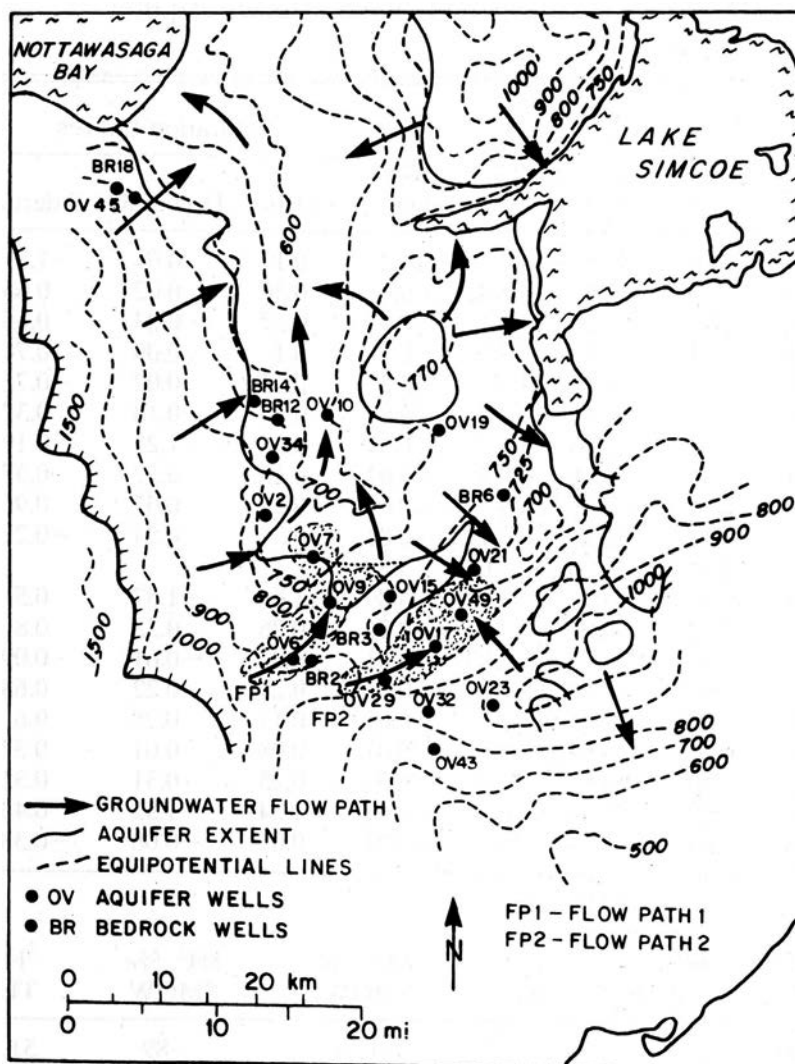
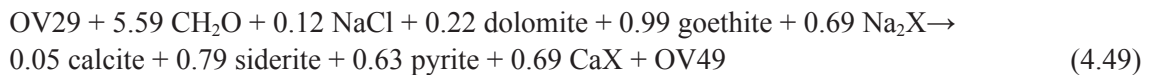


FIG. 4.7. Regional groundwater flow pattern (arrows), potentiometric contours (feet above sea level; 1 ft = 0.3048 m) and sampling sites in the Alliston Aquifer (from Aravena et al. (1995) [166]).

areas. Concentrations of  $\text{HCO}_3^-$ , Na, Cl, DOC and  $\text{CH}_4$  increased along directions of groundwater flow, while concentrations of  $\text{NO}_3$  and  $\text{SO}_4$  decreased (to below detection in some cases).

Concentrations of dissolved carbon species in the Alliston aquifer were 169–428 mg/L  $\text{HCO}_3^-$ , 2.0–18 mg/L DOC and <10 to 3550  $\mu\text{mol/L}$   $\text{CH}_4$ . The  $^{14}\text{C}$  content of DIC ranged from 0.7 to 63.8 pmc and  $\delta^{13}\text{C}_{\text{DIC}}$  ranged from  $-12.7$  to  $+2.0\text{‰}$  in the Alliston aquifer. Aravena et al. (1995) [166] applied NETPATH to calculate  $^{14}\text{C}$  model ages in the Alliston aquifer. Several representative initial waters were selected and, because these waters contained bomb tritium,  $A_{\text{oTDC}}$  ( $\text{TDC} = \text{DIC} + \text{DOC} + \text{CH}_4$ ) was computed based on the Tamers, Pearson, Fontes and Garnier, and Eichinger models, and  $A_{\text{oTDC}}$  was estimated from the available data. The data and model results are provided in Aravena et al. (1995) [166]. One example is the evolution of water from well OV29 in the recharge area to well OV49 further down gradient along flow path 2 (Fig. 4.7):



where  $\text{CH}_2\text{O}$  refers to sedimentary organic carbon of oxidation state 0, and masses of reactions are in millimoles per litre. The models were corroborated by close agreement in modelled and measured  $\delta^{13}\text{C}$  of TDC. The unadjusted  $^{14}\text{C}$  model age was 15.1 ka. By using data on the  $\delta^{13}\text{C}$  and  $^{14}\text{C}$  content of DIC, DOC and  $\text{CH}_4$  measured in the groundwater samples, the adjusted  $^{14}\text{C}$  model age of TDC ranged from

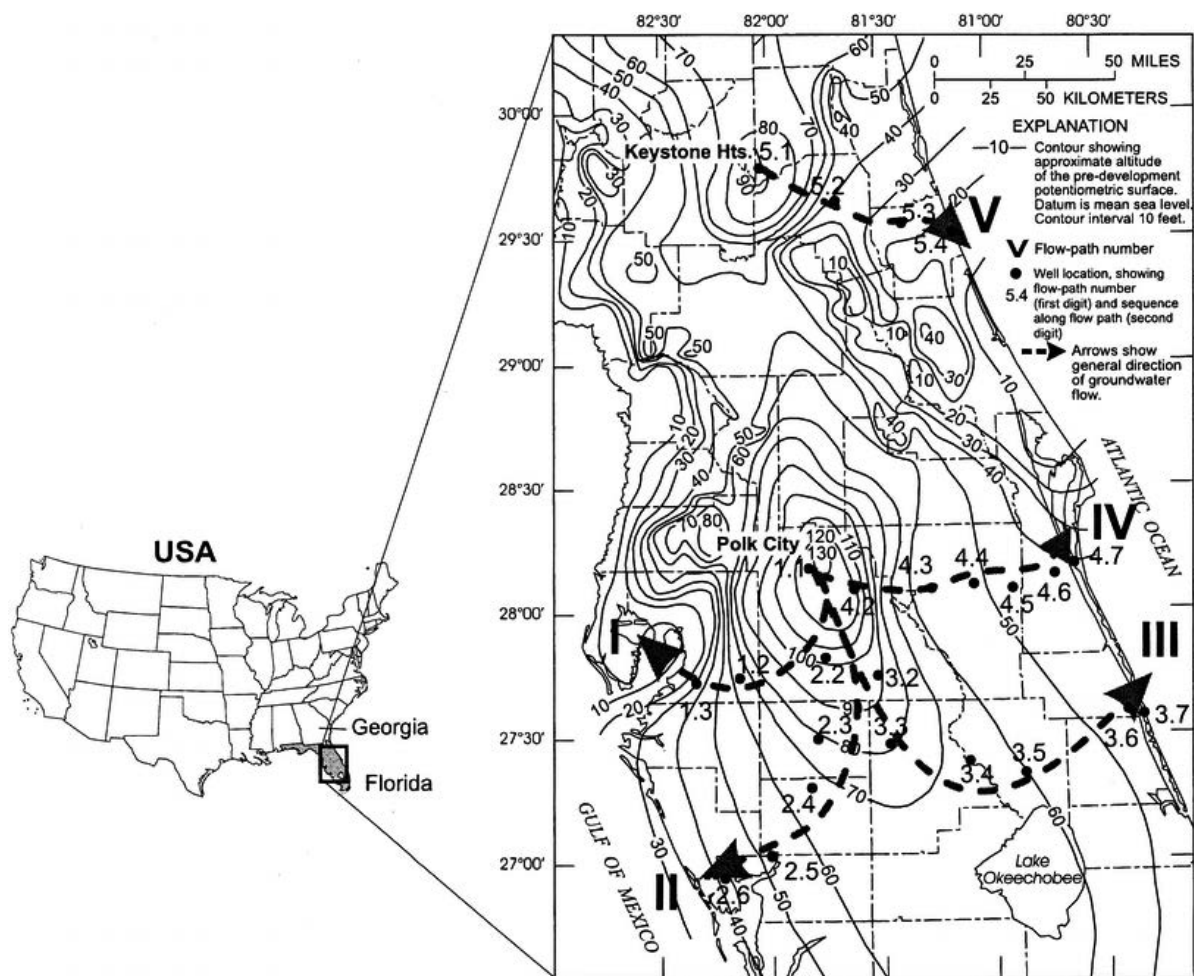


FIG. 4.8. Location of wells sampled and flow paths I–V in relation to altitude of the pre-development potentiometric surface of the Upper Floridan aquifer. Contours in feet (1 ft = 0.3048 m; from Plummer and Sprinkle (2001) [135]).

5.5 to 5.8 ka at well OV49. Overall, two groups of waters were found in the Alliston aquifer — one group of waters has  $^{14}\text{C}$  model ages of less than 13 ka, and the other group has  $^{14}\text{C}$  model ages between 15 and 23 ka. The  $^{14}\text{C}$  model age range calculated by NETPATH was in agreement with the age range based on DOC age correction models (Aravena and Wassenaar (1993) [167]).

#### 4.7.2. Floridan Aquifer System, FL, USA

Plummer and Sprinkle (2001) [135] applied geochemical modelling techniques to improve radiocarbon dating of DIC in the Floridan aquifer system, FL, USA. Water samples were obtained along five general directions of groundwater flow, based on the shape of the pre-development potentiometric surface (Fig. 4.8).

By using NETPATH, the predominant geochemical reactions that affect the  $^{14}\text{C}$  content of the DIC were: (i) dissolution of dolomite and anhydrite with accompanying calcite precipitation (de-dolomitization); (ii) sulphate reduction accompanying microbial degradation of sedimentary organic matter; (iii) recrystallization of calcite; and (iv) mixing of fresh water with as much as 7% saline water in some coastal areas. None of these processes/reactions are accounted for by any of

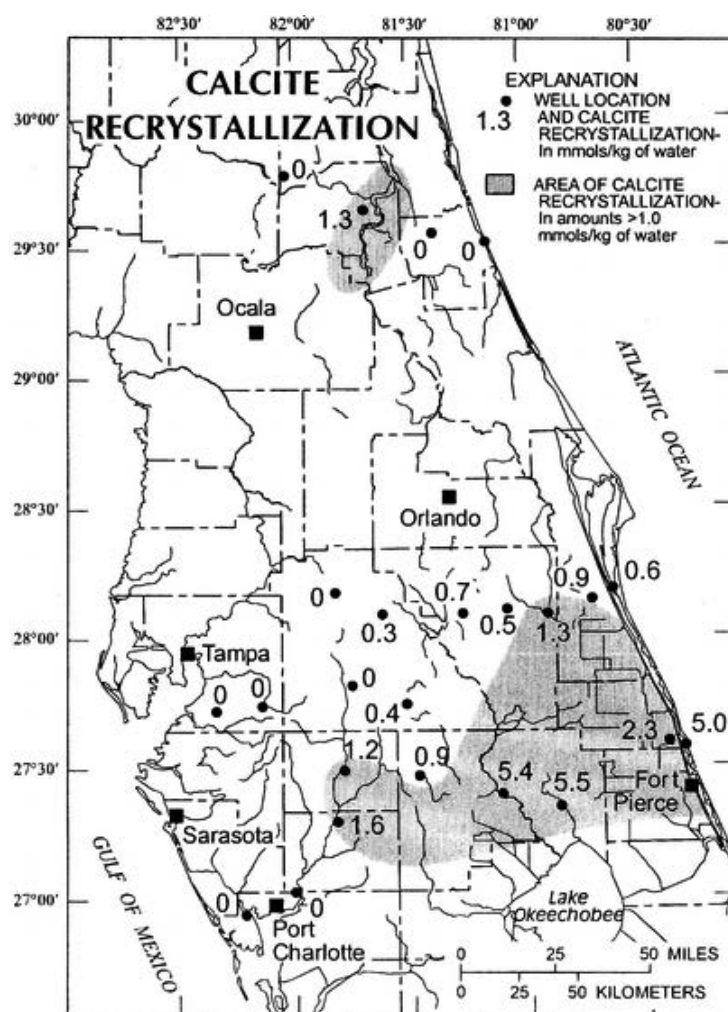
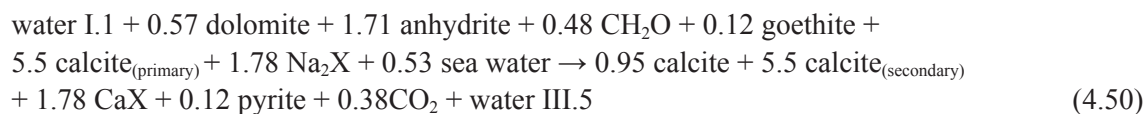


FIG. 4.9. Distribution of cumulative mass of calcite recrystallized (mmols/kg water; from Plummer and Sprinkle (2001) [135]).

the traditional inorganic adjustment models. As an example, a representative net geochemical reaction along flow path III was:



The part of the overall reaction pertaining to calcite recrystallization:



represents recrystallization of an estimated mass of 5.5 mmols of calcite (of marine origin,  $\delta^{13}\text{C}_{\text{calcite}} \equiv 0\text{‰}$ ) per litre of aquifer, to form 5.5 mmols of secondary calcite (accounting for isotopic fractionation in calcite precipitation) in fresh water. One of the findings from the NETPATH modelling was that without calcite recrystallization, the modelled values of  $\delta^{13}\text{C}_{\text{DIC}}$  were significantly depleted in  $^{13}\text{C}$ . The millimoles per kilogram of water of calcite recrystallization needed in the NETPATH models to match the observed  $\delta^{13}\text{C}_{\text{DIC}}$  were estimated and plotted on a map (Fig. 4.9). The estimated masses of recrystallization increased near the ends of flow paths and were attributed to geochemical interactions caused by upward leakage from the Lower Floridan aquifer, through semi-confining layers, and discharge into the Upper Floridan aquifer. During recrystallization, a fractionation occurs (Appendix to Chapter 4) that enriches the secondary calcite with  $^{14}\text{C}$  from the DIC, lowering the  $^{14}\text{C}$  content of

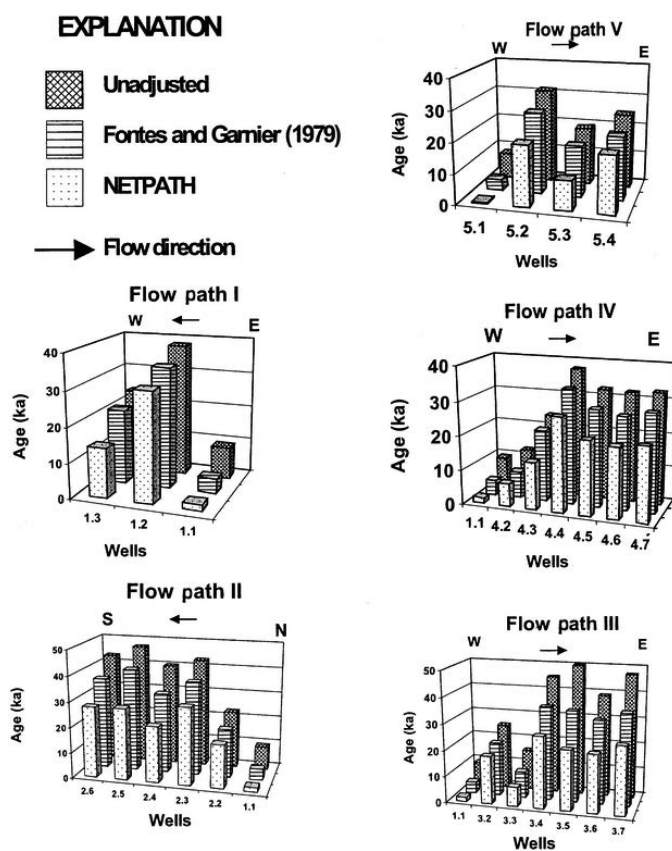


FIG. 4.10. Comparison of  $^{14}\text{C}$  model ages calculated for dissolved inorganic carbon from 24 water samples from the Upper Floridan aquifer, Florida as (i) unadjusted age, (ii) adjusted age based on the model of Fontes and Garnier (1979) [116], and (iii) adjusted age calculated using NETPATH (from Plummer and Sprinkle (2001) [135]).

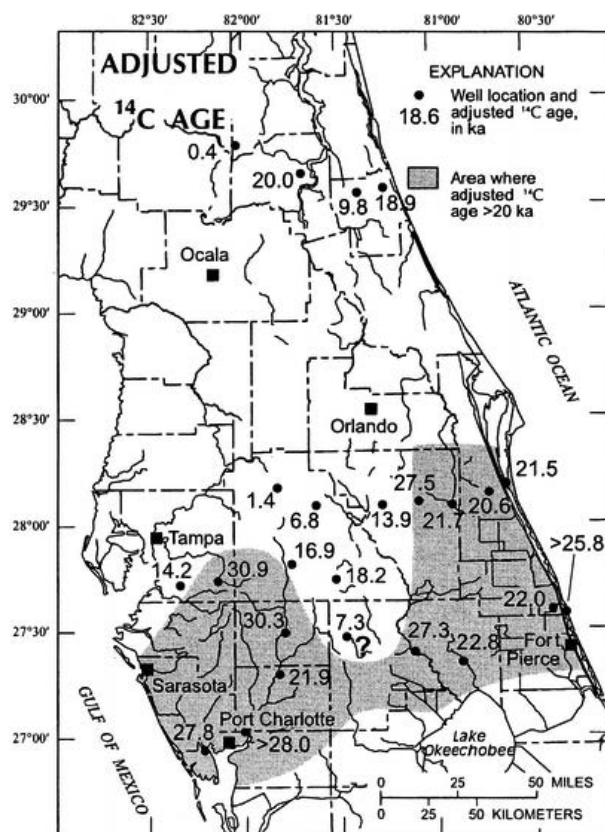


FIG. 4.11. Distribution of NETPATH adjusted  $^{14}\text{C}$  model ages of DIC in groundwater from the Upper Floridan aquifer, FL, USA (from Plummer and Sprinkle (2001) [135]).

DIC in dissolved  $\text{HCO}_3^-$ . Therefore, recrystallization of calcite lowers the value of  $A_{\text{nd}}$  and, thus, lowers the adjusted radiocarbon age.

Figure 4.10 compares the unadjusted  $^{14}\text{C}$  model age for waters along the five flow paths with the  $^{14}\text{C}$  model ages calculated from application of the Fontes and Garnier (1979) [116] model to the final water, and the NETPATH calculated  $^{14}\text{C}$  model ages, which include the geochemical mass balance models with calcite recrystallization.

Most of the waters outside of the recharge area had adjusted  $^{14}\text{C}$  model ages of 20–30 ka (Fig. 4.11).

The measured  $^{14}\text{C}$  values of DIC in the Floridan aquifer were low, and varied from about 33 pmc in the recharge area to as low as 0.23 pmc on flow path III. Along the same flow direction,  $\delta^{13}\text{C}_{\text{DIC}}$  increased from  $-11.4$  to  $-2.5\%$ . Unadjusted  $^{14}\text{C}$  model ages ranged from about 9 to more than 50 ka. The calculated  $^{14}\text{C}$  model ages using NETPATH ranged from 1.4 to about 27 ka (Plummer and Sprinkle (2001) [135]).

#### 4.8. RADIOCARBON DATING OF DISSOLVED ORGANIC CARBON

Owing to the many geochemical interactions that can lower the  $^{14}\text{C}$  content of DIC and, if not quantified, limit the usefulness of radiocarbon dating of DIC in groundwater, the feasibility of radiocarbon dating of DOC in groundwater was investigated in a series of studies (Drimmie et al. (1991) [168]; Hendry and Wassenaar (2005) [169]; Long et al. (1992) [170]; Murphy et al. (1989) [171]; Murphy et al. (1989) [172]; Purdy et al. (1992) [173]; Tullborg and Gustafsson (1999) [174]; Wassenaar et al. (1989) [175]; Wassenaar et al. (1991) [176]). A generally accepted definition of DOC is organic carbon that passes through a  $0.45\ \mu\text{m}$  filter (Drever (1997) [177]). Groundwater typically contains less than 2 mg/L (as C) of DOC with a median concentration of about 0.7 mg/L (Leenheer et al.

(1974) [178]). With the development of  $^{14}\text{C}$  AMS analysis, radiocarbon dating of DOC in groundwater is possible, although relatively large volumes of water (100–200 L) are needed to extract and separate high molecular weight (HMW) and low molecular weight (LMW) fractions of DOC (Murphy et al. (1989) [171]; Murphy et al. (1989) [172]). Although radiocarbon dating with DOC can avoid many of the geochemical complications that affect the  $^{14}\text{C}$  content of DIC, research over the past two decades has shown that two of the problems that affect radiocarbon dating of DIC must also be evaluated in radiocarbon dating of DOC; namely, definition of the initial  $^{14}\text{C}$  value of DOC,  $A_{o(\text{FA})}$ , where FA refers to the fulvic acid (HMW) fraction, and adjustment of  $A_{o(\text{FA})}$ , to  $A_{nd(\text{FA})}$ , for additional sources of (usually old) fulvic acid within the aquifer.

There are two main sources of DOC in groundwater: (i) particulate organic carbon (POC) in the soil zone and unsaturated zone that can have radiocarbon ages of zero to at least several thousand years; and (ii) sedimentary organic matter (SOM) such as lignite, peat or other forms of POC buried with the aquifer sediment that typically is radiocarbon-‘dead’. Both sources of DOC can dilute the  $^{14}\text{C}$  content of DOC in an aquifer.

Biogeochemical processes also significantly lower DOC concentrations across unsaturated zones (Pabich et al. (2001) [179]). Loss of DOC during the recharge process does not, alone, complicate the definition of  $A_{o(\text{FA})}$ . The problem is that within the soil zone and unsaturated zone, POC is not all modern and the assumption of 100 pmc for  $A_{o(\text{FA})}$  is usually not valid. Little is known about the rates of the complex series of biogeochemical processes that alters POC in soil zones, so that modelling of  $A_{o(\text{FA})}$  is currently not possible. The alternative is to measure  $A_{o(\text{FA})}$  in recharge waters of aquifers. One of the problems is that there is a spectrum of  $^{14}\text{C}$  values corresponding to the distribution of organic species and molecules recharging the groundwater system; generally, the ‘younger’ species will preferentially degrade (through fermentation or oxidation processes) relative to the ‘older’ species. Consequently, the distribution of  $^{14}\text{C}$  amongst the various organic molecular species will change through time, and generally decrease in  $^{14}\text{C}$  abundance, even in the absence of radioactive decay.

Methods of separating HMW and LMW fractions of DOC are provided in Thurman and Malcolm (1981) [180], Murphy (1987) [181], Murphy et al. (1989) [171] and Murphy et al. (1989) [172]. The HMW fraction is composed primarily of fulvic acids with a molecular weight range of 500–950 amu (Aiken and Malcolm (1987) [182]), whereas the LMW fraction consists primarily of short chain aliphatic hydrocarbons and substituted alcohols (molecular weight of <140 amu). Murphy et al. (1989) [172] found large and varying differences in the  $^{14}\text{C}$  content of the HMW and LMW fractions of DOC in individual samples from the Milk River aquifer, Canada, demonstrating the diverse origin of DOC in the aquifer and showing that radiocarbon dating of a composite DOC sample (HMW + LMW fractions) could be misleading. In the Milk River aquifer, LMW compounds generally had low  $^{14}\text{C}$  content, suggesting dilution with LMW DOC from  $^{14}\text{C}$ -‘dead’ kerogen within the aquifer. The  $^{14}\text{C}$  content of the HMW DOC generally followed that of the DIC, supporting a predominantly soil origin of the fulvic acid fraction (Murphy et al. (1989) [172]). Although the HMW (fulvic acids) DOC fractions are also mixtures of organic molecules of different age, they are thought to be predominantly of soil origin (Murphy et al. (1989) [172]) and probably better suited for radiocarbon dating than composite DOC or the LMW fraction of DOC (Clark and Fritz (1997) [52]).

Wassenaar et al. (1991) [176] found  $^{14}\text{C}$  values of the HMW fraction of DOC decreased in young, tritiated recharge waters of the Sturgeon Falls aquifer and Rodney aquifer in western Canada to 75 and 76 pmc, respectively at depths of 16–18 m. The  $^{14}\text{C}$  content of the HMW fraction of DOC ranged from 99 to 87 pmc in recharge waters from the Alliston aquifer (Canada), where the highest value was from a depth of 16–18 m and may have contained a higher fraction of fulvic acid from the bomb era than more shallow samples. The  $^{14}\text{C}$  content of the HMW fraction of DOC in recharge water from the Milk River aquifer was estimated to be as low as 30 pmc (Drimmie et al. (1991) [168]; Wassenaar et al. (1991) [176]). Measurements from a clay rich till aquitard system in Canada demonstrated that the  $^{14}\text{C}$  of the HMW fraction of DOC decreased from 97 pmc at depths of 1.2 m to 13–15 pmc at depths of 15–43 m (Hendry and Wassenaar (2005) [169]). The trend with depth was consistent with diffusive mixing

between two distinct end members: SOM formed since the Holocene (past 10 ka) and DOC in pore fluids of the aquitard (Hendry and Wassenaar (2005) [169]) suggesting, at least in this environment, that the HMW and LMW fractions of DOC were geochemically and biochemically conservative.

In studies where the  $^{14}\text{C}$  of DIC and DOC (or of the HMW fraction of DOC) are measured, the  $^{14}\text{C}$  content of DIC is usually significantly lower than that of the DOC (or of the HMW fraction of DOC) (Buckau et al. (2000) [183]; Burr et al. (2001) [184]; Drimmie et al. (1991) [168]; Murphy et al. (1989) [171]; Pettersson and Allard (1991) [185]; Purdy et al. (1992) [173]; Wassenaar et al. (1991) [176]). The differences can be attributed to the relatively large number of geochemical reactions (as well as other processes such as matrix diffusion and isotopic exchange) that can lower the  $^{14}\text{C}$  content of DIC in old groundwater. The two most significant geochemical processes are dilution of dissolved inorganic  $^{14}\text{C}$  ( $\text{DI}^{14}\text{C}$ ) from dissolution of carbonates and formation of DIC from microbial degradation of old organic carbon within the aquifer. Thomas et al. (2001) [186] found unadjusted  $^{14}\text{C}$  model ages of DIC in groundwater from Nevada as much as 20 ka, that, when corrected on the basis of  $\delta^{13}\text{C}$  for carbonate rock recrystallization in this tectonically active aquifer, were in the range of 1–7 ka and similar to  $^{14}\text{C}$  model ages of DOC in the aquifer.

Although ‘traditional’ adjustment models adequately compensate for carbonate mineral dissolution, most studies comparing  $\text{DO}^{14}\text{C}$  and  $\text{DI}^{14}\text{C}$  ages have not evaluated the organic source of DIC. Geochemical models used to adjust the initial  $^{14}\text{C}$  value that included the degradation of organic matter in the aquifer (Aravena et al. (1995) [166]; Plummer (1993) [60]; Plummer et al. (1990) [145]; Plummer and Sprinkle (2001) [135]) yielded adjusted radiocarbon ages of DIC that were ‘reasonable’; i.e. consistent with other palaeoclimate indicators (stable isotopes and palaeorecharge temperatures) or with results from numerical flow models. Buckau et al. (2000) [183] applied ‘traditional’ adjustment models to the DIC of the Gorleben aquifer, Germany, finding  $^{14}\text{C}$  model ages of 1–10 ka in tritium-containing recharge water, and DIC  $^{14}\text{C}$  model ages up to 31 ka in waters that had Holocene stable isotope signatures. By taking into account dilution of the DIC from microbial degradation of DOC in the aquifer, and determination that  $A_{\text{o(DIC)}}$  in the aquifer was near 50 pmc, Buckau et al. (2000) [183] demonstrated that the waters that contained elevated concentrations of DOC were so young that significant  $^{14}\text{C}$  decay could not be detected, and that the ages were consistent with the age limits derived from  $^2\text{H}$  and  $^{18}\text{O}$ . Buckau et al. (2000) [187] demonstrate the release of large concentrations of LMW (1.7–171 mg C/L) and HMW (2.6–22 mg C/L) DOC fractions in waters of the Gorleben aquifer compared to the relatively low DOC concentrations in the recharge waters (0–2.2 mg C/L). The contribution of DOC from sedimentary organic matter in the Gorleben aquifer overwhelms the initial DOC fractions, demonstrating the difficulty of dating DOC in organic rich aquifers. The next important advance in the application of radiocarbon dating of DOC in groundwater will likely be in the field of compound specific radiocarbon dating (Ingalls and Pearson (2005) [188]; Kalin (1999) [111]).

Long et al. (1992) [170] suggested that the most important justification for the study of  $^{14}\text{C}$  of DOC in aquifers is for comparison with travel times inferred from  $^{14}\text{C}$  in DIC. Differences in  $^{14}\text{C}$  model ages between DIC and DOC can aid in refining geochemical adjustment models of the  $^{14}\text{C}$  content of DIC as well as help to interpret the  $^{14}\text{C}$  content of DOC in aquifers. A useful approach to establishing radiocarbon chronologies in aquifers where inorganic and organic carbon sources contribute to the  $^{14}\text{C}$  DIC pool is to date the DIC. This is done by constructing geochemical adjustment models accounting for all of the predominant inorganic and microbially mediated organic degradation reactions in the TDC system, such as implemented in NETPATH (Plummer et al. (1994) [120]), and demonstrated by Aravena et al. (1995) [166] and Plummer and Sprinkle (2001) [135].

## 4.9. HYDRODYNAMIC AND AQUIFER MATRIX EFFECTS ON RADIOCARBON AGES

### 4.9.1. Mixing processes

Groundwater pumping extracts water preferentially from the most hydraulically conductive zones adjacent to well screens. This means that the waters extracted and their solutes, including DIC and DOC, generally come preferentially from one or more transmissive aquifers, transmissive zones or from highly conductive fractures. It is important, however, to consider the spatial scale of the effects of groundwater pumping and movement. In a study investigating regional groundwater depletion, Konikow and Neuzil (2007) [189] showed that most of the regional groundwater depletion caused by pumping actually came from a change in storage in confining layers. Thus, a significant fraction of a water sample pumped from a well may represent water that has not only been residing in ‘mobile’ zones of the groundwater system. Some of the water may have leaked from/through confining layers. If the leakage occurs primarily from more recently recharged (usually shallower)<sup>2</sup> horizons, the water sample will contain a fraction of younger water and, possibly, younger solutes. If the leakage occurs primarily from less recently recharged (usually deeper) horizons, the water will contain a fraction of older water and older solutes. In general, water samples extracted from given horizons will have a frequency distribution of water and tracer model ages (cf. review by Bethke and Johnson (2008) [84]; Chapter 3 in the present volume discusses this issue at length and how it affects groundwater ‘age’ concepts). This natural range in age distributions can be coupled with the following facts: (i) different solutes undergo different types and extents of reaction and, therefore, undergo varying extents of retardation in groundwater systems (Atteia et al. (2005) [190]; Glynn and Brown (2012) [154]; Maloszewski and Zuber (1991) [191]); (ii) different solutes have different histories of recharge into the groundwater system (Plummer et al. (1993) [192]), as well as different production and removal histories in their passage through the system; and (iii) different solutes may even have undergone different extents of dispersal and/or exclusion through the system (LaBolle et al. (2006) [193]; Neuzil (1986) [194]; Neuzil and Provost (2009) [195]). Consequently, it is no surprise to find that different dating techniques provide different tracer model ages for a given sample (see DePaolo (2006) [196]; IAEA (2006) [85]; Maloszewski and Zuber (1991) [191]; Plummer et al. (1993) [192]).

### 4.9.2. Subsurface production

The possibility of subsurface production of <sup>14</sup>C was investigated by Zito et al. (1980) [197] and with regard to the Stripa granite by Andrews et al. (1989) [198]. Although it is theoretically possible to produce <sup>14</sup>C in groundwater from nuclear reactions induced by emissions from U and Th nuclei, the effect is normally not important in waters younger than 50 ka (Zito et al. (1980) [197]), which is approximately the limit for <sup>14</sup>C dating. The minimum <sup>14</sup>C content from in situ production in the Stripa fracture fluids corresponded to a decay time of 32 ka, for an initial <sup>14</sup>C value of 50 pmc. However, the question of in situ production of <sup>14</sup>C would need to be investigated on a site specific basis and depends on several factors, including the localization of U- and Th-bearing minerals with respect to pore spaces and various target materials (Al, Mg, O, Si, B) in the aquifer (Zito et al. (1980) [197]).

### 4.9.3. Diffusive exchange with confining layers

In addition to the possible advective leakage of waters from other conductive zones of a groundwater system (through confining zones), diffusive exchange of water and solutes is also an

---

<sup>2</sup> One exception may occur when shallow, relatively less transmissive zones overlie deeper relatively more transmissive zones. In this situation, waters in the deeper zones may have been more recently recharged than waters in the shallower zones.

important process to consider. Any groundwater system may have a range of ‘stagnant’<sup>3</sup> zones, typically containing old water and solutes which can possibly exchange diffusively with younger water and solutes in more mobile regions of the system. Large chemical and isotopic concentration gradients are often found between mobile and stagnant zones in groundwater systems, with stagnant zones usually containing more highly concentrated, sometimes more chemically reducing waters. A wide range of stagnant zones can occur: confining beds or aquitards, clay or silt lenses, unfractured rock matrices with some connected porosity between mineral grains, connected porosity inside individual mineral grains, and internal exchange layer porosity in clay minerals. Many of the diffusion processes will involve aqueous ion diffusion through a water phase, although this phase can have varying electrochemical properties because of interfacial effects with the contacting solid surfaces. Some of the diffusion can also occur through surface diffusion processes, including surface diffusion inside the double layer of clays (Helffferich (1995) [199]). Atteia et al. (2005) [190] offer a comprehensive review examining the contributions of diffusion and leakage from low permeability layers to the geochemical evolution of groundwater systems.

#### 4.9.4. Transport models

Ideally, the complex interplay between advective, dispersive and diffusive processes, geochemical reactions and radioactive decay (or production) would be investigated using forward-modelling reactive transport codes such as PHAST (Parkhurst et al. (2004) [200]). Owing to the multiplicity of possible computer intensive simulations varying parameters, processes and configurations, inverse modelling is needed to constrain the range of possible simulations and optimize parameter values (for given configurations and processes chosen for a particular system). Inverse modelling could include inverse geochemical modelling with NETPATH/PHREEQC to determine sets of possible reactions and mixing processes that might control the geochemical evolution of the groundwater. Inverse modelling with codes such as UCODE (Poeter and Hill (1998) [74]) could also be used to estimate and constrain flow and transport models and model parameters. Having sufficient high quality data and an understanding of what is reasonable in the hydrological and geochemical behaviour of a system would be key to the useful application of the modelling process.

#### 4.9.5. Analytical solutions

In the absence of full featured but time consuming inverse and forward simulations of groundwater systems, some analytical solutions are available that can quickly quantify the potential importance of diffusive processes on observed radiocarbon ages for given groundwater samples. The solutions were first derived for the study of radionuclide transport in fractured rocks, initially for the transport of a radionuclide through a single fracture with transverse diffusion into a rock matrix (Neretnieks (1980) [201]; Neretnieks (1981) [202]; Tang et al. (1981) [203]), then for transport through a parallel set of fractures with transverse diffusion into the intervening rock matrix (Sudicky and Frind (1982) [204]; Sudicky and Frind (1984) [205]). A more general 3-D analysis for fractured rock media was provided by Therrien and Sudicky (1996) [206]. Although Tang et al. (1981) [203] recognized early on the application of their analytical solution to radiocarbon dating of groundwater in a thin aquifer bounded by thick confining beds, Sanford (1997) [207] provided an elegant analytical derivation and solution for a parallel series of stagnant and flow zones, applicable either for porous or fractured rock media. The basic equations in Sanford (1997) [207] for the analytical solution under steady-state conditions

---

<sup>3</sup> Historically, hydrologists have often considered low permeability zones as zones that were completely impervious to flow, such as aquicludes, for example. In reality, advective flow generally does occur through low permeability zones and, more often than not, can be quantitatively meaningful when integrated over large regional areas and/or over large timescales. In this chapter, ‘stagnant’ zones is simply used to indicate zones for which diffusive transport processes dominate over advective ones over the time periods and areas of interest.

(with respect to both flow and transport) of a parallel flow and stagnant zone system, with a constant tracer input concentration (e.g. a  $^{14}\text{C}$  content of 100 pmc), constant flow zone width,  $w_{\text{flow}}$ , and constant stagnant zone width,  $w_{\text{stag}}$ , are further discussed in recent papers by Cook et al. (2005) [208] and DePaolo (2006) [196]. Sanford's steady state solution can take the form of a diffusion loss constant that can be added to the radioactive decay constant for a given tracer such as  $^{14}\text{C}$ . Sanford relates the diffusion corrected,  $t_c$ , and diffusion uncorrected,  $t_u$ , ages for a sample through the following equation:

$$t_c/t_u = k/(k + k_{\text{diff}}) \quad (4.52)$$

where  $k$  and  $k_{\text{diff}}$  are the radioactive decay and diffusive loss constants, respectively. For  $^{14}\text{C}$ ,  $k$  is  $1.21 \times 10^{-4}$  per a or  $3.83 \times 10^{-12}$  per s (corresponding to a half-life of 5730 a). The diffusive loss constant,  $k_{\text{diff}}$ , can be calculated from the following equation:

$$k_{\text{diff}} = \frac{2\sqrt{kD_{\text{eff}}}}{\phi w_{\text{flow}}} \tanh\left(\frac{w_{\text{stag}}}{2} \sqrt{\frac{k}{D_{\text{eff}}}}\right) \quad (4.53)$$

where

$\phi$  is the porosity in the flow zone; and the effective diffusion coefficient,  $D_{\text{eff}}$ , can be related to the aqueous diffusion coefficient,  $D_0$ , through a variety of equations that generally include the effects of matrix (or stagnant zone) porosity,  $\theta_{\text{stag}}$ , and tortuosity,  $\tau$ .

These equations and the magnitude of  $D_{\text{eff}}$  vary significantly in different studies. Cook et al. (2005) [208] provide a fairly general formulation:

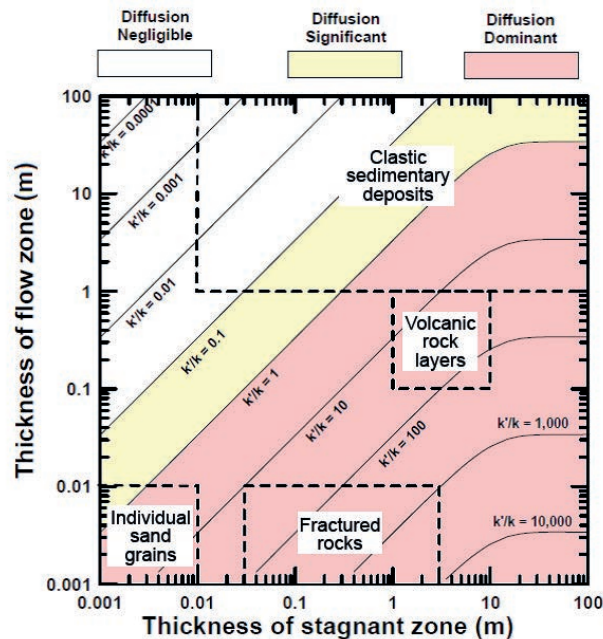


FIG. 4.12. Plot of the ratio of the diffusive rate constant,  $k'$ , to the decay constant of  $^{14}\text{C}$ ,  $k$ , over the length scales at which vertical heterogeneities occur in porous media. Shaded regions indicate where diffusion is either negligible (white), significant (pale yellow) or dominant (pink). The ratios assume a porosity of the flow zone of 0.30, a coefficient of molecular diffusion of  $1 \times 10^{-10} \text{ m}^2/\text{s}$ , and a decay constant of  $3.83 \times 10^{-1}/\text{s}$  (modified from Sanford (1997) [207]). Sanford's analytical solution and the adjacent plot will generally tend to an overestimation of the effects of  $^{14}\text{C}$  diffusive loss on  $^{14}\text{C}$  model ages as discussed in the text.

$$D_{\text{eff}} = D_0 \theta_{\text{stag}} \tau \quad (4.54)$$

The aqueous diffusion constant,  $D_0$ , for carbonate and bicarbonate species is variously cited: 0.04 m<sup>2</sup>/a ( $1.3 \times 10^{-9}$  m<sup>2</sup>/s) by Cook et al. (2005) [208], and 0.03 m<sup>2</sup>/a ( $9.5 \times 10^{-10}$  m<sup>2</sup>/s) by DePaolo (2006) [196], who may be including a tortuosity effect in his lower number. In their example describing a fractured rock system, however, Cook et al. (2005) [208] assumed a tortuosity of 0.03 and a matrix porosity of 0.02. Porous media have higher stagnant-zone porosity and tortuosity compared to fractured rock matrices. This explains the two orders of magnitude difference in the effective <sup>14</sup>C diffusivities ( $D_{\text{eff}}$ ),  $10^{-10}$  m<sup>2</sup>/s and  $7.6 \times 10^{-13}$  m<sup>2</sup>/s, used by Sanford (1997) [207] and Cook et al. (2005) [208], respectively.

Sanford used his steady state model calculations to estimate the effect of diffusive loss on radiocarbon dating of waters in the stratified basalts of the island of Oahu, where he calculated that the diffusive losses of <sup>14</sup>C could result in a <sup>14</sup>C model age that could be 100 times too old. He also applied his model to <sup>14</sup>C dating of waters in the Bangkok Basin, an alluvial system of stratified clay, sand and gravel lenses, where he estimated the near equal removal of <sup>14</sup>C through radioactive decay and diffusive loss. His calculations assumed that the clay lenses had an average thickness of about 6 m, and that the transmissive sand layers had a thickness of about 20 m. Figure 4.12 (from Sanford (1997) [207]) can be used to estimate the relative importance of diffusive <sup>14</sup>C loss in radiocarbon dating.

It must be noted that Sanford's analytical solution did not consider the possibility of sorption and isotope exchange with the solid phase, a process that can be important in carbonate (limestone, dolomite) or chalk aquifers. Małozzewski and Zuber (1991) [191] added these processes in their own analysis of diffusive effects on radiocarbon dating. The additional retardation caused by the sorption and exchange of <sup>14</sup>C leads to additional decay and loss of the isotope, even in a steady state system. In contrast to this loss, the concentrations of non-decaying constituents, such as <sup>13</sup>C, are not affected by sorption and exchange processes under steady state conditions. However, groundwater systems are probably never in complete steady state with respect to all transport processes and geochemical reactions.

Sanford's analytical solution assumes steady state conditions and may either overestimate or underestimate diffusive losses of <sup>14</sup>C in groundwater systems with changing flow and transport conditions. Sanford's analytical solution may provide a good estimate of <sup>14</sup>C diffusive loss (and the needed groundwater age correction) in the case of parallel transmissive and stagnant zones, where the water in the stagnant zones is truly stagnant. Generally, however, Sanford's analytical solution may tend to overestimate the diffusive losses of <sup>14</sup>C for the following reasons:

- (a) The solution assumes a binary layer flow system, with fast flow zones and stagnant zones. Advection is a non-fractionating transport process. By assuming that advection is insignificant in stagnant zones, the diffusive loss of <sup>14</sup>C in those zones is maximized.
- (b) The solution assumes a 'layer-cake' alternating distribution of flow and stagnant zones, with one constant width for the flow zones and one constant width for the stagnant zones, and a diffusive gradient into the stagnant zones orthogonal to the flow direction in the flow zones. In contrast, stagnant zones in alluvial basins are likely to pinch out and be limited in areal extent. If the lenticular stagnant zones are small in their individual areal extents, diffusion into the lenses may be fast enough that no significant <sup>14</sup>C decay will occur. Therefore, the 'layer-cake' configuration assumed by Sanford's analytical solution likely overestimates <sup>14</sup>C diffusive losses in systems that have stagnant zones with very limited individual areal extents.
- (c) The solution assumes that transverse dispersion is great enough in the flow zones to ensure a constant <sup>14</sup>C content across the width of each flow zone. In systems with large flow zones, such as thick aquifers, this may not be the case and this could limit the overall diffusive loss of <sup>14</sup>C.
- (d) The solution assumes that Fick's law, as applied only to the <sup>14</sup>C content in the water, controls the diffusion and the diffusive loss of <sup>14</sup>C. It assumes that the chemical counter diffusion of ions from stagnant zones into flow zones does not affect <sup>14</sup>C diffusion. In reality, major regional

aquitards often have significantly different chemistry from their neighbouring aquifers and are usually more saline. In such systems, coupled diffusion processes might have to be taken into account. Multicomponent diffusion is a complex process that can speed up the diffusion of certain ions and slow the diffusion of others, relative to the diffusive flux that might be calculated by assuming single ion diffusion. However, in the common case of stagnant zones that are significantly more saline than the flow zone of interest, intuition suggests that strong chemical counter diffusion fluxes of ions into the flow zone could potentially slow the diffusive flux and loss of  $^{14}\text{C}$  into the stagnant zones, relative to the  $^{14}\text{C}$  loss that might occur in a situation without a strong chemical counter diffusion.

In summary, Sanford's analytical solution is a useful tool for an initial estimation of potential  $^{14}\text{C}$  diffusive losses. However, it probably provides a maximum estimate of such losses, and is best applied to systems that have pervasive zones with no significant advective flow. It will probably not be applicable to alluvial basins with relatively coarse sediments and a paucity of truly stagnant zones, such as the Middle Rio Grande and San Juan Basins in New Mexico. After an examination of the geological information available for the Middle Rio Grande Basin, Sanford et al. (2004) [47] and Sanford et al. (2004) [48] did not correct  $^{14}\text{C}$  model ages for diffusive losses in that basin. In their study on the San Juan Basin, Phillips et al. (1989) [39] considered the potential effects of dispersive mixing and, more importantly, inter-aquifer leakage, on the sampled groundwater  $^{14}\text{C}$  model ages; they concluded that these effects did not significantly affect the estimated  $^{14}\text{C}$  model ages.

#### **4.9.6. Matrix diffusion in unsaturated zones**

Most of the studies that have investigated the effects of matrix diffusion on  $^{14}\text{C}$  dating of groundwater have considered only the effects that occur below the water table. There could be some situations in which the physical and chemical processes relating to diffusion, sorption, isotopic exchange and decay of  $^{14}\text{C}$  in matrices, lenses or grain pores in the unsaturated zone or near the water table might also need to be considered, even though the effects could be mitigated by gas phase exchange processes. Diffusive processes in the unsaturated zone or in perched groundwater could potentially lower the initial  $^{14}\text{C}$  content,  $A_0$ , of recharging groundwater.

#### **4.9.7. General conclusions regarding the effects of hydrodynamics and heterogeneity on $^{14}\text{C}$ model ages in groundwater**

Some general conclusions can be stated regarding the effects of matrix diffusion on  $^{14}\text{C}$  dating of groundwater. Most groundwater sampled for  $^{14}\text{C}$  analysis and radiocarbon dating is pumped from the more transmissive zones of a groundwater system. Owing to dispersive and diffusive effects (and usually their associated geochemical reactions), the groundwater flow rates obtained by using the  $^{14}\text{C}$  model ages estimated<sup>4</sup> for these transmissive zones will underestimate the actual groundwater velocities in these zones. Further, the flow rates obtained will probably greatly overestimate the mean water velocity of the system as a whole (because the sampled water may not fully reflect the slower velocities and older ages of water in less transmissive zones). Consequently, if a system is at steady state, overall recharge to the system<sup>5</sup> will be overestimated if the recharge rate is determined from  $^{14}\text{C}$  measurements insufficiently corrected for diffusive processes. From a water management perspective, the underestimation of water velocities in transmissive zones could cause a problem if water contamination is an issue; the overestimation of overall recharge to the system could be a problem from a water supply perspective.

<sup>4</sup> Without corrections for diffusion.

<sup>5</sup> The system, as defined here, is the entire groundwater system. It includes all of its transmissive, less transmissive and stagnant zones.

The geometry and distribution of more transmissive and less transmissive, and/or stagnant zones will be important in determining the relative effects of diffusive processes (and of advective leakage). The relative sizes of stagnant and transmissive zones will matter as can be seen from the equations above. The orientation and aspect ratio of the zones relative to the recharge surface, and the distribution of these orientations and geometries will also be important. The use of multiple tracers with different effective diffusivities and decay or growth characteristics can potentially provide a better understanding of the distribution of model and actual groundwater velocities through the system.

Simple, easy to use, estimation techniques and numerical modelling tools are useful and needed to obtain a good understanding of the geochemical and hydrological processes occurring in aquifers and their potential impacts on the distribution of  $^{14}\text{C}$  content throughout a groundwater system. Ultimately, however, the heterogeneous nature and the structural and process complexity of groundwater systems may require more sophisticated full-featured numerical simulation tools. The full use of these tools, however, will be warranted only when there is sufficient information and data available to describe the groundwater system under investigation. In such a situation,  $^{14}\text{C}$  age dating may be used in conjunction with the chemical and isotopic characterization of various recharge and evolved waters, and the spatial delineation of their occurrence, to help calibrate full featured flow and transport simulations of a groundwater basin. Plummer et al. (2004) [49], Plummer et al. (2004) [50], Plummer et al. (2004) [51], Sanford et al. (2004) [47] and Sanford et al. (2004) [48] provide an example of such an application in an investigation of the hydrogeology of the Middle Rio Grande Basin (see Chapter 12 for a case study on the Middle Rio Grande Basin). Their study calculated the effective modern and palaeorecharge rates for the basin. The minimal corrections needed to adjust for  $^{14}\text{C}$  dilution through geochemical reactions in the Middle Rio Grande Basin, and the extensive geochemical and hydrological data available were a great help in facilitating calibration of the flow model for the system. Several earlier efforts have also used radiocarbon dating, measured  $^{14}\text{C}$  values and geochemical modelling, to help determine regional recharge rates and the transmissivity of aquifers on large regional scales. Some notable examples of such studies include Phillips et al. (1989) [39], Plummer et al. (1990) [145], and Plummer and Sprinkle (2001) [135]. In these efforts, the collection of an extensive set of chemical and isotopic analyses was often the key to obtaining confidence that calculated tracer model ages or velocities were reasonable. In the best situations, the ages obtained correlated with recharge palaeotemperatures derived from noble gas,  $\text{N}_2/\text{Ar}$ ,  $^{18}\text{O}$  and  $^2\text{H}$  data.

#### 4.10. GUIDELINES FOR RADIOCARBON DATING OF DISSOLVED CARBON IN GROUNDWATER SYSTEMS

Nine guidelines essentially describe the application of radiocarbon measurements to groundwater dating:

- (1) Although it is sometimes possible to reconstruct the  $^{14}\text{C}$  content of DIC in water samples that are mixtures of young and old water, it is best to attempt radiocarbon dating on waters that are representative of in situ aquifer conditions. Well construction and/or drilling practices can compromise the integrity of the  $^{14}\text{C}$  content of the formation water. Tritium analyses and CFC analyses are useful in recognizing water samples or their mixtures that may be contaminated with fractions of post-bomb  $^{14}\text{C}$  and identifying those samples that may not be worthy of undergoing the expense of radiocarbon analysis. On the other side of the radiocarbon timescale,  $^{36}\text{Cl}$  measurements may be useful for samples with low  $^{14}\text{C}$  to test for the possibility that the water is very old, but contains a small fraction of relatively young (radiocarbon timescale) water. Given (i) the local tritium and  $^{14}\text{C}$  input function for the bomb era; (ii) the interpretation of initial  $^{14}\text{C}$  in recharge processes; and (iii) geochemical reaction corrections, it may be possible to test various mixing scenarios of young and old water that potentially affect interpretation of  $^{14}\text{C}$  model age for a given locality.

- (2) Most radiocarbon laboratories report the measured  $^{14}\text{C}$  content according to that of Stuiver and Polach (1977) [110], which provides values of per cent modern (pM) carbon normalized for  $^{13}\text{C}$  of the sample (see the Appendix to Chapter 4). In radiocarbon dating of DIC (or TDC) in aquifers, it is best to use unnormalized  $^{14}\text{C}$  values, pMC and/or  $\delta^{14}\text{C}$ , and use geochemical models to construct the adjusted  $^{14}\text{C}$  content. Equations to convert the normalized  $^{14}\text{C}$  to non-normalized values are provided in the Appendix to Chapter 4. Geochemical adjustment models are then constructed, such as in Fontes and Garnier (1979) [116] or through use of the code NETPATH (Plummer et al. (1994) [120]) as described above, to adjust the initial  $^{14}\text{C}$  for water–rock reactions.
- (3) Determination of the initial  $^{14}\text{C}$  value,  $A_0$ , in recharge areas of aquifers remains one of the most significant uncertainties in radiocarbon dating of DIC in groundwater. In systems open to  $\text{CO}_2$  gas exchange during recharge, such as in some arid regions,  $A_0$  can be near 100 pMC. In systems closed to  $\text{CO}_2$  gas exchange following recharge,  $A_0$  may be near 50 pMC if old carbonate rocks dissolve within the aquifer following recharge without further gas exchange with unsaturated zone air. Intermediate values, as well as values even lower than 50 pMC are also possible, depending on the extent of geochemical reactions occurring in the aquifer. The difference between open and closed system evolution — the difference between approximately 100 and 50 pMC in  $A_0$  alone — introduces 5730 a uncertainty in the adjusted  $^{14}\text{C}$  model age. However, as long as conditions in the recharge area have not substantially varied, groundwater velocities down a flow path calculated from  $^{14}\text{C}$  model ages are not affected by the  $A_0$  error after the first sample. Two approaches have been taken in estimating  $A_0$ : (i) the initial  $^{14}\text{C}$  value of DIC in the recharge area can be estimated by locating water samples in the recharge area that are low in tritium or CFC content (pre-nuclear detonation waters) and analysing the  $^{14}\text{C}$  content of DIC in these samples (Fig. 4.1); and (ii) the initial  $^{14}\text{C}$  value of DIC can be estimated by applying one or more of the ‘traditional’ adjustment models discussed above to the chemical data from recharge waters or to the water sample being studied, as in NETPATH. Alternatively, geochemical modelling techniques, such as in PHREEQC, can be used to estimate  $A_0$  values pertaining to assumed conceptualizations of the geochemical evolution of initial waters.
- (4) Consideration should be given to the possibility that the chemical, isotopic and recharge conditions occurring today in the recharge area of the aquifer may not apply to the palaeoconditions prevailing at the time of recharge of the sample being dated with radiocarbon. Changes in climatic conditions could lead to changes in the thickness of the unsaturated zone, recharge rate and the extent of open or closed system conditions. The predominant plant type in the recharge area could shift from one photosynthetic pathway to another, resulting in a change in  $\delta^{13}\text{C}$  of soil gas  $\text{CO}_2$ . As explained above, many of the models for reconstructing  $A_0$  in recharge waters are sensitive to the assumed  $\delta^{13}\text{C}$  of soil gas  $\text{CO}_2$ .
- (5) Constructing geochemical adjustments to initial radiocarbon values in aquifers can require considerable geochemical intuition related to water–rock reactions in a system. Data on the carbon isotopic composition of DIC, DOC,  $\text{CH}_4$  and POC, and reacting carbon-bearing phases in the system are usually needed or must be estimated, both within the recharge zone and the aquifer system.
- (6) If initial and final water compositions can be proposed, geochemical mass balance reaction models can be used to adjust the initial  $^{14}\text{C}$  value for geochemical reactions along the flow path. The calculated  $^{14}\text{C}$  model age is the time required for decay of the reaction corrected initial  $^{14}\text{C}$  value to the measured (non-normalized) value in the final water. Inverse geochemical modelling codes such as NETPATH and PHREEQC can estimate the effects of hydrodynamic mixing and geochemical processes on the dilution of observed  $^{14}\text{C}$  values. It may be possible to apply some analytical solutions to estimate the importance of matrix diffusion on  $^{14}\text{C}$  model ages.
- (7) In some cases, such as silicate aquifers where geochemical adjustments to  $A_0$  can be small, it may be warranted to apply radiocarbon calibration scales to convert radiocarbon years to calendar years. Before radiocarbon calibration can be applied, radiocarbon ages that have been calculated

by using the modern  $^{14}\text{C}$  half-life (5730 a, as in NETPATH) need to be converted to Libby half-life (5568 a) by using the equation

$$t_{\text{Libby}} = 0.972t_{5730} \quad (4.55)$$

This produces the adjusted  $^{14}\text{C}$  model age based on the Libby half-life. Calibrated radiocarbon ages, where warranted, are probably more reliably used in conjunction with numerical models of groundwater flow, as in Sanford et al. (2004) [47].

- (8) Efforts should be made to corroborate radiocarbon ages. Measurements of tritium and/or CFCs should always be made in conjunction with radiocarbon measurements, as discussed above. Measurements of  $^{36}\text{Cl}$  can identify mixing of pre-nuclear detonation water with very old groundwater (water on the 100 ka timescale). If the radiocarbon age places the sample near the LGM (18 ka radiocarbon age), comparison with data on the stable isotope composition of the water (Rozanski (1985) [209]) or of the dissolved gas  $\text{N}_2/\text{Ar}$  (Heaton (1981) [210]; Heaton et al. (1983) [56]; Heaton and Vogel (1981) [211]), or recharge temperatures (Herzberg and Mazor (1979) [212]; Stute et al. (1995) [213]; Stute et al. (1995) [214]; Stute and Schlosser (2000) [215]; Stute et al. (1992) [42]) can be used to corroborate the age. Examining the radiocarbon data spatially throughout the aquifer in relation to conceptualization of groundwater flow can also help to corroborate or possibly invalidate some radiocarbon ages. Measurement of vertical  $^{14}\text{C}$  gradients in unconfined or deep aquifers and/or  $^{14}\text{C}$  gradients along flow paths complement geochemical correction procedures, for example, in estimating the initial  $^{14}\text{C}$  value, and determining recharge rates (see Chapter 12). The gradient in  $^{14}\text{C}$  concentration can help to evaluate whether a  $^{14}\text{C}$  decrease with flow distance is due to radioactive decay or the combined effect of decay, retardation and geochemical processes. The process of refining age interpretation can be aided by use of numerical models of groundwater flow, recognizing ages that are consistent with the model and those that are not.
- (9) The complexity of a hydrogeological setting may require more sophisticated full featured numerical simulation tools. The use of these tools will truly be warranted only when there is sufficient information and data available to describe the groundwater system under investigation. If this is the case,  $^{14}\text{C}$  model ages can be used in conjunction with geochemical characterization to help calibrate flow and transport simulations of a groundwater system.

## ACKNOWLEDGEMENTS

This chapter was improved by technical reviews from F.M. Phillips, New Mexico Tech, USA; K. Fröhlich; P. Aggarwal, IAEA; and D.L. Parkhurst, United States Geological Survey, USA. Any use of trade, product or firm names is for descriptive purposes only and does not imply endorsement by the US Government.

## APPENDIX TO CHAPTER 4

The following appendix provides details that may be of use to hydrologists requiring additional background information. It summarizes the various reporting units of radiocarbon and their interrelationships, reviews isotopic fractionation in carbonate systems open and closed to CO<sub>2</sub> gas, summarizes radiocarbon calibration and its possible application to radiocarbon dating of DIC in groundwater, provides information on methods of collection of radiocarbon samples, provides sources for selected geochemical and radiocarbon software, and contains information on locating radiocarbon laboratories.

### A.1. RADIOCARBON REPORTING UNITS

Radiocarbon measurements are reported following specific recommendations (Stuiver and Polach (1977) [110]). These authors recommend that in reporting <sup>14</sup>C measurements, all values should be normalized for isotope fractionation effects to a common δ<sup>13</sup>C value of -25‰. These recommendations have been adopted by most radiocarbon laboratories worldwide, providing conformity in reporting units between the various radiocarbon laboratories and continuity of results with previously reported data.

The practice of normalization of <sup>14</sup>C measurements is well established in the radiocarbon community, and is an appropriate step in converting radiocarbon years to calendar years. Geochemists and hydrologists sometimes lose sight of the fact that radiocarbon dating of DIC in groundwater (Eq. (4.3)) is based on non-normalized <sup>14</sup>C specific activity values (Kalin (1999) [111]; Mook and van der Plicht (1999) [216]; Stuiver and Polach (1977) [110]). By international convention, specific activities are compared to a standard activity,  $A_{ox}$ , where  $A_{ox} = 0.95$  times the specific activity of NBS oxalic acid ( $0.95 \times 13.56$  dpm/g C, in the year A.D. 1950). The initial <sup>14</sup>C specific activity,  $A_o$ , and the measured <sup>14</sup>C specific activity of a sample,  $A$ , can be expressed as a percentage of this standard activity in pmc, where  $pmc = (A/A_{ox}) \times 100$  (Mook (1980) [109]). Here, the notation pmc is used for the non-normalized 'per cent modern carbon' and 'pM' for the commonly reported normalized <sup>14</sup>C value, denoted 'per cent modern'. The <sup>14</sup>C values in pM have been modified (normalized) for assumed <sup>13</sup>C isotope fractionation from an assumed initial value of -25‰ to the measured δ<sup>13</sup>C of the sample.

In some cases, such as in studies of <sup>14</sup>C in plants, bones and tree rings, it is convenient and scientifically justifiable to normalize <sup>14</sup>C values to a common δ<sup>13</sup>C value of -25‰, to correct for in vitro fractionation processes that affect both <sup>13</sup>C and <sup>14</sup>C. However, in groundwater, most of the isotopic variation in δ<sup>13</sup>C of DIC is caused by water-rock interaction or geochemical reactions occurring in the aquifer. For example, the δ<sup>13</sup>C of DIC is typically more positive than -25‰ (such as for C<sub>3</sub> plants) due to: (i) isotope fractionation between soil gas CO<sub>2</sub> and HCO<sub>3</sub> in recharge water; and (ii) isotope dilution from dissolution of carbonate rocks that are enriched in <sup>13</sup>C, and not due to in vitro fractionation processes. When dating DIC in groundwater, the actual number of <sup>14</sup>C atoms in the DIC is needed to determine the time elapsed since the DIC was isolated from the modern reservoir (that is, the soil CO<sub>2</sub> derived from plants and air) and its <sup>14</sup>C atoms were recharged. Corrections (adjustments) to the <sup>14</sup>C of DIC are normally made through geochemical calculations, as discussed in this chapter.

Currently, most radiocarbon measurements are made using AMS, which determines radiocarbon ages from a measured isotope ratio (<sup>14</sup>C/<sup>13</sup>C) or (<sup>14</sup>C/<sup>12</sup>C). For example, at the University of Arizona AMS facility, radiocarbon ages are determined from the measured <sup>14</sup>C/<sup>13</sup>C ratio in a sample by comparing that ratio with a similar ratio measured in known standards (Linick et al. (1986) [217]). The measured ratios of standards and samples are corrected (normalized) to values corresponding to δ<sup>13</sup>C of -25‰ by using <sup>13</sup>C/<sup>12</sup>C ratios measured in a stable isotope mass spectrometer and the 'fraction of modern',  $F$ , of the sample,  $S$ , is found using the Eq. (A.1), where the notation is that of Donahue et al. (1990) [218]:

$$F = \frac{(14/13)_{S[-25]}}{(14/13)_{1950[-25]}} \quad (\text{A.1})$$

where

$(14/13)_{S[-25]}$  denotes the  $^{14}\text{C}/^{13}\text{C}$  atom ratio in the sample,  $S$ , normalized to a  $\delta^{13}\text{C}$  of  $-25\text{‰}$ ;  
 $(14/13)_{1950[-25]}$  is the  $^{14}\text{C}/^{13}\text{C}$  atom ratio in a standard normalized to  $-25\text{‰}$  in the year 1950.

The conventional radiocarbon age (denoted ‘Age’) of the sample is then:

$$\text{Age} = -\tau \ln F \quad (\text{A.2})$$

where  $\tau$  is the Libby mean life (8033 a;  $\tau = 5568/\ln(2)$ ) and 5568 is the Libby half-life of  $^{14}\text{C}$ .

Donahue et al. (1990) [218] present equations for the conversion of measured isotope ratios to forms that can be used in Eqs (A.1) and (A.2).

Many other AMS radiocarbon laboratories measure the  $^{14}\text{C}/^{12}\text{C}$  isotope ratio rather than the  $^{14}\text{C}/^{13}\text{C}$  ratio. Equations are summarized below for results based on either the  $^{14}\text{C}/^{12}\text{C}$  or  $^{14}\text{C}/^{13}\text{C}$  ratio.

### A.1.1. Recommended reporting units

For consistency with past practice, and following the recommendations of Stuiver and Polach (1977) [110], Mook and van der Plicht (1999) [216] and Donahue et al. (1990) [218],  $^{14}\text{C}$  values will continue to be reported as pM, which has been normalized for  $^{13}\text{C}$  isotopic fractionation, and its associated  $\pm 1\sigma$  value along with the  $^{13}\text{C}$  value used to normalize pM. The nomenclature used here is as follows (Table A.1).

### A.1.2. Relation between radiocarbon reporting units

The equations that follow are based on those of Stuiver and Polach (1977) [110], and were originally intended for  $^{14}\text{C}$  measurements made by counting beta decay in which the  $^{14}\text{C}$  specific activity was measured in disintegrations per minute per gram of carbon. As that gram of carbon contains, to within about 1/10 000, almost entirely  $^{12}\text{C}$  atoms, the radiocarbon specific activity measured by beta

TABLE A.1. NOMENCLATURE USED IN REPORTING  $^{14}\text{C}$  VALUES

Value	Unit	Uncertainty	Unit	Description
$\Delta^{14}\text{C}$	‰	$\pm 1\sigma$	‰	Per mille depletion or enrichment relative to the NBS I oxalic acid standard normalized for $^{13}\text{C}$ isotopic fractionation
$\delta^{14}\text{C}$	‰	$\pm 1\sigma$	‰	Per mille depletion or enrichment relative to the NBS I oxalic acid standard, not normalized for $^{13}\text{C}$ isotopic fractionation
pM	%	$\pm 1\sigma$		Per cent modern (pM) relative to the NBS I oxalic acid standard, normalized for $^{13}\text{C}$ isotopic fractionation
pmc	%	$\pm 1\sigma$	%	Per cent modern carbon (pmc) relative to the NBS I oxalic acid standard, not normalized for $^{13}\text{C}$ isotopic fractionation
T	years	$\pm 1\sigma$	years	Conventional radiocarbon age, years before 1950

decay can be expressed as the ratio of  $^{14}\text{C}/^{12}\text{C}$ . The terms ‘fraction of modern’,  $F$ , and conventional radiocarbon age can be defined similarly as in the first two equations above, which use the  $^{14}\text{C}/^{13}\text{C}$  ratio, that is, 14/13 is replaced with 14/12. However, in further calculations, such as those necessary for denormalization of reported values of  $F$  or pM, it is necessary to know which isotope ratio was measured in the AMS facility. The equations below are based on  $^{14}\text{C}/^{12}\text{C}$  measurements, leading to squared terms in correcting for  $^{14}\text{C}$  fractionation. The exponent is changed from 2 to 1 when the isotope ratio  $^{14}\text{C}/^{13}\text{C}$  is measured. Donahue et al. (1990) [218] provided equations that relate radiocarbon AMS measurements based on  $^{14}\text{C}/^{13}\text{C}$  and  $^{14}\text{C}/^{12}\text{C}$ .

In radiocarbon dating of DIC, it may be desirable to make calculations based on  $\delta^{14}\text{C}$  or pmc, which have not been normalized with  $^{13}\text{C}$  differences from  $-25\%$ . As most radiocarbon laboratories report normalized values, it is sometimes necessary to ‘denormalize’ the reported value in making radiocarbon age calculations in groundwater environments. The actual equations used for ‘denormalization’ depend on which isotope ratio was measured at the AMS facility, for example  $^{14}\text{C}/^{12}\text{C}$  or  $^{14}\text{C}/^{13}\text{C}$ . In either case, the value of pmc is related to  $\delta^{14}\text{C}$  by:

$$\text{pmc} = \left( \frac{\delta^{14}\text{C}}{1000} + 1 \right) 100 \quad (\text{A.3})$$

If the measurement is based on the  $^{14}\text{C}/^{12}\text{C}$  isotope ratio, then  $\delta^{14}\text{C}$  is related to the normalized  $^{14}\text{C}$  by Stuiver and Robinson (1974) [219]:

$$\delta^{14}\text{C} = \left( \frac{1 + \Delta^{14}\text{C}/1000}{0.975^2 / (1 + \delta^{13}\text{C}/1000)^2} - 1 \right) 1000 \quad (\text{A.4})$$

If the basic measurement is from the  $^{14}\text{C}/^{13}\text{C}$  isotope ratio, the denormalization is:

$$\delta^{14}\text{C} = \left( \frac{1 + \Delta^{14}\text{C}/1000}{0.975 / (1 + \delta^{13}\text{C}/1000)} - 1 \right) 1000 \quad (\text{A.5})$$

The pM relative to the NBS I oxalic acid standard, normalized for  $^{13}\text{C}$  isotope fractionation is:

$$\text{pM} = \left( \frac{\Delta^{14}\text{C}}{1000} + 1 \right) 100 \quad (\text{A.6})$$

The conventional radiocarbon age,  $t$ , is expressed in years before present (BP), where present is the year 1950, and is normalized for  $^{13}\text{C}$  differences from  $-25\%$ :

$$t = -\tau \ln \left( \frac{A_{\text{SN(in1950)}}}{A_{\text{ON(in1950)}}} \right) = -\tau \ln \left( \frac{\text{pM}}{100} \right) = -\tau \ln F \quad (\text{A.7})$$

where

$A_{\text{SN(in1950)}}$  is the specific activity of  $^{14}\text{C}$  in the sample in the year 1950, normalized for  $^{13}\text{C}$  fractionation;

$A_{\text{ON(in1950)}}$  is the specific activity of the standard in 1950.

The conventional radiocarbon age applies best to the dating of wood or other forms of organic matter, or in the dating of DIC in some groundwater systems where the initial  $^{14}\text{C}$  specific activity during recharge is near modern, and geochemical reactions affecting DIC in the aquifer can be ignored, such as in some silicate aquifers (Plummer et al. (2004) [49]; Plummer et al. (2004) [50]; Plummer et al. (2004) [51]). However, generally, the conventional radiocarbon age is biased to old in the dating of DIC in groundwater due to geochemical reaction effects (referred to as ‘reservoir effects’ in radiocarbon literature).

In some cases, it is necessary to ‘denormalize’ the commonly reported normalized  $^{14}\text{C}$  pmc value (Mook and van der Plicht (1999) [216]). Normalized  $^{14}\text{C}$  pM values can be converted to non-normalized pmc values by the equation provided by Mook and van der Plicht (1999) [216], for measurements based on the  $^{14}\text{C}/^{12}\text{C}$  ratio:

$$\text{pmc} = \text{pM} \left[ \left( 1 + \frac{^{13}\delta}{1000} \right) / 0.975 \right]^2 \quad (\text{A.8})$$

where  $^{13}$  is the  $\delta^{13}\text{C}$  of the DIC.

For  $^{14}\text{C}$  measurements based on the  $^{14}\text{C}/^{13}\text{C}$  ratio:

$$\text{pmc} = \text{pM} \left[ \left( 1 + \frac{^{13}\delta}{1000} \right) / 0.975 \right] \quad (\text{A.9})$$

### A.1.3. Relationships derived from the fraction of modern, $F$

In cases where radiocarbon measurements are reported in the normalized ‘fraction of modern’,  $F$ , terminology, the following equations can be used to deduce the parameters of Table A.1 from the values of  $F$  and  $\delta^{13}\text{C}$ .

Terminology:

$F$  = fraction of modern, normalized for  $^{13}\text{C}$  variations

$f$  = fraction of modern, not normalized for  $^{13}\text{C}$  variations

Age = conventional radiocarbon age normalized for  $^{13}\text{C}$  variations (BP)

age = conventional radiocarbon age not normalized for  $^{13}\text{C}$  variations (BP)

pM = normalized per cent modern carbon

pmc = not normalized per cent modern carbon

$\delta^{14}\text{C}$  = not normalized

$\Delta^{14}\text{C}$  = normalized

*Measured as  $^{14}\text{C}/^{12}\text{C}$*

*Measured as  $^{14}\text{C}/^{13}\text{C}$*

$$\text{Age} = -8033 \ln F$$

$$\text{Age} = -8033 \ln F$$

$$\text{age} = -8033 \left( \ln F - 2 \ln(0.975) / \left( 1 + \frac{\delta^{13}\text{C}}{1000} \right) \right)$$

$$\text{age} = -8033 \left( \ln F - \ln(0.975) / \left( 1 + \frac{\delta^{13}\text{C}}{1000} \right) \right)$$

$$f = \exp(\text{age} / -8033)$$

$$f = \exp(\text{age} / -8033)$$

$$\text{pmc} = \exp(-\text{age} / 8033) 100$$

$$\text{pmc} = \exp(-\text{age} / 8033) 100$$

$$\text{pM} = \exp(-\text{Age} / 8033) 100$$

$$\text{pM} = \exp(-\text{Age} / 8033) 100$$

$$\delta^{14}\text{C} = \left( \frac{\text{pmc}}{100} - 1 \right) 1000$$

$$\delta^{14}\text{C} = \left( \frac{\text{pmc}}{100} - 1 \right) 1000$$

$$\Delta^{14}\text{C} = \left( \frac{\text{pM}}{100} - 1 \right) 1000$$

$$\Delta^{14}\text{C} = \left( \frac{\text{pM}}{100} - 1 \right) 1000$$

**Example:**

Given that  $F = 0.8633$  and  $\delta^{13}\text{C} = -13.1\text{‰}$  (based on measurement of the  $^{14}\text{C}/^{13}\text{C}$  ratio):

Parameter	Calculated
F	0.8633 (reported)
$\delta^{13}\text{C}$ (‰)	-13.1 (reported)
F	0.8738
Age (years BP)	1181
age (years BP)	1083
pmc	87.38
pM	86.33
$\delta^{14}\text{C}$ (‰)	-126
$\Delta^{14}\text{C}$ (‰)	-137

**A.1.4. Absolute per cent modern carbon**

Absolute pM and absolute pmc refer to the normalized and non-normalized values of per cent modern carbon that have been calculated, taking into account the decay of the oxalic acid standards for the elapsed time between 1950, when the standard was defined, and the date of collection of the sample. Such corrections are on the order of 50 years and are unnecessary when dealing with geological samples; they are not included here. Further details are provided in Stuiver and Polach (1977) [110], and Mook and van der Plicht (1999) [216].

**A.1.5. Age error from use of normalized  $^{14}\text{C}$  values**

Although there are many uncertainties in radiocarbon dating of DIC in groundwater, an unnecessary error is introduced if ages are based on the normalized pM value rather than the denormalized  $^{14}\text{C}$  pmc value. This difference is not always recognized but, fortunately, the error resulting from use of pM rather than pmc is relatively small. Figure A.1 shows that the error in age varies almost linearly with the value of  $\delta^{13}\text{C}$  of the DIC. If  $\delta^{13}\text{C}$  of the DIC is greater than  $-25\text{‰}$ , the calculated radiocarbon age based on pM will be too old relative to the age properly based on pmc. When  $\delta^{13}\text{C}$  is more negative than  $-25\text{‰}$ , the calculated radiocarbon age will be too young relative to the age properly based on pmc. The  $\delta^{13}\text{C}$  of DIC in most groundwater is more positive than  $-25\text{‰}$ , and commonly in the range of  $-20$  to approximately  $0\text{‰}$  (Vienna Pee Dee belemnite scale). For this range of  $\delta^{13}\text{C}$  values, the age based on pM is approximately 100–400 a too old, respectively. Considering the overall uncertainties in radiocarbon dating of DIC in groundwater, these errors are not generally significant, but do introduce an unnecessary bias in the radiocarbon age. In a few environments, such as where organic carbon is undergoing methanogenesis, the DIC may be significantly enriched in  $\delta^{13}\text{C}$ , and ages based on pM could be as much as 1000 a too old. In environments where the DIC is derived from oxidation of highly depleted carbon sources, such as methane, the radiocarbon age can be as much as 1000 a too young if based on pM rather than correctly on pmc (Fig. A.1).

In summary, radiocarbon dating of DIC in groundwater should be based on the measured  $^{14}\text{C}$  specific activity relative to the modern standard, and can be expressed in  $\delta^{14}\text{C}$  or pmc values. Small errors result if radiocarbon age is evaluated from normalized  $^{14}\text{C}$  values,  $\Delta^{14}\text{C}$  or pM. Measurements of pM should always be accompanied by the measured  $\delta^{13}\text{C}$  and associated  $1\sigma$  errors.

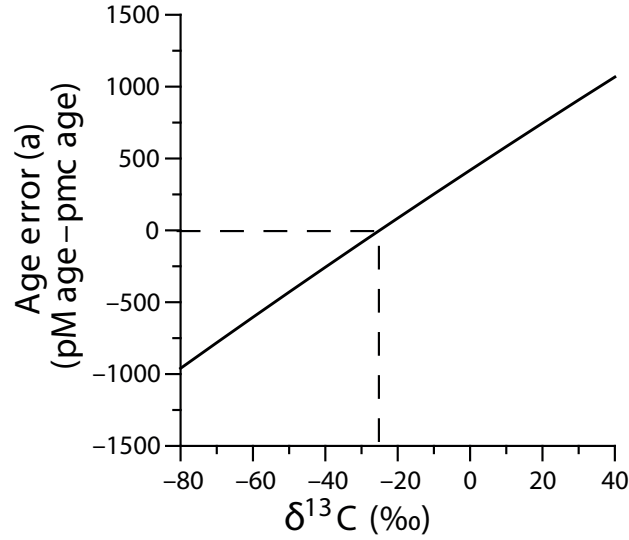


FIG. A.1. Age error resulting from use of pM instead of pmc in radiocarbon dating as a function of  $\delta^{13}\text{C}$  of DIC in the water sample.

## A.2. ISOTOPIC FRACTIONATION IN CARBONATE WATERS

### A.2.1. Definitions

Some of the basic definitions are listed that are mostly assumed in the treatment given here. Further information can be found in texts such as Clark and Fritz (1997) [52], and Mook (2005) [119].

$R$  refers to an isotope ratio and it is defined as the ratio of the abundance of the rare isotope divided by the abundance of the abundant isotope:

$$R = \frac{\text{abundance of rare isotope}}{\text{abundance of abundant isotope}}$$

Examples for  $^{13}\text{C}$  and  $^{14}\text{C}$  would be as follows:

$$^{13}R = \frac{^{13}\text{C}}{^{12}\text{C}}; \quad ^{13}R_{\text{CO}_2} = \frac{^{13}\text{CO}_2}{^{12}\text{CO}_2}; \quad ^{14}R_{\text{CO}_2} = \frac{^{14}\text{CO}_2}{^{12}\text{CO}_2} \quad (\text{A.10})$$

Isotope abundance is usually expressed in  $\delta$  notation, which expresses the value of an isotope ratio of an element in a sample,  $s$ , relative to that ratio in a standard:

$$\delta_{\text{A-ref}} = \left( \frac{R_{\text{A}}}{R_{\text{ref}}} - 1 \right) \times 10^3 \text{ per mille} \quad (\text{A.11})$$

As values of  $\delta$  are small dimensionless numbers, they are usually multiplied by  $10^3\text{‰}$ :

$$^{13}\delta = \left( \frac{(^{13}\text{C}/^{12}\text{C})_s}{(^{13}\text{C}/^{12}\text{C})_{\text{ref}}} - 1 \right) \times 10^3; \quad ^{14}\delta = \left( \frac{(^{14}\text{C}/^{12}\text{C})_s}{(^{14}\text{C}/^{12}\text{C})_{\text{ref}}} - 1 \right) \times 10^3 \quad (\text{A.12})$$

Isotope fractionation is mathematically expressed by comparing the isotope ratios of two compounds that are in isotopic equilibrium. The isotope fractionation factor,  $\alpha_{\text{B-A}}$ , is:

$$\alpha_{\text{B-A}} = \frac{R_{(\text{B})}}{R_{(\text{A})}} \quad (\text{A.13})$$

which expresses the isotope ratio of the phase or compound B relative to that in A. Combining Eqs (A.11, A.13), it can be shown that:

$$\alpha_{B-A} = \frac{1000 + \delta_{(B)}}{1000 + \delta_{(A)}} \quad (\text{A.14})$$

Generally, fractionation factors,  $\alpha$ , are near unity. Therefore, the deviation of  $\alpha$  from 1 is commonly expressed as an ‘enrichment factor’, also referred to as an ‘additive fractionation factor’, because of an approximation that is described below. The ‘enrichment factor’,  $\varepsilon$  (in ‰) is related to  $\alpha$  by:

$$\varepsilon_{B-A} = (\alpha_{B-A} - 1)(10^3) = \left( \frac{R_{(B)}}{R_{(A)}} - 1 \right) \times 10^3 \quad (\text{A.15})$$

$\varepsilon_{B-A}$  is referred to as the ‘additive fractionation factor’ because:

$$\delta_B \cong \delta_A + \varepsilon_{B-A} \quad \text{or} \quad \delta_B - \delta_A \cong \varepsilon_{B-A} \quad (\text{A.16})$$

Approximations of the form of Eq. (A.16) have been applied in the derivation of some of the traditional adjustment models for estimation of  $A_0$  described in this volume. All isotopic calculations in NETPATH and PHREEQC are made in terms of  $R$  and  $\alpha$ , without introduction of this approximation.

A further complication that arises in making isotopic calculations in  $\text{CO}_2$ -water systems stems from the fact that what is measured is the  $^{13}\text{C}$  or  $^{14}\text{C}$  isotopic composition of the total DIC in the groundwater sample. There is no means of routinely measuring the isotopic composition of individual molecules of  $\text{CO}_2(\text{aq})$ ,  $\text{HCO}_3^-$  or  $\text{CO}_3^{2-}$  in solution. Yet, isotopic fractionation occurs between molecules and phases, for which the isotopic fractionation factors are defined. A transformation is made to redefine pH dependent values of  $\alpha$  (and  $\varepsilon$ ) relative to the average isotopic composition of the solution. Accordingly,  $^{13}R_{\text{DIC}}$  is:

$$^{13}R_{\text{DIC}} = \frac{[\text{CO}_{2\text{aq}}]^{13}R_{\text{CO}_{2\text{aq}}} + [\text{HCO}_3^-]^{13}R_{\text{HCO}_3^-} + [\text{CO}_3^{2-}]^{13}R_{\text{CO}_3^{2-}}}{[\text{CO}_{2\text{aq}}] + [\text{HCO}_3^-] + [\text{CO}_3^{2-}]} \quad (\text{A.17})$$

Dividing Eq. (A.17) by  $^{13}R_{\text{HCO}_3^-}$ , and because  $^{13}\alpha_{i-\text{HCO}_3^-} = ^{13}R_i / ^{13}R_{\text{HCO}_3^-}$

$$\frac{^{13}R_{\text{DIC}}}{^{13}R_{\text{HCO}_3^-}} = \frac{[\text{CO}_{2\text{aq}}]^{13}\alpha_{\text{CO}_{2\text{aq}}-\text{HCO}_3^-} + [\text{HCO}_3^-] + [\text{CO}_3^{2-}]^{13}R_{\text{CO}_3^{2-}}}{\text{DIC}} \quad (\text{A.18})$$

Using Eq. (A.14) and defining the fraction of the concentration of the  $i$ th carbonate species to the total concentration of DIC,  $\chi_i = [i]/\text{DIC}$ :

$$\delta^{13}\text{C}_{\text{HCO}_3^-} = \frac{1000 + \delta^{13}\text{C}_{\text{DIC}}}{\chi_{\text{CO}_{2\text{aq}}}^{13}\alpha_{\text{CO}_{2\text{aq}}-\text{HCO}_3^-} + \chi_{\text{HCO}_3^-} + \chi_{\text{CO}_3^{2-}}^{13}\alpha_{\text{CO}_3^{2-}-\text{HCO}_3^-}} \quad (\text{A.19})$$

Similarly, the fractionation factor for calcite relative to DIC can be written as:

$$^{13}\alpha_{\text{calcite-DIC}} = \frac{^{13}\alpha_{\text{calcite-HCO}_3^-}}{\chi_{\text{CO}_{2\text{aq}}}^{13}\alpha_{\text{CO}_{2\text{aq}}-\text{HCO}_3^-} + \chi_{\text{HCO}_3^-} + \chi_{\text{CO}_3^{2-}}^{13}\alpha_{\text{CO}_3^{2-}-\text{HCO}_3^-}} \quad (\text{A.20})$$

and for  $\text{CO}_2$  gas relative to DIC as:

$$^{13}\alpha_{\text{CO}_{2\text{gas}}-\text{DIC}} = \frac{^{13}\alpha_{\text{CO}_{2\text{gas}}-\text{HCO}_3^-}}{\chi_{\text{CO}_{2\text{aq}}}^{13}\alpha_{\text{CO}_{2\text{aq}}-\text{HCO}_3^-} + \chi_{\text{HCO}_3^-} + \chi_{\text{CO}_3^{2-}}^{13}\alpha_{\text{CO}_3^{2-}-\text{HCO}_3^-}} \quad (\text{A.21})$$

## A.2.2. Fractionation factors

Two sets of fractionation factors in the calcite–CO<sub>2</sub>–water system are commonly in use and available in NETPATH (Plummer et al. (1994) [120]). These are identified as the ‘Mook set’ and the ‘Deines set’ of fractionation factors. The Mook set (Mook (2005) [119]) was derived from experimental data obtaining temperature dependent expressions for the additive fractionation factors (enrichment factors) as follows:

Values of  $\varepsilon_{i-j}$  over the temperature range of 0–40°C are shown in Table A.2.

Deines et al. (1974) [122] provide the following relations for the temperature dependence of selected fractionation factors in the calcite–CO<sub>2</sub> water system:

$$1000 \ln {}^{13}\alpha_{\text{CO}_2\text{aq}-\text{CO}_2\text{gas}} = -0.91 + \frac{6300}{T^2} \quad (\text{A.22})$$

$$1000 \ln {}^{13}\alpha_{\text{CO}_3^{2-}-\text{CO}_2\text{gas}} = -3.4 + \frac{870\,000}{T^2} \quad (\text{A.23})$$

$$1000 \ln {}^{13}\alpha_{\text{calcite}-\text{CO}_2\text{gas}} = -3.63 + \frac{1\,194\,000}{T^2} \quad (\text{A.24})$$

TABLE A.2. SUMMARY OF EXPRESSIONS FOR TEMPERATURE DEPENDENCE OF ADDITIVE FRACTIONATION FACTORS IN THE CALCITE–CO<sub>2</sub> WATER SYSTEM ‘MOOK SET’ (MOOK (2005) [119])

Equation	Reference
$\varepsilon_{g-b} = -9483/T + 23.89\text{‰}$ (1)	Mook et al. (1974) [220]
$\varepsilon_{a-g} = -373/T + 0.19\text{‰}$ (2)	Vogel et al. (1970) [138]
$\varepsilon_{a-b} = -9866/T + 24.12\text{‰}$ (3)	From (1) and (2)
$\varepsilon_{c-b} = -867/T + 2.52\text{‰}$ (4)	Thode et al. (1965) [221] and (1)
$\varepsilon_{\text{cal-b}} = -4232/T + 15.10\text{‰}$ (5)	Mook (2005) [119] <sup>a</sup>
$\varepsilon_{\text{cal-g}} = +5380/T - 9.15\text{‰}$ (6)	From (1) and (5)

<sup>a</sup> Based on evaluation of original data from Rubinson and Clayton (1969) [222], and Emrich et al. (1970) [223].

TABLE A.3. VALUES OF  $\varepsilon_{i-j}$  CALCULATED FROM THE ‘MOOK SET’ OVER THE TEMPERATURE RANGE OF 0–40°C

Temperature (°C)	$\varepsilon_{g-b}$	$\varepsilon_{a-g}$	$\varepsilon_{a-b}$	$\varepsilon_{c-b}$	$\varepsilon_{\text{cal-b}}$	$\varepsilon_{\text{cal-g}}$
0	-10.83	-1.18	-12.00	-0.65	-0.39	10.55
5	-10.20	-1.15	-11.35	-0.60	-0.11	10.19
10	-9.60	-1.13	-10.72	-0.54	0.15	9.85
15	-9.02	-1.10	-10.12	-0.49	0.41	9.52
20	-8.46	-1.08	-9.54	-0.44	0.66	9.20
25	-7.92	-1.06	-8.97	-0.39	0.91	8.89
30	-7.39	-1.04	-8.42	-0.34	1.14	8.60
35	-6.88	-1.02	-7.90	-0.29	1.37	8.31
40	-6.39	-1.00	-7.39	-0.25	1.59	8.03

**Note:** g = CO<sub>2</sub> (gas); a = CO<sub>2</sub> (aq); b = HCO<sub>3</sub><sup>-</sup>; c = CO<sub>3</sub><sup>2-</sup>; cal = calcite.

TABLE A.4. VALUES OF  $\epsilon_{i,j}$  CALCULATED FROM THE 'DEINES SET' OVER THE TEMPERATURE RANGE OF 0–40°C

Temperature (°C)	$\epsilon_{g-b}$	$\epsilon_{a-g}$	$\epsilon_{a-b}$	$\epsilon_{c-b}$	$\epsilon_{cal-b}$	$\epsilon_{cal-g}$
0	-10.14	-0.83	-10.95	-1.93	2.19	12.45
5	-9.62	-0.83	-10.44	-1.82	2.14	11.87
10	-9.13	-0.83	-9.95	-1.71	2.10	11.33
15	-8.66	-0.83	-9.48	-1.62	2.06	10.81
20	-8.21	-0.84	-9.04	-1.52	2.02	10.32
25	-7.79	-0.84	-8.62	-1.44	1.98	9.85
30	-7.39	-0.84	-8.23	-1.35	1.95	9.41
35	-7.01	-0.84	-7.85	-1.27	1.91	8.98
40	-6.64	-0.85	-7.48	-1.19	1.88	8.58

**Note:** g = CO<sub>2</sub> (gas); a = CO<sub>2</sub> (aq); b = HCO<sub>3</sub><sup>-</sup>; c = CO<sub>3</sub><sup>2-</sup>; cal = calcite.

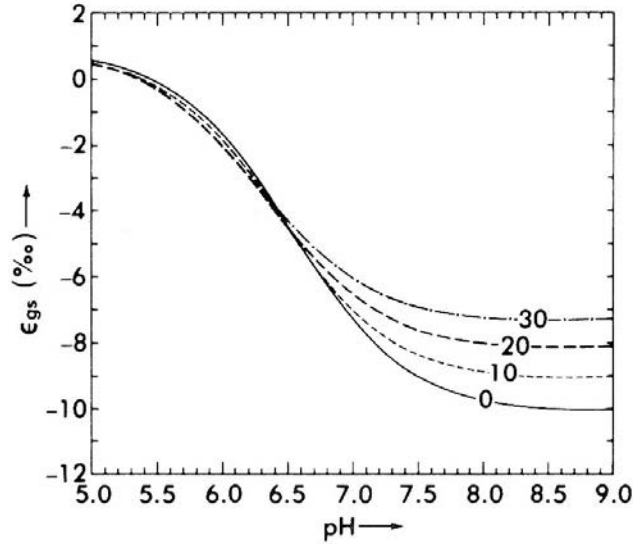


FIG. A.2. The additive fractionation factor,  $\epsilon_{CO_2 \text{ gas-DIC}}$ , between CO<sub>2</sub> gas (g) and the isotopic composition of dissolved inorganic carbon (s) as a function of solution pH from 0 to 30°C, based on the Deines set of fractionation factors (from Wigley et al. (1978) [136]).

$$1000 \ln^{13} \alpha_{HCO_3^- - CO_2 \text{ gas}} = -4.54 + \frac{1099000}{T^2} \quad (\text{A.25})$$

Table A.3 summarizes values of  $\epsilon_{i,j}$  calculated from the Mook set over the temperature range of 0–40°C, which can be compared to the values from the Deines set (Table A.4).

Values of  $\epsilon_{CO_2 \text{ gas-DIC}}$  and  $\epsilon_{calcite-DIC}$  calculated from Eqs (A.20, A.21, A.15) as a function of temperature based on the Deines set of fractionation factors are provided in Figs A.2 and A.3.

Due to the mass difference between <sup>13</sup>C and <sup>14</sup>C atoms, it can be shown that the additive fractionation factors for <sup>14</sup>C should be approximately twice those of <sup>13</sup>C (Craig (1954) [143]):

$$^{14}\epsilon \cong 2 \ ^{13}\epsilon \quad (\text{A.26})$$

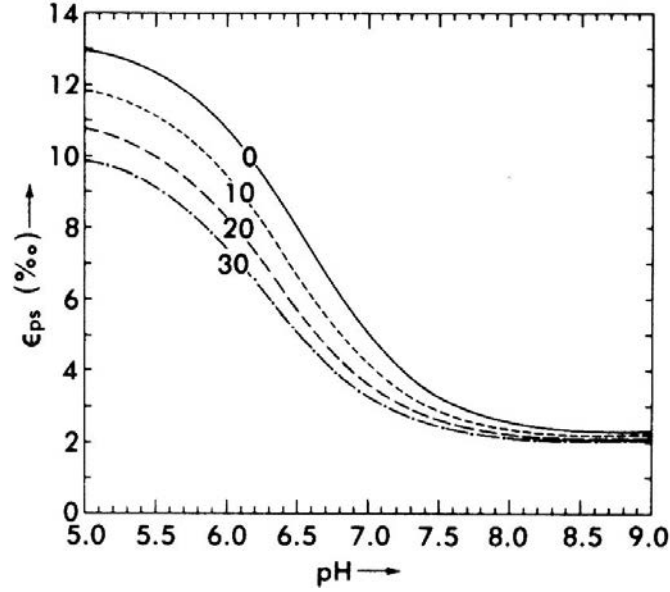


FIG. A.3. The additive fractionation factor,  $\epsilon_{\text{calcite-DIC}}$ , between calcite (p) and the isotopic composition of dissolved inorganic carbon (s) as a function of solution pH from 0 to 30°C, based on the Deines set of fractionation factors (from Wigley et al. (1978) [136]).

This relation is used in NETPATH (Plummer et al. (1994) [120]). There is some experimental and theoretical evidence that the additive fractionation factors for  $^{14}\text{C}$  may be approximately 2.3 times greater than those for  $^{13}\text{C}$  (Saliege and Fontes (1984) [224]; Wigley and Muller (1981) [225]).

### A.2.3. Total dissolved carbon

If TDC is defined as  $m_{\text{TDC}} = m_{\text{DIC}} + m_{\text{DOC}} + m_{\text{CH}_4}$ , then  $\delta^{13}\text{C}_{\text{TDC}}$  becomes:

$$\delta^{13}\text{C}_{\text{TDC}} = \frac{m_{\text{DIC}}\delta^{13}\text{C}_{\text{DIC}} + m_{\text{DOC}}\delta^{13}\text{C}_{\text{DOC}} + m_{\text{CH}_4}\delta^{13}\text{C}_{\text{CH}_4}}{m_{\text{TDC}}} \quad (\text{A.27})$$

If methane and/or DOC are present, the fractionation factors relative to the average isotopic composition of the solution need to be modified to reflect the presence of these additional species, even though they are not likely to be in isotopic equilibrium with any carbon-bearing aqueous species in the solution. Therefore, to estimate values of fractionation factors in the system of TDC, concentrations and isotopic composition of DOC and/or  $\text{CH}_4$  must be measured or defined. Following the above examples for calcite and  $\text{CO}_2$  gas, Eqs (A.20, A.21) become:

$$^{13}\alpha_{\text{calcite-TDC}} = \frac{^{13}\alpha_{\text{calcite-HCO}_3^-}}{\chi_{\text{CO}_{2\text{aq}}} ^{13}\alpha_{\text{CO}_{2\text{aq}}-\text{HCO}_3^-} + \chi_{\text{HCO}_3^-} + \chi_{\text{CO}_3^{2-}} ^{13}\alpha_{\text{CO}_3^{2-}-\text{HCO}_3^-} + \chi_{\text{DOC}} ^{13}\alpha_{\text{DOC-HCO}_3^-} + \chi_{\text{CH}_4} ^{13}\alpha_{\text{CH}_4-\text{HCO}_3^-}} \quad (\text{A.28})$$

and

$$^{13}\alpha_{\text{CO}_{2\text{gas}}-\text{TDC}} = \frac{^{13}\alpha_{\text{CO}_{2\text{gas}}-\text{HCO}_3^-}}{\chi_{\text{CO}_{2\text{aq}}} ^{13}\alpha_{\text{CO}_{2\text{aq}}-\text{HCO}_3^-} + \chi_{\text{HCO}_3^-} + \chi_{\text{CO}_3^{2-}} ^{13}\alpha_{\text{CO}_3^{2-}-\text{HCO}_3^-} + \chi_{\text{DOC}} ^{13}\alpha_{\text{DOC-HCO}_3^-} + \chi_{\text{CH}_4} ^{13}\alpha_{\text{CH}_4-\text{HCO}_3^-}} \quad (\text{A.29})$$

In Eqs (A.28, A.29),  $\alpha_{\text{DOC-HCO}_3^-}$  and  $\alpha_{\text{CH}_4-\text{HCO}_3^-}$  are treated as though they were empirical kinetic isotope fractionation factors and defined from the measured (or estimated) isotopic composition of DOC and  $\text{CH}_4$  in the groundwater sample:

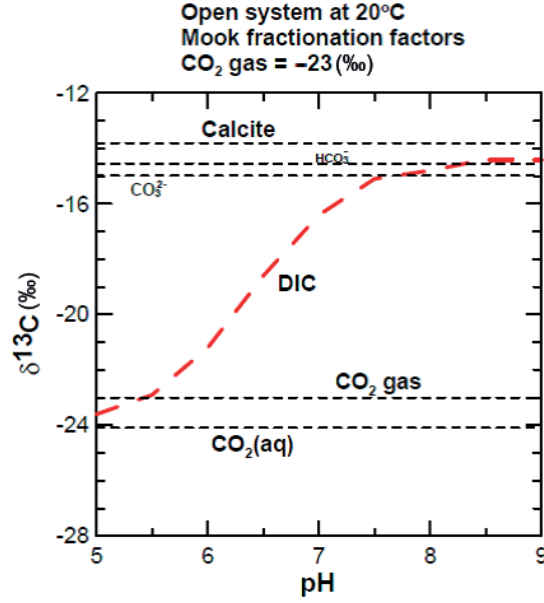


FIG. A.4. The  $\delta^{13}\text{C}_{\text{DIC}}$  of dissolved inorganic carbon in the open system calcite–CO<sub>2</sub>–water, for  $\delta^{13}\text{C}_{\text{CO}_2} = -23\text{‰}$  at 20°C (Mook's set of fractionation factors).

$$^{13}\alpha_{\text{CH}_4\text{-HCO}_3^-} = \frac{1000 + \delta^{13}\text{C}_{\text{CH}_4}}{1000 + \delta^{13}\text{C}_{\text{HCO}_3^-}} \quad (\text{A.30})$$

and

$$^{13}\alpha_{\text{DOC-HCO}_3^-} = \frac{1000 + \delta^{13}\text{C}_{\text{DOC}}}{1000 + \delta^{13}\text{C}_{\text{HCO}_3^-}} \quad (\text{A.31})$$

Values of  $\delta^{13}\text{C}_{\text{HCO}_3^-}$  are calculated from the measured  $\delta^{13}\text{C}_{\text{DIC}}$  using Eq. (A.19).

### Examples: Open system

Using the Mook set of additive fractionation factors in the inorganic calcite–CO<sub>2</sub>–water system, the  $\delta^{13}\text{C}_{\text{DIC}}$  of DIC is calculated as calcite dissolves, maintaining isotopic equilibrium among all dissolved species and calcite at 20°C for a (constant)  $\delta^{13}\text{C}_{\text{CO}_2\text{ gas}}$  value of -23‰; pointing to evolution in a system open to soil gas CO<sub>2</sub> of <sup>13</sup>C isotopic composition of -23‰. The following  $\epsilon$  values are obtained from Table A.2, at 20°C:  $\epsilon_{\text{g-b}} = -8.46\text{‰}$ ;  $\epsilon_{\text{a-g}} = -1.08\text{‰}$ ;  $\epsilon_{\text{a-b}} = -9.54\text{‰}$ ;  $\epsilon_{\text{c-b}} = -0.44\text{‰}$ ;  $\epsilon_{\text{cal-b}} = 0.66\text{‰}$ ;  $\epsilon_{\text{cal-g}} = 9.20\text{‰}$ .

Accordingly, for  $\delta^{13}\text{C}_{\text{CO}_2\text{ gas}}$ , which was defined to be -23‰,  $\delta^{13}\text{C}_{\text{calcite}} = -13.8\text{‰}$ ,  $\delta^{13}\text{C}_{\text{HCO}_3^-} = -14.5\text{‰}$ ,  $\delta^{13}\text{C}_{\text{CO}_3} = -14.9\text{‰}$  and  $\delta^{13}\text{C}_{\text{CO}_2\text{ aq}} = -24.1\text{‰}$ . Calculating the fractions of inorganic carbon species relative to DIC and using Eq. (A.19), it can be seen that the value of  $\delta^{13}\text{C}_{\text{DIC}}$  will increase with increasing pH, as calcite dissolves, from about -24‰ at pH5 and increases to about -14.5‰ at pH8.5 where nearly all of the DIC is HCO<sub>3</sub><sup>-</sup> (Fig. A.4). A similar result is obtained from the 'Deines set' using the plot of Fig. A.2 where at 20°C and pH8.5,  $\epsilon_{\text{g-DIC}}$  is approximately -8‰ and  $\delta^{13}\text{C}_{\text{DIC}}$  is about -15‰.

Next, an estimation is made of the initial <sup>14</sup>C pmc value of DIC in groundwater in equilibrium with a soil gas CO<sub>2</sub> value of 100 pmc at 20°C. As  $^{14}\epsilon_{\text{g-DIC}} \cong 2 \ ^{13}\epsilon_{\text{g-DIC}} \cong -16\text{‰}$ ,  $A_0$  in an open system at 20°C is about 102 pmc:

$$\begin{aligned}
^{13}\epsilon_{\text{g-DIC}} &\approx -8 = ^{13}\delta\text{C}_{\text{g}} - ^{13}\delta\text{C}_{\text{DIC}} \\
^{14}\epsilon_{\text{g-DIC}} &\approx 2^{13}\epsilon_{\text{g-DIC}} \approx 2(-8) \approx ^{14}\delta\text{C}_{\text{g}} - ^{14}\delta\text{C}_{\text{DIC}} = -160 \\
^{14}\delta\text{C}_{\text{DIC}} &= ^{14}\delta\text{C}_{\text{g}} + 16 \\
^{14}\delta\text{C}_{\text{g}} &= \left(\frac{\text{pmc}}{100} - 1\right)1000 = \left(\frac{100}{100} - 1\right)1000 = 00 \\
^{14}\delta\text{C}_{\text{DIC}} &\approx ^{14}\delta\text{C}_{\text{g}} + 16 = 0 + 16 = 160 \\
\text{pmc} &= \left(\frac{^{14}\delta\text{C}_{\text{s}}}{1000} + 1\right)100 = \left(\frac{16}{1000} + 1\right)100 = 101.6
\end{aligned}$$

### A.3. RADIOCARBON CALIBRATION

Regardless of the extent of geochemical corrections, use of the Libby half-life permits use of radiocarbon calibration scales (Stuiver et al. (1998) [226]; Stuiver et al. (1998) [227]). Radiocarbon calibration scales correct for past variations in the strength of the Earth's geomagnetic field and strength of the solar flux. The  $^{14}\text{C}$  content of atmospheric  $\text{CO}_2$  has varied in the past, and for the most part has been somewhat greater than 100 pM (Bard et al. (1993) [228]; Bard et al. (1990) [112]; Bartlein et al. (1995) [229]; Stuiver et al. (1986) [230]; Stuiver and Reimer (1993) [231]). By using the Libby half-life for  $^{14}\text{C}$  and making the appropriate corrections for geochemical reactions, calendar years BP can be derived using radiocarbon calibration scales (Stuiver et al. (1998) [226]; Stuiver et al. (1998) [227]). Figure A.5 shows a plot relating the conventional radiocarbon age (unadjusted for geochemical reactions) to calendar years BP (Stuiver et al. (1998) [226]; Stuiver et al. (1998) [227]). The correction to calendar years is fairly small for samples with radiocarbon ages of less than 10 ka. The correction increases for samples with radiocarbon ages of 10–20 ka. For example, if the radiocarbon age (Libby half-life, adjusted for all geochemical reactions) is 20 ka, the corresponding age in calendar years is nearly 24 ka (Fig. A.5). As adjusted radiocarbon ages are used as calibration criteria for some groundwater flow models, calendar years apply to the hydraulic timescale, not radiocarbon years.

Figure A.5 was extended to approximately 45 ka (radiocarbon years) by using lake varve chronologies (Kitagawa and van der Plicht (1998) [233]; Kitagawa and van der Plicht (1998) [234];

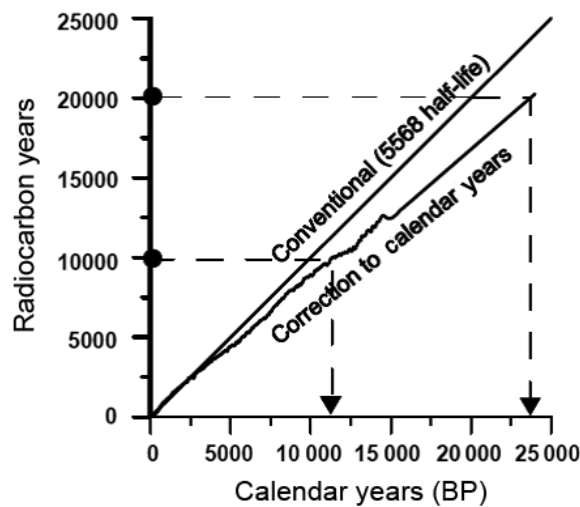


FIG. A.5. Radiocarbon calibration scale (based on data of Stuiver et al. (1998) [226] and Stuiver et al. (1998) [227]; see also Fairbanks et al. (2005) [232]).

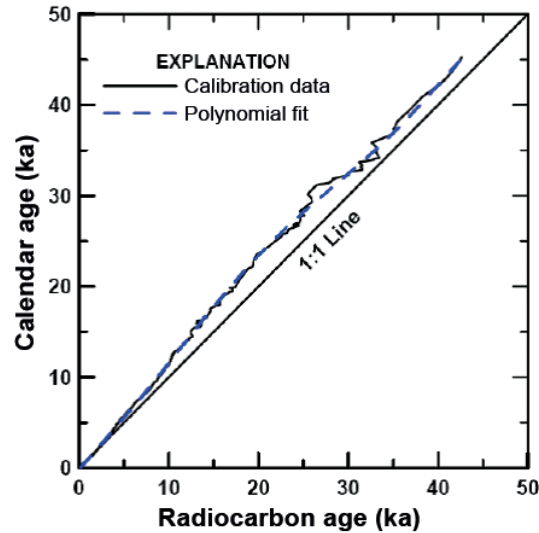


FIG. A.6. Extended radiocarbon calibration to approximately 45 ka radiocarbon years (based on the data of Bard et al. (1998) [236]; Kitagawa and van der Plicht (1998) [233]; Kitagawa and van der Plicht (1998) [234]; Kitagawa and van der Plicht (2000) [235]; Stuiver et al. (1998) [226]; Stuiver et al. (1998) [227]). The blue line is from Eq. (A.33) from Plummer et al. (2004) [49] (see Fairbanks et al. (2005) [232]).

Kitagawa and van der Plicht (2000) [235]) (Fig. A.6). A polynomial (Eq. (A.32)) was fitted to the data of Fig. A.6 and used to estimate calendar years from the unadjusted radiocarbon age (Libby half-life):

$$\begin{aligned} \text{calendar years BP} = & -173.94 + 1.1713A - 2.0521 \times 10^{-5}A^2 + 4.0150 \times 10^{-9}A^3 \\ & - 2.4519 \times 10^{-13}A^4 + 5.7738 \times 10^{-18}A^5 - 4.6915 \times 10^{-23}A^6 \end{aligned} \quad (\text{A.32})$$

where  $A$  is the unadjusted radiocarbon age (Libby half-life) in years.

Although the radiocarbon calibration data obtained from tree rings (Stuiver et al. (1998) [226]; Stuiver et al. (1998) [227]) and  $^{230}\text{Th}/^{234}\text{U}$  dating of corals (Bard et al. (1998) [236]) are relatively precise, larger uncertainties in radiocarbon calibration are associated with data obtained from varves (Kitagawa and van der Plicht (1998) [233]; Kitagawa and van der Plicht (1998) [234]). Recently, additional calibration data have been obtained from a stalagmite in the calendar year age range of 11–45 ka that indicate large variations in atmospheric  $^{14}\text{C}$  content of between 33 and 45 ka (Bard (2001) [237]; Beck et al. (2001) [238]). Although radiocarbon calibration to about 20 ka now seems well established for groundwater applications, extension of the calibration to the dating limits of the radiocarbon method (about 45 ka) has received considerable attention recently (Chiu et al. (2007) [108]; Chiu et al. (2005) [239]; Chiu et al. (2006) [240]; Fairbanks et al. (2005) [232]; Sanford et al. (2004) [47]; Sanford et al. (2004) [48]).

## A.4. FIELD COLLECTION PROCEDURES

### A.4.1. Well selection

Water samples for  $^{14}\text{C}$  determination have historically been obtained from a variety of groundwater sources, including municipal supply wells, monitoring wells, wells used for domestic or farm supply, windmills, flowing wells and springs. Prior to sampling, attention should be given to well construction,

depth and length of the interval open to an aquifer. Commonly, municipal supply wells are open to large intervals of an aquifer, resulting in mixing across  $^{14}\text{C}$  model age gradients. Samples pumped from fractured rock aquifers also tend to be mixtures. Preferred samples for radiocarbon dating are obtained from monitoring wells or flowing wells with a short open interval to the aquifer.

For recently constructed wells, a precaution is necessary; the possibility should be considered that the aquifer was contaminated with fluids used in the drilling process. During drilling, such as in mud-rotary drilling, and in well development after completing a well, water is often imported to the drilling site and pumped into the wellbore. If this imported water is not completely removed in well development, the DIC in the vicinity of the well opening can be contaminated. Plummer et al. (2004) [49] measured the concentrations of CFCs in water pumped from deep, recently completed monitoring wells in New Mexico to identify samples that were likely still contaminated with imported water used in drilling and well development. The most reliable radiocarbon data were obtained from monitoring wells that were free of CFCs, and from domestic supply wells that tended to have more use and relatively short open intervals. As a general guide, water from recently drilled monitoring wells is more likely to be contaminated than water from older wells that have a long history of sampling (or extended well development). The problem is particularly acute in sampling very old water because, due to low flow velocities in an aquifer, groundwater contaminated during drilling may still reside in the vicinity of a well screen even many years after drilling. Due to matrix diffusion into sediment pore spaces, many pore volumes may need to be pumped prior to sampling.

Flowing wells can be another good source of uncontaminated water if there is a long history of use. Finally, because of the possibility of mixing with young fractions, sampling for radiocarbon determination should always include determination of tritium (and possibly CFCs).

#### **A.4.2. Sample collection**

Water samples should be collected as close to the source as possible, and certainly before treatment, such as chlorination, ozonation or aeration, and only after sufficient flow to clear three wellbore volumes from the casing. In the case of domestic supply wells, it is recommended that samples be taken before water enters a pressure tank, where, in the case of a bladderless pressure tank, water would be exposed to a gas phase.

##### *A.4.2.1. Tritium*

Tritium samples are collected in a 1 L plastic-coated glass bottle with a polycone seal cap. A headspace of approximately 2–3 mL is left in the bottles during filling to accommodate expansion upon warming. Tritium analysis is used to detect contamination of old groundwater with water from the bomb era or contamination from drilling. In the case of very old water, as discussed here, tritium should be determined with a very low minimum detection level (<0.1–0.3 TU by electrolytic enrichment and liquid scintillation counting; or preferably <0.1 TU by the helium in-growth method (Bayer et al. (1989) [241]; Clarke et al. (1976) [242])).

##### *A.4.2.2. Carbon-13 and carbon-14 of dissolved inorganic carbon*

Water samples for the determination of  $\delta^{13}\text{C}$  and  $^{14}\text{C}$  of DIC should be filtered in the field (0.45  $\mu\text{m}$  filter), collected in safety coated glass bottles, and capped with a polycone seal cap, leaving a small 2–3 mL headspace to accommodate water expansion. Alternatively, if a sample will be analysed within a few months, a Teflon/silicon septum cap can be used; excluding headspace is recommended. In this case, the septum is normally depressed as the cap is put in place to allow for water expansion. Although it

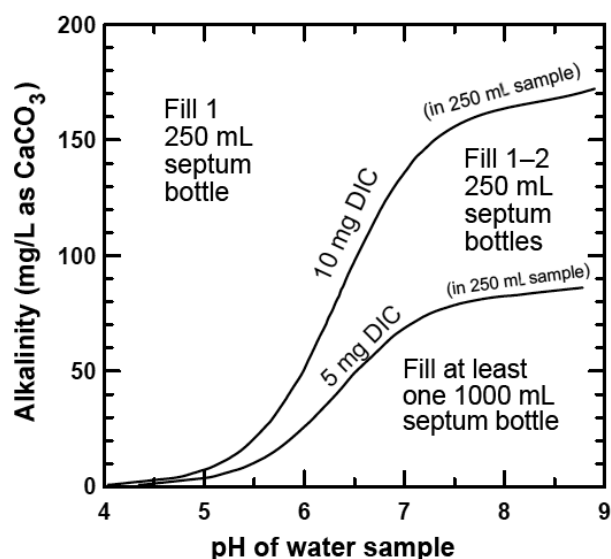


FIG. A.7. Guidelines indicating amounts of groundwater sample required for collection to obtain at least 5 mg C/L as a function of alkalinity (as  $\text{CaCO}_3$ ) and pH (note: alkalinity (in mg/L as  $\text{CaCO}_3$ ) = alkalinity (in mg/L as  $\text{HCO}_3^-$ )  $\times$  0.82014).

can be debated, addition of a preservative to stop possible microbial activity runs a risk of contamination of the sample with a fraction of modern  $^{14}\text{C}$  and is not recommended for old groundwater samples.

Although most AMS facilities can determine  $^{14}\text{C}$  content of DIC with as little as 1 mg of carbon, it is recommended that the volume of water sample collected be sufficient to contain a minimum of 5 mg of DIC (as C). For many water samples, a 250 mL sample will be sufficient. Figure A.7 provides guidelines for sample volumes required to provide a minimum of 5 mg DIC for a range of field alkalinities and pH. The two curves in the figure provide corresponding alkalinity and pH values for simple inorganic carbonate waters (at 25°C) that would contain 5 or 10 mg of DIC in a 250 mL volume. If, for example, the sample alkalinity is 150 mg/L (as  $\text{CaCO}_3$ ) or greater, a 250 mL bottle fitted with a Teflon/silicon septum is sufficient for most pH. Sample volumes of 1 L or more will be needed if field alkalinity is less than 80 mg/L (as  $\text{CaCO}_3$ ) and pH is greater than 7.0. If alkalinity is unknown at the time of sampling, it is recommended to fill two 1 L bottles.

#### A.4.3. Recommended method of collection (dissolved inorganic carbon)

Fill the appropriate bottle(s) fitted with a Teflon/silicon septum cap to provide at least 5 mg of DIC. Fill the sample container(s) from the bottom of the vessel. Use an in-line filter (0.45  $\mu\text{m}$ ) to eliminate the possibility of contamination of the DIC with particulates containing carbonate minerals. If there is concern about DOC oxidation in the sample bottle, a silver filter can be used, though this is normally not needed. Minimize contact with air while filling the bottle(s). This can be accomplished by establishing a closed path from the water source, through the filter, to the bottom of the container. Fill from the bottom, allowing overflow of several litres of filtered water. For potentially low  $^{14}\text{C}$  samples (<10 pmc) or if relatively long times are required for filtering, place the sample bottle in a small bucket or beaker containing water from the same source, flush the sample bottle from the bottom of the bottle while still immersed in the bucket or beaker (allowing overflow of several litres) and cap with a Teflon/silicon septum cap under water. It is best to depress the septum slightly, without compromising the seal, as the cap is screwed onto the bottle to provide room for water expansion as the sample warms during transit and storage prior to analysis. Use plastic coated glass bottles fitted with a Teflon/silicon septum for most samples. The septum allows laboratory extraction of the water sample without contact with air.

#### **A.4.4. Carbon-13 and carbon-14 of dissolved organic carbon**

The procedure for collection of HMW and LMW fractions of DOC is provided in Murphy et al. (1989) [172] and is based on the original work of Thurman and Malcolm (1981) [180], and Murphy (1987) [181]. The sample is filtered (0.45 µm) in the field and collected using a field column system. The fulvic acids (primarily HMW) typically make up about 30% of the DOC in groundwater, and are collected on XAD-8 resin. The LMW compounds are collected on Silicalite, a silica based molecular sieve. Prior to use, the Silicalite is preheated to 1000°C to remove organic contamination. The XAD-8 and Silicalite columns remove only about 30–60% of the total DOC in groundwater. To characterize the fulvic acid fraction completely, a minimum of 200 mg of material is typically needed, and sample volumes of the order of 100–200 L are usually processed. Further details are provided in Murphy et al. (1989) [172]. Other procedures for collection of total DOC can be found in Purdy et al. (1992) [173] and Burr et al. (2001) [184].

#### **A.5. GEOCHEMICAL MODELLING SOFTWARE**

United States Geological Survey (USGS) geochemical modelling software of use in interpreting radiocarbon data (NETPATH, NETPATH-WIN, NetpathXL, PHREEQC, PhreeqcI) and associated documentation can be downloaded from the web site:

[http://wwwbrr.cr.usgs.gov/projects/GWC\\_coupled/](http://wwwbrr.cr.usgs.gov/projects/GWC_coupled/)

Other USGS geochemical software is available from:

<http://water.usgs.gov/software/geochemical.html>

The CALIB Radiocarbon Calibration Programme is available from:

<http://calib.qub.ac.uk/calib/>

#### **A.6. SELECTED ACCELERATOR MASS SPECTROMETRY FACILITIES FOR RADIOCARBON ANALYSIS**

A list of active radiocarbon laboratories (conventional beta-counting facilities and AMS facilities), and known personnel is published annually in the journal Radiocarbon (see, for example, List of Laboratories, Radiocarbon **51**(4) (2009) 1187–1211 and <http://www.radiocarbon.org/Info/lablist.html>).



## Chapter 5

### KRYPTON-81 DATING OF OLD GROUNDWATER

R. PURTSCHERT  
Physics Institute,  
University of Bern,  
Bern, Switzerland

R. YOKOCHI, N.C. STURCHIO  
Department of Earth and Environmental Sciences,  
University of Illinois,  
Chicago, Illinois,  
United States of America

#### 5.1. INTRODUCTION

##### 5.1.1. Krypton in the environment

The abundance of krypton in the atmosphere has been quoted for nearly half a century as  $1.14 \pm 0.01$  ppm, which corresponds to a total atmospheric inventory of  $4.51 \times 10^{12}$  m<sup>3</sup> STP (Verniani (1966) [243]). A recent re-evaluation yielded a value of  $1.099 \pm 0.009$  ppm, which is about 4% lower than the previously used value (Aoki and Makide (2005) [244]).

Krypton has six stable isotopes of which <sup>84</sup>Kr is the most abundant, comprising about 57% of natural Kr (Table 5.1). Eleven major radioactive isotopes of Kr exist but only <sup>81</sup>Kr and <sup>85</sup>Kr, with half-lives of 229 000 and 10.76 a, respectively, exceed 2 d and are, therefore, suitable for the investigation of environmental processes. Krypton-81 is produced in the atmosphere by cosmic ray induced spallation of heavier stable Kr isotopes and by the nuclear reactions <sup>80</sup>Kr(n,  $\gamma$ )<sup>81</sup>Kr and <sup>82</sup>Kr( $\gamma$ , n)<sup>81</sup>Kr.

The atmospheric <sup>81</sup>Kr/Kr ratio has been measured three times by different methods and research groups (Fig. 5.1; Collon et al. (1997) [245]; Kuzminov and Pomansky (1983) [246]; Loosli and Oeschger (1969) [247]). The mean value of  $5.2 \pm 0.6 \times 10^{-13}$  corresponds to a specific activity in the modern atmosphere of  $1.47$  mBq  $\cdot$  L<sup>-1</sup> Kr.<sup>1</sup> Variations in the production rate, for example, due to modulations of the geomagnetic field intensities with a period of 10–30 ka (Plummer et al. (1997) [248]), are likely to be averaged out on the timescale of the <sup>81</sup>Kr mean lifetime (the atmosphere is well mixed within a timescale of  $\sim 1$  a). This, and the fact that the atmosphere represents the main terrestrial Kr reservoir, provides evidence that the <sup>81</sup>Kr abundance in the atmosphere is rather constant over its applicable age dating range.

The production of <sup>81</sup>Kr from <sup>235</sup>U or <sup>238</sup>U fission is expected to be very small because the nuclide is shielded by stable <sup>81</sup>Br. The direct fission yield of <sup>81</sup>Kr is estimated to be only  $7 \times 10^{-11}$  atoms <sup>81</sup>Kr/atoms U<sub>decayed</sub>. For this reason, anthropogenic sources such as nuclear weapon testing and releases from the nuclear industry are probably insignificant. This has been confirmed by the comparison of post-bomb and pre-bomb atmospheric samples, for which the most recent measurements resulted in an agreement at the 8% precision level (Du et al. (2003) [249]). Likewise, subsurface production of <sup>81</sup>Kr in rocks is expected to be very small; the equilibrium concentration of <sup>81</sup>Kr from fission production is  $5 \times 10^{-6}$  <sup>81</sup>Kr atoms  $\cdot$  kg<sup>-1</sup><sub>rock</sub>  $\cdot$  ppm<sup>-1</sup> U. Production due to neutron capture by <sup>80</sup>Kr is probably of the same order of magnitude (Lehmann et al. (1993) [250]).

<sup>1</sup>  $10^{-3}$  dis  $\cdot$  s<sup>-1</sup>  $\cdot$  L<sub>STP</sub><sup>-1</sup> Kr.

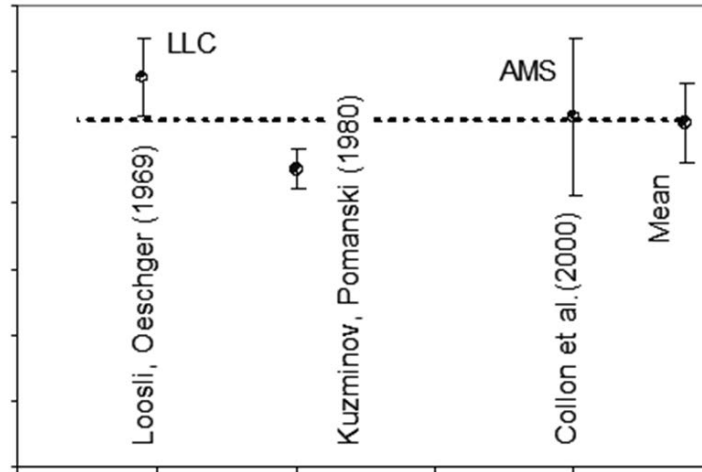


FIG. 5.1. Measurements of the modern atmospheric  $^{81}\text{Kr}/\text{Kr}$  ratio.

## 5.1.2. Krypton in hydrology

### 5.1.2.1. Dating principles

During recharge, water approaches solubility equilibrium with the atmosphere according to the local temperature and barometric pressure at the water table (Fig. 5.2). Gas partitioning at the free air–water interface is described by Henry’s law:

$$c_{\text{gas}}/c_{\text{water}} = H(T, S) \quad (5.1)$$

where

$c_{\text{gas}}$  and  $c_{\text{water}}$  denote the concentration of a given gas species in the gas phase and water phase, respectively;

$H(T, S)$  is the dimensionless Henry coefficient, which depends on water temperature  $T$  and salinity  $S$ .

Water in equilibrium with the atmosphere at  $10^\circ\text{C}$  and 1 atm contains  $\sim 1300$  atoms  $^{81}\text{Kr}/\text{L}$  water (Table 5.1). This is more than seven orders of magnitude larger than the equilibrium concentration of fission  $^{81}\text{Kr}$  in the crust (see above), indicating that subsurface production of  $^{81}\text{Kr}$  is negligible compared with the groundwater source. In the (unlikely) case of a 100%  $^{81}\text{Kr}$  release rate from the rock into the water filled pore volume, for a rock porosity of 30% and a uranium concentration of 50 ppm, a  $^{81}\text{Kr}$  activity in the water of less than 1‰ of the modern level would result. For a temperature of  $10^\circ\text{C}$ , a mean ocean salinity of 35‰ and a total world ocean water volume of  $1.4 \times 10^{18} \text{ m}^3$ , a total ocean Kr inventory of  $10^{11} \text{ m}^3$  is estimated, which corresponds to about 2% of the global inventory. Therefore, exchange between ocean and atmosphere (e.g. as a result of changing temperature) has little impact on the atmospheric Kr inventory.

During recharge, Kr (and other atmospheric gases) may additionally be introduced by the dissolution of excess air (Fig. 5.2) (Heaton and Vogel (1981) [211]). In contrast to other gaseous tracer methods, which rely on absolute concentrations of dissolved constituents (such as  $^3\text{H}/^3\text{He}$ ,  $\text{SF}_6$  or  $^4\text{He}$ ),  $^{81}\text{Kr}$  and  $^{85}\text{Kr}$  (and  $^{39}\text{Ar}$ ), gas tracers are insensitive to absolute concentration that is affected by the addition of excess air, degrees of degassing (both in nature and during sampling; see also Chapter 8) and recharge conditions because these methods are based on isotope ratios of the same element ( $^{81}\text{Kr}/\text{Kr}$ ,  $^{85}\text{Kr}/\text{Kr}$ ,  $^{39}\text{Ar}/\text{Ar}$ , etc.).

TABLE 5.1. KRYPTON IN THE ENVIRONMENT: SOME USEFUL NUMBERS

Kr species/physical characteristic	Value	Unit	Reference
Kr concentration in the atmosphere	1.1	ppm	Aoki and Makide (2005) [244]
Isotopic composition (stable)			
Kr-78	0.35	%	Ozima and Podosek (2002) [251]
Kr-80	2.26	%	Ozima and Podosek (2002) [251]
Kr-82	11.52	%	Ozima and Podosek (2002) [251]
Kr-83	11.48	%	Ozima and Podosek (2002) [251]
Kr-84	57	%	Ozima and Podosek (2002) [251]
Kr-86	17.4	%	Ozima and Podosek (2002) [251]
Kr-85/Kr (2008)	2.4	$\times 10^{-11}$	Winger et al. (2005) [252]
Kr-81/Kr (air)	$5.2 \pm 0.6$	$\times 10^{-13}$	Du et al. (2003) [249]; Collon et al. (1997) [245]
Kr-85/Kr-81 (2008)	46.2		Du et al. (2003) [249]; Collon et al. (1997) [245]
Half-life Kr-85	10.76	a	Firestone and Shirley (1996) [253]
Half-life Kr-81	229 000	a	Firestone and Shirley (1996) [253]
Kr-85 atoms/L water (2008)	57 845		Du et al. (2003) [249]; Collon et al. (1997) [245]
Kr-81 atoms/L water (modern)	1253		Du et al. (2003) [249]; Collon et al. (1997) [245]
Kr solubility in water (10°C)	0.081	$\text{cm}^3_{\text{STP}} \cdot \text{cm}^{-3}_{\text{water}} \cdot \text{atm}^{-1}$	Weiss and Kyser (1978) [254]
Diffusion coefficient of Kr in air (20°C)	$\sim 0.13$	$\text{cm}^2/\text{s}$	Weast (1981) [255]
Diffusion coefficient of Kr in water (20°C)	$\sim 6.2$	$10^{-5} \text{ cm}^2/\text{s}$	Weast (1981) [255]

After the air saturated water parcel has moved to depths of greater than about 20 m, the  $^{81}\text{Kr}$  (or  $^{39}\text{Ar}$ ) exchange with the source (atmosphere) stops and the  $^{81}\text{Kr}/\text{Kr}$  ratio decreases due to radioactive decay (Fig. 5.2). According to the exponential decay law, the time elapsed since the water was in contact with the atmosphere can be calculated according to:

$$t_{\text{Kr}} = -\frac{1}{\lambda_{81}} \ln \left( \frac{R_{\text{sample}}}{R_{\text{air}}} \right) \quad (5.2)$$

where

$\lambda_{81}$  is the  $^{81}\text{Kr}$  decay constant ( $3.03 \pm 0.14 \times 10^{-6}/\text{a}$ );

$R_{\text{sample}}$  and  $R_{\text{air}}$  are the  $^{81}\text{Kr}/\text{Kr}$  ratios of the sample and modern air respectively (Table 5.1).

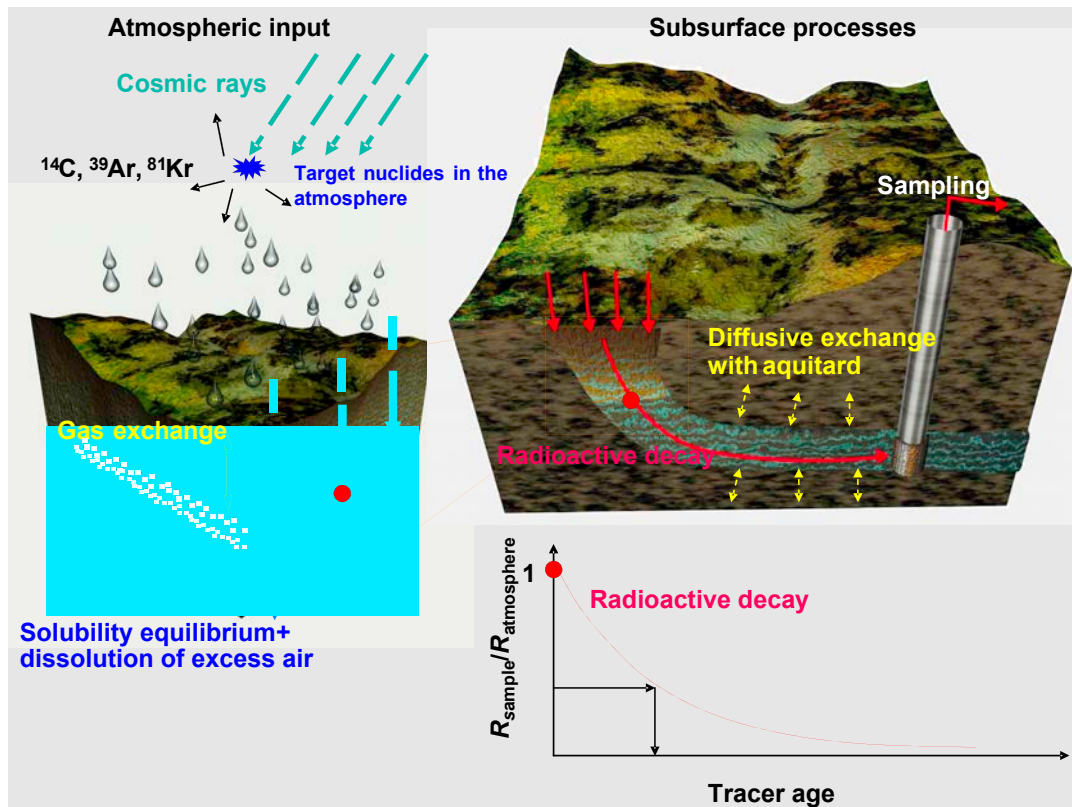


FIG. 5.2. Scheme of relevant processes for radio-noble gas dating. Cosmic ray induced production in the atmosphere, gas dissolution in the recharge water due to solubility equilibrium and trapped air bubbles in the quasi-saturated soil zone (excess air) and radioactive decay in the subsurface.

$R_{\text{sample}}$  can also be expressed as  $\%_{\text{modern}}$  in relation to  $R_{\text{air}} = 100\%_{\text{modern}}$ . As underground production can be neglected, the only process other than decay that might change the isotopic ratio in the groundwater system is mixing driven by diffusive/dispersive processes (especially with aquitards) and/or convergent flow (Lehmann et al. (2003) [256]).

The suitable dating range of  $0.2 \times 10^5$ – $10^6$  a ( $\sim 5$  half-lives), the presumably constant and known input concentration, the potential absence of underground production and the fact that dating is based on an isotope ratio ( $^{81}\text{Kr}/\text{Kr}_{\text{total}}$ ) which is not sensitive to climate variations and phase transition processes, makes  $^{81}\text{Kr}$  an ideal tracer for dating old groundwater or ice. The fundamental limitation hindering the routine use of  $^{81}\text{Kr}$  in environmental science is the analytical challenge of sampling and measuring  $^{81}\text{Kr}$  concentrations at natural levels.

#### 5.1.2.2. Diffusive exchange with stagnant zones

There are only a few processes that may affect the interpretation of  $^{81}\text{Kr}$  activities in terms of groundwater age. The two most potentially critical processes are: (i) mixing of different water flow path components as for any radiometric dating tracer and (ii) diffusive exchange between the aquifer (active flow zone) and the less permeable adjacent aquitards ('stagnant zones'). In (i), ages calculated on the basis of the radioactive decay law yield a lower age limit for mixtures due to the concave shape of the exponential function (see Chapters 3 and 9). For (ii), diffusive loss of  $^{81}\text{Kr}$  atoms into stagnant zones of the system, on the other hand, dilutes tracer concentration in the active flow zone and results in tracer model ages which are too old compared with pure decay based idealized ages (see also Section 4.9.3). The larger the tracer diffusion accessible volume in relation to the advective system volume,

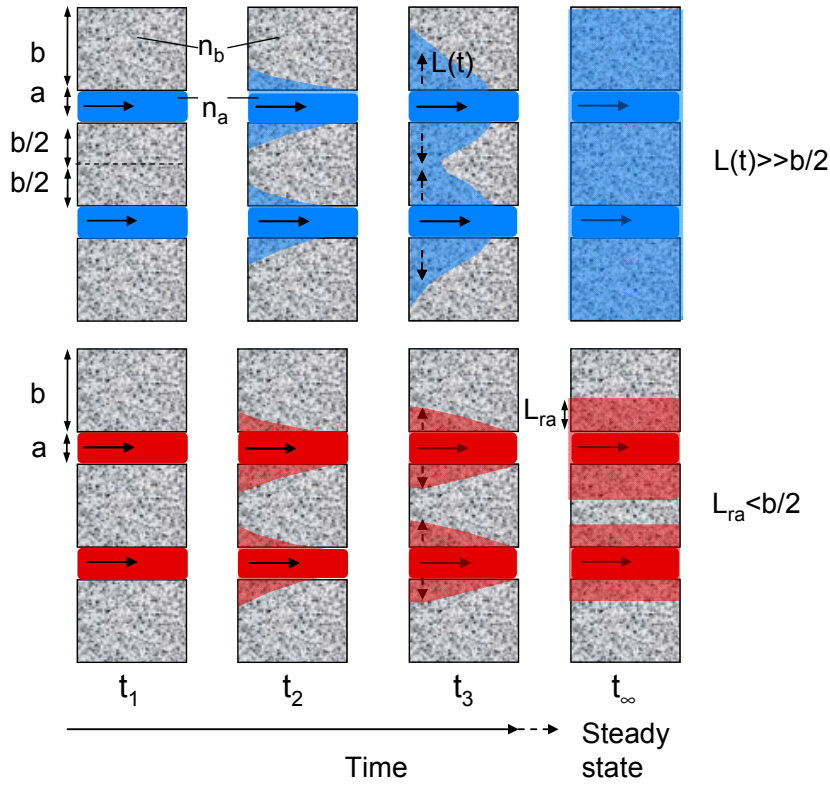


FIG. 5.3. Diffusive tracer retardation in simplified double porous media. The advective flow system with aperture  $a$  and porosity  $n_a$  may either be a fracture ( $n_a = 1$  in this case) surrounded by a rock matrix (with porosity  $n_b$ ) or an aquifer between two aquitards, each with thickness  $b$ . The process is depicted at a specific location as a function of time increasing from left to right.

the older the tracer model age becomes compared with the hydraulic age. The ratio of tracer model age to hydraulic age is expressed by the effective retardation factor  $R$  (Małozzewski and Zuber (1985) [257]). Both processes are competitive in terms of their effect on  $^{81}\text{Kr}$  model age (Fig. 5.3). The top image in Fig. 5.3 depicts the evolution of a stable tracer (in blue). The initially tracer free stagnant zone is increasingly penetrated due to the concentration gradient between the active and stagnant zones. Steady state is achieved when concentration gradients are equalized in the whole system. The bottom image depicts the diffusion limit of a radioactive tracer (brown) with a diffusion length  $L < b/2$  (Fig. 5.3 modified after Cook et al. (2005) [208]).

The accessible system volume is tracer (half-life) specific and depends on the effective tracer diffusion coefficient  $D_{\text{eff}}$  in the pore space of the stagnant zones. For a stable tracer, the diffusion path length  $L(t)$  increases steadily and indefinitely as a function of time (Einstein (1905) [258]):

$$L(t) \cong \sqrt{D_{\text{eff}} t} \quad (5.3)$$

For radioactive tracers on diffusion, length at steady state is constrained by the mean lifetime  $\tau = 1/\lambda$  of the tracer.

$$L_{\text{ra}} \cong \sqrt{D_{\text{eff}} \tau} = \sqrt{\frac{D_{\text{eff}}}{\lambda}} \quad (5.4)$$

The situation is illustrated in Fig. 5.3 for an idealized system of parallel flow and stagnant zones with thicknesses  $a$ ,  $b$  and porosities  $n_a$ ,  $n_b$ , respectively. It is assumed that the tracer concentration in

the stagnant zone is initially zero and that sorption reactions are negligible. The retardation factor  $R$  is provided by the ratio of the total tracer accessible pore volume to the mobile water volume.

$$R(t) \cong \frac{a \cdot n_a + 2 \cdot L(t) \cdot n_b}{a \cdot n_a} \quad (5.5)$$

For short flow times and/or slow diffusion  $L(t)$  becomes small and the retardation factor  $R(t)$  is  $\sim 1$  (Fig. 5.3,  $t_1$ ). With increasing flow time,  $L(t)$  increases according to Eq. (5.3) and the tracer delay  $R(t)$  increases as well ( $t_2-t_3$ ). The steady state situation depends on the half-life of the tracer, the diffusion coefficient and the spacing  $b$  between the mobile zones. A diffusion length  $L(t)$  or  $L_{ra}$  exceeding  $b/2$  (Fig. 5.3,  $t_\infty$  top) will result in a retardation factor  $R$  which is simply provided by the ratio of total system porosity to the porosity of the advective flow system (Małozewski and Zuber (1985) [257]):

$$R \cong \frac{a \cdot n_a + b \cdot n_b}{a \cdot n_a} \quad (5.6)$$

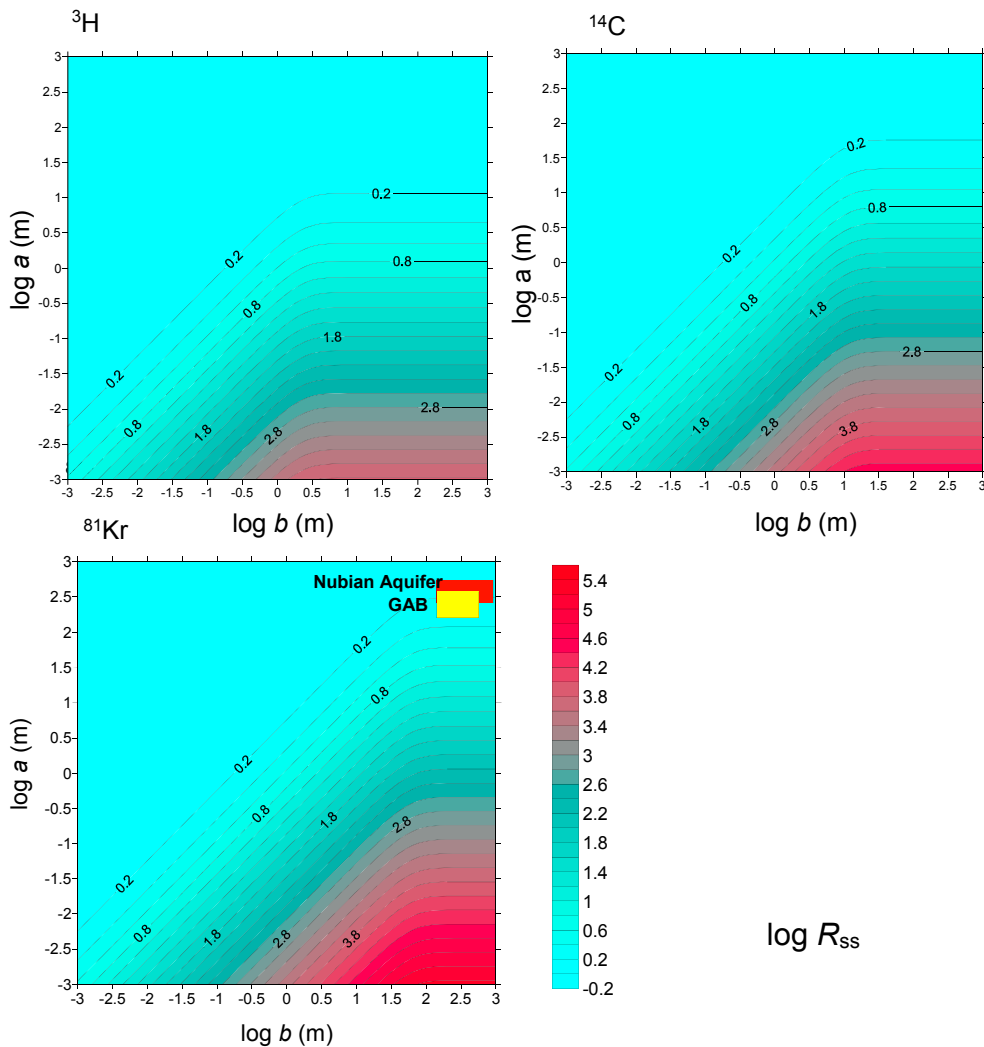


FIG. 5.4. Plots of the logarithm of steady state retardation factor  $R_{ss}$  as a function of the logarithm of the thickness of the stagnant zone ( $b$ ) and the thickness of the transmissive zones ( $a$ ). The relations are shown for  $^3\text{H}$ ,  $^{14}\text{C}$  and  $^{81}\text{Kr}$  assuming reasonable effective diffusion coefficients and a porosity of the flow zone of 0.3 (Sanford (1997) [207]). The system characteristics of the Great Artesian Basin (Section 5.5) and the Nubian aquifer (Chapter 14) are also indicated in the  $^{81}\text{Kr}$  plot.

For fast decaying radioactive tracers and/or slow diffusion in large impermeable zones ( $L_{ra} < b/2$ ), the retardation factor is limited to a maximal steady state value  $R_{ss}$  (Fig. 5.3, Case D bottom).

$$R_{ss} \cong \frac{a \cdot n_a + 2 \cdot L_{ra} \cdot n_b}{a \cdot n_a} \quad (5.7)$$

with  $L_{ra}$  given in Eq. (5.3). The mobile and stagnant zones can be interpreted either as aquifers surrounded by aquitards or as fractures within a rock matrix. In the latter case,  $n_a = 1$ .

Steady state retardation factors for  $^3\text{H}$ ,  $^{14}\text{C}$  and  $^{81}\text{Kr}$  are shown in Fig. 5.4 as functions of the system parameters  $a$  and  $b$  for reasonable porosities and effective tracer diffusion coefficients (Sanford (1997) [207]). As deduced above, diffusive retardation is small for thick aquifers (large  $a$ ) with thin aquitards (small  $b$ ; blue area) and increases with increasing  $b$  for constant  $a$ . If the extension of the stagnant zones exceeds the tracer diffusion length  $L_{ra}$  (the location of the sharp bend on the  $b$  axes),  $R$  levels off with increasing  $b$ . The longer the diffusion length (or half-life of the tracer), the higher the maximal retardation factor for a given geometry of the system. Fractures with small apertures ( $a$ ) and long flow times may produce retardation factors  $R$  of up to  $10^3$  (Fig. 5.4; Cook et al. (2005) [208]). For several hundred metre thick regional aquifers such as the J-sandstone aquifer in the Great Artesian Basin or the Nubian aquifer in Egypt (see case studies), relatively moderate steady state  $^{81}\text{Kr}$  retardation factors can be expected (coloured boxes in Fig. 5.4). Equations (5.5–5.7) probably, in most circumstances, overestimate the retardation  $R$  of the tracer. This is because (i) the permeability in ‘stagnant zones’ in most cases still allows some advective flow and (ii) because timescales may be too short to achieve a steady state equilibrium between the active and passive flow systems.

### 5.1.2.3. Additional noble gas tracers ( $^{85}\text{Kr}$ , $^{37}\text{Ar}$ and $^{39}\text{Ar}$ )

With the current status of analytical techniques,  $^{81}\text{Kr}$  sampling and measurement require large volume water degassing in the field (see next sections). The collected gas offers the possibility to measure not only  $^{81}\text{Kr}$  but also three other shorter lived noble gas radionuclides that may provide additional valuable information.

#### *Krypton-85*

Krypton-85 is the second radioactive Kr isotope that is suitable for groundwater dating for reasons similar to that of  $^{81}\text{Kr}$ . However, the shorter half-life ( $t_{1/2} = 10.76$  a) limits the dating range of  $^{85}\text{Kr}$  to  $<50$  a. Krypton-85 is produced as a fission product of uranium and plutonium decay. Over the past 50 a, the increasing release of  $^{85}\text{Kr}$  from nuclear fuel reprocessing plants (such as Sellafield, La Hague) has completely overwhelmed the natural activity of about  $10^{-7}$  Bq/cm $^3_{\text{STP}}$  Kr (Lehmann and Loosli (1984) [259]). The current specific activity in the atmosphere is about 1.4 Bq/cm $^3_{\text{STP}}$  Kr, which corresponds to an atomic ratio of  $^{85}\text{Kr}/\text{Kr}_{\text{total}}$  of  $2 \times 10^{-11}$  (see also Fig. 5.10). Air saturated water (10°C, 1 atm) contains about 58 000  $^{85}\text{Kr}$  atoms/L water (Table 5.1). Krypton-85 detected in gas extracted from groundwater indicates either the admixture of young groundwater (Althaus et al. (2007) [260]) or, in the case of very old groundwater, can be used as an indication of atmospheric air contamination during sampling and gas purification (Loosli et al. (2000) [261]).

#### *Argon-39*

Argon-39 is produced through the interaction of cosmic rays with nuclides of potassium and argon in the atmosphere. The resulting atmospheric equilibrium activity is constant at  $1.67 \times 10^{-2}$  Bq/m $^3$  of air (Loosli (1983) [262]), corresponding to an atmospheric  $^{39}\text{Ar}/\text{Ar}$  ratio of  $\sim 10^{-15}$  (anthropogenic sources are negligible). With a half-life of 269 a,  $^{39}\text{Ar}$  fills the dating gap between young residence time indicators

(CFC,  $^3\text{H}/^3\text{He}$ , etc.) and the radiocarbon method (Corcho et al. (2009) [263]; Corcho et al. (2007) [264]). Owing to the very low isotopic abundance of  $^{39}\text{Ar}$ , a relatively large amount of water (~2000 L) has to be degassed in the field to obtain a sufficient number of  $^{39}\text{Ar}$  atoms. Although first attempts have been made to use the accelerator mass spectrometry (AMS) technique which would reduce this volume (Collon et al. (2004) [265]), and laser atom trap methods are currently being developed (Williams et al. (2010) [266]), the detection of  $^{39}\text{Ar}$  is currently only practical using the radioactive decay counting technique (Loosli (1983) [262]). The  $^{39}\text{Ar}$  activity of the argon separated from groundwater is measured in high pressure proportional counters in an ultra-low background environment (see Section 5.4.1).

The interpretation of  $^{39}\text{Ar}$  activities in terms of groundwater residence time may be complicated because of subsurface production of  $^{39}\text{Ar}$  via the  $^{39}\text{K}(n, p)^{39}\text{Ar}$  reaction (Loosli et al. (1989) [267]). In such rarely occurring cases, more care has to be taken in the interpretation of the data (Purtschert et al. (2001) [268]).

In the investigation of very old groundwater systems,  $^{39}\text{Ar}$  can be useful (i) as an indicator of the presence of water components in the age range 60–1000 a which cannot be identified by  $^3\text{H}$ ,  $^{85}\text{Kr}$  or CFC measurement, and (ii) as a formation specific indicator with a ‘flow history memory’ of a few hundred years (Purtschert et al. (2001) [268]).

### *Argon-37*

Argon-37 is produced in the atmosphere by cosmic rays in spallation reactions. The resulting specific activity is about  $1 \text{ mBq/m}^3_{\text{air}}$  (see also Fig. 5.10), corresponding to an  $^{37}\text{Ar}/\text{Ar}$  ratio of  $\sim 2 \times 10^{-20}$ . Because of the short half-life of  $^{37}\text{Ar}$  ( $t_{1/2} = 35 \text{ d}$ ), any atmospheric components would have decayed in water which was underground for more than about half a year. Owing to the similarities in  $^{39}\text{Ar}$  and  $^{37}\text{Ar}$  production,  $^{37}\text{Ar}$  provides a monitor for the strength of underground production of  $^{39}\text{Ar}$ . This underground release strength is also an important factor for the interpretation of helium data (Chapter 8).

## 5.2. LARGE VOLUME GAS SAMPLING TECHNIQUES

### 5.2.1. Sampling requirements

Although future increases in the detection efficiency of  $^{81}\text{Kr}$  are likely to eventually decrease the sample size to practically transportable amounts (less than tens of litres of water), existing studies of  $^{81}\text{Kr}$  have used gases obtained from 17 t (Lehmann et al. (2003) [256]) to 3 t (Sturchio et al. (2004) [5]) of water, requiring gas extraction in the field. Such a degassing system has to (i) be leaktight to avoid sample contamination by modern air, (ii) have a high extraction yield to reduce sampling and extraction time and also the volume of water necessary, and (iii) be suitable for fieldwork (e.g. be simple, light and robust). The performance of a gas extraction system is determined by the extraction efficiency at a given water flow rate. Maximal water flow rate is limited by the productivity of a well and the pressure drop through a system.

As old water usually has lower tracer concentrations than the atmosphere, a very small amount of air contamination could seriously affect dating results. A rigorous leak check is, therefore, mandatory (see box for an example of a leak check method).

There is a series of technical measures for efficiency optimization if an extraction is carried out in a laboratory or on a research ship (Smethie and Mathieu (1986) [269]). It is also possible to pre-enrich extracted gases in the field (Sidle and Fischer (2003) [270]). However, the operational practicality is more critical for groundwater hydrology, which demands sampling at remote locations.

### Method of leak checking

Prior to gas collection, the entire degassing system needs to be evacuated, and carefully checked for leaks. Commonly, the system is evacuated in the field and pressure increase is monitored to evaluate the leak rate of the entire system. To guarantee a leak rate of less than  $X\%$ , the following conditions have to be fulfilled:

$$\frac{\Delta p}{\Delta t} \cdot V < Q \cdot c \cdot e \cdot X\%$$

where

$\Delta p$  is the pressure increase (mbar) in time  $\Delta t$  (min);

$V$  is the volume of the gas part of the system (L);

$Q$  is water flux (L/min);

$c$  is gas content of water ( $\text{cm}^3_{\text{STP}}/\text{L}$ );

$e$  is extraction yield (%).

The typical parameters for an extraction system such as those used by Patterson et al. (2005) [43], are a water flow rate of 20 L/min, a gas content of 16  $\text{cm}^3_{\text{STP}}/\text{L}$  (ASW 10°C), an extraction yield of 80% and a volume of the extraction system (including sample container) of 30 L. For <1% air contamination, the pressure increase during a leak test must be less than 0.1 mbar/min or 2.5 mbar/30 min. A leak test of at least 30 min is, therefore, adequate in this case. During a leak test, all gas pumps and compressors should be in operation in a closed circuit (active test).

After a leak test, the system must be flushed with sample water and gas for at least three system volumes. Alternatively, a flushing gas such as helium or pure  $\text{N}_2$  may be used.

### 5.2.2. Physical principles of gas extraction

Physical extraction of  $^{81}\text{Kr}$  from water requires the opposite process of the air equilibration process discussed earlier. According to Henry's law, the amount of gas dissolved in a liquid is proportional to the partial pressure of the gas in equilibrium with the liquid at a constant temperature, i.e. gas and liquid phases in contact will eventually reach solubility equilibrium. At recharge, groundwater dissolves atmospheric gases at atmospheric pressure ( $\approx 1$  bar). By exposing the air saturated water to a gas phase having lower partial pressure of a component than the previous equilibrium, the dissolved gas component becomes repartitioned into the gas phase to attain a new solubility equilibrium. In practice, low Kr partial pressure is achieved either by applying a vacuum so that the partial pressure of any dissolved gas component is lower than that of the atmospheric air previously equilibrated with the sampled groundwater, or by putting the water in contact with a pure and inert gas phase such as He or  $\text{N}_2$  in which Kr partial pressure is nominally zero.

The efficiency of gas extraction from groundwater, therefore, depends on: (i) the partial pressure of the gas phase in equilibrium with the water, (ii) the solubility of Kr in the water, and (iii) the rate of gas transfer. The pressure in the gas phase depends on the capability of the pump and the gas flux, which is a function of the water flux and the gas content of the water. The limiting factor of the gas transfer rate from water to gas phase is the rate of gas diffusion in water. The most effective method of enhancing the efficiency of the apparatus is to increase the specific gas–water interfacial surface area by spraying the water or by using a membrane contactor characterized by a large surface area.

During these gas extraction processes, the elemental and isotopic ratios of noble gases are expected to fractionate, depending on their solubility. Extraction efficiency of two substances  $i$  and  $r$  ( $E_i$  and  $E_r$ ) with solubility  $S_i$  and  $S_r$  are expected to follow a relation:

$$S_r \frac{E_r}{1-E_r} = S_i \frac{E_i}{1-E_i} \quad (5.8)$$

in the case where solubility equilibrium is attained. A theoretical limit on the maximum possible isotopic fractionation is provided by assuming Rayleigh fractionation using the square root of the mass ratio as the isotopic fractionation factor. For an extraction efficiency of >50%, the isotopic fractionation of the  $^{81}\text{Kr}/^{84}\text{Kr}$  ratio is expected to be <1%, much smaller than the uncertainty of the current measurements. Thus, the measured isotopic abundance of  $^{81}\text{Kr}$  does not require any correction for isotopic fractionation during sample processing and the same applies to other noble gas radionuclides of interest.

### 5.2.3. Gas extraction system designs

Two categories of systems have been applied in the field for large volume gas extraction: (i) vacuum extraction using an extraction chamber and (ii) membrane contactors. In both systems, sample water is transferred from the well into the system and discharged after gas extraction (Fig. 5.5). Large particles in the water are filtered out, and water flux and inlet pressure are monitored using a flow meter and a pressure gauge. Check valves are used to prevent flows of water or gas in undesired directions.

In the extraction units, the contact area between the water and the gas phase is increased either by producing small water droplets (spraying) or by means of hydrophobic microporous hollow fibre membrane contactors. In the vacuum cylinder gas extraction system, the groundwater sample is sprayed through nozzles of optimal size (2–6 mm) into a transparent cylinder containing two phases, gas and water, separated by gravity. The water is continuously removed from the bottom of the cylinder at a desired rate regulated with magnetic floating sensors to maintain a range of water

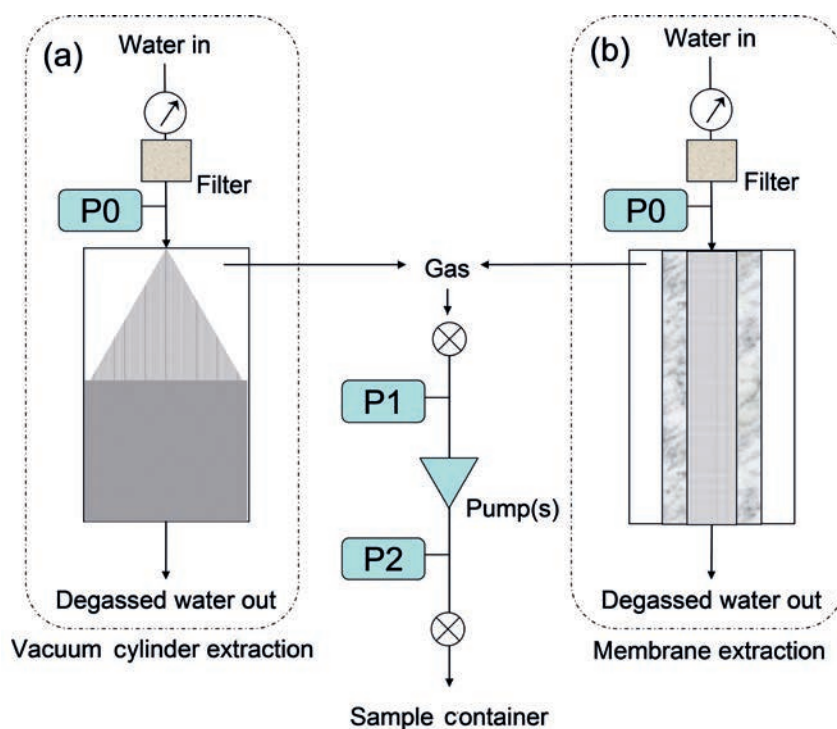


FIG. 5.5. Schematic diagram of water degassing systems: (a) vacuum cylinder extraction; (b) membrane extraction ( $P_0$ : water inlet pressure;  $P_1$ : gas extraction pressure;  $P_2$ : gas pressure in the sampling container).

levels while the gas–vapour phase is transferred to a sample container by a compressor (Fig. 5.5(a)). The hydrophobic microporous hollow-fibre membrane contactor has a cylindrical shape, and consists of two volume sections partitioned by the membrane material. Since the membrane is hydrophobic, it will not allow liquid water to pass through the pores, and diffusion of gas from the liquid water into the gas-filled pores is the mechanism by which gases are extracted from the groundwater (Wiesler (1996) [271]). Because water and gas phases are separated by the membrane instead of gravity, water level tuning is not required. The gas phase in contact with water is maintained at a pressure of 20–150 mbar (P1)<sup>2</sup>, and the gas released from the water is pumped via pump/compressor into pre-evacuated sampling containers (P2, Fig. 5.5). The gas handling portion of the extraction apparatus is commonly constructed of stainless steel tubing connected with stainless steel Swagelok fittings. Pressure gauges monitor the sampling condition (P1, pressure of the gas phase in equilibrium with water) and gas yield (P2, total pressure of the sampled gas).

#### 5.2.4. Specific parameters, remarks and extraction efficiencies

##### 5.2.4.1. Vacuum cylinder extraction system

The extraction cylinder is 20 cm in diameter and 100 cm in height, made of an acrylic tube with PVC end caps. For air saturated water and a water flux of 20 L/min, a typical extraction pressure of 20–50 mbar is reached (Fig. 5.6). This leads to an extraction efficiency of 80–90% for a water temperature of 10°C (Kropf (1996) [272]). The flow rate and, thus, the sampling capacity of the system is primarily limited by the pump rate of the drainage pump (WP2), which is about 30 L/min.

A number of technical features have been devised for enhanced sampling efficiency with minimal problems. An additional centrifugal pump (WP1) is used to increase inlet water pressure (up to 26 bar), and thus the flow rate, to supplement the pressure drop (4–8 bar) caused by the spray nozzle. The differential range of attainable pressure is widened significantly, both on the vacuum (20 mbar) and pressure side (12 bar), by installing two pump/compressors of different pressure capacities in series. An emergency stop function is also installed, which is triggered either by manual switching or by a forbidden physical parameter (such as rising water levels in the extraction cylinder) to protect the system and the sample.

The vacuum cylinder extraction system, which has been used successfully in several field campaigns for large volume <sup>39</sup>Ar, <sup>85</sup>Kr and <sup>81</sup>Kr sampling (Corcho et al. (2007) [264]; Lehmann et al. (2003) [256]; Sturchio et al. (2004) [5]), was developed at the Physics Institute at the University of Bern. A similar apparatus has been used in oceanography (Smethie and Mathieu (1986) [269]) and is currently in operation at other institutes or environmental research companies (University of Freiburg, University of Leipzig, Hydroisotop GmbH).

##### 5.2.4.2. Extraction system using membrane contactors

The availability of commercially available membranes facilitated the construction of compact field degassing systems (Ohta et al. (2009) [273]; Probst et al. (2007) [274]). The membrane contactor currently used at the University of Illinois in Chicago (Liqui-Cel® Extra-Flow 4×28) handles water flow rates up to 30 L/min. For air saturated water with a water flux of 20 L/min at a typical vacuum pressure of 130 mbar, the extraction efficiency is 80–90% for Ar and O<sub>2</sub> and >70% for Kr. No significant Kr isotopic fractionation has been observed through this extraction process. The operating pressure of the vacuum is limited to >65 mbar to avoid damaging the membrane structure, which sets a theoretical limit on extraction efficiency. The original system (EDGAR: Extraction of Dissolved Gases for Analysis of Radiokrypton) weighed about 180 kg (Probst et al. (2007) [274]), whereas a recent modification

<sup>2</sup> Depending on the performance of the pump system and the water and gas fluxes, respectively.

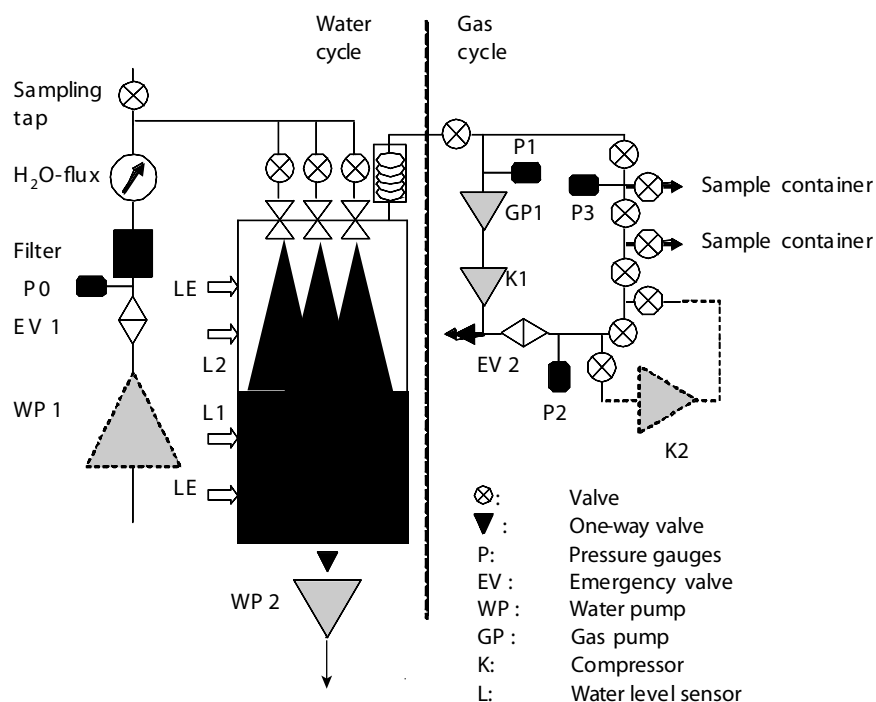


FIG. 5.6. Vacuum cylinder apparatus for field gas extraction of dissolved gases. Components indicated with dotted lines are optional (see text). In the water part (left side), the water is filtered and transferred to the extraction cylinder from where it is pumped out after degassing. An emergency valve (EV1) protects the cylinder from overflow (closed when the water level reaches LE). The gas is extracted with a vacuum pump (GP1) compressed (K1) into the sampling container. An additional compressor (K2) can be attached if higher pressures are required because of high gas contents and/or small sample containers ( $P_{max} \sim 15$  bar).

halved the size. Smaller membrane contactors are now available with lower water flow capacity (<5 L/min), and may be applied for smaller sampling (Ohta et al. (2009) [273]).

### 5.2.5. Optimal design of gas extraction units

The systems described above are complementary, and a suitable or optimal gas extraction method needs to be adjusted according to the local environmental conditions at the sampling site, the required sample size and the isotope of interest. Table 5.2 summarizes the most important features, benefits and disadvantages of the two systems.

## 5.3. GAS PREPARATION AND PURIFICATION

### 5.3.1. Introduction

Existing analytical methods for  $^{81}\text{Kr}$  (and  $^{39}\text{Ar}$ ) require relatively large quantities ( $\sim 15 \mu\text{L}$ ) of pure Kr gas. The gas phases extracted in the field have to be processed and purified in the laboratory. Alternatively, an initial noble gas pre-enrichment can already be achieved in the field (Sidle and Fischer (2003) [270]). The composition of dissolved gas in groundwater can be highly variable (Fig. 5.7). The air saturated seepage water may acquire different amounts of excess air through the partial or complete dissolution of air bubbles that are trapped at the capillary fringe in the unsaturated soil zone. Carbon dioxide can be accumulated from different sources in the unsaturated (biogenic  $\text{CO}_2$ ) or

TABLE 5.2. COMPARISON OF DIFFERENT GAS EXTRACTION SYSTEMS

Benefits	Disadvantages
Extraction chamber	
Insensitive to chemical and physical water composition (pH, temperature, hydrocarbons, suspended matter, etc.)	Requires low extraction pressure and is, therefore, more sensitive to leaks
Easy to repair by experienced personnel in case of breakdown (important in remote areas)	Careful leak testing and set-up requires experienced personnel
Operational for a large range of water fluxes	Relatively high flow resistance may limit water flow rate
Allows a low extraction pressure, thus higher extraction efficiency	Not commercially available and, therefore, expensive to construct
Benefits	Disadvantages
Membrane contactors	
Commercially available membrane contactors, relatively inexpensive	Sensitive to chemical and physical water composition: Not suitable in the presence of substances which reduce the surface tension of water
Modular: several contactors can be combined in parallel (increased water flux) and/or in series (increased extraction efficiency)	Not suitable for a high temperature environment (i.e. >70°C)
Compact and relatively easy to operate in the field	Suspended or precipitated matter may clog the pores
Low inlet water pressure facilitates high water flux; operational over large flux range	A damaged membrane requires a relatively complex regeneration processes

the saturated zone (biogenic, chemogenic or thermogenic). Under reducing conditions, O<sub>2</sub> is consumed and CH<sub>4</sub> can be produced by methanogenesis or CO<sub>2</sub> reduction (Klass (1984) [275]). As a result of denitrification, N<sub>2</sub> is another common subsurface gas source in many aquifers. Thus, a Kr purification system must be able to separate Kr efficiently from large quantities of gas of variable composition. In the case of multitracer studies, including, for example, additional <sup>39</sup>Ar measurements, a combined Kr and Ar purification process is necessary. There are several methods of separating noble gases from gas mixtures. Some of the most common processes used in large volume Kr–Ar purification systems are outlined below.

### *Distillation*

Isolating and/or enriching components from a gas mixture based on differences in condensation points of the gas components (such as cooling traps for CO<sub>2</sub> or water vapour removal from the gas mixture).

### *Adsorption*

Separating gas mixtures using microporous solids (adsorbents) that have strong affinities for one or more of the components in the mixtures at variable temperature and partial pressure.



that are in use for stable noble gas isotopic analyses (Beyerle et al. (2000) [276]). The procedures described here or elsewhere in recent literature (Loosli and Purtschert (2005) [277]; Smethie and Mathieu (1986) [269]; Yokochi et al. (2008) [278]) are, therefore, to be regarded as a ‘snapshot’ of the present capability. In the following sections, two selected large volume noble gas purification systems will be presented in more detail.

### 5.3.2. Purification system at the University of Bern

The low level counting laboratory at the Physics Institute of the University of Bern has a long history in the separation and analysis of noble gas radionuclides through low level counting (LLC) (Loosli (1983) [262]; Loosli et al. (2000) [261]; Loosli et al. (1986) [279]; Loosli and Purtschert (2005) [277]). The required amount of gas extracted from groundwater for LLC is constrained by the decay rate of the isotope of interest. Measuring  $^{81}\text{Kr}$  in groundwater via decay counting is not feasible, but LLC was used for the first detection of  $^{81}\text{Kr}$  in the atmosphere (Loosli and Oeschger (1969) [247]). The powerful combination of  $^{85}\text{Kr}$  and  $^{39}\text{Ar}$  dating in hydrology (Corcho et al. (2007) [264]; Purtschert (2008) [280]) requires purification of both Ar and Kr. If Ar or Kr is exclusively of interest, the procedure can be optimized and simplified accordingly. With the separation system of the LLC laboratory in Bern, samples with a gas volume between ten (for  $^{85}\text{Kr}$  measurements) and several hundred litres can be processed serially in portions of about 2 L.

#### *Combined Ar–Kr separation procedure*

The gas is transferred from the sample cylinder into a first cooling trap filled with activated charcoal (AC). Using the bulk gas as a carrier, water vapour and  $\text{CO}_2$  are removed using a molecular sieve 5A, and  $\text{O}_2$  is removed by oxidation of Cu to CuO in a Cu furnace at  $600^\circ\text{C}$ . The sample is then released into a buffer volume, and injected as a sequence of 2 L aliquots into the gas chromatograph (GC) separation system. The two large packed columns of the GC (1 m long, 7 cm diameter,  $T = 20^\circ\text{C}$ ) are filled with AC and with a molecular sieve 5A, respectively, and sequentially. Helium is used as a carrier gas, and the gas effluent is analysed by a thermal conductivity detector. The fractions containing Ar and Kr are collected separately in cooling traps filled with AC at  $\text{N}_2(\text{l})$  temperature. This procedure separates Ar from Kr, so that the Kr in the Ar fraction is reduced by a factor of at least  $10^4$  to eliminate present day atmospheric  $^{85}\text{Kr}$  activity. The argon fraction is then passed a second time through the GC columns and finally purified from any remaining traces of  $\text{O}_2$  and  $\text{N}_2$  in a Ti-furnace at  $800^\circ\text{C}$ . If present, a fraction of  $\text{CH}_4$  is collected together with Kr because the Kr and  $\text{CH}_4$  retardation times overlap if more than  $1 \text{ cm}^3$  STP  $\text{CH}_4$  was present in the original sample. The final Kr purification is done with a separation system optimized for Kr. Any traces of radon (released, for example, from AC in the system) are removed in a cold finger filled with glass pellets at  $\text{N}_2(\text{l})$  temperature.

#### *Krypton purification*

Krypton typically extracted from 300–500 L of water, or from the residual gas from the Ar–Kr system described above (the Kr enriched portion), is separated by three GC separation steps. If only Kr (for  $^{85}\text{Kr}$  or  $^{81}\text{Kr}$  measurements) is of interest, the procedure starts at this point (Collon et al. (2000) [281]).

The sample gas is exposed to a molecular sieve (5A (MS1)) bed for water vapour and  $\text{CO}_2$  removal and subsequently adsorbed on an AC cold finger (AC1).

The trap (AC1) is then heated to room temperature, and the desorbed gases (mainly  $\text{N}_2$  and Ar) are pumped away during the first five minutes. The trap is then flushed with the carrier gas (He) and the effluent is monitored using a thermal conductivity detector. After the Ar( $\text{O}_2$ ) and  $\text{N}_2$  peaks have

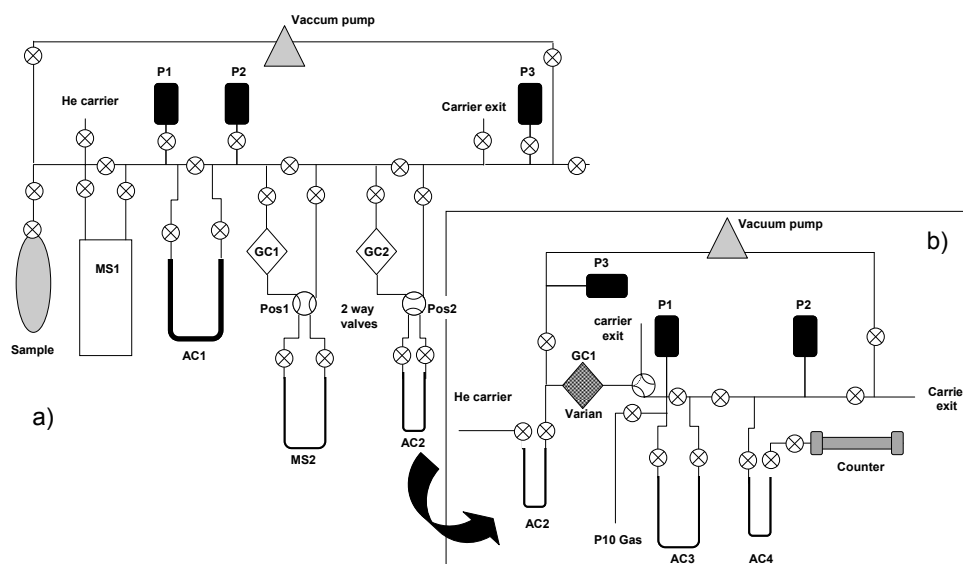


FIG. 5.9. Krypton purification system (for details, see text). Pure Kr is obtained by several GC separation steps (a). Krypton is then transferred into a cooling trap (AC2), purified, mixed with P10 gas, and finally fed into the proportional counter (b).

passed, the two way valve is switched to divert the gas flow through the second trap (MS2) filled with a 5A molecular sieve cooled at  $N_2(l)$  temperature. From this trap, the desorption procedure is repeated to further purify and freeze Kr in the third cooling trap (AC2), filled with AC. In each step, the gas volume is reduced by a factor of  $\sim 10$  and the remaining gas volume in AC2 is about 20–100  $\mu\text{L}$  STP (Collon et al. (2000) [281]). AC2 is then removed from the system and connected to a commercial GC system (Varian Star 3400) where the Kr is further purified, mixed with a P10 mixture as a quench gas (90% argon and 10%  $\text{CH}_4$ ) and finally transferred into the low level counter for activity measurement in the underground laboratory (Fig. 5.9(b)). If the Kr and  $\text{CH}_4$  abundances in the sample are comparable, they can be easily separated and the final amount of recovered Kr is determined from the area of the Kr peak. If the methane and Kr peaks cannot be separated, the Kr content in the counter gas has to be measured after the activity measurement by mass spectrometry.

Large  $\text{CH}_4$  concentration in the sample gas requires further measures in order to purify Kr. For example,  $\text{CH}_4$  can be used as a carrier gas for GC separation (Sidle and Fischer (2003) [270]). In the laboratories of the University of Bern,  $\text{CH}_4$  is oxidized in a CuO coated furnace at  $800^\circ\text{C}$ , followed by the separation of the resulting  $\text{CO}_2$  and  $\text{H}_2\text{O}$ .

### 5.3.3. Purification system at the University of Illinois, Chicago

Major constituents of the atmosphere,  $\text{N}_2$ ,  $\text{O}_2$  and Ar, have much higher vapour pressure than Kr. Consequently, cryogenic distillation enriches the residual phase in Kr. Large scale cryogenic distillation with refined engineering control has indeed been the most widely applied method of producing pure gas substances from the atmosphere. Eliminating sophisticated engineering controls, a simple method of cryogenic Kr enrichment at an easily attainable constant temperature (77 K) was developed at the University of Illinois, Chicago (Yokochi et al. (2008) [278]). Pure Kr is obtained through subsequent GC separation and Ti-gettering. The system uses a quadrupole mass spectrometer (QMS) to monitor gas effluent composition during separation, which enables (i) small scale cryogenic distillation in a controlled manner, (ii) gas chromatographic separation of parts per million by volume (ppm<sub>v</sub>) level

of Kr from a significantly large quantity of gas (up to a few litres), and brings (iii) the applicability of the method to natural groundwater samples characterized by variable chemical compositions.

After H<sub>2</sub>O and CO<sub>2</sub> removal using a molecular sieve 4A, sample gas is condensed in an empty container at liquid N<sub>2</sub> temperature, then distilled at that temperature assisted by a vacuum compressor. The rate of the cryogenic distillation is about 3 L/min for a system dominated by N<sub>2</sub>, and 0.5 L/min for a system dominated by O<sub>2</sub>. The N<sub>2</sub>/Ar ratio of the distillation gas effluent is continuously monitored to determine the progress of the distillation based on a model calculation assuming gas–liquid equilibrium partitioning. Efficient separation of Kr and CH<sub>4</sub> from Ar, O<sub>2</sub> and N<sub>2</sub> can be achieved for up to a few litres of the distillation residue gas by using an AC column (AC2) at room temperature. The Kr peak following these major species overlaps with the peak tails, but the use of a QMS for monitoring gas composition enables identification and further selective processing of the Kr enriched portion. A molecular sieve 5A separates Kr from CH<sub>4</sub> (up to a few hundred cubic centimetres STP) at low temperature (around –20°C). Pure Kr is collected in a small (0.7 cm<sup>3</sup>) stainless steel container filled with AC.

#### 5.4. DETECTION METHODS OF NOBLE GAS RADIONUCLIDES

Despite their excellent tracer properties, radioactive noble gases are still not used on a routine basis in environmental science; for <sup>81</sup>Kr, only three field investigations have been completed to date (Lehmann et al. (1991) [282]; Lehmann et al. (2003) [256]; Sturchio et al. (2004) [5]). The main issue limiting the widespread use of noble gas radionuclides has been a lack of convenient analytical methods to measure these isotopes at natural concentrations. The problem is depicted in Fig. 5.10, where typical values of atmospheric activities, concentrations and specific isotope ratios are plotted as a function of the half-lives of corresponding noble gas isotopes. The numbers can vary depending on the specific situation, but correspond roughly to modern waters under average environmental conditions. First, the extremely low isotopic abundances (<10<sup>-11</sup>) of these noble gas radionuclides far exceed the dynamic range of conventional gas source mass spectrometers. The activities in 1 L of water for <sup>37</sup>Ar, <sup>39</sup>Ar, <sup>85</sup>Kr and <sup>81</sup>Kr are 10<sup>-4</sup>, 10<sup>-1</sup>, 10<sup>-3</sup> and 10<sup>-7</sup> mBq, respectively. While the <sup>85</sup>Kr activity of a modern sample

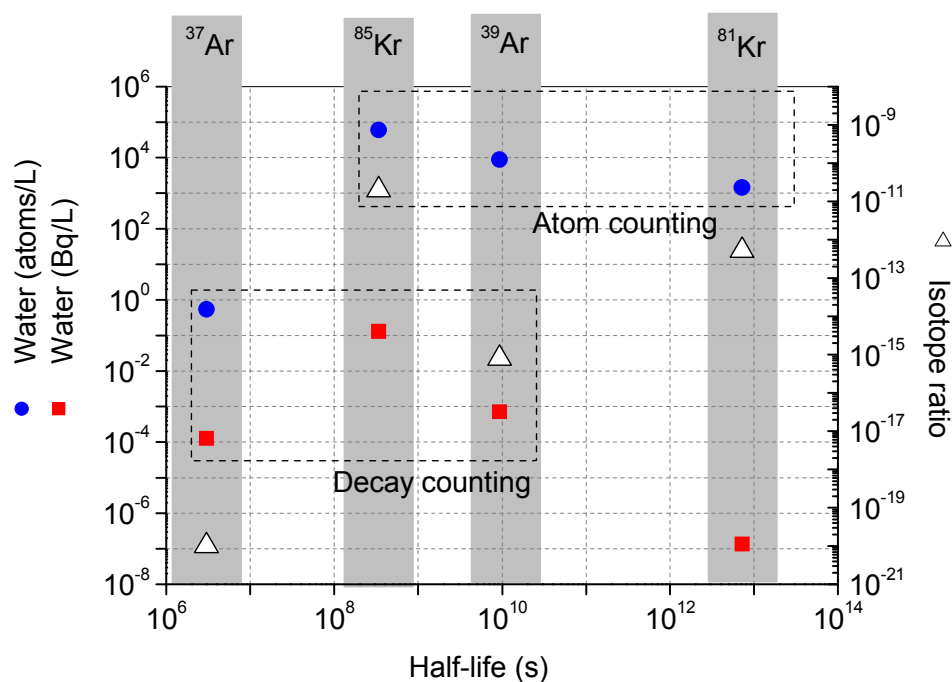


FIG. 5.10. Typical values of atmospheric activities (squares), concentrations (circles) and specific isotope ratios (e.g. <sup>81</sup>Kr/Kr; triangles) dissolved in 1 L of water at 10°C versus half-life of noble gas radionuclides (Lehmann and Loosli (1984) [259]).

can be measured in a number of laboratories worldwide,  $^{39}\text{Ar}$  and  $^{37}\text{Ar}$  can currently only be measured in one underground laboratory at the University of Bern, using Ar extracted from a few tons of water. As seen in Fig. 5.10, the specific  $^{81}\text{Kr}$  activity is out of range of any reasonable sampling and decay counting system, thus  $^{81}\text{Kr}$  has to be measured by other atom counting methods. AMS (Collon et al. (2000) [281]) and new ultrasensitive atom counting methods (Chen et al. (1999) [283]; Du et al. (2003) [249]) have been applied in studies of  $^{81}\text{Kr}$  in hydrology. The analytical methods that are suitable for noble gas radionuclides, particularly  $^{81}\text{Kr}$ , will be briefly discussed in the following section.

#### 5.4.1. Low level counting

For decades, LLC was the only method for detecting radioisotopes of Ar and Kr at atmospheric levels. The first determination of  $^{81}\text{Kr}$  activity in the atmosphere was undertaken using proportional counting with 5 L of pre-bomb Kr (Loosli and Oeschger (1969) [247]). The current LLC laboratory at the University of Bern is shown in Fig. 5.11 (Acosta-Kane et al. (2007) [284]). The laboratory is located at a depth of 35 m, providing a reduction of the muon flux by a factor of  $\sim 10$ . The laboratory walls utilize special concrete selected for its low radioactivity content to minimize gamma ray flux within the laboratory. The proportional counters are built of high conductivity, oxygen free Cu and filled with the sample gas at a pressure of 2–30 bar, then placed in a cylindrical lead shield 5 cm thick. Only a fraction of the particle decay energy is released within the counter before it reaches the counter wall. The deposited energy increases with increasing pressure and is recorded by a 7-bit multi-channel analyser (MCA) with a linear energy range of 0–35 keV. For further background reduction, the proportional counter is constructed with low background materials and uses an anti-coincidence proportional counter to reduce background. The small volume of the counters reduces the background

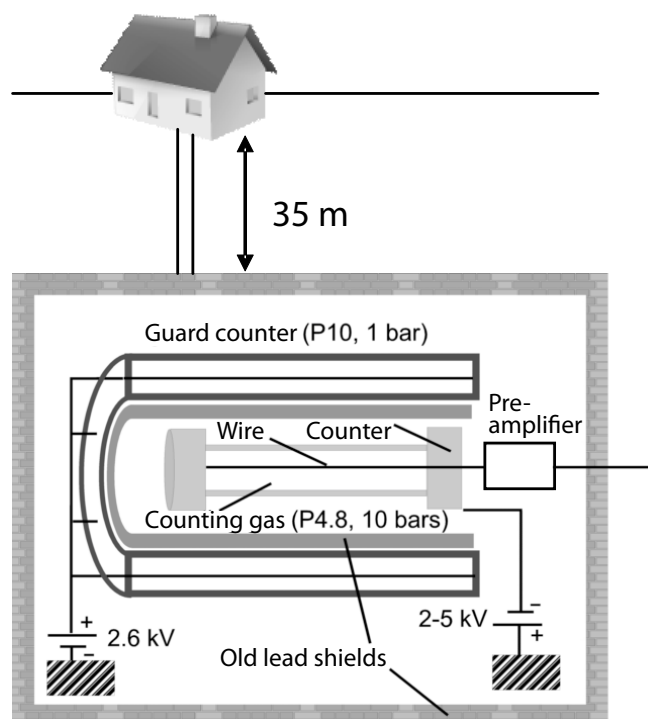


FIG. 5.11. Schematic of the set-up utilized to measure noble gas radionuclides at the Low Level Counting Underground Laboratory at the University of Bern. For  $^{85}\text{Kr}$  measurements, the counters are filled with a P10 mixture (10% methane, 90% argon) at pressures in the range of 2–10 bar. The measurements are performed at a depth of 35 m. Low activity lead shielding and an anti-coincidence arrangement provide a further reduction in the background count rate.

because the counter surfaces, thus the influence of self-activity of the counter material (mostly Cu), are smaller. The assembly is inserted in a second, larger cylindrical proportional detector, which acts as an anti-coincidence counter. The passive shielding is complemented by an external lead shield approximately 12 cm thick. The lead shields were built using lead from pre-industrial shipwrecks with very low intrinsic  $^{210}\text{Pb}$  activity.

Gas purity may change slightly from one sample to the next; gas quality may also slowly worsen over a counting time of several weeks. To be able to apply exactly the same gas multiplication factor, 8 keV X ray radiation of Cu is induced in the wall of the counter by an external  $^{241}\text{Am}$  source and fixed for each counting system at a given channel of the energy spectrum.

For  $^{39}\text{Ar}$ , a precision of about 5% modern is reached for young samples, corresponding to an age uncertainty of  $\pm 20$  a. For ages comparable to the  $^{39}\text{Ar}$  half-life, an error of about 7% modern is typical, corresponding to about  $\pm 30$  a. The limit of dating corresponds to a detection limit of about 5% modern, which results in an age indication of more than 1000 a (Pearson Jr. et al. (1991) [285]). The modern  $^{85}\text{Kr}/\text{Kr}$  ratio can be measured with a precision of better than 3% using 5–10 L of atmospheric air or 200–500 L of water, respectively.

## 5.4.2. Accelerator mass spectrometry

When analysing long lived isotopes, atom counting has a number of advantages over decay counting (Collon et al. (2004) [265]). The efficiency and speed of atom counting is not fundamentally limited by the long half-lives of isotopes, nor is it affected by radioactive backgrounds in the environment or in samples.

In an AMS analysis, ions are first produced from a sample in an ion source, and are then passed through a first set of low energy analysing magnets in order to select those with the correct charge to mass ratio. The selected ions are accelerated and, in some cases, passed through a stripper foil which largely removes molecular isobars. The surviving ions are passed through an additional series of magnetic and electrostatic analysers before being further analysed and counted in a detector system (Fig. 5.12). The high sensitivity and selectivity of the method makes it possible to measure a trace nuclide at a rate of several counts per hour from a microrampere primary beam ( $\sim 10^{16}$  ions/h) (Collon et al. (2004) [265]).

The main technical problems for the detection of  $^{81}\text{Kr}$  with AMS arise from (i) the inability of noble gases to form negative ions, which excludes the application of tandem accelerators, and (ii) the high background due to isobaric, stable and abundant  $^{81}\text{Br}$ . This was recently overcome by Collen et al. (1997) [245] using the full stripping technique. Once all of the electrons are removed,  $^{81}\text{Kr}^{36+}$

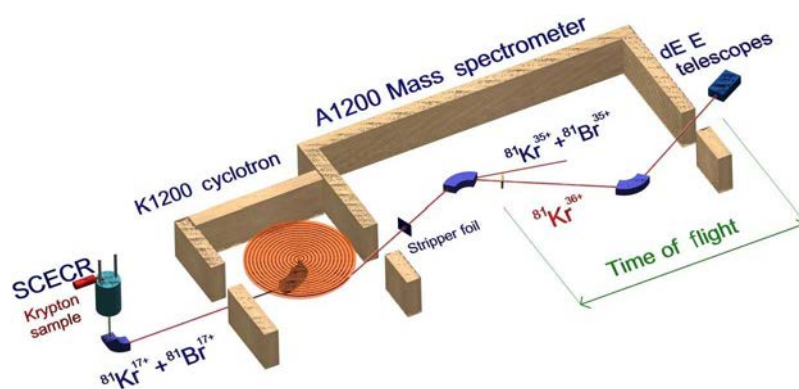


FIG. 5.12. Schematic of the accelerator mass spectrometry experimental set-up at the National Superconducting Cyclotron Laboratory, Michigan State University (Collon et al. (1997) [245]).

( $Z = 36$ ) can be cleanly separated from  $^{81}\text{Br}^{35+}$  ( $Z = 35$ ). The AMS measurements of  $^{81}\text{Kr}$  in atmospheric Kr were performed using the K1200 Superconducting Cyclotron at Michigan State University, which accelerated ions to an energy (3.6 GeV) high enough for efficient full stripping. After the acceleration in the cyclotron, the  $^{81}\text{Kr}^{17+}$  ions were passed through a Be foil (18.8 mg/cm<sup>2</sup>), which provided a 70% stripping efficiency to reach the 36+ charge state. The fully stripped  $^{81}\text{Kr}^{36+}$  was then separated from the  $^{81}\text{Br}^{35+}$  using the A1200 mass spectrometer, and detected with two  $\Delta E$ -E telescope detectors (Collon et al. (1997) [245]).

The nuclear reaction products induced by the high  $^{81}\text{Br}^{17+}$  background in the stripper foil heavily dominated the final spectrum and had to be suppressed by several orders of magnitude before  $^{81}\text{Kr}$  in natural samples could be detected. As Kr and Br have very different melting temperatures ( $-156.6^\circ\text{C}$  and  $-7.2^\circ\text{C}$ , respectively), Br in the sample was suppressed by freezing the sample with liquid nitrogen. In addition, tests revealed that the largest suppressor of  $^{81}\text{Br}$  was the support gas used in the ion source. By using Ar as a support gas, reductions in Br contamination by two orders of magnitude were obtained (Collon et al. (1999) [286]). These steps opened the door to possible measurements of  $^{81}\text{Kr}$  below the natural level of  $5 \times 10^{-13}$ . This AMS set-up was used to perform  $^{81}\text{Kr}$  dating of groundwater samples (Collon et al. (2000) [281]) and to compare pre-bomb and post-bomb abundances of atmospheric  $^{81}\text{Kr}/\text{Kr}$  (Collon et al. (1999) [286]).

### 5.4.3. Atom trap trace analysis

In atom trap trace analysis (ATTA), an atom of a particular isotope is selectively captured by a laser trap and then detected by observing its fluorescence while in the trap (Chen et al. (1999) [283]). A magneto-optical trap (MOT) — a type of robust and efficient atom trap — is used as a selective concentrator (Chen et al. (1999) [283]; Du et al. (2003) [249]). When the laser frequency is tuned to within a few natural line widths of the low frequency side of the targeted isotope resonance, only atoms of this particular isotope are trapped. Atoms of other isotopes are either deflected before reaching the trap or are allowed to pass through the trap without being captured. This method allows for the counting of single atoms with a high signal to noise ratio and, since selectivity depends exponentially on the number of photons detected in a burst, also ensures superb selectivity. Indeed, ATTA is practically immune to contamination from other isotopes, elements or molecules.

The vacuum system consists of the following components: the sample reservoir, the source chamber, the transverse cooling chamber and the trap chamber. A getter pump in the source chamber removes reactive gases, such as hydrogen, water, etc. from the vacuum system while leaving the Kr sample intact. Either a Ti-sapphire ring laser system or a diode laser system can be used to generate the 811 nm light needed to trap Kr atoms in the metastable  $5s [3/2]2$  level by repeatedly exciting

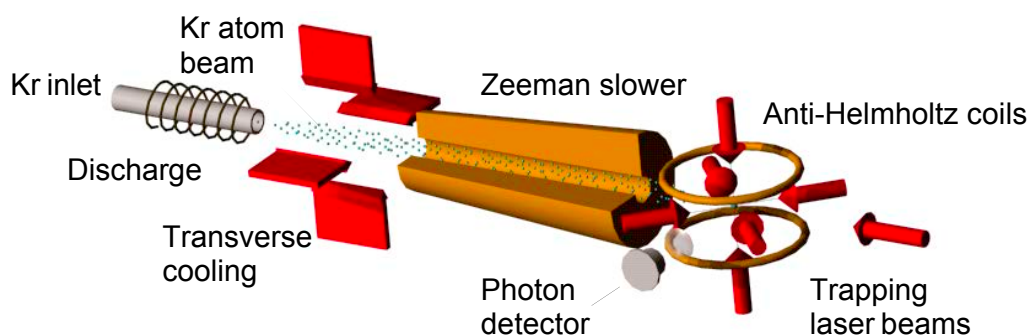


FIG. 5.13. Schematic layout of the krypton ATTA-2 apparatus. Metastable krypton atoms are produced in the discharge. The atoms are then transversely cooled, slowed and trapped by laser beams, shown as solid red arrows. The total length of the set-up is about 2.5 m (Lu and Mueller (2010) [287]).

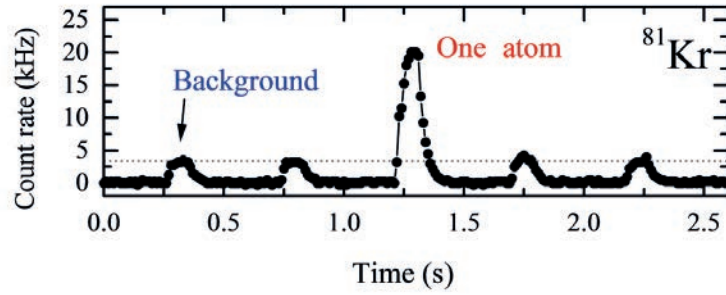


FIG. 5.14. Signal of a single  $^{81}\text{Kr}$  atom. The background is due to photons scattered off the surrounding wall of the vacuum chamber (Du et al. (2003) [249]).

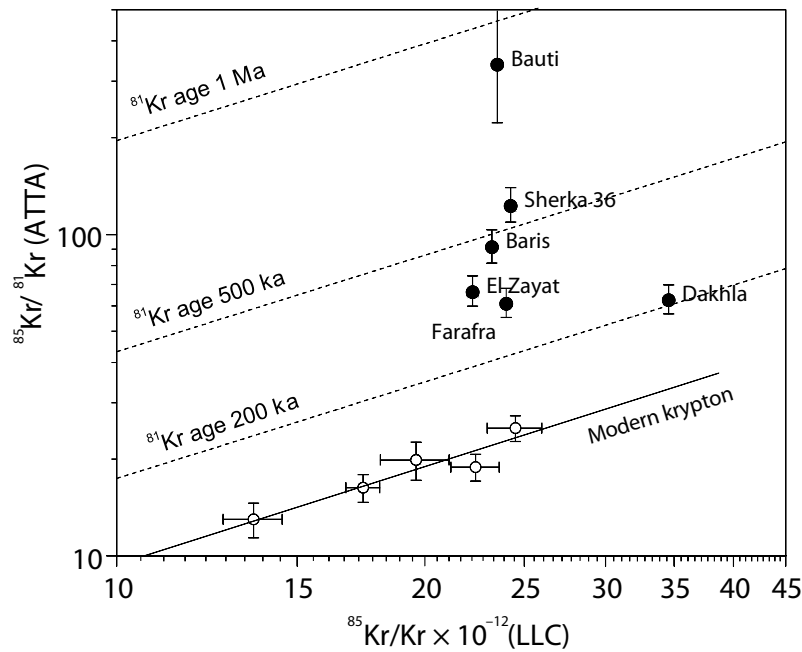


FIG. 5.15. Correlation between the  $^{85}\text{Kr}/^{81}\text{Kr}$  ratios measured using ATTA and  $^{85}\text{Kr}/\text{Kr}$  ratios measured using LLC. Line through open symbols: measured relation for modern Kr (Du et al. (2003) [249]). Solid symbols:  $^{81}\text{Kr}$  depleted values for ancient groundwater samples (Sturchio et al. (2004) [5]). Ratios of equal age are indicated by dashed lines.

the  $5s [3/2]2 - 5p [5/2]3$  cycling transition. A novel feature of the system is that it can be switched into a mode that recirculates the Kr atoms repeatedly through the system, which dramatically improves counting efficiency.

In an ATTA analysis, a Kr gas sample is injected into the system through a discharge region (Fig. 5.13), where approximately  $1 \times 10^{-3}$  of the atoms are excited into the metastable level  $5s [3/2]2$  via collisions with energetic electrons and ions. The thermal (300 K) atoms are then transversely cooled, decelerated using the Zeeman slowing technique and captured into an MOT (Fig. 5.13). The MOT can capture the abundant  $^{83}\text{Kr}$  (isotopic abundance = 11.5%) at a rate of  $1 \times 10^9/\text{s}$ . Since an atom typically lasts 0.5 s in a trap before being bumped out in collisions with thermal background atoms or molecules, rare atoms are not accumulated in the trap; instead, they are usually captured and counted one at a time. A single trapped atom can be unambiguously observed with a signal to noise ratio of 40 by detecting its strong fluorescence induced by the trapping laser beams (Fig. 5.14).

The capture rates for  $^{81}\text{Kr}$  and of stable  $^{83}\text{Kr}$  differ by 11 orders of magnitude. At present, the  $^{81}\text{Kr}/^{83}\text{Kr}$  ratio cannot be measured directly due to an inadequate dynamic range in the ATTA

detector system. Instead, a controlled amount of  $^{85}\text{Kr}$  is introduced into the sample and the  $^{81}\text{Kr}/\text{Kr}$  ratio is determined based upon two measurements: the  $^{85}\text{Kr}/^{81}\text{Kr}$  ratio measured using ATTA and the  $^{85}\text{Kr}/\text{Kr}$  ratio measured using LLC (Fig. 5.15). This ratio was measured for modern atmospheric Kr (Du et al. (2003) [249]). The obtained linear relation is the reference zero age line for  $^{81}\text{Kr}$  dating. The detection limit depends on the sampled Kr volume, the resulting ATTA and LLC counting statistics and the reliability of the spiking process. The current detection limit of  $\sim 5\%_{\text{modern}}$  for  $\sim 2000$  L water samples will likely be reduced in the near future with the next generation of ATTA instruments (see below).

An ATTA system developed at Argonne National Laboratory has been used to analyse  $^{81}\text{Kr}$  and  $^{85}\text{Kr}$  in the atmosphere and in groundwater (Du et al. (2003) [249]; Sturchio et al. (2004) [5]). The counting efficiency of this second generation system (ATTA-2) was  $\sim 10^{-4}$ , with a required Kr sample size of  $50 \mu\text{L}$ , corresponding to a water volume of about  $3000$  L. The elevated  $^{85}\text{Kr}/^{81}\text{Kr}$  ratios measured for six samples from the Nubian aquifer compared with the modern reference line (Fig. 5.15) are due to radioactive decay of  $^{81}\text{Kr}$  and were directly converted to groundwater  $^{81}\text{Kr}$  model age (Sturchio et al. (2004) [5]). As the absolute calibration of  $^{81}\text{Kr}/^{85}\text{Kr}$  and, thus, the  $^{81}\text{Kr}/\text{Kr}$  ratio was not feasible up until now, the atmospheric value measured by ATTA is not indicated in Fig. 5.1.

On the basis of the knowledge and experience provided by the ATTA-2 set-up, an optimized ATTA-2 apparatus is currently under development at several institutions, including the Argonne National Laboratory (Lu and Mueller (2010) [287]). Improvements in trapping and counting efficiency by two orders of magnitude aim to reduce the sample size required to less than  $10$  kg of water or ice (Fig. 5.8). This will considerably facilitate the gas sampling and purification procedures and finally open  $^{81}\text{Kr}$  dating method applications to a wide field of possibilities, thus answering many scientific questions.

#### 5.4.4. Resonance ionization mass spectrometry

For many years, extensive efforts have been undertaken to measure  $^{81}\text{Kr}$  using laser resonance ionization mass spectrometry (RIS) (Lehmann (2000) [288]; Lehmann et al. (1985) [289]; Thonnard et al. (1987) [290]). Similar to the ATTA technique, Kr atoms are selectively excited and ionized with laser pulses. This process is very element sensitive, but generally not isotope selective, because the bandwidth of the pulsed ionization lasers is larger than the isotope effects in the Kr spectra. Isotope selectivity is achieved in combination with mass spectrometers. However, the very small isotope ratio requires rather complicated isotopic pre-enrichment procedures prior to the final measurement. Despite some encouraging results (Lehmann et al. (1991) [282]), problems remained unsolved and the RIS method has so far not successfully been applied to a multisample field investigation.

### 5.5. FIRST ATTEMPTS AT $^{81}\text{Kr}$ DATING: THE MULTITRACER COMPARISON IN THE SOUTH-WESTERN GREAT ARTESIAN BASIN

#### 5.5.1. Introduction

A pioneering attempt to use  $^{81}\text{Kr}$  for groundwater dating was performed at the Milk River aquifer in Canada at one selected well (Lehmann et al. (1991) [282]) as discussed in Chapter 11. Although the obtained  $^{81}\text{Kr}/\text{Kr}$  ratio measured using the RIS technique was indistinguishable within uncertainties in the  $^{81}\text{Kr}/\text{Kr}$  ratio of modern krypton, it was encouraging that a maximum  $^{81}\text{Kr}$  tracer age of  $140$  ka could be estimated (Lehmann et al. (1991) [282]), consistent with findings from  $^{36}\text{Cl}/\text{Cl}$  data (Nolte et al. (1991) [291]).

In the south-western Great Artesian Basin of Australia,  $^{81}\text{Kr}$  was applied for the second time in a groundwater study but for the first time at more than one sampling location (Lehmann et al. (2003) [256]). Sites were chosen on the basis of hydraulic age estimates and  $^{36}\text{Cl}$  data, which indicated groundwater ages on the order of several hundred thousand years (Love et al. (2000) [292]). The  $^{81}\text{Kr}/\text{Kr}$

ratios of four wells were measured using the AMS technique (Collon et al. (2000) [281]; Section 5.4.2) and for the first time allowed for a check of the applicability of  $^{81}\text{Kr}$  methods and a cross-check with tracer ages and conclusions derived from  $^{36}\text{Cl}$  and  $^4\text{He}$  data. The comparison of all data in such a multitracer study yields more information about the flow system than is possible from single tracer measurements. Moreover, limitations and uncertainties about individual tracer methods can be reduced and possibly quantified. Specifically, the following issues are addressed in the following pages.

Krypton-81 dating is a new method and its validity must be demonstrated in comparison to the more established  $^{36}\text{Cl}$  and  $^4\text{He}$  methods. Although theoretical considerations indicate that variations in  $^{81}\text{Kr}$  input activity and underground production should be low (Lehmann et al. (1993) [250]), this has to be verified in field studies. The strength of diffusive exchange between an aquifer and its surrounding aquitards is another potential problem that needs further investigation (Section 5.1.2.2).

For  $^4\text{He}$ , the most critical factor is quantification of the local accumulation rate, which is composed of an 'on-line' in situ production rate (easy to calculate) and an influx of helium that was produced either external to the aquifer (Torgersen and Clarke (1985) [293]; Torgersen et al. (1992) [294]; Torgersen and Ivey (1985) [93]) or helium that accumulated 'off-line' in the past which is now being released within an aquifer via diffusion from rocks into pore spaces (Solomon et al. (1996) [295]; Chapter 8).

For  $^{36}\text{Cl}$  dating, the 'initial value problem' (Davis et al. (1998) [296]) concerns the  $^{36}\text{Cl}/\text{Cl}$  ratio at the recharge area's geographical location, as well as an estimate of the Cl concentration of recharging water, which depends strongly on prevailing climatic conditions which may change as a function of time. During groundwater flow, subsurface processes other than radioactive decay may alter the number of  $^{36}\text{Cl}$  atoms and/or the number of Cl atoms dissolved in the water (Chapter 6).

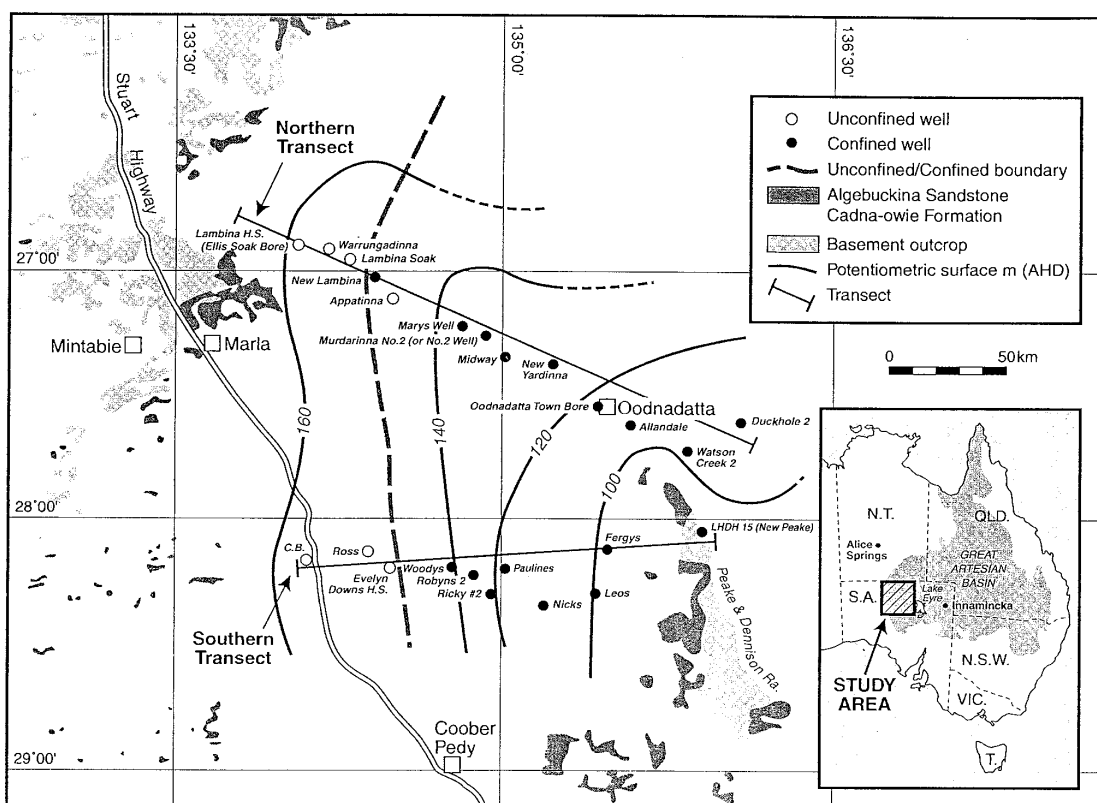


FIG. 5.16. Location map of the south-west margin of the Great Artesian Basin, showing the locations of wells for  $^{36}\text{Cl}$  dating (●) (Love et al. (2000) [292]) and the four sites that have been sampled for  $^{81}\text{Kr}$  measurements (★) (Lehmann et al. (2003) [256]). The shaded areas indicate the sandstone aquifer outcrop. The dashed line represents the transition from unconfined to confined conditions (where the water level of the aquifer is above the overlying Bulldog Shale).

The part of the Great Artesian Basin investigated here (see below) provides unfavourable conditions for the interpretation of  $^{36}\text{Cl}$  data due to high and variable evaporation rates and the occurrence of subsurface Cl sources. The systematic use of helium as a dating tool is also complicated by the presence of different helium sources (Torgersen and Clarke (1985) [293]). It is, therefore, an ideal area to demonstrate the interrelation between different tracer methods in such 'real world scenarios' and the potential of multitracer studies. The intention is not to favour any of the applied methods or to explain the flow system in this hydrologically complex part of the Great Artesian Basin. Significantly more data would be required, including  $^{81}\text{Kr}$ , to reach this goal.

### 5.5.2. Study area

The study area is located in the Great Artesian Basin south-western flow system of the Eromanga Basin. Piezometric contours indicate that the major direction of groundwater flow is from the western margin towards the south-east and east (Fig. 5.16). Chlorine-36 dating was previously performed along two transects and based on these data the test sites for  $^{81}\text{Kr}$  measurements were chosen (Love et al. (2000) [292]). The southernmost site (RC) was sampled because other sites along the northern transect were inaccessible due to inclement weather and poor road conditions.

All wells tap the J-K sandstone aquifer that is overlain by the 200–400 m thick Bulldog Shale aquitard. The transects start in the outcrops and unconfined parts of the aquifer. Further downstream, the aquifer becomes confined or eventually artesian (Love et al. (2000) [292]).

### 5.5.3. Krypton-81 groundwater ages

The four wells, RC, OD, DH and WC (Fig. 5.16), were sampled during a field campaign in 1998 in collaboration with the Department of Water, Land and Biodiversity Conservation of South Australia, the Institute of Isotope Research Vienna (AMS measurements) and the University of Bern (sampling and sample preparation). The project was partly supported by the IAEA within the framework of a research programme called "Isotope Techniques for the Assessment of Slow Moving Deep Groundwaters". About 16 t of water was degassed in the field and the extracted gas was processed in the University of Bern laboratories according to the procedures explained above. The purified Kr samples ( $\sim 0.5 \text{ cm}^3_{\text{STP}}$ ) were shipped to the AMS laboratory at Michigan State University for  $^{81}\text{Kr}/\text{Kr}$  ratio determination.

Measured  $^{81}\text{Kr}$  activities expressed in terms of the air normalized ratio  $(^{81}\text{Kr}/\text{Kr})_{\text{sample}} / (^{81}\text{Kr}/\text{Kr})_{\text{modern air}}$  range from 51% to 30%<sub>modern</sub>. A simple age calculation using the exponential law for radioactive decay yields  $^{81}\text{Kr}$  model ages of between 230 and 400 ka (Table 5.3), in agreement with expectations from  $^{36}\text{Cl}$  data (Love et al. (2000) [292]). The uncertainty in calculated groundwater tracer age is about 10–20% because of the analytical error in these first  $^{81}\text{Kr}$  measurements using cyclotron AMS. Contamination during sampling was excluded through  $^{85}\text{Kr}$  measurements carried out on subsamples of the same gas used for AMS.

These  $^{81}\text{Kr}$  model ages are piston flow ages and, thus, neglect dispersion in the aquifer, possible diffusive exchange with aquitards and any underground production of  $^{81}\text{Kr}$ . The effect of dispersion is minor for tracers with a constant input because the concentration gradient is small in the direction of flow (in contrast to peak shape inputs as for  $^3\text{H}$ ). For reasonable dispersivities (Gelhar et al. (1992) [297]), the effect would lead to an underestimation of groundwater age on the order of <15% for  $^{81}\text{Kr}$  piston flow ages <500 ka. Underground production is expected to be very likely <10%<sub>modern</sub> and likely to be <4%<sub>modern</sub> (Lehmann et al. (1993) [256]). However, upper limits for the subsurface production of  $^{81}\text{Kr}$  and its escape to groundwater still need to be established by field measurements. Underground production would lead to an underestimation of age if not considered in the model age calculation (the produced activity feigns a younger age). Diffusive exchange with stagnant aquitards (depleted in  $^{81}\text{Kr}$  compared with the studied aquifer) would cause an overestimation of model ages if not considered

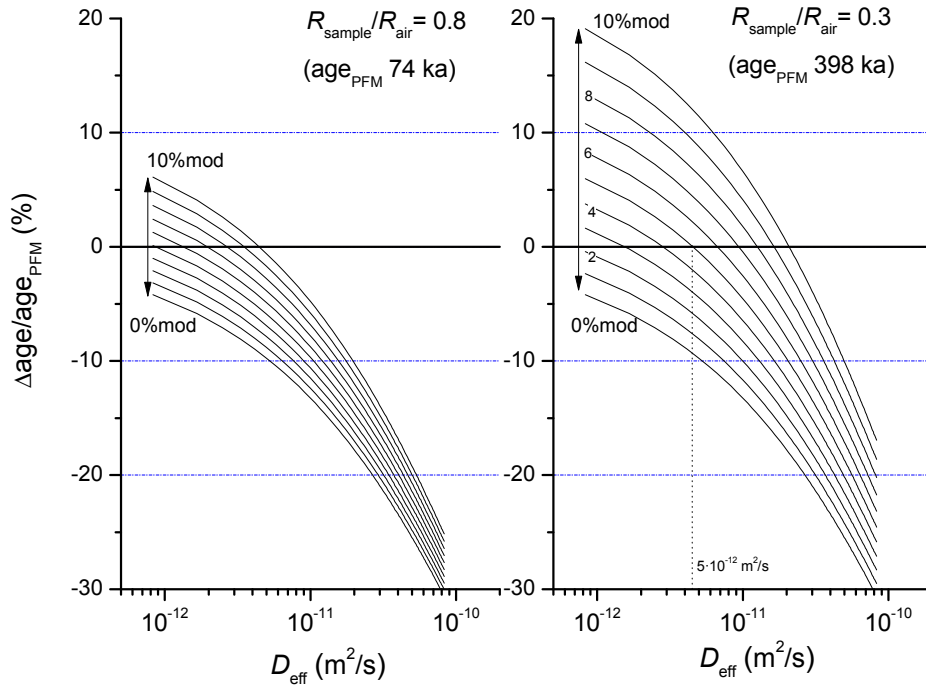


FIG. 5.17. Steady state relative  $^{81}\text{Kr}$  model age differences between model ages considering diffusion and underground production and piston flow model (PFM) ages. The relation is plotted as a function of the effective diffusion coefficient of  $^{81}\text{Kr}$  in the aquitard ( $D_{\text{eff}}$ ), for an underground production of between 0–10% modern and for two piston flow model age ranges. It is thereby assumed that the aquifer is 100 m thick and lies between two layers of indefinite aquitards (Sudicky and Frind (1981) [299]). The supposed porosities of the aquifer and the aquitards are 0.2 and 0.3, respectively. Flow velocity is 1 m/a.

in the decay law piston flow age calculation (the aquitards act as an additional sink for  $^{81}\text{Kr}$ ). Relative deviations between groundwater and  $^{81}\text{Kr}$  tracer ages are shown in Fig. 5.17 and provide a realistic range of diffusion coefficients, subsurface secular equilibrium activities and measured  $^{81}\text{Kr}/\text{Kr}$  ratios (Lehmann and Purtschert (1997) [298]; Sanford (1997) [207]; Sudicky and Frind (1981) [299]). Underground production causes a positive shift in  $^{81}\text{Kr}/\text{Kr}$  ratios, whereas aquitard diffusion results in a negative shift. The assumed aquifer geometry and porosity are comparable to values typical for the investigated part of the Great Artesian Basin. The resulting maximal age difference is in the range  $\pm 20\%$  and thus not much larger than the current analytical error. Additionally, for a groundwater sample with an age of 400 ka, the effect due to 5% underground production is compensated by diffusion with an effective diffusion coefficient of  $\sim 5 \times 10^{-12} \text{ m}^2/\text{s}$ . For the following discussion,  $^{81}\text{Kr}$  model ages based on radioactive decay only are used.

#### 5.5.4. Comparison with helium data

Calculated  $^{81}\text{Kr}$  model ages now allow for an assessment of the concentration of radiogenic  $^4\text{He}$ , which increases with increasing groundwater age (Fig. 5.18). Two samples (DH, WC) showed a high accumulation rate of  $9 \times 10^{-10} \text{ cm}^3_{\text{STP}} \cdot \text{cm}^{-3}_{\text{water}} \cdot \text{a}^{-1}$ , whereas RC and OD accumulated  $^4\text{He}$  at a much lower rate of  $0.2 \times 10^{-10} \text{ cm}^3_{\text{STP}} \cdot \text{cm}^{-3}_{\text{water}} \cdot \text{a}^{-1}$ . However, the in situ  $^4\text{He}$  accumulation rate in the J-K sandstone is only  $6.9 \times 10^{-12} \text{ cm}^3_{\text{STP}} \cdot \text{cm}^{-3}_{\text{water}} \cdot \text{a}^{-1}$  (dotted line in Fig. 5.18) as calculated from the known U and Th concentrations and an average sandstone porosity of 20% (Lehmann et al. (2003) [256]). In accordance with observations at other locations in the Great Artesian Basin, the dominant source of helium is apparently external to the aquifer. By comparing the measured  $^3\text{He}$  and  $^4\text{He}$  concentrations

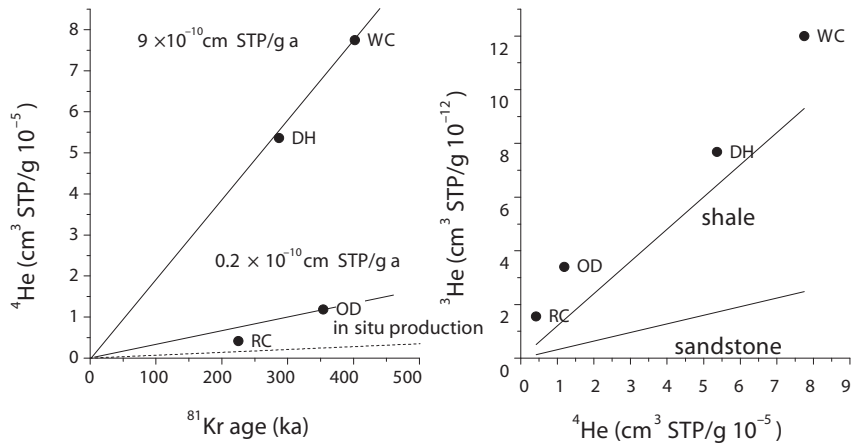


FIG. 5.18. Helium-4 accumulation as a function of  ${}^{81}\text{Kr}$  model ages (left panel) and  ${}^3\text{He}/{}^4\text{He}$  signatures compared with calculated values in the sandstone and the Bulldog Shale (right panel). The dotted line indicates the increase of helium due to in situ U and Th decay within the aquifer.

in four groundwater samples to the calculated in situ  ${}^3\text{He}/{}^4\text{He}$  production ratio (Fig. 5.18, right), it appears at least plausible that the source of the excess helium is located in the rocks and pore waters of the Bulldog Shale. This He exchange between the sandstone and the shale seems to be more effective at the end of the northern transect where DH and WC are located than for the locations of the other two wells, OD and RC.

### 5.5.5. Comparison with chlorine-36 data

The chloride and  ${}^{36}\text{Cl}$  data along the two sampled transects are shown in Fig. 5.19. In the confined part (solid symbols) of the aquifer for the  ${}^{81}\text{Kr}$  study, both  ${}^{36}\text{Cl}$  and  ${}^{36}\text{Cl}/\text{Cl}$  decrease with decreasing hydraulic head (and distance), indicating increasing ages along the flow path. Chloride concentrations are relatively high and range from 600 to 3000 mg/L. The Cl decrease along the southern transect is likely the result of lower rates of evapotranspiration in the past (Love et al. (2000) [292]). This was also demonstrated by a good correlation between Cl concentrations and  $\delta^{18}\text{O}$  values for the southern transect (not shown here). Concentrations of Cl along the northern transect are lower and show less variability, indicating that the input conditions were more humid and more constant in the recharge area of those samples. This observation is in line with other studies that also indicate spatially variable recharge and input conditions in this part of the Great Artesian Basin (Torgersen et al. (1991) [300]). In this study area,  ${}^{36}\text{Cl}$  dating is apparently complicated by the unfortunate situation that both evaporative Cl enrichment during recharge ( $C_i$ ) and varying subsurface Cl sources ( $C_a$ ) occur simultaneously and with varying (and a priori unknown) strengths. The hypothesis of a spatially and temporally varying contribution of subsurface Cl is further strengthened by the weak correlation between  $\delta^{18}\text{O}$  and the Cl concentration along the northern transect (Love et al. (2000) [292]). This implies once more that processes other than evaporation control Cl concentration. Neither dating by the  ${}^{36}\text{Cl}/\text{Cl}$  ratio (insensitive to evaporation) nor by the  ${}^{36}\text{Cl}$  concentration (rather insensitive to the addition of  ${}^{36}\text{Cl}$ -‘dead’ chloride) offers an evident solution to this problem.

In light of the calculated  ${}^{81}\text{Kr}$  model ages, it is possible to demonstrate how such an ambiguity can be reduced by means of a multitracer comparison. As a starting point, the temporal evolution of the different  ${}^{36}\text{Cl}$  components in a groundwater sample and their corresponding initial parameters (expressed as isotope ratios  $R = {}^{36}\text{Cl}/\text{Cl}$  multiplied with the Cl concentrations  $C$ ) are reconsidered (Bentley et al. (1986) [301]):

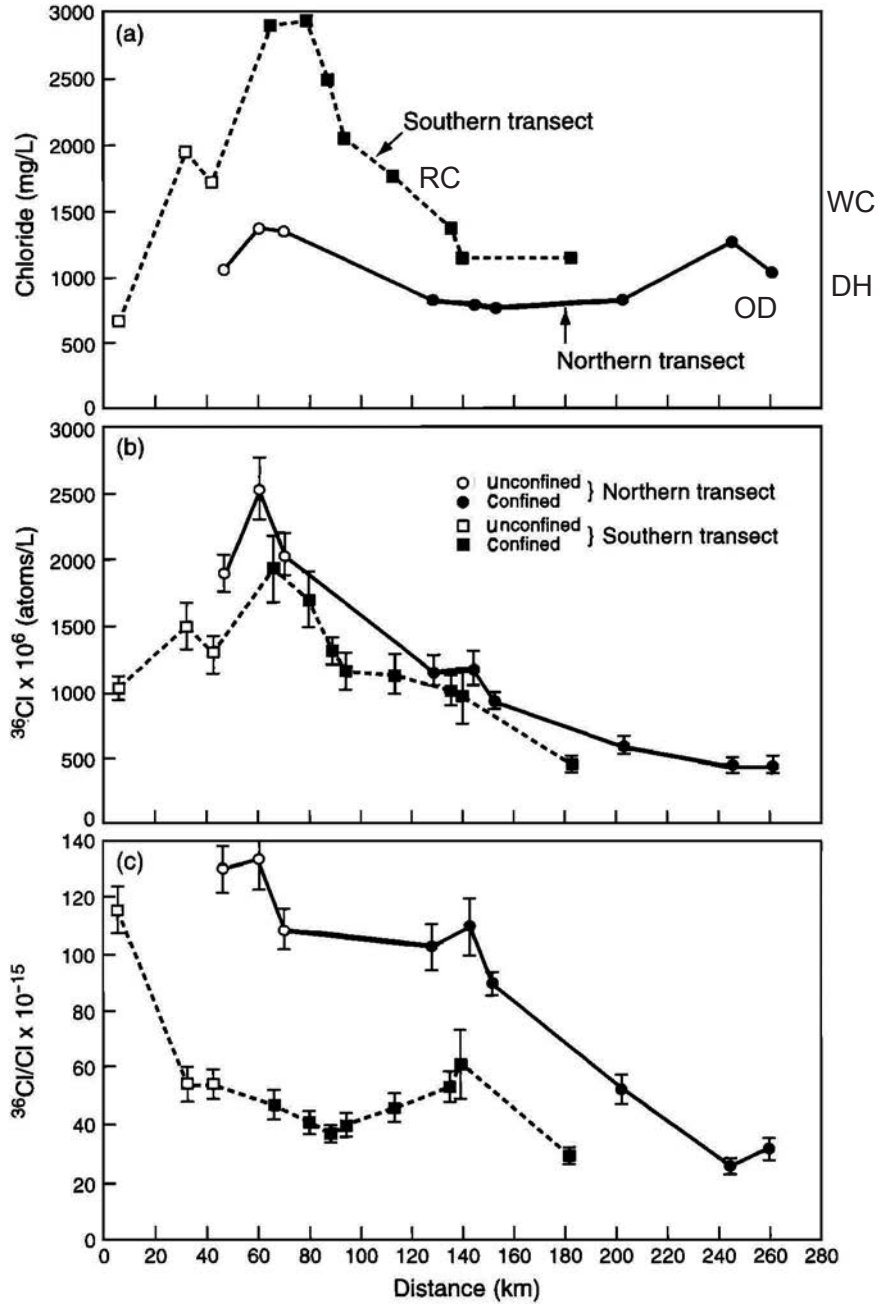


FIG. 5.19. Chloride and  $^{36}\text{Cl}$  versus distance for south-western Great Basin groundwaters (from Love et al. (2000) [292]).

$$\underbrace{RC}_A = \underbrace{R_i C_i \exp(-\lambda_{36} t)}_B + \underbrace{R_{Se} C_i (1 - \exp(-\lambda_{36} t))}_C + \underbrace{(C - C_i) R_{ex}}_D \quad (5.9)$$

where

- $A$  is measured  $^{36}\text{Cl}$  concentration (atoms/L water);
- $B$  is decay of the initial  $^{36}\text{Cl}$  concentration in recharge water;
- $C$  is the in-growth of a secular subsurface equilibrium  $^{36}\text{Cl}$  concentration within the aquifer ( $R_{Se}$ );
- $D$  is  $^{36}\text{Cl}$  accumulation due to the addition of Cl from subsurface sources with a  $^{36}\text{Cl}/\text{Cl}$  ratio of  $R_{ex}$ .

TABLE 5.3. RECONSTRUCTED CONTRIBUTIONS OF METEORIC ( $C_i$ ) AND SUBSURFACE ( $C_a$ ) Cl SOURCES IN THE SOUTH-WESTERN GREAT ARTESIAN BASIN

	RC	OD	DH	WC
$^{81}\text{Kr}$ age $t$ (ka)	$230 \pm 40$	$350 \pm 50$	$290 \pm 40$	$400 \pm 50$
$C$ (mg/L)	1260	680	850	1040
$C_i$ (mg/L)	1050	620	120	210
$C_a = C - C_i$ (mg/L)	210	60	730	830
$K = C_a/t$ ( $\text{mg} \cdot \text{ka}^{-1} \cdot \text{L}^{-1}$ )	0.95	0.15	2.54	2.07

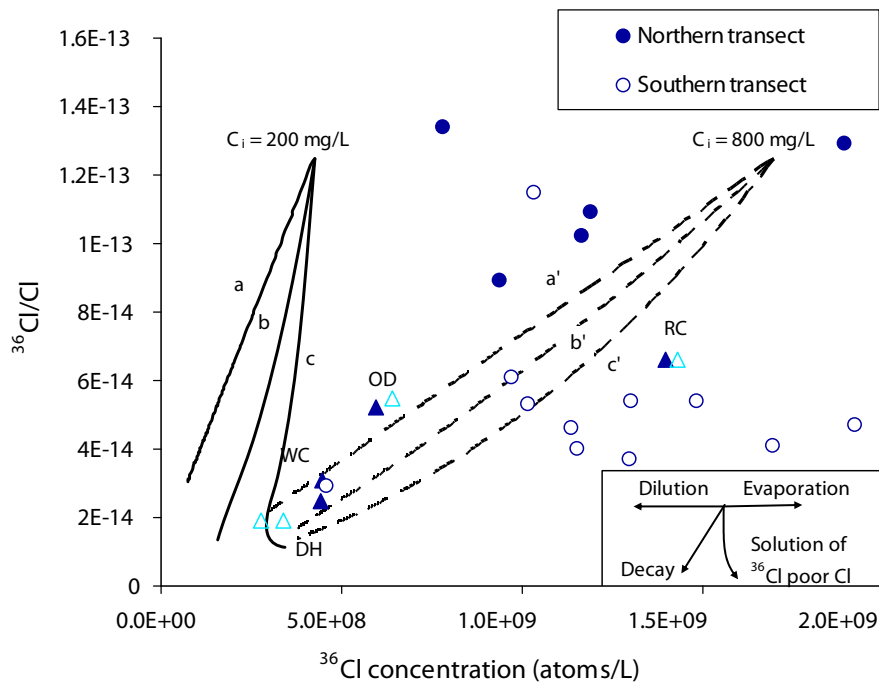


FIG. 5.20. Variations in  $^{36}\text{Cl}/\text{Cl}$  and  $^{36}\text{Cl}$  concentrations down two transects of the south-western Great Artesian Basin. Triangles indicate  $^{81}\text{Kr}$  dated locations (sampling date:  $\blacktriangle$  1995  $\triangle$  1998). Lines represent the evolution for (a) decay, (b) a temporally linear Cl accumulation rate  $k$  of  $0.5 \text{ mg} \cdot \text{ka}^{-1} \cdot \text{L}^{-1}$  and (c)  $k = 1.6 \text{ mg/L ka}$  starting with Cl concentrations of 200 mg/L and 800 mg/L, respectively. A  $^{36}\text{Cl}/\text{Cl}$  ratio of  $20 \times 10^{-15}$  for the accumulated Cl was assumed for cases b and c.

Apart from the groundwater age  $t$ , which is the target parameter for dating, it is necessary to estimate the meteoric  $^{36}\text{Cl}/\text{Cl}$  initial ratio  $R_i$ , the recharge of Cl concentrations  $C_i$ , the secular equilibrium ratio  $R_{\text{Se}}$  within the aquifer, and the ratio  $R_{\text{ex}}$  of any admixed or dissolved Cl. For this area of the Great Artesian Basin, a  $R_i$  of  $125 \times 10^{-15}$  was estimated based on relatively young samples in the recharge area which are  $^3\text{H}$  free and, therefore, not affected by thermonuclear  $^{36}\text{Cl}$  (Love et al. (2000) [292]; Torgersen et al. (1991) [300]). It was further assumed that higher frequency variations of the  $^{36}\text{Cl}$  fallout (Plummer et al. (1997) [248]) were smoothed out due to hydrodynamic dispersion (see Section 5.6).

A secular equilibrium ratio  $R_{\text{Se}}$  of  $6.5 \times 10^{-15}$  for J-K aquifer sandstone was calculated based on the measured elemental composition of several rock samples from the aquifer (Lehmann et al. (2003) [256]). Similarly, a ratio  $R_{\text{ex}}$  of  $20 \times 10^{-15}$  was obtained for the adjacent Bulldog Shale formation. The only residual free parameter is the chloride concentration that represents a recharge value ( $C_i$ ), and

that depends on the climatic conditions during recharge. It is known that several glacial cycles occurred over the timescales of the  $^{36}\text{Cl}$  method dating range. The four well case study ( $C_i$ ) can now be calculated because the second unknown  $t$  in Eq. (5.5) can be independently determined using  $^{81}\text{Kr}$  dating. In other words, the  $C_i$  value for each sample was determined by inserting the  $^{81}\text{Kr}$  age  $t = t_{81}$  into Eq. (5.9) and solving for  $C_i$ . The subsurface input ( $C_a$ ) corresponds to the difference between measured ( $C$ ) and the initial Cl concentration ( $C_i$ ). Finally, the Cl accumulation rate  $k = C_a/t = t_{81}$  can be calculated (Table 5.3).

Reconstructed input concentrations  $C_i$  vary over almost one order of magnitude between 120 mg/L (DH) and 1050 mg/L (RC). The subsurface Cl accumulation rate  $k$  is small for two of the samples ( $<1 \text{ mg} \cdot \text{ka}^{-1} \cdot \text{L}^{-1}$  for RC, OD) but more significant for DH and WC ( $2\text{--}3 \text{ mg} \cdot \text{ka}^{-1} \cdot \text{L}^{-1}$ ). In Fig. 5.20,  $^{36}\text{Cl}/\text{Cl}$  ratios are plotted as a function of the  $^{36}\text{Cl}$  concentrations. Straight lines ( $a, a'$ ) indicate the theoretical evolution for decay and an underground secular equilibrium ratio of  $20 \times 10^{-15}$  but without any addition of subsurface Cl (terms  $B$  and  $C$  in Eq. (5.9)). The curved lines ( $b, b', c, c'$ ) represent cases for different Cl accumulation rates (term  $D$  in Eq. (5.9)). It is thereby assumed that Cl concentration increases linearly with time, starting with initial  $C_i$  concentrations of 200 mg/L ( $b, c$ ) and 800 mg/L ( $b', c'$ ), respectively. The large scatter of measured values on both transects is one more indication that evaporative enrichment and the accumulation of subsurface Cl are both significant processes which possibly overwhelm the decay signal. Data along the southern transect can only be explained by a high evaporative Cl enrichment during recharge and/or an elevated Cl accumulation rate in the subsurface. Samples low in  $^{36}\text{Cl}$  (DH and WC) can either be the result of a high input concentration  $C_i$  ( $\sim 800 \text{ mg/L}$ ) and a low accumulation rate (scenario  $a'$ ) or a low Cl input (200 mg/L) and a higher accumulation rate of  $\sim 1\text{--}2 \text{ mg} \cdot \text{ka}^{-1} \cdot \text{L}^{-1}$  (scenario  $c$ ).

The best estimate setting has either to be identified by a clear trend along a flowline (e.g. in Fig. 5.20) or by means of supplementary data such as  $^{81}\text{Kr}$  in this case. The results provided in Table 5.3 point to scenario  $c$  for DH and WC and scenarios  $a'\text{--}c'$  for RC and OD.

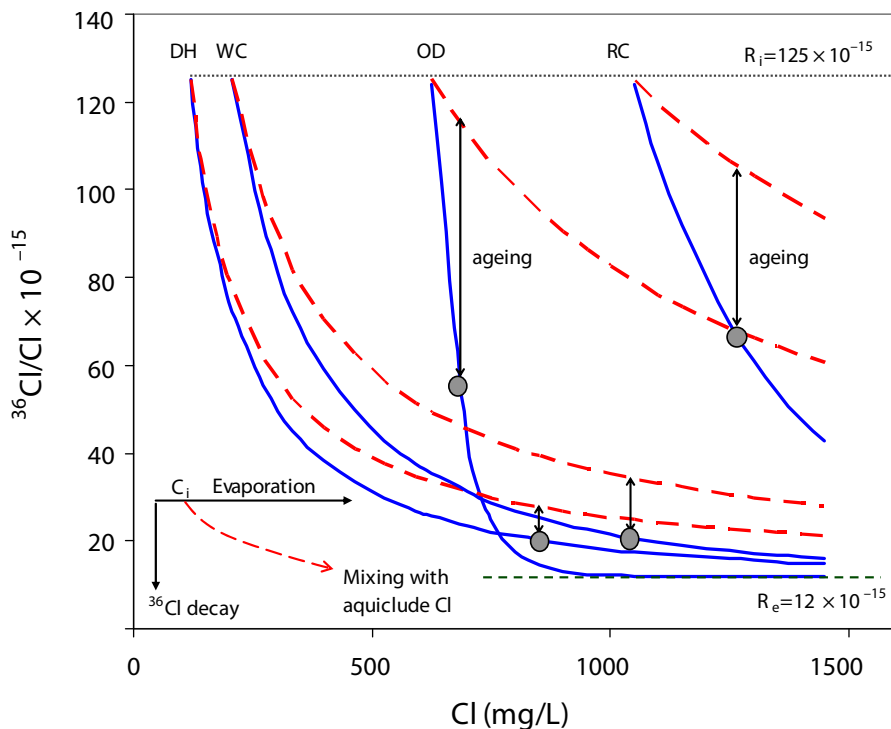


FIG. 5.21.  $^{36}\text{Cl}/\text{Cl}$  ratios versus Cl concentration of  $^{81}\text{Kr}$  dated samples (dashed red lines: pure mixing; blue solid lines: mixing + decay). Initial Cl concentrations as well as the quantification of  $^{36}\text{Cl}/\text{Cl}$  reduction due to ageing are based on  $^{81}\text{Kr}$  data (Table 5.3).

The impact of the different scenarios on  $^{36}\text{Cl}$  dating results becomes more evident upon looking at the relation between the Cl concentration and the  $^{36}\text{Cl}/\text{Cl}$  ratio (Fig. 5.21). The dashed lines represent pure mixing lines of the initial chloride with chloride in secular equilibrium with the Bulldog Shale (no radioactive decay). The solid lines include radioactive decay as quantified by  $^{81}\text{Kr}$  measurements. The same initial  $^{36}\text{Cl}/\text{Cl}$  ratio of  $125 \times 10^{-15}$  was assumed for all of the samples. For samples DH and WC, 93% and 89% of the  $^{36}\text{Cl}/\text{Cl}$  ratio decrease is caused by the addition of subsurface chloride. Only the remaining 10% drop of the  $^{36}\text{Cl}/\text{Cl}$  ratio is attributed to radioactive decay and, thus, to ageing. For OD and RC, on the other hand, the situation is quite different. The decrease in  $^{36}\text{Cl}/\text{Cl}$  is dominated by the decay of atmospheric input. Chlorine-36 dating for these samples, therefore, seems to be straightforward. The identification and quantification of relative amounts of meteoric and subsurface Cl has to be based on additional tracers such as  $^{81}\text{Kr}$ , as deduced in Section 6.6.3.

### 5.5.6. Additional evidence for the correctness of krypton-81 ages

Sparse experience with  $^{81}\text{Kr}$  dating can raise questions about the conclusions discussed above. Fundamentally, it poses the question of whether  $^{81}\text{Kr}$  ages are correct. Is it possible that processes other than admixture of Cl from the underlying shale are responsible for the disagreement of  $^{81}\text{Kr}$  and  $^{36}\text{Cl}$  model ages for two of the samples? Again, the answer to these questions can only be obtained with additional evidence from other tracer measurements. The importance of multitracer approaches is once more emphasized (this is true for any groundwater investigation, not only for old groundwater).

The evaporative enrichment of initial Cl concentration  $C_i$  as a function of recharge temperature  $T$  is found using:

$$C_i(T) = \frac{C_p \cdot P}{R(T)} \quad (5.10)$$

where

$R(T)$  is the recharge rate (mm/a) as a function of the evaporation rate that is closely related to the recharge temperature  $T$  ( $^{\circ}\text{C}$ );

$C_p$  is the Cl concentrations in precipitation (mg/L);

$P$  is the mean annual precipitation rate (mm/a).

From this simple chloride mass balance, a positive correlation is expected between recharge temperature  $T$  and the initial chloride concentration (warmer temperatures lead to a higher Cl enrichment in the recharge). Recharge temperatures can be reconstructed based on concentrations of dissolved noble gases (Aeschbach-Hertig et al. (1999) [302]; Mazor (1972) [303]). Noble gas recharge temperatures (NGRT) of the four wells are compared with reconstructed Cl input concentrations  $C_i$  in Fig. 5.22(a) (Lehmann et al. (2003) [256]). The reasonable correlation provides supporting evidence for the plausibility of estimated initial Cl concentrations (and derived  $^{81}\text{Kr}$  ages) because the parameters  $C_i$  and NGRT are analytically completely independent.

The second line of evidence comes from the comparison between accumulated radiogenic helium and accumulated Cl concentrations ( $C_a$ ). Model calculations have shown that downward diffusion from the Bulldog Shale aquitard is most likely the process by which variable amounts of subsurface Cl are added (Love et al. (2000) [292]). Measured  $\delta^{37}\text{Cl}$  values in rocks and groundwater support that the Bulldog Shale is the main source of Cl in the aquifer (see Zhang et al. (2007) [304] and Section 6.4.2). Moreover, the Bulldog Shale has already been identified to be the probable source for most of the accumulated He in the aquifer based on  $^3\text{He}/^4\text{He}$  ratios (Fig. 5.18). It is an intriguing further piece of evidence that subsurface chloride accumulation ( $C_a$ ) reconstructed on the basis of the  $^{81}\text{Kr}$  ages correlates well with the amount of accumulated  $^4\text{He}$  (Fig. 5.22(b)). It should be noted that the  $^4\text{He}$  concentration and noble gas temperatures are again completely independent parameters. A correlation

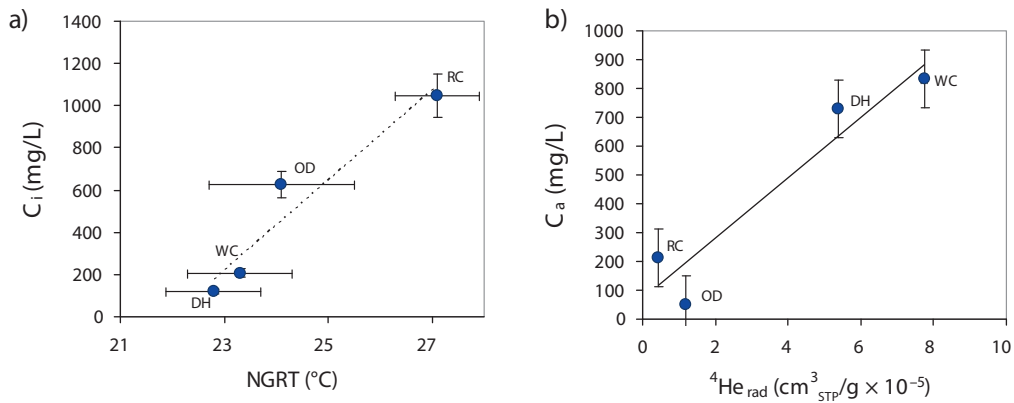


FIG. 5.22. (a)  ${}^{81}\text{Kr}$  derived initial chloride concentrations  $C_i$  versus calculated NGRT; (b) chloride of subsurface origin ( $C_a$ ) versus concentration of radiogenic  ${}^4\text{He}_{\text{rad}}$ .

between  ${}^4\text{He}$  and Cl concentrations was also observed in other deep aquifer systems (Lehmann et al. (1996) [305]).

Despite the small number of samples, the conclusion has been drawn that the consistency of a whole set of different independent isotope tracers ( ${}^{81}\text{Kr}$ ,  ${}^{36,37}\text{Cl}$ ,  ${}^3,4\text{He}$ , NGRT) points to:

- The validity of  ${}^{81}\text{Kr}$  model ages in the range of 200–450 ka, which seem not to be significantly affected by secondary processes such as underground production, diffusion or variations in input concentration;
- Distinct Cl accumulation histories with lower input concentrations and high Cl accumulation for two samples (DH, WC) and higher input concentrations and low subsurface accumulation for the other samples (RC, OD);
- External sources of helium and chloride that are at least correlated.

### 5.5.7. Summary

The ten currently (2010) available  ${}^{81}\text{Kr}$  measurements in old groundwater<sup>3</sup> certainly do not yet permit a comprehensive evaluation of the  ${}^{81}\text{Kr}$  method. Despite the sparse amount of data, some important conclusions can be drawn with regard to the analytical procedure of the  ${}^{81}\text{Kr}$  method and the applicability of  ${}^{81}\text{Kr}$  for dating old groundwater. An assessment of a novel technique is not meaningful without a comparison with more established methods. Owing to the comparable half-lives and dating ranges of  ${}^{36}\text{Cl}$  and  ${}^{81}\text{Kr}$ , the focus is on the relationship between these two methods.

#### 5.5.7.1. Krypton-81 methodology

In the past 15 years, significant progress has been made in the development of instruments for analysing  ${}^{81}\text{Kr}$  at natural concentration levels. The required amount of water has been reduced from about 17 t to about 1 t (2010) and is likely to be reduced further in the near future to approximately a few tens of litres (Lu and Mueller (2010) [287]). Sampling via gas extraction in the field has been proven to be practical and reliable. The gas processing and Kr separation procedure can be done using standard methods and will be further facilitated in the future with a probable decrease in sample volume.

<sup>3</sup> Milk-River: 1 sample; GAB: 4 samples; Nubian aquifer (see Chapter 14): 6 samples.

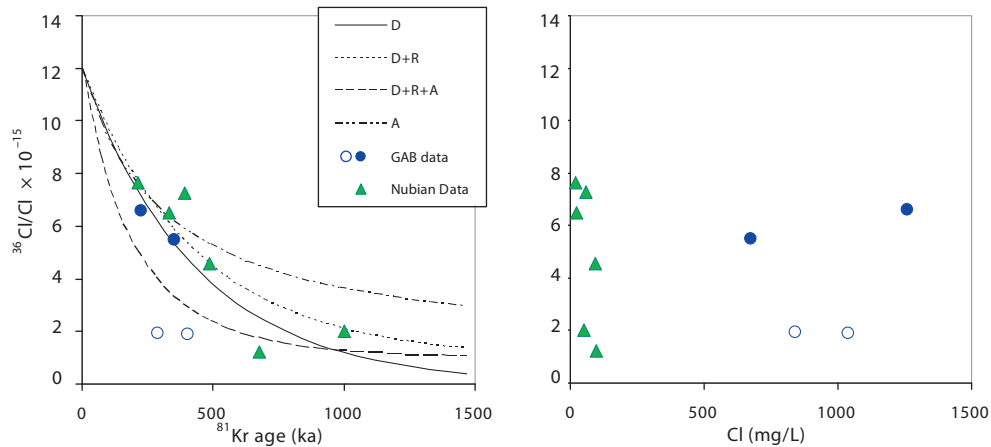


FIG. 5.23.  $^{36}\text{Cl}/\text{Cl}$  ratios as a function of  $^{81}\text{Kr}$  model ages (left plot) and Cl concentrations (right plot). Green triangles: samples from the Nubian aquifer; blue circles: samples from the Great Artesian Basin; solid circles:  $^{36}\text{Cl}/\text{Cl}$  evolution dominated by decay; open circles:  $^{36}\text{Cl}/\text{Cl}$  evolution dominated by the accumulation of Cl from subsurface sources. The lines indicate different calculated temporal  $^{36}\text{Cl}/\text{Cl}$  evolutions (see text. D: Pure decay starting from  $^{36}\text{Cl}/\text{Cl} = 120 \times 10^{-15}$ , R: Considering a subsurface secular equilibrium  $R_{se} = 10 \times 10^{-15}$ , A: Considering a subsurface Cl accumulation at a rate of  $2 \text{ mg} \cdot \text{ka}^{-1} \cdot \text{L}^{-1}$ )

#### 5.5.7.2. Krypton-81 application

So far, nine out of ten  $^{81}\text{Kr}$  analyses from groundwater were significantly depleted compared with modern atmospheric krypton, with the lowest activity of  $5\%_{\text{modern}}$  found in the Nubian aquifer (Sturchio et al. (2004) [5]). The proof-of-principle test of the  $^{81}\text{Kr}$  method is, therefore, fulfilled. The initial results confirm — within remaining uncertainties — the expected advantageous characteristics of the  $^{81}\text{Kr}$  method, namely a constant input concentration and negligible underground production. This can be concluded from a comparison of  $^{36}\text{Cl}/\text{Cl}$  data and  $^{81}\text{Kr}$  model ages from all currently available data pairs (Fig. 5.23, left). The lines in the plot indicate the calculated and expected relationship assuming different scenarios for the  $^{36}\text{Cl}$  evolution. The first two scenarios represent pure decay (D) and decay with a subsurface  $^{36}\text{Cl}/\text{Cl}$  equilibrium ratio of  $10 \times 10^{-15}$  (D + R). The scenario (D + R + A) assumes, in addition, a subsurface Cl accumulation with a  $^{36}\text{Cl}/\text{Cl}$  ratio of  $10 \times 10^{-15}$  at a rate of  $2 \text{ mg} \cdot \text{ka}^{-1} \cdot \text{L}^{-1}$ . All samples from the Nubian aquifer and two samples from the Great Artesian Basin agree with uncertainties within the range of the above mentioned  $^{36}\text{Cl}$  accumulation scenarios. Without going into details of the local hydrology, this is already an encouraging coincidence, indicating the validity of the basic assumption for  $^{81}\text{Kr}$  model ages. It is also a demonstration of the applicability of the  $^{36}\text{Cl}$  dating method despite some factors that could potentially affect the age interpretation of this isotope. However, for two of the Great Artesian Basin samples,  $^{81}\text{Kr}$  and  $^{36}\text{Cl}$  ages disagree. The possible reasons are numerous and could originate from both tracers, but a look at Cl concentrations (right panel in Fig. 5.23) makes simplified  $^{36}\text{Cl}$  interpretation more doubtful. In the Nubian aquifer, chlorinity is low and rather constant over time, representing ideal conditions for  $^{36}\text{Cl}$  dating. In comparison, Cl concentrations in the Great Artesian Basin case study are much higher and more variable. This is just another element of the unfavourable  $^{36}\text{Cl}$  dating conditions prevailing in this part of the Great Artesian Basin. However, if the fraction of subsurface Cl addition can be estimated using other means, it is nevertheless possible to calculate realistic tracer ages within the age of  $<1 \text{ Ma}$ , even if a large fraction of Cl is of subsurface origin (Phillips (2000) [306]). The problem associated with DH and WC samples (open symbols) is that a high subsurface Cl accumulation rate goes together with a reduced meteoric

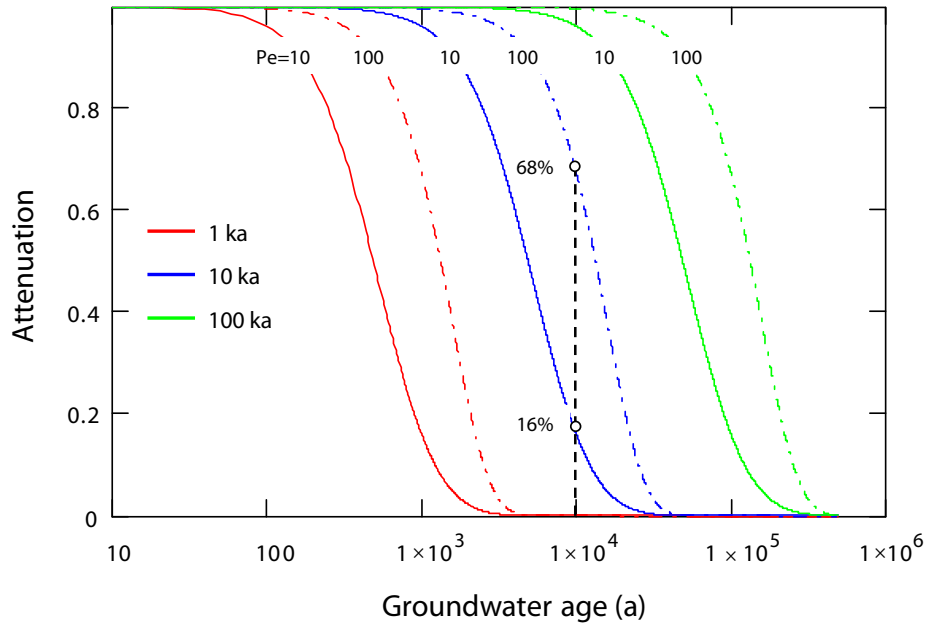


FIG. 5.24. Attenuation of a periodic climate signal as a function of groundwater age for different signal periods and Pe numbers (solid lines:  $Pe = 10$ ; broken lines:  $Pe = 100$ ).

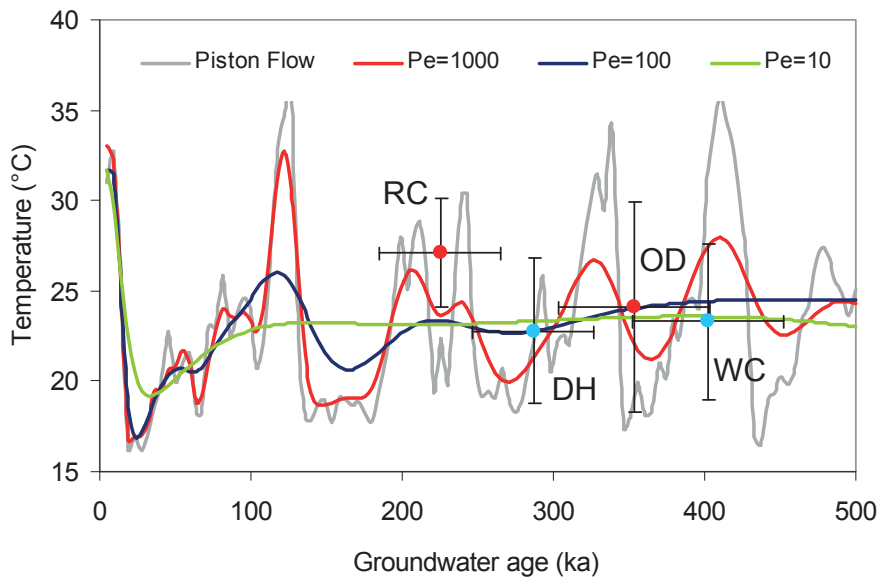


FIG. 5.25. Temperature variations reconstructed from the Dome C ice core record (Luethi et al. (2008) [308]) compared with noble gas temperatures of four Great Artesian Basin wells.

input concentration. Future studies and more data are required for the verification of this hypothesis, which is based on the results of only four wells.

### 5.6. ADDENDUM: SIGNAL ATTENUATION DUE TO HYDRODYNAMIC DISPERSION

Fluctuations of initial recharge conditions and climate signal variations are propagated into the aquifer by advection and dispersion. These input signals are attenuated and phase shifted due to hydrodynamic dispersion. Attenuation factor  $A$  defined as the ratio of the remaining amplitude to

the initial amplitude of the signal as a function of the period ( $T$ ) of the initial (climate) signal, the flow time  $t$  in the aquifer and the strength of the hydrodynamic dispersion which can be expressed by means of the dimensionless Peclet number  $Pe = vx/D$  (Roberts and Valochi (1981) [307]) is:

$$A = \exp(-\alpha) \text{ with } \alpha = \frac{Pe}{2} \left( \sqrt{0.5 + 0.5 \sqrt{1 + \left( \frac{8 \cdot \pi \cdot t}{T \cdot Pe} \right)^2}} - 1 \right) \quad (5.11)$$

For example, an attenuation factor  $A$  of 0.7 corresponds to a reduction of the initial periodic (sinusoidal) signal by 30%. In Fig. 5.24,  $A$  is plotted as a function of groundwater age (assuming a flow velocity of 1 m/a) for different periods of the initial signal and for two different Peclet numbers, 10 and 100.

The remaining amplitude of a signal with a period of 10 ka after a flow time of 10 ka is 16% for a Pe number of 10 and 68% for a Pe number of 100 (Fig. 5.24). An aquifer system acts consequently as a low pass filter. Only long term low frequency input variations are recorded in old groundwater systems. An example are the noble gas temperatures (NGTs) of the four wells of the present Great Artesian Basin study compared in Fig. 5.25 with estimated temperature variations as recorded in  $\delta^{18}\text{O}$  values from the Antarctic Dome C ice core (Luethi et al. (2008) [308]). The  $\delta^{18}\text{O}/T$  relation was arbitrarily adjusted to local climate conditions. Despite the relatively large uncertainties in  $^{81}\text{Kr}$  ages and the NGTs, it can be concluded that small amplitudes of the observed variations are roughly in accord with the model calculations for a reasonable range of Peclet numbers between 10 and 100 (Gelhar et al. (1992) [297]). Larger temporal variations cannot be expected or are, if present, possibly the result of different recharge areas with distinct recharge conditions.

## Chapter 6

### CHLORINE-36 DATING OF OLD GROUNDWATER

F.M. PHILLIPS

Department of Earth and Environmental Science,  
New Mexico Tech,  
Socorro, New Mexico,  
United States of America

#### 6.1. BASIC PRINCIPLES OF CHLORINE-36

Chlorine-36 has been widely used for dating old groundwater. The  $^{36}\text{Cl}$  used for this purpose is produced in the atmosphere through the interaction of cosmic rays with argon atoms. The  $^{36}\text{Cl}$  then mixes with ordinary atmospheric chloride (mostly derived from the ocean). The mixture is deposited on the land surface dissolved in rain or snow or as dry aerosols. Groundwater recharge carries the  $^{36}\text{Cl}$  into the subsurface where the radiometric 'clock' is set. Chloride is conservative in the subsurface and, thus, the  $^{36}\text{Cl}$  is rarely retarded with respect to the water velocity by adsorption or geochemical reactions. Groundwater age can be estimated using the radiometric decay equation and the decrease in  $^{36}\text{Cl}$  from the amount in the recharge water. The main complication is variations in the Cl concentration of groundwater. This can potentially be due to variable evapotranspiration during recharge or to the addition of Cl in the aquifer. If the cause of Cl concentration variations is understood, the age calculation can be corrected to account for the process. Chlorine-36 dating is generally applicable to water in the age range 100 ka–1 Ma.

##### 6.1.1. Chlorine-36 in the hydrological cycle

The principal application of  $^{36}\text{Cl}$  to the dating of old groundwater is defining age through measuring the decay of atmospheric  $^{36}\text{Cl}$ . Chlorine-36 is produced in the atmosphere by cosmic ray spallation of  $^{40}\text{Ar}$  (Lal and Peters (1967) [309]). It decays to  $^{36}\text{Ar}$  with a half-life of  $301\,000 \pm 4000$  a (Bentley et al. (1986) [310]). The average global production rate lies between 20 and 30 atoms  $\text{m}^2/\text{s}$  (Phillips (2000) [306]). This meteoric  $^{36}\text{Cl}$  then mixes with stable oceanic Cl in the atmosphere, resulting in relatively low ratios of  $^{36}\text{Cl}$  to stable Cl ( $^{36}\text{Cl}/\text{Cl}$ ) near coastlines, but these ratios increase to high values near the centres of continents owing to the decrease in the atmospheric concentration of stable chloride (Davis et al. (2003) [311]; Keywood et al. (1997) [312]; Moyses et al. (2003) [313]).

The mixture of  $^{36}\text{Cl}$  and stable chloride is deposited on the land surface dissolved in precipitation and as dry aerosols. Groundwater recharge transports the chlorine isotopes to the water table where they begin to be advected along with the flowing groundwater. As groundwater age increases,  $^{36}\text{Cl}$  decays. In an ideal system (i.e. one with no subsurface sources of either  $^{36}\text{Cl}$  or stable Cl and no sinks except radiodecay), calculating the  $^{36}\text{Cl}$  model age is a simple matter of entering the initial and measured  $^{36}\text{Cl}$  concentrations (or  $^{36}\text{Cl}/\text{Cl}$  ratios) into the radioactive decay equation and solving for time.

In actual aquifers, although anomalous loss of either  $^{36}\text{Cl}$  or stable Cl is seldom a problem, both species are often introduced in the subsurface. Concentrations of Cl and  $^{36}\text{Cl}$  can also vary due to temporal or spatial changes in evapotranspiration in the aquifer recharge area. The challenge of  $^{36}\text{Cl}$  dating of old groundwater is, thus, separating the changes in  $^{36}\text{Cl}$  due to radioactive decay from these other processes (Phillips (2000) [306]). A representative schematic of  $^{36}\text{Cl}$  in the hydrological cycle is shown in Fig. 6.1. The grey lines in the graphs on the bottom part of the figure show the simple exponential evolution of the  $^{36}\text{Cl}/\text{Cl}$  ratio and  $^{36}\text{Cl}$  concentration as a function of distance when no Cl

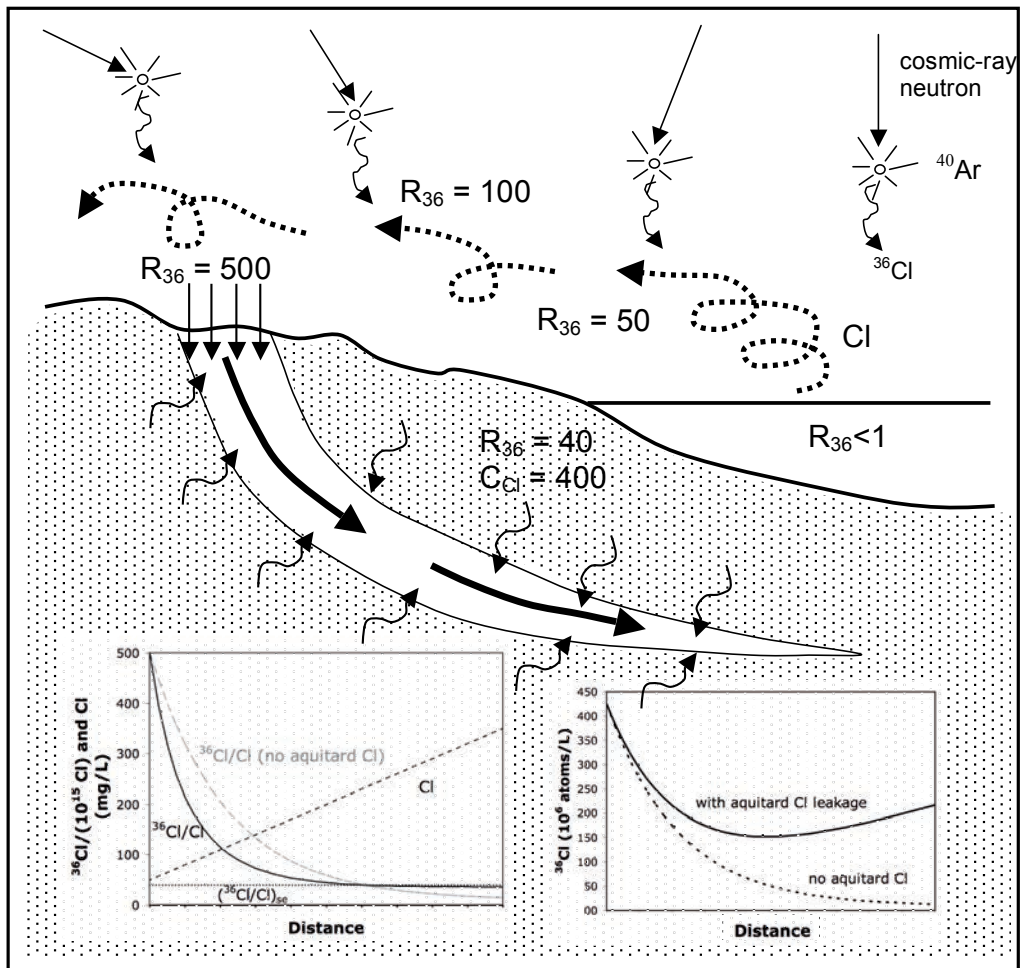


FIG. 6.1. Schematic of  $^{36}\text{Cl}$  in the hydrological cycle. Numerical values are only representative. At the right hand side, marine Cl containing very little  $^{36}\text{Cl}$  is lofted into the troposphere and over the continents. As it is advected inland, it mixes with  $^{36}\text{Cl}$  produced by cosmic ray reaction with argon in the upper atmosphere. This mixture is deposited on the recharge area of an aquifer and the  $^{36}\text{Cl}$  decays during groundwater flow.

is added in the subsurface. When Cl is added from bounding formations (which is common), the black lines show the evolution with distance. For the purposes of illustration, the assumed Cl concentration and  $^{36}\text{Cl}/\text{Cl}$  ratio (which is shown by  $^{36}\text{Cl}/\text{Cl}_{\text{sc}}$  in the right hand graph) are unusually high. The  $^{36}\text{Cl}/\text{Cl}$  ratio varies only moderately from the exponential case, but the  $^{36}\text{Cl}$  concentration actually increases (due to the high equilibrium concentration in the bounding formation).

#### 6.1.1.1. Historical summary

Application of  $^{36}\text{Cl}$  to geochronology was first suggested by Davis and Schaeffer (1955) [314]. Although they did perform a few successful measurements on rocks and water containing fallout from nuclear weapons testing, the screen-wall beta counter technology of the time was incapable of quantifying  $^{36}\text{Cl}$  in typical groundwater. This problem was partially solved with the development of liquid scintillation counting (Ronzani and Tamers (1966) [315]; Tamers et al. (1969) [316]). This method could measure  $^{36}\text{Cl}$  at, and below, the levels typical of groundwater recharge, but suffered from the limitation that several grams of Cl were required. Inasmuch as groundwater recharge with high values of  $^{36}\text{Cl}/\text{Cl}$  is typically fairly dilute, and subsurface water with high concentrations of Cl

typically shows fairly low  $^{36}\text{Cl}/\text{Cl}$ , this analytical advance was limited to only a small number of practical applications.

The real breakthrough in the application of  $^{36}\text{Cl}$  was the development of accelerator mass spectrometry (AMS) as an analytical tool (Elmore et al. (1979) [317]). This technique was capable of measuring down to background levels of  $^{36}\text{Cl}/\text{Cl}$  on milligram-sized samples and, thus, enabled analysis of nearly any groundwater sample (Davis et al. (1983) [318]). The first successful applications to old groundwater were in the Great Artesian Basin (Australia) and the Milk River aquifer (Canada) (Bentley et al. (1986) [310]; Phillips et al. (1986) [319]). These studies both illustrated the feasibility of  $^{36}\text{Cl}$  as a method for dating old groundwater and pointed out the complications that result from variable evapotranspiration combined with subsurface sources of Cl and  $^{36}\text{Cl}$ . Since the mid-1980s, the technique has been widely applied around the world (see Phillips (2000) [306], and Phillips and Castro (2003) [77] for a summary of studies).

## 6.2. SAMPLING TECHNIQUES FOR CHLORINE-36

Ease of sampling is one of the advantages of  $^{36}\text{Cl}$ . Sampling is normally done by collecting sufficient water to contain at least  $\sim 10$  mg of Cl in a clean container and precipitating the Cl as AgCl by adding excess  $\text{AgNO}_3$  solution. Acidification is helpful in promoting the precipitation and flocculation of the AgCl.

The only case in which significant difficulty is likely to be encountered is if the water to be sampled contains very low Cl concentrations ( $< \sim 5$  mg/L). In this case, a large water sample (5–10 L) must be collected. Flocculation for such dilute solutions is typically poor and isolation of the AgCl precipitate may be difficult or impossible. This problem can be addressed in two ways. The first is the use of an anion exchange resin column. Typically, the exchange resin is loaded with nitrate, which is displaced by  $\text{Cl}^-$  as the water sample flows through the column. However, anion exchange resins, as sold, typically have significant amounts of  $\text{Cl}^-$  adsorbed and great care must be taken to ensure that all of this  $\text{Cl}^-$  is flushed before the column is used for sampling. As the water being sampled is dilute, even small amounts of  $\text{Cl}^-$  contamination may be a serious problem. This method has been described in detail (Jannik (1989) [320]).

An alternative approach to dealing with low Cl concentrations is the addition of carrier. The carrier can either be  $^{36}\text{Cl}$ -free ordinary Cl or one in which either  $^{35}\text{Cl}$  or  $^{37}\text{Cl}$  has been enriched. If an isotopically enriched carrier is used, the Cl concentration of the sample can be determined by means of isotope dilution mass spectrometry (IDMS) (Desilets et al. (2006) [321]) during AMS analysis. This offers a very significant advantage over separate measurement of the Cl concentration due to the difficulties involved in conventional measurement of Cl at low concentrations. Disadvantages of this approach are that if both the Cl concentration and the  $^{36}\text{Cl}/\text{Cl}$  ratio are low, dilution of the ratio by addition of a carrier may significantly increase the uncertainty of the AMS measurement, and that carrier addition must be performed with great precision, which can be difficult under field conditions. For this reason, unless practical problems prevent shipment of the water sample to the laboratory, it is preferable to add the spike and precipitate the sample in the laboratory where the spike can be precisely weighed out. There is no single reliable source of isotopically enriched Cl and researchers are encouraged to contact the AMS laboratory that will provide their analyses for recommendations.

## 6.3. CHLORINE-36 SAMPLE PREPARATION AND MEASUREMENT

Chlorine-36 measurements in natural waters are almost entirely performed using AMS (Elmore et al. (1979) [317]; Elmore and Phillips (1987) [322]). This technique employs a tandem van de Graaff particle accelerator, originally designed for particle physics research, as a high energy mass spectrometer. One advantage of this instrument is that when the charge of the ion beam is reversed

in the high voltage terminal by passing through a thin foil (the ‘tandem’ aspect of the accelerator), all molecular species are broken up, eliminating molecular interference that would otherwise overwhelm the  $^{36}\text{Cl}$  detector. A second advantage is that the very high energies imparted to the ion beam allow the use of a rate of energy loss detector that separates  $^{36}\text{Cl}$  from its isobar  $^{36}\text{S}$ , based on their differences in proton number. The history of AMS and recent advances have been surveyed (Elmore and Phillips (1987) [322]; Gove (1992) [323]; Muzikar et al. (2003) [324]; Suter (2004) [325]).

One recent advance that is now becoming frequently used for analysis of  $^{36}\text{Cl}$  in environmental water samples is IDMS (Desilets et al. (2006) [321]). In this approach, an isotopically enriched spike of Cl (usually enriched in  $^{35}\text{Cl}$ ) is added to the sample before the Cl is precipitated as AgCl. Knowing the isotope ratio of the Cl spike and the masses of spike and sample, the Cl concentration of the sample (and, thus, also the  $^{36}\text{Cl}$  concentration) can be calculated from the  $^{35}\text{Cl}/^{37}\text{Cl}$  ratio that is measured during the AMS analysis.  $R_{36,\text{sample}}$ , the actual sample  $^{36}\text{Cl}/\text{Cl}$  ratio ( $\text{atoms } ^{36}\text{Cl} \cdot (\text{atoms } ^{35}\text{Cl} + ^{37}\text{Cl})^{-1}$ ), is calculated from the following formula, given  $R_{36,\text{meas}}$ , the  $^{36}\text{Cl}/\text{Cl}$  ratio measured by the AMS;  $SS$ , the atomic  $^{35}\text{Cl}/^{37}\text{Cl}$  ratio measured by the AMS;  $R_{35,\text{n}}$ , the atomic  $^{35}\text{Cl}/\text{Cl}$  ratio (i.e.  $^{35}\text{Cl}/(^{35}\text{Cl} + ^{37}\text{Cl})$ ) of natural Cl (0.7573); and  $R_{35,\text{sp}}$ , the  $^{35}\text{Cl}/\text{Cl}$  ratio of the isotopically labelled spike:

$$R_{36,\text{sample}} = R_{36,\text{meas}} \left[ 1 + \frac{(1 - R_{35,\text{n}})SS - R_{35,\text{n}}}{R_{35,\text{sp}} - SS(1 - R_{35,\text{sp}})} \right] \quad (6.1)$$

The Cl concentration of the sample ( $C_{\text{Cl},\text{sample}}$ ) in mg Cl/kg solution is correspondingly shown by:

$$C_{\text{Cl},\text{sample}} = \frac{(1000)C_{\text{Cl},\text{soln}}M_{\text{soln}}A_{\text{n}}(R_{35,\text{sp}} - SS(1 - R_{35,\text{sp}}))}{M_{\text{water}} \left[ (R_{35,\text{sp}}A_{35} + (1 - R_{35,\text{sp}})A_{37})(SS(1 - R_{35,\text{n}}) - R_{35,\text{n}}) \right]} \quad (6.2)$$

where

$C_{\text{Cl},\text{soln}}$  is the Cl concentration of the spike solution (mg Cl/g solution);

$M_{\text{soln}}$  is the mass of spike solution added to the sample (g);

$A_{\text{n}}$  is the atomic mass of natural Cl (35.4527 g/mol);

$M_{\text{water}}$  is the mass of the aqueous sample (g);

$A_{35}$  is the atomic mass of  $^{35}\text{Cl}$  (34.9688 g/mol);

$A_{37}$  is the atomic mass of  $^{37}\text{Cl}$  (36.9659 g/mol).

This methodology takes advantage of the high precision and accuracy of isotope ratio mass spectrometry to obtain a very reliable value for the Cl concentration of the sample. It is especially valuable for samples with low Cl concentration, where it not only provides a superior measurement of the Cl concentration, but also increases the Cl content of the water sample, thus facilitating precipitation and isolation of the AgCl and reducing the volume of water that must be collected.

As described above, Cl for  $^{36}\text{Cl}$  analysis is collected through precipitation of AgCl. Fortunately, AgCl can be used as the target in the ion source of an AMS system. However, the sample must first be purified of S. Although the rate of energy loss detector is highly efficient at separating  $^{36}\text{Cl}$  from  $^{36}\text{S}$ , concentrations of S greater than a few milligrams per litre in the AgCl can still produce enough  $^{36}\text{S}$  counts to seriously degrade the precision of the  $^{36}\text{Cl}$  analysis, especially if the  $^{36}\text{Cl}/\text{Cl}$  ratio is low. The sample preparation procedure, therefore, focuses on reducing the S concentration to make it as low as possible.

The standard  $^{36}\text{Cl}$  preparation procedure was originally developed by H.W. Bentley (Bentley et al. (1986) [310]; Bentley et al. (1986) [301]; Phillips et al. (1986) [319]). The procedure consists of first dissolving the AgCl precipitate in  $\text{NH}_4\text{OH}$ , reprecipitating it through the addition of  $\text{HNO}_3$ , redissolving it and then adding  $\text{BaNO}_3$  solution. The  $\text{Ba}^{2+}$  precipitates sulphur as  $\text{BaSO}_4$ . The solution is then separated from the  $\text{BaSO}_4$  precipitate and the AgCl reprecipitated through the addition of  $\text{HNO}_3$ . The repeated dissolution/reprecipitation steps also lower the S content of the AgCl by partitioning the S

TABLE 6.1. STATISTICAL EVALUATION OF INTERLABORATORY COMPARISON DATA (from Mahara et al. (2004) [327])

	Average coefficient of variation (%)				Analytical bias relative to average (%)		
	Analytical	Sample	Sample	Sample	Lab A	Lab B	Lab C
	Both treatments	Both treatments	Uniform preparation	Laboratory preparation			
All data	46	37	30	38	0	6	21
$^{36}\text{Cl}/\text{Cl} > 10 \times 10^{-15}$	10	14	12	16	3	-1	-3

into the solution with each precipitation. Depending on the sulphur concentration of the water sampled, this procedure may be repeated two or three times.

The main disadvantages of this procedure are that it may require one to several days, depending on the number of  $\text{BaNO}_3$  steps, and that a small amount of Cl is lost with each cycle. An alternative procedure has recently been developed (Jiang et al. (2004) [326]). This procedure employs ion exchange columns to concentrate the Cl and reduce S contamination. The authors claim that Cl recovery is  $>90\%$  and that the procedure takes less than one day, however, it has not yet been widely tested.

After drying, the AgCl can be packed into a holder and placed in the ion source of an accelerator mass spectrometer. The machine measures the  $^{36}\text{Cl}/\text{Cl}$  ratio and the  $^{35}\text{Cl}/^{37}\text{Cl}$  ratio (assuming an isotopically enriched spike has been added) of the AgCl. This analysis typically uses between 15 min and 1 h of beam time. The analyses are standardized by normalization to recognized international standards (unlike  $^{14}\text{C}$ , these standards are arbitrary and do not reflect any natural material). From these ratios and associated information on sample volume and the mass of the sample spike  $^{36}\text{Cl}/\text{Cl}$  ratio, the Cl concentration and  $^{36}\text{Cl}$  concentration can be calculated. If IDMS has not been employed, the Cl concentration must be analysed using an independent method. Ion chromatography is generally the preferred method.

Assuming the sample has been spiked with  $^{35}\text{Cl}$  or  $^{37}\text{Cl}$ , the AMS laboratory will report back either the  $^{36}\text{Cl}/(^{35}\text{Cl} + ^{37}\text{Cl})$  ratio or the  $^{36}\text{Cl}/^{35}\text{Cl}$  ratio and the  $^{35}\text{Cl}/^{37}\text{Cl}$  ratio. The user must combine this with data on the sample mass, the spike isotope ratio, and the mass of spike added in Eqs (6.1, 6.2), to obtain the sample  $^{36}\text{Cl}/\text{Cl}$  and Cl concentration.

Until recently, any systematic comparisons of  $^{36}\text{Cl}$  analyses' reliability have been very limited in scope. However, Mahara et al. (2004) [327] have recently published a very thorough interlaboratory comparison. They sent 15 natural water samples to three AMS laboratories around the world (the laboratories were not identified by name). Each of the 15 samples was subjected to two treatments: the first aliquot was processed in Mahara's laboratory using a uniform processing procedure, while the second aliquot was sent to the AMS laboratory as an untreated water sample and processed there by whatever procedure was standard in that laboratory. This constituted a total sample of 90 AMS analyses, which is a sufficient basis for statistical evaluation. The chloride concentrations of the samples ranged from 9 to 17 900 mg/L and the mean  $^{36}\text{Cl}/\text{Cl}$  ratios ranged from 0.5 to  $410 \times 10^{-15}$ , a typical range for deep groundwater samples.

The outcome of this comparison is summarized in Table 6.1 and shown graphically in Fig. 6.2. The results are divided into 'all samples' (a total of either 90 or 45 analyses, depending on whether both treatments or only one are being considered) and ' $^{36}\text{Cl}/\text{Cl} > 10 \times 10^{-15}$ ', which constituted 9 of the 15 samples. The 'analytical standard deviation' is the mean of the  $1\sigma$  standard deviations for each analysis, converted to a coefficient of variation using the mean of the six replicate analyses. The next three columns provide the coefficients of variation for both treatments combined and each

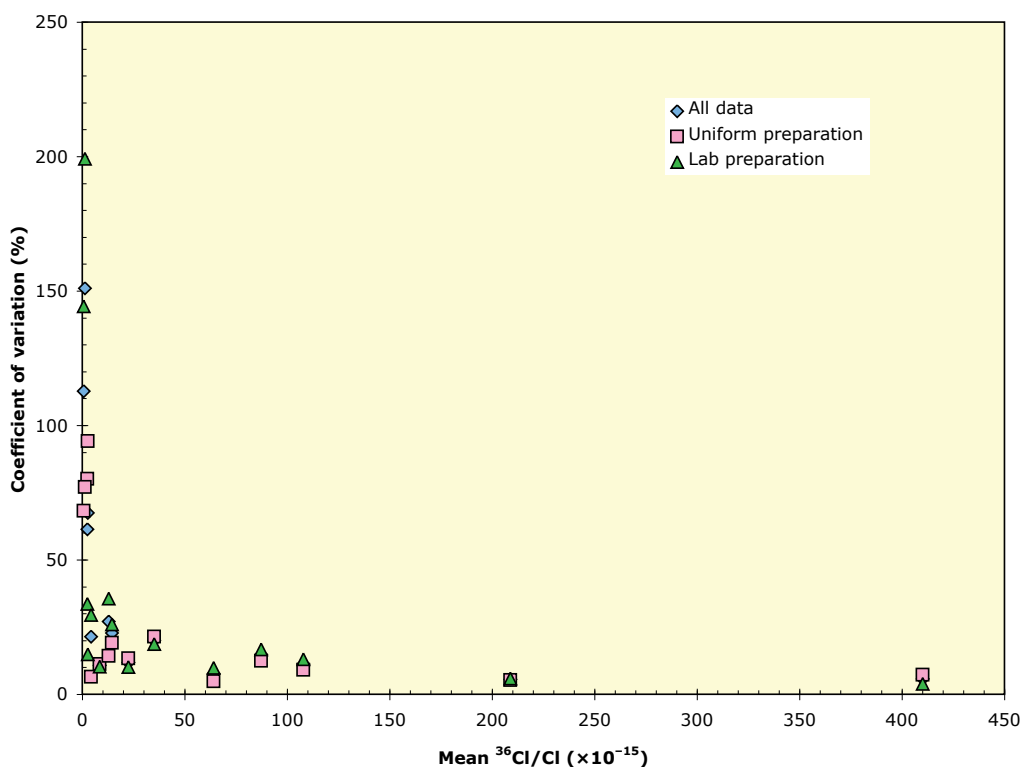


FIG. 6.2. Reproducibility of AMS  $^{36}\text{Cl}/\text{Cl}$  measurements on water samples as a function of the  $^{36}\text{Cl}/\text{Cl}$  ratio of the sample, based on data from Mahara et al. (2004) [327]. 'Uniform preparation' refers to samples prepared in Mahara's laboratory, 'Lab preparation' to samples prepared at several AMS laboratories, and 'All data' to the two data sets combined.

separately. Finally, the last three columns summarize the analytical bias (relative to the mean of all six replicates) for the three AMS laboratories. Figure 6.2 shows that for samples with  $^{36}\text{Cl}/\text{Cl}$  less than  $\sim 20 \times 10^{-15}$ , the coefficients of variation are reasonably small, but that they in some cases rise to values over 100% as the  $^{36}\text{Cl}/\text{Cl}$  ratio approaches zero. The reported analytical standard deviations appear to predict the actual measured standard deviations reasonably well. For samples with  $^{36}\text{Cl}/\text{Cl}$  greater than  $10 \times 10^{-15}$ , having the sample preparation performed in three separate laboratories, as opposed to a single laboratory, increased the coefficient of variation from 12% to 16%. This difference of 4% would appear to be a reasonable estimate of the magnitude of variability that might be expected as a result of differing laboratory preparation procedures. The bias evaluation indicates that samples can be expected to be reproducible between laboratories to  $\sim 3\%$ , which is quite adequate for the purposes of groundwater dating.

#### 6.4. CHLORINE-36 RESEARCH GROUPS AND LABORATORIES

Owing to the size and expense of accelerator mass spectrometers, the number of laboratories around the world that are capable of  $^{36}\text{Cl}$  analysis on typical deep groundwater samples is limited. However, because such major laboratories are almost always operated as shared facilities, they are accessible to outside investigators, and as a result there are many research groups employing  $^{36}\text{Cl}$  in groundwater studies.

The institution that performed the original  $^{36}\text{Cl}$  AMS analyses was the tandem accelerator laboratory at the University of Rochester (New York, USA), but this facility has since been closed down. Analyses were taken over by the Center for Accelerator Mass Spectrometry at Lawrence Livermore National Laboratory (Livermore, CA, USA) (Roberts et al. (1996) [328]), the Purdue Rare Isotope

Measurement Laboratory (West Lafayette, IN, USA; 'PRIME Lab') (Elmore et al. (1996) [329]), the AMS laboratory at the Paul Scherrer Institute (Zurich, Switzerland) (Synal et al. (1994) [330]), the Research Group and Laboratory of the Technical University of Munich (Garching, Germany), and the laboratory at Australia National University (Canberra, Australia) (Fifield (2000) [331]). For many years, these facilities have performed the bulk of  $^{36}\text{Cl}$  analyses around the world, but they have recently been joined by several laboratories that have more recently developed the  $^{36}\text{Cl}$  capability. These include the Scottish Universities Environmental Research Centre (East Kilbride, United Kingdom) (Freeman et al. (2004) [332]), the China Institute of Atomic Energy (Jiang et al. (2004) [326]), the University of Tokyo (Tokyo, Japan) (Aze et al. (2007) [333]), the University of Tsukuba (Tsukuba, Ibaraki, Japan) (Sasa et al. (2007) [334]), the University of Uppsala (Uppsala, Sweden) (Alfimov et al. (2007) [335]), and Oak Ridge National Laboratory (Oak Ridge, TN, USA) (Galindo-Uribarri et al. (2007) [336]).

## 6.5. SPECIFICS OF THE $^{36}\text{Cl}$ METHOD

Unlike many groundwater tracers and dating agents that may undergo complex chemical reactions in the subsurface (such as  $^{14}\text{C}$  or uranium isotopes),  $^{36}\text{Cl}$  is virtually inert. This greatly simplifies the interpretation of its behaviour. In spite of this relative simplicity, the interpretation is often not straightforward. The major complications in using  $^{36}\text{Cl}$  to estimate groundwater age are the introduction of subsurface chloride, subsurface production of  $^{36}\text{Cl}$ , and variation in the input of  $^{36}\text{Cl}$  due to changes in evapotranspirative concentration or changes in cosmogenic production. High chloride concentrations arising from connate waters, evaporite dissolution, or possibly rock–water interaction are common in sedimentary basins and deep crystalline rocks. These may either diffuse upward or be advected into aquifers by cross-formational flow. In general, this subsurface-source chloride is not  $^{36}\text{Cl}$  free, because  $^{36}\text{Cl}$  is produced at low levels (compared with meteoric chloride) in the subsurface by absorption by  $^{35}\text{Cl}$  of thermal neutrons produced by U and Th series decay and U fission (Fabryka-Martin et al. (1988) [337]; Lehmann et al. (1993) [250]; Phillips (2000) [306]). In addition to subsurface addition of Cl isotopes, the production of  $^{36}\text{Cl}$  in the atmosphere and, thus, the input at the recharge area may also change with time as a result of fluctuations in the intensity of the terrestrial and solar magnetic fields (Plummer et al. (1997) [248]; Wagner et al. (2001) [338]). Finally, changes in climate can affect both the distance from the ocean shore (Bentley et al. (1986) [310]; Purdy et al. (1996) [339]) and, thus, the accession of stable marine chloride to the recharge area, and the amount of evapotranspiration of the recharge water (Love et al. (2000) [292]; Zhu et al. (2003) [340]), which concentrates Cl and  $^{36}\text{Cl}$  equally.

As a general working principle,  $^{36}\text{Cl}$  dating of old groundwater is most straightforward and least ambiguous in situations where the meteoric  $^{36}\text{Cl}/\text{Cl}$  ratio at the aquifer recharge area is high relative to the steady state subsurface ratios and where subsurface input of chloride is minimal. Subsurface equilibrium ratios typically vary from about  $5 \times 10^{-15}$  to  $50 \times 10^{-15}$ . The ratios at the higher end of this range are most commonly found in acidic plutonic or volcanic formations and the large sedimentary aquifers in which  $^{36}\text{Cl}$  is commonly employed usually have subsurface equilibrium ratios of less than  $20 \times 10^{-15}$ . Meteoric  $^{36}\text{Cl}/\text{Cl}$  in aquifer recharge may be below this ratio close to the ocean, but rises to values of  $100\text{--}1000 \times 10^{-15}$  in continental interior settings. Thus, the 'cleanest' applications of the method are likely to be found in large sedimentary basin aquifers with recharge in the continental interior and permeabilities high enough to flush most connate solutes. Recent studies in the Australian interior at Palm Valley (Wischusen et al. (2004) [341]), the Amadeus Basin (Cresswell et al. (1999) [342]; Kulongoski et al. (2008) [343]), the Coonamble embayment in the Great Artesian Basin (Mahara et al. (2007) [344]), and, in North Africa, the Nubian aquifer (Patterson et al. (2005) [43]; Sturchio et al. (2004) [5]) provide good examples of this favourable situation.

### 6.5.1. Meteoric sources of $^{36}\text{Cl}$

In most cases, as described above, the fundamental basis for  $^{36}\text{Cl}$  dating of groundwater is the radiodecay, during subsurface residence, of relatively high concentrations of  $^{36}\text{Cl}$  introduced to aquifers, along with recharging groundwater. Successful dating, thus, requires knowledge of  $^{36}\text{Cl}$  in atmospheric deposition.

The ultimate source of  $^{36}\text{Cl}$  in the atmosphere is the interaction of high energy cosmic rays (principally protons and neutrons) with the nucleus of  $^{40}\text{Ar}$  atoms (see Phillips (2000) [306] for more information on the nuclear reactions). This production is highest near the geomagnetic poles and lowest near the geomagnetic equator because the magnetic field of the earth deflects primary cosmic ray protons where the field lines are quasi-horizontal near the equator, but allows the cosmic ray particles to reach the atmosphere following the near-vertical field lines at the poles (Desilets and Zreda (2003) [345]; Lal and Peters (1967) [309]; Powell (1955) [346]; Simpson and Uretz (1953) [347]). Chlorine-36 deposition on the land surface, however, does not peak at the geomagnetic poles. Most of the  $^{36}\text{Cl}$  production takes place in the stratosphere because the cosmic ray flux is higher there than in the troposphere, and it is the position of maximum stratosphere–troposphere mixing that largely determines the concentration distribution of  $^{36}\text{Cl}$  in the troposphere. This mixing is greatest at  $\sim 40^\circ$  latitude, during the spring season. This produces the characteristic maximum in deposition at this latitude, decreasing towards both the pole and equator as deposition removes  $^{36}\text{Cl}$  from the atmosphere during turbulent transport northward and southward (Fig. 6.3) (Bentley et al. (1986) [310]; Phillips (2000) [306]).

Were the tropospheric  $^{36}\text{Cl}$  concentration is directly proportional to  $^{36}\text{Cl}$  deposition on the land surface,  $^{36}\text{Cl}$  in groundwater recharge would be straightforward to predict. In reality, the processes involved in  $^{36}\text{Cl}$  deposition are considerably more complex. Chlorine-36, along with stable Cl, adheres to atmospheric aerosols. Depending on their size, these aerosols are deposited at differing rates (Buseck and Schwartz (2003) [348]). They may serve as nuclei for the condensation of water droplets or be engulfed by droplets after they have formed. Depending on the degree of water saturation of the atmosphere, the droplets may grow rapidly and precipitate to the land surface or may simply persist in the atmosphere. As a result of these interactions,  $^{36}\text{Cl}$  may have both varying residence times and varying deposition rates in different parts of the troposphere.

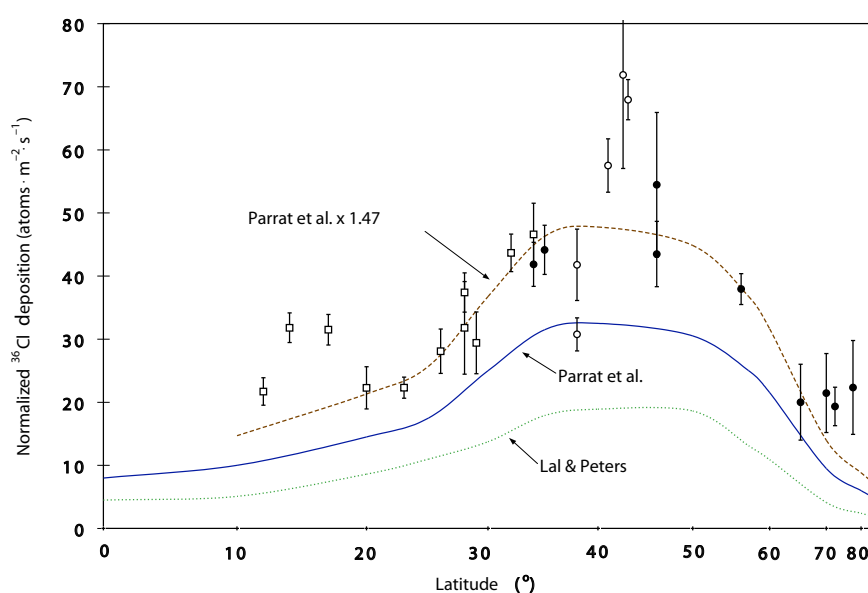


FIG. 6.3. Estimated latitudinal distribution of  $^{36}\text{Cl}$  deposition. Empirical data are compared to calculations by Parrat et al. (1996) [349], and Lal and Peters (1967) [309]. (Figure modified from Phillips (2000) [306].)

The most detailed time series of  $^{36}\text{Cl}$  in precipitation was produced by Knies (1994) [350], who measured over 350 samples from West Lafayette, Indiana, USA, between June 1992 and June 1993. Concentrations in individual samples (multiple samples were collected during storms) varied from  $10^5$  to  $10^7$  atoms/L and the range of concentrations in an individual event sometimes spanned an order of magnitude. Averaged over a large number of storm events,  $^{36}\text{Cl}$  concentrations and deposition rates do form spatially coherent patterns, but a very high degree of short term variability shows that the controls on deposition are very sensitive to environmental conditions.

The average monthly  $^{36}\text{Cl}$  deposition rate of the samples from Knies' data set exhibited a strong correlation to average monthly precipitation ( $0.052 \pm 0.006$  atoms  $^{36}\text{Cl} \cdot \text{m}^{-2} \cdot \text{s}^{-1} \cdot (\text{mm/a})^{-1}$  converted to annual units;  $r^2 = 0.85$ ) (Phillips (2000) [306]). This suggests that some of the variability in  $^{36}\text{Cl}$  deposition can be explained by variations in precipitation. Phillips (2000) [306] used this correlation to normalize  $^{36}\text{Cl}$  deposition measurements spanning the globe, obtaining a global average value of  $\sim 30$  atoms  $\cdot \text{m}^{-2} \cdot \text{s}^{-1}$ . He also used it, in concert with an estimate of the latitudinal distribution of  $^{36}\text{Cl}$  deposition and the geographic distribution of precipitation and stable chloride deposition, to calculate the distribution of the  $^{36}\text{Cl}/\text{Cl}$  ratio over the USA. However, other data sets bearing on this relation have not showed as strong a correlation (Hainsworth et al. (1994) [351]; Moysey et al. (2003) [313]). A large set of data on  $^{36}\text{Cl}$  in groundwater collected yielded a slope for the  $^{36}\text{Cl}$  deposition/precipitation relation that was about half that of the Knies data (Davis et al. (2003) [311]; Moysey et al. (2003) [313]).

This observation may help to reconcile previous estimates of  $^{36}\text{Cl}$  deposition and the distribution of the  $^{36}\text{Cl}/\text{Cl}$  ratio. If the slope from the Moysey/Davis data ( $\sim 0.025$  atoms  $^{36}\text{Cl} \cdot \text{m}^{-2} \cdot \text{s}^{-1} \cdot (\text{mm/a})^{-1}$ ) is used in the Phillips (2000) [306] equation for calculating global average  $^{36}\text{Cl}$  deposition, a value of  $\sim 25$  atoms  $\cdot \text{m}^{-2} \cdot \text{s}^{-1}$  is obtained, which is closer to that calculated by Moysey et al. (2003) [313] and several other authors. The empirical map of  $^{36}\text{Cl}/\text{Cl}$  ratios over the USA produced by Davis et al. (2003) [311] and Moysey et al. (2003) [313] (Fig. 6.4) showed a pattern similar to that predicted by Phillips (2000) [306], but in general lower values. If both the lower slope from Moysey et al. (2003) [313] and the lower global deposition value calculated above are substituted in the algorithm from Phillips (2000) [306] for the distribution of the  $^{36}\text{Cl}/\text{Cl}$  ratio, the match is markedly improved. However,  $^{36}\text{Cl}/\text{Cl}$  ratios in the south-eastern USA are still lower than calculated. The most likely explanation for this

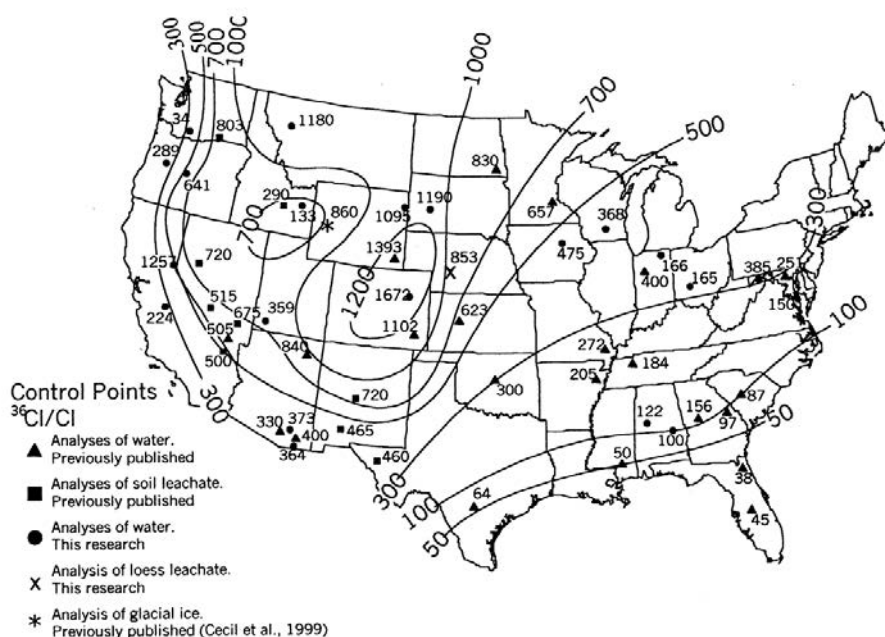


FIG. 6.4. The distribution of meteoric  $^{36}\text{Cl}/\text{Cl}$  ratios over the USA estimated by Davis et al. (2003) [311], based on empirical data.

systematic deviation is that much of the Cl deposited over the south-eastern region originates from the lower latitudes of the north Atlantic Ocean, where  $^{36}\text{Cl}$  atmospheric concentration is less than in the area where the  $^{36}\text{Cl}$  is eventually deposited on the land surface.

The strongest correlation that Moysey et al. (2003) [311] found for the  $^{36}\text{Cl}/\text{Cl}$  ratio was an inverse one with stable Cl deposition. This is encouraging, suggesting that the deposition of  $^{36}\text{Cl}$  is fairly uniform, with dependence on amount of precipitation as a second order effect, and that the geographical variation of the  $^{36}\text{Cl}/\text{Cl}$  ratio can be explained mostly by the amount of dilution from stable Cl deposition. For the remainder of the globe that has been studied for  $^{36}\text{Cl}$  deposition less intensively than the USA, this indicates that with current knowledge of the latitudinal variation of  $^{36}\text{Cl}$  deposition, precipitation distribution and stable Cl deposition (which is much easier to measure than  $^{36}\text{Cl}$  deposition), ratios of  $^{36}\text{Cl}/\text{Cl}$  in groundwater recharge might be satisfactorily estimated.

### **6.5.2. Secular variation in the atmospheric deposition of $^{36}\text{Cl}$**

As described above, the penetration of the primary cosmic radiation into the atmosphere of the earth is modulated by the strength of the terrestrial magnetic field (Elsasser et al. (1956) [352]). Large fluctuations in both the intensity of the dipole magnetic field and in the position, configuration and intensity of the non-dipole field have been well documented (Korte and Constable (2006) [353]; Valet et al. (2005) [354]). Cosmogenic production of  $^{36}\text{Cl}$  has, therefore, varied with time. This inference has been verified by measurement of  $^{36}\text{Cl}$  in the meteoric proxy archives of ice cores (Baumgartner et al. (1998) [355]; Wagner et al. (2001) [338]) and fossil rat urine (Plummer (1996) [356]) (Fig. 6.5). The magnitude of variation in both of these records was about a factor of two. The extent to which these fluctuations in atmospheric production are reflected in the initial  $^{36}\text{Cl}$  content of old groundwater samples has not been determined. Over the long timescales usually considered (>100 ka), dispersion and mixing may average out the input variations. In one of the few continental archives over this timescale, a very deep vadose zone profile from the Mojave Desert, these variations in production were not readily apparent, although the deep chloride did have higher  $^{36}\text{Cl}/\text{Cl}$  ratios than expected based on modern samples (Tyler et al. (1996) [357]).

In addition to the atmospheric production variation, the  $^{36}\text{Cl}/\text{Cl}$  ratio of atmospheric deposition can vary as a result of changes in the stable Cl deposition. Such changes could be produced by variation in the distance between the aquifer recharge area and the ocean, driven by sea level changes. Trends in the  $^{36}\text{Cl}/\text{Cl}$  ratio down flowlines in the Carrizo aquifer (Texas, USA) (Bentley et al. (1986) [310]) and the Aquia aquifer (Maryland, USA) (Purdy et al. (1996) [339]) have been attributed to this mechanism.

### **6.5.3. Chlorine-36 from nuclear weapons fallout**

The USA tested numerous thermonuclear weapons in the Pacific Ocean during the 1950s and 1960s. Thirty-five of these, between 1954 and 1958, were conducted with devices placed on barges in the ocean (Zerle et al. (1997) [358]). The resultant thermal neutron activation of  $^{35}\text{Cl}$  in sea water and dispersion in the stratosphere produced a global pulse of  $^{36}\text{Cl}$  fallout between 1954 and 1965. This peaked at deposition rates approximately two orders of magnitude greater than natural atmospheric  $^{36}\text{Cl}$  production. Phillips (2000) [306] has presented a global reconstruction of the latitudinal distribution of the fallout pulse.

Owing to the magnitude and duration of this pulse, it presents a potential complication to the  $^{36}\text{Cl}$  dating of old groundwater. Contamination of old groundwater samples by relatively small proportions of bomb era recharge could markedly increase the apparent  $^{36}\text{Cl}$  concentration of old groundwater. For this reason, it is common to analyse samples for  $^{36}\text{Cl}$ , for  $^3\text{H}$  or for  $^3\text{H}/^3\text{He}$  in order to provide assurance that such contamination is negligible.

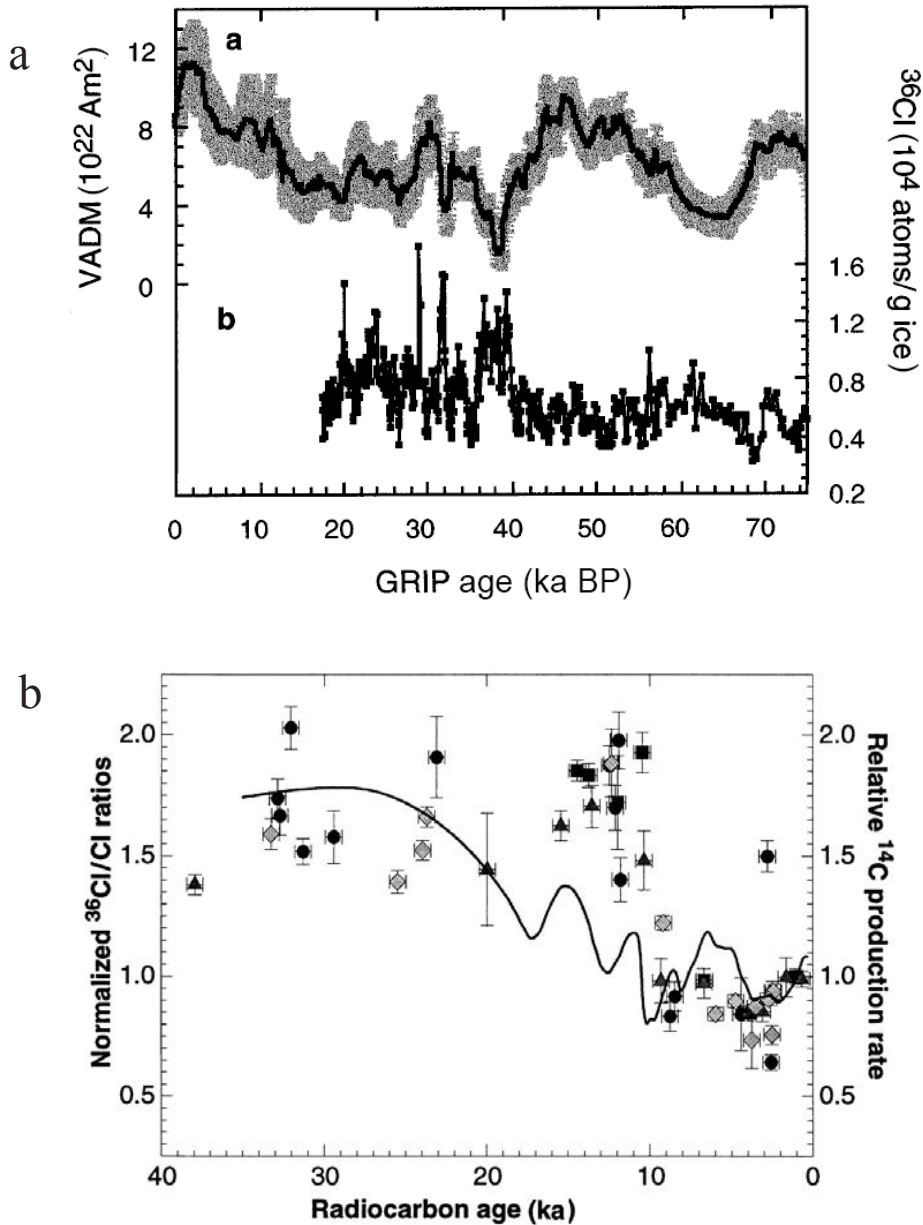


FIG. 6.5. (a) Chlorine-36 deposition variations in a Greenland ice core (Wagner et al. (2001) [338]) (a) variation in the virtual axial dipole moment of the earth over the past 75 ka, (b)  $^{36}\text{Cl}$  concentration in the ice. It should be noted that  $^{36}\text{Cl}$  concentration varies as a function of ice deposition rate as well as production. (b)  $^{36}\text{Cl}/\text{Cl}$  in fossilized rat urine from the south-western USA over the past 40 ka (from Plummer et al. (1997) [248]).

The bomb  $^{36}\text{Cl}$  pulse can also complicate the estimation of the initial  $^{36}\text{Cl}$  ratio or concentration by contamination of young samples collected to assess the initial condition. Samples of post-bomb recharge (as established by CFC or  $^3\text{H}/^3\text{He}$  dating) could potentially be used for this purpose, but this is complicated by retention of bomb  $^{36}\text{Cl}$  in vegetation and subsequent soil/plant recycling (see Section 6.5.4.2).

Scheffel et al. (1999) [359] have reported  $^{36}\text{Cl}$  deposition rates several times the expected natural ones for post-bomb precipitation samples. They attributed this to recycling of bomb  $^{36}\text{Cl}$ . If this attribution is correct, then precipitation samples should also not be used to establish the initial  $^{36}\text{Cl}$  for groundwater dating. However, the Cl concentration data in precipitation reported by Scheffel et

al. (1999) [359] also appear to be unreasonably high (cf. values reported in Berner and Berner (1987) [360]). This process, rather than bomb  $^{36}\text{Cl}$  recycling, may explain anomalous  $^{36}\text{Cl}$  deposition rates.

#### 6.5.4. Processes affecting $^{36}\text{Cl}$ during recharge

During deposition on the land surface and infiltration through the vadose zone,  $^{36}\text{Cl}$  concentrations and ratios can potentially be affected by several processes. The most prominent of these are evaporation, transpiration, biological uptake, differential transport through fast and slow flow paths, and weathering release of  $^{36}\text{Cl}$  from minerals.

##### 6.5.4.1. *Effects of evapotranspiration*

Virtually all recharge water is concentrated to some extent by evapotranspiration (Lerner et al. (1990) [361]). In arid regions,  $\text{Cl}^-$  in recharge water can be enriched over precipitation by up to 500-fold (Scanlon et al. (2006) [362]; Tyler et al. (1996) [357]). Climate variations at the glacial/interglacial timescale can produce large changes in the evapotranspirative concentration of recharge (Walvoord et al. (2002) [44]). Trends in  $\text{Cl}$  concentration down flow paths that were produced by this mechanism have been noted in the Great Artesian Basin (Airey et al. (1983) [363]) and other aquifers. This phenomenon can produce significant problems in attempts to date such groundwater using changes in  $^{36}\text{Cl}$  concentration. Use of the  $^{36}\text{Cl}/\text{Cl}$  ratio is generally preferable in this case, since  $^{36}\text{Cl}$  and  $\text{Cl}$  are concentrated equally by evapotranspiration.

##### 6.5.4.2. *Effects of plant uptake of $\text{Cl}$ and $^{36}\text{Cl}$*

Chlorine is an essential nutrient for plants and is, thus, taken up by their roots and utilized in plant tissues and fluids (Sheppard et al. (1999) [364]). Scarce nutrients such as  $\text{NO}_3^-$  and P exhibit concentration profiles through the root zone that decrease with depth; this is an indication that they are being semi-quantitatively retained in the soil via biological recycling. In contrast,  $\text{Cl}^-$  typically shows concentration profiles that increase with depth, reflecting predominant control by evapotranspirative concentration (Jobbagy and Jackson (2001) [365]). In general, the effect of plant uptake is most prominent when  $\text{Cl}^-$  concentrations in soil water are low.

The  $\text{Cl}^-$  taken up by plant roots is incorporated into organic compounds within the plant. The concentration of  $\text{Cl}$  in plant tissue (dry mass basis) is typically ten times that of the  $\text{Cl}^-$  in the soil water from which the plants grew, and in some plants may be 150 times the soil water concentration (Kashparov et al. (2007) [366]; Sheppard et al. (1999) [364]). Most of this  $\text{Cl}$  is released back to the soil by decomposition, either after leaves are shed or after the plant dies, but some fraction may be incorporated in volatile organic molecules such as chloroform, tetrachloromethane and 1,1,1-trichloroethane (Laternus and Matucha (2008) [367]). Chlorine-36 in these compounds may then be volatilized to the atmosphere, although the fraction lost this way is probably generally small.

Some of the  $\text{Cl}$  incorporated in plant tissues is directly released to the soil water as  $\text{Cl}^-$  during decomposition, but a significant fraction can be retained in relatively refractory humic and fulvic acids in the soil (Myneni (2002) [368]). These, and similar, compounds in soil can then adsorb additional  $\text{Cl}^-$  from the soil water (Lee et al. (2001) [369]). A small fraction of the  $\text{Cl}^-$  deposited on the soil surface may be immobilized over geological time in these refractory compounds, but a strong trend towards increasing concentration with depth (Jobbagy and Jackson (2001) [365]) shows that most  $\text{Cl}^-$  eventually passes through the soil column. The effect of vegetation uptake and chemical transformation is, thus, to retard and homogenize  $\text{Cl}^-$  deposited from the atmosphere.

This retardation (relative to the flux of associated water) is clearly evidenced by the slowness in passing through the hydrological system of the pulse of  $^{36}\text{Cl}$  released by nuclear weapons testing in

the late 1950s (Elmore et al. (1982) [370]; Zerle et al. (1997) [358]). Numerous studies have noted that in situations where consideration of hydrological fluxes indicate that surface water or soil water should have been flushed of the bomb pulse, fallout  $^{36}\text{Cl}$  is still found at high levels in the system (Alvarado et al. (2005) [371]; Hogan et al. (2007) [372]; Milton et al. (1997) [373]; Van Valkenburgh (1996) [374]). Measurements of  $^{36}\text{Cl}$  in various species of conifers in Canada have verified that twenty or more years after the bomb fallout peak, the vegetation retained  $^{36}\text{Cl}/\text{Cl}$  ratios similar to that of the peak (Milton et al. (1997) [375]). Cornett et al. (1997) [376] estimated a mean residence time of  $\sim 40$  a for Cl in vegetation and soil under relatively humid, heavily vegetated conditions in Ontario, Canada. Given the subsequent discovery of Cl sequestration in relatively refractory organo-chlorine compounds (Myneni (2002) [368]), the residence time distribution is undoubtedly skewed, with a tail of quite long residences.

The net effect of biological uptake of  $^{36}\text{Cl}$  is to provide a low pass filter at the front end of the groundwater system. Residence times in the organic reservoir (plants plus soil) are almost certainly quite short compared with the residence time in aquifers being considered for  $^{36}\text{Cl}$  dating, but the retention helps to smooth short term fluctuations in  $^{36}\text{Cl}$  and Cl deposition.

#### 6.5.4.3. *Effects of transport through the vadose zone*

Transport through the vadose zone is a necessary step prior to atmospherically deposited  $^{36}\text{Cl}$  becoming a groundwater solute. In most cases, this constitutes a geologically instantaneous transfer and has little influence on  $^{36}\text{Cl}$  dating of old groundwater. However,  $\text{Cl}^-$  residence times in the vadose zone can vary widely depending on climate and vadose zone thickness, varying from a few days to  $>10^5$  a. In arid regions with thick vadose zones, the residence time of  $\text{Cl}^-$  may be significant in comparison to subsurface residence times of interest. For example, Tyler et al. (1996) [357] has shown that  $^{36}\text{Cl}$  is retained in deep ( $>200$  m) vadose zones of the Mojave Desert for over 120 000 a. Modelling of this system by Walvoord et al. (2002) [44] indicates that plausible climate change events are capable of flushing this accumulated  $\text{Cl}^-$  into underlying aquifers in a matter of a few thousand years.

Large contrasts in the hydraulic properties of vadose zones can produce similar effects without the necessity for a very arid climate. For example, Foster and Smith-Carrington (1980) [377] have shown that diffusion into low permeability matrix blocks has retarded the arrival of agricultural nitrate by decades during transport through a fractured chalk vadose zone in England. Conversely, at least small amounts of bomb  $^{36}\text{Cl}$  are apparently bypassing large amounts of  $\text{Cl}^-$  that entered the vadose zone at Yucca Mountain, Nevada, during the Pleistocene and are now entering a tunnel at hundreds of metres depth (Campbell et al. (2003) [378]; Cizdziel et al. (2008) [379]). Dual media vadose zones (usually high permeability fractures in a low permeability but high porosity matrix) can have the apparently paradoxical property of retaining large reservoirs of solutes while permitting the rapid transmission of water. If aquifer recharge areas intended for  $^{36}\text{Cl}$  dating have dual media characteristics, the effect on the recharge value for the  $^{36}\text{Cl}$  should be carefully evaluated.

#### 6.5.4.4. *Effects of weathering release of cosmogenic in situ $^{36}\text{Cl}$*

In addition to the effects of the vegetation–soil–vadose zone on  $^{36}\text{Cl}$  transport, this zone can also be a source of the nuclide. Nuclear reactions provoked by the actions of cosmic radiation on the nuclei of atoms making up soil and rock can produce  $^{36}\text{Cl}$  within the mineral phases (Gosse and Phillips (2001) [380]). The production rate of  $^{36}\text{Cl}$  increases quasi-exponentially with altitude. Phillips (2000) [306] has described the production reactions in some detail and evaluated their importance for groundwater dating. Given normal weathering rates, these in situ reactions are of negligible importance for most rock types at sea level. However, at elevations  $>3$  km, this source can increase the flux of  $^{36}\text{Cl}$  to the water table by more than 50%, especially at tropical latitudes where atmospheric deposition rates are low. Limestone is of particular importance in this regard because it has both a high concentration of the target element

calcium and it weathers unusually rapidly. Even at sea level at mid-latitudes, weathering of  $^{36}\text{Cl}$  from limestone can contribute  $\sim 10\%$  of the atmospheric flux, whereas at high elevations near the equator it can release  $^{36}\text{Cl}$  amounting to  $>200\%$  of the atmospheric flux. The release of this ‘epigene’  $^{36}\text{Cl}$  (Bentley et al. (1986) [310]) should always be considered in evaluating the accession rate of  $^{36}\text{Cl}$  to the aquifer if the recharge area is above a  $\sim 2$  km elevation.

### 6.5.5. Subsurface processes influencing $^{36}\text{Cl}$ concentrations and $^{36}\text{Cl}/\text{Cl}$

#### 6.5.5.1. Hypogene production of $^{36}\text{Cl}$

Chlorine-36 is unusual (although not unique) among nuclides used for groundwater tracing in that it can be produced by a thermal neutron absorption reaction, in this case  $^{35}\text{Cl}(n, \gamma)^{36}\text{Cl}$  (Davis and Schaeffer (1955) [314]). This means that any water that contains  $\text{Cl}^-$ , which is virtually ubiquitous, and undergoes a neutron flux will produce  $^{36}\text{Cl}$ . Neutrons are released in the subsurface below the reach of cosmic radiation by nuclear reactions, principally neutrons directly emitted from the nuclei of uranium atoms undergoing spontaneous fission and as a secondary result of  $\alpha$  particles released during the decay of uranium series nuclides and absorbed by light nuclei that then eject a neutron (Feige et al. (1968) [381]). These neutrons are rapidly slowed to thermal energies and may then be absorbed by  $^{35}\text{Cl}$ . The reaction  $^{39}\text{K}(\alpha, n)^{36}\text{Cl}$  can also produce  $^{36}\text{Cl}$  in the subsurface, but it is generally insignificant in comparison to the neutron absorption reaction on  $\text{Cl}$  (Lehmann et al. (1993) [250]).

The production of neutrons as a result of spontaneous fission emission is simply a function of the concentration of U in the rock:

$$P_{n,\text{sf}} = 0.429C_U \quad (6.3)$$

where

$P_{n,\text{sf}}$  is the production rate in neutrons  $\cdot (\text{g rock})^{-1} \cdot \text{a}^{-1}$ ;

$C_U$  is the concentration of U in parts per million (Fabryka-Martin (1988) [382]).

The production by alpha-n reactions is shown by:

$$P_{n,\alpha} = \frac{\sum_i S_i C_i Y_n^U + \sum_i S_i C_i Y_n^{\text{Th}}}{\sum_i S_i C_i} \quad (6.4)$$

where

$P_{n,\alpha}$  is the production rate in neutrons  $\cdot (\text{g rock})^{-1} \cdot \text{a}^{-1}$ ;

$S_i$  is the mass stopping power of element  $i$  for  $\alpha$  particles of a given energy in  $\text{MeV} \cdot \text{cm}^2 \cdot \text{g}^{-1}$ ;

$C_i$  is the concentration of element  $i$  in parts per million;

$Y_n^U$  and  $Y_n^{\text{Th}}$  are the neutron yields of element  $i$  per parts per million of U or Th in secular equilibrium with their daughters (Fabryka-Martin (1988) [382]; Feige et al. (1968) [381]).

Values for these constants are given in Table 6.2.

When neutrons are emitted by the reactions described above, they are at energies well above the thermal level dictated by the ambient temperature ( $<0.5$  eV). They are slowed and lose energy principally by collision with light atomic nuclei. During this energy moderation process, some of the neutrons may be absorbed by nuclei they encounter. The equilibrium neutron flux (neutrons  $\cdot \text{cm}^{-2} \cdot \text{a}^{-1}$ ) is provided by a balance between the neutron production rate and the rates of absorption in the thermal energy range and the epithermal energy range just above the thermal level:

TABLE 6.2. VALUES FOR PARAMETERS USED IN CALCULATING  $^{36}\text{Cl}$  PRODUCTION BY NEUTRON FLUX IN THE SUBSURFACE (from Fabryka-Martin (1988) [382])

Element	$S_i$	$Y_n^U$	$Y_n^{\text{Th}}$	$\sigma_{\text{th},i}$	$I_{a,i}$	$\sigma_{\text{sc},i}$	$A_i$	$\xi_i$
	Mass stop- ping power ( $\text{MeV} \cdot \text{cm}^2 \cdot \text{g}^{-1}$ )	Neutron yield (n per ppm U)	Neutron yield (n per ppm Th)	Thermal n abs. cross-section ( $10^{-24} \text{ cm}^2/\text{atom}$ )	Dilute resonance integral ( $10^{-24} \text{ cm}^2/\text{atom}$ )	Neutron scattering cross-section ( $10^{-24} \text{ cm}^2/\text{atom}$ )	Atomic weight (g/mol)	Energy loss per collision (unitless)
H	1542			0.33	0	20.5	1.0	1.000
Li	548	21.1	9.6	70.5	0	0.95	6.9	0.264
Be	529	265	91.2					
B	527	62.3	19.2	767	343	4.27	10.8	0.174
C	573	0.45	0.18	0.0034	0.0016	4.74	12.0	0.158
O	527	0.23	0.079	0.0002	0.0002	3.76	16.0	0.12
F	472	30.8	11.8					
Na	456	14.5	6.8	0.53	0.311	3.025	23.0	0.084
Mg	461	5.8	2.6	0.063	0.038	3.42	24.3	0.08
Al	444	5.1	2.6	0.23	0.17	1.41	27.0	0.072
Si	454	0.69	0.335	0.17	0.082	2.04	28.1	0.07
Cl	420			33.5	13.7	15.8	35.45	0.055
P	433	0	0	0.165	0.079	3.13	31.0	0.063
S	439	0	0					
K	414	0.45	0.305	2.15	1.00	2.04	39.1	0.05
Ca	428	0	0	0.43	0.235	2.93	40.1	0.049
Ti	375	0	0	6.1	3.1	4.09	47.9	0.041
Cr				3.1	1.6	3.38	52.0	0.038
Mn	353			13.3	13.4	2.20	54.9	0.036
Fe	351	0.19	0.205	2.56	1.39	11.35	55.8	0.035
Sm				9640	1400	38	150.4	0.013
Gd				41 560	390	172	157.3	0.013
UO <sub>2</sub>	74.7	0.077	0.027					

$$\Phi_n = \frac{p(E_{th})}{\sigma_m} P_{n,total} + \frac{(1-p(E_{th}))}{I_{eff}} P_{n,total} \quad (6.5)$$

where

- $P_{n,total}$  is equal to the sum of  $P_{n,sf}$  and  $P_{n,\alpha}$ ;
- $p(E_{th})$  is the probability that a neutron will escape the epithermal energy range without being absorbed, called the resonance escape probability (unitless);
- $\sigma_m$  is the macroscopic thermal neutron absorption cross-section (cm<sup>2</sup>/g);
- $I_{eff}$  is the effective dilute resonance integral (cm<sup>2</sup>/g) (Fabryka-Martin (1988) [382]).

The first term on the right hand side of Eq. (6.5) is the thermal neutron flux and the second term is the epithermal neutron flux. The macroscopic thermal neutron absorption cross-section and the effective dilute resonance integrals are equivalent to the total absorption cross-sections of all of the elements in the rock and pore fluid in the thermal and epithermal energy ranges, respectively, and are shown by:

$$\sigma_m = \sum_i N_i \sigma_{th,i} \quad (6.6)$$

$$I_{eff} = \sum_i N_i I_{a,i} \quad (6.7)$$

where

- $N_i$  is the concentration of element  $i$  in atoms<sup>-1</sup>;
- $\sigma_{th,i}$  is the thermal neutron absorption cross-section of element  $i$  (cm<sup>2</sup>);
- $I_{a,i}$  is the dilute resonance integral for element  $i$ .

The elemental concentrations are referenced per gram of rock plus pore fluid and the summations should include concentrations in the pore fluid as well as rock.

The resonance escape probability is found by:

$$p(E_{th}) = \exp \frac{-I_{eff}}{\sum_i \xi_i N_i \sigma_{sc,i}} \quad (6.8)$$

where

- $\sigma_{sc,i}$  is the neutron scattering cross-section for element  $i$ ;
- $\xi_i$  is the average log decrement of energy loss per collision with an atom of element  $i$ .

For hydrogen,  $\xi_i$  is equal to 1.0 and for heavier elements it is a function of the atomic number,  $A$ :

$$\xi_i = \frac{2}{A_i + 0.667} \quad (6.9)$$

Values for  $\sigma_{th,i}$ ,  $\sigma_{sc,i}$ ,  $I_{a,i}$ ,  $A_i$  and  $\xi_i$  are provided in Table 6.2.

Given the fluxes as calculated above, the production rate for <sup>36</sup>Cl in the pore water (atoms <sup>36</sup>Cl in pore water · (g aquifer)<sup>-1</sup> · a<sup>-1</sup>) is then simply the product of the neutron fluxes at the two energy levels and the cross-sections for the reactions yielding <sup>36</sup>Cl at those energies:

$$P_{36,pw} = \frac{N_{35,pw} \sigma_{35}}{\sigma_m} p(E_{th}) P_{n,total} + \frac{N_{35,pw} I_{a,35}}{I_{eff}} (1-p(E_{th})) P_{n,total} \quad (6.10)$$

where

- $N_{35,pw}$  is the concentration of <sup>35</sup>Cl in the pore water (atoms <sup>35</sup>Cl in pore water · (g aquifer)<sup>-1</sup>);

- $\sigma_{35}$  is the cross-section for the reaction  $^{35}\text{Cl}(n, \gamma)^{36}\text{Cl}$  in the thermal energy range, equal to  $(43.6 \pm 0.4) \times 10^{-24}$  cm<sup>2</sup>/atom;
- $I_{a,35}$  is the dilute resonance integral for the same reaction in the epithermal energy range, equal to  $(18 \pm 2) \times 10^{-24}$  cm<sup>2</sup>/atom (Fabryka-Martin (1988) [382]).

For the purpose of estimating the age of old groundwater, the quantities of interest are usually the secular equilibrium  $^{36}\text{Cl}$  concentration (atoms  $^{36}\text{Cl} \cdot (\text{L pore water})^{-1}$ ) and the secular equilibrium  $^{36}\text{Cl}/\text{Cl}$  ratio in the pore water (unitless):

$$C_{36,se} = \frac{P_{36,pw}}{\lambda_{36}} \left( \frac{\rho_B + n_e \rho_{sol}}{n_e} \right) 10^3 \quad (6.11)$$

$$R_{36,se} = \frac{P_{36,pw} A_{n,Cl}}{C_{Cl} \lambda_{36} A_v} \left( \frac{\rho_B + n_e \rho_{sol}}{n_e} \right) 10^6 \quad (6.12)$$

where

- $\lambda_{36}$  is the decay constant of  $^{36}\text{Cl}$  ( $2.303 \times 10^{-6}/\text{a}$ );
- $\rho_b$  is the dry bulk density of the aquifer (g/cm<sup>3</sup>);
- $C_{Cl}$  is the concentration of  $\text{Cl}^-$  in the pore water (mg/L);
- $\rho_{pw}$  is the density of the pore water solution (g/cm<sup>3</sup>);
- $n_e$  is the effective porosity (unitless);
- $A_{n,Cl}$  is the atomic mass of natural Cl (35.4527 g/mol);
- $A_v$  is Avogadro's number ( $6.023 \times 10^{23}$  atoms/mol).

It should be noted that, strictly, the 'secular equilibrium' concentration or ratio refers to the theoretical value of these quantities for a chloride solution in contact with a specific rock over a very long period (>2 Ma). Actual groundwater may move through formations of varying chemistry or porosity, or change Cl concentration with time, and thus not achieve true equilibrium with the rock.

Typical values for  $R_{36,se}$  range from  $<1 \times 10^{-15}$  in ultramafic rocks to  $\sim 50 \times 10^{-15}$  in granites or rhyolites (Bentley et al. (1986) [310]; Fabryka-Martin (1988) [382]; Lehmann et al. (1993) [250]; Phillips (2000) [306]). Lithologies having exceptionally high concentrations of U and Th can support ratios as large as  $10^{-10}$ , but these are rarely encountered (Fabryka-Martin (1988) [382]). Phillips (2000) [306] compared  $^{36}\text{Cl}$  secular equilibrium ratios measured on 56 water samples with the ratios calculated (by the authors of the papers) from chemical analyses of the host rocks. The average bias of the calculated ratios relative to the measured ones was <3% and the average absolute error was 33%. This constitutes an acceptable level of accuracy and precision for most hydrological purposes.

#### 6.5.5.2. Subsurface systematics of $^{36}\text{Cl}$

As described above, the simplest and most straightforward applications of  $^{36}\text{Cl}$  dating are to aquifers recharging in the continental interior and permeable enough that subsurface sources of  $\text{Cl}^-$  have been flushed away. In this case,  $^{36}\text{Cl}$  model age as a function of flow distance can be obtained by application of the radioactive decay equation to the measured distribution of  $^{36}\text{Cl}/\text{Cl}$  ratios. Figure 6.6 shows an example of this simple type of behaviour from the Nubian sandstone aquifer of north Africa (Patterson et al. (2005) [43]). Here, one set of samples (in blue) follows a clearly defined decay line between the initial recharge value and the subsurface secular equilibrium value. A second set (in red) has a more complicated history, evidently originating from a more evaporated recharge source and in some cases showing evidence of subsurface  $\text{Cl}^-$  addition. Nevertheless, both sets can be at least approximately dated by their positions down their respective decay lines.

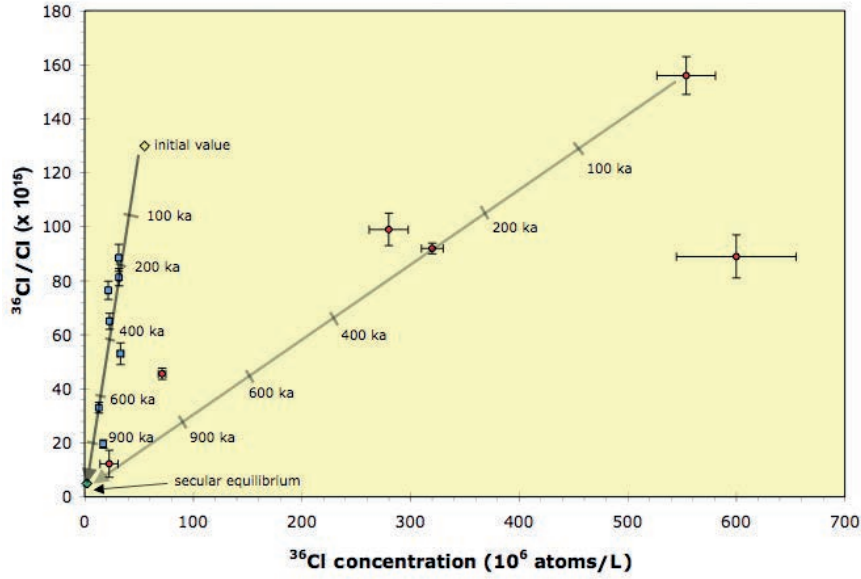


FIG. 6.6. Variation in  $^{36}\text{Cl}/\text{Cl}$  and the  $^{36}\text{Cl}$  concentration down two flow paths in the Nubian sandstone aquifer of north Africa (Patterson et al. (2005) [43]).

In many cases, however, significant increases or fluctuations in Cl concentration, often accompanied by corresponding variations in the  $^{36}\text{Cl}$  concentration or ratio are encountered. The most important processes affecting  $^{36}\text{Cl}$  in the subsurface are radioactive decay, hypogene production (discussed above), mixing with other subsurface water, and the addition of  $\text{Cl}^-$  from evaporite dissolution. The basic equations for evaluating these systematics were laid out by Bentley et al. (1986) [301] and Phillips et al. (1986) [319] (see also Michelot (1988) [383]). They are based on the simultaneous interpretation of the  $^{36}\text{Cl}$  concentration, the  $^{36}\text{Cl}/\text{Cl}$  ratio and the Cl concentration. If the systematics of Cl variation can be reliably inferred, the simple mixing/decay equations from these sources can be employed to calculate  $^{36}\text{Cl}$  model ages. Even if unambiguous arguments for one mechanism cannot be asserted, it is often possible to calculate  $^{36}\text{Cl}$  model ages based on alternative hypotheses and, thus, provide useful bounds on the possible range of groundwater ages (Phillips (2000) [306]). Although more sophisticated numerical models can yield a detailed understanding of  $^{36}\text{Cl}$  systematics in specific situations (e.g. Park et al. (2002) [90]), these fundamental equations still provide a sound basis at least for initial interpretations.

A mass balance of  $^{36}\text{Cl}$  in the subsurface can be expressed as follows:

$$C_{36} = R_{\text{meas}} C_{\text{meas}} = R_{36,\text{re}} C_{\text{re}} \exp(-\lambda_{36} t) + ((1-f)R_{36,\text{se1}} + fR_{36,\text{se2}}) C_{\text{re}} (1 - \exp(-\lambda_{36} t)) + R_{36,\text{se2}} (C_{\text{meas}} - C_{\text{re}}) \quad (6.13)$$

where

$C_{36}$  is the  $^{36}\text{Cl}$  concentration (atoms  $^{36}\text{Cl}/\text{L}$ );

$R_{36,\text{re}}$  is the recharge  $^{36}\text{Cl}/\text{Cl}$  ratio;

$C_{\text{re}}$  is the recharge  $\text{Cl}^-$  concentration (atoms  $\text{Cl}^-/\text{L}$ );

$R_{36,\text{se1}}$  is the secular equilibrium  $^{36}\text{Cl}/\text{Cl}$  ratio in the aquifer;

$R_{36,\text{se2}}$  is the secular equilibrium  $^{36}\text{Cl}/\text{Cl}$  ratio in some source of  $\text{Cl}^-$  (such as a brine, an evaporite, diffusion out of an aquitard) being added to the system;

$C_{\text{meas}}$  is the measured  $\text{Cl}^-$  concentration of the sample (atoms/L);

$R_{\text{meas}}$  is the measured  $^{36}\text{Cl}/\text{Cl}$  ratio of the sample and  $f = (dC/dt)(\lambda C_{\text{re}})$  is a term that accounts for the rate of addition of aquifer external subsurface Cl to the sample.

$R_{36,se2}$  may or may not be the same as  $R_{36,se1}$ . If  $R_{36,se1}$  is the same as  $R_{36,se2}$ , the solution of Eq. (6.13) is:

$$t = \frac{-1}{\lambda_{36}} \ln \frac{C_{meas} (R_{36,meas} - R_{36,se})}{C_{re} (R_{36,re} - R_{36,se})} \quad (6.14)$$

There are several circumstances that allow simplification of this formulation. One is that the  $Cl^-$  being added originates from dissolution of bedded halite. In this case,  $R_{se}$  equals zero (Fabryka-Martin et al. (1987) [384]; Phillips (2000) [306]), no additional  $^{36}Cl$  is added, and Eq. (6.14) reduces to:

$$t = \frac{-1}{\lambda_{36}} \ln \frac{C_{meas} R_{36,meas}}{C_{re} R_{36,re}} \quad (6.15)$$

Alternatively, variations in the concentration of  $^{36}Cl$  and  $Cl^-$  down the flow path may arise from temporal variations in the amount of evapotranspiration during recharge, or from subsurface enrichment due to ion filtration. In either case, the  $^{36}Cl$  and  $Cl^-$  are concentrated equally, the  $^{36}Cl/Cl^-$  ratio does not change and Eq. (6.13) becomes:

$$t = \frac{-1}{\lambda_{36}} \ln \frac{R_{36,meas} - R_{36,se}}{R_{36,re} - R_{36,se}} \quad (6.16)$$

Equation (6.16) also applies when there is no change in the  $Cl^-$  concentration. Finally, there is the case where the  $Cl^-$  concentration increases due to diffusion of, or mixing with, brine that has a secular equilibrium  $^{36}Cl/Cl^-$  different from that of the aquifer itself (i.e.  $R_{36,se1} \neq R_{36,se2}$ ). In this case, the solution is:

$$t = \frac{-1}{\lambda_{36}} \ln \frac{C_{re} (R_{36,se2} - R_{36,se1}) + C_{meas} (R_{36,meas} - R_{36,se2})}{C_{re} (R_{36,re} - R_{36,se1})} \quad (6.17)$$

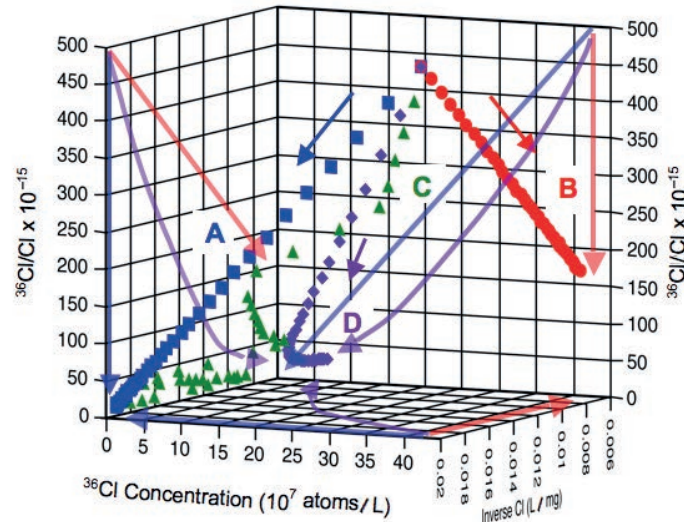


FIG. 6.7. Hypothetical evolution of  $^{36}Cl$  and  $Cl^-$  down four flow paths having a common initial composition, which is  $Cl^- = 50 \text{ mg/L}$ ,  $^{36}Cl/Cl^- = 500 \times 10^{-15}$  and  $^{36}Cl$  concentration =  $4.25 \times 10^8 \text{ atoms/L}$ . The aquifer is assumed to have a secular equilibrium of  $^{36}Cl/Cl^-$  of  $10 \times 10^{-15}$ . Arrows indicate the direction of the evolution. For all flow paths except B, the symbols are spaced at 50 ka intervals. Case A is simple decay towards  $R_{36,se}$ . Case B is dilution by 'dead'  $Cl^-$  without ageing. Case C is variable evapotranspiration during recharge. Case D is the addition of  $Cl^-$  due to diffusion out of an aquitard having  $R_{36,se}$  of  $50 \times 10^{-15}$ . Colour keyed translucent arrows show the corresponding evolution paths in the two dimensional bounding planes.

Figure 6.7 illustrates four different evolutionary paths for water having a common initial composition, which is  $\text{Cl}^- = 50 \text{ mg/L}$ ,  $^{36}\text{Cl}/\text{Cl} = 500 \times 10^{-15}$  and  $^{36}\text{Cl}$  concentration =  $4.25 \times 10^8$  atoms/L (this is equivalent to the closest vertex of the cube formed by the three coordinates in Fig. 6.7). The aquifer is assumed to have a secular equilibrium  $^{36}\text{Cl}/\text{Cl}$  of  $10 \times 10^{-15}$ . Case A is simply constant recharge conditions and radiodecay down the flow path. The evolution is modelled over 2 Ma and the points are at 50 ka intervals (this is the same for all cases except B). Case A shows the linear correlation of  $C_{36,\text{meas}}$  and  $R_{36,\text{meas}}$ , together with invariant  $\text{Cl}^-$ , that is characteristic of simple decay in a closed system. Case B illustrates a situation in which the flow is so fast that  $^{36}\text{Cl}$  decay is negligible but  $\text{Cl}^-$  progressively increases due to dissolution of halite ( $R_{36,\text{se}} = 0$ ). The decrease in the  $^{36}\text{Cl}/\text{Cl}$  ratio down the flow path may give the appearance of decay, but the invariant  $^{36}\text{Cl}$  concentration and linear relation with inverse  $\text{Cl}^-$  identifies this path as merely dilution by ‘dead’  $\text{Cl}^-$ . Case C features variable  $\text{Cl}^-$  concentrations, ranging between 50 and 100 mg/L, and observed down the flow path due to climate driven changes in evapotranspirative concentration in the recharge area. The characteristic signature of this process is correlated changes in  $\text{Cl}^-$  and  $^{36}\text{Cl}$  concentration (the snaky path followed by the dots in the figure), but a relatively smooth decrease in  $^{36}\text{Cl}/\text{Cl}$  with flow distance. Instead of following Case B in a linear pattern to the right (low inverse  $\text{Cl}^-$ ), the data points lie in the same plane as Cases A and D. Finally, Case D is similar to Case A, except that  $\text{Cl}^-$  concentration increases steadily down the flow path to 150 mg/L due to the diffusion of  $\text{Cl}^-$  having a  $^{36}\text{Cl}/\text{Cl}$  of  $50 \times 10^{-15}$  out of a bounding shale. Here, instead of the linear pattern produced by simple decay, the various measures of concentration show a pronounced curvature ‘hooking’ to the right (i.e. towards low inverse  $\text{Cl}^-$ ). Figure 6.7 illustrates how differing histories produce characteristic and distinctive patterns that can be used to diagnose the appropriate approach to estimating groundwater age.

### 6.5.5.3. Examples of subsurface systematics

Three examples of  $^{36}\text{Cl}$  systematics are provided in Fig. 6.8. The first (Fig. 6.8(a)) is from the Nubian sandstone aquifer (Patterson et al. (2005) [43]). As noted above, the  $^{36}\text{Cl}$  systematics of this aquifer are very simple, having a relatively high meteoric input and simple decay without significant subsurface addition of  $\text{Cl}$  or  $^{36}\text{Cl}$ . In Fig. 6.8, the  $^{36}\text{Cl}$  evolution exhibits a linear trend sloping diagonally downwards towards low  $^{36}\text{Cl}$  concentration and low  $^{36}\text{Cl}/\text{Cl}$ . This is similar to the trend of line ‘A’ in Fig. 6.7, for simple  $^{36}\text{Cl}$  decay.

The data points from the Milk River aquifer (Nolte et al. (1991) [291]; Phillips et al. (1986) [319]) differ from the Nubian sandstone in that they start at a lower inverse  $\text{Cl}$  concentration and form a trend that curves towards higher  $1/\text{Cl}$  as the  $^{36}\text{Cl}$  concentration and  $^{36}\text{Cl}/\text{Cl}$  ratio decrease. Figure 6.8(b) is expanded from Fig. 6.8(a) in order to illustrate this trend in more detail for the distal flow path, but it leaves out the samples from the proximal portion of the flow path. This curved trajectory is similar to that of line ‘D’ in Fig. 6.7. Line ‘D’ modelled an increase of  $\text{Cl}$  concentration in the aquifer due to diffusion of  $\text{Cl}$  out of bounding aquitards. The same mechanism is believed to be operative in the Milk River aquifer (Fabryka-Martin et al. (1991) [385]; Nolte et al. (1991) [291]).

The third data set in Fig. 6.8(a) is from the Tokachi Basin in Japan (Mahara et al. (2007) [344]). This trend first shows a decrease in  $^{36}\text{Cl}/\text{Cl}$  accompanied by an increase in  $\text{Cl}$  (decrease in  $1/\text{Cl}$ ), but without a significant decrease in the  $^{36}\text{Cl}$  concentration. After the samples reach an inverse  $\text{Cl} < 0.05 \text{ L/mg}$  ( $\text{Cl}$  concentration  $> 20 \text{ mg/L}$ ), they ‘turn the corner’ and the  $^{36}\text{Cl}$  concentration increases along with  $\text{Cl}$  concentration, but the  $^{36}\text{Cl}/\text{Cl}$  remains relatively constant. This pattern is unusual. The trend in the first part of the flow path is indicative of decay of meteoric  $^{36}\text{Cl}/\text{Cl}$  accompanied by increasing  $\text{Cl}$ . Once the  $^{36}\text{Cl}/\text{Cl}$  approaches secular equilibrium, it stabilizes but the  $\text{Cl}$  and  $^{36}\text{Cl}$  increase. The stable  $^{36}\text{Cl}/\text{Cl}$  is maintained by the  $\text{Cl}$  and  $^{36}\text{Cl}$  increasing at the same rate. Mahara et al. (2007) [344] attribute this pattern to progressive solute concentration increase driven by ion filtration (reverse osmosis) and the trend shown in Fig. 6.8 is consistent with this explanation. However, the trend also resembles that of case ‘D’ in Fig. 6.7 (subsurface  $\text{Cl}$  addition) with an extended ‘tail’. Inferences drawn from

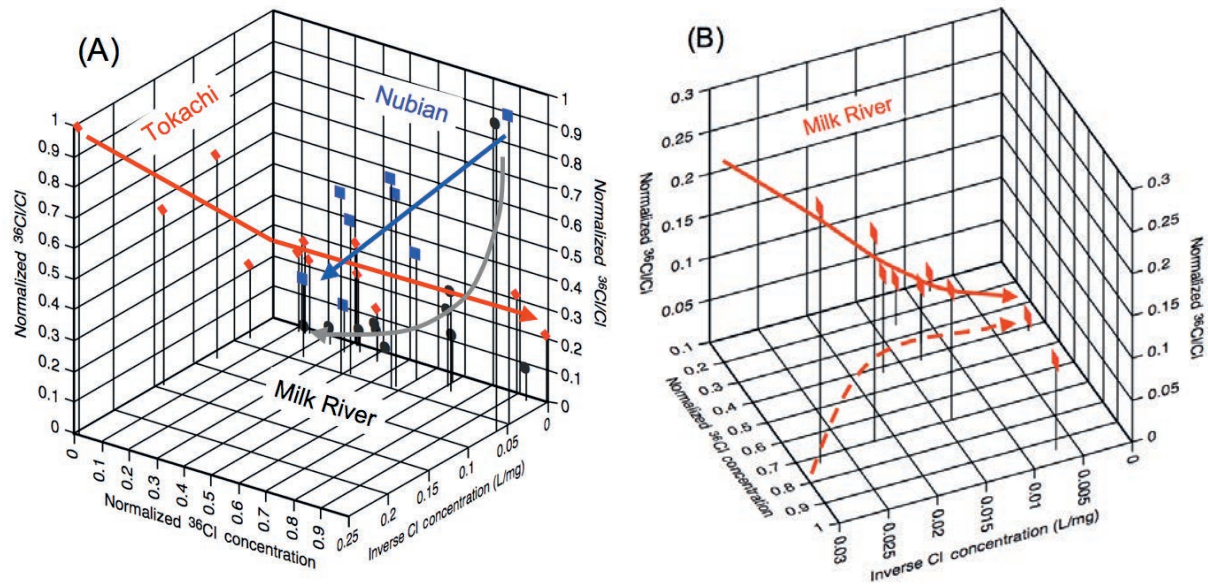


FIG. 6.8. Examples of  $^{36}\text{Cl}$  systematics. (a) Trends of  $^{36}\text{Cl}/\text{Cl}$ ,  $^{36}\text{Cl}$  concentration and inverse Cl concentration in the Nubian sandstone aquifer (blue points; Patterson et al. (2005) [43]), the 'eastern flow path' on the Milk River aquifer (grey points; Nolte et al. (1991) [291]; Phillips et al. (1986) [319]), and the Tokachi Basin of Japan (red points; Mahara et al. (2007) [344]). The  $^{36}\text{Cl}$  concentration and  $^{36}\text{Cl}/\text{Cl}$  data have been normalized by dividing by the highest values in each data set in order to facilitate plotting on a single graph. (b) Expansion of (a) to more clearly illustrate trends in the Milk River aquifer. The dashed line shows the trend projected onto the  $^{36}\text{Cl}$  concentration–inverse Cl plane.

additional environmental tracers might be useful to distinguish these possibilities, and this topic is discussed below.

A fourth example of subsurface  $^{36}\text{Cl}$  systematics may be adduced from the south-western portion of the Great Artesian Basin aquifer in Australia. This aquifer, originally studied by Love et al. (2000) [292], has been reassessed in detail by R. Purtschert in Section 5.5 of this book. The figures and discussion will, therefore, not be reproduced here. The data from this study area are particularly informative because, as in the Nubian sandstone aquifer system, results from the independent  $^{81}\text{Kr}$  method are also available for comparison. This comparison reveals considerable complications in the subsurface systematics of the  $^{36}\text{Cl}$ .

One notable characteristic of this aquifer is the very high chloride concentrations, ranging from  $>500$  to  $3000$  mg/L. These are vastly above the Cl concentrations in precipitation, indicating that recharge water is evapotranspiratively concentrated by two to three orders of magnitude (Love et al. (2000) [292]). The aquifer is also bounded by a unit, the Bulldog Shale, that contains relatively large concentrations of Cl (up to  $18\,000$  mg/L) and sufficient concentrations of radioactive elements to raise the subsurface equilibrium ratio to about  $20 \times 10^{-15}$ , four times that in the aquifer. In spite of these complications, the distribution of the  $^{36}\text{Cl}/\text{Cl}$  ratio in the aquifer is a relatively regular function of flow distance (Figs 5.19 and 5.20), and, thus, creates the possibility that  $^{36}\text{Cl}$  might produce useful groundwater age estimates.

The comparison with the  $^{81}\text{Kr}$  results given in Chapter 5 shows that the relatively smooth decline of  $^{36}\text{Cl}/\text{Cl}$  ratios may be fortuitous. The measured Cl concentrations and  $^{36}\text{Cl}/\text{Cl}$  appear to be a result of markedly varying contributions by evapotranspirative concentration during recharge and diffusive input from the Bulldog Shale during flow, rendering very difficult the calculation of a useful  $^{36}\text{Cl}$  tracer age without independent quantification of at least one of these processes.

The results from the  $^{81}\text{Kr}$  comparison bear out the concerns of Love et al. (2000) [292], who warned that “The preceding discussion emphasizes that estimates of ‘absolute’ groundwater age using  $^{36}\text{Cl}$  data are subject to large uncertainties because of problems of estimating the initial concentration of  $^{36}\text{Cl}$ ... and correcting for sources or sinks of chloride...”. As emphasized above in this chapter,  $^{36}\text{Cl}$  dating is most likely to yield useful results when the Cl and  $^{36}\text{Cl}$  systematics are simple and the subsurface  $^{36}\text{Cl}$  is dominated by meteoric input. The south-western Great Artesian Basin offers strong support for this caution. The combination of extreme (and, therefore, potentially highly variable) evapotranspirative concentration and large subsurface sources of Cl and  $^{36}\text{Cl}$  warns of complications that are too large for reliable dating corrections. Potential users of the method should carefully evaluate their study areas for similar problems.

### 6.5.6. Use of other environmental tracers to interpret chloride systematics

As illustrated above, although the end member cases illustrated in Fig. 6.6 are clearly distinguishable, in some real world cases there may be multiple processes influencing  $^{36}\text{Cl}$  and Cl patterns, or there may be insufficient data to distinguish fully between alternative hypotheses. The past 20 years have seen a major advance in the development of additional tracers that can be examined in conjunction with the  $^{36}\text{Cl}$  and Cl patterns and that can provide independent constraints on chloride systematics.

Probably the simplest and most cost effective of these is measurement of the concentration of  $\text{Br}^-$  along with  $\text{Cl}^-$  (Davis et al. (1998) [296]; Davis et al. (2004) [386]; Whittemore (1995) [387]). Most meteoric waters over the continents have a Cl/Br (mass:mass) value lower than that of sea water, which is 290. This is because during the formation of marine aerosols, Br is preferentially fractionated into the smaller particles which persist longer in the atmosphere and are, thus, more readily transported towards the continental interiors (Davis et al. (2004) [386]). Cl/Br ratios between 50 and 150 are characteristic of continental interiors.

In contrast, solutions originating from dissolution of marine evaporites or from connate fluids tend to have ratios of between 300 and 1000 (Whittemore (1995) [387]). Such solutions start at the marine

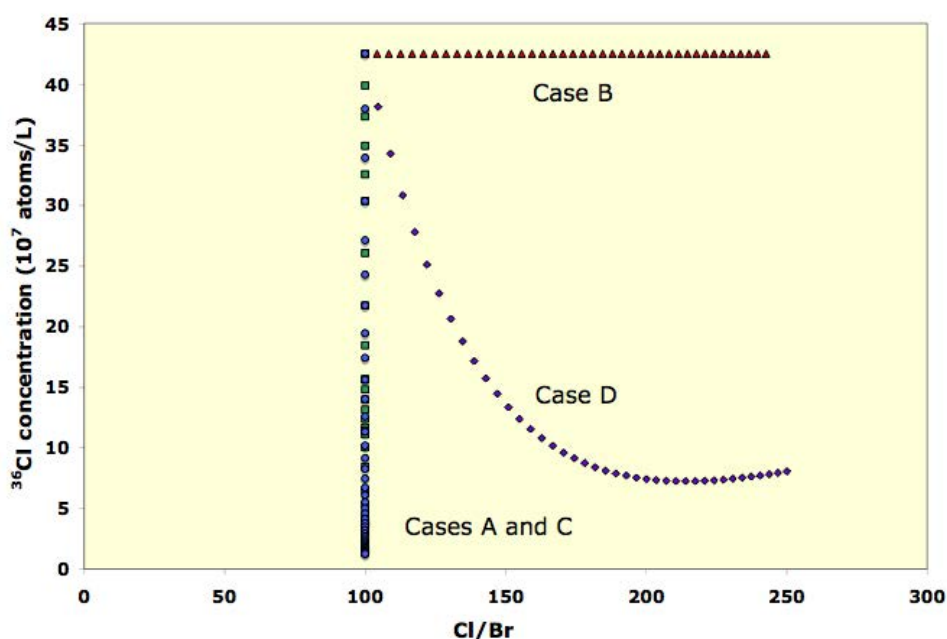


FIG. 6.9. The evolution of the  $^{36}\text{Cl}$  concentration and the Cl/Br ratio for the same hypothetical cases as in Fig. 6.7.

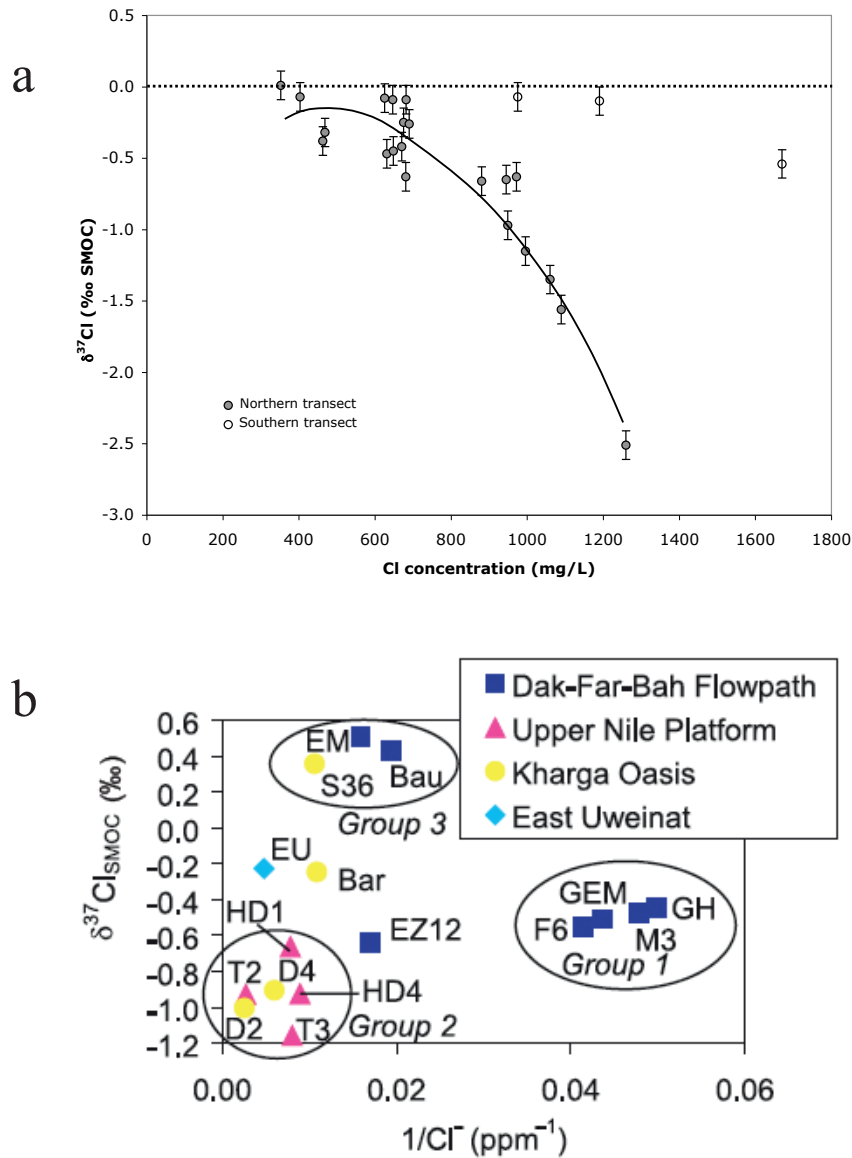


FIG. 6.10. (a) Relation between  $\delta^{37}\text{Cl}$  and the Cl concentration in groundwater from the Great Artesian Basin of Australia (Zhang et al. (2007) [304]); (b) relation between  $\delta^{37}\text{Cl}$  and  $1/\text{Cl}$  in the Nubian aquifer of north Africa (Patterson et al. (2005) [43]).

ratio of 290 and, inasmuch as Br is excluded during the precipitation of halite, can have ratios of up to several thousand. These characteristics are convenient for the differentiation of Cl sources, since recharge water will generally possess a low Cl/Br value and subsurface sources of Cl will have high Cl/Br values. Figure 6.9 illustrates the use of Cl/Br to distinguish sources of Cl in the scenarios illustrated in Fig. 6.6. The recharge water is assumed to have a Cl/Br ratio of 100 and the subsurface source a ratio of 1000. The cases in which subsurface Cl is added show an evolution to the right of the graph whereas those where changes in Cl are not subsurface related only evolve in the vertical.

The stable isotope composition of the Cl is another environmental tracer that is integral to the halides and can help elucidate the origins of Cl within aquifer systems (Rao et al. (2005) [388]; Stewart and Spivack (2004) [389]; Whittemore (1995) [387]). The  $\delta^{37}\text{Cl}$  of the ocean and of marine evaporites has apparently been within  $\pm 0.5\%$  of  $0\%$  throughout the Phanerozoic (Eastoe et al. (2007) [390]). However, the  $\delta^{37}\text{Cl}$  of  $\text{Cl}^-$  in pore fluids of shales seems to range between  $-1$  and  $-2\%$  (Zhang et al. (2007) [304]) and addition of Cl from this source is probably responsible for the generally negative

(~0 to -2‰) values often found in sedimentary basin waters (Weaver (2000) [391]). In contrast, marine aerosols usually have positive  $\delta^{37}\text{Cl}$ , varying between +0.5 and +2.5‰ (Volpe and Spivack (1994) [392]). This difference in atmospheric and subsurface isotopic signatures can help to fingerprint the origin of  $\text{Cl}^-$  in water being dated with  $^{36}\text{Cl}$ .

Figure 6.10 relates  $\text{Cl}^-$  and  $\delta^{37}\text{Cl}$  in two systems: the Great Artesian Basin (Zhang et al. (2007) [304]) and the Nubian aquifer (Patterson et al. (2005) [43]). The Great Artesian Basin data show a clear trend of decreasing  $\delta^{37}\text{Cl}$  with increasing  $\text{Cl}^-$  concentration. Direct measurement of  $\text{Cl}^-$  in pore water from bounding shale units confirmed that diffusion of  $\text{Cl}^-$  out of the shale was the likely source of the increased  $\text{Cl}^-$  with flow distance in this aquifer. However, three samples show increased  $\text{Cl}^-$  with relatively constant  $\delta^{37}\text{Cl}$ . These are from a distinct portion of the basin and the likelihood that this  $\text{Cl}^-$  increase is due to recharge area evaporation is supported by independent evidence.

The data from the Nubian aquifer (Patterson et al. (2005) [43]) exhibit a more complex pattern. The spacing of wells in the Western Desert of Egypt is irregular and does not permit as comprehensive a view of the spatial distribution of water quality. However, the  $\delta^{37}\text{Cl}$  clearly aids in distinguishing different groups of waters characterized by differing  $\text{Cl}^-$  concentrations and, thus, aids in interpreting  $^{36}\text{Cl}$  data.

In summary, even though Cl has unusually simple geochemistry, the evolution of the  $^{36}\text{Cl}$  concentration and the  $^{36}\text{Cl}/\text{Cl}$  ratio down flow paths can still exhibit considerable complexity that reflects the heterogeneity of water sources and transport mechanisms in the subsurface. These trends have generally been thought of as requiring ‘correction’ of the calculated  $^{36}\text{Cl}$  model ages, but are perhaps better considered as hallmarks of the water history. For example, diffusion of low  $^{36}\text{Cl}/\text{Cl}$  chloride out of an aquitard into an aquifer is also indicative of diffusion of ‘old’ water molecules out of the aquitard, and correspondingly, diffusion of ‘young’ aquifer water into the aquitard. Variable  $^{36}\text{Cl}$  ratios due to variable evapotranspiration during recharge probably also indicate variations in the recharge rate, and hence groundwater velocity. As noted in Chapter 1, the interpretation of age tracer data is most valuable when it is comprehensive, in other words, when a large number of different tracers can be interpreted within a reasonably well defined hydrogeological framework and be reconciled with a single, coherent history and set of processes. This chapter has focused on the calculation of single valued  $^{36}\text{Cl}$  tracer ages, but integrating the  $^{36}\text{Cl}$  patterns into a more comprehensive data set may permit estimation of actual frequency distribution of groundwater age.

A significant amount of recent research has explored the use of additional environmental tracers to yield information on halide systematics. Examples include  $^{129}\text{I}$  (Fabryka-Martin et al. (1991) [385]; Snyder and Fabryka-Martin (2007) [393]), the  $\text{Cl}/\text{Br}$  ratio (Davis et al. (2000) [394]; Hurwitz et al. (2005) [395]; Metcalfe et al. (2007) [396]; Rao et al. (2005) [388]),  $\delta^{37}\text{Cl}$  (Lehmann et al. (2003) [256]; Zhang et al. (2007) [304]) and  $^4\text{He}$  (Kulongoski et al. (2008) [343]; Mahara et al. (2007) [344]; Patterson et al. (2005) [43]). The application of one or several of these tracers, all associated with the systematics of Cl or  $^{36}\text{Cl}$  in some way, can greatly help to constrain sources of Cl and  $^{36}\text{Cl}$  or to explain variations in their distributions.

## 6.6. COMPARISON OF $^{36}\text{Cl}$ WITH OTHER METHODS OF DATING

As discussed in the introduction to this book, interpretation of age dating tracers is most informative when multiple methods can be compared. In this section, the patterns of  $^{36}\text{Cl}$  are compared with those of other tracers in several aquifer systems.

### 6.6.1. Comparison with radiocarbon

Unfortunately, the useful range of  $^{36}\text{Cl}$  in groundwater does not overlap with that of radiocarbon. The decay of  $^{36}\text{Cl}$  is still small when  $^{14}\text{C}$  has decayed beyond the limit of practical application. This is

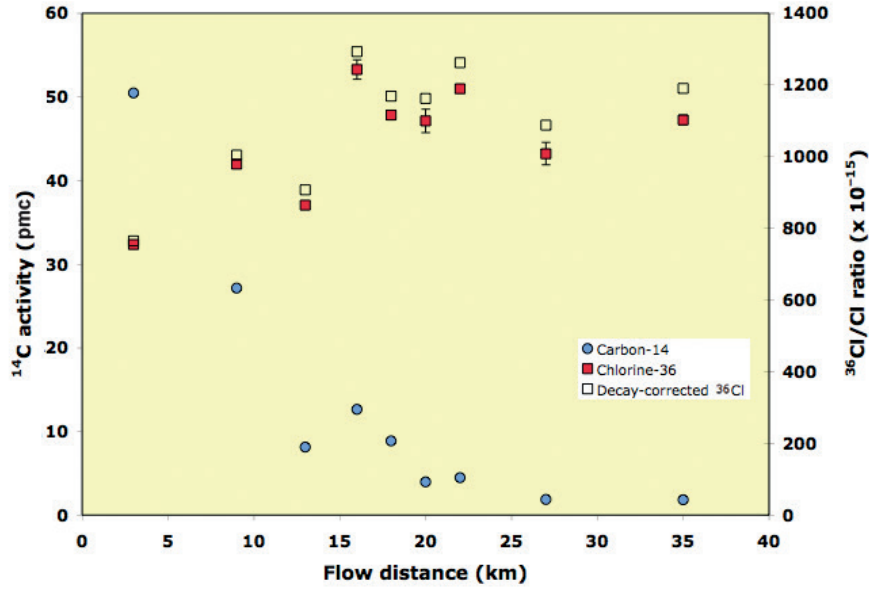


FIG. 6.11. Variation of  $^{14}\text{C}$  activity and  $^{36}\text{Cl}/\text{Cl}$  with flow distance in the Ojo Alamo and Nacimiento aquifers of the San Juan Basin, south-western USA. Data are from Phillips (2000) [306], Plummer (1996) [356] and Stute et al. (1995) [213]. The open squares are  $^{36}\text{Cl}/\text{Cl}$  corrected for radioactive decay using the inferred  $^{14}\text{C}$  model age.

illustrated in Fig. 6.11, where radiocarbon and  $^{36}\text{Cl}$  are compared in the Ojo Alamo and Nacimiento aquifers of the San Juan Basin, south-western USA (Phillips (2000) [306]; Plummer (1996) [356]; Stute et al. (1995) [213]). The  $^{14}\text{C}$  activity exhibits a quasi-exponential decrease with flow distance, as expected. By ~30 km, the activity is too low to yield useful groundwater age estimates. As predicted, the  $^{36}\text{Cl}/\text{Cl}$  is approximately constant over this interval. The open squares in Fig. 6.11 show the  $^{36}\text{Cl}/\text{Cl}$  corrected for decay using the radiocarbon model age. Given the observed variability in the  $^{36}\text{Cl}/\text{Cl}$ , this decay is too small to be useful for groundwater age estimation. The pattern of lower Holocene  $^{36}\text{Cl}/\text{Cl}$  compared with the late Pleistocene is due to secular variation of the  $^{36}\text{Cl}$  production, modulated by the dipole geomagnetic field strength.

### 6.6.2. Comparison with $^4\text{He}$

Only a few age tracers significantly overlap with  $^{36}\text{Cl}$ . One of the best is  $^4\text{He}$  accumulation. Figure 6.12 compares  $^4\text{He}$  accumulation,  $^{36}\text{Cl}$  and  $^{14}\text{C}$  along the ‘eastern flow path’ in the Milk River aquifer (Drimmie et al. (1991) [168]; Nolte et al. (1991) [291]; Phillips et al. (1986) [319]). The  $^{14}\text{C}$  adds little information, but is consistent with the other tracers. The first sample on the flow path contains about 10 pmc and the rest negligible  $^{14}\text{C}$ .

The  $^{36}\text{Cl}$  shows a quasi-exponential decay with flow distance. In Fig. 6.12, this profile has been fitted using the following equation:

$$R_{36}(x) = R_{0,36} \exp\left(-\lambda_{36} \frac{x}{q_s}\right) \quad (6.18)$$

where

$R_{36}(x)$  is the  $^{36}\text{Cl}/\text{Cl}$  ratio as a function of flow distance;

$R_{0,36}$  is the initial  $^{36}\text{Cl}/\text{Cl}$  ratio;

$q_s$  is the seepage velocity of the groundwater.

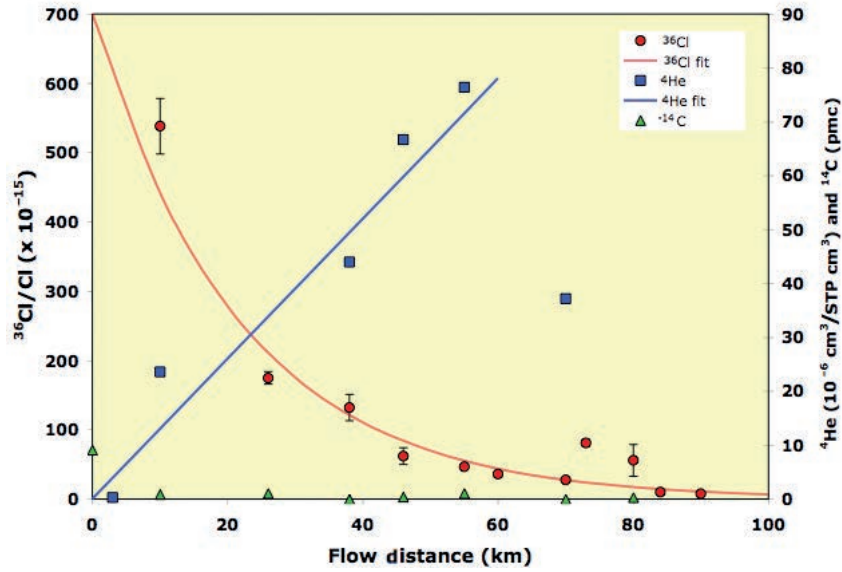


FIG. 6.12. Trends of  $^{36}\text{Cl}/\text{Cl}$ ,  $^4\text{He}$  and  $^{14}\text{C}$  with flow distance down the Milk River aquifer. Data are taken from Drimmie et al. (1991) [168], Nolte et al. (1991) [291] and Phillips et al. (1986) [319]. The red line illustrates the fit of an exponential decay model (Eq. (6.18)) to the  $^{36}\text{Cl}/\text{Cl}$  data and the blue line the fit of a linear accumulation model to the  $^4\text{He}$  model. Details are discussed in the text.

The fit illustrated employed  $R_{0,36} = 700 \times 10^{-15}$  and  $q_s = 5 \text{ cm/a}$ . This simplistic dating approach neglects subsurface addition of Cl and  $^{36}\text{Cl}$ , which is undoubtedly significant in this case (Nolte et al. (1991) [291]; Phillips (2000) [306]), but gives a first order idea of the behaviour of the system.

The good fit to this simple equation (Eq. (6.18)) indicates that flow velocity is approximately constant. If this is the case, and if  $^4\text{He}$  is introduced to the aquifer at a constant rate, then  $^4\text{He}$  should accumulate linearly with distance. Figure 6.12 shows that there is indeed a linear accumulation, with  $^4\text{He}$  increasing at the rate of  $1.3 \times 10^{-6} \text{ cm}^3 \text{ STP} \cdot \text{cm}^{-3}_{\text{H}_2\text{O}} \cdot \text{km}^{-1}$ . Assuming a seepage velocity of  $5 \text{ cm/a}$ , this is equivalent to a helium influx of  $6 \times 10^{-11} \text{ cm}^3 \text{ STP} \cdot \text{cm}^{-3}_{\text{H}_2\text{O}} \cdot \text{a}^{-1}$ . The calculated contribution rate of  $^4\text{He}$  from the rock matrix is approximately one order less than this value, if all the  $^4\text{He}$  produced is assumed to diffuse into the pore water (Andrews et al. (1991) [397]). If the  $^4\text{He}$  is instead assumed mostly to access the aquifer water by upward diffusion from the crust beneath, the  $^4\text{He}$  flux would be approximately  $5 \times 10^{-4} \text{ cm}^3 \text{ STP} \cdot \text{m}^{-2} \cdot \text{a}^{-1}$ . This is not an especially large flux. In any case, the exponential dependence of the  $^{36}\text{Cl}/\text{Cl}$  ratio with distance and the linear dependence of the  $^4\text{He}$  confirm that the trends are consistent with the basic conceptual models for both isotopes that have been presented in this volume.

### 6.6.3. Comparison with $^{81}\text{Kr}$

Another dating method that overlaps very well with  $^{36}\text{Cl}$  is  $^{81}\text{Kr}$ , with a half-life of 229 000 a. Although the technology for  $^{81}\text{Kr}$  measurement is relatively new and has, therefore, only been studied in relatively few localities, both nuclides have been measured in the Nubian sandstone aquifer system (Sturchio et al. (2004) [5]). Figure 6.13 shows the  $^{36}\text{Cl}/\text{Cl}$  ratio as a function of the model  $^{81}\text{Kr}$  age. If the two dating methods are consistent,  $^{36}\text{Cl}/\text{Cl}$  should fall along a trend determined by the following equation:

$$^{36}\text{Cl}/\text{Cl}_{\text{meas}} = \left[ ^{36}\text{Cl}/\text{Cl}_o - ^{36}\text{Cl}/\text{Cl}_{\text{se}} \right] \exp(-\lambda_{36} t_{81}) + ^{36}\text{Cl}/\text{Cl}_{\text{se}} \quad (6.19)$$

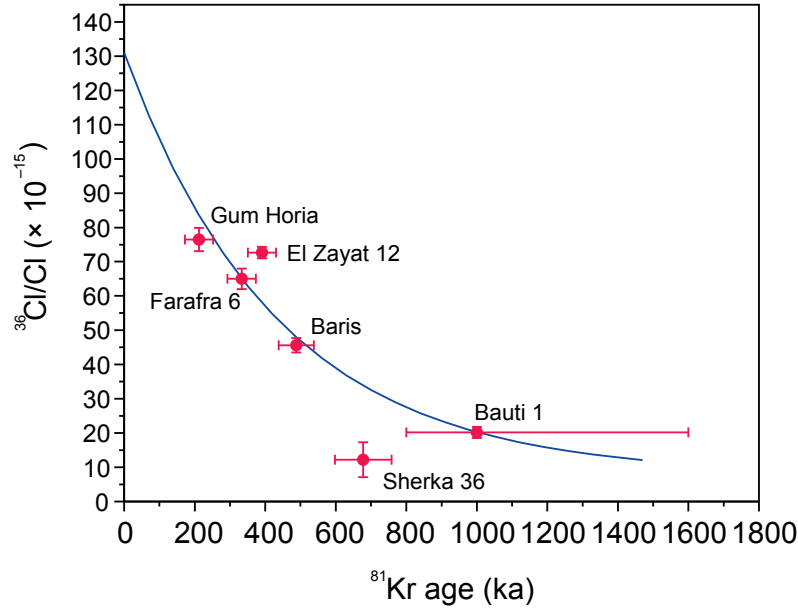


FIG. 6.13.  $^{36}\text{Cl}/\text{Cl}$  ratios measured in the Nubian sandstone aquifer of Egypt as a function of groundwater age calculated using measured  $^{81}\text{Kr}/\text{Kr}$  ratios, from Sturchio et al. (2004) [5]. The blue line is the  $^{36}\text{Cl}/\text{Cl}$  ratio calculated from the  $^{81}\text{Kr}$  model age using Eq. (6.19).

where

- $^{36}\text{Cl}/\text{Cl}_0$  is the recharge ratio;
- $^{36}\text{Cl}/\text{Cl}_{\text{se}}$  is the secular equilibrium ratio;
- $t_{81}$  is the model  $^{81}\text{Kr}$  age.

In Fig. 6.12, the data have been fitted to Eq. (6.19) with  $^{36}\text{Cl}/\text{Cl}_0 = 131 \times 10^{-15}$  and  $^{36}\text{Cl}/\text{Cl}_{\text{se}} = 8 \times 10^{-15}$ . An initial  $^{81}\text{Kr}/\text{Kr}$  ratio of  $1.10(\pm 0.05) \times 10^{-12}$  was used in calculating the simple exponential decay  $^{81}\text{Kr}$  model age. The agreement between the calculated and measured  $^{36}\text{Cl}/\text{Cl}$  ratios is generally good, especially considering that no effort was made to correct the model  $^{36}\text{Cl}$  ages for subsurface additions of Cl and  $^{36}\text{Cl}$ .

#### 6.6.4. Comparison without a well defined flow path

In some cases, general concordance between  $^{36}\text{Cl}$  trends and those of independent tracers can be established even if a clear-cut flow path cannot be distinguished. This is illustrated in Fig. 6.14, where  $^{36}\text{Cl}$  and  $^4\text{He}$  data from the Tokachi Basin in Japan are plotted (Mahara et al. (2007) [344]). Here, the data are too scattered and irregular to allow evaluation of a flow path. However, the relation between the temporal patterns of accumulation of  $^{36}\text{Cl}$  and  $^4\text{He}$  can still be evaluated. A simplistic model for the dependence of  $^{36}\text{Cl}/\text{Cl}$  on time is shown by:

$$^{36}\text{Cl}/\text{Cl}(t) = ^{36}\text{Cl}/\text{Cl}_0 \exp(-\lambda_{36}t) + ^{36}\text{Cl}/\text{Cl}_{\text{se}} [1 - \exp(-\lambda_{36}t)] \quad (6.20)$$

where  $^{36}\text{Cl}/\text{Cl}_0$  is the recharge  $^{36}\text{Cl}/\text{Cl}$  ratio and  $^{36}\text{Cl}/\text{Cl}_{\text{se}}$  the secular equilibrium ratio. The  $^4\text{He}$  accumulation is equally simplistically given by:

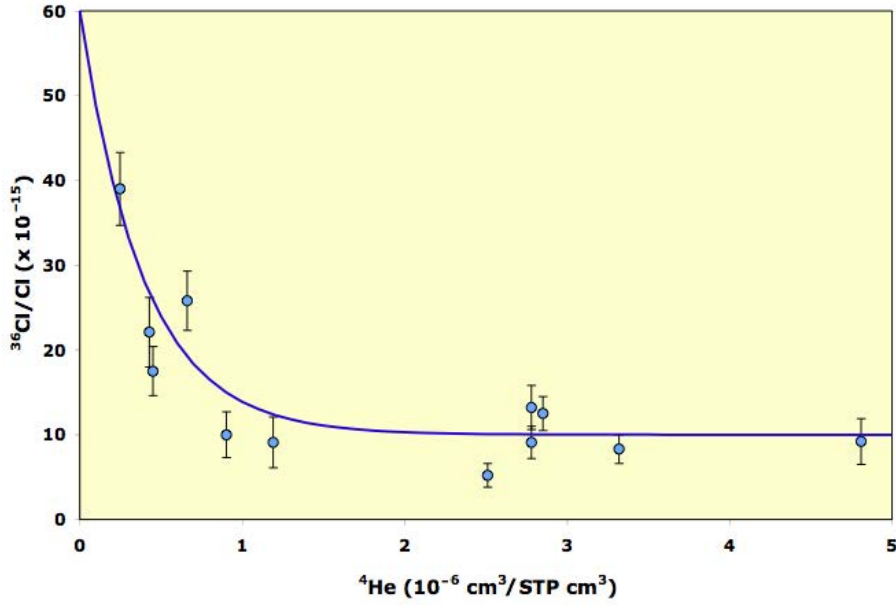


FIG. 6.14.  $^{36}\text{Cl}/\text{Cl}$  ratio as a function of  $^4\text{He}$  content in groundwater from the Tokachi Basin, Japan. Data are from Mahara et al. (2007) [344]. The blue line is  $^{36}\text{Cl}/\text{Cl}$  as a function of  $^4\text{He}$  accumulation, calculated from Eq. (6.22).

$$^4\text{He}(t) = A_{4\text{He}}t \quad (6.21)$$

where  $A_{4\text{He}}$  is the accumulation rate of  $^4\text{He}$ . Equation (6.21) can be substituted into Eq. (6.22) to yield:

$$^{36}\text{Cl}/\text{Cl}(t) = ^{36}\text{Cl}/\text{Cl}_0 \exp\left(-\lambda_{36} \frac{^4\text{He}}{A_{4\text{He}}}\right) + ^{36}\text{Cl}/\text{Cl}_{\text{se}} \left[1 - \exp\left(-\lambda_{36} \frac{^4\text{He}}{A_{4\text{He}}}\right)\right] \quad (6.22)$$

In Fig. 6.14, the solution of equation 6.22 is shown for  $^{36}\text{Cl}/\text{Cl}_0 = 60 \times 10^{-15}$ ,  $^{36}\text{Cl}/\text{Cl}_{\text{se}} = 10 \times 10^{-15}$ , and  $A_{4\text{He}} = 9 \times 10^{-7} \text{ cm}^3 \text{ STP} \cdot \text{cm}^{-3} \cdot \text{a}^{-1}$ . This calculated curve matches the data well, confirming that both  $^{36}\text{Cl}$  and  $^4\text{He}$  are following the expected conceptual models and allowing the  $^4\text{He}$  accumulation rate to be estimated. As for the Milk River aquifer, the original authors offer a more nuanced interpretation.

### 6.6.5. Summary

Chlorine-36 has been used to estimate groundwater ages in numerous old groundwater systems over the past 20 years. The systematics are well understood, with  $^{36}\text{Cl}$  principally produced in the atmosphere and entering the aquifer along with groundwater recharge. Once in the subsurface,  $^{36}\text{Cl}$  acts quite conservatively, leaving radiodecay as the only significant sink. The main complication for  $^{36}\text{Cl}$  dating of old groundwater is the subsurface introduction of chloride, with accompanying  $^{36}\text{Cl}$ . However, straightforward corrections for this mixing are possible if the nature of the subsurface processes is evaluated. Results from  $^{36}\text{Cl}$  dating of old groundwater can now be compared with those from a variety of other methods of dating. These comparisons are generally internally consistent and support the widespread use of  $^{36}\text{Cl}$  for dating old groundwater.

## Chapter 7

### DATING OF OLD GROUNDWATER USING URANIUM ISOTOPES — PRINCIPLES AND APPLICATIONS

K. FRÖHLICH

Vienna, Austria

#### 7.1. INTRODUCTION

This chapter provides background on the behaviour of uranium isotopes in groundwater and shows that uranium isotope disequilibrium presents a method that has the potential to play an important role within the concerted application of techniques to date old groundwater. Depending on the geochemistry of the aquifer system, the potential dating range extends from about 10 ka up to 1 Ma, which overlaps the  $^{14}\text{C}$  and the  $^{36}\text{Cl}/^{81}\text{Kr}$  dating ranges. Uranium isotopes can provide independent information relevant to groundwater age that complements other dating approaches and may help resolve ambiguities in data interpretation. Moreover, uranium isotopes in groundwater have the potential for quantifying geochemical parameters of the water–rock interaction and represent natural analogues for radioactive waste. Any multitracer application to date old groundwater should integrate uranium isotope measurements, which can easily be afforded by the use of modern mass spectrometric techniques.

Among the natural decay series radionuclides, the uranium isotopes  $^{234}\text{U}$  and  $^{238}\text{U}$  and the ratio of activity of these isotopes ( $^{234}\text{U}/^{238}\text{U}$ ) provide the greatest potential to trace natural water and to date old groundwater. Moreover, they are very useful as natural analogues in assessing the behaviour of radionuclides in nuclear waste disposal sites.

##### 7.1.1. History

In 1955, V.V. Cherdyn'tsev and P.I. Chalov discovered that in secondary minerals and natural water,  $^{234}\text{U}$  and  $^{238}\text{U}$  predominantly occur in radioactive disequilibrium, i.e. the activity ratio  $^{234}\text{U}/^{238}\text{U}$  is different from unity (Cherdyn'tsev et al. (1955) [398]). Subsequent studies have shown that this disequilibrium is a consequence of the energetic alpha decay of  $^{238}\text{U}$  that causes recoil fractionation between  $^{234}\text{U}$  and  $^{238}\text{U}$  due to differential release of  $^{234}\text{U}$  and  $^{238}\text{U}$  from the rock into the surrounding water (Chalov and Merkulova (1966) [399]; Cherdyn'tsev (1969) [400]; Osmond and Cowart (1976) [401]; Osmond and Cowart (1982) [402]). This disequilibrium found wide application in surface and groundwater studies.

In aerobic aqueous systems, measurements of uranium and  $^{234}\text{U}/^{238}\text{U}$  have been used to trace the flow of river water and groundwater (Plater et al. (1992) [403]; Porcelli and Swarzenski (2003) [404]; Sarin et al. (1990) [405]; Tuzova (1986) [406]; Tuzova and Novikov (1991) [407]), establish timescales of weathering processes (Andersen et al. (2009) [408]; Dosseto et al. (2008) [409]; Vigier et al. (2006) [410]), quantify mixing of surface and groundwater (Briel (1976) [411]), and identify groundwater inflow into surface water (Durand et al. (2005) [412]).

The suitability of uranium isotope disequilibrium as a tracer and timer of groundwater was first demonstrated by Osmond et al. (1968) [413] and later by Chalov et al. (1979) [414], Osmond and Cowart (1976) [401], and Osmond et al. (1983) [415]. Given the long half-life of  $^{234}\text{U}$  ( $2.45 \times 10^5$  a), many attempts have been made to apply  $^{234}\text{U}/^{238}\text{U}$  and/or the  $^{234}\text{U}$  excess (difference in the activity concentration of  $^{234}\text{U}$  and  $^{238}\text{U}$ ) to date old groundwater up to hundreds of thousands of years (Andrews et al. (1982) [416]; Andrews and Kay (1983) [417]; Barr et al. (1979) [418]; Cowart and Osmond (1974) [419]; Eshova (1981) [420]; Fröhlich et al. (1984) [421]; Ivanovich et al. (1991) [422]; Kigoshi (1973)

[423]; Kronfeld and Adams (1974) [424]; Pearson et al. (1983) [425]). Cowart and Osmond (1974) [419] noted that groundwater age derived from the decay of  $^{234}\text{U}$  excess may represent the migration time of the uranium tracer rather than the travel time of the groundwater. Consequently, any attempt to use the uranium isotope disequilibrium for groundwater studies requires a thorough knowledge of the sorption behaviour of these isotopes in the aquifer system (Fröhlich and Gellermann (1987) [426]).

The past two decades have seen a rapid expansion in the use of uranium series disequilibrium in a variety of disciplines such as geochronology, geochemistry and hydrology. Among others, applications of uranium isotopes to groundwater studies are reported by Bonotto (2000) [427], Bonotto (2006) [428], Deschamps et al. (2004) [429], Luo et al. (2000) [430], Rogojin et al. (1998) [431] and Tricca et al. (2001) [432]. Many recent studies take advantage of new analytical techniques, which began in the late 1980s with the use of thermal ionization mass spectrometry for the measurement of uranium isotopes and other radionuclides of the natural decay series (Chen et al. (1986) [433]). The application of multicollector inductively coupled plasma mass spectrometry (MC-ICP-MS) especially allowed measurement of much smaller water samples with greater accuracy and a significant increase in the measuring capacity in comparison to alpha spectrometry (Goldstein and Stirling (2003) [434]). The MC-ICP-MS technique enables high precision measurements of previously undetectable variations in many elements, including isotopic fractionation between  $^{235}\text{U}$  and  $^{238}\text{U}$  in water (Rademacher et al. (2003) [435]). Achievements have also been made in quantifying the effects of preferential release of  $^{234}\text{U}$  in weathering and erosion studies both by laboratory and field experiments (Andersen et al. (2009) [408]). In conclusion, the advent of mass spectrometric analysis of uranium isotopes, which is quicker and more precise, may enable broader application of this method and its practical application.

### 7.1.2. Scope and objective

This review is focused on the uranium isotope disequilibrium in groundwater and its relevance to dating of old groundwater. First, the natural abundance of uranium isotopes and their geochemical behaviour in groundwater will briefly be discussed. Second, a critical review of the models used to derive information from uranium isotope measurements on groundwater age will be given. Special emphasis is placed on a conceptual model incorporating water-rock interaction that has been used for dating old groundwater. Finally, some case studies will be discussed which demonstrate the strengths and limitations of the uranium isotope groundwater dating technique and its integration into multitracer approaches to date old groundwater. Developments in the use of uranium and  $^{234}\text{U}/^{238}\text{U}$  have been reviewed by Cherdyntsev (1971) [436], Osmond (1980) [437], Osmond and Cowart (1976) [401], Osmond and Cowart (1992) [438], and Osmond and Cowart (2000) [439]. Monographs on this subject have been published by Ivanovich and Harmon (1982) [440], Ivanovich and Harmon (1992) [441] and, more recently, by Bourdon et al. (2003) [442].

## 7.2. NATURAL ABUNDANCE OF URANIUM ISOTOPES

Naturally occurring uranium consists of three alpha active isotopes:  $^{238}\text{U}$ ,  $^{235}\text{U}$  and  $^{234}\text{U}$ . The first two isotopes are initial members of the corresponding natural radioactive decay series and the latter one is a decay product of  $^{238}\text{U}$  (Fig. 7.1). The  $^{235}\text{U}$  activity in natural uranium is less than 5% of the  $^{238}\text{U}$  activity and, thus, has not been used for hydrological applications. Given the relatively short half-life of  $^{234}\text{U}$  ( $2.455 \times 10^5$  a) compared with  $^{238}\text{U}$  ( $4.468 \times 10^9$  a), these two uranium isotopes are expected to be globally in secular radioactive equilibrium, i.e.  $^{234}\text{U}/^{238}\text{U} = 1$ . It was, therefore, a surprise when Cherdyntsev et al. (1955) [398] reported that in some geological objects, radioactive equilibrium is disturbed. In groundwater, the  $^{234}\text{U}/^{238}\text{U}$  ratio is usually  $>1$ , while in weathered rock, for instance, this ratio can be distinctly  $<1$ .

<b>U</b>	$^{238}\text{U}$ 4.468×10 <sup>9</sup> a		$^{234}\text{U}$ 2.455×10 <sup>5</sup> a
<b>Pa</b>	↓ α	$^{234}\text{Pa}$ 1.17 m	↓ α
<b>Th</b>	$^{234}\text{Th}$ 24.1 d	↗ β	$^{230}\text{Th}$ 75.38×10 <sup>3</sup> a
<b>Ac</b>			↓ α
<b>Ra</b>			$^{226}\text{Ra}$ 1602 a
<b>Fr</b>			↓ α
<b>Rn</b>			$^{222}\text{Rn}$ 3.824 d

FIG. 7.1. Part of the  $^{238}\text{U}$  decay series (from  $^{238}\text{U}$  to  $^{222}\text{Rn}$ ).

The quantities used to express uranium abundance and measuring results include the following:

- Uranium activity concentration = uranium activity (Bq or mBq) divided by volume of water (L) in which uranium is dissolved.
- Uranium concentration = mass of uranium (mg or  $\mu\text{g}$ ) divided by volume of water (L) in which uranium is dissolved.
- Specific activity of uranium = uranium activity (Bq or mBq) divided by mass of substance (kg) containing the uranium.
- (Relative) uranium content = mass of uranium divided by mass of substance containing the uranium (g/g, ppm = 1 mg U/1 kg of substance, or 1 ppb = 1  $\mu\text{g}$  U/1 kg of substance).
- Uranium activity ratio = activity of  $^{234}\text{U}$  divided by activity of  $^{238}\text{U}$  in a given sample.

It should be noted that 1 ppm uranium corresponds to a specific activity of 12.4 Bq/kg.

In ocean water, related to a salinity of 35‰, uranium concentration ranges from 3.162 to 3.281  $\mu\text{g/L}$  (Chen et al. (1986) [433]) and the activity ratio is  $1.147 \pm 0.001$  (Andersen et al. (2007) [443]; Robinson et al. (2004) [444]) (Table 7.1). In continental surface water, the uranium content varies between  $10^{-3}$  and  $10^3$  ppb, and the activity ratio ranges from 1 to 2 (Osmond and Cowart (1976) [401]). Most of the  $^{234}\text{U}/^{238}\text{U}$  values of lakes and rivers are between 1.1 and 1.4 (Chabaux et al. (2003) [445]; Ferronsky and Polyakov (1982) [446]).

Groundwater shows the largest variation both of uranium concentration and the activity ratio. An evaluation of nearly 800 measurements published at the beginning of the 1980s (Gellermann and Fröhlich (1984) [447]) uncovered a logarithmic normal distribution of uranium concentration with an average value of 1 ppb and a range from  $10^{-3}$  to  $10^4$  ppb. The lower end of this distribution corresponds to the analytical detection limit by alpha spectrometric measurements of uranium made in 1984; in reality, uranium concentrations may be even lower. The activity ratios in groundwater ranged from 0.5 to about 30; values  $>5$  were mainly associated with low uranium concentrations. None of the published activity ratio values were below 0.5; this appears to be in agreement with theoretical considerations of Bondarenko (1981) [448]. The frequency distribution of the  $^{234}\text{U}/^{238}\text{U}$  activity ratio is generally asymmetric and strongly depends on the type of water-bearing rocks. In an extensive study of groundwater from Kazakhstan, Syromyatnikov (1961) [449] found characteristic frequency distributions of  $^{234}\text{U}/^{238}\text{U}$  for various rock types (Fig. 7.2).

TABLE 7.1. URANIUM CONTENT AND  $^{234}\text{U}/^{238}\text{U}$  IN ROCKS AND NATURAL WATERS

Object	Uranium content (ppm)	$^{234}\text{U}/^{238}\text{U}$
Sedimentary rocks		
carbonates	$0.6 \pm 0.5$	$0.92 \pm 0.01$
clays	$2 \pm 1$	$0.9 \pm 0.1$
phosphorites	100	1.0–1.15
Igneous rocks		
mafic	0.9	(1.0)
diorites	2	(1.0)
granodiorites	2.6	(1.0)
silicic volcaneous	5	(1.0)
Magma (basalt)	0.078	(1.0)
Ocean water	$3.3 \times 10^{-3}$	$1.147 \pm 0.001$
Groundwater	$1 \times 10^{-3}$ ( $1-10^{-6}$ )	1.5 (0.5–30)

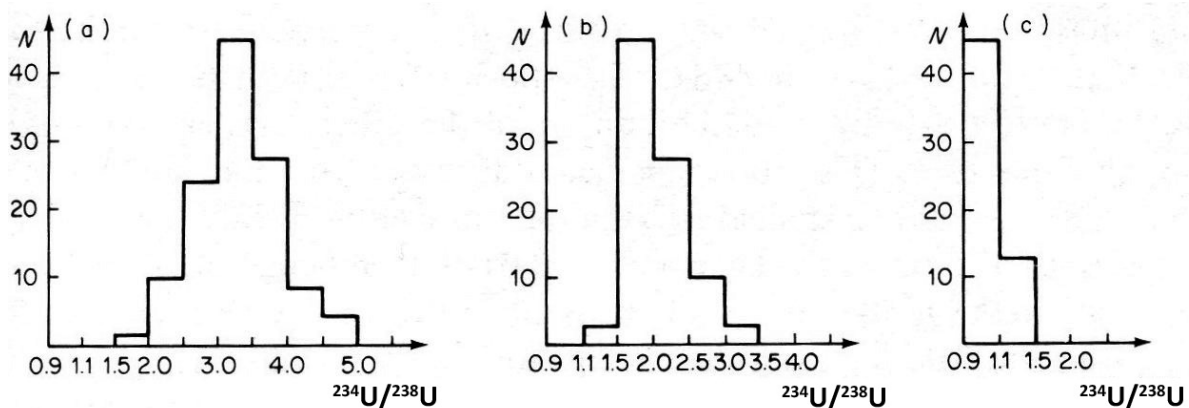


FIG. 7.2. Histograms of  $^{234}\text{U}/^{238}\text{U}$  distribution in the groundwater of igneous rocks (a), sedimentary and metamorphic rocks (b) and uranium ores (c) (from Ferronsky and Polyakov (1982) [446]).

### 7.3. URANIUM GEOCHEMISTRY

In natural waters, the prevailing valence states of uranium are +4 and +6. During weathering, uranium is oxidized to the hexavalent uranyl ion  $\text{UO}_2^{2+}$  which forms soluble complexes with  $\text{CO}_3^{2-}$  and  $\text{PO}_4^{3-}$  under near-neutral conditions, and with  $\text{SO}_4^{2-}$ ,  $\text{F}^-$  and  $\text{Cl}^-$  at lower pH values (Langmuir (1978) [450]). The presence of these complexing ions inhibits adsorption and, hence, is mainly responsible for the mobility of uranium observed in natural waters (Rose and Wright (1980) [451]). Under oxidizing conditions, typical uranium concentrations in water are close to 1 ppb (Osmond and Cowart (1992) [438]). Under reducing conditions, uranium occurs in the tetravalent state and is stable as  $\text{U}(\text{OH})_4$ ; the maximum uranium concentration is at about 0.06 ppb, which corresponds to the solubility limit of uraninite ( $\text{UO}_2$ ) (Gascoyne (1992) [452]).

Adsorption and precipitation processes are important in controlling the uranium isotope migration in groundwater. Dissolved  $\text{UO}_2^{2+}$  is susceptible to adsorption, especially by organic matter such as humic acids (Lenhart and Honeyman (1999) [453]), iron oxyhydroxides and micas (Ames et al. (1983) [454]; Arnold et al. (1998) [455]; Duff et al. (2002) [456]; Hsi and Langmuir (1985) [457]; Liger et al. (1999) [458]). The retention of adsorbed uranium, and thus also of  $^{234}\text{U}$  excess, depends on the pH of the solution. Silicate mineral surfaces generally have high uranium retention at a pH of 5–10, while at  $\text{pH} < 4$  the uranium retention is low (Krawczyk-Barsch et al. (2004) [459]). During crystallization of Fe minerals, uranium that has been exchangeably adsorbed by the originally amorphous Fe hydroxides can irreversibly be incorporated into more stable sites (Ohnuki et al. (1997) [460]; Payne et al. (1994) [461]). This long term precipitation of Fe minerals can transfer a significant fraction of adsorbed uranium onto surface coatings. Uranium sorption on goethite was found to be initially reversible, but after some months a portion of this uranium was no longer readily exchangeable (Giammar and Hering (2001) [462]). If the rate of such uranium removal is of the order of, or higher than, the decay constant of  $^{234}\text{U}$ , it may be difficult to disentangle the effects of the two processes on uranium evolution over greater distances.

Studies of the uranium isotopic composition along the groundwater flow from the outcrop to confined deeper regions of aquifers revealed the existence of three zones (Fig. 7.3) with different  $^{234}\text{U}/^{238}\text{U}$  ratios and uranium contents (Andrews and Kay (1983) [417]; Andrews and Kay (1982) [463]; Osmond and Cowart (1982) [402]): (i) an oxidizing zone (often coinciding with the vadose zone where weathering takes place) characterized by high uranium content and a moderate  $^{234}\text{U}/^{238}\text{U}$  ratio; (ii) a redox front with decreasing uranium concentration due to reduction of hexavalent uranium to rather insoluble tetravalent uranium and with a high  $^{234}\text{U}/^{238}\text{U}$  ratio due to enhanced recoil of  $^{234}\text{U}$  from precipitated phases; and (iii) a reduced zone with low uranium content and varying  $^{234}\text{U}/^{238}\text{U}$ .

There are three effects that give rise to the observed disequilibrium between  $^{234}\text{U}$  and  $^{238}\text{U}$ : (i) preferential release of more loosely bound  $^{234}\text{U}$  from damaged mineral lattice sites; (ii) release of  $^{234}\text{U}$  excess adsorbed on mineral grain surfaces in contact with the aqueous phase; and (iii) direct recoil of  $^{234}\text{Th}$  (the immediate short lived daughter of  $^{238}\text{U}$ ) from near mineral surface boundaries into the surrounding aqueous phase. The first effect is a consequence of the nuclear recoil by the energetic alpha decay of  $^{238}\text{U}$  and  $^{234}\text{Th}$ . This recoil induces bond breaks and lattice damage and displaces decay products into weakly bound interstitial (surficial) sites of the mineral grains (Chalov and Merkulova (1966) [399]; Cherdynstev (1971) [436]; Fleischer (1980) [464]; Fleischer (1982) [465]; Hussain and Lal (1986) [466]; Rosholt et al. (1963) [467]; Zielinski et al. (1981) [468]). A further cause for the disequilibrium is the ionization of  $^{234}\text{U}$  from a  $4^+$  to  $6^+$  valence state by stripping two of its electrons

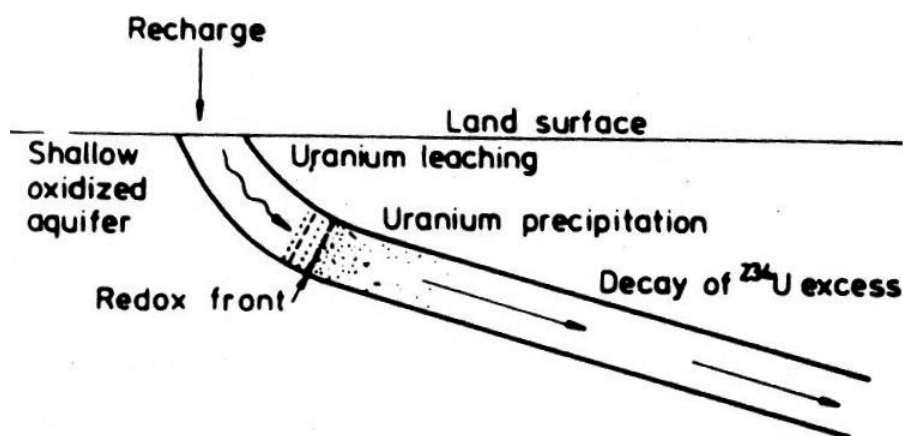


FIG. 7.3. Schematic of uranium isotope evolution along a confined aquifer; preferential leaching under oxidizing conditions, precipitation in the redox zone and recoil ejection and radioactive decay of  $^{234}\text{U}$ .

during the decay sequence  $^{238}\text{U}(4^+) \rightarrow ^{234}\text{Th}(4^+) \rightarrow ^{234}\text{Pa}(5^+) \rightarrow ^{234}\text{U}(6^+)$  (Dooley et al. (1966) [469]). An alternative explanation of the  $^{234}\text{U}$  oxidation has been found by computer simulations of the recoil process (Adloff and Roessler (1991) [470]). These simulations suggest that recoiling  $^{234}\text{Th}$  atoms push the oxygen atoms of the mineral in front of it so that the final resting location of  $^{234}\text{Th}$  becomes enriched in oxidizing species. These species subsequently oxidize  $^{234}\text{U}$  after decay of  $^{234}\text{Th}$ .

The various mineral phases of a given rock type do not only have different susceptibility to lattice damage induced by alpha decay, but also differing ability to anneal (recover from) this damage. In general, lattice defect recovery is a slow process at normal groundwater temperatures and, thus, some silicate minerals are comparatively susceptible to preferential release of  $^{234}\text{U}$  from damaged lattice sites (Andersen et al. (2009) [408]; Eyal and Fleischer (1985) [471]). In contrast, minerals such as monazite and apatite show a rapid recovery (Chaumont et al. (2002) [472]; Eyal and Olander (1990) [473]; Hendriks and Redfield (2005) [474]).

Kigoshi (1971) [475] found that  $^{234}\text{U}/^{238}\text{U}$  ratios  $>3$  cannot be explained by this preferential  $^{234}\text{U}$  release alone, but require a combination with an additional fractionation mechanism based on direct alpha recoil ejection of  $^{234}\text{Th}$  from the solid into the aqueous phase (see also Hussain and Krishnaswami (1980) [476], and Rama and Moore (1984) [477]). At the transition from oxic to anoxic conditions, high groundwater  $^{234}\text{U}/^{238}\text{U}$  ratios are produced due to recoil effects and preserved by the anoxic water. Thus, uranium is concentrated on secondary phases by precipitation. As a consequence, uranium concentrations strongly decrease and  $^{234}\text{U}/^{238}\text{U}$  ratios increase due to recoil from these phases (Osmond and Cowart (1992) [438]). The recoil effect depends on the uranium concentration in the mineral, the grain size of the mineral, the recoil range of  $^{234}\text{Th}$  (about 20 nm) and the time (DePaolo et al. (2006) [478]; Kigoshi (1971) [475]). Provided the  $^{234}\text{Th}$  residence time in the aqueous phase is long enough compared with its half-life,  $^{234}\text{U}$  is produced directly within the aqueous phase by the decay of recoil ejected  $^{234}\text{Th}$ . If, however,  $^{234}\text{Th}$  is quickly adsorbed by mineral surfaces (Langmuir and Herman (1980) [479]), then  $^{234}\text{U}$  is produced at these surface sites from which it can easily enter the surrounding groundwater. Note that over long timescales (of the order of 100 ka) in slow moving groundwater and at low leaching (weathering) rates ( $<10^{-6}/\text{a}$ ), direct recoil may overcompensate radioactive decay of  $^{234}\text{U}$  and, thus, cause an increase of  $^{234}\text{U}/^{238}\text{U}$  along the groundwater flow (Andersen et al. (2009) [408]).

#### 7.4. URANIUM ISOTOPE MEASUREMENTS

The uranium isotopes  $^{238}\text{U}$  and  $^{234}\text{U}$  are alpha emitters and thus, until recently, have been measured by alpha spectrometry combined with isotope dilution methods using  $^{232}\text{U}$  or  $^{236}\text{U}$  as analytical tracers (Lally (1992) [480]). This technique is still cost effective and well suited for applications where higher detection limits and lower precision and longer measuring (counting) times (several days per sample) are acceptable. Alpha spectrometry laboratories often simultaneously operate dozens of solid state alpha detectors and small vacuum chambers. In the late 1980s and early 1990s, mass spectrometry became an alternative to decay counting techniques (Chen et al. (1992) [481]). Although much more expensive, it facilitates more accurate measurements in a shorter time and with much smaller samples (Table 7.2).

For alpha spectrometry of uranium isotopes, at least 10 L of water is necessary. When using mass spectrometry, water samples of the order of 10 mL are sufficient for analysis. If water samples contain particulate matter, filtering (usually with 0.45  $\mu\text{m}$  membranes) is required. Adsorption of uranium onto the container walls or suspended matter can be avoided by adding, as soon as feasible during sampling, enough nitric acid to lower the pH of the water to approximately 1. (If other U–Th series nuclides are to be measured also, a more sophisticated sampling procedure is necessary, which, for example, is described by Tricca et al. (2001) [432]).

In the laboratory, a weighed amount of spike solution (usually with the shorter lived  $^{232}\text{U}$  for alpha spectrometry and the longer lived  $^{233}\text{U}$  or  $^{236}\text{U}$  for mass spectrometry) has to be added to the water sample. For alpha spectrometric analysis, the water volume must be reduced by evaporation or through co-precipitation of uranium with, for example, ferric hydroxide as carrier. The precipitate is re-dissolved

TABLE 7.2. COMPARISON OF ANALYTICAL METHODS FOR URANIUM ISOTOPE ANALYSIS (*Goldstein and Stirling (2003) [434]*)

		Alpha spectrometry	Thermal ionization mass spectrometry	Multiple-collector thermal ionization mass spectrometry	Inductive coupled plasma mass spectrometry	Multiple-collector inductive coupled plasma mass spectrometry
Sample size ( $\mu\text{g}$ )	Uranium	1–100	0.1–2	0.01–1	0.01–0.45	0.01–0.45
Precision ( $2\sigma$ ) (%)	$^{238}\text{U}$	2–10	0.1	0.1	0.1–5	<0.1
	$^{234}\text{U}/^{238}\text{U}$	2–10	0.5	0.1–0.2	0.1–10	0.05–0.2
Meas. time	Uranium	1–28 d	4 h	1–2 h	1–10 min	15–30 min

in an acid medium and then passed through an anion exchange column to isolate uranium from other nuclides that might cause interference during counting. Finally, the uranium is deposited on a suitable substrate (e.g. electrodeposition on polished stainless steel planchets) for alpha spectrometric analysis. More details of this laboratory procedure can be found in Lally (1992) [480]. For mass spectrometric measurements, the following procedure is used: addition of a spike ( $^{233}\text{U}$  or  $^{236}\text{U}$ ), drying, anion exchange and loading onto filaments for analysis.

Table 7.2 compiles parameters that allow comparison of the various methods currently available for the measurement of  $^{234}\text{U}$  and  $^{238}\text{U}$  in natural water samples (Goldstein and Stirling (2003) [434]). There are several suitable mass spectrometric methods which basically differ regarding the type of ion source, ionization method and ion collector system. The first mass spectrometric measurements of uranium and thorium isotopes were performed with thermal ionization mass spectrometers (TIMS) (Chen et al. (1986) [433]; Edwards et al. (1987) [482]; Goldstein et al. (1989) [483]). Sample size, measuring precision and time of analysis have improved at least one order of magnitude since that time. Since the 1990s, inductive coupled plasma mass spectrometry (ICPMS) has become more commonly used as an alternative to TIMS with comparable or even better precision. ICPMS facilitates a fast and easy acquisition of data. Analysis times are typically less than 10 min (Goldstein and Stirling (2003) [434]). Since the end of the 1990s, MC-ICPMS (multiple-collector-ICPMS) is increasingly being used. It facilitates an even better precision than conventional ICPMS. The cost per sample analysis is presently about US \$25.

## 7.5. URANIUM ISOTOPE DATING METHOD

### 7.5.1. Introduction

A straightforward dating of old groundwater by uranium isotope disequilibrium would be possible if: (i) the initial state of disequilibrium were known and (ii) the concentrations of both isotopes had not changed by chemical and physical processes other than radioactive decay. The initial state of disequilibrium can be estimated empirically by extrapolation of measured values along the groundwater flow direction. However, the second requirement is difficult to satisfy because of the various geochemical processes (including dissolution, precipitation, sorption/desorption) involved in the water–rock interaction that affect the evolution of uranium in groundwater. A range of attempts have been made by various authors to interpret uranium isotope measurements in terms of groundwater age. In the following, a model is described that allows a critical review of such approaches and helps

better define potential and limitations of the groundwater dating using uranium isotope disequilibrium. The model is based on the approach published by Fröhlich et al. (1984) [421] and, in its present version, has been used by Ivanovich et al. (1991) [422] to evaluate the uranium isotope data of the Milk River aquifer. A similar model was used by Pearson et al. (1983) [425] for the numerical evaluation of  $^{14}\text{C}$  and uranium isotope data of the Carrizo aquifer. Furthermore, a detailed description of radionuclide transport models has been given by Ku et al. (1992) [484]. More recently, Porcelli and Swarzenski (2003) [404] reviewed the general principles and evaluated the controlling processes incorporated in the models.

### 7.5.2. Mathematical formulation of the model

The basic model (Fröhlich et al. (1984) [421]) describes the radionuclide evolution in a one dimensional groundwater flow of constant velocity. The following notation is used:

$N_m, N_{im}, N_a$	number of radionuclide atoms in the mobile (m), immobile (im) and adsorbed (a) phase
$N$	total number of radionuclide atoms in the mobile, immobile and adsorbed phase: $N = N_m + N_{im} + N_a$
$N_r$	number of radionuclide atoms in the solid (rock) phase
$V_m, V_{im}, V_r$	volume of the mobile, immobile and rock phase
$V$	total (unit) volume: $V = V_m + V_{im} + V_r$
$n$	flow (effective) porosity: $n = V_m/V$
$n_{im}$	matrix porosity: $n_{im} = V_{im}/V$
$n_t$	total porosity: $n_t = (V_m + V_{im})/V = n + n_{im}$
$m_r$	mass of rock: $m_r = \rho \times V_r$
$x$	distance along flow path
$t$	time
$v_f$	Darcy velocity
$v$	flow velocity: $v = v_f/n$
$D$	dispersion/diffusion coefficient
$\lambda$	radioactive decay constant
$p$	precipitation rate constant
$e$	dissolution (leaching) rate constant
$\gamma$	recoil efficiency
-1	subscript denoting the radioactive parent nuclide. Given the short half-life of $^{234}\text{Th}$ and its short lifetime in the liquid phase, the parent nuclide of $^{234}\text{U}$ is assumed to be $^{238}\text{U}$
$\frac{\partial N}{dt}$	time derivative of the amount of the given radionuclide in the liquid and adsorbed phases of the unit volume
$D \frac{\partial^2 N_m}{\partial x^2}$	change of the dispersive/diffusive flux, assuming that $D$ is constant
$v \frac{\partial N_m}{\partial x}$	change of the advective flux, assuming $v$ is constant
$\lambda N$	radioactive decay in liquid and adsorbed phase
$\lambda_{-1} N_{-1}$	radioactive decay of parent nuclide in liquid and adsorbed phases
$p(N_m + N_{im})$	irreversible precipitation from liquid to rock phase
$eN_r$	dissolution from rock phase
$\gamma\lambda_{-1} N_{-1r}$	recoil ejection from rock phase

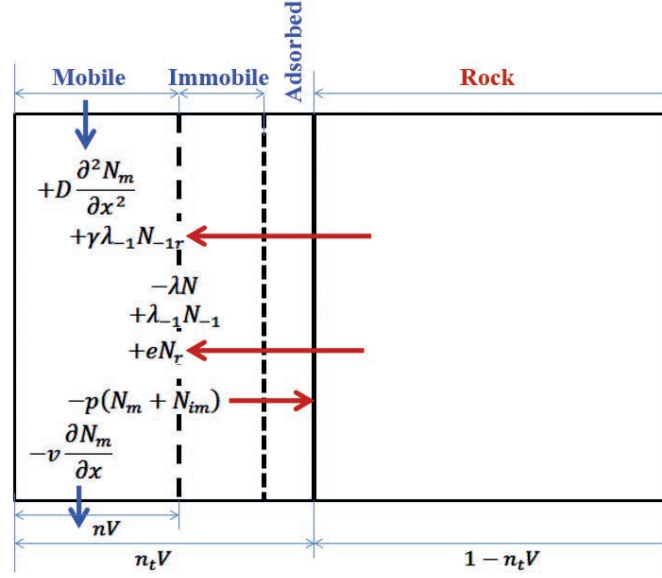


FIG. 7.4. Schematic diagram of a unit volume ( $V$ ) of an aquifer and of the processes controlling the temporal change of the radionuclide content in the liquid (mobile and immobile) phase (see text).

Figure 7.4 schematically represents a unit volume of the aquifer with the physicochemical processes controlling the radionuclide evolution. The processes considered in the model include dispersive/diffusive transport through and advective transport in the liquid phase, sorption/desorption and precipitation/dissolution across the solid–liquid interface, radioactive decay and ingrowth (due to radioactive decay of the precursor) in the liquid phase, and alpha recoil input. It is assumed that dissolution and precipitation of solids occur irreversibly and that sorption/desorption are reversible processes following a linear adsorption isotherm which is characterized by a constant equilibrium distribution coefficient ( $K_d$ ). This  $K_d$  value is defined as the ratio of the specific activity of the given radionuclide in the adsorbed phase and the activity concentration of the radionuclide in the liquid phase:

$$K_d = \frac{N_a / m_r}{N_m / V_m} \quad (7.1)$$

It should be noted that this approach is appropriate as long as the decay rate of the given radionuclide is considerably smaller than the rate constants of reversible sorption and desorption (Fröhlich et al. (1995) [485]). Alpha decay induced recoil ejection is assumed to be proportional to the activity of the parent nuclide in the rock matrix.

The liquid phase (groundwater) is divided into a mobile and an immobile component and, thus, the total porosity of the rock  $n_t$  is the sum of flow (effective) porosity  $n$  and matrix porosity  $n_{im}/n_t = n + n_{im}$ . It should be noted that in porous rock aquifers the matrix porosity is usually negligible ( $n_{im} \ll n$  or  $n_t \approx n$ ), while in fractured rocks the effective (fracture) porosity is generally small in comparison with the matrix porosity  $n \ll n_{im}$ . It is further assumed that the given radionuclide is able to penetrate fully into the immobile groundwater, i.e. mobile and immobile groundwater are assumed to have the same radionuclide concentration:

$$\frac{N_m}{V_m} = \frac{N_{im}}{V_{im}} \quad (7.2)$$

The mathematical formulation of the model is based on the mass balance equation of the radionuclide in the unit volume of the aquifer (Fig. 7.4). The temporal change of the amount of

the radionuclide is given by the difference between the input and output of the radionuclide as well as by its production and decay. The mass balance includes both the liquid and adsorbed phases in the unit volume:

$$\frac{\partial N}{\partial t} = D \frac{\partial^2 N_m}{\partial x^2} - v \frac{\partial N_m}{\partial x} - \lambda N + \lambda_{-1} N_{-1} - p(N_m + N_{im}) + eN_r + \gamma \lambda_{-1} N_{-1r} \quad (7.3)$$

The various terms of Eq. (7.3) are schematically shown in Fig. 7.4 and are explained in the above notation. Considering that:

$$N = N_m + N_{im} + N_a$$

taking into account Eqs (7.1, 7.2) and the definitions of the various porosities, it can be shown that:

$$N = R \times N_m$$

where  $R$  is the retardation factor:

$$R = \frac{n_t}{n} + \frac{1-n_t}{n} \rho K_d \quad (7.4)$$

Similarly, it can be shown that  $N_m + N_{im}$  of the precipitation term in Eq. (7.3) can be replaced by  $\frac{n_t}{n} N_m$ . Thus, with Eq. (7.3), it follows that:

$$R \frac{\partial N_m}{\partial t} = D \frac{\partial^2 N_m}{\partial x^2} - v \frac{\partial N_m}{\partial x} - (R\lambda + \frac{n_t}{n} p) N_m + R_{-1} \lambda_{-1} N_{-1m} + eN_r + \gamma \lambda_{-1} N_{-1r} \quad (7.5)$$

Finally, replacing the number of radionuclide atoms in Eq. (7.5) by the corresponding activity concentration  $a = \frac{\lambda N_m}{V_m}$ ,  $a_{-1} = \frac{\lambda_{-1} N_{-1m}}{V_m}$ ,  $a_r = \frac{\lambda N_r}{V}$  and  $a_{-1r} = \frac{\lambda_{-1} N_{-1r}}{V}$ , and multiplying both sides by  $\frac{V_m}{\lambda}$  leads to:

$$R \frac{\partial a}{\partial t} = D \frac{\partial^2 a}{\partial x^2} - v \frac{\partial a}{\partial x} - \left( R\lambda + \frac{n_t}{n} p \right) a + R_{-1} \lambda a_{-1} + e a_r / n + \gamma \lambda a_{-1r} / n \quad (7.6)$$

This equation describes the evolution of any radionuclide of the natural decay series (Fröhlich et al. (1995) [485]). For the determination of  $^{234}\text{U}/^{238}\text{U}$  disequilibrium, Eq. (7.6) represents a system of three partial differential equations that has to be solved for the three members of the decay sequence  $^{238}\text{U} \rightarrow ^{234}\text{Th} \rightarrow ^{234}\text{U}$ . The following simplifying assumptions allow a straightforward analytical solution of these equations. In aquifer systems with old groundwater, the radionuclide distributions are supposed to be in steady state ( $\frac{\partial a}{\partial t} = 0$ ). Thus, the partial differential equations change to ordinary differential equations. The  $^{234}\text{Th}$  activity concentration in groundwater is, in general, very low or even negligible, which reduces the system to two equations. Furthermore, it is assumed that the parameters characterizing the water–rock interaction ( $R$ ,  $p$ ,  $n_t$ ,  $n$ ) and the activity concentrations in the rock phase ( $a_r$  and  $a_{-1r}$ ) are constant along the considered groundwater flow path. Consequently, the system of Eq. (7.6) reduces to two ordinary linear differential equations of second order with constant coefficients, for which the following solutions for the  $^{238}\text{U}$  and  $^{234}\text{U}$  activity concentrations can easily be obtained:

$$a_8(\tau) = a_{8s} + (a_{80} - a_{8s}) \exp(\kappa_8 \tau) \quad (7.7)$$

$$a_4(\tau) = a_{4s} + (a_{40} - a_{4s}) \exp(\kappa_4 \tau) \quad (7.8)$$

TABLE 7.3. COMPILATION OF EARLIER ATTEMPTS TO DATE OLD GROUNDWATER USING URANIUM ISOTOPES (from Fröhlich and Gellermann (1987) [426])

Authors	Study area; aquifer rock type	Dating formula(s)	Results
Kronfeld (1971) [486], Kronfeld and Adams (1974) [424]	Hosston aquifer (Texas, USA); sandstone	$AR = AR_0 \exp(-\lambda_4 \tau)^*$ (water rock interaction neglected)	Flow velocity 0.2–1.0 m/a derived
Cowart and Osmond (1974) [419], Cowart and Osmond (1977) [487]	Carrizo aquifer (Texas, USA); sandstone	$X = X_s + (X_0 - X_s) \exp(-\lambda_4 \tau)^{**}$ (retardation, precipitation, leaching neglected)	Apparent groundwater flow rate of 8 cm/a about 20 times lower than the one determined by other techniques
Pearson et al. (1983) [425]	Carrizo aquifer (Texas, USA); sandstone	Groundwater and radionuclide transport equation incorporating water rock exchange	$^{14}\text{C}$ data (uncorrected) used to validate numerical solution of the transport equation; uranium retardation factor in reducing zone about 30
Barr et al. (1979) [418]	Delaware Basin (New Mexico–Texas, USA); evaporite, limestone	$AR = AR_s + (AR_0 - AR_s) \exp(-\lambda_4 \tau)$ (retardation, precipitation, leaching neglected)	$AR_s = 1$ assumed and $AR_0$ estimated; calculated ages between 0.3 and 1.1 Ma
Eshova (1981) [420]	Bachardensky aquifer (Turkmenistan)	$AR = 1 + (AR_0 - 1) \exp(-\lambda_4 \tau)$ (retardation, precipitation, leaching neglected)	Estimated groundwater age 60 ka
Fritz et al. (1980) [488]	Stripa test site (Sweden); granite	$AR = 1 + (AR_0 - 1) \exp(-\lambda_4 \tau)$	Vertical age differences of 0.14 Ma estimated; model assumptions not supported by chemical data
Andrews et al. (1982) [416]		$AR = 1 + (AR_0 - 1) \exp(-\lambda_4 \tau) + \beta_A [1 - \exp(-\lambda_4 \tau)]$ , where $\beta_A \approx a_{87}/a_8$	
Andrews and Kay (1983) [417], Andrews et al. (1984) [489]	East Midlands aquifer (United Kingdom); sandstone	$AR = 1 + (AR_0 - 1) \exp(-\lambda_4 \tau) + \beta_A [1 - \exp(-\lambda_4 \tau)]$ , where $\beta_A \approx a_{87}/a_8$	U isotopes are related to the hydrochemistry and difficult to relate to groundwater age
Fröhlich et al. (1984) [421]	Triassic aquifer (Germany); sandstone	Groundwater and radionuclide transport equation incorporating water–rock exchange	Combined measurements of $^{14}\text{C}$ and uranium isotopes; for reducing zone, the uranium retardation factor is between 30 and 80
Ivanovich et al. (1991) [422]	Milk River sandstone aquifer, Canada	Groundwater and radionuclide transport equation incorporating water–rock exchange	$^{234}\text{U}$ ( $^{238}\text{U}$ ) age in good agreement with results obtained by hydraulic and $^{36}\text{Cl}$ methods (see Table 7.4)

The subscripts 8 and 4 indicate  $^{238}\text{U}$  and  $^{234}\text{U}$ , respectively, 0 and s indicate initial and stationary values, respectively, and  $\tau$  is the groundwater age, or more precisely the time the groundwater parcel needs to travel along a distance  $x$  of the flow path:

$$\tau = x / v \quad (7.9)$$

The parameters included in Eqs (7.7, 7.8) are defined as follows:

$$\kappa_i = \frac{v^2}{2D} \left[ 1 - \left( 1 + \frac{4DK_i}{v^2} \right)^{1/2} \right] \quad (7.10)$$

$$K_i = R\lambda_i + \left( \frac{n_t}{n} \right) p \quad (7.11)$$

$$a_{8s} = e_8 a_{8r} / (nK_8) \quad (7.12)$$

$$a_{4s} = (e_4 a_{4r} + \gamma \lambda_4 a_{8r}) / (nK_4) \quad (7.13)$$

The dispersivity  $D/v$  in deep aquifer systems is assumed to be small, i.e.  $D/v \ll v/4K_i$ . Thus, expressing the square root in Eq. (7.10) by a Taylor series, the terms  $\left( \frac{4DK_i}{v^2} \right)^{1/2}$  with  $v > 1$  can be neglected, so that Eq. (7.10) reduces to:

$$\kappa_i \approx -K_i \quad (7.14)$$

A numerical example of the practical application of the above equations represents the evaluation of uranium isotope data of the Continental Intercalaire aquifer provided in Section 7.6.

Using Eqs (7.7, 7.8) (with the parameters defined by Eqs (7.9–7.14)), Fröhlich and Gellermann (1987) [426] reviewed earlier attempts of groundwater dating using uranium isotopes. They found that the dating equations used in most of these studies (Table 7.3) represent special cases of Eqs (7.7, 7.8) for which the uranium isotope exchange between water and rock were neglected. As can be seen in Table 7.3, the uranium isotope results are often expressed by the  $^{234}\text{U}/^{238}\text{U}$  activity ratio (AR) and  $^{234}\text{U}$  excess ( $X$ ). With the notation used in Eqs (7.7, 7.8), it follows that:

$$\text{AR} = ^{234}\text{U}/^{238}\text{U} = a_4/a_8$$

$$X = ^{234}\text{U} - ^{238}\text{U} = a_4 - a_8$$

It should be noted that, apart from analytical solutions of the radionuclide transport equation, numerical solution techniques have also been used (e.g. Pearson et al. (1983) [425]). Such numerical solutions have certain advantages over analytical solutions if spatial variations of the hydraulic and geochemical properties of the aquifer systems are significant. Moreover, in order to simulate real field problems, transport in two or even three dimensions must be evaluated; this can only be realized with numerical techniques.

### 7.5.3. Identification of model parameters

In the following, the properties (behaviour) and values of the geochemical parameters that are incorporated in the model, are discussed.

### 7.5.3.1. Generalized dating equation and dating range

Model Eqs (7.7–7.14) indicate that groundwater age can be derived from uranium isotope measurements provided that the parameters quantifying water–rock exchange processes are known for the given aquifer system. Combining Eqs (7.7, 7.8), it follows that:

$$\tau = \frac{1}{R\lambda_4} \ln \left( \frac{a_8 - a_{8s}}{a_4 - a_{4s}} \times \frac{a_{40} - a_{4s}}{a_{80} - a_{8s}} \right) \quad (7.15)$$

This equation shows that groundwater dating with uranium isotopes requires knowledge (determination) of the uranium retardation factor and the initial and stationary activity concentrations of both isotopes. It should be noted that in deriving this relationship the precipitation rate has been eliminated, recognizing that precipitation is an element specific rather than isotope specific process. Figure 7.5 illustrates the dating range that can be covered under favourable conditions, in particular for those cases where the  $^{238}\text{U}$  activity concentration is found to be constant along the studied groundwater flow path (negligible precipitation).

For the sake of simplicity, Fig. 7.5 assumes that the stationary value of the  $^{234}\text{U}$  activity concentration is zero. Using the error propagation law, the relative error of the model age  $\frac{d\tau}{\tau}$  has been calculated: re-arranging Eq. (7.8), replacing  $\kappa_4$  by  $K_4$  and neglecting  $p$  and  $a_s$ , it follows that:

$$\frac{d\tau}{\tau} = \frac{da_4/a_{40}}{R\lambda_4\tau} \sqrt{1 + \exp(2R\lambda_4\tau)}$$

where  $da_4/a_{40}$  is the relative analytical error of the uranium isotope measurement.

Fig. 7.5 clearly shows that the dating range depends on the analytical accuracy and on the retardation factor. If the dating range is defined as the age range for which the relative error of the uranium isotope model age is lower than 25%, then Fig. 7.5 shows that for  $R = 1$  the dating range is from about 50 to 1000 ka, while for  $R = 5$  this range goes from about 10 to 200 ka. Therefore, Fig. 7.5 clearly demonstrates that the retardation factor is a key parameter that controls the dating range. If there

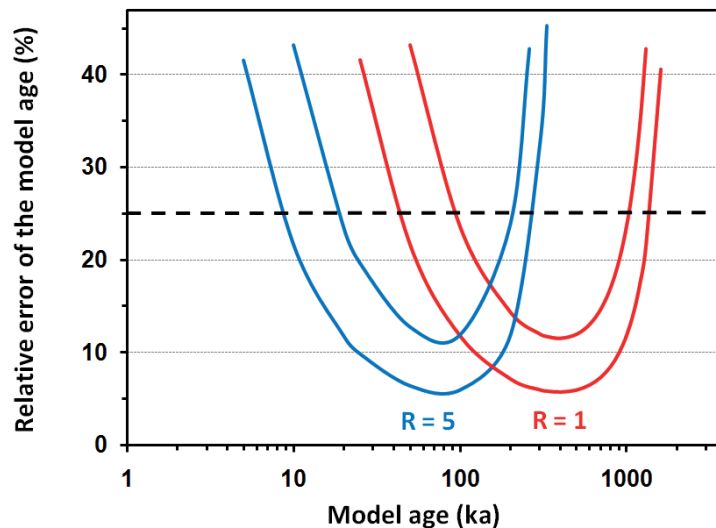


FIG. 7.5. Characterization of the uranium isotope dating range (see text). The red curves correspond to a retardation factor of  $R = 1$  and the blue curves  $R = 5$ . The curves have been calculated assuming a relative analytical error of the uranium isotope measurement  $da_4/a_{40}$  of 2% (lower red and blue curves) and 4% (upper red and blue curves), respectively.

is a retardation factor  $>1$ , the uranium isotope dating range may overlap the one of  $^{14}\text{C}$  dating and, in this way, fill the gap between the upper limit of  $^{14}\text{C}$  and the lower limit of  $^{36}\text{Cl}$  and  $^{81}\text{Kr}$  dating.

### 7.5.3.2. Retardation factor

First of all, it should be noted that the retardation factor  $R$  is relevant to all radiometric dating methods: conservative radionuclides ( $^3\text{H}$ ,  $^{81}\text{Kr}$ ) can be subject to retardation in groundwater of fractured rocks because of the double porosity ( $n_i/n$  in Eq. (7.4)); non-conservative radionuclides (such as  $^{14}\text{C}$ , uranium and radium isotopes) are subject to sorption/desorption processes and, thus, to retardation in all rock types (Eq. (7.4)). Garnier (1985) [164] concluded from  $^{14}\text{C}$  field studies that “the interaction between  $^{14}\text{C}$  species (in the mobile and immobile phases) make ages obtained by  $^{14}\text{C}$  overestimated”. The  $K_d$  value defining the effect of sorption processes on the radionuclide retardation (Eq. (7.4)) can be determined by laboratory experiments. However, deviations between laboratory and field results may occur due to differences between laboratory and field conditions. For example, Fjeld et al. (2001) [490] in laboratory experiments with aquifer rocks found a uranium retardation factor of 30. Porcelli and Swarzenski (2003) [404] noticed that this value was different from values derived from field study and attributed this difference to “difficulties of using laboratory data as an average for the larger scales of the aquifer or limitations of the mathematical model that was applied to the field data”. Pearson et al. (1983) [425] estimated, from  $^{14}\text{C}$  and uranium isotope data of the Carrizo sandstone aquifer, a uranium retardation factor of 30. For a Permian–Triassic sandstone, Ivanovich et al. (1991) [422] found considerably higher values of  $0.8\text{--}7 \times 10^3$ . Given the variability of the retardation factor values, it is essential to determine this parameter for the groundwater formation of interest. In the following, examples of the determination of the retardation factor will be discussed; further practical aspects will be included under Section 7.6.

Constant  $^{238}\text{U}$  activity concentrations under reducing conditions suggest that leaching and precipitation are negligible and that any increase of  $^{234}\text{U}$  can be attributed to recoil ejection. A typical example is shown in Fig. 7.6, where at an almost constant  $^{238}\text{U}$  value along a flow path in the reducing part of a sandstone aquifer the  $^{234}\text{U}$  activity concentration increases remarkably with the  $^{14}\text{C}$  piston flow model age as suggested by Eq. (7.8). The  $^{14}\text{C}$  ages were determined without geochemical adjustment

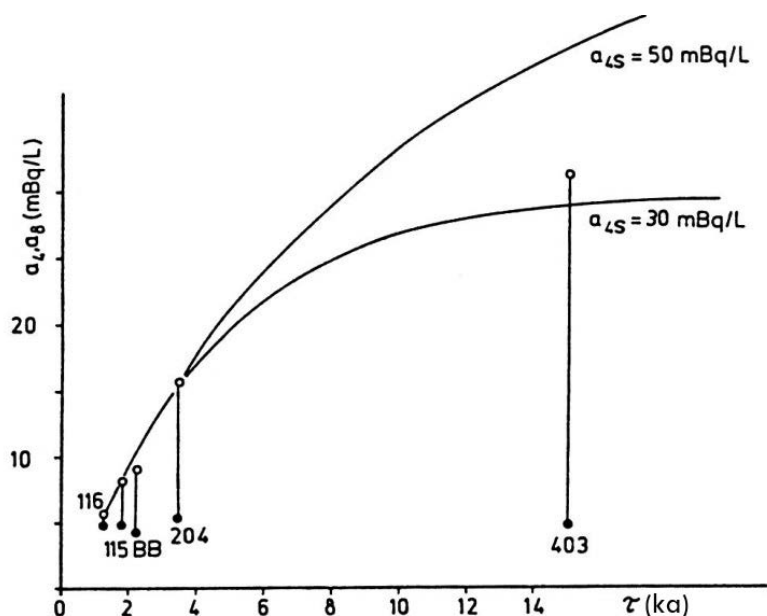


FIG. 7.6. Activity concentration of  $^{238}\text{U}$  ( $\bullet$ ) and  $^{234}\text{U}$  ( $\circ$ ) as a function of the  $^{14}\text{C}$  model age in the reducing zone of a Triassic sandstone aquifer in Thuringia, Germany (from Fröhlich et al. (1984) [421]).

of the  $^{14}\text{C}$  initial concentration. Fitting the measured to the calculated data (Eq. (7.5)),  $K_4$  has been determined:  $K_4 = (1.1 - 2.4) \times 10^{-4}/\text{a}$ . Given that precipitation is negligible, from Eq. (7.11) it follows that the retardation factor is between about 40 and 80. This result is in rather good agreement with the one found by Pearson et al. (1983) [425] for the Carrizo sandstone aquifer, and it underlines that, under reducing conditions, the ‘effective decay constant’  $K_4$  can be about one order of magnitude higher than the radioactive decay constant, i.e. the ‘effective life time’ of  $^{234}\text{U}$  in the investigated groundwater can be accordingly shorter than the radioactive lifetime of  $^{234}\text{U}$  of  $1/\lambda_4 = 3.54 \times 10^5$  a.

### 7.5.3.3. Precipitation rate

Although the dating formula (Eq. (7.15)) does not explicitly include the precipitation rate, knowledge of this parameter is important. If its value is of the same order of magnitude or even higher than the radioactive decay rate of  $^{234}\text{U}$ , groundwater dating with uranium isotopes becomes a geochemical rather than a radiometric dating method (see Eq. (7.11)). An approach to determine the precipitation rate is demonstrated in Figs 7.7(a) and 7.7(b), where the relationship between  $^{234}\text{U}$  and  $^{238}\text{U}$  is shown; this has been calculated with Eqs (7.7, 7.8) for given ratios between stationary and initial concentrations of both uranium isotopes. It can be seen that with increasing removal rate  $r = (n_v/n)p/R$ , the curves come close to a straight line. Furthermore, a concave curve shape indicates an increase in uranium isotope concentrations along the flow path (Fig. 7.7(a)); when concentrations decrease, the shape is convex (Fig. 7.7(b)).

A practical example of the diagrams in Fig. 7.7 is provided by the  $^{234}\text{U}$ – $^{238}\text{U}$  diagrams in Fig. 7.8, where the uranium isotope data of the Hosston aquifer (Kronfeld (1971) [486]) are plotted together with trend lines calculated for different values of the parameter  $r$ . The data appear to fit trend lines with  $r \geq 2\lambda_4$ , i.e. precipitation may not be negligible in these aquifer sections. Overall, trend line analysis appears to be an important approach to constrain precipitation effects as well as initial and stationary uranium isotope concentration. Typical values of the parameter  $r$  derived from earlier uranium isotope

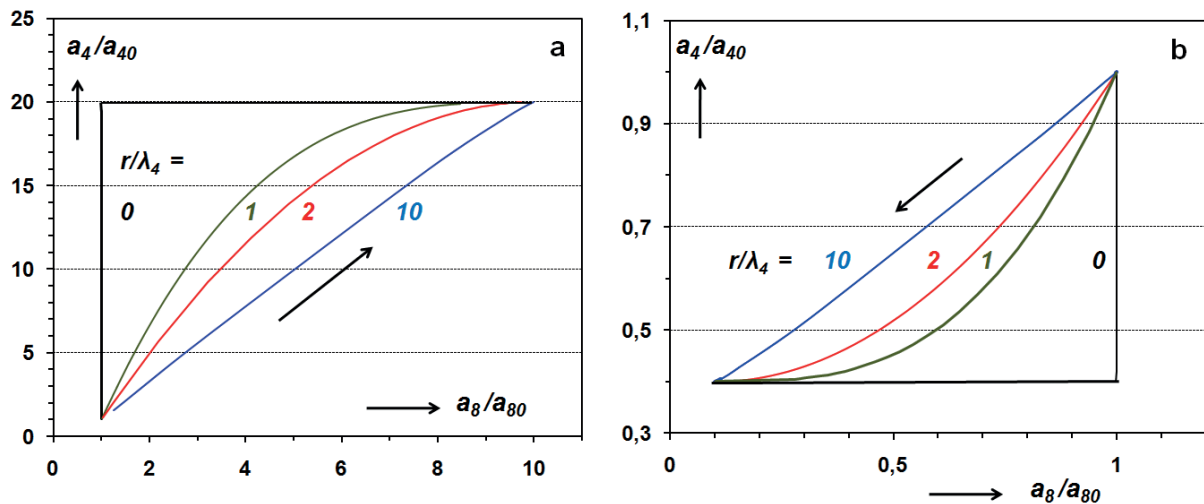


FIG. 7.7. Uranium isotope evolution along a flow path at given ratios between saturation and initial concentrations:  $a_4/a_{40} = 20$ ;  $a_8/a_{80} = 10$  (a) and  $a_4/a_{40} = 0.4$ ;  $a_8/a_{80} = 0.1$  (b) (see text for a definition of  $r/\lambda_4$ ).

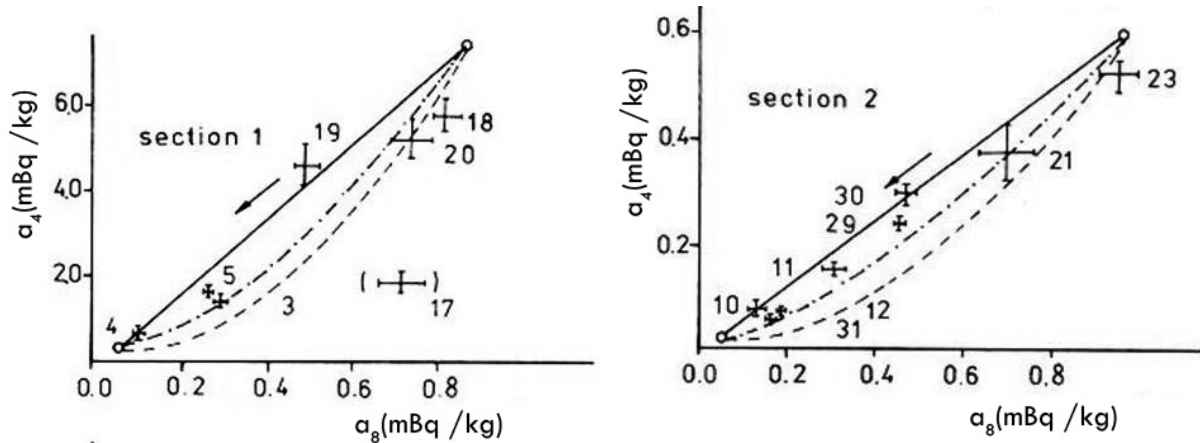


FIG. 7.8. Uranium isotope evolution in the Hosston aquifer (Sections 1 and 2) and theoretical trend curves for selected values of the removal rate  $r$ . Full line:  $r \gg \lambda_4$ ; dot dashed line:  $r = 2\lambda_4$ ; broken line:  $r = \lambda_4$  (after Fröhlich and Gellermann (1987) [426]).

studies by this approach range from about  $10^{-6}$  to  $10^{-4} \text{ a}^{-1}$  (Fröhlich and Gellermann (1987) [426]). Thus, irreversible uranium precipitation cannot a priori be disregarded in uranium isotope groundwater dating.

#### 7.5.3.4. Leaching and recoil ejection

Under oxidizing conditions, the recoil ejection of  $^{234}\text{U}$  appears to be negligible compared to leaching because of the very low  $^{234}\text{U}$  decay rate (Eq. (7.13)). Such conditions usually exist in the shallow unconfined part of an aquifer system in which the groundwater age is comparatively short, so that  $K_4\tau \ll 1$  can be assumed. Thus, from Eqs (7.7, 7.8), it follows that the activity of  $^{238}\text{U}$  ( $^{234}\text{U}$ ) increases in proportion to groundwater age, where the proportional factor is the leaching terms  $e_8 a_{8r}/n$  and  $e_4 a_{4r}/n$ , respectively. In fact, combined  $^{14}\text{C}$  and uranium isotope measurements in the unconfined part of a Triassic sandstone aquifer in Thuringia, Germany, have shown a linear increase in the activity of both uranium isotopes with slopes  $e_8 a_{8r}/n = 0.1 \text{ mBq} \cdot \text{L}^{-1} \cdot \text{a}^{-1}$  and  $e_4 a_{4r}/n = 0.15 \text{ mBq} \cdot \text{L}^{-1} \cdot \text{a}^{-1}$  (Fröhlich et al. (1984) [421]). With typical values of  $a_{8r}/n \approx a_{4r}/n$  for sandstone of this aquifer, the following values have been found:  $e_8 \approx 0.2 \times 10^{-6}/\text{a}$  and  $e_4 \approx 0.4 \times 10^{-6}/\text{a}$ . The higher value for  $^{234}\text{U}$  is attributed to preferential leaching.

For the reducing part of this aquifer, the stationary value of  $^{234}\text{U}$  was estimated to be in the range of 30 to 50 mBq/L (Fig. 7.6), and for the 'effective decay rate' a value of  $K_4 = (1.1-2.4) \times 10^{-4}/\text{a}$  was obtained (see also Section 7.5.3.2). Finally, with Eq. (7.13), it follows for the recoil ejection term that  $\gamma\lambda_4 a_{8r}/n \approx a_{4s} \times K_4 \approx (3-12) \times 10^{-3} \text{ mBq} \cdot \text{L}^{-1} \cdot \text{a}^{-1}$ . Thus, the recoil ejection rate for  $^{234}\text{U}$  appeared to be about one to two orders of magnitude lower than the leaching rate under oxidizing conditions.

#### 7.5.3.5. Summary

The retardation effect is relevant to all radiometric dating methods. Retardation affects dating with conservative radionuclides ( $^3\text{H}$ ,  $^{81}\text{Kr}$ ) in fractured rocks owing to double porosity ( $n_t/n$  in Eq. (7.4)) and affects non-conservative radionuclides ( $^{14}\text{C}$ , uranium and radium isotopes) in all aquifer rocks owing to reversible water-rock exchange.

Given the observed variability of the retardation factor, it is essential to determine the uranium retardation for each location of interest. Reliable values for the retardation factor of uranium should be derived from field (rather than laboratory) studies that include the use of other dating tools, for

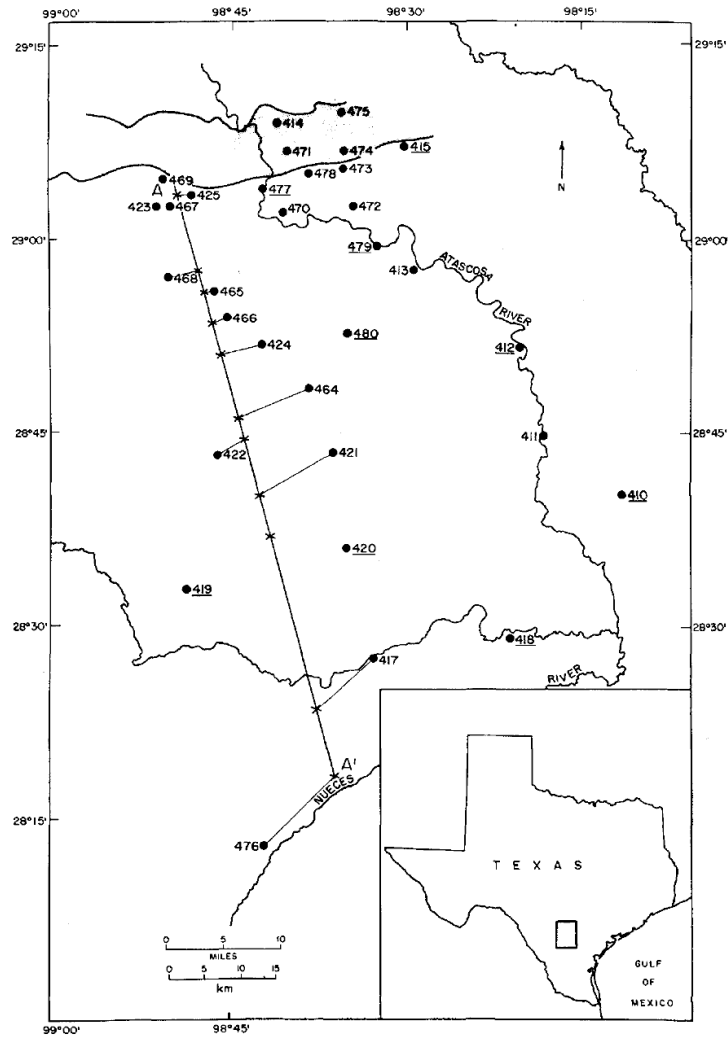


FIG. 7.9. The study area in southern Texas. The Carrizo sandstone dips gently towards the south–southeast. A–A' is the line of the cross-section of Fig. 7.10. The projections of sample points onto this line are made parallel to the strike of the formation. An underlined sample number, such as 410, indicates that no uranium data are available for that location (from Cowart and Osmond (1974) [419]).

example,  $^{14}\text{C}$  dating of the upstream section of the aquifer flow, where the relatively young groundwater is amenable to  $^{14}\text{C}$  dating.

Analysis of uranium isotope trend lines can help constrain values of the precipitation rate. Using data from earlier uranium isotope dating attempts, it has been shown that the precipitation rate,  $p$ , can be remarkably higher than the 'apparent decay rate',  $R\lambda_4$ ; i.e. under such conditions, uranium isotope dating would be a geochemical rather than a radiometric dating method (see Figs 7.7 and 7.8). More generally, it can be concluded that the study of trend lines ( $^{234}\text{U}$  as a function of  $^{238}\text{U}$  or the  $^{234}\text{U}/^{238}\text{U}$  ratio as a function of  $1/^{238}\text{U}$  (e.g. Osmond and Cowart (2000) [439])) are a prerequisite for any attempt to derive values of the groundwater age from uranium isotope measurements.

Oxidizing zones typically contain relatively young groundwater with ages below the dating range of uranium isotopes. However, measurements of uranium isotopes together with suitable dating tools, such as  $^{14}\text{C}$ , may be used to determine the leaching rates under field conditions, which may be relevant for other applications of uranium isotopes, in particular as natural analogues in connection with nuclear

waste disposal (IAEA (1989) [491]). Typical values of the leaching rate found for  $^{238}\text{U}$  and  $^{234}\text{U}$  are at about  $0.2 \times 10^{-6}/\text{a}$  and  $0.4 \times 10^{-6}/\text{a}$ , respectively.

Under reducing conditions, a steady increase of  $^{234}\text{U}$  activity concentration at constant  $^{238}\text{U}$  activity concentration can be attributed to the effect of recoil ejection. Characteristic activities have been found to range from  $3\text{--}12 \times 10^{-3} \text{ mBq} \cdot \text{L}^{-1} \cdot \text{a}^{-1}$  (IAEA (1989) [491]), which is about one to two orders of magnitude lower than the leaching rate under oxidizing conditions.

## 7.6. CASE STUDIES

There are numerous studies on the use of the uranium isotope disequilibrium to date old groundwater. Early attempts are summarized in Table 7.3. Here, the uranium isotope dating results of the Carrizo aquifer, USA are discussed and evaluation is made of recently published uranium isotope data of the Continentale Intercalaire aquifer, in the north-western Sahara. The discussion is aimed at demonstrating the potential and limitations of uranium isotope dating in practical applications. The uranium isotope studies of groundwater from the Milk River aquifer, Canada, are discussed in Chapter 11.

### 7.6.1. Carrizo sandstone aquifer, South Texas, USA

One of the earliest uranium isotope studies of old groundwater was related to the Carrizo sandstone aquifer, South Texas, USA (Cowart and Osmond (1974) [419]). The Carrizo formation is Eocene coastal plain sandstone which crops out nearly parallel to the coast and dips towards the Gulf of Mexico (Fig. 7.9). The Carrizo is a well confined aquifer with little leakage in or out of the sand; it was hydrogeologically and hydraulically well studied and had many observation wells for sampling.

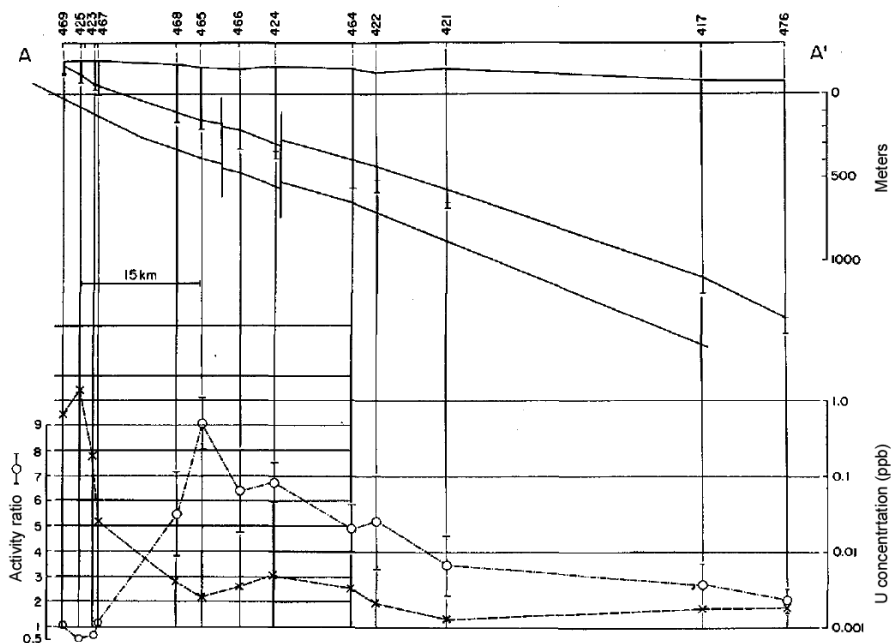


FIG. 7.10. Cross-section along A–A' of Fig. 7.7, showing the sample well locations relative to the dipping Carrizo aquifer (upper). The  $^{234}\text{U}/^{238}\text{U}$  activity ratios (linear scale on left) and the U concentration values (logarithmic scale on right) as a function of corresponding well positions (lower) (from Cowart and Osmond (1974) [419]).

Moreover, earlier  $^{14}\text{C}$  data were used to determine flow velocity and age of the groundwater (Pearson and White (1967) [492]).

The water of the Carrizo is of meteoric origin and infiltrates in the outcrop area under oxidizing conditions. The aquifer consists mainly of quartz sand with a thickness varying from about 180 m near the outcrop to ca. 400 m at a distance downdip of some 90 km (Fig. 7.10, upper part). In the outcrop region, relatively high uranium concentrations associated with low  $^{234}\text{U}/^{238}\text{U}$  ratios were found (Fig. 7.10, lower part), which is characteristic for oxidizing conditions. Somewhat downdip, a sharp decrease in the uranium concentration indicated a change to reducing conditions with strong uranium precipitation. Radioactive decay of the precipitated uranium at the grain surfaces associated with recoil ejection of the daughter nuclide  $^{234}\text{Th}$  were suggested to be the cause of increasing  $^{234}\text{U}$  excess and, thus, high activity ratios. The activity ratio reached a maximum of nine at about 33 km, and further downdip it decreased, while low  $^{238}\text{U}$  values remained comparatively constant. The boundary between low and high activity ratios was rather well defined.

Cowart and Osmond (1974) [419] ascribed this decrease in the activity ratio to radioactive decay of  $^{234}\text{U}$  excess  $X$  according to the relationship:

$$X_p = X_s + (X_0 - X_s)\exp(-\lambda_4 \tau) \quad (7.16)$$

where

$X_p$  is the observed  $^{234}\text{U}$  excess at any point;

$X_s$  is the steady state (stationary) excess;

$X_0$  is the initial excess;

$\tau$  is the time elapsed between the initial condition ( $X_0$ ) and the time of measurement ( $X_p$ );

$\lambda_4$  is the radioactive decay rate of  $^{234}\text{U}$ .

Replacing time,  $\tau$ , by the distance,  $x$ , down the flow direction  $\tau = x/v$ ,  $v$  = flow velocity, Eq. (7.16) corresponds to a straight line in a semi-logarithmic plot of  $(X_p - X_s)$  versus  $x$ , where the slope of the line is shown by  $\lambda_4/v$ . Figure 7.11 shows the plot of the measured data and the best fit line in

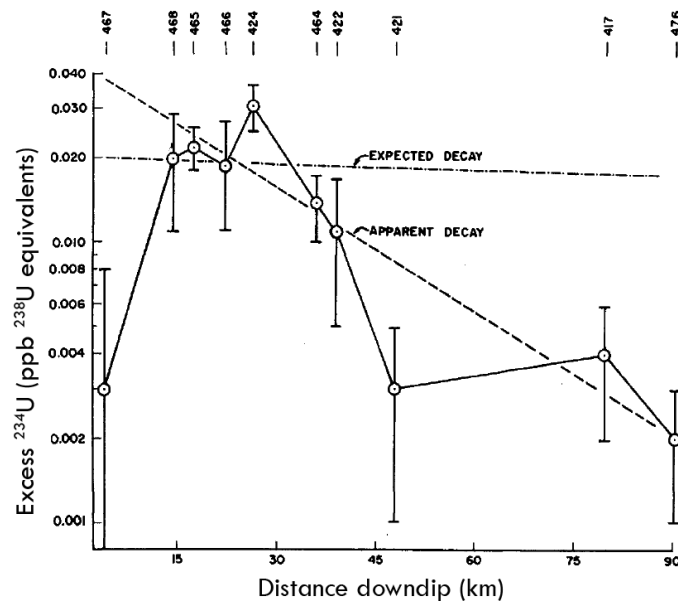


FIG. 7.11. Plot of  $^{234}\text{U}$  excess as a function of distance down the flow direction and in the direction of increasing water age. The dash dotted line has been drawn assuming a velocity of 150 cm/a and a radioactive decay of  $^{234}\text{U}$  excess from an initial value of 0.020 ppb ( $^{238}\text{U}$  equivalents). The broken line is the best fit to the data points and corresponds to an 'apparent flow velocity' of about 8 cm/a (from Cowart and Osmond (1974) [419]).

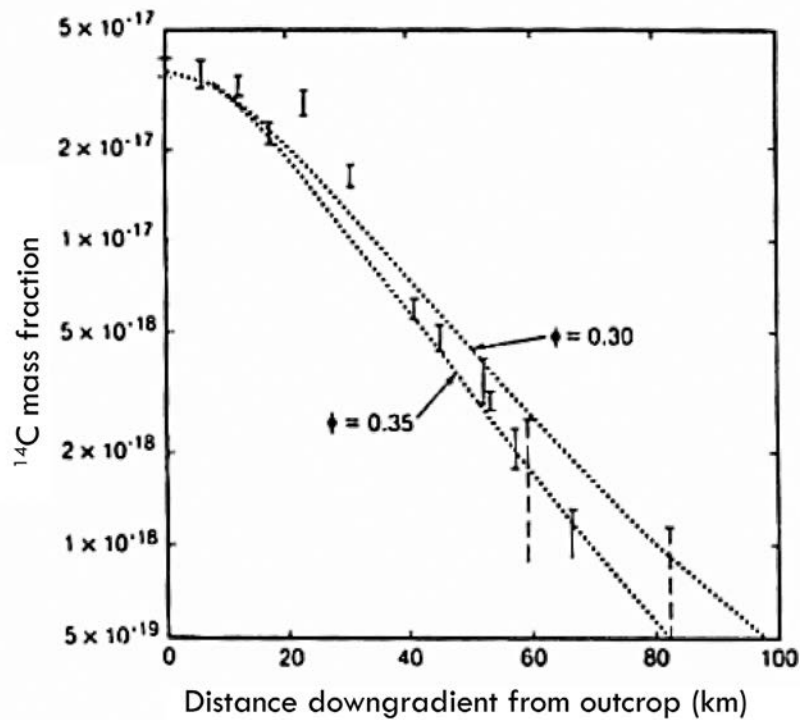


FIG. 7.12. Measured and simulated  $^{14}\text{C}$  contents with distance down gradient from outcrop (from Pearson et al. (1983) [425]).

a semi-logarithmic diagram. The slope of this line corresponds to an apparent flow velocity (also called ‘uranium migration velocity’) of less than 8 cm/a. However, hydrological estimates (Alexander and White (1966) [493]) and  $^{14}\text{C}$  dating (Pearson and White (1967) [492]) indicated a value of at least 150 cm/a, which is about 20 times higher.

Pearson et al. (1983) [425] followed up the evaluation of these  $^{14}\text{C}$  and uranium isotope data, using a groundwater flow and radionuclide transport model that incorporates water–rock exchange similar to Eq. (7.6). The solute transport equation (conservation of mass for one dimensional groundwater flow) was solved by a numerical technique, validated using the  $^{14}\text{C}$  data (Fig. 7.12) and then applied to simulate  $^{234}\text{U}$  and  $^{238}\text{U}$  movement in the reducing part of the Carrizo. Calculating the  $^{234}\text{U}/^{238}\text{U}$  ratio for several  $K_d$  values and comparing the simulated with the measured ratios, the authors were able to determine the best fit  $K_d$  value and, thus, the uranium retardation in the system.

Figure 7.13 demonstrates that uranium transport in the reducing zone down gradient of about 33 km in the Carrizo is best simulated using a  $K_d$  of 6.0. From Eq. (7.4), it follows with  $n_t \approx n = 0.35$  and  $\rho_r = 2.6 \text{ g/cm}^3$  (Pearson et al. (1983) [425]) that the retardation factor is 30, or that the uranium migration velocity in the Carrizo is only 1/30th of the flow velocity of groundwater movement. This result explains the disparity in the flow velocities of water and uranium found by Cowart and Osmond (1974) [419]. Their model (Eq. (7.16)) did not account for the reversible sorption of uranium in the Carrizo aquifer. However, it is interesting to note that the ratio between groundwater flow velocity derived from hydrological estimates and  $^{14}\text{C}$  determinations, and the velocity derived from the decrease of  $^{234}\text{U}$  excess was of the same order as the retardation factor obtained by Pearson et al. (1983) [425].

Overall, the Carrizo case study clearly demonstrates that, in sandstone aquifers, exchange between dissolved and adsorbed uranium may occur that retards the velocity of uranium movement relative to that of the water itself. Therefore, determination of the retardation factor through combined  $^{14}\text{C}$  and uranium isotope measurements in the upstream part of an aquifer (younger groundwater) can facilitate

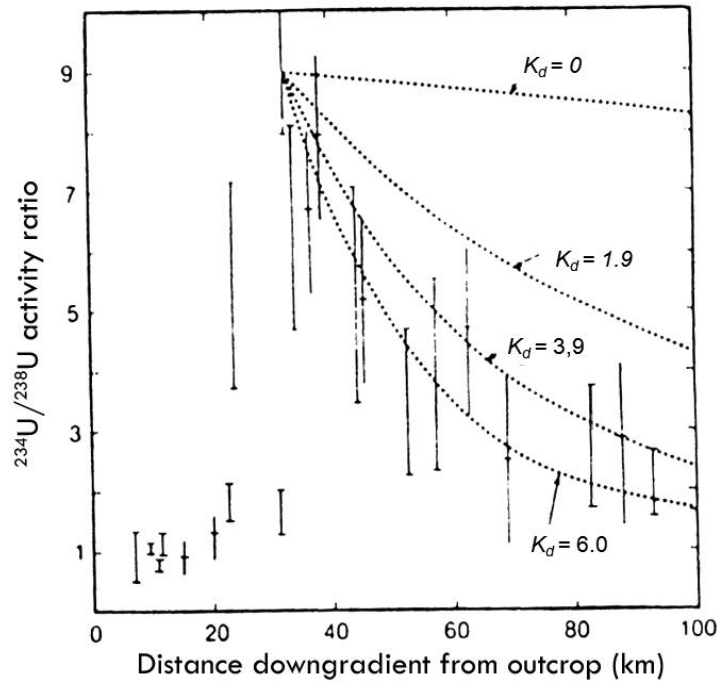


FIG. 7.13. Measured and simulated uranium activity ratios with distance down gradient from outcrop (from Pearson et al. (1983) [425]).

the use of uranium isotope dating downstream where the age of the groundwater is beyond the  $^{14}\text{C}$  dating range.

### 7.6.2. Continental Intercalaire aquifer, north-west Sahara

The Continental Intercalaire is one of the largest confined aquifer systems in the world. It is located in the north-western part of the Sahara and covers an area of some 600 000 km<sup>2</sup>. It occupies the continental formations of the Lower Cretaceous (Neocomian, Barremian, Aptian, Albian) and extends from the Saharan Atlas in the north to the Tassili mountains of the Hoggar in the south, and from western Algeria in the west to the Libyan desert in the east (Fig. 7.14). The depth of the aquifer roof is approximately 1000 m below the surface in the lower Sahara in the south and reaches 2000 m in the north in the region of the saline lakes of Chott Melrhir (Algeria) and Chott Djerid (Tunisia). There are three groundwater flow paths which all converge towards a single discharge zone in Tunisia (Chott Djérid/Chott Fejej region and Gulf of Gabès). The main flow path comes from the Saharan Atlas and reaches up to the Chott Djérid and the Gulf of Gabès in Tunisia (see lower part of Fig. 7.14).

The groundwater of the Continental Intercalaire aquifer system was subject to various isotopic investigations over the past 50 years (Edmunds et al. (2003) [494]; Edmunds et al. (1997) [495]; Gonfiantini et al. (1974) [496]; UNESCO (1972) [497]). Using radiocarbon as a dating tool, it was found that, except near outcrops, the radiocarbon ages are at or below the dating limit. First attempts to date the old Continental Intercalaire groundwater by  $^{36}\text{Cl}$  were published by Michelot et al. (1989) [498], followed in 1994 by additional sampling for  $^{36}\text{Cl}$ . Guendouz and Michelot (2006) [499] published all of their data and their evaluation in terms of groundwater age; values of up to 1 Ma were obtained. The first uranium isotope measurements of Continental Intercalaire groundwater were carried out by Chkir et al. (2009) [500] to study the variability of these isotopes in the aquifer system.

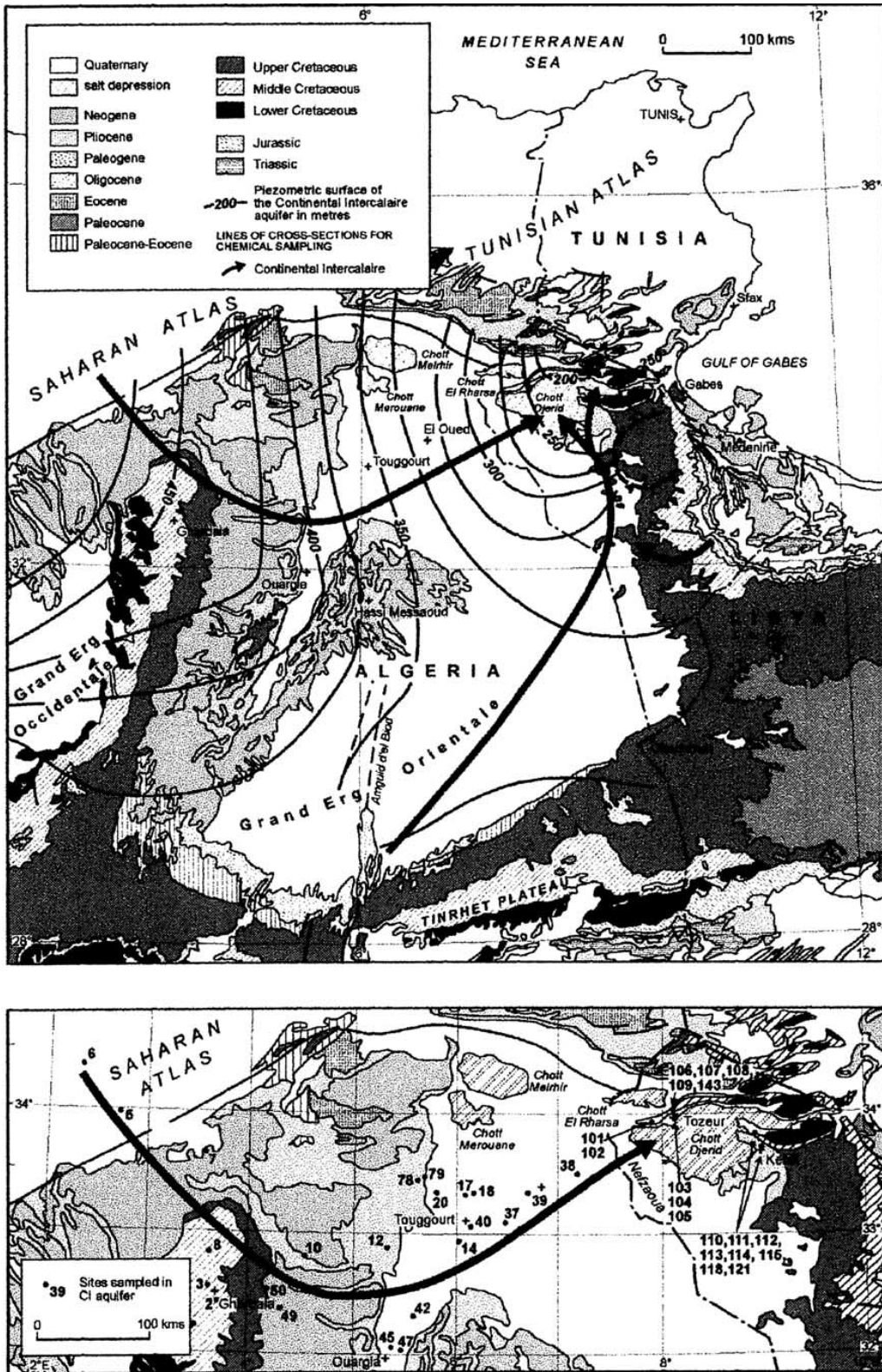


FIG. 7.14. The Lower Cretaceous outcrops forming the Continental Intercalaire aquifer system and its piezometric surface leading to discharge in the area of the Chotts of Tunisia. The lower part shows the sites chosen by Edmunds et al. (2003)[494] for sampling along the cross-section from the Saharan Atlas (Algeria) to the Tunisian Chotts (main flow path) (from Edmunds et al. (2003) [494]).

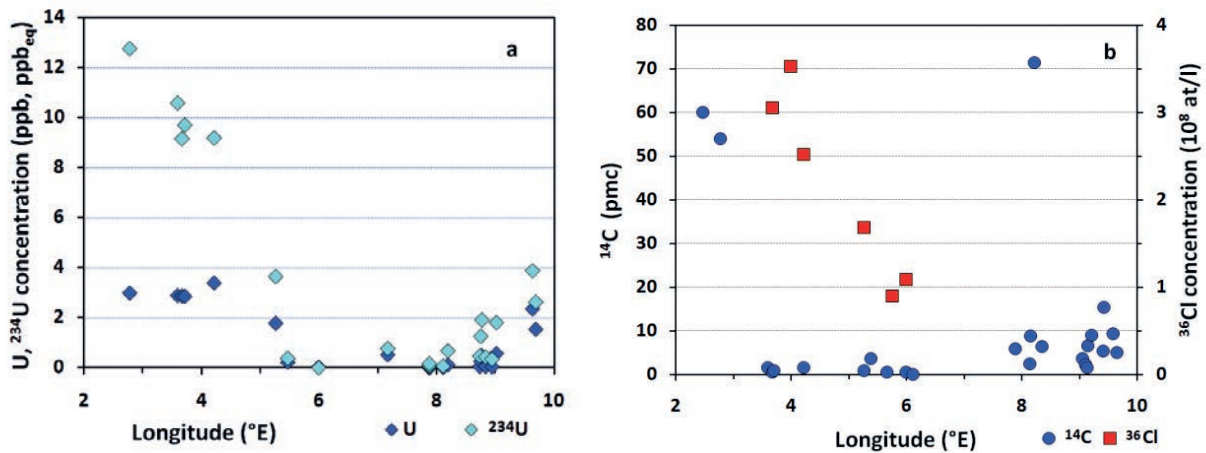


FIG. 7.15. Distribution of  $^{238}\text{U}$  and  $^{234}\text{U}$  (a), and of  $^{14}\text{C}$  and  $^{36}\text{Cl}$  (b) along the main flow path of the Continental Intercalaire from its outcrop to its discharge area (about 2°E to 10°E). It should be noted that in the given latitude region, a longitude difference of 1° corresponds to a distance of about 90 km.

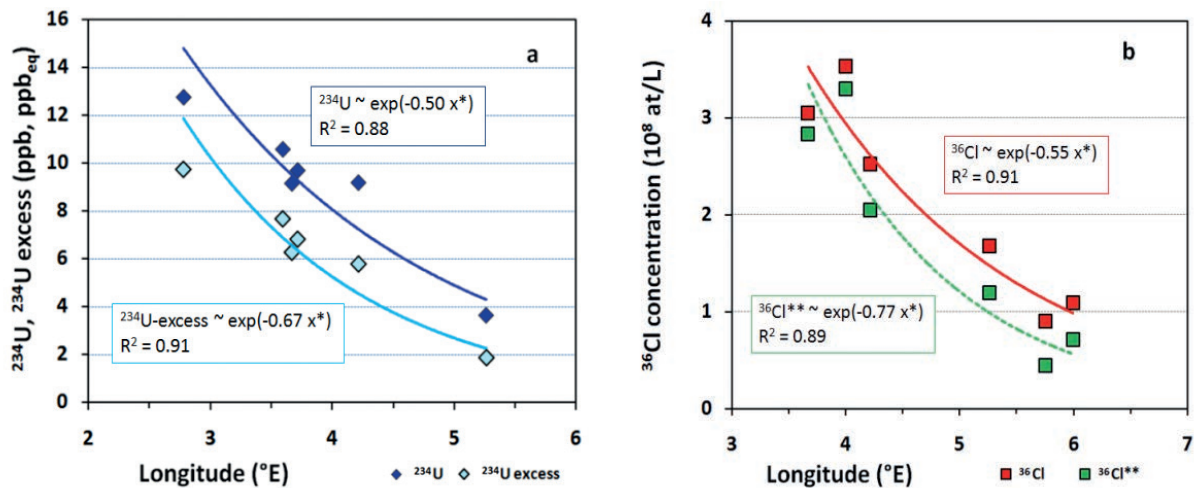


FIG. 7.16. Exponential regression lines fitting the uranium isotope and  $^{36}\text{Cl}$  data of the selected section along the main flow part: (a)  $^{234}\text{U}$  concentration and  $^{234}\text{U}$  excess concentration, (b)  $^{36}\text{Cl}$  concentration and  $^{36}\text{Cl}^{**}$  concentration corrected for in situ production equivalent to a stationary  $^{36}\text{Cl}/\text{Cl}$  ratio of  $5 \times 10^{-15}$ . It should be noted that  $x^*$  is the longitude (in °E) along the flow path. For the sake of simplicity, the curvature of the flow path (Fig. 7.14, lower part) has been ignored. Thus, a longitude difference of 1° is approximately equivalent to a flow path distance of 93 km.

In the following, the uranium isotope composition of groundwater from the Continental Intercalaire is examined to determine groundwater age. To this end, data available for the main flow path (region extending from 2°E to 10°E and 32°N to 34°N; see Fig. 7.14) were selected. The  $^{14}\text{C}$  and  $^{36}\text{Cl}$  data of this region (Edmunds et al. (2003) [494]; Guendouz and Michelot (2006) [499]) are also examined in terms of groundwater age.

Figure 7.15(a) shows that the uranium concentration remains nearly constant from about 2.5°E to about 4.5°E from where it rapidly decreases to about 0 ppb. This abrupt decrease matches the sudden increase in the Fe concentration (Edmunds et al. (2003) [494]) which indicates that the groundwater becomes reducing. Therefore, the decrease of  $^{234}\text{U}$  at nearly constant  $^{238}\text{U}$  can be attributed to radioactive decay of  $^{234}\text{U}$ . Except near outcrop, where  $^{14}\text{C}$  indicates Holocene groundwater,  $^{14}\text{C}$  is virtually absent (Fig. 7.15(b)) and, thus, the groundwater age is beyond the  $^{14}\text{C}$  dating range. It should, however, be

TABLE 7.4. COMPILATION OF THE DATING RESULTS ESTIMATED ON THE BASIS OF URANIUM ISOTOPE AND <sup>36</sup>Cl MEASUREMENTS OF GROUNDWATER OF THE CONTINENTAL INTERCALAIRE

Dating method	$v/R$ (m/a)	$v$ (m/a)	age <sup>a</sup> (Ma)
<sup>234</sup> U	0.53		0.94
<sup>234</sup> U excess	0.39		1.3
<sup>36</sup> Cl		0.39	1.3
<sup>36</sup> Cl** (in situ production)		0.28	1.8

<sup>a</sup> At a distance of 500 km from the outcrop.

noted that downstream of about 8°E the <sup>14</sup>C values increase above the detection limit. This behaviour, also replicated by the uranium isotope concentrations, can be associated with the convergence of all Continental Intercalaire groundwater flowlines near the Tunisian Chotts between about 8°E and 9°E (Edmunds et al. (2003) [494]). In particular, the higher <sup>14</sup>C values point to a second recharge area located in the Dahar uplands in southern Tunisia (Edmunds et al. (1997) [495]). Therefore, only uranium isotope and <sup>36</sup>Cl data from about 3°E to 7°E along the main flow path appear to be suitable for estimating the groundwater flow velocity (age).

Since uranium and <sup>234</sup>U stationary values approach zero (Fig. 7.15(a), from about 5.5°E to 7.5°E), a simple exponential decrease can be assumed for <sup>234</sup>U as well as <sup>234</sup>U excess which, according to Eqs (7.7–7.14), should be proportional to  $\exp(-R\lambda_4\tau)$ , where  $\tau = x/v$ . In fact, Fig. 7.16(a) suggests that the data fit an exponential function reasonably well. Similarly, <sup>36</sup>Cl values can be fitted to an exponential function  $\exp(-\lambda_{36}\tau)$ . Apart from the directly measured <sup>36</sup>Cl values, the evaluation also includes <sup>36</sup>Cl values corrected for in situ production (<sup>36</sup>Cl\*\*, Fig. 7.16(b)). A ‘reasonable’ value for the situ production was assumed that corresponded to a stationary <sup>36</sup>Cl/Cl ratio of  $5 \times 10^{-15}$ . From the coefficients of the exponential functions given in Figs 7.16(a) and 7.16(b) and the decay constants of <sup>234</sup>U and <sup>36</sup>Cl, groundwater flow velocity was estimated. The results compiled in Table 7.4 show that the flow velocity estimated by <sup>36</sup>Cl is lower than the one derived from <sup>234</sup>U and <sup>234</sup>U excess. Thus, the uranium retardation appears to be negligible ( $R = 1$ ). Given the uncertainties inherent in the approach, it can be concluded that the estimated flow velocities overlap. Consequently, the uranium isotopes have provided estimates of groundwater flow velocity and ages which are close to the ones derived from <sup>36</sup>Cl.

## 7.7. SUMMARY

Old groundwater typically occurs under reducing conditions in deep aquifer formations where, in addition to radioactive decay, processes of reversible sorption (retardation factor), irreversible precipitation (precipitation rate) and recoil ejection may affect the evolution of uranium isotopes. So far, attempts to date old groundwater using uranium isotopes have only been of limited success, mainly because of the inappropriate modelling that did not match the geochemical conditions in the studied aquifers. This chapter has provided evidence that any dating model must take full recognition of water–rock interaction processes controlling the behaviour of the uranium isotopes in groundwater.

Favourable conditions for groundwater dating exist where uranium (<sup>238</sup>U) concentration along a given section of the groundwater flow is constant (but  $\neq 0$ ), so that irreversible precipitation of uranium can be assumed to be negligible. In these cases, the only remaining unknowns are retardation factor and the stationary value of <sup>234</sup>U. The latter parameter can be determined by extrapolation of the <sup>234</sup>U trend (‘evolutionary trend’) along the flow path. The retardation factor can be determined by combining

uranium isotope dating with an independent dating method, for example,  $^{14}\text{C}$  dating of groundwater in the upstream region of the flow path (as in the case of the Carrizo aquifer) or  $^{36}\text{Cl}$  dating (as in the case of the Continental Intercalaire aquifer). In this context, it should also be noted that determination of uranium isotope geochemical parameters such as precipitation rate and retardation factor are highly relevant for the use of uranium isotopes as natural analogues in assessment of nuclear waste disposals (IAEA (1989) [491]).

The discussion of the Carrizo case study has shown that in sandstone aquifers exchange between dissolved and adsorbed uranium may occur, retarding the movement of uranium relative to the water. This retardation causes a faster decrease of  $^{234}\text{U}$  (see Eq. (7.11)) than expected from pure radioactive decay of  $^{234}\text{U}$  and, thus, results in an accordingly older ' $^{234}\text{U}$  based age' than the age of the groundwater itself. Assuming that in the upstream part of the aquifer, which is amenable to  $^{14}\text{C}$  dating, the flow velocity derived from  $^{14}\text{C}$  data represents groundwater velocity, the retardation factor (ratio of groundwater velocity and uranium migration velocity) can be determined. In the case of the Carrizo aquifer, the estimated value was about 30 and, thus, considerably higher than that derived from the Continental Intercalaire aquifer where uranium retardation was found to be negligible (retardation factor = 1). For this aquifer, flow velocities derived from  $^{36}\text{Cl}$  data and the one determined by uranium isotope data show fairly good agreement (Table 7.4).

Although the interpretation of uranium isotope data in terms of groundwater age is not an easy task, this method shows potential for playing an important role within the concerted application of techniques to date old groundwater. Depending on the geochemistry of the aquifer system, the potential dating range extends from about 10 ka up to 1 Ma, which overlaps the  $^{14}\text{C}$  and the  $^{36}\text{Cl}/^{81}\text{Kr}$  dating range. Uranium isotopes can provide independent information relevant to groundwater age that complements other dating approaches and may help to resolve ambiguities in data interpretation. Moreover, uranium isotopes in groundwater have the potential to quantify geochemical parameters of the water–rock interaction and represent natural analogues for radioactive waste. Any multitracer application to date old groundwater should integrate uranium isotope measurements which can easily be afforded by the use of modern mass spectrometric techniques.



## Chapter 8

### HELIUM (AND OTHER NOBLE GASES) AS A TOOL FOR UNDERSTANDING LONG TIMESCALE GROUNDWATER TRANSPORT

T. TORGERSEN  
Department of Marine Sciences,  
University of Connecticut,  
Groton, Connecticut,  
United States of America

M. STUTE  
Barnard College and Lamont Doherty Earth Observatory,  
Columbia University,  
Palisades, New York,  
United States of America

#### 8.1. INTRODUCTION

Helium-4 is the alpha decay product from the radioactive decay of U–Th series elements that occur naturally in the Earth. As both U and Th have long half-lives in comparison to typically anticipated groundwater ages, the accumulation of  $^4\text{He}$  along a groundwater flow path has long been explored and evaluated as a groundwater dating tool. A simple age,  $\Delta t$ , can be defined in the following way:

$$\Delta t = \frac{\Delta C}{[\Sigma I]} \quad (8.1)$$

where

$\Delta C$  is the change in concentration of  $^4\text{He}$  with respect to an initial condition;  
 $\Sigma I$  is the sum of  $^4\text{He}$  inputs the groundwater parcel.

$\Delta t$  is usually called the  $^4\text{He}$  model age, which using certain assumptions under favourable conditions can be interpreted with respect to an idealized water age. It should then be possible to estimate, for example, flow velocities, provided there is some additional evidence that the suite of  $^4\text{He}$  samples is along a flowline. However, because  $^4\text{He}$  diffusion coefficients are higher than that of water, and because groundwater is an open system with regard to both locally produced  $^4\text{He}$  (which can accumulate or be lost) supplied on the grain scale as well as externally imposed sources and sinks for  $^4\text{He}$  which can exert influences on the kilometre scale, the methodology becomes considerably more complex. This paper presents the  $^4\text{He}$  methodology as a geochemical construct and then illustrates how such information can be interpreted and applied to problems of basin scale groundwater flow. The goal is to enable a valuable groundwater tracer ( $^4\text{He}$  and other noble gases) to be understood from a practical standpoint and interpreted in a realistic environment.

#### 8.2. THE GEOCHEMICAL CONSTRUCT FOR APPARENT $^4\text{He}$ TRACER AGES

Helium-4 is present in the atmosphere at levels of 5.24 ppm and is sparingly soluble in water (Ozima and Podosek (2002) [251]). As water accumulates near the water table, it equilibrates with soil gas (idealized as air) and acquires an initial concentration of  $^4\text{He}$ . When the vertical recharge

velocity of the groundwater isolates the water parcel from the atmosphere (e.g. the recharge velocity moves the water parcel away from the groundwater table faster than diffusion-like exchange can re-equilibrate the water parcel with the soil gas; Peclet number ( $v\Delta x/D > 1$ )), the water is initialized to a concentration of  $^4\text{He}$  controlled by the partial pressure of He at the water table, temperature, salinity and the dissolution of soil air bubbles due to water table fluctuations ('excess air'). For systems such as  $^{36}\text{Cl}$ , the assumption is that the water parcel then acts as a closed system and loses  $^{36}\text{Cl}$  through radioactive decay without mixing with other water parcels. The comparable assumption for  $^4\text{He}$  would be that radioactive decay of dissolved U–Th series elements produces alpha particles ( $^4\text{He}^{++}$ ) which then accumulate in the water parcel. However, for most systems, the contribution from dissolved phase U–Th series alpha decay is insignificant and the idealized geochemical construct must be altered to allow  $^4\text{He}$  sources from the solid phase (which changes as a function of time/space as determined by the groundwater flow velocity). The simplifying assumptions are that the solid phase composition and its porosity are homogeneous along the flow path. However, given this is an open system,  $^4\text{He}$  sources from outside the moving water parcel and outside the sample collection space ( $\Delta x\Delta y\Delta z$ ) can contribute to the accumulation of  $^4\text{He}$  within the water parcel. Thus, the calculation of a  $^4\text{He}$  model age for the water parcel is dependent upon specific knowledge of an open system for which the source and sink terms for  $^4\text{He}$  are known. Inadequate knowledge of the open system sources and sinks (potentially heterogeneous in time and space) will limit the interpretability or applicability of the  $^4\text{He}$  model age in addition to the conditions discussed above. Thus, the calculation of an appropriate  $^4\text{He}$  model age in a groundwater parcel is dependent upon the definition of a known initial condition, including:

- (a) Initial solubility equilibrium;
- (b) Excess air incorporated during the water table initialization process;
- (c) Possible gas loss (by, for example, bubble ebullition in situ);
- (d) Specific knowledge of the local, grain scale source strengths for  $^4\text{He}$  in the solid phase (which is changing as the water parcel moves) and how such sources vary in time and space with:
  - The volume of solid phase associated with the water parcel (as determined by the porosity,  $\Phi = f(x,y,z,t)$ );
  - Direct release of alpha particles from the solid phase (which may vary in space and time) to the fluid phase;
  - Diffusive release of solid phase, accumulated  $^4\text{He}$  and its variability over time/space;
  - Weathering release of solid phase, accumulated  $^4\text{He}$  and its variability over time/space by the dissolution of the solid phase during chemical reaction (a function of  $x,y,z,t$ );
  - Mechanically or thermally induced fracturing and subsequent diffusion of solid phase, accumulated  $^4\text{He}$  to the pore space (this term is applicable on both the microscale and the macroscale);
  - Specific knowledge of the external sources (and loss terms) for  $^4\text{He}$  to the pore space groundwater and how such external sources (and loss terms) vary with time/space including:
    - Fluxes across local aquifer/aquitard boundaries (sources and losses);
    - Sources from fluxes that permeate the crust and degas to the atmosphere;
    - Magma based sources as evidenced by excess  $^3\text{He}$  attributable to mantle sources and the  $^4\text{He}$  that accompanies such a source;
    - Tectonically controlled  $^4\text{He}$  fluxes and their variability that induce  $^4\text{He}$  fluxes as a result of extension, intrusion, volcanism and basin deformation.

The above forms a conceptual outline for the following discussion. As a part of the discussion, it will become apparent that calculation of a  $^4\text{He}$  model age requires measures of gases in addition to  $^4\text{He}$  (e.g. Ne,  $^{36}\text{Ar}$ , Kr, Xe,  $\text{N}_2$ ), some of which can also be used to provide temporal constraints with differing sensitivities to sources, sinks and variability (e.g.  $^{40}\text{Ar}$ , fissionogenic  $^{136}\text{Xe}$ ,  $^{84}\text{Kr}$  and nucleogenic ( $\alpha, n$ ) $^{21}\text{Ne}$  and ( $n, \alpha$ ) $^3\text{He}$ ). Details about these other gases are provided elsewhere (Matsuda (1994) [501]; Ozima and Podosek (2002) [251]; Porcelli et al. (2002) [502]) and only those details especially pertinent to the discussion of  $^4\text{He}$  will be addressed. Information is also included on sampling

techniques, instrumentation and mass spectrometric constraints to enable intelligent negotiation when seeking collaborative  $^4\text{He}$  analyses.

### 8.3. SAMPLING AND ANALYSIS

#### 8.3.1. Sampling methods

Sampling groundwater for  $^4\text{He}$  requires collection of in situ water that is (i) not subject to gas loss by the sampling process and (ii) not subject to air contamination during the sampling process. Additionally,  $^4\text{He}$  diffuses through typical glass/plastic containers with/without special caps on a timescale (hours to weeks) that is typically incompatible with shipping samples to the laboratory and mass spectrometer analysis schedules. Helium-4 also diffuses through borosilicate glass on a timescale of hours to weeks even when closed by flame sealing (Suckow et al. (1990) [503]). Consequently, the traditional method for collecting  $^4\text{He}$  samples has been in  $\sim 1$  cm outer diameter crimped copper tubes (Weiss (1968) [504]). Soft refrigeration-type (dehydrated) copper tubing is used to avoid contamination by tritiogenic  $^3\text{He}$  and loss of gas (the crimping device creates a cold weld as opposing walls of the copper tube are pressed together). Such sampling devices are also suitable for other (non-reactive) gases although the volumes required for some gases may be larger, so multiple samples would need to be collected. In such cases, it is necessary to ensure that samples represent ‘duplicates’ of the groundwater and at least one gas should be measured in both sampling devices. Even for the case of He, Ne-only, replicate copper tube samples are often taken to evaluate the sampling procedure and the suitability of the well/borehole preparation.

The most common sampling approach for wells is to use a submersible pump connected via pressure tight tubing to a tee. One branch leads to an outflow that can be regulated and acts as a bypass. The other branch is connected to the copper tube with a clear piece of tubing and a needle valve on the other end. By adjusting the pump rate and the flow rates in the two outflows, it is usually possible to set the pressure in the copper tube to a level larger than the sum of the partial pressures of all dissolved gases to avoid degassing. The clear tube can be monitored for signs of bubbles, indicating leaks or degassing (for details, see, for example, <http://water.usgs.gov/lab/3h3he/sampling/>). Many old groundwaters are free of dissolved oxygen and a simple  $\text{O}_2$  measurement with a chemical kit or an  $\text{O}_2$  sensor can place an upper limit on contamination with atmospheric air during sampling. For wells with short screens, several bore volumes should be pumped out before a sample is collected. Wells with long screens should be packed-off at appropriate intervals to avoid cross-flow self-contamination (wellbore induced mixing). Alternatives to submersible pumps include borehole fluid samplers that can be used to retrieve water at depth (e.g. Kuster sampler (Solbau et al. (1986) [505])). If wells tap into artesian aquifers, flow at the surface is often sufficient to ensure a good sample but depressurization as water flows up the well may induce bubble formation which can strip gases from the fluid. As wellhead conditions are often not known before sampling and return visits are often not possible, backup sampling systems and variations on the sampling procedure are common, and creativity in the field is required.

Copper tube sampling has been shown to be robust and samples can be shipped with minimal concern and stored for considerable time prior to analysis. The most common shipping problem is loss of the crimped/exposed end of the copper tube which may lead to crimp failure and leakage of  $^4\text{He}$  or may create sample processing issues if one or both ends are lost (connection to vacuum processing line becomes difficult). As only the gas within the water parcel needs to be collected, some investigators have relied on gas only sampling in the field. Sanford et al. (1996) [506] describe a vacuum extraction technique. Sheldon (2002) [507] and Loose et al. (2009) [508] summarize techniques in which the dissolved gases are equilibrated with a sample host across a gas permeable membrane. After equilibrium is achieved, the sampler is removed and the equilibrium headspace in the sampler can be analysed. Sanford et al. (1996) [506] describe the use of a semi-permeable silicon tubing to sample for dissolved gases. Dyck and Silva (1981) [509], and Gascoyne and Sheppard (1993) [510] used ping-pong balls to collect gases for  $^4\text{He}$  analysis (but these cannot be stored for long periods and require

measurement in the field). Spalding and Watson (2006) [511] used silicon tubing attached to a syringe for sampling and direct injection of samples analysed for H<sub>2</sub>, O<sub>2</sub> and CO<sub>2</sub>. Gardner and Solomon (2009) [512] recently described a passive headspace diffusion sampler that maintains the total dissolved gas pressure. In cases where wells are not available or the specific yield of the formation is too small, rock samples have been collected and stored in evacuated stainless steel vessels. Over time (often weeks to months), gases dissolved in the pore fluids accumulate in the headspace and can subsequently be extracted for measurement (Ali et al. (2010) [513]; Osenbrück (1996) [514]; Osenbrück et al. (1998) [515]).

### 8.3.2. Laboratory processing methods

Typical extraction procedures for the laboratory involve attaching the free end of the crimped copper tube to the processing line, opening the crimp or container into an evacuated processing system, degassing of the water under vacuum (or vacuum boiling) and isolation of the extracted gases on the downstream side of a fine capillary (Rudolph (1981) [516]; Torgersen (1977) [517]). The capillary allows a large flow rate of water vapour so that gases of interest cannot effectively back-diffuse against the large scale advection of water vapour. The isolated gases are then cleaned of water vapour and unwanted gases (CH<sub>4</sub>, CO<sub>2</sub>, O<sub>2</sub>, etc.) with a series of traps that may retain gases (e.g. water vapour), adsorb gases or react gases to absorbable species (e.g. Smith and Kennedy (1983) [518]; Smith and Kennedy (1985) [519]). Gases are then quantitatively transferred into a sample container or directly into the mass spectrometer, originally by a toepler pump (Torgersen (1977) [517]), but now most commonly with a set of one or two cryogenically cooled traps used to accumulate the gases and separate the He/Ne fraction from the other gases. Reactive gases are removed using titanium (heated sponge or filament), Cu/CuO or alloy (ST101 or 707) getter pumps, either right after extraction and removal of water vapour; or after desorption from the cryogenic traps. Sample aliquots can be stored for analysis at a later time in all metal containers; or in flame sealed borosilicate (Ne, Ar, Kr, Xe), Corning 1720 or Pb (He) glass ampoules. The diffusion coefficients of He in these specific glasses are sufficiently low that samples can be stored for years at temperatures typically <0°C (depending on gas and glass type (Suckow et al. (1990) [503])). In recent years, more and more analysis systems have been automated, at least from the water sample extraction step onwards, which has improved the reproducibility of the measurements and the sample throughput.

### 8.3.3. Mass spectrometry

Helium-4 and noble gases are measured mass spectrometrically and require specialized machines with defined resolution. For helium, measurement of <sup>4</sup>He and <sup>3</sup>He are often necessary (identification of mantle sources and tritiogenic <sup>3</sup>He). Clear measurement of <sup>3</sup>He requires separation of the HD<sup>+</sup> peak from the <sup>3</sup>He<sup>+</sup> peak and, thus, machine resolution of over 630 is required. If only measures of <sup>4</sup>He are required, much simpler mass spectrometers can be employed and very high concentrations can be measured with gas chromatography. However, unless the field site and the problem are well determined, <sup>4</sup>He ‘dating’ in the research mode usually requires the use of a well equipped and specialized noble gas mass spectrometer which can produce (at a minimum) <sup>3</sup>He, <sup>4</sup>He, Ne, <sup>36</sup>Ar, <sup>40</sup>Ar, Kr and Xe measures. Measures of the complete noble gas suite aid in the definition of the initial condition and the recharge temperature. The better laboratories can additionally provide measures of <sup>20,21,22</sup>Ne (to potentially support <sup>4</sup>He model age times with nucleogenic Ne model ages); and Ar, Kr and Xe isotopes (to potentially support <sup>4</sup>He model ages with <sup>40</sup>Ar model ages as well as fissionogenic <sup>136</sup>Xe and <sup>84</sup>Kr model ages). A suite of noble gas isotopic measures is also important in the identification of mass dependent fractionation as an analytical problem. For analytical detail, the reader is referred to Bayer et al. (1989) [241], Beyerle et al. (2000) [276], Clarke et al. (1976) [242], Ludin et al. (1998) [520], Mamyrin and

Tolstikhin (1984) [521], Rudolph (1981) [516], Smith and Kennedy (1983) [518], Smith and Kennedy (1985) [519], Stute (1989) [522] and Torgersen (1977) [517].

#### 8.4. IDENTIFYING MULTIPLE $^4\text{He}$ COMPONENTS FROM MEASUREMENTS

The total  $^4\text{He}$  in a measured sample is a composite of  $^4\text{He}$  from multiple sources as well as sampling induced  $^4\text{He}$  additions and losses (e.g. degassing in situ or during sampling). These components can be generally expressed for any noble gas ( $^i\text{Ng}$ ) as:

$${}^i\text{Ng}_{\text{tot}} = {}^i\text{Ng}_{\text{eq}} + {}^i\text{Ng}_{\text{exc}} + {}^i\text{Ng}_{\text{rad}}^{\text{is}} + {}^i\text{Ng}_{\text{nuc}}^{\text{is}} + {}^i\text{Ng}_{\text{fiss}}^{\text{is}} + {}^i\text{Ng}_{\text{rad}}^{\text{terr}} + {}^i\text{Ng}_{\text{nuc}}^{\text{terr}} + {}^i\text{Ng}_{\text{fiss}}^{\text{terr}} + {}^i\text{Ng}_{\text{man}}^{\text{terr}} - \Sigma L \quad (8.2)$$

where the subscripts tot, eq, exc, rad, nuc, fiss and man indicate total (=measured), equilibrium with air, excess air, radiogenic, nucleogenic, fissiogenic (only relevant for Ne, Kr, and Xe) and mantle origin, which correspond to the various source (sum of inputs,  $\Sigma I$ ) terms as well as potential gas losses which are included as  $\Sigma L$  (sum of loss terms). All components marked 'is' (in situ) represent sources inside the water parcel (contained within a mobile  $\Delta x \Delta y \Delta z$ ), while those with 'terr' (terrigenic) have their origin outside.

For  $^4\text{He}$ , the rad term is U–Th series alpha decay and for  $^3\text{He}$  the rad term is  $^3\text{H}$  decay, often termed  $^3\text{He}_{\text{tri}}$ . Fissiogenic He is not relevant, and nucleogenic  $^3\text{He}$  is produced by the reaction  $^6\text{Li}(n, \alpha)^3\text{H}(\beta^-)^3\text{He}$ . He of mantle origin can often be found in areas affected by tectonic activity. The  $^3\text{He}/^4\text{He}$  ratio of radiogenic and mantle He is on the order of  $10^{-8}$  or  $10^{-5}$ , respectively. For He, separation of components in the total measured gas by a source/production process is easier than by origin (in situ or terrigenic). Additionally, the analysis must be able to recognize and correct for several gas loss,  $L$ , possibilities that presumably reduce each Ng component via equilibrium fractionation or bulk non-fractionating loss. Calculation of a  $^4\text{He}$  model age is based on in situ and terrigenic components.

##### 8.4.1. Equilibrium with air, $^4\text{He}_{\text{eq}}$

The  $^4\text{He}_{\text{eq}}$  is governed by the solubility of noble gases in water as a function of Henry's law. As solubility is a function of temperature, pressure and salinity, most calculations of  ${}^i\text{Ng}_{\text{eq}}$  are generalized from a limited suite of laboratory measurements. Weiss (1970) [523], Weiss (1971) [524], and Weiss and Kyser (1978) [254] provide empirical equations that yield solubility concentrations from air. Clever (1979) [525], Clever (1979) [526] and Clever (1979) [527] provide mole fraction solubilities which Aeschbach-Hertig et al. (1999) [302] have combined with the salting-out coefficients (Smith and Kennedy (1983) [518]) to provide solubilities as a function of pressure, temperature and salinity. Table 8.1 (after Kipfer et al. (2002) [528]) provides the equations by which to calculate noble gas solubilities.

It should be noted that calculation of  ${}^i\text{Ng}_{\text{eq}}$  requires the definition of an assumed recharge elevation and pressure. Additional assumptions are required with regard to changes in temperature and salinity that may occur along the flow path from recharge to the sampling point. It is often assumed that recharge occurs and  ${}^i\text{Ng}_{\text{eq}}$  is established at the mean annual temperature and pressure of the (assumed) recharge zone and that subsequent changes in temperature (as a result of heat gain along a geothermal gradient) have no impact on this initial equilibrium solubility. Changes in 'salinity' as a result of weathering and/or opening of fluid inclusions may also be assumed to have no impact on this initial equilibrium solubility. However, changes in salinity by mixing from different sources and/or halite dissolution cannot be viewed in such a simplistic sense: strong increases in salinity by halite dissolution were demonstrated to impact transport of noble gases (Suckow and Sonntag (1993) [529]). It is unknown to what extent mixing of waters impacts Ng concentrations versus the impacts that are the result of in situ increases in T and P. Some correlations between Cl and  $^4\text{He}$  could be the result of progressive NaCl addition by halite dissolution, whereas other changes in Cl could be the result of weathering and

The equilibrium concentrations of He, Ne, Ar and Kr can be calculated as:

$$C_{eq}^i = \exp\{t + t2(100/T) + t3 \ln(T/100) + t4(T/100) + S[s1 + s2(T/100) + s3(T/100)^2]\} \left( \frac{(ptot - ew)}{(pnorm - ew)1000} \right)$$

The equilibrium concentrations of Xe can be calculated as:

$$C_{eq}^{Xe} \exp[x1 + x2(100/T) + x3 \times \ln(T/100)] \times 0.00011 \times \exp[S(x4 + x5(100/T) + x6 \times \ln(T/100))]$$

Solubilities of <sup>3</sup>He and <sup>4</sup>He expressed as a function of the <sup>3</sup>He/<sup>4</sup>He ratio ( $R_{eq}$ ):

$$R_{eq} = 1.384 \cdot 10^{-6} [\exp((r1 + r2)/T + r3/T^2)(1 + r4S)]^{-1}$$

where

$C_{eq}^i, C_{eq}^{Xe}$  concentration of noble gas (cm<sup>3</sup> STP/g);  
 ptot, pnorm local and reference (1 atm) atmospheric pressure (atm);  
 ew water vapour pressure;  
 T, S water temperature (K) and salinity (g<sub>salt</sub>/kg).

The coefficients are given after Kipfer et al. (2002) [528].

TABLE 8.1. NOBLE GAS SOLUBILITIES

	Coefficient, i					
	$R_{eq}$	He	Ne	Ar	Kr	Xe
t1	—	-167.2178	-170.6018	-178.1725	-112.684	—
t2	—	216.3442	225.1946	251.8139	153.5817	—
t3	—	139.2032	140.8863	145.2337	74.469	—
t4	—	-22.6202	-22.629	-22.2046	-10.0189	—
s1	—	-0.044781	-0.127113	-0.038729	-0.011213	—
s2	—	0.023541	0.079277	0.017171	-0.001844	—
s3	—	-0.0034266	-0.0129095	-0.0021281	0.0011201	—
r1	-0.0299645	—	—	—	—	—
r2	19.8715	—	—	—	—	—
r3	-1833.92	—	—	—	—	—
r4	0.000464	—	—	—	—	—
x1	—	—	—	—	—	-74.7398
x2	—	—	—	—	—	105.21
x3	—	—	—	—	—	27.4664
x4	—	—	—	—	—	-14.1338
x5	—	—	—	—	—	21.8772
x6	—	—	—	—	—	6.5527

release of fluid inclusions (presumably rich in Cl). Ballentine et al. (2002) [530] provide a discussion of the background theory. Nonetheless, the isolation and quantification of  ${}^i\text{Ng}_{\text{eq}}$  and  ${}^4\text{He}_{\text{eq}}$  requires a suite of assumptions not all of which have been checked and not all of which can be checked. This is a theme that will continue.

#### 8.4.2. Excess ‘air’ components, ${}^4\text{He}_{\text{exc}}$

The creation of  ${}^4\text{He}_{\text{exc}}$  is the result of soil processes by which excess air is occluded in the recharge process and is eventually dissolved as pressure increases. Bulk dissolution of unfractionated air is one possibility that requires the use of an Ng tracer that is controlled primarily by dissolution of air (e.g. Ne) rather than in situ and external sources (e.g.  ${}^4\text{He}$ ). Early research used a definition of the Ne components in groundwater to define the excess air component of Ne which, for unfractionated air, could then be scaled to the  ${}^4\text{He}_{\text{exc}}$ , rewriting Eq. (8.2) for Ne:

$$\text{Ne}_{\text{tot}} = \text{Ne}_{\text{eq}} + \text{Ne}_{\text{exc}} - \sum L \quad (8.3)$$

and assuming no losses:

$$\text{Ne}_{\text{exc}} = \text{Ne}_{\text{tot}} - \text{Ne}_{\text{eq}} \quad (8.4)$$

This allows the excess  ${}^4\text{He}$  component to be calculated as:

$${}^4\text{He}_{\text{exc}} = \text{Ne}_{\text{exc}} \left( \frac{\text{He}}{\text{Ne}} \right)_{\text{air}} \quad (8.5)$$

As Ne solubility is the least temperature sensitive of the noble gases, such an assumption and calculation were tenable. However, this assumes that air is in excess and that its process of dissolution is non-fractionating and non-equilibrating. Cross-checking these assumptions with the noble gas suite has shown this to be oversimplified (Aeschbach-Hertig et al. (1999) [302]). Yet, in most cases, the  $\text{Ne}_{\text{exc}}$  component is less than 30% and, thus, the calculated  ${}^4\text{He}_{\text{exc}}$  is also small, especially considering that the  ${}^4\text{He}_{\text{terr}}$  and the  ${}^4\text{He}_{\text{rad}}$  are often orders of magnitude larger. As mass spectrometric measurement of  ${}^4\text{He}$  usually also acquires Ne, analytical costs can often be reduced by making these assumptions and acquiring He and Ne concentrations only.

If measures of the complete noble gas suite are acquired, such measures can be evaluated in terms of the palaeorecharge temperature that has found application in palaeoclimate research (Stute et al. (1995) [213]; Stute et al. (1995) [214]; Stute et al. (1992) [42]). Considerable research has been devoted to evaluating the  ${}^i\text{Ng}_{\text{exc}}$  component in order to best fit the  ${}^i\text{Ng}_{\text{eq}}$  components to a recharge temperature. Stute et al. (1995) [213] and Stute et al. (1995) [214] explored partial re-equilibration where an initial air bubble was dissolved and partial re-equilibration occurred by molecular processes across the water table. Peeters et al. (2002) [531] suggested the use of  ${}^{20}\text{Ne}/{}^{22}\text{Ne}$  ratios to test the partial re-equilibration model but where measures have been made, no significant diffusive fractionation of the isotopes has been uniquely identified. Kipfer et al. (2002) [528] propose a multistep re-equilibration model that would allow for large excess air (accommodated at pressure well beyond the water table). However, as multistep re-equilibration reduces to partial re-equilibration in the limiting case and the lack of evidence for diffusive fractionation of  ${}^{20}\text{Ne}/{}^{22}\text{Ne}$  (Peeters et al. (2002) [531]), such a model is also less than adequate. The closed system equilibration model (Aeschbach-Hertig et al. (2001) [532]; Aeschbach-Hertig et al. (1999) [302]; Aeschbach-Hertig et al. (2000) [55]; Peeters et al. (2002) [531]) appears to allow direct physical interpretation of the excess air component and its variance across the Ng suite in most cases. Direct verification of a mechanistic link between excess Ne and water table fluctuations is not available (Kipfer et al. (2002) [528]) but experiments with sand columns appear to support the basic

mechanistic possibilities (Holocher et al. (2002) [533]). A widely used Excel/Matlab routine can be downloaded from: [http://www.eawag.ch/organisation/abteilungen/wut/schwerpunkte/umweltisotope/methoden/interp\\_EN](http://www.eawag.ch/organisation/abteilungen/wut/schwerpunkte/umweltisotope/methoden/interp_EN)

### 8.4.3. Radiogenic production, ${}^4\text{He}_{\text{rad}}$

Radiogenic production via alpha decay of U–Th series elements creates  ${}^4\text{He}_{\text{rad}}$ . Other sources of  $\alpha$  particles (e.g. Nd decay) and  ${}^4\text{He}$  as a result of (n,  $\alpha$ ) interactions can be considered quantitatively insignificant. Under the assumption that U–Th series elements have reached radioequilibrium, the  ${}^4\text{He}$  production rate from rock can be expressed as:

$${}^4\text{He cm}^3 \text{ STP} \cdot \text{g}_{\text{rock}}^{-1} \cdot \text{a}^{-1} = J'_{\text{He}} = 0.2355 \times 10^{-12}([U](1 + 0.123([Th]/[U] - 4))) \quad (8.6)$$

$${}^4\text{He atoms} \cdot \text{g}_{\text{rock}}^{-1} \cdot \text{a}^{-1} = J_{\text{He}} = 2.688 \times 10^{19}(0.2355 \times 10^{-12}([U](1 + 0.123([Th]/[U] - 4))) \quad (8.7)$$

where [U] and [Th] are concentrations expressed in parts per million (Craig and Lupton (1976) [534]; Torgersen (1980) [535]).

For groundwater calculations, it is then necessary to quantify how much of this in situ production becomes available to the fluid phase. This has been generalized as a release factor  $\Lambda_{\text{He}}$  and the accumulation of  ${}^4\text{He}$  in the fluid phase can be calculated as:

$${}^4\text{He cm}^3\text{STP} \cdot \text{g}_{\text{H}_2\text{O}}^{-1} \cdot \text{a}^{-1} = J_{\text{He}} = J'_{\text{He}}(\rho\Lambda_{\text{He}}((1 - \Phi)/\Phi)) \quad (8.8)$$

where

$\rho$  is the density of the solid ( $\text{g}/\text{cm}^3$ );

$\Phi$  is the porosity ( $\text{cm}^3_{\text{H}_2\text{O}}/\text{cm}^3_{\text{total}}$ ).

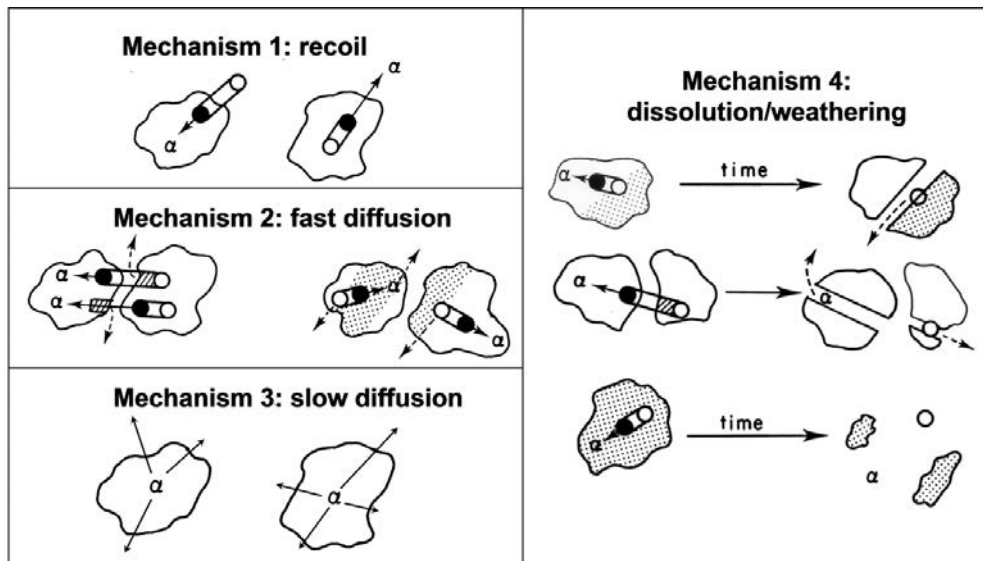


FIG. 8.1. Mechanisms for the release of  $\alpha$  decay  ${}^4\text{He}$  from rock: (1) recoil of the  $\alpha$  particle (30–100  $\mu\text{m}$ ); (2) recoil followed by rapid diffusion along recoil damage tracks, grain imperfections and microfractures; (3) molecular diffusion in the solid state with no advantages from recoil damage or grain imperfections; (4) weathering and dissolution release (after Torgersen (1980) [535]).

Quantification of  $\Lambda_{\text{He}}$  is a challenge. Figure 8.1 (modified from Torgersen (1980) [535]) shows schematically the various mechanisms by which  $^4\text{He}$  can enter the pore space from the solid phase: (i) direct recoil, (ii) rapid diffusion in imperfections, (iii) slow diffusion in the solid phase and (iv) weathering or dissolution.

#### 8.4.3.1. Mechanism 1: direct recoil

The recoil path length of an  $\alpha$  particle in silicate material ( $R_\alpha$ ) is of the order of 30–100  $\mu\text{m}$  (Andrews (1977) [536]) and the direct recoil loss of  $\alpha$  particles by the solid phase has been evaluated by Flügge and Zimens (1939) [537], and summarized by Torgersen (1980) [535]. From the grain size and the recoil path length,  $\Lambda_{\text{He}}$  can be calculated as:

$$\Lambda_{\text{He}} = \frac{3R_\alpha}{4r} - \frac{1}{16} \left( \frac{R_\alpha}{r} \right)^3 \quad \text{for } 2r \geq R_\alpha \quad (8.9)$$

$$\Lambda_{\text{He}} = 1 \text{ for } R_\alpha > r \quad (8.10)$$

where

$r$  is the grain radius;

$R_\alpha$  is the recoil path length.

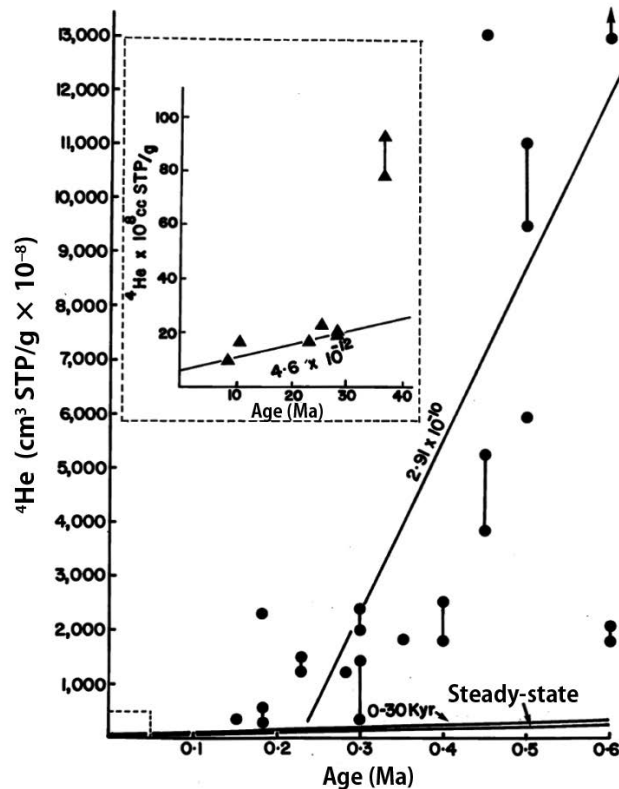


FIG. 8.2. Helium concentrations versus groundwater hydraulic (flow model) age (as supported by  $^{36}\text{Cl}$  model ages) for the Great Artesian Basin, Australia. For groundwaters younger than 40 ka, the accumulation rate is  $4.6 \times 10^{-12} \text{ cm}^3 \text{ STP } ^4\text{He} \cdot \text{cm}^{-3} \text{H}_2\text{O} \cdot \text{a}^{-1}$  which agrees with the calculated rate ( $\Lambda_{\text{He}} = 1$ ) of  $3.95 \times 10^{-12} \text{ cm}^3 \text{ STP } ^4\text{He} \cdot \text{cm}^{-3} \text{H}_2\text{O} \cdot \text{a}^{-1}$ . For groundwaters greater than 100 ka, the rate of accumulation is  $2.91 \times 10^{-10} \text{ cm}^3 \text{ STP } ^4\text{He} \cdot \text{cm}^{-3} \text{H}_2\text{O} \cdot \text{a}^{-1}$  or 74 $\times$  in situ production. An external bottom boundary flux provides the best explanation for the source and the timescale over which it can be seen (from Torgersen and Clarke (1985) [293]).

Most aquifer grain sizes (of the order of millimetres) are large compared to the recoil path length (of the order of 0.1 mm) and  $\Lambda_{\text{He}}$  can be approximated as:

$$\Lambda_{\text{He}} = \frac{3R_{\alpha}}{4r} \quad \text{for } R_{\alpha}/r < 0.5 \quad (8.11)$$

Calculations indicate that direct recoil release of  $\alpha$  particles should be low ( $\Lambda_{\text{He}}$  of the order of 0.075), yet it is often observed (e.g. Heaton (1984) [538]; Torgersen and Clarke (1985) [293]) that  $^4\text{He}$  in the pore water increases as if  $\Lambda_{\text{He}} = 1$  (Fig. 8.2). The implication of this common assumption ( $\Lambda_{\text{He}} = 1$ ) implies that the diffusive (rapid or slow) loss of  $^4\text{He}$  from the solid phase to the fluid phase is balanced by the production of  $^4\text{He}$  in the solid phase by radioproduction of  $^4\text{He}$ . This is equivalent to the assumption that the grain has reached a condition of diffusive (rapid or slow) equilibrium with the local pore water. It should be noted that the timescale on which diffusive equilibrium is reached is much shorter for fast diffusion (mechanism 2) than for slow diffusion (mechanism 3) (see Fig. 8.1).

#### 8.4.3.2. Mechanisms 2 and 3: rapid and slow (molecular) diffusion release

Using an idealized spherical geometry and the solution of Carslaw and Jaeger (1959) [539] (see Fig. 32 of Ref. [539]), a condition of diffusive (rapid or slow) equilibrium with the local pore water occurs in a grain with an initial concentration of  $^4\text{He} = 0$  at a scaled time of  $D_{\text{solid}}t/\Delta x^2 > 0.5$  (for spherical geometries, such as a sand grain,  $\Delta x$  is equivalent to the radius). As a generalization, the diffusive timescale  $Dt/\Delta x^2 > 0.5$  implies that a  $>50\%$  change has been achieved. With the (slow) molecular diffusion coefficient of  $^4\text{He}$  in silicate material on the order of  $10^{-18}$ – $10^{-22}$   $\text{cm}^2/\text{s}$  (typical crustal minerals; Lippolt and Weigel (1988) [540]; Trull et al. (1991) [541]), the ‘steady state’ condition (production in the grain = loss from the grain) can apply to a 0.1 cm grain on the timescale of  $10^8$  a ( $10^{-18}$   $\text{cm}^2/\text{s}$ ) (Fig. 8.3). However, when grains are laced with imperfections, it is important to differentiate the screened grain size from the effective grain size (Ballentine et al. (2002) [530]; Torgersen (1980) [535]). For the effective grain size, internal defects, imperfections, dislocations and

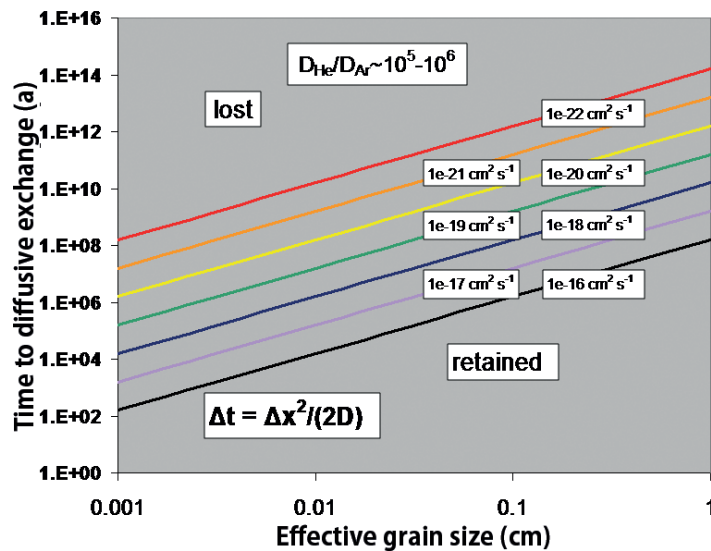


FIG. 8.3. Simple scaled rates of diffusion for various grain sizes as a function of diffusion coefficient. The timescale  $\Delta x^2/2D$  approximates the timescale for loss of the solid phase, accumulated  $^4\text{He}$ . Significant fluxes ( $>10\%$  of max.) would be observable at timescales of  $0.1\Delta x^2/2D$  and all initial  $^4\text{He}$  would be effectively lost by  $3\Delta x^2/2D$ . It should be noted that  $D_{\text{He}}/D_{\text{Ar}} \sim 10^5$  and, therefore, closure for Ar is maintained for far longer timescales than closure for  $^4\text{He}$ .

microfractures render the distance to a pore space-available boundary to be significantly less than the screen-sorted grain size (the rapid diffusion case of Torgersen (1980) [535]; see Fig. 8.1). For example, an effective grain size of 0.01 cm will reach steady state (production = loss) on a timescale of the order of  $10^6$  a (100 times faster) if transport time in the ‘imperfection pathway’ is not considered significant. Additionally, the (slow) diffusion coefficient of  $^4\text{He}$  in grains may increase with time due to radiation damage, microfracturing, etc. and the effective grain size may, therefore, decrease with time. As this loss of  $^4\text{He}$  from a grain is typically not measureable in the laboratory on a reasonable timescale, a measure of loss at a higher temperature can often be scaled to the in situ lower temperature (Mamyrin and Tolstikhin (1984) [521]). Although such measures are possible, this laboratory measure of  $D_{\text{solid}}$  will only reflect conditions now rather than conditions over the timescale of the  $^4\text{He}$  model age (the time over which solid material contributed to the fluid parcel). Of additional concern is the possibility of variability in  $\Lambda_{\text{He}}$  in space or time. Is the rock sample acquired representative of the ‘average’ rock the water parcel has seen over its residence time? As effective grain sizes in aquifers are typically small and the diffusion coefficients for  $^4\text{He}$  in the solid phase are typically large, an in situ production rate equivalent to  $\Lambda_{\text{He}} = 1$  is often assumed.

#### 8.4.3.3. Mechanism 4: bulk dissolution or weathering

Bulk dissolution or weathering of grains should also result in the release of  $^4\text{He}$  accumulated within the grain (see Fig. 8.1). As grains dissolve from the outside and diffusion will create gradients in the solid phase that decrease the concentration towards the outside of grains, quantification of a priori dissolution release of  $^4\text{He}$  is difficult. Both Torgersen and Clarke (1985) [293], and Heaton (1984) [538] calculate a simple rate for dissolution release of  $^4\text{He}$  based on an assumed uniform concentration of  $^4\text{He}$  in the grain. These concentrations are usually based on the metamorphic or depositional age of the formation and, hence, represent a maximum value. Both Torgersen and Clarke (1985) [293], and Heaton (1984) [538] calculate the rate of ‘weathering’ release of  $^4\text{He}$  from their systems to be  $<1\%$  of the  $\Lambda_{\text{He}} = 1$  condition and, thus, weathering release may be unimportant. However, it is still to be determined whether this is a general condition.

Heaton (1984) [538] estimates a bulk rate of surface chemical weathering from the chemistry of world rivers to be  $3 \text{ mg}_{\text{rock}} \cdot \text{kg}^{-1}_{\text{rock}} \cdot \text{a}^{-1}$ . Simplistically, this is equivalent to a timescale for dissolution of 0.3 Ma. However, Heaton (1984) [538] advises that subsurface dissolution will be of the order of  $0.1\text{--}0.01\times$  slower, indicating subsurface timescales for dissolution of the order of 3–30 Ma. This ‘dissolution timescale’ can be compared to the timescale for solid phase loss of  $^4\text{He}$  by molecular diffusion. Using a ‘fast’ molecular diffusion coefficient ( $10^{-18} \text{ cm}^2/\text{s}$ ) for grains of 0.1 cm, yields of the order of 300 Ma as a timescale for loss (Fig. 8.3). Thus, one might expect weathering release or chemical dissolution to be an important release mechanism. However, the observation that release equivalent to  $\Lambda_{\text{He}} = 1$  is often observed suggests that effective grain sizes for diffusion might be as small as  $0.5 \times 10^{-3} \text{ cm}$  ( $\Delta x = (D\Delta t)^{0.5}$ , where  $D = 10^{-18} \text{ cm}^2/\text{s}$  and  $\Delta t = 10 \text{ ka}$ ; Fig. 8.3). These arguments suggest that  $^4\text{He}$  release via chemical dissolution should be considered but may often be dismissed.

#### 8.4.3.4. Effective release at low rates ( $\Lambda_{\text{He}} < 1$ )

Under conditions where  $D_{\text{solid}}/\Delta x \ll 0.5$ , the solid phase can release  $^4\text{He}$  at a rate that is equivalent to  $\Lambda_{\text{He}} < 1$ . However, the authors are aware of no documented cases for which  $\Lambda_{\text{He}} \ll 1$  has been unequivocally shown. This condition may require formation of new grains from new material (authigenic material) with no pre-existing  $^4\text{He}$ , which is likely an artificial case.

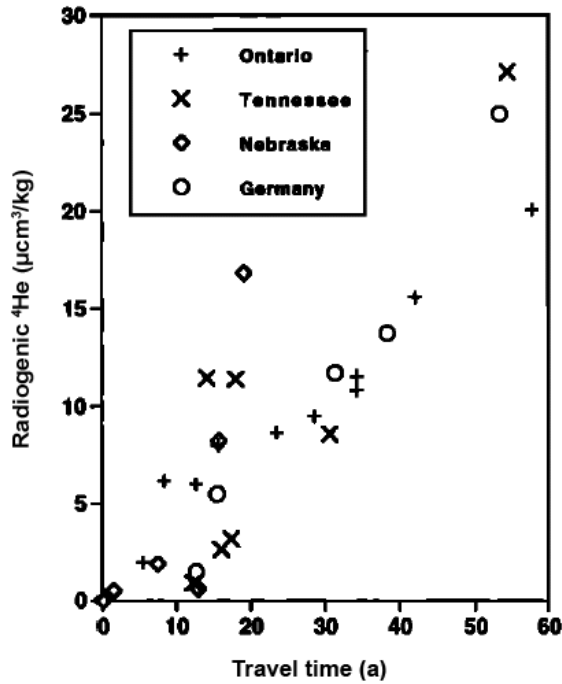


FIG. 8.4. The accumulation of  $^4\text{He}$  in various groundwater aquifers as a function of travel time (flow model age). Typical in situ production is  $0.18 \mu\text{cm}^3/\text{kg}$  over 60 a. The data indicate rates  $>100$  times the expected in situ production via radiodecay. This enhanced source is the result of slow release of solid phase, accumulated  $^4\text{He}$  (accumulated over the metamorphic age of the rock) that occurs as a result of comminution of large blocks/grains into smaller grains. The source is exemplary of mechanism 3 of Fig. 8.1. (From Solomon et al. (1996) [295], reproduced with permission of the American Geophysical Union.)

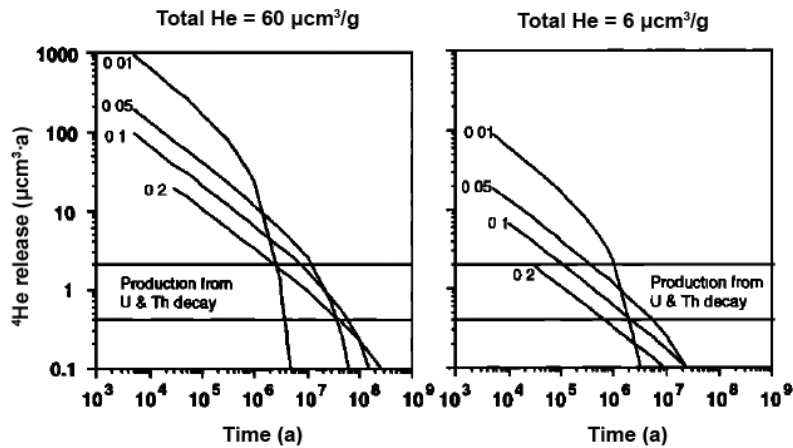


FIG. 8.5. Model calculations showing the timescale over which solid phase, accumulated  $^4\text{He}$  can be released into the groundwater. The fluxes from the solid phase to the groundwater are a function of the grain size (labelled on various curves), the initial  $^4\text{He}$  concentration before comminution (metamorphic age of the solid; compare initial concentration of  $60 \mu\text{cm}^3/\text{g}$  to  $6 \mu\text{cm}^3/\text{g}$ ) and the diffusion coefficient for  $^4\text{He}$  in the solid (graphs present the case for only a single diffusion coefficient  $D^{\text{He}} = 4.5 \times 10^{-21} \text{ cm}^2/\text{s}$ ). (From Solomon et al. (1996) [295], reproduced with permission of the American Geophysical Union.)

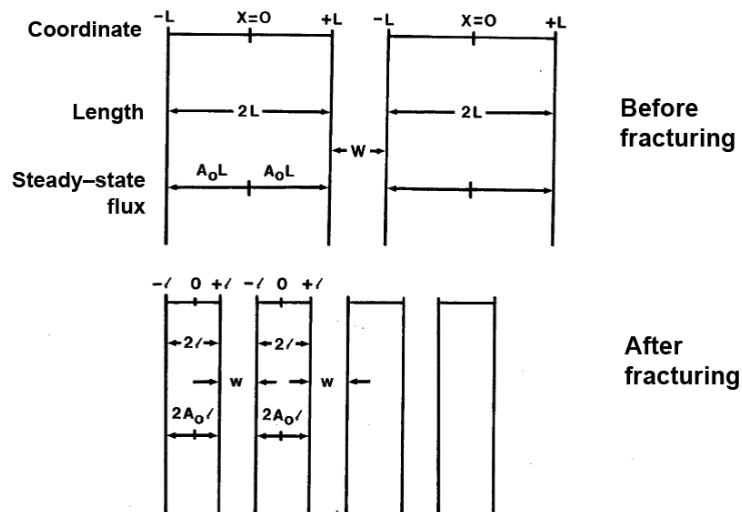


FIG. 8.6. The bulk fracturing model of Torgersen and O'Donnell (1991) [543] illustrated the 1-D case for simple comminution. Before fracturing, the slab of thickness  $L$  can acquire a noble gas concentration that is (initial condition 1) 0.005 times the steady state or (initial condition 2) the steady state concentration of  $A_0L/2D$ . Fracturing then reduces the slab thickness from  $L$  to  $l$ . Fracturing is quantified as the ratio  $L:l$  and can have any value  $>1$ . It should be noted that the higher  $L:l$ , the larger the surface area available for diffusion into the pore space. (From Torgersen and O'Donnell (1991) [543], reproduced with permission of the American Geophysical Union.)

#### 8.4.3.5. Enhanced release ( $\Lambda_{He} > 1$ ) by comminution, microfracturing and macrofracturing

The case where  $\Lambda_{He} > 1$  can and does occur as a result of a decrease in effective grain size by comminution, micro- and macrofracturing. In such a case, a large effective grain size ( $>1$  cm) may retain most of its in situ production of  $^4He$  but release that  $^4He$  when the grain size is reduced. In the case of the Sturgeon Falls site in Ontario, Canada, Solomon et al. (1996) [295] hypothesized that Precambrian Canadian Shield rocks ( $>1$  Ga) that occur in large blocks (fracture to fracture spacing on the order of 1–10 m) were reduced by glacial action to the 1 mm grains that comprise the aquifer. The accumulated  $^4He$  would then be released from 1 mm grains on a timescale of the order of  $10^8$  a ( $10^{-18}$  cm $^2$ /s) to  $10^{10}$  a ( $10^{-20}$  cm $^2$ /s) (see Fig. 8.3). Such release ( $\Lambda_{He}$  order 100) was confirmed by laboratory measurements (Solomon et al. (1996) [295]). Based on a comparison of groundwater  $^4He$  accumulation rates and independently estimated travel times (Fig. 8.4), this scenario (glacially produced comminution and  $\Lambda_{He} \gg 1$ ) may be common at high latitudes. The enhanced release of  $^4He$  ( $\Lambda_{He} \gg 1$ ) can continue for a considerable time (Fig. 8.5) and may provide a dominant  $^4He$  input within an aquifer.

This concept of comminution/fracturing is scalable. Honda et al. (1982) [542] have shown in laboratory experiments that rock fracturing can lead to the release of  $^4He$ . In the 1-D case, Torgersen and O'Donnell (1991) [543] have shown that fracturing creates large gradients and surface areas that lead to high  $^4He$  fluxes ( $\Lambda_{He} \gg 1$ ) (Fig. 8.6). The resultant 'pieces' continue to lose  $^4He$  ( $\Lambda_{He} \gg 1$ ) for timescales on the order of  $2 < Dt/\Delta x^2 < 5$  depending on the initial condition. It should be noted that the flux from the slab (Fig. 8.7) is reduced by half in the timescale defined by  $Dt/\Delta x^2 = 1$ , but that, in some cases, the flux remaining to be released may still be larger than in situ production. Thus, increased stress leading to microfracturing can result in  $\Lambda_{He} \gg 1$  through new surfaces and/or the creation of imperfections and microcracks which creates shorter routes and higher gradients to enable high transport rates to imperfections. At the larger scale (1–1000 m), it has been shown that 1 km of uplift

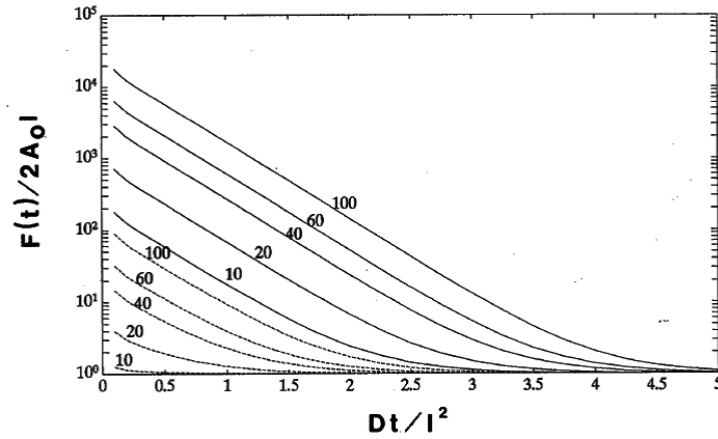


FIG. 8.7. The flux of noble gas (y axis) to the pore space relative to in situ production as a function of diffusion time,  $Dt/l^2$  (from the general case  $Dt/\Delta x^2$ ). Dashed lines are calculated for the IC1 (0.005 times steady state concentration at time of fracturing) and solid lines are calculated for IC2 (steady state concentration at time of fracturing). (From Torgersen and O'Donnell (1991) [543], reproduced with permission of the American Geophysical Union.)

or downdrop will result in thermal stresses sufficient to produce stresses approaching the yield strength of rock (Knapp and Knight (1977) [544]; Savage (1978) [545]). The 1-D modelling of Torgersen and O'Donnell (1991) [543] shows that stress-induced macrofracturing leads to large fluxes from blocks ( $\Lambda_{\text{He}} > 10^4$ ) and although such fluxes decrease with time, they can produce  $\Lambda_{\text{He}} \gg 1$  for timescales on the order of  $2 < Dt/\Delta x^2 < 5$  (see Fig. 8.7). The results in Fig. 8.7 show that fracturing/comminution can result in large local sources of  $^4\text{He}$  to the pore space that can persist for characteristic timescales of  $1 < Dt/l^2 < 5$  but  $Dt/l^2 = 0.5$  marks the point where approximately half of the accumulated noble gas has been lost to the pore space. Given that  $D_{\text{He}}/D_{\text{Ar}} \sim 10^5$ , the entire accumulated  $^4\text{He}$  could be lost from the slab while  $^{40}\text{Ar}$  loss continues for a considerable longer time. It should be noted that the concentration in the pore fluid is governed not only by the flux from the slab but also by the residence time in the post-fractured system.

The net result of microscale fracturing coupled to larger scale (km) macrofracturing is that retention of  $^4\text{He}$  in the crust becomes difficult and there can be a resultant significant flux of  $^4\text{He}$  from the crust to the atmosphere.

#### 8.4.3.6. Crustal fluxes of $^4\text{He}_{\text{rad}}$

The concentration and residence time of  $^4\text{He}$  in the atmosphere suggest that on a continental space scale and a megayear (Ma) timescale, the flux of  $^4\text{He}$  from the Earth's crust to the atmosphere is comparable to the net in situ production by U–Th series element  $\alpha$  decay in 30–40 km of the crust (Torgersen (1989) [546] and Torgersen (2010) [547]). This is not equivalent to a steady state loss of  $^4\text{He}$  from the crust to the atmosphere as implied by Ballentine et al. (2002) [530], as any measure of flux contains within it a characteristic time and space scale, whereas steady state implies that the flux is constant in time and space. However, the implication of the atmospheric  $^4\text{He}$  mass balance is that in situ crustal production of  $^4\text{He}$  must both be released to a mobile phase (see above discussion of  $\Lambda_{\text{He}}$ ) and that that mobile phase must be transportable to the Earth's surface on timescales of the order of 1 Ma although it may take longer ( $10^9$  a) for that flux to be established (see Fig. 8.8).

With regard to the interpretation of  $^4\text{He}$  in groundwater systems, the issue becomes one of a possible dominant flux of  $^4\text{He}$  into a water parcel from external sources rather than the internal production terms encountered in the space  $\Delta x\Delta y\Delta z$  (acknowledging that  $\Delta x\Delta y\Delta z$  is heterogeneous and that the solid phase

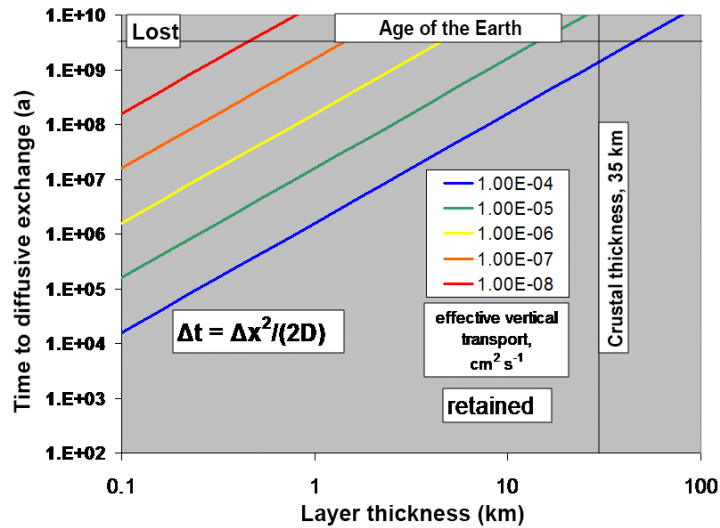


FIG. 8.8. The effective time for diffusive transport as a function of layer thickness and effective diffusion coefficient. The timescale  $\Delta x^2/2D$  approximates the timescale for diffusive exchange of produced/accumulated  $^4\text{He}$ . Significant fluxes into the layer and/or out of the layer ( $\sim 20\%$  of the max.) would be observable at timescales of  $0.1\Delta x^2/2D$  and all exchangeable species would be effectively lost/gained in  $3\Delta x^2/2D$ .

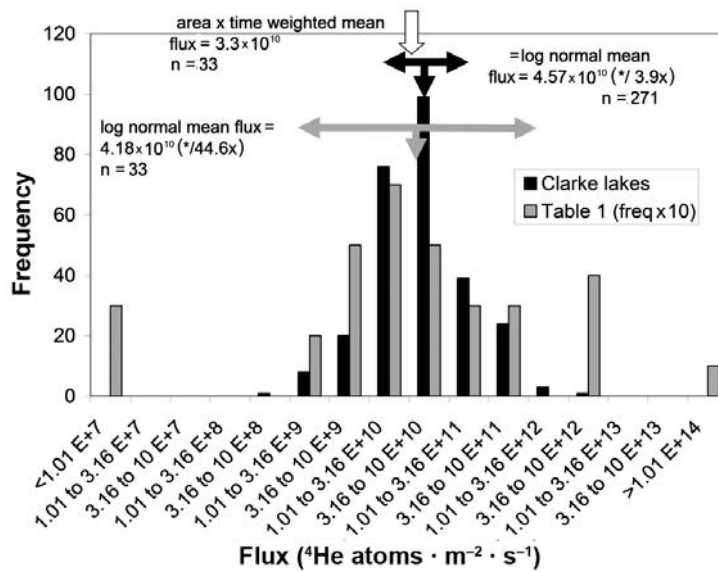


FIG. 8.9. A statistical analysis of the measured flux of  $^4\text{He}$  into 271 Canadian Shield lakes using the data of Clarke et al. (1977) [548], Clarke et al. (1983) [549], and Top and Clarke (1981) [550]. These data typically provide one sample per lake, including both a measure of excess  $^4\text{He}$  and the  $^3\text{H}/^3\text{He}$  model age.

remains in place while the water flows). Table 8.2 shows the measured  $^4\text{He}$  degassing flux in locations around the world. Although the analysis of Torgersen and O'Donnell (1991) [543] suggests fluxes from individual blocks can be  $10^4$  times in situ production and that  $\Lambda_{\text{He}} < 1$  remains an unobserved possibility, it is of note that area- and time-weighted mean flux ( $3.3 \times 10^{10} \text{ } ^4\text{He atoms} \cdot \text{m}^{-2} \cdot \text{s}^{-1}$ ) is approximately equivalent to the mean crustal production. When the fluxes of Table 8.2 are evaluated with respect to their log-normal mean ( $4.18 \times 10^{10} \text{ } ^4\text{He atoms} \cdot \text{m}^{-2} \cdot \text{s}^{-1}$ ), the variability in measured  $^4\text{He}$  flux is approximately  $\pm 1.5$  orders of magnitude (Torgersen (2010) [547]; see also Fig. 8.9).

TABLE 8.2. THE HELIUM FLUX FROM CONTINENTAL REGIONS

Region	${}^4\text{He}$ flux (atoms·m <sup>-2</sup> ·s <sup>-1</sup> × 10 <sup>10</sup> )	Method	Plotted, evaluated ${}^4\text{He}$ flux (atoms·m <sup>-2</sup> ·s <sup>-1</sup> × 10 <sup>10</sup> )	Timescale	Space scale (km)	Reference
Continents	2.8	calculation from U,Th	2.8	2 Ma	>5000	1,2,3
Great Artesian Basin	3.1	Measured accum in gw	3.1	1 Ma	500	2
Great Hungarian Plain	0.07-0.45	Measured accum in gw	0.2	1 Ma	200	7
Great Hungarian Plain	8	Measured accum in gw	8	1 Ma	200	8
Paris Basin	0.4-4	Measured accum in gw and model	1	10 ka	100-500	11,12,13,14
Paris Basin	0.4	Measured accum in gw and model	0.4	10 ka	100-500	11
Molasse Basin	0.2	Measured accum in gw	0.2	250 ka	50	9
Carrizo Aquifer, TX	1	Measured accum in gw and model	1	100 ka	75	23
Black Sea	1.3	Profile and model	1.3	440 a	661	26
San Juan Basin, NM	0.8	Measured accum in gw and model	0.8	40 ka	40	23
Eastern Paris Basin	3.8-15	Measured accum in gw and model	10	10 ka	75	15
Auob Sandstone	0.09-3	Measured accum in gw	1	20 ka	50	5
Auob Sandstone	2.6	Measured accum in gw	2.6	20 ka	50	2
Serra Grande, Brazil	2.4	Measured accum in gw	2.4	20 ka	40	24, 28
Caspian Sea	1.9-5.9	Lake profile	4	25 a	609	22
Lake Baikal	14-28	Lake profile	21	10 a	177	22
Lake Huron	Not detectable	Lake profile	0.001*	0.5 a	243	20, 28
Lake Erie	Not detectable	Lake profile	0.001*	0.5 a	161	20, 28
Lake Ontario	Not detectable	Lake profile	0.001*	0.5 a	136	20, 28
Lake Van	25	Lake profile, volcanic area	25	2 a	60	22

Lake Taupo	3	Lake profile, volcanic area	3	10 a	15	19, 28
Lake Nyos	30 000	Lake profile, volcanic area	30 000	18 a	1	22
Lake Lugano	4.8	Lake profile	4.8	12 a	7	22
Lake Nemrut	600	Ice covered, volcanic area	600	36 a	3	22
Crater Lake	55	Lake profile, volcanic area	55	3 a	7	22
Lake Lucerne	2.1–14	Lake profile	8	1 a	10.7	22
Lake Zug	1.6	Lake profile	1.6	3 a	6	22
Lake Mashu	92	Lake profile, kz, volcanic area	92	2 a	5	22
Teggau Lake	300–600	Lake profile	450	1 a	4	18, 28
Lake Alpnoch	1.1	Lake profile	1.1	0.5 a	5	22
Green Lake	811	Lake profile	811	10 a	1	16, 28
Lake 120	14	Lake profile	14	3 a	0.5	17, 28
Lac Pavin	60	2 Lake profiles, volcanic area	60	1–2 a	0.66	22
Laacher Lake	1000	2 Lake profiles, volcanic area	1000	0.26 a	1.4	22
271 Clarke Lakes	4.6 <sup>a</sup> /3.9×	271 Lakes; 1 sample each		0.3 a	0.5	21, 28
World Ocean	0.1	Profile	0.1	500 a	22 609	25
Ocean flux	0.04–0.26	Theory	0.1	510 a	22 609	27

<sup>a</sup> the flux is  $<10^9$   $^4\text{He atoms} \cdot \text{m}^{-2} \cdot \text{s}^{-1}$ ; the flux is chosen to be the best estimates (symmetric log-normal error bounds).

- 1) O’Nions and Oxburgh (1983)
- 2) Torgersen and Clarke (1985)
- 3) Torgersen and Ivey (1985)
- 4) Craig et al. (1975)
- 5) Heaton (1984)
- 6) Sano et al. (1986)
- 7) Stute et al. (1992)
- 8) Martel et al. (1989)
- 9) Andrews et al. (1985)
- 10) Tolstikhin et al. (1996)
- 11) Marty et al. (1993)
- 12) Pinti and Marty (1995)
- 13) Pinti et al. (1997)
- 14) Castro et al. (1998)
- 15) Dewonck et al. (2001)
- 16) Torgersen et al. (1981)
- 17) Campbell and Torgersen (1980)
- 18) Torgersen and Clarke (1978)
- 19) Torgersen (1983)
- 20) Torgersen et al. (1977)
- 21) Clarke et al. (1977), Clarke et al. (1983), Top and Clarke (1981)
- 22) Kipfer et al. (2002)
- 23) Castro et al. (2000)
- 24) Stute et al. (1995)
- 25) Well et al. (2001) (ref. in Schlosser and Winckler (2002))
- 26) Top and Clarke (1983)
- 27) Torgersen (1989)
- 28) This study

It is acknowledged that the fluxes in Table 8.2 represent fluxes distributed over an area appropriate to the measurement. For instance, the quantified external flux into the Great Artesian Basin (Torgersen and Clarke (1985) [293]) is roughly equivalent to whole crustal production and is influxed to the base of the aquifer over the space/timescale of the basin. This, of necessity, means that the flux above the aquifer directly from the soil to the atmosphere is very low. Furthermore, the net flux to the atmosphere in the discharge zone would be locally very large since it reflects the input of crustal production over the whole basin and not just the discharge zone. These measures of the degassing fluxes of  $^4\text{He}$  must, therefore, be carefully interpreted with respect to their applicable time and space scale. For the range of basin scale fluxes to be this constrained, vertical transport must not be only relatively rapid but also relatively pervasive.

Figure 8.9 shows a simple analysis of the U prospecting data of Clarke and others (Clarke et al. (1977) [548]; Clarke et al. (1983) [549]; Top and Clarke (1981) [550]) for 271 lakes for which only one sample is obtained per lake. The calculation in the figure assumes the depth of sampling (most often below the thermocline) is an approximation of the mean lake depth. The calculation likely has an error based on assumptions that is of the order of three times. Also shown are fluxes based on the data in Table 8.2 for which both an area multiplied by a time weighted mean has been calculated, as well as a log-normal mean and deviation. The agreement between the mean and standard deviation for the Clarke lakes and Table 8.2 data suggest the magnitude of the crustal degassing flux is approximately equivalent to whole crustal production with variance of a factor of 44.6 times or 1.5 orders of magnitude. One, therefore, has a 68% probability of measuring a flux between  $0.1 \times 10^{10}$  and  $186 \times 10^{10}$  atoms  $^4\text{He} \cdot \text{m}^{-2} \cdot \text{s}^{-1}$  in any one study. The analysis suggests strong spatial and temporal variability in the measured flux.

Although such data only captures of the order of 0.5 a of  $^4\text{He}$  flux over a specific lake area and is likely subject to errors on the order of three times due to the assumptions necessary (the assumptions also suggest the estimate is  $\sim 50\%$  too high), the mean flux measured by these lakes is  $4.57 \times 10^{10}$   $^4\text{He}$  atoms  $\cdot \text{m}^{-2} \cdot \text{s}^{-1}$  (log-normal mean with a standard deviation of a factor of 3.9 times written as  $\times/3.9$ ). The lake regions sampled by Clarke and others is an area of the Precambrian Canadian Shield which was depressed by about 1 km due to coverage by 3 km of ice sheet approximately 20 ka ago. Thus, it is noteworthy both that the mean measured flux ( $4.57 \times 10^{10}$   $^4\text{He}$  atoms  $\cdot \text{m}^{-2} \cdot \text{s}^{-1}$  log-normal mean with a standard deviation of  $\times/3.9$ ) is not much larger than whole crustal production ( $3 \times 10^{10}$   $^4\text{He}$  atoms  $\cdot \text{m}^{-2} \cdot \text{s}^{-1}$  (Torgersen (1989) [546]; Torgersen and Clarke (1985) [293])); and that the variance of the flux is consistent with the range reported from much larger basins (see Table 8.2). While the coverage of the planet with regard to crustal flux measurements remains limited, these measurements (Table 8.2, Fig. 8.9) support a hypothesis that the mean flux of  $^4\text{He}$  from the continental crust is of the same order as the in situ production from U–Th series decay in the continental crust. However, the variance of the crustal degassing flux is significant (a factor of  $10^6$  (95th per centile) for short time (0.5 a) and short space scales (1 km) (Torgersen (2010) [547])) and is likely unpredictable, thus, complicating the potential use of  $^4\text{He}$  as a method of groundwater ‘dating’. Such a conclusion also requires that the net rate of vertical transport in the crust be examined.

#### 8.4.3.7. *Vertical transport of $^4\text{He}_{\text{terr}}$ in the crust*

Simple scaling arguments can be used to evaluate the necessary rates of vertical transport in the continental crust in order to achieve surface crustal fluxes equivalent to the rate of whole crustal in situ production. As the data in Fig. 8.9 and Table 8.2 represent multiple time and space scales, the problem is constrained by the limit: continental degassing and basin scale measures of the degassing flux (on the time and space scale of  $10^6$  a and 1000 km) can be approximated as equivalent to the in situ production from 30–40 km of crust but with considerable variance (Torgersen (2010) [547]). This does not imply steady state degassing is applicable everywhere at all times; but it does acknowledge that the range exhibited in Table 8.2 and Fig. 8.9 is relatively small. In order to achieve the crustal degassing

flux in the Great Artesian Basin, Torgersen and Clarke (1985) [293] used a timescale of  $2 \times 10^8$  a (corresponding to a Jurassic age for the aquifer material) and assumed that most of the U–Th resided in the upper 7 km of crust to calculate a scaled effective diffusion coefficient (Fig. 8.8) of  $8 \times 10^{-6}$  cm<sup>2</sup>/s for that 7 km of crust. Torgersen (1989) [546], using a solution from Carslaw and Jaeger (1959) [539], scaled these observations to effective vertical diffusivities of  $10^{-5}$ – $10^{-6}$  cm<sup>2</sup>/s (Torgersen (1989) [546]) or vertical velocities of 0.1–1 cm/s. Given the diffusivity of gas in water is of the order of  $10^{-5}$  cm<sup>2</sup>/s and that the porosity ( $\Phi = 0.1$ ) and tortuosity effects will reduce this quiescent water to  $D\Phi^2 = 10^{-7}$  cm<sup>2</sup>/s, it is clear that over the long time and space scale, continental crust must transport significant quantities of <sup>4</sup>He and water at rates that are significantly faster than would be measured by typical (short time and space scale) well tests.

Such rates of transport are surprising when one considers the hydraulic conductivity of consolidated, non-granular rocks (Freeze and Cherry (1979) [11]) but less surprising when the rates of metamorphic processes are considered (Etheridge et al. (1984) [551]; Etheridge et al. (1983) [552]). The low hydraulic conductivities and transport often encountered in bulk non-granular rock are measured over small timescales (<1 a) with small space scale (of the order of centimetres) pieces of rock. In contrast, metamorphic processes reflect the transport in the crust on the larger time/space scales. This conclusion of rapid transport and high volumes of water is consistent with the requirements of the observed products in metamorphic geology (e.g. Etheridge et al. (1984) [551]; Etheridge et al. (1983) [552]). Metamorphic rock structure also suggests that fluid transport is episodic with periods of ‘no transport’ followed by periods of ‘very high transport’. Thus, the effective degassing of continental crust is supportive of and supported by the fluid transport required by metamorphic processes. When the time/space scale for transport is large, the effective rate of crustal scale transport is higher than might be predicted. However, any specific quantification of vertical transport in the crust may yield numbers which suggest that such crustal scale transport is not viable. This feature was specifically addressed by the Torgersen and Clarke (1992) [294] study at Cajon Pass drillhole, where the vertical transport measured by borehole tests showed rates of  $10^{-5}$  cm/a while effective rates estimated from the apparent <sup>4</sup>He tracer ages of the fluid implied vertical rates of 0.04–0.6 cm/a. Vertical transport in the continental crust must, therefore, be episodic (as required by metamorphic geology; Etheridge et al. (1984) [551]; Etheridge et al. (1983) [552]), with long periods of slow transport and short periods with a very high transport rate. Thus, what is ‘seen’ in the crustal scale transport of <sup>4</sup>He is comparable to travel in city subway systems: one can travel by subway from downtown Manhattan to uptown in a specific period of time (effectively several kilometres per hour) but when viewed in detail, this transport is accomplished by a series of stops (velocity of 0 km/h) interrupted by bursts of high speed (tens of kilometres per hour) travel. It would, thus, not be surprising for the external flux of <sup>4</sup>He (<sup>4</sup>He<sub>terr</sub>) to become quite important in many aquifer systems. For a more detailed discussion of vertical transport of <sup>4</sup>He<sub>terr</sub>, see Torgersen (2010) [547].

#### 8.4.3.8. *In situ production of <sup>3</sup>He*

Radiogenic production of <sup>4</sup>He is accompanied by a small but important nucleogenic production of <sup>3</sup>He as a result of thermal neutron interactions with <sup>6</sup>Li in the solid phase:



Helium-3 produced according to Eq. (8.12) is defined as nucleogenic <sup>3</sup>He whereas radiogenic (tritogenic) <sup>3</sup>He is produced by an atmospheric source of <sup>3</sup>H. To initiate the reaction (Eq. (8.12)), the production of neutrons in the solid matrix by ( $\alpha, n$ ) reactions and spontaneous fission neutrons must be calculated:

$$n = (n, \alpha)\text{U} + (\text{sf}, n)\text{U} + (\alpha, n)\text{Th} \quad (8.13)$$

TABLE 8.3. PARAMETERS FOR CALCULATION OF  $^3\text{He}/^4\text{He}$  PRODUCTION RATIOS (after Andrew and Kay (1982) [463])

Element	Molecular weight (g/mol)	$\phi_{\text{th}}$ (barns)
Li	6.94	71
B	10.81	755
Na	22.989	0.534
Mg	24.305	0.064
Al	26.981	0.232
Si	28.086	0.16
Cl	35.453	32.6
K	39.098	2.07
Ca	40.080	0.44
Ti	47.900	6.1
Cr	51.996	3.1
Mn	54.938	13.3
Fe	55.847	2.56
Ni	58.71	4.54
Co	58.933	37.5
Sm	150.4	5820
Gd	157.25	49 000

The dominant target elements for the  $(\alpha, n)$  reactions are Na, Mg, Al, Si and C (although water is also a viable and variable sink for neutron capture) and the net production of thermal neutrons ( $n$  (neutrons  $\cdot$  g $^{-1}$   $\cdot$  a $^{-1}$ )) can be expressed as (Ballentine and Burnard (2002) [553]):

$$n = 0.01[\text{U}](13.8[\text{Na}] + 5.4[\text{Mg}] + 5.0[\text{Al}] + 1.31[\text{Si}] + 2.0[\text{C}]) + 0.4788[\text{U}] + 0.01[\text{Th}](6.0[\text{Na}] + 2.45[\text{Mg}] + 2.55[\text{Al}] + 0.56[\text{Si}] + 0.83[\text{C}]) \quad (8.14)$$

where [U] and [Th] are expressed in parts per million and the remaining components are in per cent.

These thermal neutrons are captured by further interactions with the solid phase where typical slow neutron path lengths in silicate are of the order of 1 m. This suggests that the bulk solid phase composition can be used to estimate  $^3\text{He}$  production. Such calculations are well developed. Based on the initial work by Morrison and Pine (1955) [554] and Fiegge et al. (1968) [555], the fraction of the thermal neutron flux captured by  $^6\text{Li}$  ( $F_{\text{Li}}^{\text{Thn}}$ ) can be calculated as (Andrews (1985) [556]; Andrews and Kay (1982) [463]):

$$F_{\text{Li}}^{\text{Thn}} = \frac{\sigma_i N_i}{\sum \sigma_i N_i} \quad (8.15)$$

where

$\sigma_i$  is the thermal neutron cross-section;

$N_i$  is the molar abundance for important components of the rock composition (see Table 8.3).

TABLE 8.4.  $^3\text{He}/^4\text{He}$  PRODUCTION RATIOS (after Ballentine and Burnard (2002) [553])

Rock type	$^3\text{He}/^4\text{He}$ calculated $\times 10^8$	$^3\text{He}/^4\text{He}$ measured $\times 10^8$	Reference
Upper continental crust	3.90	—	Torgersen and Clarke (1987), Torgersen (1989)
Lower continental crust	0.21	—	Torgersen and Clarke (1987), Torgersen (1989)
Upper crust	1.08	—	Ballentine and Burnard (2002)
Middle crust	0.40	—	Ballentine and Burnard (2002)
Lower crust	0.37	—	Ballentine and Burnard (2002)
Oceanic crust	0.029	—	Torgersen and Clarke (1987), Torgersen (1989)
Basalt	1.3	—	Andrews (1985)
Ultramafic	0.114	—	Andrews (1985)
Hooray sandstone	2.2–3.3	—	Torgersen and Clarke (1987)
Sandstone, UK	2.23	—	Andrews (1985)
Sandstone, avg	0.58	—	Andrews (1985)
Clay and shale	1.99	—	Andrews (1985)
Limestone	0.1	—	Torgersen et al. (1981)
Limestone, UK	1.14	—	Andrews (1985)
Limestone, avg	0.23	—	Andrews (1985)
Typical granite	5–15	—	Fiege et al. (1968)
Granite	2.23	—	Andrews (1985)
Wr, stripa	0.594	—	Andrews et al. (1989)
Whole rock	1.6	1.6	
Orthoclase	—	40	
Biorite	—	12	
Plagioclase	—	5	Gerling et al. (1971), samples from Rapakiwi
Quartz	—	15	
Amphibole	—	4.5	
Zircon	—	2	
1-Whole rock	1.6	1.6	
2-Whole rock	1.7	1.9	
4-Whole rock	1.4	0.3	Tolstikhin and Drubetskoy (1977), Mamyrin and Tolstikhin (1984)
43-Whole rock	0.7	0.8	
27-Whole rock	0.09	6	
ss1-WR	—	0.21	
ss1-feldspar	—	0.238	
ss1-mica	—	0.462	
ss1-quartz	—	0.0084	Martel et al. (1990), samples from Carnmenellis
rh1g-WR	6.4	0.21	
rh12d-WR1	6.7	0.154	
rh12d-WR2	6.7	0.49	
Uraninite	—	0.0098	

Combining Eqs (8.14, 8.15) yields a rate of production of  $^3\text{He}$  which can be further combined with Eq. (8.7) to calculate the  $^3\text{He}/^4\text{He}$  production ratio. It should be noted that the rate of  $^3\text{He}$  production is based on the neutron production rate which is a function of [U] and [Th], but the  $^3\text{He}/^4\text{He}$  production ratio is determined by the rock composition and is a function of the Li/U–Th ratio.

Table 8.4 shows the  $^3\text{He}/^4\text{He}$  production ratio for average crust as well as selected rock types based on specific rock compositions from the literature. While there is a large degree of agreement, the observed differences and variability are significant. Table 8.4 further shows that differences between the observed  $^3\text{He}/^4\text{He}$  production rate and the calculated  $^3\text{He}/^4\text{He}$  production rate are also significant. As ( $\alpha$ , n) reactions occur within one alpha path length (0–40  $\mu\text{m}$ ) of the decaying nuclei, inhomogeneities in rock chemistry on the space scale of 40  $\mu\text{m}$  can impact the specific  $^3\text{He}$  yield. Furthermore, the assumption of homogeneous rock over a space scale of 1 m may be problematic for the thermal neutron capture and the relative siting/separation of the trace elements, U, Th, Li, Gd and Sm (the last two elements have very large cross-sections), or the relative presence of water may significantly impact the specific  $^3\text{He}$  yield. Such issues were discussed by Martel et al. (1990) [557] who investigated Carnmenellis granite  $^3\text{He}/^4\text{He}$  production (see also discussion by Ballentine and Burnard (2002) [553]). Chazal et al. (1998) [558] revisited Stripa granite and found that the measured  $^3\text{He}/^4\text{He}$  ratio was 4 times the calculated ratio. Specific causes for the differences between the observed/measured  $^3\text{He}/^4\text{He}$  ratios and calculated production ratios have not been unequivocally identified but the data in Table 8.4 and analysis of studies mentioned above serve to provide context for the use of calculated  $^3\text{He}/^4\text{He}$  production ratios and an interpretation of the errors that might be appropriate to that value. Based on the data in Table 8.4 and the discussion of Martel et al. (1990) [557], Ballentine and Burnard (2002) [553], and Tolstikhin et al. (1996) [559], it would appear that a calculated  $^3\text{He}/^4\text{He}$  production ratio is uncertain up to a factor of ten of the given figure. The best way to determine the  $^3\text{He}/^4\text{He}$  production ratio is by collecting a number of  $^3\text{H}$  free groundwater samples from the aquifer and to use the component separation process described below.

#### 8.4.3.9. Separation of He components

As multiple He sources are likely in groundwater systems and each source may have a different isotope composition, separating the various components and specifically identifying the He isotope ratio associated with that component can improve the analysis of He. Transforming the isotopic mass balances for  $^4\text{He}$  and  $^3\text{He}$  (e.g. Eq. (8.2)) to a measured ratio:

$$\left(\frac{^3\text{He}}{^4\text{He}}\right)_{\text{tot}} = \left(\frac{^3\text{He}}{^4\text{He}}\right)_{\text{measured}} = \frac{^3\text{He}_{\text{eq}} + ^3\text{He}_{\text{exc}} + ^3\text{He}_{\text{tri}} + ^3\text{He}^{\text{is}} + ^3\text{He}^{\text{terr}}}{^4\text{He}_{\text{eq}} + ^4\text{He}_{\text{exc}} + ^4\text{He}^{\text{is}} + ^4\text{He}^{\text{terr}}} \quad (8.16)$$

where

$^3\text{He}_{\text{tri}}$  is tritiogenic  $^3\text{He}$ ;

$^i\text{He}_{\text{is}}$  and  $^i\text{He}_{\text{terr}}$  represent in situ produced and terrigenic contributions, respectively.

The latter two contain He of radiogenic, nucleogenic and sometimes mantle origin. Using the method of Weise (1986) [560] (see also Castro et al. (2000) [88]; Stute et al. (1992) [561]; Weise and Moser (1987) [562]) yields an equation in the form of  $(y) = [m]x + b$ :

$$\left(\frac{^3\text{He}_{\text{tot}} - ^3\text{He}_{\text{exc}}}{^4\text{He}_{\text{tot}} - ^4\text{He}_{\text{exc}}}\right) = \left[R_{\text{eq}} - R_{\text{is,terr}} + \frac{^3\text{He}_{\text{tri}}}{^4\text{He}_{\text{eq}}}\right] \frac{^4\text{He}_{\text{eq}}}{^4\text{He}_{\text{tot}} - ^4\text{He}_{\text{exc}}} + R_{\text{is,terr}} \quad (8.17)$$

where  $R_{\text{is,terr}}$  represents the  $^3\text{He}/^4\text{He}$  ratio originating from both in situ and terrigenic sources.

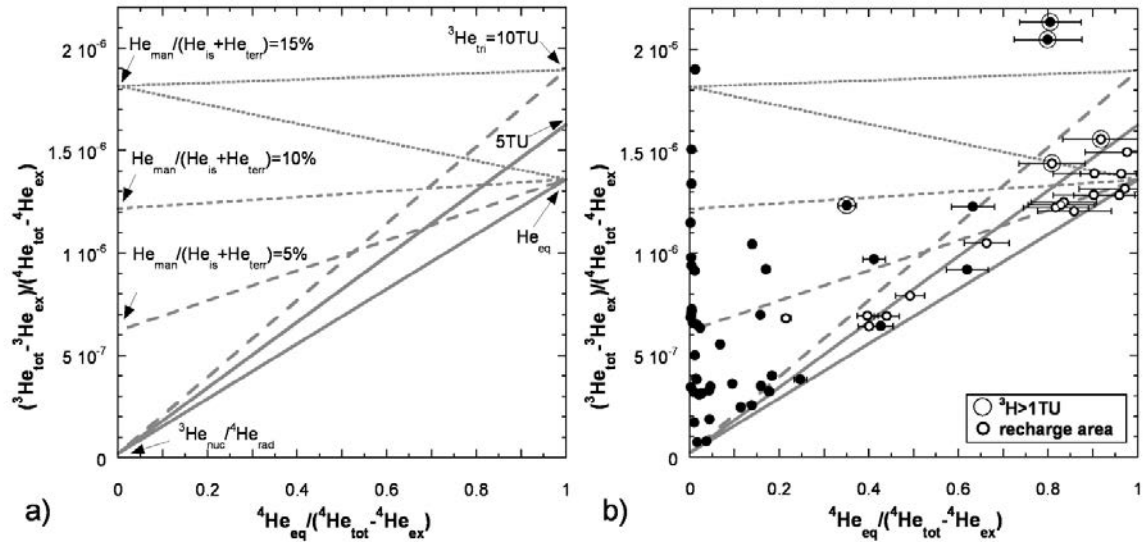


FIG. 8.10. Graphical separation of the individual He components. (a) This panel outlines the meaning of the various mixing lines with their end members; (b) Data from the Great Hungarian Plain. Samples containing more than 1 TU of tritium and samples collected in recharge areas (with vertical downward hydraulic gradient) are highlighted with open circles. (After Stute et al. (1992) [561]).

They are merged into one isotope ratio, because they are difficult to separate based on field measurements only:

$$R_{is,terr} = \frac{{}^3\text{He}_{is,terr}}{{}^4\text{He}_{is,terr}} = \frac{{}^3\text{He}_{nuc}^{is} + {}^3\text{He}_{nuc}^{terr} + {}^3\text{He}_{man}^{terr}}{{}^4\text{He}_{rad}^{is} + {}^4\text{He}_{rad}^{terr} + {}^4\text{He}_{man}^{terr}} \quad (8.18)$$

As radiogenic and mantle helium may both contribute to in situ and terrigenic  ${}^4\text{He}$ , the graphical determination of the ratio  $R_{is,terr}$  provides specific information regarding the source of non-atmospheric  ${}^4\text{He}$  in the system. The y axis is the measured  ${}^3\text{He}/{}^4\text{He}$  isotope ratio corrected for the excess air addition; the x axis measures the relative importance of  ${}^4\text{He}_{eq}$  to the other  ${}^4\text{He}$  components minus  ${}^4\text{He}_{exc}$ .  ${}^3\text{He}_{exc}$  and  ${}^4\text{He}_{exc}$  can be either derived from Ne measurements using Eq. (8.5) or by using concentrations of all stable noble gases and the inverse model as discussed above (Aeschbach-Hertig et al. (2001) [532]; Aeschbach-Hertig et al. (2000) [55]).

Data plot along linear (He component) mixing lines if  $R_{is,terr}$  is constant for the data set and if the amount of  ${}^3\text{He}_{tri}$  is constant or negligible (Fig. 8.10(a)). If  ${}^3\text{He}_{tri}$  is present, data will scatter somewhat around the mixing line because the variable  ${}^4\text{He}_{eq}$  is part of the slope in Eq. (8.17). However, the temperature and recharge elevation dependence of  ${}^4\text{He}_{eq}$  is small and slopes typically do not vary by more than 2% due to this effect. The addition of mantle derived helium (assuming  $R_{man} = 1.2 \times 10^{-5}$ , e.g. Craig and Lupton (1981) [563]) increases the y axis intercept, while the presence of  ${}^3\text{He}_{tri}$  anchors the right end of the mixing lines (Fig. 8.10(a)). If  $R_{is,terr}$  is variable in a data set and  ${}^3\text{He}_{tri}$  is present and variable, He components cannot be separated in a unique way. Assuming that the pre-nuclear bomb  ${}^3\text{H}$  concentrations in precipitation were fairly constant, a  ${}^3\text{H}$  measurement on the samples can be used as an indicator of anthropogenic  ${}^3\text{He}_{tri}$  and serve as a flag for those cases where a separation may be more complicated or impossible. It should be noted that the area underneath the lowest mixing line in Fig. 8.10(a) is a forbidden area because no known process can produce data that fall into this domain. Similar appearing graphs can be obtained by plotting  ${}^3\text{He}/{}^4\text{He}_{tot}$  versus  $\text{Ne}/{}^4\text{He}_{tot}$  or just versus  $1/{}^4\text{He}_{tot}$ . However, because of variable amounts of  ${}^4\text{He}_{exc}$ , it is not possible to draw accurate mixing lines in these diagrams.

As an example of the component separation, the He data set from the Great Hungarian Plain aquifers (Stute et al. (1992) [561]) is discussed. For the purpose of this paper,  $\text{He}_{cq}$  and  $\text{Ne}_{cq}$  were

calculated using the solubility data of Weiss (1971) [524], assuming an elevation of the recharge area of 200 m and an average recharge temperature of  $6 \pm 6^\circ\text{C}$ , which covers the glacial/interglacial temperature range derived from noble gas temperatures in the Great Hungarian Plain (Stute (1989) [522]; Stute and Deak (1989) [564]).  $\text{He}_{\text{exc}}$  was then determined with Eq. (8.5) by using Ne concentration data.

Samples from recharge areas (characterized by a downward hydraulic gradient) and samples containing  $^3\text{H} > 1$  TU at the time of sampling (1985) are highlighted by open symbols (Fig. 8.10(b)). Error bars reflect  $1\sigma$  analytical errors and the uncertainty in recharge temperature. The inverse model (see Aeschbach-Hertig et al. (2001) [532] and Aeschbach-Hertig et al. (2000) [55] discussed above) was also used to determine  $\text{He}_{\text{exc}}$  from all of the noble gas concentrations. It yields slightly smaller error bars, but the two plots (not shown) are identical within the error bars of Fig. 8.10(b).

Assuming  $^3\text{He}_{\text{tri}} = 0$ , the upper limit of  $R_{\text{is,terr}}$  may be estimated by placing an envelope line below the data points (Fig. 8.10(b)). The resulting intercept with the y axis,  $(4 \pm 4) \times 10^{-8}$ , is consistent with isotope ratios of He released from sediments (Mamyrin and Tolstikhin (1984) [521]) and is our best estimate for the  $^3\text{He}_{\text{nuc}}/^4\text{He}_{\text{rad}}$  ratio in the Great Hungarian Plain. If  $R_{\text{is,terr}}$  is assumed to be constant, data points above the lower line in Fig. 8.10(b) have to contain either  $^3\text{He}_{\text{tri}}$  or  $^3\text{He}_{\text{man}}$ . There are no  $^3\text{H}$  data for many of the deeper samples. However, they can be assumed not to contain  $^3\text{H}$  because of their low radiocarbon content (Stute and Deak (1989) [564]; Stute et al. (1992) [561]). Samples from the recharge areas plot slightly above the lower envelope line, and are unlikely to contain significant amounts of mantle He. Tritium measurements indicate that samples are of pre-nuclear bomb test origin. The sum of derived  $^3\text{He}_{\text{tri}}$  ( $1.6 \pm 1.7$  TU) and measured  $^3\text{H}$  ( $0.5 \pm 0.2$  TU) is  $2.1 \pm 1.7$  TU, providing an estimate of the natural  $^3\text{H}$  in recharge before anthropogenic  $^3\text{H}$  was added to the hydrological cycle. This value is lower than the pre-bomb estimate by Roether (1967) [565] of  $5 \pm 1.5$  TU, possibly as a result of partial loss of  $^3\text{He}_{\text{tri}}$  across the water table due to low recharge rates in Hungary (Schlosser et al. (1989) [566]; Stute et al. (1992) [561]). Assuming  $^3\text{He}_{\text{nuc}}/^4\text{He}_{\text{rad}} = 4 \pm 4 \times 10^{-8}$ ,  $^3\text{He}_{\text{tri}} = 1.6 \pm 1.7$  TU and  $R_{\text{man}} = 1.2 \pm 0.1 \times 10^{-5}$  are representative for the Great Hungarian Plain, the mantle component ( $^4\text{He}_{\text{man}}/(^4\text{He}_{\text{is}} + ^4\text{He}_{\text{terr}})$ ) yields values up to 16%, consistent with the geological history of the Pannonian Basin undergoing extension. A detailed discussion of the interpretation of this He data set can be found in Stute et al. (1992) [561].

#### 8.4.3.10. Nucleogenic and fissionogenic noble gases: $^i\text{Ng}_{\text{nuc}}$ , $^i\text{Ng}_{\text{fiss}}$

The contribution of nucleogenic and fissionogenic processes in the production of other noble gas isotopes can be an important diagnostic for  $^4\text{He}$ . In particular, nucleogenic  $^{20,21,22}\text{Ne}$ , and fissionogenic  $^{83,84,86}\text{Kr}$  and  $^{129,131,132,134,136}\text{Xe}$  can be produced, although only the dominant isotope can be observed in very old groundwater systems (Kennedy et al. (2002) [567]; Lippmann et al. (2003) [568]). In such cases, the nucleogenic isotope and fissionogenic isotope accumulation can be compared to the accumulation of  $^4\text{He}$ . If the release factor for each noble gas isotope is assumed to be  $\Lambda_{\text{Ng}} = 1$ , then apparent  $^{21,22}\text{Ne}$ ,  $^{86}\text{Kr}$  and  $^{136}\text{Xe}$  tracer model ages should concur with apparent  $^4\text{He}$  tracer model ages. However, because  $D_{\text{Ng}}$  decreases with increasing atomic mass, the release factor for each noble gas is likely to follow the order  $\Lambda_{\text{He}} > \Lambda_{\text{Ne}} > \Lambda_{\text{Kr}} > \Lambda_{\text{Xe}}$  (Drescher et al. (1998) [569]), and one might expect the simple noble gas tracer model age ( $\tau_{\text{Ng}}$ ) to reflect the order  $\tau_{\text{He}} > \tau_{\text{Ne}} > \tau_{\text{Kr}} > \tau_{\text{Xe}}$ . Such diagnostics can be critical in the evaluation of noble gas model ages from very old groundwaters (Lippmann et al. (2003) [568]).

The difference between  $^i\text{Ng}_{\text{rad}}$ ,  $^i\text{Ng}_{\text{nuc}}$ ,  $^i\text{Ng}_{\text{fiss}}$  and  $^i\text{Ng}_{\text{terr}}$  is often defined by whether the observed isotopic ratios can be produced in the host rock ( $^i\text{Ng}_{\text{rad}}^{\text{is}}$ ,  $^i\text{Ng}_{\text{nuc}}^{\text{is}}$ ,  $^i\text{Ng}_{\text{fiss}}^{\text{is}}$ ) or whether the isotopic ratio indicates that it must have its source in another type of rock ( $^i\text{Ng}_{\text{rad}}^{\text{terr}}$ ,  $^i\text{Ng}_{\text{nuc}}^{\text{terr}}$ ,  $^i\text{Ng}_{\text{fiss}}^{\text{terr}}$ ), including the aquitard.  $^3\text{He}/^4\text{He}$  ratios can often suggest a terrigenous (external) contribution to the groundwater, especially where aquitard rock has significantly different bulk compositions to the aquifer rock, although the reader is cognizant of the error in calculation of the  $^3\text{He}/^4\text{He}$  production ratio. However, because the external terrigenous sources are not known a priori, a comparison with the possible production ratio

calculated for an adjacent rock may not constrain the problem when the observed anomalous isotopic composition could also be explained by a mixture between local aquifer rock and an external ‘exotic’ rock. While one could feel fairly confident regarding the input of a mantle source of  $^3\text{He}$ , calculation of a per cent mantle contribution is potentially misleading because the mantle end member has inherent variability (hot spots have  $^3\text{He}/^4\text{He}$  ratios of 4–35  $R_a$  where  $R_a$  is the ratio in air,  $R_a = 1.384 \times 10^{-6}$  (Clarke et al. (1976) [242]) and such ratios will also vary with the age (time since eruption; Torgersen (1993) [570] and Torgersen et al. (1994) [571]). This suggests that evidence of a non-local contribution ( $\text{Ng}^{\text{terr}}$ ) based on measured isotopic ratios should be seen as evidence to evaluate and model several different mechanisms by which such observations could be produced and observed in situ. The calculation of the per cent mantle  $^3\text{He}$  contribution when that mantle source is of the order of millions of years old begins to lose meaning.

#### 8.4.3.11. The special case of $^{40}\text{Ar}$

The above discussion can be generalized to include  $^{40}\text{Ar}_{\text{rad}}$  which is the decay product of  $^{40}\text{K}$ . The production rate for  $^{40}\text{Ar}_{\text{rad}}$  (atoms  $\cdot \text{g}^{-1} \cdot \text{a}^{-1}$ ) is:

$$^{40}\text{Ar}_{\text{rad}} = 102.2[\text{K}] \quad (8.19)$$

where  $[\text{K}]$  is the concentration of potassium in parts per million.

The  $^4\text{He}_{\text{rad}}/^{40}\text{Ar}_{\text{rad}}$  production ratio can be derived from Eqs (8.19, 8.7) to give:

$$^4\text{He}_{\text{rad}}/^{40}\text{Ar}_{\text{rad}} = \{3.242 \times 10^6 [\text{U}] + 7.710 \times 10^5 [\text{Th}]\} / \{102.2[\text{K}]\} \quad (8.20)$$

In many cases,  $^{40}\text{Ar}_{\text{rad}}$  model ages can be calculated for comparison to  $^4\text{He}$  model ages. For the calculation of  $\Lambda_{40\text{rad}}$ , the above criteria generally apply. However, it should be noted that K is typically associated with major phases within the rock whereas U–Th series elements are associated with minor phases. In this sense, K may be located in very large grains and/or U–Th may be associated with the surface of grains. Thus, it is often encountered that the release factor for  $^{40}\text{Ar}_{\text{rad}}$  ( $\Lambda_{40\text{rad}}$ ) is less than the release factor for  $^4\text{He}$  ( $\Lambda_{40\text{rad}} < \Lambda_{4\text{rad}}$ ). This has been confirmed by the experiments of

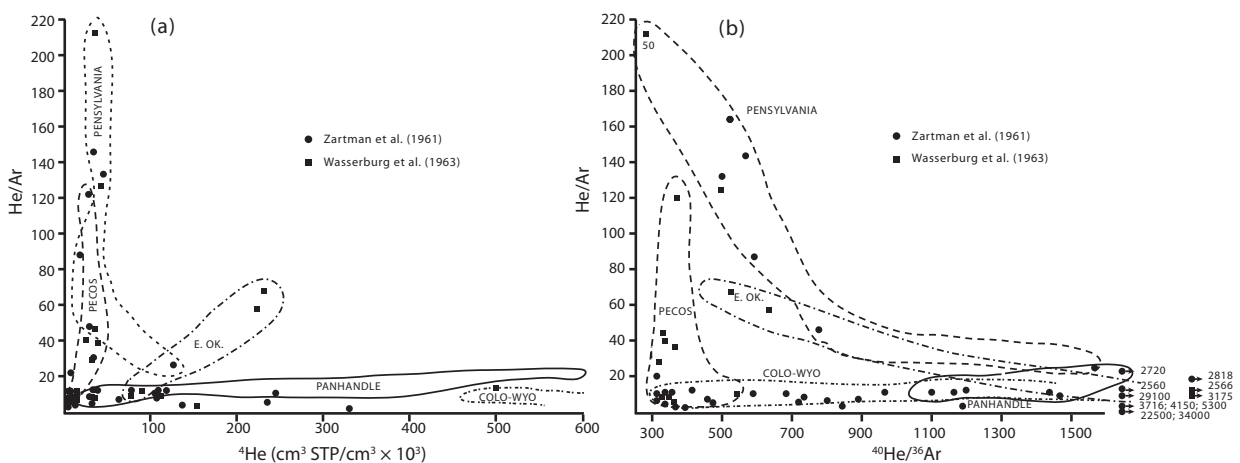


FIG. 8.11. The  $^4\text{He}/^{40}\text{Ar}_{\text{rad}}$  ratio measured in gas/oil reservoirs which reflect the accumulation of local and crustal degassing sources and their mode of release from the solid phase production. It should be noted that as time increases (as defined by increasing  $^{40}\text{He}$  or  $^{40}\text{Ar}/^{36}\text{Ar}$ ), the  $^4\text{He}/^{40}\text{Ar}_{\text{rad}}$  ratio decreases from values well above the production ratio to values that integrate and approach the production ratio. (From Torgersen et al. (1989) [573].)

Krishnaswami and Seidemann (1988) [572], and is intuitive with regard to the difference in their respective diffusion coefficients ( $D_{Ar}/D_{He} = 10^{-5}$ – $10^{-6}$ ; see Ballentine and Burnard (2002) [553]; for calculating diffusion coefficients, see Table 9 of Ref. [553]). Alternatively, the combination of grain size and diffusion coefficient may have enabled  $^4\text{He}$  to reach steady state after comminution, whereas the slower loss of  $^{40}\text{Ar}_{\text{rad}}$  may still impose a local input of  $^{40}\text{Ar}_{\text{rad}}$  that is significantly in excess of local production (Torgersen and O'Donnell (1991) [543]). Thus,  $^{40}\text{Ar}_{\text{rad}}$  model ages can be non-confirmatory of  $^4\text{He}$  model ages, but yet still provide knowledge about processes within the aquifer system. This separation of  $^4\text{He}$  and  $^{40}\text{Ar}_{\text{rad}}$  can be explicitly seen as noble gases accumulate in oil production reservoirs (see Fig. 8.11). Initially, with short times suggested by low concentrations of  $^4\text{He}$  or small  $^{40}\text{Ar}/^{36}\text{Ar}$  ratios,  $^4\text{He}/^{40}\text{Ar}_{\text{rad}}$  ratios are far in excess of in situ production. However, with time and the integrated accumulation of the late release of  $^{40}\text{Ar}_{\text{rad}}$ , the  $^4\text{He}/^{40}\text{Ar}_{\text{rad}}$  ratio approaches that typical of crustal production ( $\sim 5$ ; Torgersen et al. (1989) [573]).

In the case where  $^{40}\text{Ar}_{\text{rad}}$  and  $^4\text{He}_{\text{rad}}$  may both have viable external (to the aquifer) sources ( $^{40}\text{Ar}_{\text{rad}}^{\text{terr}}$  and  $^4\text{He}_{\text{rad}}^{\text{terr}}$ ), the above possibilities, with respect to relative release factors in the external source, apply. Additionally, diffusive transport into the local water parcel may separate  $^{40}\text{Ar}_{\text{rad}}$  and  $^4\text{He}_{\text{rad}}$ . Torgersen et al. (1989) [573] found that the Great Artesian Basin was dominated by external fluxes of  $^4\text{He}_{\text{rad}}$  and  $^{40}\text{Ar}_{\text{rad}}$ , both of which were approximated by the whole crustal rate of in situ production (with some degree of variation). Yet, Torgersen et al. (1989) [573] emphasize that  $^{40}\text{Ar}_{\text{rad}}$  has spatial heterogeneity not apparent in  $^4\text{He}_{\text{rad}}$ . Additionally, Castro et al. (1998) [96] and Castro et al. (1998) [97] found that diffusive separation of  $^4\text{He}_{\text{rad}}$  and  $^{40}\text{Ar}_{\text{rad}}$  across aquitards within the Paris Basin created differing and contrasting mechanisms of  $^4\text{He}_{\text{rad}}$  or  $^{40}\text{Ar}_{\text{rad}}$  accumulation in different layers. Thus, a comparison of terrigenic  $^{40}\text{Ar}_{\text{rad}}^{\text{terr}}$  and  $^4\text{He}_{\text{rad}}^{\text{terr}}$  may again not be confirmatory, and  $^{40}\text{Ar}_{\text{rad}}$  requires additional boundary and initial conditions that make any solution non-unique.

#### 8.4.4. Summary

The various components that contribute to the total measured  $^4\text{He}$  in a groundwater sample show that noble gas isotopic measures in addition to  $^4\text{He}$  are a requirement for the separation of components. Furthermore, the overall complexity of noble gas groundwater processes suggests that any tracer model age calculation should be cross-checked with other methods (e.g.  $^{36}\text{Cl}$ ,  $^{40}\text{Ar}_{\text{rad}}$ ). It is then necessary to use such information within a simplified basin flow model (Bethke and Johnson (2008) [84]; Bethke et al. (2002) [574]; Castro and Goblet (2003) [89]; Castro et al. (1998) [96]; Castro et al. (1998) [97]; Castro et al. (2000) [88]; Fritzel (1996) [575]; Zhao et al. (1998) [98]) to arrive at the best conceptualization of the aquifer and its timescale of transport, which may still provide a non-unique solution.

### 8.5. CASE STUDIES

#### 8.5.1. Setting the stage

In spite of the potential for the application of  $^4\text{He}$  model ages to groundwater transport, it was recognized early that the method raises considerable questions. Geochemists are, of necessity, sceptical of direct application of concepts and have rightly devoted considerable time to testing the underlying assumptions for the use of  $^4\text{He}$  in groundwater systems. Marine (1979) [576] evaluated  $^4\text{He}$  model ages in groundwater based on assumptions regarding  $\Lambda_{\text{He}}$  but cross-checked  $\Lambda_{\text{He}}$  with measures from the solid phase indicating  $0.73 < \Lambda_{\text{He}} < 0.97$ . However, his analysis did not include external, open system sources of  $^4\text{He}$  (large fluxes from the crust and/or aquitards) that could transport  $^4\text{He}$  into the system (it should be noted that solid phase measures indicating  $\Lambda_{\text{He}} \sim 1.0$  almost demands a resultant crustal flux). Andrews and Lee (1979) [577] evaluated  $^4\text{He}$  model ages of the Bunter sandstone based on only-local  $^4\text{He}$  inputs but cross-checked such ages with  $^{14}\text{C}$  analysis. The results indicated significant excess  $^4\text{He}$

(four times) and excessively large  $^4\text{He}$  model ages. Torgersen (1980) [535] evaluated  $^4\text{He}$  model ages based on only-local sources from gas wells, geothermal systems and groundwater, and found  $^4\text{He}$  model ages of the order of 1000 times in excess of  $^3\text{H}$ – $^3\text{He}$  model ages for cold springs. Heaton (1984) [538] compared  $^4\text{He}$  model ages to  $^{14}\text{C}$  model ages for two aquifer systems and found only-local source  $^4\text{He}$  model ages were 10–100 times the calculated  $^{14}\text{C}$  model ages. Heaton (1984) [538] calculated the rate of  $^4\text{He}$  addition due to weathering (dissolution) input of  $^4\text{He}$  (Torgersen (1980) [535]) but dismissed that source as insignificant. Torgersen and Clarke (1985) [293] also evaluated a  $^4\text{He}$  source associated with weathering input and also found that source to be insignificant. Notable in the Heaton (1984) [538], and Torgersen and Clarke (1985) [293] studies was an increase in the rate of  $^4\text{He}$  accumulation down the presumed flowline (assuming a flow model). These studies clearly demonstrated an inherent complication in the calculation of  $^4\text{He}$  model ages in groundwater that had yet to be specifically identified, although Heaton (1984) [538] did note that an external flux of  $^4\text{He}$  from below the aquifer could be an important source.

### 8.5.2. Simple open system aquifer models

In a study of the Great Artesian Basin in Australia, Torgersen and Clarke (1985) [293], and Torgersen and Ivey (1985) [93] had the good fortune of evaluating a well defined system with existing and available hydraulic ages (flow model ages based on Darcy's law),  $^{14}\text{C}$  model ages and  $^{36}\text{Cl}$  model ages (Airey et al. (1983) [363]; Airey et al. (1979) [578]; Bentley et al. (1986) [301]). After evaluating local  $^4\text{He}$  production and its downflow variability via  $^{222}\text{Rn}$ , in situ U–Th-series abundances and possible sources via weathering release from the solid phase, Torgersen and Clarke (1985) [293] concluded  $^4\text{He}$  in the Great Artesian Basin must have a dominant external source from outside (below) the aquifer. A key component in this analysis is that simple local-source-only  $^4\text{He}$  concentrations agree with  $^{14}\text{C}$  model ages and hydraulic flow model ages for timescales less than 40 ka. Yet, for longer timescales,  $^4\text{He}$  concentrations exceeded the local-source-only  $^4\text{He}$  concentration by 74 times (see Fig. 8.2). Within this largely uniform aquifer, the local-source-only production rate is likely to be constant throughout the aquifer without large scale variation and this was confirmed with  $^{222}\text{Rn}$  analyses (Torgersen and Clarke (1985) [293]). Torgersen and Ivey (1985) [93] used a simple, piston flow, 2-D model adapted from Carslaw and Jaeger (1959) [539] which included a 2-D aquifer of uniform vertical diffusion and uniform horizontal velocity:

$$v_x \frac{\partial C}{\partial x} = D_z \frac{\partial^2 C}{\partial z^2} + I \quad (8.21)$$

With  $v_x$ ,  $D_z$  and  $I$  constant, a constant flux across the bottom boundary and zero flux across the top boundary, Torgersen and Ivey (1985) [93] were able to evaluate the variability of  $^4\text{He}$  as a tracer of groundwater processes rather than as a groundwater dating methodology. They demonstrated that the change in the apparent rate of  $^4\text{He}$  accumulation with time/distance along the aquifer was related to the time needed to diffuse a bottom boundary flux vertically through the aquifer. Secondly, they were able to demonstrate that the external bottom flux dominated the sources of  $^4\text{He}$  at long timescales. Although the simple model (Torgersen and Ivey (1985) [93]) did not allow a loss term for the  $^4\text{He}$  flux out the top of the aquifer, their analysis shows that such a flux would be minimal on the timescale of the Great Artesian Basin system. Their analysis proceeded to evaluate simply the parameter sensitivity of the tracer flow model (from Carslaw and Jaeger (1959) [539]) by evaluating the sensitivity of the  $^4\text{He}$  measures obtained with regard to relative depth within the aquifer, aquifer thickness, aquifer porosity and the vertical rate of diffusion/dispersion. The model was also applied to the Aoub sandstone data of Heaton (1981) [210], which was much thinner and much younger and allowed a sensitivity analysis of the impact of the bottom boundary input flux. Castro et al. (2000) [88] ultimately re-sampled and re-evaluated the (Stampriet) Auob aquifer (Heaton (1981) [210]; Heaton (1984) [538]), and obtained

a bottom boundary  $^4\text{He}$  flux  $\sim 2$  times larger than estimated by Torgersen and Ivey (1985) [93]. Castro et al. (2000) [88] additionally quantified the Carrizo aquifer in Texas and the Ojo Alamo and Nacimiento aquifers (San Juan Basin, NM). These crustal fluxes are reported in Table 8.2. Torgersen et al. (1989) [573] showed that the accumulation of  $^{40}\text{Ar}_{\text{rad}}$  from an external bottom boundary flux of  $^{40}\text{Ar}_{\text{rad}}$  in the Great Artesian Basin system also dominated in situ production of  $^{40}\text{Ar}_{\text{rad}}$  in the aquifer. The key contribution of these papers is the transition from a theoretical calculation of a  $^4\text{He}$  model age to the incorporation of  $^4\text{He}$  into simplified groundwater flow models as a component subject to reaction and transport in the groundwater systems. As such,  $^4\text{He}$  allows finer scale tuning of knowledge about transport, mixing, sources and sinks to/in aquifer systems. The disadvantage is that some prior knowledge about the structure of the aquifer system is required.

Stute et al. (1992) [561] used a 2-D model of flow in the Great Hungarian Plain with a bottom boundary flux equivalent to 0.25 times the value of Torgersen and Ivey (1985) [93]; equivalent to whole crustal production, but allowing flux out of the top boundary. Fitting the observed  $^4\text{He}$  and  $^3\text{He}$  concentrations to the 2-D model, Stute et al. (1992) [561] were able to constrain vertical flow velocities in this aquifer system and provide an estimate of groundwater turnover in the system to be of the order of  $10^5$  a. An important contribution of this work is the ability to examine the discharge region of an aquifer system in terms of the Peclet number ( $\Delta z v_z / D_z$ ) which defines the basic transport of the system. Castro et al. (2000) [88] further evaluated the model of Torgersen and Ivey (1985) [93] for the Carrizo aquifer system and verified the basic assumptions of the system, including the assumption of a topmost no-flux boundary. Although emphasizing that fluxes across boundaries can be the result of advection, dispersion and diffusion, they concluded that many systems are sufficiently young or short to operate as if there were no flux across the top boundary. The corollary to this observation is that  $^4\text{He}$  fluxes measured at the land surface will be highly variable; for such an aquifer, the flux leaving the ground surface to the atmosphere will be very low, while the  $^4\text{He}$  flux to the atmosphere at the discharge zone will be very high. The transport properties and mechanisms of the continental crust dictate a high degree of spatial variability.

### 8.5.3. Helium-4 as a component in groundwater flow models evolves

Fritzel (1996) [575] and Zhao et al. (1998) [98] inserted  $^4\text{He}$  (and  $^3\text{He}$ ) within established groundwater flow models (Bethke et al. (1993) [579]). Zhao et al. (1998) [98] show (Fig. 8.12) that for a base case (in situ production plus a large basal bottom flux; Fig. 8.12.2),  $^4\text{He}$  in the vertical section of the aquifer increases from the top to the bottom, reflecting the importance of the basal flux. However, for the exemplar case in which the bottom boundary flux is insignificant (Fig. 8.12.3), the  $^4\text{He}$  concentration in the aquifer increases from the top to the bottom, reflecting the importance of ‘old water’ in the upper confining shale as a source of high  $^4\text{He}$  concentration. The Zhao et al. (1998) [98] examination of an irregular basal flux (Fig. 8.12.4) shows that if  $^4\text{He}$  basal flux is confined to an area one tenth of the original and is ten times the original, then  $^4\text{He}$  decreases downstream of the basal flux region as a result of hydrodynamic dispersion and mixing. As shown by both Torgersen and Ivey (1985) [93], and Zhao et al. (1998) [98], increasing the vertical rate of dispersion/mixing results in a shorter period of local in situ production dominance, less vertical variation and a system dominated by horizontal variability over vertical variability (Fig. 8.12.5). Zhao et al. (1998) [98] also evaluate the impact of subregional flow cells induced by basin topography as a control on aquifer  $^4\text{He}$  distribution (Fig. 8.12.6). These studies show how the quantification of large scale average aquifer transport properties can be fine-tuned with the inclusion of  $^4\text{He}$  in reaction and transport models, even under conditions where the details of the basal flux variability may not be explicitly defined.

In relation to Fig. 8.12, the utilization of He data for quantification of groundwater flow requires consideration of the aspects listed below. It should be noted that in all cases in the figure, the (a) panel shows  $^4\text{He}$  concentrations in units of  $10^{-5}$  cm<sup>3</sup> STP  $^4\text{He}/\text{cm}^3_{\text{H}_2\text{O}}$  while the (b) panel shows the  $^3\text{He}/^4\text{He}$  ratio in units of  $10^{-8}$ .

- Fig. 8.12.1: The conceptual model for numerical simulations is as follows: 1000 km basin with a basin tilt of 0.7 km/1000 km and an aquifer thickness of 1 km.
- Fig. 8.12.2: The base case scenario proscribed with a basal flux from Torgersen and Ivey (1985) [93] shows (Fig. 8.12.2(a)) an increase in  $^4\text{He}$  along flowlines and from the top to the bottom of the aquifer. Figure 8.12.2(b) shows a decrease in the  $^3\text{He}/^4\text{He}$  ratio downstream that is the result of both in situ dilution of the air-saturated initial condition with in situ production as well as the basal flux which has been set to have a greater  $^3\text{He}/^4\text{He}$  ratio than in situ production.
- Fig. 8.12.3: The condition where the basal flux is zero shows (Fig. 8.12.3(a)) the  $^4\text{He}$  concentration decreasing with increasing depth in the aquifer as a result of input from the overlying shale aquitard and (Fig. 8.12.3(b)) a lower  $^3\text{He}/^4\text{He}$  ratio resulting from the lower in situ production ratio.
- Fig. 8.12.4: The condition where the basal flux is highly localized (one tenth of the area but at ten times the flux). Fig. 8.12.4(a) shows that the localized basal flux is significantly diluted downstream by dispersion.
- Fig. 8.12.5: The variability of the  $^4\text{He}$  concentration as a result of different dispersivities (Fig. 8.12.5(a)) used assumes no mechanical dispersion (Fig. 8.12.5(b)), and shows the condition for a longitudinal dispersivity of 100 m and transverse dispersivity of 10 m. It should be noted that Fig. 8.12.2(a) shows the intermediate case of longitudinal dispersivity of 10 m and a transverse dispersivity of 1 m.

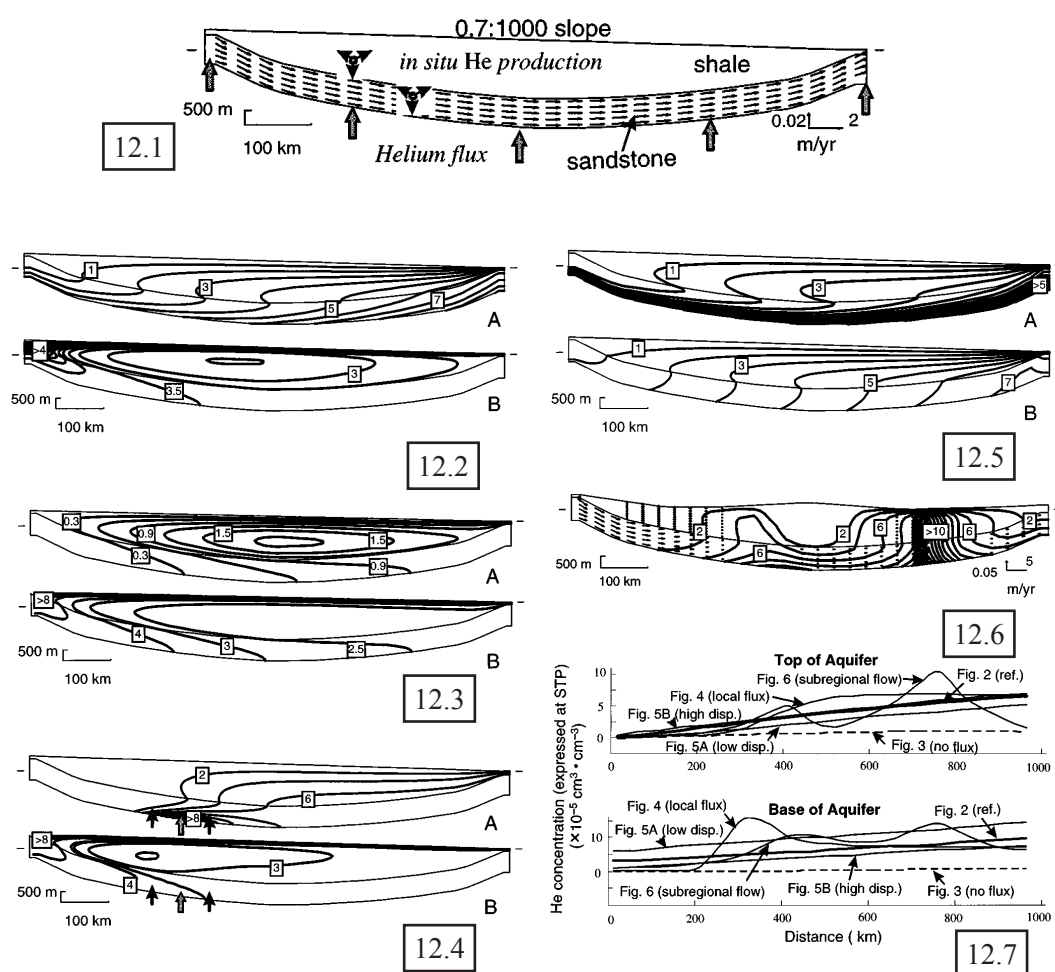


FIG. 8.12. The utilization of He data in the quantification of groundwater flow and transport problems (from Zhao et al. (1998) [98]) in the Great Artesian Basin, Australia.

- Fig. 8.12.6: The variability of  $^4\text{He}$  under the influence of subregional flow cells is imposed by regional topography.
- Fig. 8.12.7: A comparison of the  $^4\text{He}$  concentrations along the top of the aquifer and the bottom of the aquifer is shown for each illustrated case. It should be noted that all cases show a general increase with distance but that variability along the flow path can be identified with specific cause/effect hypotheses that are model testable.

Unless otherwise specified, the model is defined with:

Aquifer length	1000 km
Aquifer thickness	1 km
Topographic slope	700 m/1000 km
Permeability sandstone	$1 \mu\text{m}^2$
Permeability shale	$5 \times 10^{-5} \mu\text{m}^2$
Dispersivity longitudinal	10 m
Dispersivity transverse	1 m
Diffusion coefficient	$3 \times 10^3 \text{ cm}^2/\text{a}$
In situ production of $^4\text{He}$ , sandstone	$3.07 \times 10^{-13} \text{ cm}^3 \text{ STP } ^4\text{He} \cdot \text{cm}^{-3}_{\text{H}_2\text{O}} \cdot \text{a}^{-1}$
In situ production of $^4\text{He}$ , shale	$8.78 \times 10^{-12} \text{ cm}^3 \text{ STP } ^4\text{He} \cdot \text{cm}^{-3}_{\text{H}_2\text{O}} \cdot \text{a}^{-1}$
Basal flux	$0.14 \times 10^{-5} \text{ cm}^3 \text{ STP } ^4\text{He} \cdot \text{cm}^{-2}_{\text{tot}} \cdot \text{a}^{-1}$
$^3\text{He}/^4\text{He}$ meteoric recharge	$138.6 \times 10^{-8}$
$^3\text{He}/^4\text{He}$ production in sandstone	$1.80 \times 10^{-8}$
$^3\text{He}/^4\text{He}$ production in shale	$1.85 \times 10^{-8}$
$^3\text{He}/^4\text{He}$ of basal flux	$3.5 \times 10^{-8}$

Bethke et al. (1999) [95] re-evaluated the  $^4\text{He}$  data of Torgersen and Clarke (1985) [93] with the helium capabilities of the enhanced basin flow model (Bethke et al. (1993) [579]). They show that  $^4\text{He}$  measurements obtained in the upper 20% of the aquifer vertical section are controlled not only by the lateral flow ( $v_x$ ) and the vertical mixing ( $D_z$ ) of the basal flux up into the aquifer, but also by the vertical water velocity encountered in the recharge area and the discharge area, a subject that was also addressed in simpler form by Stute et al. (1992) [561]. Such dependency is not discernable in the simplistic model of, for example, Torgersen and Ivey (1985) [93] because it is based on a piston flow concept. Significantly, Bethke et al. (1999) [95] were able to address the high concentrations and variability of  $^4\text{He}$  in this Great Artesian Basin aquifer system without resorting to stagnant zones (Mazor (1995) [580]). This did much to reconcile the geochemical concepts of  $^4\text{He}$  inputs, sources and accumulation with established concepts of flow in large aquifer systems. Bethke et al. (2000) [94] combined the use of  $^{36}\text{Cl}$  and  $^4\text{He}$  to conclude that isotope distributions can be used to obtain internally consistent descriptions of deep groundwater flow directions and rates.

Castro et al. (1998) [96] and Castro et al. (1998) [97] used a finite element code model of transport in the Paris Basin (Wei et al. (1990) [581]), with multiple aquifers arranged vertically. Within this study, Castro et al. (1998) [96] and Castro et al. (1998) [97] examined the vertical flux of not only  $^4\text{He}$  and  $^3\text{He}$  but also  $^{40}\text{Ar}_{\text{rad}}$  and  $^{21}\text{Ne}$ . This study demonstrated the potential for diffusive separation of noble gases as they are transported across various aquitards in the system (very small Peclet numbers). While this analysis is not disputed here, Castro et al. (1998) [96] admit that the model is extremely sensitive to parameter variations, in particular to changes in flow rate and permeability. Given the degree of structural complexity in the model, the sheer number and spatial variability of parameters that control water flow and noble gas transport, together with the relatively few noble gas measures and aquifer transport parameter measures from the Paris Basin, the question is raised as to whether the conclusion (diffusion controlled separation of  $^4\text{He}$  and  $^{40}\text{Ar}_{\text{rad}}$ ) is unique. Sensitivity to parameter choice/variability is an important constraint in modelling and the tests run by Zhao et al. (1998) [98] (see Fig. 8.12) and Bethke et al. (2000) [94] provide for greater interpretation around the conclusions. The study

of Castro and Goblet (2003) [89] in the Carrizo aquifer system suggests that  $^4\text{He}$  can and often does constrain the conceptual transport model for the aquifer system as only one of five conceptual models of the Carrizo successfully captured the  $^4\text{He}$  distributions that had been measured. Berger (2008) [92], reported in Bethke and Johnson (2008) [84], used the Paris Basin model and optimized the flow field with constraints provided by  $^4\text{He}$ , head, salinity and temperature.

Bethke and Johnson (2008) [84] discuss in detail the use of  $^4\text{He}$ ,  $^{36}\text{Cl}$ , etc. as tracers in groundwater modelling, and assimilate a rigorous definition of groundwater age. The concept of groundwater age incorporates many complexities, as discussed in Chapter 3, because groundwater flow systems are subject to: (i) lateral dispersion/diffusion; (ii) vertical groundwater velocity distributions resulting from recharge area downflow and discharge area upflow; and (iii) convergence and divergence of streamlines. The interpretation of, for example, a  $^4\text{He}$  model age as an idealized groundwater age is, thus, specific and limited. The most important of the groundwater flow field complexities is the mixing of water parcels. Such issues of groundwater mixing are well established in short timescale groundwater flow where multiple tracers ( $^3\text{H}$ – $^3\text{He}$ , CFC, bomb  $^{14}\text{C}$ , etc.) are often used to quantify both  $v_x$  and  $D_x$  in a 1-D system (Ekwurzel et al. (1994) [582]; Plummer et al. (2004) [50]). This is possible because the input function for  $^3\text{H}$  is much different to, for example, the input function for CFCs, and a comparison of the distribution of both tracers enables the quantification of two controlling parameters. In very old groundwater systems, the viable groundwater ‘dating’ methods are  $^{14}\text{C}$ ,  $^4\text{He}$ ,  $^{81}\text{Kr}$  and  $^{36}\text{Cl}$ . Since  $^4\text{He}$  is typically controlled by (i) an internal production of  $^4\text{He}$  that is often constant and (ii) a large external flux that may be assumed to be constant, the use of combined dating methods of, for example,  $^4\text{He}$  and  $^{36}\text{Cl}$  (with its exponential decay control) provides a powerful means by which to constrain the parameter values describing flow and mixing in aquifer systems, although model optimization with other tracers including temperature (Berger (2008) [92]) are possible and enlightening.

#### 8.5.4. Summary

The concept of using  $^4\text{He}$  to derive an idealized groundwater age has largely been abandoned in favour of the use of  $^4\text{He}$  (other noble gas isotopes,  $^{36}\text{Cl}$  and  $^{81}\text{Kr}$ ) as a component in groundwater reaction and transport models to constrain the complexity of transport in specific aquifers. The inclusion of  $^4\text{He}$  in standard groundwater transport models has the ability to constrain the fundamental aquifer flow conceptualization as well as to refine the quantification of the controlling flow parameter values and their distribution. Building such conceptual transport models of aquifer systems requires some degree of foreknowledge about the basic aquifer structure, the general transport properties of the structure (hydraulic conductivity of the aquitards versus hydraulic conductivity of the aquifer) as well as the in situ  $^4\text{He}$  production (concentration of U–Th and porosity) of the basin structural components. In such cases, the use of  $^4\text{He}$  and adequate samples of  $^4\text{He}$  across the groundwater flow system can provide significant constraints on flow. Still to be addressed, however, are systems for which little structural information is known and for which the basic parameters controlling flow are poorly known in space/time. These issues are exemplified by drillhole sampling that present unique opportunities and problems.

### 8.6. CONCEPTUAL $^4\text{He}$ TRACER AGES AS A CONSTRAINT ON GROUNDWATER AGE

The material presented above shows the simple concept of  $^4\text{He}$  model ages as a proxy for idealized groundwater age is likely inapplicable in most systems. This does not negate the value of  $^4\text{He}$  tracer applications, but it does imply that the physical meaning of the  $^4\text{He}$  model age must be evaluated. Simple  $^4\text{He}$  model age calculations in the idealized 1-D system (piston flow and vertical gradients of  $^4\text{He}$  as a result of bottom flux) demonstrate that direct comparison of 1-D piston flow model ages and

$^4\text{He}$  model ages is inappropriate at best. Furthermore, the possibility that a bottom boundary flux could also be lost out of the top of the control volume further indicates that the  $^4\text{He}$  model age calculated is applicable only to  $^4\text{He}$  and that it has no parallel in groundwater flow.

The calculation of a  $^4\text{He}$  model age, in most cases, will involve the amount of  $^4\text{He}$  in a control volume (atoms/m<sup>3</sup>) as well as fluxes (atoms · m<sup>-2</sup> · s<sup>-1</sup>) across boundaries of that control volume. This necessitates the definition of a layer thickness to which the  $^4\text{He}$  concentration measures apply. Even if one can obtain closely spaced  $^4\text{He}$  concentrations to define a gradient, one would be pressed to define whether the influx across the bottom boundary were advection controlled or diffusion controlled, and knowledge of  $v_z$  and/or  $D_z$  would require additional knowledge about the aquifer structure, its composition and its transport properties. The calculation of  $^4\text{He}$  model age as a proxy for groundwater age, thus, becomes a geochemical ‘artform’.

Calculations of the  $^4\text{He}$  model age are more specifically generalized as:

$$\tau_{\text{He}} = [^4\text{He}] \left( \Lambda_4 J'_{\text{He}} \rho_{\text{rock}} \frac{1-\Phi}{\Phi} + \frac{\Sigma F_{\text{He}}}{\rho_{\text{H}_2\text{O}} \Phi z} \right)^{-1} \quad (8.22)$$

where

$J'_{\text{He}}$  is the internal rate of  $^4\text{He}$  production from U–Th series decay (Eqs (8.6, 8.7));

$\rho_{\text{rock}}$  is rock density;

$\rho_{\text{H}_2\text{O}}$  is water density;

$\Phi$  is porosity;

$\Sigma F_{\text{He}}$  are the boundary fluxes of  $^4\text{He}$  into/out-of the system (atoms · m<sup>-2</sup> · a<sup>-1</sup>) of thickness  $z$  (m).

The first term in Eq. (8.22) bracket represents the local source of  $^4\text{He}$  as a result of local U–Th series element decay and the second term in the same equation represents the external flux to the system across a (bottom) boundary. The ‘artform’ comes not only in choosing  $\Lambda_{\text{He}}$ ,  $F_{\text{He}}$  and  $z$  but also in explicitly defining meaning for  $\tau_{\text{He}}$  in relation to a  $^4\text{He}$  model age and an idealized groundwater age. One example is the case where the vertical flux through the system has reached a steady state and the flux into the bottom is equal to the flux out of the top.  $\Sigma F_{\text{He}}$  for this case is zero but the concentration in the vertical position is linearly variable, giving linearly variable  $^4\text{He}$  model ages in the vertical. The loss terms will be specifically avoided in the following analysis for this reason. Nonetheless, the concept of a  $^4\text{He}$  model age calculation is worth exploring in unique opportunities.

### 8.6.1. Helium-4 fluxes determined by vertical borehole variation in $^3\text{He}/^4\text{He}$

Sano et al. (1986) [583] examined natural gas wells in Taiwan and identified a  $^3\text{He}/^4\text{He}$  ratio that decreased as samples approached the surface. This scenario can be modelled if the base of the system is ‘tagged’ with a mantle  $^3\text{He}$  ( $^3\text{He}/^4\text{He} \sim 10^{-5}$ ) signature, the system is vertically controlled and in situ production by radioactive decay of U–Th series elements in the layer (thickness =  $z_i$ ) between measures supplies an input of crustal He of known ratio ( $^3\text{He}/^4\text{He} \sim 10^{-8}$ ) that dilutes the mantle  $^3\text{He}$  flux with crustal production as it is transported vertically in the rock column. For a horizontally homogeneous system with both a  $^3\text{He}$  enriched component at depth and an in situ production of helium, the flux of helium from the top of the layer ( $F_1$ ) is (generalized from Sano et al. (1986) [583]):

$$F_1 = \frac{P_i z_i (R_2 - R_1)}{(R_2 - R_1)} \quad (8.23)$$

and the flux into the bottom of a layer ( $F_2$ ) is:

$$F_2 = \frac{P_i z_i (R_1 - R_1)}{(R_2 - R_1)} \quad (8.24)$$

where

- $P_i$  is the production rate of  $^4\text{He}$ ;  
 $R_1$  and  $R_2$  are the isotopic ratios of  $^3\text{He}/^4\text{He}$  at the top and bottom of the layer, respectively;  
 $R_i$  is the production ratio of  $^3\text{He}/^4\text{He}$  in the layer;  
 $z_i$  is the thickness of a layer.

If the system contains multiple layers with differing rates of in situ production, the appropriate equations are:

$$F_1 = \frac{\sum P_i z_i R_1 - [\sum P_i z_i] R_2}{(R_1 - R_2)} \quad (8.25)$$

and

$$F_2 = F_1 - \sum P_i z_i \quad (8.26)$$

where  $P_i z_i$  is the in situ production of individual layers between the surfaces defining  $F_1$  and  $F_2$ .

Using Eqs (8.23) and (8.24), Sano et al. (1986) [583] quantified the fluxes of  $^4\text{He}$  in two Taiwan natural gas fields to be  $2.7 \pm 0.6 \times 10^{10}$  atoms  $^4\text{He} \cdot \text{m}^{-2} \cdot \text{s}^{-1}$  and  $2.4 \pm 0.8 \times 10^{10}$  atoms  $^4\text{He} \cdot \text{m}^{-2} \cdot \text{s}^{-1}$  (Table 8.2). These continental degassing fluxes are in agreement with measures from the Great Artesian Basin (Torgersen and Clarke (1985) [293]; Torgersen and Ivey (1985) [93]) and the atmospheric mass balance (Torgersen (1989) [546]), and could have been used to calculate apparent  $^4\text{He}$  model ages as per Eq. (8.22). Torgersen and Marty (unpublished data)<sup>1</sup> applied such relations to the Paris Basin and obtained ages that were roughly ten times larger for the Dogger aquifer than were obtained by Castro et al. (1998) [96] and Castro et al. (1998) [97] using a full scale hydrological flow model. These results suggest that although the mathematics of the approach is appealing, the underlying assumptions are likely too restrictive to apply to the general case. It would be interesting to apply Eqs (8.23–8.26) to modelled results of Zhao et al. (1998) [98], for example, to determine when/whether these simple relations have meaning.

### 8.6.2. Cajon Pass

Torgersen and Clarke (1992) [294] evaluated the  $^4\text{He}$  model age for waters collected in the Cajon Pass scientific drillhole to constrain groundwater flow and heat transport in and around the San Andreas Fault. Samples were collected with a downhole sampler (Solbau et al. (1986) [505]) after the drillhole had been given over wholly to fluid inflow during a prolonged period of no drilling (due to lack of funds). The drillhole was pumped and the water remaining was spiked with fluorescein to differentiate contaminant water from fracture water inflow. Specific intervals were packed-off to define layers of fracture water inflow that were allowed to accumulate over periods of months. Careful sampling enabled some vertical structure in the inflow water to be defined but the evaluation of  $^4\text{He}$  tracer model ages was based on bulk concentrations of the fluorescein (contaminate)-corrected inflow water  $^4\text{He}$  concentration.

CASE (1) calculations in Torgersen and Clarke (1992) [294] assumed  $F_{\text{He}} = 0$ , used a  $\Lambda_{\text{He}}$  value quantified by the  $^{222}\text{Rn}$  concentration after the method of Torgersen (1980) [535] and calculated the source function from U–Th series decay ( $J'_{\text{He}}$ ) from estimated rock composition. The resultant apparent  $^4\text{He}$  model age was 0.9–5 Ma which implies a vertical fluid velocity of 0.04–0.2 cm/a ( $v = \Delta z / \Delta t$  where  $\Delta z = 2000$  m). CASE (2) calculations in Torgersen and Clarke (1992) [294] assumed a release factor of  $\Lambda_{\text{He}} = 1$ . The resultant  $^4\text{He}$  model age was 33–330 ka, implying a vertical fluid velocity

<sup>1</sup> TORGERSEN, T., Marine Sciences, University of Connecticut, MARTY, B., Centre de Recherches Pétrographiques et Géochimiques, Nancy, unpublished data.

of 0.6–6 cm/a. They further evaluated the possibility of a non-steady state source (loss of  $^4\text{He}$  as a result of fracturing (Torgersen and O'Donnell (1991) [543])) which possibly mimics the  $\Lambda_{\text{He}} > 1$  defined by Solomon et al. (1996) [295] and concluded that  $\Lambda_{\text{He}} = 1$  was a good approximation. This gives a range for the vertical fluid velocity of 0.04–6 cm/a. CASE (3) is added to their analysis, where it is assumed that the accumulation of  $^4\text{He}$  in the Cajon Pass groundwater was dominated by the crustal degassing flux. Assuming an externally imposed degassing flux equivalent to the whole crustal production and assuming the concentration measured at  $\sim 2000$  m applies to the whole layer from 0–2000 m depth, a  $^4\text{He}$  model age of 1667 a would be calculated, giving a vertical fluid velocity of 120 cm/a. Torgersen and Clarke (1992) [294] show that excess heat generated by fault zone friction is not significantly removed by vertical fluid flow estimate for CASE (1), demonstrating that the San Andreas Fault system is likely a low strength/low coefficient of friction system. Furthermore, the vertical fluid velocity estimated from  $^4\text{He}$  model ages was compared to drillhole well tests that estimate vertical fluid velocities of  $10^{-5}$  cm/a. If one assumes that both quantifications represent reality but over different timescales (the drillstem test provides an estimate of fluid velocity on the timescale of months for a space equivalent to the open hole section; and the  $^4\text{He}$  tracer age based velocity is applicable over the residence time (tracer age) and the 2000 m depth of the sample), then the comparison suggests that fluid transport is episodic with short intervals of rapid fluid transport and longer timescales of very slow fluid transport. Such a conclusion is in agreement with metamorphic geology literature and the mechanisms of fluid transport suggested by Nur and Walder (1990) [584]. Adding CASE (3) does not change the conclusion with regard to episodic transport but it does enable hydrothermal heat flow (estimated to be  $<65\text{--}130$  W/m $^2$ ) to remove any fault zone generated heat (estimated to be  $<85\text{--}90$  W/m $^2$ ) if such a vertical fluid transport rate can be verified. Thus, the principles of  $^4\text{He}$  model age calculations can be applied to constrain systems for which little information is available.

### 8.6.3. South African ultra-deep mine waters

Lippmann et al. (2003) [568] evaluated the noble gas isotope composition of groundwaters collected from seeps in the ultradeep mines of South Africa. They calculated noble gas tracer ages based on  $^4\text{He}$ ,  $^{40}\text{Ar}_{\text{rad}}$ ,  $^{134}\text{Xe}$  and  $^{138}\text{Xe}$  on the basis of the generalization of Eq. (8.22) from  $^4\text{He}$  to other noble gases. Scenario 1 calculations were based on in situ local-only sources of noble gas isotopes ( $\Sigma F_{\text{He}} = 0$ ) with an assumed  $\Lambda_{\text{He}} = 1$  and  $\Lambda_{\text{Ar}} = 1$ . For Xe isotopes,  $0.1 < \Lambda_{\text{Xe}} < 0.5$  was artfully fit based upon a much smaller recoil distance involved in the fissionogenic production of these isotopes. Scenario 2 includes the possibility of a whole crustal production degassing flux ( $F_{\text{He}} = 8 \times 10^9$  atoms  $^4\text{He} \cdot \text{cm}^{-2} \cdot \text{s}^{-1}$ ; see Table 8.2) applicable over the layer from the surface to the depth of sampling. Their calculations indicate noble gas tracer model ages on the order of 10–100 Ma (scenario 1) and 0.1–20 Ma (scenario 2). Given that  $^{36}\text{Cl}$  measures in the same water indicate  $^{36}\text{Cl}$  model ages in excess of 1.5 Ma, the noble gas estimated ranges for tracer age can be used as a zeroth order estimate of the idealized groundwater age. The vertical fluid velocities estimated (sample depth is of the order of 2000–3000 m) from these noble gas tracer ages are 0.003–0.02 cm/a which are consistent with hydraulic conductivity in tight rock (Freeze and Cherry (1979) [11]; unfractured metamorphic and igneous rocks assuming hydrostatic gradients) as well as in situ measures of vertical transport rates at the Cajon Pass, California (Coyle and Zoback (1988) [585]; Torgersen and Clarke (1992) [294]).

### 8.6.4. Deep borehole sampling

Osenbrück (1996) [514] explored a new sampling method for deep borehole rock in which either inflow of water was minimal and/or the restrictions of the drilling schedule/cost were such that direct groundwater sampling was not feasible. The method (Osenbrück (1996) [514]) depends upon the relatively slow diffusion of noble gases in the matrix pore fluids of intact rock (hours) to enable

rock sampling (drillcore retrieval) that preserves noble gas concentrations from matrix pore fluids recovered from depth. The principle assumption is that matrix pore fluids are equivalent to fracture filling pore fluids which are likely the major mode of transport. In a typical sampling operation, drillcore is recovered at the surface within hours of being cut and intact rock is subcored to avoid rock on the exterior of the drillcore that had already been microfractured and had begun to release pore fluids. The subcored rock is then introduced into a vacuum container, purged of air and left either under low  $N_2$  pressure or vacuum for an extended period of time. The natural relaxation of the rock then causes expansion, dilatation and draining of pore fluids into the sealed container. The container may be maintained at room temperature or at elevated temperatures (e.g. equivalent to in situ temperatures) to increase the diffusivity in water and, thus, speed the release of pore fluid to the container (Ali et al. (2008) [586]; Ali et al. (2010) [513]). Opening the container to the mass spectrometer will then enable measures of the amount of water released as well as the noble gases contained in those pore fluids.

Using the method of Osenbrück (1996) [514] to obtain pore fluid samples, Osenbrück et al. (1998) [515] explored the tracer model ages in a potential nuclear waste repository in Morsleben, Germany. Their results show a profile of  $^4He$  in pore fluids that is consistent with vertical diffusive transport in a horizontally homogeneous system. They assume that transport occurs at a rate determined by tortuosity- and porosity-corrected molecular diffusivity, and calculate a diffusion coefficient of  $D = 2 \times 10^{-6} \text{ cm}^2/\text{s}$ . Using this diffusion coefficient and the measured gradient in pore fluid  $^4He$  concentration, they calculate a vertical flux of  $2 \times 10^{-7} \text{ cm}^3 \text{ STP } ^4He \cdot \text{cm}^{-2} \cdot \text{a}^{-1}$  which is in agreement with other measured fluxes (see Table 8.2). Using the characteristic timescale for such a steady state profile to be obtained (from Carslaw and Jaeger (1959) [539]):

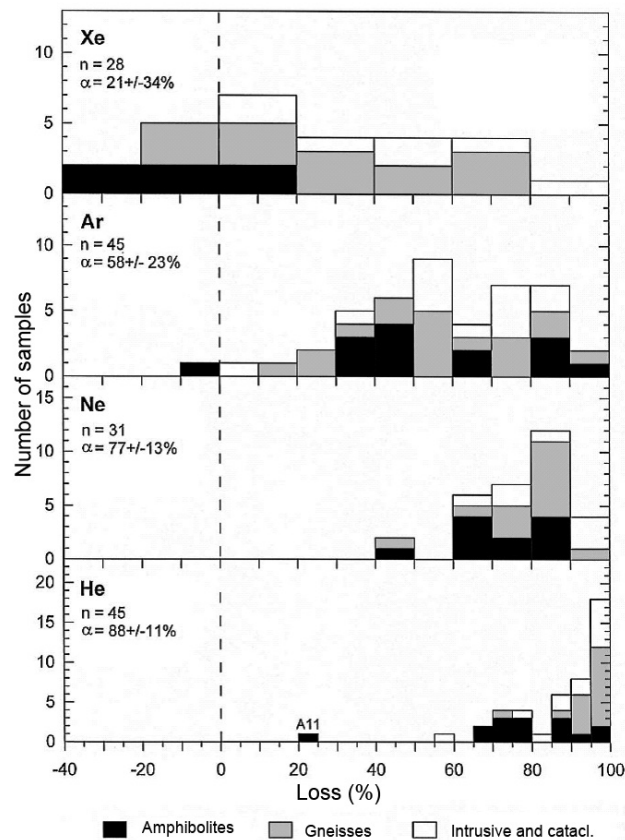


FIG. 8.13. The release fraction,  $A_{Ng}$ , as determined from whole rock samples recovered from the German Continental Deep Drilling programme borehole (Drescher et al. (1998) [569]). The results represent an analysis of rock and the results confirm the general trend of  $A_{He} > A_{Ne} > A_{Ar} > A_{Xe}$  as would be expected from their respective diffusion coefficients in the solid phase. (From Drescher et al. (1998) [569].)

$$\tau = 4 \frac{\Delta x^2}{\pi^2 D} \quad (8.27)$$

they calculate a lower limit on the pore water age of 6 Ma. Here, the tracer model age based on the  $^4\text{He}$  concentration and the sum of the in situ production and the crustal flux can be calculated for comparison. For depths of 300–700 m, where  $^4\text{He}$  is approximately constant at  $4 \times 10^{-4}$  ccSTP  $^4\text{He}/\text{g}_{\text{H}_2\text{O}}$ , the tracer model age is given by Eq. (8.22). The data of Osenbrück et al. (1998) [515] yield 7.5 Ma using the calculation of the local crustal flux (which is circular reasoning) or 4.3 Ma if the local  $^4\text{He}$  crustal flux is equivalent to the whole crustal production as estimated from the measures in Table 8.2.

The Osenbrück (1996) [514] methodology for sampling pore fluids opens the more general case for dating deep borehole pore fluids. Drescher et al. (1998) [569] collected deep borehole rock samples from the German Continental Deep Drilling (KTB) programme (depths from 100–9000 m) and measured the solid phase concentration of  $^4\text{He}$ ,  $^{40}\text{Ar}_{\text{rad}}$ ,  $^{21}\text{Ne}$ ,  $^{84,86}\text{Kr}$  and  $^{134,136}\text{Xe}$ . These are converted to an effective noble gas tracer model age of the rock which can be compared to the metamorphic age of the rock as determined by, for example,  $^{87}\text{Sr}/^{86}\text{Sr}$ ,  $^{40}\text{Ar}_{\text{rad}}/\text{K}$  and/or other dating methods. The release fraction for each noble gas to the pore fluid can then be quantified as (Drescher et al. (1998) [569]):

$$\Lambda_{\text{Ng}}^{\text{meas}} = 1 - \frac{\tau_{\text{Ng}}^{\text{rock}}}{\tau_{\text{meta}}} \quad (8.28)$$

Direct measurements and Eq. (8.28) (Drescher et al. (1998) [569]) indicate the release factor from the KTB borehole rock to be  $\Lambda_{\text{He}} = 0.88 \pm 0.11$  (Fig. 8.13), which is in agreement with the generally assumed value of  $\Lambda_{\text{He}} = 1.0$ . Similar values can be obtained from the case study of Tolstikhin et al. (1996) [559]. Assuming the rock samples of Drescher et al. (1998) [569] are representative of the crust, they imply a crustal flux of 0.88 times whole crustal production with similar estimates for  $^{21}\text{Ne}$ ,  $^{40}\text{Ar}_{\text{rad}}$  and  $^{136}\text{Xe}$  (Fig. 8.13). It should be noted that the depth at which these samples were collected removes a significant fraction of the crust as a contributor to the net crustal flux. The approach can be further generalized.

These simple measures of  $\tau_{\text{rock}}$  need to be corrected for the time necessary to establish a gradient through which to diffuse the in situ production.  $\tau_{\text{rock}}$ , therefore, establishes a minimum constraint on the true value of  $\Lambda_{\text{He}}$  and a best estimate for  $\Lambda_{\text{He}}$  might be:

$$1 - \frac{\tau_{\text{Ng}}^{\text{rock}}}{\tau_{\text{meta}}} < \Lambda_{\text{Ng}}^{\text{meas}} < 1 - \frac{\tau_{\text{Ng}}^{\text{rock}} - \Delta x^2 / D_{\text{He}}}{\tau_{\text{meta}}} = \frac{\tau_{\text{corr-Ng}}^{\text{rock}}}{\tau_{\text{meta}}} \quad (8.29)$$

where

$\Delta x$  is the effective grain size;

$D_{\text{He}}$  is the diffusion coefficient of He in the grain.

Since  $D_{\text{He}} > D_{\text{Ne}} > D_{\text{Ar}} > D_{\text{Xe}}$ , the correction will be relatively more important for the heavier noble gases.

Drescher et al. (1998) [569] were unable to collect pore fluid samples from the KTB by the method of Osenbrück et al. (1998) [515], but this analysis can proceed in the theoretical sense. Parts of this analysis are applied to Ali et al. (2010) [513]. Any one sample obtained at depth can be evaluated with respect to local or external sources with measures of  $[\text{Ng}]_{\text{H}_2\text{O}}$  and  $[\text{Ng}]_{\text{rock}}$ , and a metamorphic age of the rock. If it is assumed that the sample operated as a closed system, then conservation of mass indicates that:

$$[\text{Ng}]_{\text{rock}} \cdot (1 - \Phi) + [\text{Ng}]_{\text{H}_2\text{O}} \cdot \Phi = J_{\text{internal}} \cdot \rho \cdot \tau_{\text{meta}} (1 - \Phi) \quad (8.30)$$

and all (for example)  ${}^4\text{He}$  produced in the metamorphic age of the rock (at which time it was assumed that  ${}^4\text{He}$  was initialized to zero) is contained in either the rock or the pore fluid. Rearranging Eq. (8.30) and including the internal production from the solid phase with regard to the release fraction gives:

$$\frac{[\text{Ng}]_{\text{rock}}}{J_{\text{internal}} \cdot \rho} + \frac{[\text{Ng}]_{\text{H}_2\text{O}}}{\Lambda_{\text{Ng}} J_{\text{internal}} \cdot \rho} \cdot \frac{\Phi}{(1-\Phi)} = \tau_{\text{meta}} \quad (8.31)$$

or:

$$\tau_{\text{rock}} + \tau'_{\text{H}_2\text{O}} \Lambda_{\text{Ng}} = \tau_{\text{meta}} \quad (8.32(a))$$

where  $\tau'_{\text{H}_2\text{O}}$  is the  ${}^4\text{He}$  tracer model age in the water calculated with the assumption that (Eq. (8.22))  $F_{\text{He}} = 0$  and the appropriate solution should be bracketed by corrected (Eq. (8.29)) and uncorrected values of  $\tau_{\text{rock}}$ . Thus, for the closed system sample volume,  $\Delta x \Delta y \Delta z$ , for example, the helium age of the rock ( $\tau_{\text{rock}}$ ) plus a portion ( $\Lambda_{\text{He}}$ ) of the  ${}^4\text{He}$  tracer model age in the fluid ( $\tau'_{\text{H}_2\text{O}}$ ) is equal to the metamorphic age of the rock (as determined by  ${}^{40}\text{Ar}$  and/or  ${}^{87}\text{Sr}/{}^{86}\text{Sr}$  dating of specific mineral separates). Clear indications of an open system with respect to, for example,  ${}^4\text{He}$  in the volume  $\Delta x \Delta y \Delta z$ , but with distinctly different meanings, are expressed as:

$$\tau_{\text{rock}} + \tau'_{\text{H}_2\text{O}} \Lambda_{\text{Ng}} < \tau_{\text{meta}} \quad \text{open system, 'no' external source} \quad (8.32(b))$$

$$\tau_{\text{rock}} + \tau'_{\text{H}_2\text{O}} \Lambda_{\text{Ng}} > \tau_{\text{meta}} \quad \text{open system, significant external source} \quad (8.32(c))$$

For the inequality expressed by Eq. (8.32(b)), there has been a net loss of Ng from the local crustal volume  $\Delta x \Delta y \Delta z$ . The most likely means to lose  ${}^4\text{He}$  (or  ${}^{40}\text{Ar}$ ) is by transport in the fluid phase. Thus,  $\tau'_{\text{H}_2\text{O}}$  (Eq. (8.22) with the assumption  $F_{\text{He}} = 0$ ) provides a first order estimate of the age of fluids within the matrix porosity in the sample and the tracer model age. With the assumption that matrix pore fluids have equilibrated in situ with the fracture-filling and transporting pore fluids, the Ng tracer model ages and the transport in the deep crust can be estimated.

For the inequality expressed by Eq. (8.32(c)), there is a clear indication of an external source of noble gas to the system (or noble gas enrichment due to phase separation and re-dissolution which must be handled in an alternative manner). Again, the mechanism of transport is most likely to be via the fluid phase in fractures and, as was seen above, the first order estimate of the external flux is  $3.63 \times 10^{10} {}^4\text{He atoms} \cdot \text{m}^{-2} \cdot \text{s}^{-1}$  with a variability of 36 times. The methods discussed in this section are actively being applied for samples recovered from the San Andreas Fault Observatory at Depth (Ali et al. (2008) [586]; Ali et al. (2010) [513]; Stute et al. (2007) [587]).

### 8.6.5. Summary

The application of  ${}^4\text{He}$  model ages in groundwater as a proxy for the idealized groundwater age and a method for groundwater 'dating' has proven to be difficult to apply but ultimately valuable. The most common complication is the dominance of external fluxes of noble gas which occurs as the result of small and large scale transport within the crust. Estimates of the crustal flux of  ${}^4\text{He}$  range from 0.03 to 36 times the total crustal in situ production and have been documented in a number of areas. It is to be appreciated that such crustal fluxes have associated with them a specific time and space scale. Furthermore, it is to be recognized that these fluxes are generally conceptualized as near-uniform over the basin in question. Hence, a flux into an aquifer may result in little vertical flux to layers above as well as a concentrated outflux at the discharge zone.

Over the past several decades, research has moved the application of  ${}^4\text{He}$  model ages from the case where individual samples might be 'datable' to the case where large suites of samples are utilized and

$^4\text{He}$  is incorporated as a constituent tracer in large scale reaction and transport models. Such models then optimize the groundwater transport parameters and the  $^4\text{He}$  tracer distributions relative to the various in situ production and crustal flux terms. However, the field has also enlightened the subject to the degree that open system methodologies for placing bounds on groundwater ages using  $^4\text{He}$  are possible and may be applicable. This is especially true in the field of deep borehole sampling where the number of samples is limited and samples are limited to vertical profiles.

## Chapter 9

### SYSTEM ANALYSIS USING MULTITRACER APPROACHES

A. SUCKOW

Leibniz-Institute of Applied Geophysics,  
Hannover, Germany

Previous chapters of this book (i) introduced the subject of dating ‘old’ groundwater (Chapter 1); (ii) reviewed information needs and approaches for refining conceptualization of flow in groundwater systems and how the aquifer properties can be constrained with geoscientific knowledge (Chapter 2); (iii) provided more detailed discussion of the concept of groundwater ‘age’ and its implications for groundwater systems (Chapter 3); and (iv) summarized approaches for estimating the age of old groundwater, based on measurements of chemical and isotopic environmental tracers in groundwater ( $^{14}\text{C}$ ,  $^{81}\text{Kr}$ ,  $^{36}\text{Cl}$ ,  $^{234}\text{U}/^{238}\text{U}$  and  $^4\text{He}$ ), and the special strengths and problems connected with each of these methods (Chapters 4–8, respectively). The present chapter offers a qualitative or semi-quantitative step towards a synthesis of the information that the different tracers provide. It also offers some criteria that can be used to help assess the reliability of selected tracer data in evaluating tracer model ages from measurements of concentrations of multiple environmental tracers in the system. In most of the literature on isotope hydrology, the term ‘apparent age’ is used instead of ‘tracer model age’, and within this chapter the two terms are considered synonymous. This approach testing reliability of tracer data is only a first step and performs a black and white selection of the tracer data. Some consistency tests are performed, and for data passing these tests there is at least no obvious reason known that the tracer model age is not a valid description. For data that fail these tests, it is obvious that a straightforward calculation of tracer model ages will not give the intended result.

This enables the user to perform the following two steps: (i) find a description of the groundwater system which consistently describes all of the tracer model ages for those data that pass the test and (ii) find a system description which can explain the measured values for all (tracer) data. It should be noted that, during the second step, calculation of ages is no longer necessary. This chapter is complemented by the modelling chapter (Chapter 10), which presents a more detailed and quantitative approach to such a synthesis. Finally, four case studies are presented that demonstrate how the techniques in this book have been applied in actual groundwater systems.

In Chapter 3, there was discussion of some of the terminological and practical questions arising when a term such as ‘age’, with an obvious meaning for human beings, is applied to groundwater, where this meaning is by no means obvious. One of the statements was that for principal reasons it is impossible to deduce the exact shape of the frequency distribution of ages in a single sample. This remains true in general terms. However, this chapter presents some methods and approaches to constrain the age distribution when tracer data for many samples or data from multiple tracers (or ideally both) are available. For a single sample, this is achieved by excluding parts of the age distribution when combining the results for several tracers. For the aquifer as a whole, this is achieved by examining patterns in measured tracer concentrations in vertical profiles or along horizontal transects. This way, the tracer data can be tested against observations which are to be expected based on very simple hypothetical models of groundwater flow. It was also demonstrated in the introductory chapters how the conceptual model of groundwater flow is refined and evolves as new data, including environmental tracer data, are considered. This chapter presents some graphical methods that can test aspects of the conceptual model of groundwater flow.

As seen in Chapters 4–8, each tracer has weaknesses and every tracer needs to constrain parameters and assumptions to allow interpretation in terms of age of groundwater. Examples include:

(i) determination of the initial  $^{14}\text{C}$  content; (ii) estimating the strength and isotopic composition of external helium fluxes or internal helium production; (iii) accounting for the secular variations in the  $^{36}\text{Cl}$  production, initial values of the  $^{36}\text{Cl}/\text{Cl}$  ratio and underground production of  $^{36}\text{Cl}$ . Therefore, another purpose of this chapter is to demonstrate how some of the necessary parameters for one tracer can be deduced by using other tracers.

This chapter uses some examples of groundwater flow for which the idealized groundwater age is described analytically by mathematical functions, and in all but one case the discussion is made without calculating an age from tracer data. The intention is to provide a toolbox for estimating hypothetical tracer patterns where tracer model ages are close to idealized ages and to distinguish these patterns from mixing scenarios where idealized ages and tracer model ages are very different and, consequently, the tracer model ages are not very meaningful. Utilizing data from a single tracer, the distinction between dominant advective flow and mixing cases is almost never possible, which is why, in this chapter, multiple tracers are considered in the same groundwater system.

## 9.1. VERTICAL PROFILES

Vertical profiles of tracer values in an aquifer system are among the most valuable data to understanding the flow system. As a general rule, discrete samples from well defined depths in a vertical profile can provide more insight into the flow system than samples taken along an assumed flowline or samples randomly selected over an aquifer system. However, samples from well defined depths in vertical profiles within an aquifer are often difficult to obtain. Although the number of multilevel well nests used in scientific studies is increasing, and although these wells are probably optimal in detailed aquifer studies, the number of vertical profiles that can be sampled is often limited. Therefore, most groundwater studies rely on sampling of ‘wells of opportunity’, that is, single wells, often with several screens or fracture zones within one borehole, or wells that are open to wide intervals of the aquifer, which may be all that are available. Sophisticated packer systems can be used to sample some wells with multiple completions. Other methods employ dual-valve bailers, and, for some gas tracers, chains of passive samplers have been used. There will be discussion on some of the effects of large-screen mixing to demonstrate how to identify mixed samples and why they are difficult to interpret, although they start with ideal sampling conditions.

As a general accepted geoscientific convention, depth profiles are always presented with depth increasing downwards along the  $y$  axis. The presentation in this chapter proceeds from simple to more complicated hydrological systems, starting with a very simple flow system in a homogeneous aquifer, continuing with a more complicated flow system in a homogeneous aquifer and finally discussing inhomogeneous cases.

### 9.1.1. Unconfined homogeneous aquifer

Although homogeneous phreatic (unconfined) aquifers with long travel times are uncommon and very often an oversimplification, this conceptual model presents a useful starting point for examining tracer patterns in aquifers. First, vertical profiles will be considered at one site and with two simple cases for which analytical solutions exist.

First, consider the hypothetical case where groundwater flow is purely vertical downward, with a constant speed, as might conceptually apply to infiltration at a groundwater divide in an unconfined homogeneous aquifer. On a small scale, this could be an infiltration area, and the downward movement could be caused by recharge. In this case, the distance velocity is the recharge rate divided by the aquifer porosity. Any tracer evolution with time will be translated into a tracer evolution with depth, as shown in Fig. 9.1. A radioactive tracer showing exponential decay with time, such as  $^{14}\text{C}$  (green line), will show exponential decrease with depth, a tracer with linear increase in time, such as  $^4\text{He}$  (red line), will

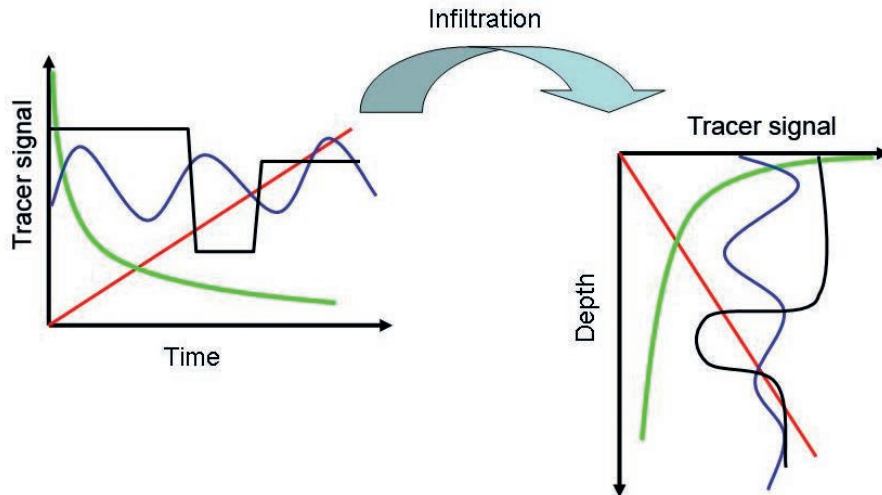


FIG. 9.1. Conversion of time evolution into a depth profile for the hypothetical case of purely downward vertical movement.

show a linear increase with depth, and any historical change in tracer concentration, such as the seasonal pattern of stable isotopes (blue) or the shift in stable isotopes and noble gas recharge temperatures at the last glaciation (black), will be translated into a corresponding depth pattern.

This simple conceptual construct is sometimes a valid approach for short timescales: seasonal variations in stable isotope signals are discernible after crossing several metres of unsaturated zone in the outflow of a lysimeter and can be used to age-date the water (Stumpp et al. (2009) [588]; Vitvar and Balderer (1997) [589]), and tritium depth profiles can show the historical record in precipitation over the past 50 a (Lin and Wei (2006) [590]). For long timescales, however, this approach is completely unrealistic, since the following simplifications are not valid:

- (a) On long timescales, the vertical downward movement changes into horizontal and later to upward movement, simply because with increasing depth there is not enough space for all of the groundwater.
- (b) Diffusion and dispersion will dampen any sharp transitions, such as the palaeoclimate signal, as well as the amplitude of any variations as discussed in Section 5.5.6. This is shown for the blue and black lines in Fig. 9.1.
- (c) Mixing of different groundwaters, infiltrated at different locations and times, will create new patterns which are an averaged combination of those in Fig. 9.1 for the corresponding point in time and the mixing ratio.

This chapter cannot discuss all of these effects in detail but will outline the impact of some of them. The first step is to consider the influence of the transition into horizontal groundwater movement if the aquifer depth is limited. Two analytical solutions exist for this problem.

#### 9.1.1.1. The 'Vogel' aquifer

Vogel (1967) [137] described a simple homogeneous 2-D aquifer system and derived analytical solutions for the resulting frequency distribution of ages that can be used to calculate the resulting tracer depth profiles. The concept of the Vogel aquifer is illustrated in Fig. 9.2. The aquifer is assumed to have a rectangular vertical cross-section of thickness,  $L$ , to be of homogeneous transmissivity and homogeneous porosity  $\Phi$  and to receive uniform recharge at a rate of  $R$  at the top. The left

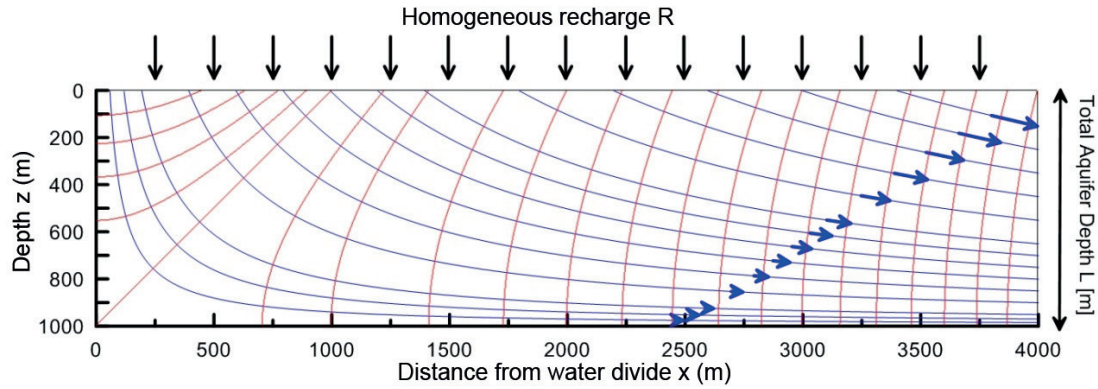


FIG. 9.2. Geometry and boundary conditions of the Vogel aquifer.

and bottom boundaries are impervious, such that all recharge has to leave the flow system through the right boundary.

Vogel (1967) [137] deduced the following formula which describes the idealized groundwater age as a function of depth ( $z$ ) within the aquifer:

$$t = \frac{\phi L}{R} \ln\left(\frac{L}{L-z}\right) \quad (9.1)$$

This age distribution is independent of the horizontal position  $x$  within the Vogel aquifer. While this aquifer model has been used widely to interpret age distributions for young groundwater (0–50 a timescale) using environmental tracers, such as tritium,  $^{85}\text{Kr}$  and the CFCs (IAEA (2006) [85]), it can of course be easily scaled to large timescales if the parameters  $R$ ,  $L$  and  $\Phi$  are chosen accordingly. It is, therefore, a good starting point to derive the expected pattern for age-dating tracers in general. In the following, idealized ages were computed from Eq. (9.1) and converted into tracer concentrations using the equation for first order decay for an assumed initial tracer activity and a decay time of the idealized age. These tracer concentrations were then averaged numerically over the well-screen lengths.

#### 9.1.1.2. Tracer depth profiles for the Vogel aquifer

A depth profile for an exponentially decaying tracer such as  $^{14}\text{C}$ ,  $^{81}\text{Kr}$  or  $^{36}\text{Cl}$  in a Vogel aquifer will always decrease with depth due to radioactive decay with increasing age. However, this decrease will be visible in the depth profile of the aquifer only if the timescale of the aquifer is similar to the timescale of the tracer. A tracer with too short a half-life ( $1/\lambda \ll \Phi L/R$ ) will decay within the topmost part of the aquifer. A tracer with too long a half-life ( $1/\lambda \gg \Phi L/R$ ) will show its decay only at the very bottom of the aquifer, which in many practical cases may not be observed.

#### **Radiocarbon**

Figure 9.3 shows the case for a set of parameters describing an aquifer in which radiocarbon shows a discernible decay ( $\Phi = 0.2$ ,  $L = 1000$ ,  $R = 0.01$ ). Initial radiocarbon content is assumed to be 100 pmc in this and all following computations in this chapter, such as might be observed under open-system conditions, and  $^{14}\text{C}$  activity changes only by radioactive decay, as might be observed in a siliciclastic aquifer (Chapter 4).

The red squares in Fig. 9.3, which closely follow the blue line, represent mixed samples from 100 m filter screens with midpoints at depths of 50, 250, 450, 650 and 950 m below the water table.

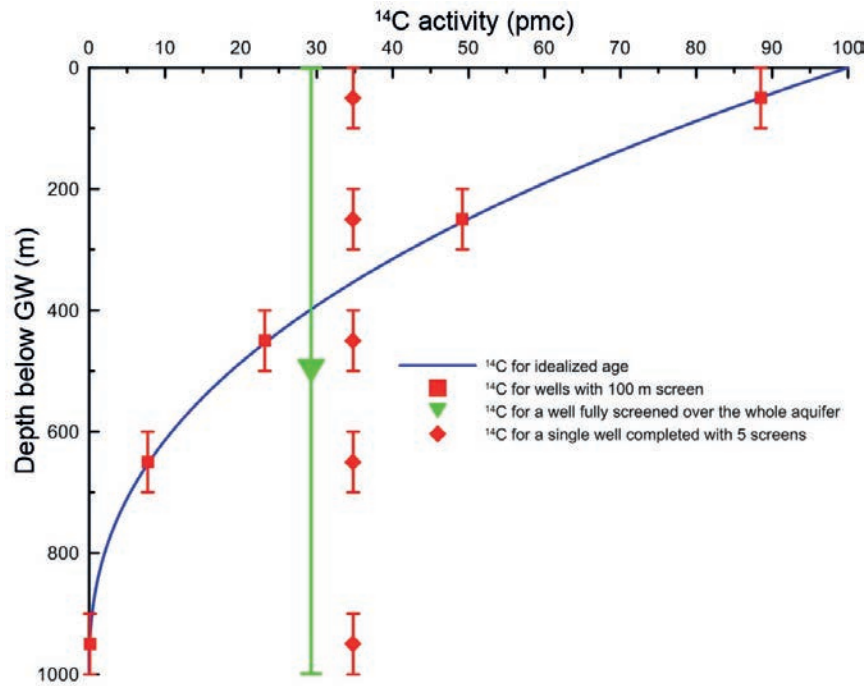


FIG. 9.3. Depth profile for  $^{14}\text{C}$  activity to be expected in a Vogel aquifer: the blue line indicates idealized point sampling and a direct conversion of idealized age (Eq. (9.1)) into  $^{14}\text{C}$  activity. Vertical error bars represent hypothetical screen lengths of 100 m. Red squares give the average  $^{14}\text{C}$  activity of five separate samples, if averaged over each 100 m screen length for each depth range. The red diamonds indicate the average  $^{14}\text{C}$  activity from a single well with five contributing zones, corresponding to those of the red squares — 34.8 pmc. A larger green triangle displays the average  $^{14}\text{C}$  activity if the whole aquifer is sampled with homogeneous inflow — 29.3 pmc.

At the topmost sample, it is obvious that the initial radiocarbon activity can only be observed if near the groundwater surface and sampling is possible with a very narrow depth resolution. As it is, the topmost sample with a screen length from the groundwater surface down to 100 m results in an average  $^{14}\text{C}$  activity of 88.5 pmc. Often, this screen resolution from five separate zones is not feasible in practice, but wells are encountered having several screens at different depths. Such a case in this example results in an averaged  $^{14}\text{C}$  activity of 34.8 pmc if all five depth zones contributed equally to a single well. Also indicated in Fig. 9.3 as a green triangle with error bars over the whole thickness of the aquifer is the  $^{14}\text{C}$  activity of 29.3 pmc which is obtained if a sample is taken from a well that is fully screened from the top to the bottom of the aquifer.

If the radiocarbon data in this simple case were to be converted into  $^{14}\text{C}$  tracer model age with an initial condition of 100 pmc, the  $^{14}\text{C}$  tracer model ages from the single screens would correspond well to the idealized age (Fig. 9.4, idealized ages indicated as a blue line). The three shallowest samples would fit a linear relation of age to depth, which can be used to deduce the recharge rate of the system. In the case of the chosen parameters, a fit would result in a vertical distance velocity of 0.04 m/a, which is indicated by the broken red line in Fig. 9.4. The slope of this fit corresponds nearly but, due to the non-linearity of the system, not exactly to the vertical distance velocity at the groundwater surface ( $\Phi \times R = 0.05$ ). The deepest two samples, however, would not follow this trend, but indicate a much older age due to the non-linearity of idealized ages versus depth in Eq. (9.1).

The more common sampling situation of all five screens averaged in one single sample will result in a  $^{14}\text{C}$  tracer model age of 8726 a, indicated by the vertical line of red diamonds and error bars. The continuous flow-weighted sampling over the whole depth of the aquifer results in a  $^{14}\text{C}$  tracer model age of 10 150 a and is indicated as a green triangle in Fig. 9.4. The blue curve in the figure indicates

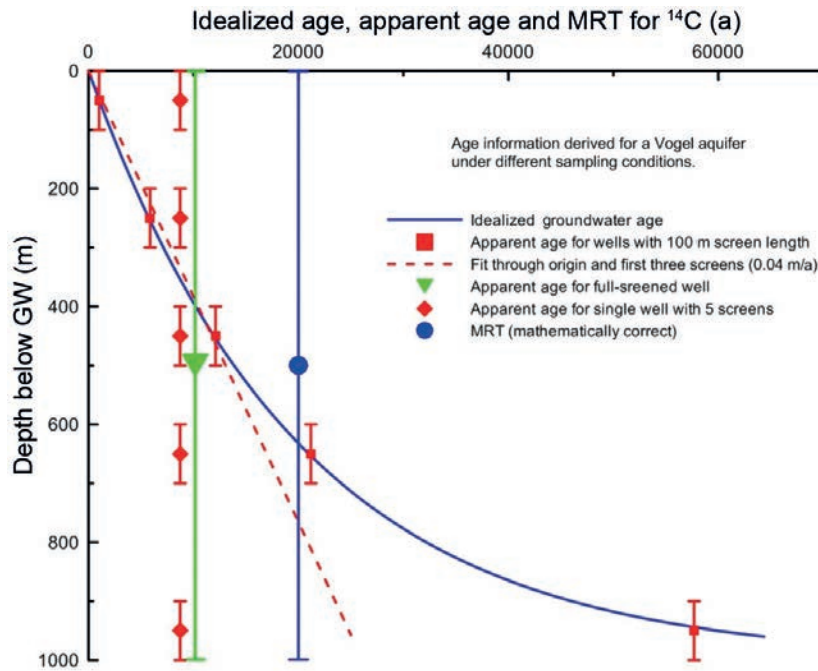


FIG. 9.4. Depth profile for  $^{14}\text{C}$  idealized ages,  $^{14}\text{C}$  tracer model ages and mean age (MRT) to be expected in a Vogel aquifer.

idealized ages, assuming neither mixing nor dispersion/diffusion and corresponding to Eq. (9.1). Red squares, following the blue line, with vertical error bars indicating screen length, display  $^{14}\text{C}$  tracer model ages calculated for five screens averaging the sampled waters and  $^{14}\text{C}$  values over a depth of 100 m in each sample. The vertical line of red diamonds corresponds to the tracer model age resulting when all five screens are mixed together in one sample. A bigger green triangle displays the value of 10 150 a resulting for the  $^{14}\text{C}$  tracer model age if the whole aquifer is sampled. In contrast, the blue diamond indicates the (mathematically true) mean age of 20 000 a for the system.

The Vogel aquifer corresponds to the exponential model, which is one of the standard lumped parameter models described in various textbooks (see, for example, IAEA (2006) [85]). It obtains its name for the exponential function that is used as frequency distribution of ages. As described in Chapter 3 and in more detail in IAEA (2006) [85], lumped parameter models are described by the mean residence time (MRT), which for the case of the Vogel aquifer is:

$$\text{MRT} = \frac{\phi L}{R} \quad (9.2)$$

In the context of this book, the term ‘mean age’ is used instead of the more common term ‘mean residence time’. As for ‘apparent age’ and ‘tracer model age’, the terms ‘mean age’ and ‘mean residence time’ are treated as synonyms. For the parameters chosen above, the mean age has a numerical value of 20 000 a. This value corresponds to the average of idealized ages in the aquifer and is, therefore, indicated as a blue diamond and vertical line in Fig. 9.4.

The radiocarbon results discussed here for the Vogel aquifer once more illustrate the statement in Chapter 3 that the ‘idealized age’, the average value of the frequency distribution of ages (the ‘mean age’ or MRT) and the ‘tracer model age’ are three fundamentally different numerical values that can all be attributed to the same hydrogeological system. Figure 9.4 simply displays these different values and provides visual evidence for their differences. Evidently, any study aiming for a tracer model age representing the idealized age as closely as possible, should try to obtain samples with the highest depth resolution practically possible.

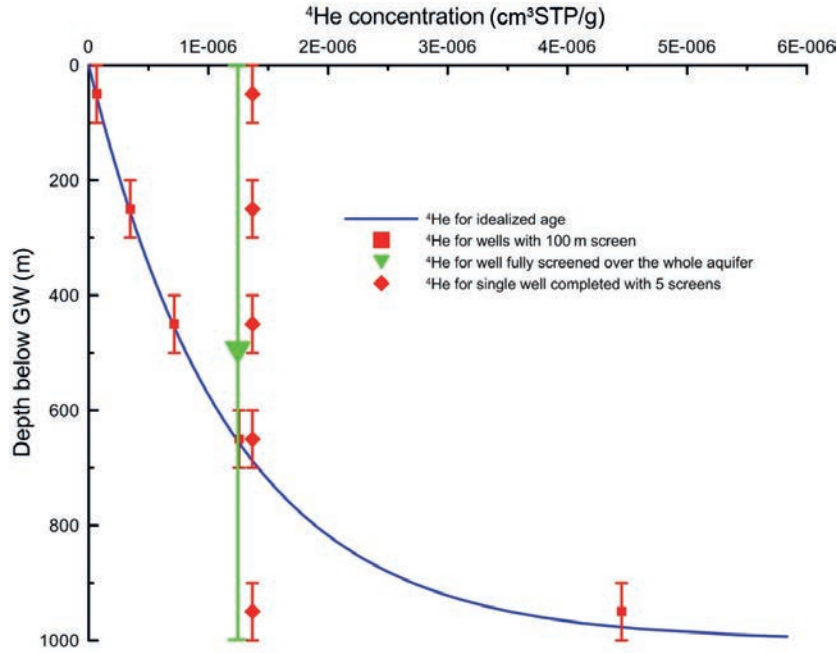


FIG. 9.5. Depth profile for helium in a Vogel aquifer. Parameters are indicated in the text and correspond to the cases in Fig. 9.2.

### Helium

All computations for helium in this chapter assume homogeneity of in situ production and no external flux source (see Chapter 8). Under these assumptions, the amount of in situ produced helium can be computed according to Eqs (8.6–8.8) in Chapter 8 and is proportional to the idealized age. Andrews and Lee (1979) [577] gave an equation for the in situ production rate of helium which is mathematically equivalent to Eq. (8.6) but more easily formulated and comprehensible with any nuclide chart:

$$J(^4\text{He}) = \Lambda \cdot \frac{\rho_R}{\rho_W} \frac{1 - \varphi_{\text{tot}}}{\varphi_{\text{eff}}} (1.19 \times 10^{-13} [\text{U}] + 2.88 \times 10^{-14} [\text{Th}]) \quad (9.3)$$

where

- $J(^4\text{He})$  is the helium flux into the groundwater (in units of  $\text{cm}^3 \text{STP} \cdot \text{g}_{\text{water}}^{-1} \cdot \text{a}^{-1}$ );
- $\Lambda$  is the release factor;
- $\rho_R$  is the rock density;
- $\rho_W$  is the water density;
- $\varphi_{\text{tot}}$  and  $\varphi_{\text{eff}}$  are the total and effective porosities.

For all computations in this chapter, a rock density of  $2.655 \text{ g/cm}^3$ , a water density of  $1 \text{ g/cm}^3$ , a release factor of one, and uranium and thorium concentrations of 40 and 30 ppm, respectively, are assumed. Together with the earlier mentioned porosity ( $\varphi = 0.2$ ), assuming total and effective porosity being equivalent, this results in an in situ helium production rate of  $6 \times 10^{-11} \text{ cm}^3 \text{STP} \cdot \text{g}^{-1} \cdot \text{a}^{-1}$ ). This in situ production has been used throughout this chapter for all plots and model computations.

A depth profile of helium concentration in a Vogel aquifer, thus, shows a logarithmic shape as indicated in Fig. 9.5.

It is observed that the highest  $^4\text{He}$  concentrations in the aquifer (corresponding in this case to the highest tracer model ages) will not be observed in most sampling campaigns because they require a very high depth resolution of sampling very near the base of the aquifer. It is also observed that in

the case of helium, the fully screened sample (green triangle in Fig. 9.5) corresponds more closely to the average of screens (red triangles in Fig. 9.5), since helium concentration increase with time is linear and mixing is linearly weighted. However, an additional crustal flux of helium from below the aquifer would further increase the helium concentration at the bottom of the aquifer. In this case, helium would not show identical depth profiles for every  $x$  coordinate within the aquifer, but higher helium concentrations would be observed at  $x$  coordinates of elevated crustal flux.

### Tracer combination

In this section, consideration is taken of possible interpretations resulting from measurement of concentrations of a suite of environmental tracers (in this case, tritium,  $^{14}\text{C}$  and  $^{81}\text{Kr}$ ) in discharge from a multilevel well in a Vogel aquifer (Fig. 9.6). Keeping the parameters constant, tritium as a tracer for the time range younger than 60 a can, of course, only be observed near the water table, down to a depth of approximately 3 m where the idealized age in this model reaches 60 a. However, because the uppermost screen in the multilevel well receives water from this layer, tritium is detectable in this sample, and for a northern hemisphere tritium input function, the sample contains nearly 1 TU if measured in the year 2000. As the half-lives of  $^{81}\text{Kr}$  and  $^{36}\text{Cl}$  are considerably greater than that of  $^{14}\text{C}$ , the decay effect of  $^{81}\text{Kr}$  (and  $^{36}\text{Cl}$ , not shown in Fig. 9.6) is much less visible than for  $^{14}\text{C}$  (Fig. 9.6) in the depth profile from the five open intervals in the well.

Combining various tracers in a simple homogeneous aquifer such as that described by Vogel (1967) [137], thus, gives age information specific to each of the tracers, each tracer displaying more details of the whole aquifer system. Only if the sampling conditions are good, do tracer model ages for the different tracers agree. Good sampling conditions include short screens and the tracer chosen fitting to the time range of ages in the mixture. Table 9.1 displays the calculated results for samples obtained in the screens for each of the tracers and for the case of equal mixing across each screen

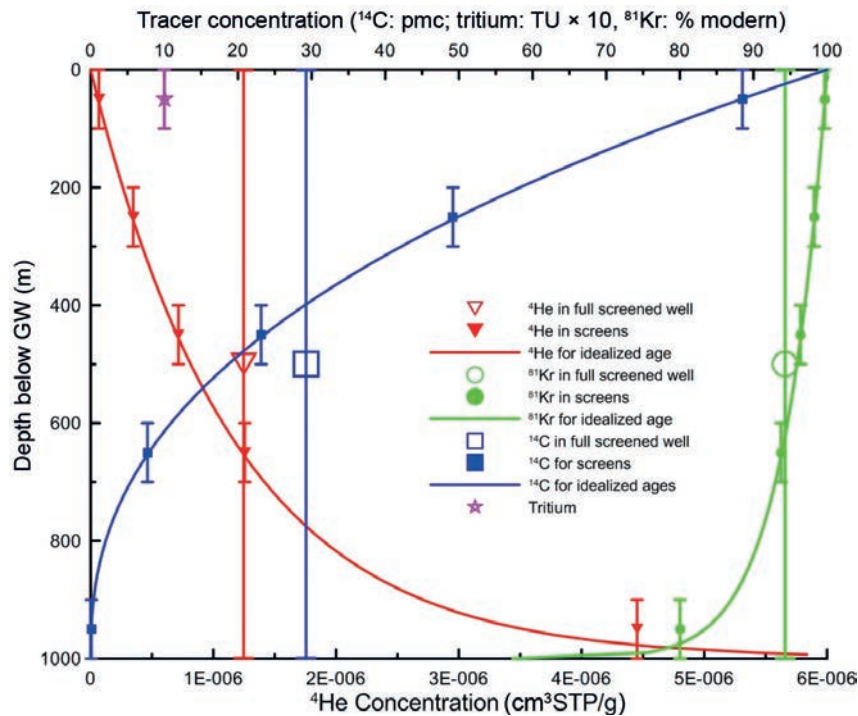


FIG. 9.6. Depth profiles of tritium,  $^{14}\text{C}$  and  $^{81}\text{Kr}$  in a Vogel aquifer. Solid lines represent concentrations obtained for idealized ages. Full symbols with error bars represent values obtained for sampling a screened well, where the error bar represents the screened interval. Vertical lines with open symbols represent concentrations obtained for a full-screened well. Colours represent tritium (purple),  $^{14}\text{C}$  (blue),  $^4\text{He}$  (red) and  $^{81}\text{Kr}$  (green).

TABLE 9.1. TRACER VALUES AND TRACER MODEL AGES FOR THE VERTICAL PROFILE IN THE VOGEL AQUIFER DISCUSSED IN THE TEXT

Well	<sup>4</sup> He		<sup>14</sup> C		<sup>81</sup> Kr		<sup>36</sup> Cl	
	Value (cm <sup>3</sup> STP/g)	Tracer model age (a)	Value (pmc)	Tracer model age (a)	Value (% mod.)	Tracer model age (a)	Value ( <sup>36</sup> Cl/Cl × 10 <sup>-15</sup> )	Tracer model age (a)
0–100 m	6.71e <sup>-8</sup>	1140	88.5	1010	99.7	1140	498	1140
200–300 m	3.47e <sup>-7</sup>	5902	49.2	5866	98.2	5901	493	5901
400–500 m	7.15e <sup>-7</sup>	12 167	23.1	12 100	96.4	12 166	486	12 166
600–700 m	1.23e <sup>-6</sup>	21 353	7.71	21 186	93.7	21 350	476	21 351
900–999 m	4.45e <sup>-6</sup>	75 710	0.09	57 697	80.0	73 657	422	74 117
Mix of all screens	1.37e <sup>-6</sup>	23 254	34.8	8726	93.7	21 390	476	21 703
Full screened	1.26e <sup>-6</sup>	21 197	29.2	10 163	94.3	19 418	477	20 334

and for mixing across the full screened aquifer. As expected, high resolution sampling yields the most consistent results over most of the tracers. However, there is poor agreement between <sup>14</sup>C and the other tracers at the deepest screen, because a significant part of the flowlines entering the screen has idealized ages that are beyond the radiocarbon dating range.

The results demonstrate that, for the case in which the sample represents a mixture of very different ages, the radiocarbon age is significantly too young, because exponential decay biases a mixture to the young side as shown in Fig. 3.3 (Bethke and Johnson (2008) [84]). This is evident in the results of tracer model ages for the fully screened case and the case of equal mixture of all screens. In any case, the disagreement of a factor of two between tracer model ages for different tracers should be taken as an indication that the tracer model ages — at least for some tracers — do not represent a meaningful water age.

With the exception of the fully screened wells, the assumed sampling conditions were quite idealistic. Section 9.3 further elaborates on the resulting patterns, if, for example, mixing between different depths occurs. The Vogel aquifer type represents the infiltration area of a large aquifer system. Thus, it is of interest to investigate whether an aquifer system as a whole, still described as a homogeneous case, will display different patterns in zones of infiltration, of horizontal flow or in zones of upward groundwater flow.

### 9.1.2. Homogeneous aquifer with different recharge and discharge zones

Tóth (1963) [28] analytically described a simple flow system which displays different areas of recharge and discharge in a homogeneous aquifer. The flow system shown in Fig. 9.7 consists of a trough with impervious left, bottom and right boundaries. The groundwater surface consists of a constant gradient which is modulated by an overlain sine function. As such, the concept is a possible description of one side of a large valley, having a water divide on the right and a discharge system (e.g. a river) on the left. Tóth describes in his classical paper that — depending on the parameters chosen, where the ratio of depth to horizontal extension is probably the most important — different hierarchical orders of flow systems emerge, which correspond to more local or regional flow (Fig. 9.7). This system is still an idealization because it considers a homogeneous aquifer only and neglects mixing, dispersion,

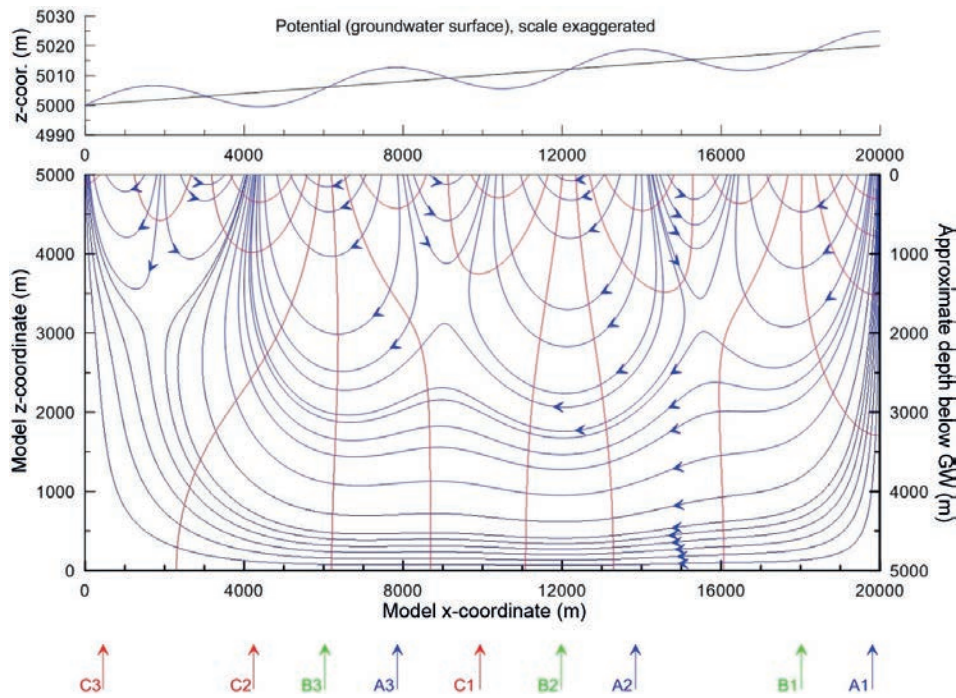


FIG. 9.7. Vertical cross-section for a groundwater flow system in a homogeneous aquifer as described by Tóth (1963) [28]. Lines of equal groundwater potential are shown in red, lines of groundwater flow in blue, with arrows indicating the flow direction. The vertical exaggerated profile on top indicates the groundwater surface creating this flow field. Vertical age and tracer profiles at horizontal positions A (infiltration), B (horizontal flow) and C (upward flow) are discussed in the text.

diffusion and external fluxes. Nevertheless, it is useful to distinguish age patterns observed in recharge areas, areas of horizontal flow and discharge areas.

The parameters chosen for this example are: depth  $L = 5000$  m, horizontal extension = 20 000 m, linear gradient = 0.001, amplitude and wavelength of the hills around this gradient = 5 and 6100 m, respectively, porosity = 0.3 and the  $k_f$  value =  $10^{-6}$  m/s. Tóth (1963) [28] gives an equation for the potential as a function of horizontal extent,  $x$ , and the vertical coordinate,  $z$ . To create depth profiles, an approximate depth below groundwater surface is also displayed, which is computed as  $L-z$  (right  $z$  axis in Fig. 9.7) and will be used in all subsequent graphs. For the discussion in the following, this formula was differentiated and multiplied by porosity to obtain the (distance) velocities. Idealized ages were computed by integration of this flow field to obtain idealized ages. The tracer values were computed from these idealized ages. These tracer values were then averaged over different screen positions as above in the Vogel case.

#### 9.1.2.1. Infiltration areas

The horizontal locations indicated with the large letter A in Fig. 9.7 correspond to infiltration areas of different flow systems and are always associated with the hilltops in the groundwater surface. Evidently, these infiltration areas feed different flow (sub)systems in the Tóth aquifer: A1 at  $x = 19\,800$  m corresponds to the infiltration area of the largest flow system, whereas A2 ( $x = 14\,000$ ) and A3 ( $x = 8000$ ) correspond to smaller watersheds with one (A2) or two (A3) underlying larger flow systems. For each of the depth profiles, the calculations that follow assume that there are eleven screens, the shallowest one centred at  $z = 4985$  with 28 m screen length and the deeper ones built with

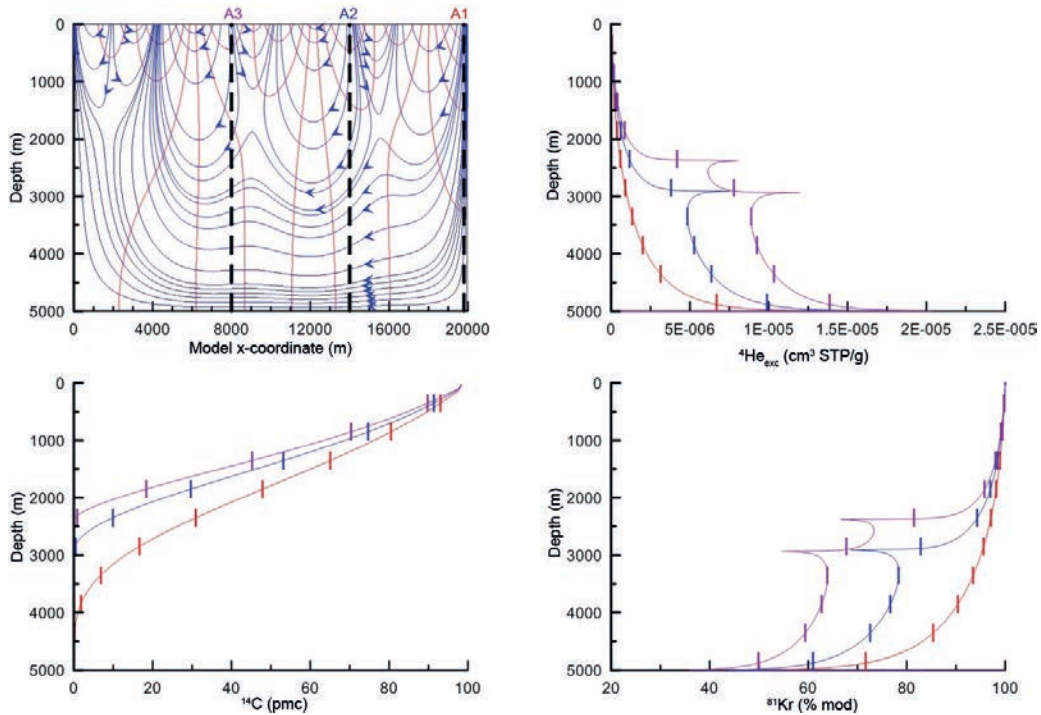


FIG. 9.8. Depth profiles of  $^4\text{He}$ ,  $^{14}\text{C}$ ,  $^{81}\text{Kr}$  in infiltration areas. Locations of profiles A1 (red), A2 (blue) and A3 (purple) are indicated in the flow field (top left). Vertical bars correspond to extension of well-filter screens.

a 280 m screen length at regular intervals of 500 m starting at a centre of  $z = 4650$  (Fig. 9.8). Figure 9.8 shows the resulting depth profiles for  $^4\text{He}$ ,  $^{14}\text{C}$  and  $^{81}\text{Kr}$ .

The mathematical solution of the Tóth model has zones of very low groundwater velocity between the first and the second flow system. This results in high idealized ages that create high  $^4\text{He}$  concentrations and low  $^{14}\text{C}$  and  $^{81}\text{Kr}$  activities in areas of low groundwater velocity. However, unless the depth resolution in sampling is extremely high, these ‘stagnant’ zones will probably not be sampled and in most cases will be of no practical importance. The transition from one flow system to the next, however, results in concentration steps in the tracer depth profile. Depending on the depth resolution during sampling, probably not all of these transitions are visible in the tracer depth profile: it would be possible from the  $^4\text{He}$  and  $^{81}\text{Kr}$  depth profiles of filtered screens, to postulate a second circulation system at greater depth, but hard to decide whether there are one or two different ones in the A3 case in Fig. 9.8. With the parameters used here,  $^{14}\text{C}$  will not be measurable in the older, underlying flow systems.

With the appropriate combination of tracers covering the timescales of the aquifer, and with suitable depth resolution, it is feasible to determine recharge rates, to discern whether a recharge area belongs to a regional or only-local flow system, and if further flow systems are beneath. It is, thus, of interest if depth profiles for the more vertical downward flow of an infiltration area can be distinguished from areas of horizontal flow.

#### 9.1.2.2. Areas of horizontal flow

The horizontal locations indicated with the large letter B in Fig. 9.7 correspond to areas where the flowlines are mainly horizontal in the selected Tóth model. They are associated with the maximum head gradient, where the sine wave determining the local groundwater gradient in Fig. 9.7 equals the straight line determining the regional groundwater gradient. In all cases, the depth profiles tap

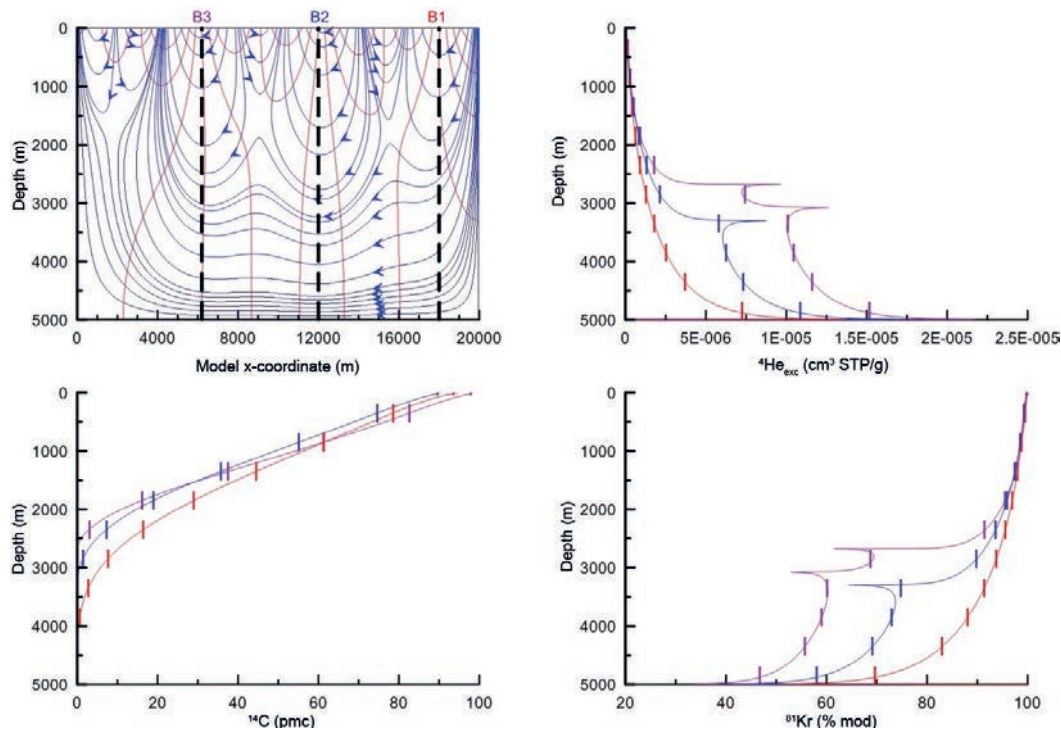


FIG. 9.9. Depth profiles of  $^4\text{He}$ ,  $^{14}\text{C}$ ,  $^{81}\text{Kr}$  in areas of horizontal flow. Locations of profiles B1 (red), B2 (blue) and B3 (purple) are indicated in the flow field (top left). Vertical bars correspond to extension of well-filter screens.

different flow systems, and the positions chosen for further discussion are B1 at  $x = 18\,000$  m, B2 at  $x = 12\,000$  m and B3 at  $x = 6\,200$  m. Figure 9.9 shows the resulting depth profiles for  $^4\text{He}$ ,  $^{14}\text{C}$  and  $^{81}\text{Kr}$ .

At first glance, there seems to be little difference in the shape of the tracer profiles between Figs 9.8 and 9.9. Again, the transition from a shallow flow system to the next deeper flow system appears as a step in the depth profile of the age tracers. A closer comparison reveals that the numerical values are different: there is more  $^4\text{He}$  and less of the radioactive tracers at similar depths in the profiles of the horizontal flow situation as compared to infiltration areas. For  $^{14}\text{C}$ , it is remarkable that the different profiles cross each other (Fig. 9.9, lower left):  $^{14}\text{C}$  has the highest time resolution since its half-life is best suited for the timescale of flow in the shallow systems. Therefore, the different age gradients of the shallow flow systems become more evident here — although they are present in the top parts of the depth profiles of  $^4\text{He}$  and  $^{81}\text{Kr}$ , they are not as clearly discernible as in the  $^{14}\text{C}$  profile. Profile B1 represents the infiltration area of the largest regional flow system. For the chosen parameters, groundwater on this profile infiltrates down to a depth of 4000 m within the dating range of  $^{14}\text{C}$  (50 000 a). Profile B3 represents the shallowest system. Here, the idealized ages cover values between zero and the dating range of  $^{14}\text{C}$  within a depth interval of 0–2500 m.

Without a conceptualization of the hydrology of the flow system, it would be difficult to even distinguish recharge areas from regions of dominant horizontal flow on the basis of tracer data alone. This illustrates that hydrogeological knowledge of the flow system is necessary before age studies are initiated (see Chapter 2), and that the purpose of the age tracers is to help quantify the flow system, not to a priori investigate its dominant direction of groundwater flow. However, this similarity of patterns between recharge area and area of horizontal flow raises the question of whether the regions of upward directed flow, where groundwater discharges to surface water or to shallower systems, show different patterns.

### 9.1.2.3. Areas of upward flow

A naive understanding of ‘upward flow’ might lead to the expectation that water ages increase in the upward direction, because this is the flow direction. Basically, it would be as though the patterns in the right part of Fig. 9.1 were flipped upside down. This would result in an upward increase of  $^4\text{He}$  and an upward decrease of the radioactive tracers  $^{14}\text{C}$  and  $^{81}\text{Kr}$  and is called an ‘age inversion’ in stratigraphy. Closer investigating the details of the flowlines in Fig. 9.7 reveals that a vertical profile in an area of upward directed flow will hardly ever sample only one flowline. This easily explains why the tracer depth profiles for  $^4\text{He}$ ,  $^{14}\text{C}$  and  $^{81}\text{Kr}$ , in regions with partly or dominant upward flow, seldom show an age inversion (Fig. 9.10). Vertical profiles for this case are situated at  $x = 10\,000$  m for profile C1 and at  $x = 4830$  m and  $x = 80$  m for profiles C2 and C3, respectively. Regions of upward directed flow may show age inversions in part of the vertical profile, as the upper three screens in profile C1 show for  $^4\text{He}$  and  $^{81}\text{Kr}$ . However, even in this profile, the values for  $^{14}\text{C}$  do not show this inversion for the last two screens, because the screen at a depth of  $350 \pm 150$  m samples a mixture of very different  $^{14}\text{C}$  concentrations and, as such, is biased young. For the aquifer parameters chosen here, radiocarbon is measurable only in profiles C1 and C2, and in these radiocarbon content is so small ( $<1$  pmc) that in many practical cases it will probably provoke discussions about contamination during sampling among the scientists in the project.

As a summary, depth profiles in areas of upward flow are generally characterized by large depth regions where the age-indicating tracers are constant with depth. This is observed on a level of activity ( $^{14}\text{C}$  and  $^{81}\text{Kr}$ ) or concentration ( $^4\text{He}$ ) that indicates considerable age. In areas where the upward directed flow belongs only to the local groundwater systems, such as the C3 profile, again steps in the tracer profile may occur, but these are less pronounced as in the case of horizontal flow. With these characteristic features, discharge zones should, in many cases, be clearly discernible from recharge zones and areas of horizontal flow, given an adequate resolution in the vertical scale of sampling.

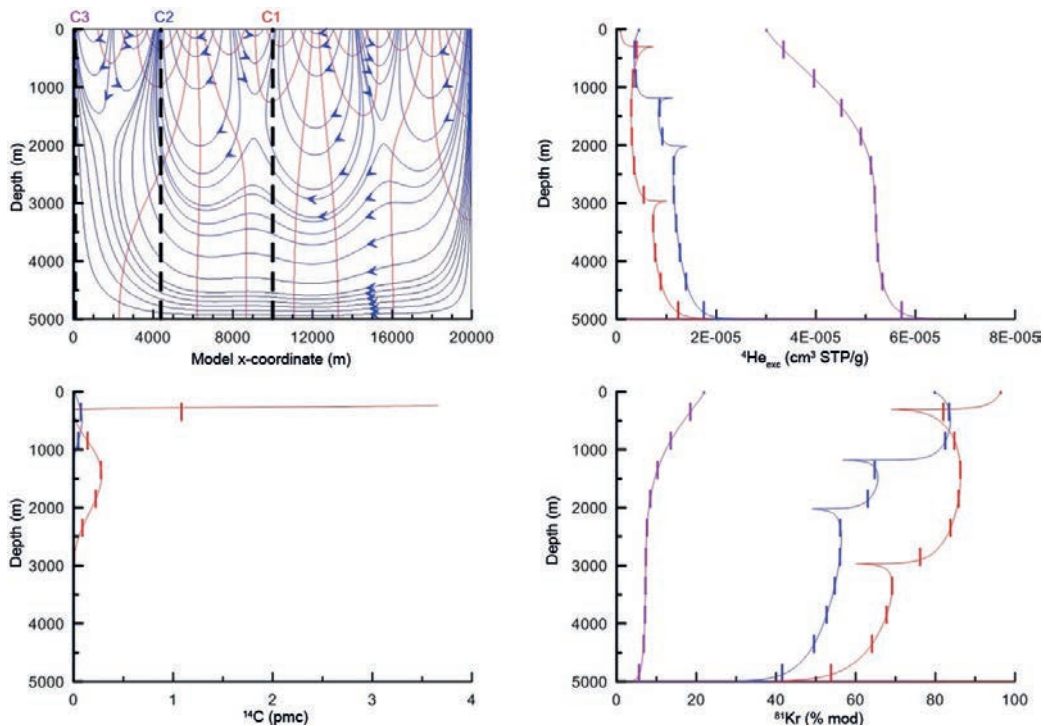


FIG. 9.10. Depth profiles of  $^4\text{He}$ ,  $^{14}\text{C}$  and  $^{81}\text{Kr}$  in discharge areas. Locations of profiles C1 (red), C2 (blue) and C3 (purple) are indicated in the flow field (top left). Vertical bars correspond to extension of well-filter screens.

All of these considerations of course neglect two natural processes important for the depth profiles: first, dispersion and diffusion are neglected. Taking these into consideration, the ‘singularities’ shown in Figs 9.8–9.10 at the transition zones from one flow system to the next will be considerably smoothed. The general shape of the depth profiles computed for screened well intervals, however, will not be altered. Second, external fluxes are neglected. Especially for the  $^4\text{He}$  depth profiles, this may be an unrealistic assumption, as pointed out in detail in Chapter 8. Qualitatively, external fluxes will increase the  $^4\text{He}$  concentration towards the bottom of the aquifer in all depth profiles. If this mainly diffusion driven flux is not too large, the profile in the ‘global’ infiltration area (profile A1, Fig. 9.8) will not be altered too much, since the downward groundwater movement will flush the helium influx from the bottom of the aquifer. In areas of horizontal flow, however,  $^4\text{He}$  gradients with depth will be considerably larger, especially near the base of the aquifer. In the areas of upward flow,  $^4\text{He}$  concentrations will be orders of magnitude higher, although the general shape of the profiles is not necessarily altered.

The most unrealistic assumption of the Tóth model (Tóth (1963) [28]) is to assume homogeneous aquifer transmissivity. The next step is, thus, to consider a layered aquifer with varying transmissivity. This is not as easily examined in a quantitative and detailed manner, because analytical solutions to the flow system are not available as they are for the Vogel or Tóth models.

### 9.1.3. Aquifer systems — confined or partly confined

While the case considered in Section 9.1.2 is easily understandable, it is not very realistic. In natural systems, a sediment layer of 5 km thickness with only one  $k_f$  value is rarely the case. Although sedimentary basins of this thickness exist in various areas of the world, the sedimentation processes changed, and these changes created layers of varying grain size, different sorting of grain sizes and different compaction, resulting in different transmissivity. This transmissivity can vary by orders of magnitude, as discussed in Chapter 2. Deep systems tend to be layered into aquifers (comparably high transmissivity), aquitards (smaller transmissivity) and aquicludes (transmissivity so low that groundwater flow is negligible as compared to flow in aquifers). Even if a layer is regarded to be ‘homogeneous’ from the sedimentological point of view, variations of a factor of five in the  $k_f$  value are still possible, simply because deducing the  $k_f$  from sedimentological information involves an uncertainty of this magnitude. All smaller variations are very difficult to detect by sedimentological methods or even from data obtained from sophisticated pump tests.

#### 9.1.3.1. Single depth profile in various aquifers

As an example, the depth profile sketched in Fig. 9.11 is considered. The sediment consists of several aquifers of different thicknesses, separated by aquitards, which are assumed to be impervious with respect to flow and diffusion. Horizontal flow is assumed through each aquifer layer, the distance velocity is calculated from Darcy’s law and porosity, and this idealized age is converted into tracer concentrations as in the previous sections. In detail, this implies the following assumptions: the aquifers are assumed to have different  $k_f$  values. For the sake of simplicity, all aquifers (i) are assumed to be recharged in the same area at a distance of 100 km, (ii) are assumed to have the same gradient of  $1 \times 10^{-4}$  in hydraulic potential and (iii) are assumed to have the same porosity of 20%. Further, (iv) it is assumed that all aquifers have the same properties in the infiltration area which leads to identical  $^4\text{He}$  production rates, and all have  $^{14}\text{C}$  and  $^{36}\text{Cl}$  (‘no decay’) initial conditions. In fact, the only varying parameter is the  $k_f$  value, which is indicated for the aquifers in Fig. 9.11.

The first impression looking at the tracer depth profiles is the absence of the systematic patterns observed in the homogeneous aquifers. In the homogeneous case, the radioactive tracers  $^{14}\text{C}$  and  $^{81}\text{Kr}$  decreased in a more or less monotonic manner with depth in nearly all cases, whereas  $^4\text{He}$  increased

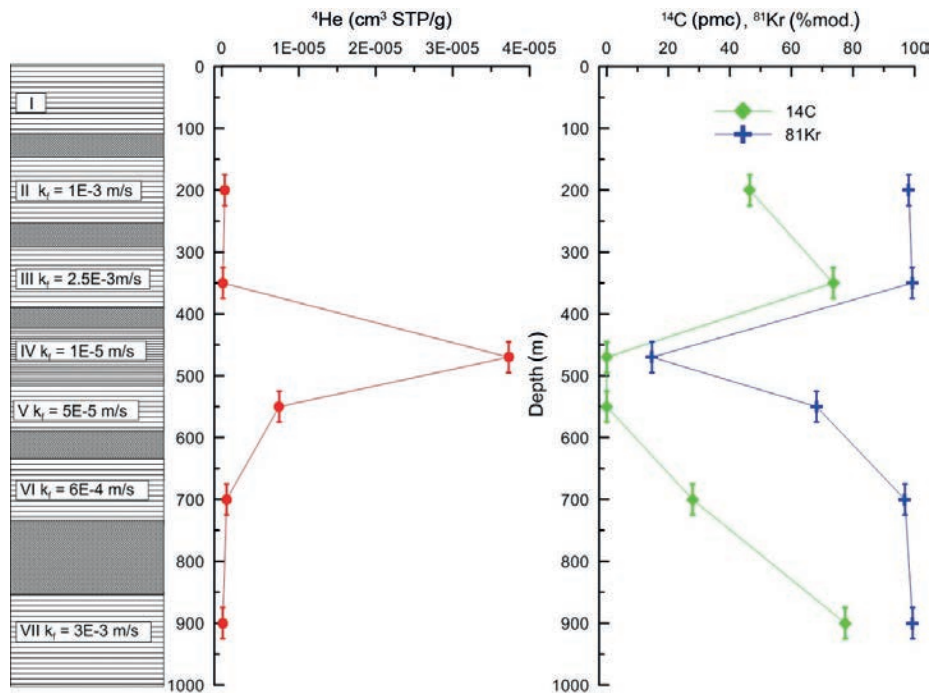


FIG. 9.11. Vertical tracer profiles in an aquifer system with separating aquitards.

with depth. The inhomogeneous case is completely dominated by the transmissivity values and shows a very irregular pattern of decreasing and increasing tracer values with depth.

A closer inspection of the depth profile of different tracers in this multi-aquifer system shows the expected pattern with lower values for the radioactive decaying tracers  $^{14}\text{C}$  and  $^{81}\text{Kr}$  (larger age) in aquifers of lower  $k_f$  value. Important to note is that a comparably small difference in  $k_f$  values can be easily discerned from the tracer results: the difference of  $1 \times 10^{-3}$  and  $2.5 \times 10^{-3}$  m/s between the topmost two aquifers results in clearly different  $^{14}\text{C}$  signals. It is also important to note that different tracers with different timescales are necessary to cover the transmissivity values in this example: aquifers IV and V show ‘infinitely old’ water on the  $^{14}\text{C}$  timescale whereas  $^4\text{He}$  and  $^{81}\text{Kr}$  give results which are clearly different from the aquifers of high transmissivity above and below, and which are still discernible from each other.

Since purely advective flow to simulate the tracers is again considered, a qualitative discussion is helpful with regard to the difference between the derived tracer values in this artificial case and tracer values in a more realistic case. One important but neglected parameter is aquitard leakage between aquifers. Only rarely do aquifer stacks in nature have the same hydraulic potential; often, pressures are different between aquifers. This means that flow is induced in the vertical direction through the aquitards. Although the amount of water flowing per square meter through the aquitards between adjacent aquifers may be very small, it has to be multiplied by the entire area over which the pressure difference exists; an area that may amount to many square kilometres. Therefore, the amount of cross-aquifer flow will, in many cases, have a measurable effect on the tracer values, caused by mixing of different waters. Cross-aquifer flow will generally decrease the differences of tracer values between aquifers. In this case, this will probably influence aquifers III, IV and V the most, because these have the largest differences in tracer values compared to their neighbours. If the flow through the aquitard needs a considerable amount of time, however, it will not cause water of the age  $a_B$  of the adjacent aquifer B to mix into aquifer A but water of an age  $a_B + t$  where  $t$  is the time needed for the transfer through the aquitard. The same also holds true for any other parameter changed within the aquitard (amount of dissolved solids, ion exchange, etc.).

Diffusion of radioactive tracers into the aquitards or of helium out of the aquitards may also have a noticeable influence. This can be simulated with the theory of dual porosity aquifer systems which are discussed in Chapters 4, 5, 8 and 10. Finally, any helium flux from external sources was neglected, in this case from below the whole aquifer system sketched in Fig. 9.11. As discussed in detail in Chapter 8, such an external flux will increase the helium concentration in the deepest aquifers, until an aquifer is reached which is able to transport all of the helium of this flux to the surface. Above this aquifer — in this case probably the deepest one, VII — helium from crustal flux is negligible, but helium from the adjacent aquitards may still increase the concentration above the one produced in situ.

#### 9.1.4. Summary

Section 9.1 has demonstrated possible tracer patterns that can be obtained sampling an aquifer with multilevel wells. It also demonstrated how mixing of waters from different depths with different age can influence the result. It demonstrated that it will be difficult or impossible from tracer data alone to distinguish recharge areas from areas of horizontal flow, because their tracer patterns are very similar. Therefore, a conceptual model of the groundwater flow system is necessary before starting the tracer study. In contrast, discharge areas can be more easily detected. Section 9.1 also demonstrated that in aquifer systems consisting of aquifers and intercalated aquitards, tracer results will be dominated by the transmissivity of the aquifer.

There are some conclusions of this section which can be translated into practical advice for the application of environmental tracers to study groundwater age:

- (a) Optimum wells for the purpose of age dating of groundwater are constructed to obtain an unmixed sample from a defined depth with a depth range being very small as compared to the total depth of the well. Well nests constructed this way to obtain a depth profile of samples are the optimum choice.
- (b) Optimum depth resolution of multilevel well nests should be higher near the groundwater surface and near the bottom of the aquifer. This is because, at these interfaces, the largest variation of tracer data is to be expected.
- (c) Whenever it is possible in the early stage of a groundwater study to influence the construction of observation wells, the facts above should be taken into consideration.
- (d) Section 9.1 also allows the following conclusions to be drawn for most practical cases where sampling conditions are not optimal, for example, where only wells completed with multiple screens are available, where open boreholes in fractured rock have to be sampled, etc.

Geotechnical methods should be considered to obtain samples with optimum depth resolution for the given case (packer systems, sampling with the dual-pumping technique (Rapp et al. (1998) [591]), chains of passive samplers, etc.).

Different (hydrochemical and isotopic) tracers should be applied to enable the deconvolution of mixtures (see Section 9.3 for further multitracer techniques to detect mixtures).

Direct conversion of tracer values to tracer model ages in most such cases will give no useful results; therefore, this should be considered only after the deconvolution of mixtures was possible.

Tracer concentrations and activities for these samples should be directly described (without converting them to tracer model ages), applying the knowledge about the sampling conditions and using an interpretation model that describes the transport conditions as closely as possible.

For instance, for the Vogel case discussed in Section 9.1.1.1 where the sample was obtained from a full screened well penetrating the whole aquifer, the direct conversion of tracer values into tracer model ages will not give a reasonable result. Fitting the tracer values for the fully screened well to an exponential model, however, will result in the correct mean age time of 20 000 a. An exponential model applied to interpret the single well completed with five screens will also give a more useful result than the direct conversion of the tracer data into a tracer model age.

As discussed, vertical profiles will only in rare cases display an evolution along a line of groundwater flow. Given the fact that most aquifers have a much larger horizontal than vertical extension, horizontal transects seem better suited to show development along a flowline.

## 9.2. HORIZONTAL TRANSECTS

Vertical tracer transects provide useful insight into the age structure of an aquifer or aquifer system. Horizontal sampling along assumed flowlines in aquifers can also provide very useful information on the flow field, including estimation of distance velocities. However, one of the most difficult problems in this approach is in recognizing the flowlines and sampling along actual flowlines in aquifers.

### 9.2.1. Transect along an assumed flowline

Figure 9.12 qualitatively displays a possible scenario for horizontal flow in an ideally confined aquifer. The top part sketches the aquifer, which shows a constant thickness for a flow distance of 100 km until the thickness increases by a factor of four, possibly due to intersection of a fault. A constant  $k_f$ , potential gradient and porosity are assumed and a constant distance velocity at least up to  $x = 100$  km is calculated. This means that distance linearly translates into age and, for tracers with exponential decay, this situation results in an exponential decrease in tracer concentration with flow distance, starting with whatever the initial value was at the first sampling point along the flow path. With parameters  $k_f = 4 \times 10^{-4}$  m/s, gradient =  $1 \times 10^{-4}$  and porosity = 20%, such curves are shown for  $^{14}\text{C}$  and  $^{81}\text{Kr}$  in Fig. 9.12 (right y axis). For tracers increasing linearly with age, for example  $^4\text{He}$ , a linear increase with flow distance results and is also shown in Fig. 9.12 (left y axis).

Also shown in Fig. 9.12 is the effect of change in thickness for a confined aquifer. In the present case, the thickness changes at flow distance  $x = 100$  km to be four times larger than before. As in this

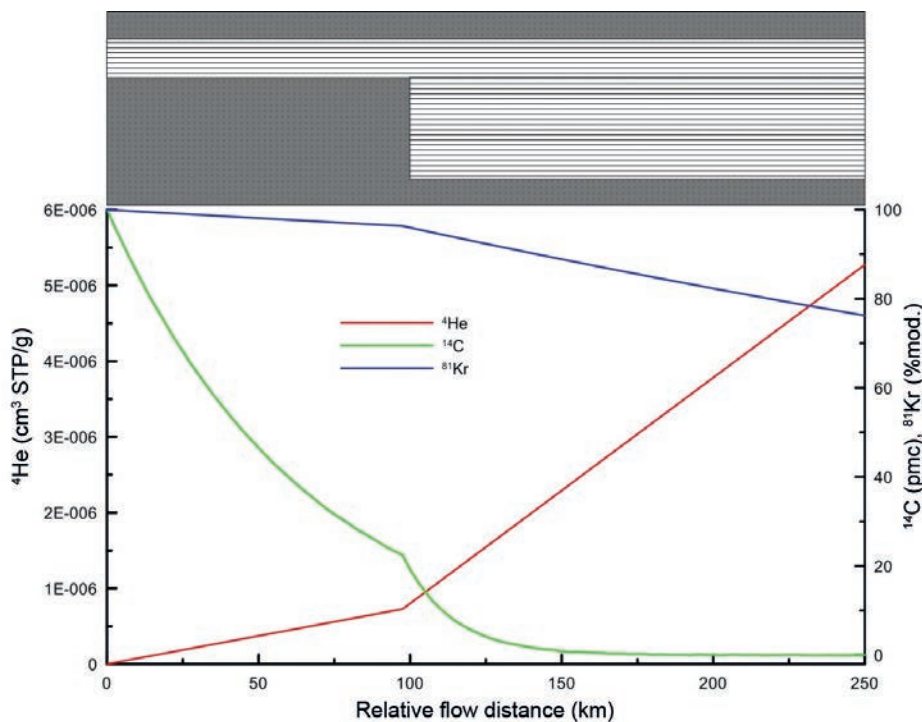


FIG. 9.12. Transects of  $^4\text{He}$  (left axis),  $^{14}\text{C}$  and  $^{81}\text{Kr}$  (right axis) along a flowline in a confined aquifer where aquifer thickness and, therefore, flow velocity vary.

example the aquitards above and below the aquifer are impervious, and all other parameters are assumed to be constant, the new aquifer thickness results in a flow velocity that is a factor of four lower than in the thinner section of the aquifer. This lower flow velocity changes the relation between flow distance and age, and results in new rates of decrease of radioactive tracer concentration with distance for  $^{14}\text{C}$  and  $^{81}\text{Kr}$ , and new rates of linear increase with distance for  $^4\text{He}$ . Calculation of distance velocity as the difference in tracer model ages divided by flow distance provides an estimate for the combination of  $k_f$  and porosity. Provided enough samples were taken at flow distances smaller and larger than 100 km, the result will be two significantly different numbers for effective aquifer transmissivity. Estimates for these important hydrogeological parameters are often difficult to obtain by other means. If the fault zone and the possibility of varying aquifer thickness are known from hydrogeological information, it can be taken into account for calculation of different distance flow velocities from the tracer transects. In this case, the two parts of the transect will result in two different distance (and Darcy) velocities. On the other hand, information on actual aquifer thickness is comparably difficult to obtain. Therefore, the example above demonstrates that calculation of distance velocity from tracer transects along a flow path may, in some cases, be more cost effective and easier to obtain than a detailed hydrogeological or seismic study.

As in all cases before, this case contains several simplifications that probably are not generally valid in all aquifer systems: diffusion of tracers into aquitards (radioactive tracers such as  $^{14}\text{C}$ ,  $^{36}\text{Cl}$  and  $^{81}\text{Kr}$ ) and from aquitards ( $^4\text{He}$ ) is neglected as well as a possible crustal flux of helium from below. These effects will not be homogeneous with depth or distance and will tend to change the tracer values towards larger ages. More important, the discussed case is only valid if the samples are actually located along the same flowline. This is less severe an assumption in a confined aquifer although many aquifers will likely have a flow component perpendicular to the plane of Fig. 9.12. This can only be studied with a case of higher dimension — sampling for a map of tracer values in one aquifer, instead of sampling only along an assumed flowline. Using the analytical Vogel and Tóth flow models, discussed in Section 9.1, will give further insight as to how severe the effect of not being on the same flowline might be.

### 9.2.2. Horizontal transects intersecting different flowlines

The Vogel model described in Fig. 9.2 obviously describes not only an infiltration area but also a horizontal flow of groundwater in this idealized aquifer as a whole. However, the ages in the Vogel aquifer are described by Eq. (9.1), which does not depend on the  $x$  coordinate, but only on the depth within the aquifer. This means that a horizontal transect of samples, all taken from the same depth in a Vogel aquifer, will result in identical tracer values and identical tracer model ages. This is a result of the fact that none of the flowlines in the Vogel model (Fig. 9.2) are horizontal, so no horizontal transect will sample the same flowline twice. Of course, any real sample will originate from a well with a finite screen interval and, therefore, will integrate Eq. (9.1) over the depth between the lower screen coordinate,  $z_L$ , and the upper screen coordinate,  $z_U$ . However, if the screen lengths are equal for all samples, this integral is still a constant. Thus, the average of idealized age over the screened interval and, therefore, the tracer concentrations will be identical along a horizontal transect.

If the screen lengths vary, different tracer values and different tracer model ages will result, even if the centre of the screen is always at the same depth. If, for this reason, the tracer model age increases on a horizontal transect, this age increase would lead to incorrect estimates of distance velocities. The two examples of horizontal transects discussed up to now demonstrate two extreme cases: in the first, the confined aquifer, horizontal distance directly translates into age and the corresponding tracer values; in the second, the unconfined (Vogel) aquifer, horizontal distance is completely independent of age and will, therefore, result in identical tracer values. This once more emphasizes that a depth profile in the practical case may give more insight into the flow system than many horizontal samples, because a detailed understanding of the flow system is already necessary to perform a useful horizontal sampling.

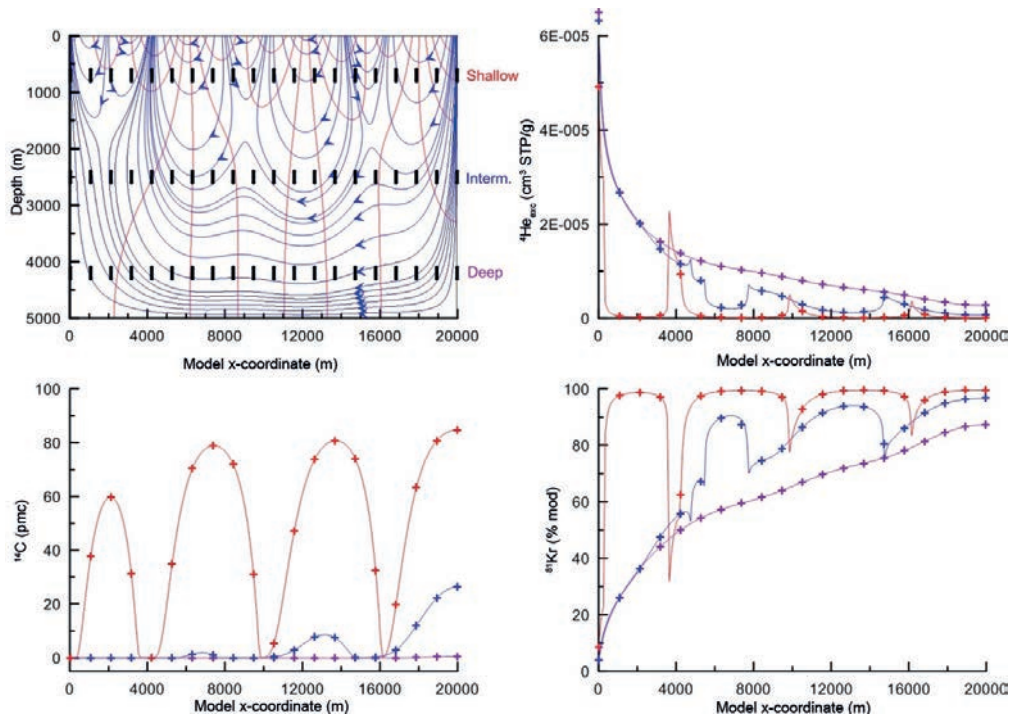


FIG. 9.13. Three horizontal transects for  $^4\text{He}$ ,  $^{14}\text{C}$  and  $^{81}\text{Kr}$  in the Tóth aquifer of Fig. 9.7. The depth of the transects is 4200 m (purple), 2500 m (blue) and 700 m (red), corresponding to model-z coordinates of 800, 2500 and 4300 m, respectively.

The case of the Tóth aquifer is more complicated, since local infiltration and upward directed flow alternate in this case. Figure 9.13 shows three horizontal transects, sampled at depths of 700 m (shallow, red curves), 2500 m (intermediate, blue curves) and 4200 m (deep, purple curves) for  $^4\text{He}$ ,  $^{14}\text{C}$  and  $^{81}\text{Kr}$  in the Tóth aquifer discussed in Fig. 9.7. As before, computed tracer values were averaged over depths corresponding to 200 m of well-screen.

From all tracers, it is evident that the shallow transect samples the local circulation systems and only the deep transect shows an increase of age with flow distance. For example,  $^4\text{He}$  in the deep transect shows monotonous increase in flow direction (right to left in this picture). The shallow  $^4\text{He}$  transect in contrast in most areas shows hardly any excess  $^4\text{He}$  but does contain local spikes that might be missed without detailed horizontal sampling. A similar pattern is observed for  $^{81}\text{Kr}$ , although in the opposite sense, since this tracer shows radioactive decay. The values for  $^{81}\text{Kr}$  in most screens of the shallow transect show minimal variation; only if, by chance, one of the screens is situated at a position of upward directed flow, a sudden decrease in  $^{81}\text{Kr}$  values may be observed. The deep transect shows the expected decrease of  $^{81}\text{Kr}$  with flow distance. Both of these tracers,  $^4\text{He}$  and  $^{81}\text{Kr}$  (and  $^{36}\text{Cl}$ ), are on a timescale too long to produce discernable age variations in the shallow transect.

Radiocarbon, in contrast, has a decay constant that is on an appropriate timescale for the shallow transect and partly also for the intermediate transect. Carbon-14 clearly reflects the infiltration areas with high radiocarbon values and the zones of upward directed flow with low radiocarbon values. In the intermediate transect,  $^{14}\text{C}$  also indicates evidence of young water at the right side, close to the deep-reaching infiltration area. Later in the intermediate transect and in the whole deep transect, groundwater circulates on a timescale too large for detection of flow patterns using  $^{14}\text{C}$ .

The assumption to sample the same flowline along a horizontal transect following the gradient of groundwater potential may be a reasonable and valid approach in confined aquifers. It is, however, normally invalid in phreatic aquifers with only small variations in aquifer transmissivity. In phreatic

aquifers, horizontal transects along an assumed flow direction can result in constant tracer values as demonstrated in the Vogel case, or in tracer values reflecting a series of locally young and old waters in the regional flow direction. This may seem unexpected on first sight, but is nevertheless in accordance with the general direction of flow. As Tóth (1963) [28] pointed out, a regional flow system circulation on long timescales may be present depending on aquifer parameters, but will then be observable only with very good depth resolution and only in the deep parts of the aquifer.

### 9.2.3. Summary

Section 9.2 demonstrated that horizontal tracer transects along an assumed flowline can help to obtain important information on the groundwater flow system such as distance velocity and aquifer transmissivity. The discussion of the Vogel aquifer in Section 9.1.1 also demonstrated that a horizontal transect in the direction of groundwater flow does not necessarily result in an increase of tracer model age in the flow direction. The discussion of the Tóth aquifer even demonstrated the possibility of locally decreasing ages in the general flow direction which pointed to the existence of local flow systems.

The first two sections of this chapter, 9.1 and 9.2, demonstrate the following:

- (a) To understand the details of a flow system, many measurements of age-dating tracers are necessary, not just a single measurement of one particular tracer.
- (b) A combination of different tracers covering different timescales is necessary, if a flow system as a whole is to be understood.
- (c) If development of a conceptual understanding of the flow system is still in its initial state, a depth profile of tracer measurements is advantageous to gain further understanding.
- (d) Horizontal transects aiming to sample a single flowline promise further useful details if the flow system is well constrained — either because it is a confined aquifer or because a detailed flow model has already been constructed. Only this allows the choice of sampling wells that may be on a flowline.
- (e) Horizontal transects not showing the tracer pattern expected are a clear indication that either the flow model needs refinement or that unexpected tracer specific phenomena are occurring. Possible reasons include changes in aquifer thickness, changes in flow direction, flow convergence, changes in tracer fluxes in or out of the aquifer (especially for  $^4\text{He}$ ) and geochemical alteration of the tracer (in the case of  $^{14}\text{C}$  or  $^{36}\text{Cl}$ ). Isotope hydrological tracers demonstrated their suitability to boost the necessary model refinements (see Chapters 11–14). Often, new sampling on a different spatial scale is necessary to achieve the necessary insight for such refinements.

The results here were obtained assuming excellent sampling conditions: multilevel sampling with several well isolated screens at different depths was a prerequisite for the considerations in Sections 9.1 and 9.2. Of course, this gives rise to the question of what may happen if the sampling conditions were not as ideal. What happens if there are several screens, but all in one borehole, leading to mixed samples from different depths? The next section presents methods that use measurements of several different tracers to resolve instances of borehole mixing.

## 9.3. IMPORTANT PATTERNS OF TRACER VERSUS TRACER

The combination of tracers reflecting different timescales is both a powerful and necessary approach when studying old groundwater. Whenever a tracer for a long timescale is used with the final goal of deriving an age, it should be supplemented by tracers for young components and, if possible, also by tracers for the next longer timescale. The reason is that most groundwater samples represent mixtures of an a priori unknown kind. As discussed in the introductory chapters, it is very

improbable that the frequency distribution of ages represented by a water sample consists only of one (idealized) age. In most cases, it will at least be broadened by diffusion and dispersion. As discussed using the Vogel and Tóth aquifer models, it can also show different, sometimes systematically varying idealized ages over the length of the screen. It may also consist of different non-overlapping age ranges (see Fig. 3.1) which normally are described as (binary, ternary, etc.) mixtures. Such mixtures will result in tracer model ages that may be very different from the ages of the (two or more) water end members that dominate the mixture. As seen in Table 9.1, such a multicomponent mixture manifests itself by tracer model ages that are different for each tracer. Often, these mixtures can be identified plotting one tracer versus another. In addition, if the age of the groundwater approaches the maximum dating range of a certain tracer, any small admixture of younger water will keep this tracer close to but not within the dating range. For example, a 2% admixture of 150 a old water to a 100 ka old water body will keep the  $^{14}\text{C}$  value near 2 pmc and the tracer model age near 32 ka — which surely will not be a representative age for the bulk of the water. However, combining the measurements of two different tracers with very different dating ranges can make the presence of such mixtures obvious by showing discrepant ages for the different tracers. Even before calculating any ages with the tracers, simple plots of one tracer relative to another can characterize samples consisting of waters of different age. Such tracer–tracer plots are presented below.

### 9.3.1. Combination of tracers for different timescales

Plotting a tracer A which decays fast or is relevant only for a small timescale versus another tracer B for a larger timescale gives insights into mixtures, initial conditions and practical detection limits. A typical plot is sketched in Fig. 9.14: in this case, the short-time tracer is plotted on the y axis and the long-time tracer on the x axis. If the long-time tracer is radioactive, it is best to plot the x axis with a logarithmic and descending scale. Doing so, a distance on the x axis represents a distance in time, independent of any initial ‘no decay’ value and without calculating an age. A possible tracer combination might be tritium on the y axis and  $^{14}\text{C}$  on the x axis. Instead of tritium, CFCs can be used

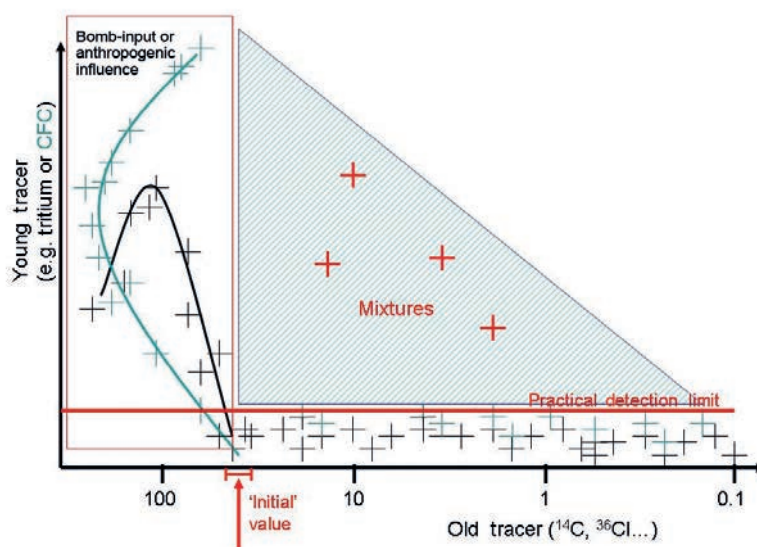


FIG. 9.14. A plot of tracers of different timescales reveals initial values for the old tracer; shows practical detection limits for the young tracer and makes mixtures of waters with different ages obvious.

(see Chapter 4). However, the same principle applies for radiocarbon as a short-time tracer on the y axis in combination with  $^{36}\text{Cl}$  as a long-time tracer on the x axis.

What are the patterns that can be observed on such a plot? In the simplest case, showing only idealized ages, all samples would plot along and very close to the x and y axes of Fig. 9.14. This is because short timescale tracers (e.g. tritium or CFCs) will decrease with age to zero before long timescale tracers (e.g.  $^{14}\text{C}$ ) will show any noticeable decrease. The young samples containing short timescale tracers plot along the y axis, with the x value (long timescale tracer) close to the initial value. As age further increases, the long-time tracer will decrease while the short-time tracer is already at zero, plotting the older samples along and close to the x axis. However, because many other processes and factors can affect tracer concentrations, this simple picture is disturbed.

First, the short-time tracer may show some behaviour with time. Tritium and the CFCs show peaks with time, the peak of tritium being around 1963 and the peaks of CFCs in the early 1990s. If the long-time tracer shows no such anthropogenic influence, such as  $^{81}\text{Kr}$ , then still all points containing the short-time tracer lie along the y axis. However, as discussed in Chapter 4, radiocarbon in atmospheric  $\text{CO}_2$  raised by nearly a factor of two above natural values due to the bomb tests, and this happened and remained measurable during the same time span as the peaks in tritium and CFCs. As a consequence, a plot of tritium and CFCs versus radiocarbon will — even for idealized ages — plot along a curve close to the y axis. This is similar for the combination  $^{14}\text{C}/^{36}\text{Cl}$ , because both show anthropogenic increase due to bomb production.

Second, some long-time tracers have no well defined initial value. This is true for  $^{14}\text{C}$  because the ‘no decay’ value is influenced by chemical processes in the unsaturated zone and in the aquifer, as discussed in detail in Chapter 4. This is true for  $^{36}\text{Cl}$ , since the initial  $^{36}\text{Cl}/\text{Cl}$  ratio depends on the recharge area and the climatic conditions during recharge, as discussed in Chapter 6. Therefore, a plot of tritium versus  $^{14}\text{C}$  or of  $^{14}\text{C}$  versus  $^{36}\text{Cl}/\text{Cl}$  can give information on the initial value of the long-time tracer on the x axis ( $^{14}\text{C}$  and  $^{36}\text{Cl}/\text{Cl}$ , respectively) as indicated by the red bracket ‘initial value’ in Fig. 9.14.

Third, all tracers have practical detection limits. These depend on the method of measurement and on the sampling conditions. For tritium, the analytical detection limit is typically around 0.5–0.1 TU for beta-counting after enrichment; for the  $^3\text{He}$  ingrowth technique, it can be as low as 0.005 TU; and for CFCs it is around 0.01–0.03 pmol/L. For  $^{14}\text{C}$  and  $^{36}\text{Cl}/\text{Cl}$ , it is around 0.1 pmc and  $10 \times 10^{-15}$ , respectively, as discussed in Chapters 4 and 6. Practical detection limits due to the sampling conditions (leaky well casing, reagents used in the field, contamination due to difficult field conditions, etc.) may be higher than these analytical detection limits. For instance, using normal sampling and transport methods, one would not interpret tritium values greater than 0.05 TU as representing samples containing significant amounts of young water, or treat samples with 0.3 pmc as ‘radiocarbon free’. The plot in Fig. 9.14 can provide an estimate of these practical detection limits, because this is the range where the concentrations of the short term tracers level off as the long-time tracer concentration decreases, as indicated by the horizontal red line and the crosses below.

Fourth, actual groundwater samples do not contain water of only one idealized age. Instead, a sample consists of waters containing a narrow or wide age distribution, or can even be a mixture of two or more waters with disjunctive ages. Imagine, for instance, a deep borehole with several screens or an open borehole in fractured rock with several water-bearing fractures. Such binary or multicomponent mixtures will plot in the triangle area in Fig. 9.14, denoted ‘mixtures’. Any sample plotting in this triangle area of Fig. 9.14 is a mixture of young and old water and, generally, within this triangle the tracer model age is not a good estimate for the groundwater age.

In principle, mixtures from the triangle area may be deconvoluted into the components, and ages for the mixing components may be computed. This is a difficult task, however, and often not possible in the practical case. Deconvolution of the mixture needs at least as many analysed parameters as mixing components are present, to narrow down the original water masses and their ‘initial’ tracer values. In general, the age of the two components is also unknown, which needs at least two additional age-tracer

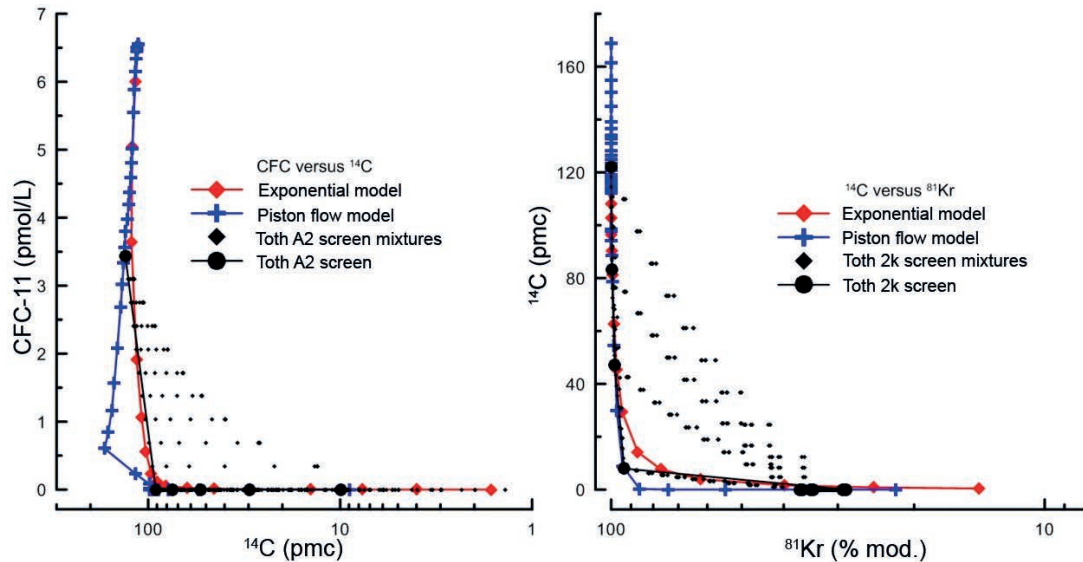


FIG. 9.15. Plots of tracers with different timescales. Example curves are for a piston flow model (blue line) and an exponential model (red line), and for two multilevel screens of the Tóth model (at  $x = 2000$ , exfiltration conditions and at  $x = 14\,000$ , infiltration conditions, black dots) together with binary mixtures between screens (small dots).

values per sample. Since each tracer has an age range over which it is sensitive (Fig. 1.3), each tracer can only resolve mixing components within the valid dating range of the tracer. For further numerical modelling approaches as discussed in Chapter 10, the samples from the triangle area in Fig. 9.14 should be avoided, or, if this is impossible, at least be treated with the necessary caution during modelling.

Two examples for the plots using tracers of different timescales are given in Fig. 9.15. The curves in Fig. 9.15 represent the piston flow model, which corresponds to the idealized age since it assumes no mixing (blue curves). Figure 9.15 also shows tracer concentrations for the exponential model, corresponding to the Vogel aquifer with a full screened well as discussed in Section 9.1.1 for different mean ages (red curves). As a mixing example, two multilevel screens from the Tóth model in Section 9.1 are displayed as black dots connected by a line. The left pane focuses on the shorter timescales and displays results computed for screens from the infiltration area at  $x = 14\,000$  m, and plots CFC-11 versus radiocarbon. The right pane for the longer timescale displays results computed for screens from the combined infiltration-upward flow area at  $x = 2000$  m, and plots radiocarbon versus  $^{81}\text{Kr}$ . Since screens in the discussed Tóth case are short enough, the large black dots are very close to the piston flow and exponential model curves (blue and red lines, respectively). In both plots, small black dots show binary mixtures between all possible screen combinations in steps of 10% for the mixing ratios.

The plots show that the curves for the exponential model (= full screened Vogel aquifer) are similar to the curves assuming idealized ages for tracers of very different timescales. However, the numerical values for the average age and the idealized age are very different for single pairs of blue and red symbols situated close to each other. The initial condition for  $^{14}\text{C}$  ('no decay' 100 pmc) could be easily deduced from these plots, and from both model assumptions. Values for  $^{14}\text{C}$  in both plots are higher than 100 pmc for small idealized ages and mean ages due to the presence of anthropogenic bomb  $^{14}\text{C}$  in the atmospheric input function. The comparably clear picture of the blue and red line, however, is considerably complicated if binary mixtures between screens of different depth are taken into account. In this case, tracer combinations are possible which could not occur assuming idealized ages or the simple mixture and dispersion patterns used in lumped parameter modelling.

Whereas CFC-11 is measurable only in the topmost screen in the Tóth aquifer, radiocarbon is also present at a greater depth. Consequently, the clear patterns of the piston flow or exponential model can be disturbed with a higher probability in the plot of  $^{14}\text{C}$  versus  $^{81}\text{Kr}$ , because more screens contain  $^{14}\text{C}$ .

This seems initially to be an unsatisfactory result; however, on the contrary, if the absence of CFCs, tritium and even  $^{14}\text{C}$  can be demonstrated, this leads to the conclusion that even small admixtures of young water can be excluded, ‘young’ meaning, in this case, waters up to several thousand years of age.

Plotting tracers of different timescales versus each other is, therefore, a useful tool for the detection of unwanted mixtures, possibly created during sampling. It also allows the necessary determination of initial values for  $^{14}\text{C}$  and  $^{36}\text{Cl}$  close to the infiltration area. A direct comparison of ages, or a detection of processes that influence the long time tracer only, needs a comparison of tracers with similar timescales.

### 9.3.2. Combination of tracers with similar decay timescales

The combination of different age-dating tracers with similar timescales is always desirable since the assumptions of one tracer application can be checked against another tracer, providing greater confidence in the interpretation of both sets of tracers. Many details of this approach were discussed in the CFC guidebook (IAEA (2006) [85]) for young groundwaters. For old groundwaters, however, there are only two radioactive tracers available that operate on the same timescale, namely  $^{36}\text{Cl}$  and  $^{81}\text{Kr}$ . The basic effects that can influence the comparison of these two tracers were described in Chapters 5 and 6, and are summarized in Fig. 9.16.

No study has yet (as of 2012) been published with enough  $^{81}\text{Kr}$  data for a detailed comparison, but the number of available  $^{81}\text{Kr}$  data will probably increase soon, and in view of the comparably low effort needed, measurements of  $^{36}\text{Cl}$  will probably always be included for the same samples. Since  $^{36}\text{Cl}$  and  $^{81}\text{Kr}$  have very similar half-lives, their evolution with increasing idealized groundwater age should follow a straight line with a slope close to one as indicated by the thin black line (Fig. 9.16). As was shown for radiocarbon and  $^{36}\text{Cl}$ , the comparison of  $^{81}\text{Kr}$  and  $^{36}\text{Cl}$  should enable the determination of ‘initial’  $^{36}\text{Cl}/\text{Cl}$  ratios. Furthermore, small deviations of measured values from the straight line may be attributed to secular variations in the initial  $^{36}\text{Cl}/\text{Cl}$  ratio. Possible reasons were discussed in Chapter 6 and may include variations in proximity of recharge areas to marine coastal areas resulting from changes in sea level, or variations in cosmic  $^{36}\text{Cl}$  production. Addition of chlorine from sediments will influence only the  $^{36}\text{Cl}/\text{Cl}$  ratio but not  $^{81}\text{Kr}$ , and should be visible as a horizontal shift towards lower  $^{36}\text{Cl}/\text{Cl}$  ratios as indicated by the green arrow (Fig. 9.16). More problematic for the ages but nearly invisible in the plot are mixtures of waters with different age. These are evident for tracers with very different

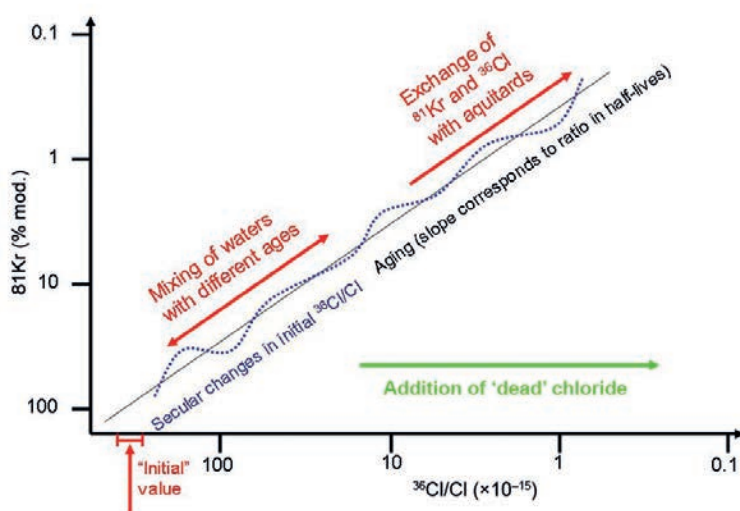


FIG. 9.16. Comparison of  $^{36}\text{Cl}/\text{Cl}$  and  $^{81}\text{Kr}$ , and possible changes in one or both tracers relevant for age dating.

timescales because the evolution according to idealized age creates a very convex curve. Since both  $^{36}\text{Cl}$  and  $^{81}\text{Kr}$  radioactively decay with similar half-lives, the plot of  $^{36}\text{Cl}$  versus  $^{81}\text{Kr}$  creates a straight line. Mixtures will also follow this line and with the present accuracy in measurement and interpretation will not be detectable. In addition, invisible in the plot of  $^{81}\text{Kr}$  versus  $^{36}\text{Cl}$  is a possible loss of  $^{81}\text{Kr}$  and  $^{36}\text{Cl}$  by diffusion into aquitards. This process was described in Chapter 5 and will influence both isotopes in a similar manner, since their diffusion constants are not very different.

### 9.3.3. Linear accumulating tracer versus exponential decay tracer

Chapter 8 discussed and demonstrated many of the uncertainties connected with the use of helium as a tracer for age dating. However, despite these uncertainties, helium has some significant advantages. First, due to its linear increase with time, its concentration changes during mixing the same way as average age changes during mixing. Second, a stable isotope which is produced linearly with time has no limit concerning the dating range. This allows helium results to be compared both with  $^{14}\text{C}$  and with  $^{81}\text{Kr}$  and  $^{36}\text{Cl}$ . Finally, helium can be measured with much less cost than  $^{36}\text{Cl}$  and  $^{81}\text{Kr}$ , even if the  $^3\text{He}/^4\text{He}$  isotope ratio and Ne concentration are to be determined as well. This allows helium to be applied to a larger number of samples than might be possible for measurement of  $^{14}\text{C}$ ,  $^{36}\text{Cl}$  or, particularly,  $^{81}\text{Kr}$ .

The comparison of the linearly increasing tracer helium with the tracers observing radioactive decay, such as  $^{14}\text{C}$ ,  $^{36}\text{Cl}$  and  $^{81}\text{Kr}$ , in some aspects is similar to the case of comparing  $^{81}\text{Kr}$  with  $^{36}\text{Cl}$ , but there are some very important and sometimes useful differences, which are illustrated in Fig. 9.17.

In the simplest case, helium concentrations increase only by in situ production or by a constant flux at a constant rate and the radioactive tracer decreases only by radioactive decay due to idealized age. In this case, the plot of excess helium (see Chapter 8 for the definition of excess helium) versus the log of a radioactive tracer should display a straight line, starting at a point where the radioactive tracer has its initial condition and at an excess helium value of zero. The slope of this line is a function of the in situ production rate and the radioactive decay constant only. The in situ production rate, as described by Eq. (9.3), can vary within a single aquifer due to changes in U and Th content, and probably differs between different aquifers. This implies that different aquifers may have different slopes, as indicated with the blue and black line of in situ production in Fig. 9.17.

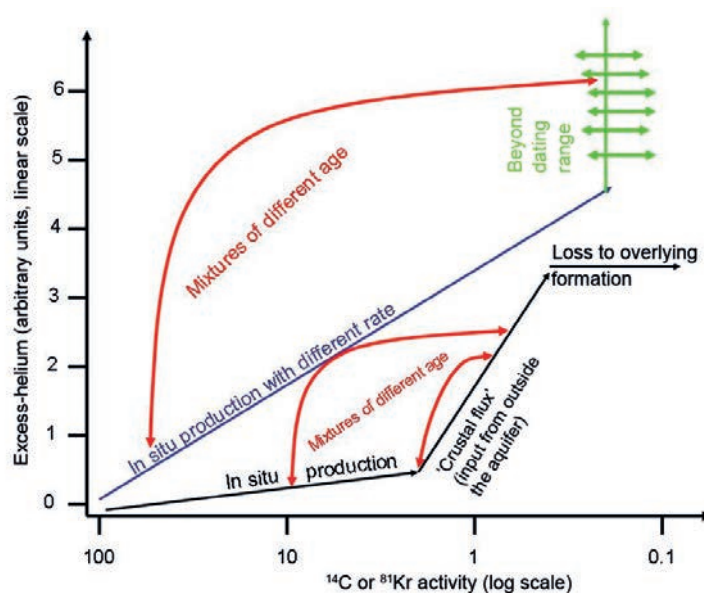


FIG. 9.17. Plot of helium versus a radioactive tracer concentration, with development lines due to the different processes in in situ production, external flux, mixing and helium loss.

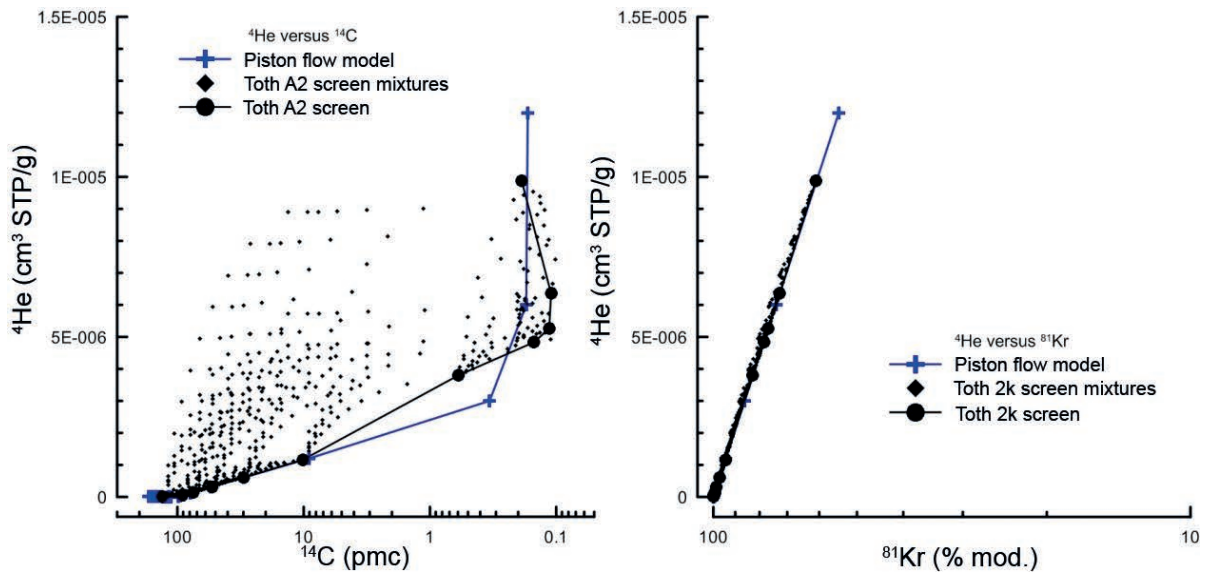


FIG. 9.18. Helium in comparison with the radioactive tracers  ${}^{14}\text{C}$  and  ${}^{81}\text{Kr}$ . Blue lines represent the piston flow model. Black dots represent tracer values as computed with the Toth model and presented in Section 9.1.2. In the left panel, black dots display profile A2 in infiltration area at  $x = 14\,000$  m; in the right panel, a depth profile with same screen depths, but located at  $x = 2000$  m. Small black diamonds represent binary mixtures between pairs of screens of these depth profiles. Low  ${}^{14}\text{C}$  values in the left panel are fixed to be not smaller than a practical detection limit of  $0.1 \pm 0.1$  pmc.

As waters grow older along a flowline, helium from external sources, such as the ‘crustal flux’ discussed in Chapter 8, will become prominent and these external sources will generally show a much higher slope in Fig. 9.17. Of course, the slope of the in situ production might also vary due to different uranium and thorium contents of the aquifer rocks. However, a different in situ production is generally a smaller variation (around a factor of two to five typically) as compared to external fluxes, which was described to be as much as a factor of 70 higher than in situ production in Chapter 8. If helium is lost to overlying formations as well, then a balance of influx and diffusive loss may be reached, resulting in constant helium concentrations with further increases in age. This, in most cases, will require very large timescales.

On the timescale of radiocarbon, another process is important, which applies to samples approaching the dating limit for radiocarbon. The analytical detection limit for radiocarbon may be as low as 0.1 pmc. However, in practice, this corresponds to an admixture of less than 0.1% young water, and such ‘clean’ samples may be difficult to obtain. Regardless of whether the practical detection limit is 1 or 0.1 pmc, eventually the  ${}^{14}\text{C}$  detection limit will be reached along the flowline. In this case, the samples will follow the vertical green arrow indicated in Fig. 9.17, because the radiocarbon value will not decrease further and the helium concentration will continue to increase with time.

Mixtures of waters with a different age along a single in situ production line will be difficult to detect: they will manifest themselves by following an evolution that is linear for both tracers in Fig. 9.17 instead of an exponential evolution for radioactive decay. On a semi-logarithmic plot, this linear relation is a curved line which does not differ very much from the straight line. Admixtures of waters which are beyond the dating range for the radioactive tracer, however, will plot above the in situ production line. Mixtures will also be discernible if waters with considerable contributions from external sources mix with those still on the in situ production line. These cases are indicated by red double-arrows in Fig. 9.17.

The case of mixtures can also be easily demonstrated using the infiltration depth profile A2 at  $x = 14\ 000\ \text{m}$  in the Tóth aquifer and is shown in Fig. 9.18: the waters in the underlying regional flow system are beyond the dating range for radiocarbon. To illustrate their possible radiocarbon values, taking into account that their measurement uncertainty is different from zero, a random number of  $(0.1 \pm 0.1)$  pmc was added to the model results computed and displayed in Fig. 9.8.

It is evident from the left plot in Fig. 9.18 that binary mixtures between pairs of different screens do not follow the in situ production line in the plot versus radiocarbon. Mixtures can, thus, be easily identified. In the plot of binary mixtures of different screens for the tracer pair  $^4\text{He}$  versus  $^{81}\text{Kr}$ , however, these fall close to the in situ production line (right panel in Fig. 9.18). Here, a depth profile at  $x = 2000\ \text{m}$  was chosen to display larger ages. Ages of waters are not beyond the dating range of  $^{81}\text{Kr}$  in this case. Therefore, mixtures of waters with different age plot very close to the lines of the piston flow model and to the Tóth screens. Mixtures will not be detectable with the right plot in Fig. 9.18.

### 9.3.4. Noble gas patterns

Water in solubility equilibrium with the atmosphere has helium concentrations between  $3 \times 10^{-8}$  and  $5 \times 10^{-8}\ \text{cm}^3\ \text{STP/g}$ , the former value being for  $25^\circ\text{C}$  and  $2500\ \text{m}$  above mean sea level and the latter at sea level for a temperature of  $0^\circ\text{C}$ . This value and the presence of a possible excess-air component (see Chapter 8 for details) can be determined with an accuracy of better than 10%, which means that excess values of  $^4\text{He}$  as small as  $6 \times 10^{-9}\ \text{cm}^3\ \text{STP/g}$  can be detected. With the in situ production of  $6 \times 10^{-11}\ \text{cm}^3\ \text{STP} \cdot \text{g}^{-1} \cdot \text{a}^{-1}$  used in this chapter, this implies that the excess helium concentration of a water with an idealized age of 100 a or larger may be detectable. While this is not an age within the scope of the present book and although the estimate may vary from aquifer to aquifer, such small helium excess values may be of interest for other tracers; if attempts are made to determine the initial  $^{14}\text{C}$  value from a plot of CFCs or tritium versus  $^{14}\text{C}$  as shown in Fig. 9.15, it is surely of interest if the CFC or tritium value represents an unmixed sample or one with a contribution of water older than 100 a. To obtain this kind of information, a plot of neon versus helium is useful, which is indicated in Fig. 9.19.

Helium and neon in solubility equilibrium plot along a curve on which the noble gas content is given for a range of (infiltration) temperatures, indicated with blue crosses. The black straight line

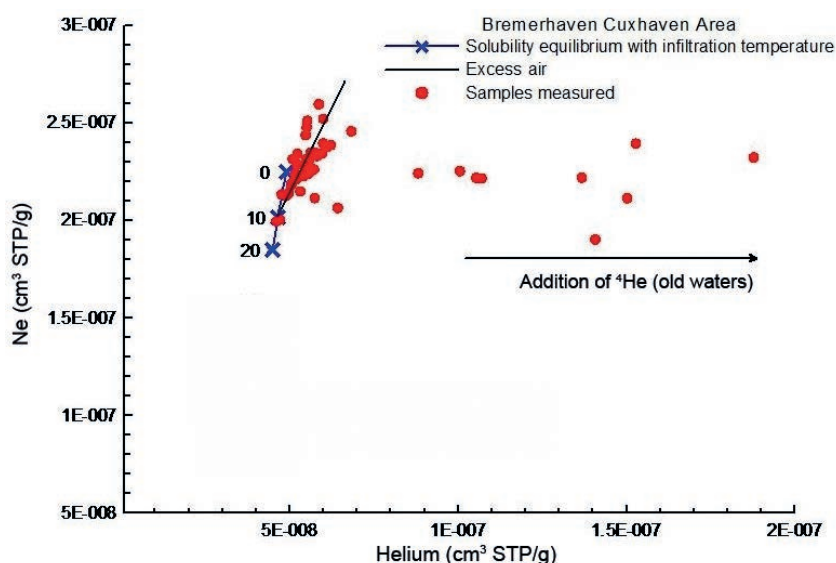


FIG. 9.19. Neon versus helium concentration with lines for solubility equilibrium, excess air and excess helium.

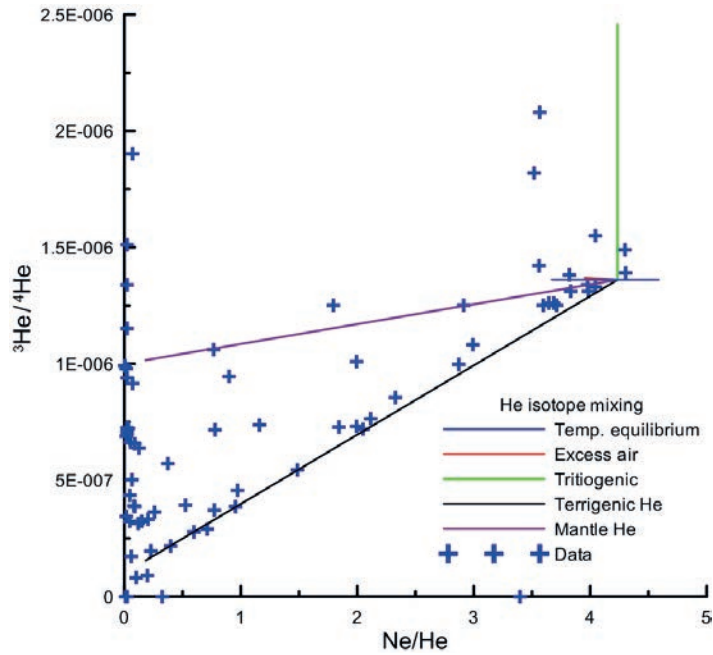


FIG. 9.20. Helium isotope mixing plot. Data are identical to those in Fig. 8.10.

indicates excess air added to the solubility concentration at 8°C. Most samples — here from a case study with young waters — plot along this excess air line. Some samples, however, show higher values as indicated by a horizontal shift to the right, towards higher helium concentrations. This can help to further constrain details, when plotting tracers of different timescales versus each other, as in Figs 9.14 and 9.15. In case these samples shifted to the right in Fig. 9.19 contain tritium, they should be regarded as mixed and, for example, not be used to determine initial  $^{14}\text{C}$  values in Fig. 9.15. Of course, a similar plot is possible with any other noble gas instead of neon, for example Ar or Kr.

Very old water contains so much helium, that the equilibrium and the excess air lines are not discernible from the y axis in this plot. In the case of old water, another plot is useful (similar to the Weisse plot in Fig. 8.10) and is demonstrated in Fig. 9.20.

In Fig. 9.20, the measured  $^3\text{He}/^4\text{He}$  isotopic ratio is plotted versus the Ne/He ratio. Together with the data, several lines are plotted: the green vertical line displays additional  $^3\text{He}$  as produced by radioactive decay from tritium. The blue and red lines display the concentration and isotope ratio of solubility equilibrium (Weiss (1971) [524]), and excess air, respectively. The blue line is horizontal and nearly coincides with the excess air line because any isotope fractionation during solution as well as its temperature dependence is nearly invisible on the scale of this plot (Benson and Krause (1980) [592]). The place where all lines meet corresponds to the  $^3\text{He}/^4\text{He}$  isotopic ratio of air and to the (slightly temperature dependent) Ne/He ratio in equilibrium with the atmosphere. The red and purple lines are mixing lines of this equilibrium helium with excess helium of different isotopic composition, namely with a  $^3\text{He}/^4\text{He}$  ratio of  $1 \times 10^{-6}$  and  $1 \times 10^{-7}$ . This plot, as compared to Fig. 8.10 (Weiss and Moser (1987) [562]), has the advantage of displaying only measured values, without needing any model for excess air correction. It is, therefore, a better choice to plot a whole data set at an early stage, if the mechanism of excess air correction is still under discussion or if perhaps different mechanisms of excess air and different infiltration temperatures are possible. Figure 8.10, in contrast, should be used if the excess air model is well constrained, because then the characterization of  $^3\text{He}/^4\text{He}$  ratios in the external sources is sharper. The important patterns, however, are discernible in both plots, and the isotopic ratio of the excess helium component can be estimated from both plots. If neon measurements are not available, a similar plot can be produced for any other noble gases as nominator (e.g. Ar), or even choosing  $1/\text{He}$  as the x coordinate.

## Chapter 10

### NUMERICAL FLOW MODELS AND THEIR CALIBRATION USING TRACER BASED AGES

W. SANFORD

United States Geological Survey,  
Reston, Virginia,  
United States of America

#### 10.1. INTRODUCTION

Any estimate of ‘age’ of a groundwater sample based on environmental tracers requires some form of geochemical model to interpret the tracer chemistry (Chapter 3) and is, therefore, referred to in this chapter as a tracer model age. The tracer model age of a groundwater sample can be useful for obtaining information on the residence time and replenishment rate of an aquifer system, but that type of data is most useful when it can be incorporated with all other information that is known about the groundwater system under study. Groundwater flow models are constructed of aquifer systems because they are usually the best way of incorporating all of the known information about the system

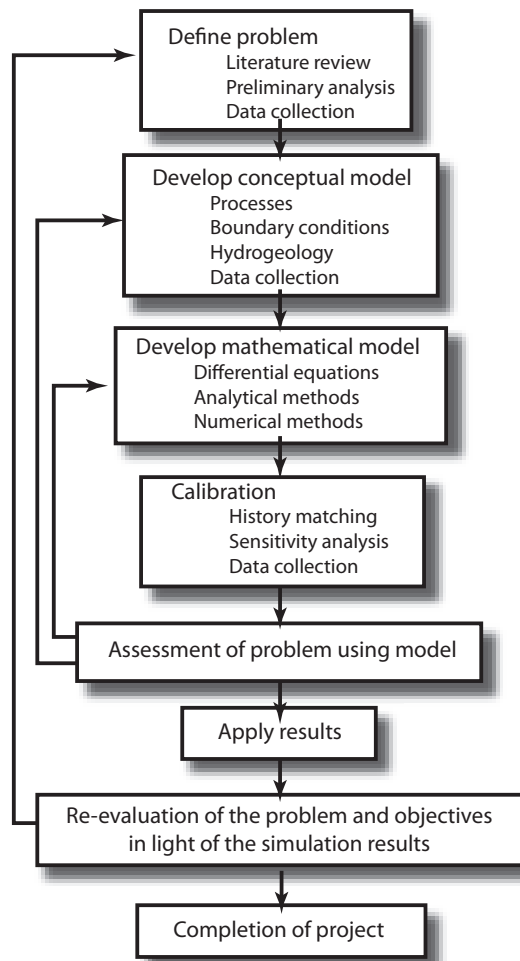


FIG. 10.1. Flow chart of the groundwater flow modelling process (after Reilly (2001) [72]).

in the context of a mathematical framework that constrains the model to follow the known laws of physics and chemistry as they apply to groundwater flow and transport. It is important that the purpose or objective of the study be identified first before choosing the type and complexity of the model to be constructed, and to make sure such a model is necessary. The purpose of a modelling study is most often to characterize the system within a numerical framework, such that the hydrological responses of the system can be tested under potential stresses that might be imposed given future development scenarios. As this manual discusses dating as it applies to old groundwater, most readers are likely to be interested in studying regional groundwater flow systems and their water resource potential.

Model development occurs in stages (Fig. 10.1) where the model developer must (i) define the problem and the purpose for the model; (ii) develop the conceptual model; (iii) design the model grid; (iv) calibrate the model (adjusting the hydraulic parameters to fit the available data); and (v) apply the model to predict future responses. In some cases, the purpose of the model may be only to improve the understanding of the flow system, in which case stage (v) might never be employed. Given the high uncertainties associated with future predictions based on most models that have relatively limited data and complex hydrogeology, models are often most useful when used to understand and quantify the flow system at the end of stage (iv), or when the results of the predictions are still useful in spite of large accompanying error bars. All models represent systems based on data that are currently available, and so many studies require a return to the data collection phase after an initial model reveals where additional data are needed to improve model predictions. This feedback between data and modelling results is often carried out as an interaction between the hydrologist constructing the model and the geochemist collecting and analysing the data. It is important for the two to have good communication and a working relationship. The feedback can happen both ways — the data control how the model is developed, and the model results can indicate where and what type of additional data need to be collected. This chapter will cover the basics of model design, development and calibration, especially with the use of tracer model ages.

## 10.2. EQUATIONS AND NUMERICAL METHODS

A groundwater flow model describes the distribution of heads within an aquifer system based on the solution of the fundamental groundwater flow equation, which can be derived solely from the principles of mass balance and Darcy's law. A general form of this equation for three dimensions, transient flow and constant fluid density can be written as:

$$\frac{\partial}{\partial x} \left( K_x \frac{\partial h}{\partial x} \right) + \frac{\partial}{\partial y} \left( K_y \frac{\partial h}{\partial y} \right) + \frac{\partial}{\partial z} \left( K_z \frac{\partial h}{\partial z} \right) = S_s \frac{\partial h}{\partial t} - Q(x, y, z, t) \quad (10.1)$$

where

- $h$  is the hydraulic head within the flow system;
- $K_x, K_y$  and  $K_z$  are hydraulic conductivity in the  $x, y$  and  $z$  directions, respectively;
- $S_s$  is the specific storage;
- $Q$  is a general source (+) or sink (–) of water to the aquifer system that can vary in space and time to represent injections or withdrawals at points in space or over regions or boundaries;
- $t$  is time.

The derivation of this equation can be found in standard textbooks on hydrogeology (Domenico and Schwartz (1998) [8]; Schwartz and Zhang (2003) [593]).

To solve this partial differential equation, a description of the hydraulic properties ( $K$  and  $S_s$ ) are needed in three dimensions, head and/or flux conditions at the boundaries of the domain, and initial conditions at the simulation starting time. For steady state conditions (often assumed for aquifers

under pre-development conditions), the left term on the right side of Eq. (10.1) becomes zero and the specific storage is not a required parameter, nor is an initial condition required. The solution to this equation gives the distribution of head,  $h$ , in three dimensions, and then by using Darcy's law, flow rates within the aquifer can subsequently be calculated. The seepage velocity (that taken by a solute or water molecule) is the specific discharge divided by the porosity and, therefore, by using an estimate of porosity, one can simulate a velocity field within the aquifer by first solving the flow equation. Given two points within the system along a flow path, the seepage velocity between those points divided by the distance yields a time of travel for water or, if the point of origin is the water table, a flow model age.

In some cases, it may be useful initially to consider the flow system as having a simple geometry and boundary conditions, to the extent that an analytical solution might be available. An analytical solution is a continuous solution across the domain where the head or hydraulic (or flow model) age value, for example, can be evaluated at any point. For some simple flow systems, the distribution of the flow model age can be represented by such a function (Cook and Böhlke (1999) [594]). A number of other analytical solutions have been taken from the heat flow literature (Carslaw and Jaeger (1959) [539]), as heat flow is mathematically analogous to fluid flow in porous media. In most cases though, the geometry, boundary conditions and hydraulic parameter distribution are complicated to the extent that no analytical solution exists. For these cases, a numerical solution is the next best alternative. A numerical solution to the flow equation is a distribution of head values at a finite number of discrete, pre-specified points (or nodes) within the aquifer system. The two numerical solution techniques most commonly used to solve the flow equation are finite difference and finite elements. The former requires the user to define a rectangular grid of points or cells at which the solution will be obtained, and the latter requires points that are connected by elements that are usually triangular or rectangular in shape, but not necessarily arranged along a regular grid. The more points in the grid, the more detailed and accurate the solution to the equation, but the more computer time and storage are required. With current computer capabilities, it is possible to have of the order of one million nodes in a grid. Finite elements provide the flexibility of arranging the nodes freely to fit the geometric features of the system, but such an arrangement requires more sophisticated graphical user interfaces to construct the 'mesh', as this could not be reasonably constructed manually if the node number were in the thousands or more.

Many modelling codes have been developed that solve the equations of groundwater flow and solute transport, most of which are adequate for modelling a groundwater system. The only codes chosen to be listed here are those published and supported by the United States Geological Survey (USGS), not because they are necessarily superior, but because they have been the most widely used in the world (and, thus, widely tested), and perhaps more importantly for this manual because the codes and their user guides can all be downloaded free from the Internet (<http://water.usgs.gov/software/>). The most widely used groundwater flow code has been MODFLOW (McDonald and Harbaugh (1988) [71]), of which the latest release is MODFLOW2005 (Harbaugh (2005) [595]). The code uses integrated finite differences and has a number of different 'modules' that can be used to incorporate different conceptual grid designs and different types of boundary conditions. One recent addition to MODFLOW is the ability to refine the grid in subdomains of local interest within a more regional coarse grid in a process known as local grid refinement (Mehl and Hill (2005) [596]; Mehl and Hill (2007) [597]). Several graphical user interfaces for MODFLOW are available on the open market, but the USGS has also created one recently (Winston (2009) [598]) that is free of charge. Viewing three dimensional results from MODFLOW is possible through the post-processing programme MODELVIEWER (Hsieh and Winston (2002) [599]).

### 10.3. AQUIFER GEOMETRY AND GRID DESIGN

Once a decision has been made to create a numerical model of an aquifer system, one of the first steps is to begin to conceptualize how the system will be represented by a grid or mesh of nodes. A basic understanding of the aquifer system and its geometry (Chapter 2) should be obtained before this grid

is created. Although three dimensional simulation is now tractable computationally for most systems, sometimes a two dimensional model may be sufficient to meet the desired objective, or it may serve as a good preliminary model that will provide some key understanding for a much smaller investment of time and resources. A two dimensional areal model could be appropriate for an aquifer that is essentially a single hydrogeological layer. On the other hand, in sedimentary basins, a two dimensional cross-section along a flowline can often provide the necessary vertical detail between multiple aquifers and aquitards, and can be simulated such that a great deal is learned about the contrast between the hydraulic conductivity of layers and how flow model ages would be influenced by such contrasts.

If a three dimensional model is to be constructed, some thought must go into how finely the layers are to be discretized in the vertical dimension, and how to balance the vertical resolution requirement with the horizontal grid resolution that is desired to represent landscape features. Aquifers and aquitards can be represented by single layers, but if solute transport and dispersion are to be represented (Chapter 10.8), more than one model layer per hydrogeological layer is usually desirable. There are many issues to consider in grid design (Anderson and Woessner (1992) [600]). All of the boundaries of the flow system of interest must be identified; sometimes, these boundaries are at a substantial distance from the sections of the system that are of most interest. Some hydrologists prefer the analytical element method (Haitjema (1995) [601]) in this case, which can more efficiently handle distant boundary conditions. Finite elements can be arranged to fit boundaries exactly. As finite difference grids are rectangular by nature and flow systems are not, certain sections of the grid will ultimately be outside of the flow system and must be characterized as inactive cells. Refinement of the grid in certain subdomains can be accomplished either by using a finite element method or local grid refinement with finite differences. Grid refinement can also be accomplished with finite differences by using variable grid spacing, which is usually a standard option, but this is somewhat less efficient (although less complicated) than using local grid refinement.

Hydrogeological units in sedimentary basins can be represented either by having them coincide exactly with model layers (Fig. 10.2), or by treating them independently and then calculating the effective hydraulic parameters for each model cell depending on how the model layers intersect the hydrostratigraphy. The latter approach can be more efficient when dealing with highly complex stratigraphy, and has been made easier with the development of software specifically designed for this purpose (Anderman and Hill (2000) [602]; Anderman and Hill (2003) [603]). Finite element models are better designed to handle hydraulic conductivity fields whose directions of maximum and minimum values do not coincide with the rectangular grids of finite-difference methods (e.g. Yager et al. (2008) [604]).

#### 10.4. BOUNDARY CONDITIONS

In order to solve the flow equation for the domain of interest, boundary conditions must be specified at the domain boundaries. Mathematically, these boundary conditions take the form of constant head, specified flux or mixed type. In order to create a model that simulates the conditions that occur in the real system, the real hydraulic boundaries must be expressed in terms of one of the three mathematical types.

Constant head is for boundaries where the head will remain constant no matter what stress is placed within the system; the internal changes in head will not affect the head at this boundary. An ideal example of this would be a large body of water, such as the ocean, that has such a large reservoir of water whose level will not be affected by changing flow conditions within the domain. Specified flux can represent a number of different field conditions. On the external boundaries, a flux of zero represents an impermeable surface. This is often the condition placed on the bottom boundaries or lateral edges of the domain. A groundwater divide would also represent a specified flux of zero. Recharge at the top boundary is a very common flux that is specified at the top boundary of the domain. Recharge can be distributed across the top of the model in a fashion that is consistent with field conditions. In humid

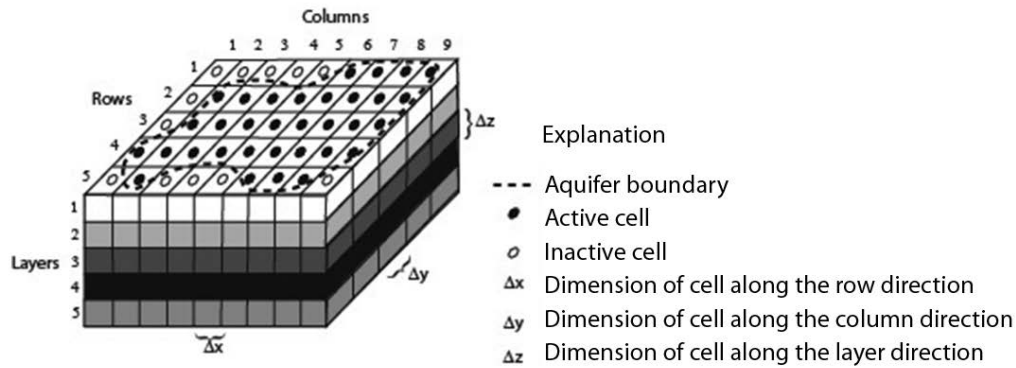


FIG. 10.2. A discretized hypothetical aquifer system (modified from McDonald and Harbaugh (1988) [71]).

climates, this is often represented by a rather even distribution of recharge across the domain, whereas in arid climates recharge is more often distributed at focal areas such as along mountain fronts or in ephemeral streams. Internal specified fluxes can be used to specify withdrawal or injection rates of water at individual wells.

Mixed type boundary conditions represent situations where the head at the boundary of the system may change, but only in a manner that can be described directly by an equation containing a head value outside of the boundary and a hydraulic conductance term across the boundary. Although a large river could be specified as a head, it could also be specified as a mixed type where the flux through the river bed sediments is a function of the vertical hydraulic conductivity of the river bed and the head in the river. A drain or seepage face is another type of mixed boundary where outflow is allowed to occur as a function of the soil conductance when the head in the aquifer exceeds that of the drain or land surface, but inflow is prohibited if the head in the aquifer is below that of the drain or land surface. Evapotranspiration directly from the groundwater can be specified as a mixed type boundary condition where the evapotranspiration upward flux varies depending on three different head conditions. When the head is below the root zone, the flux is zero. When the head is above land surface, the flux is at a maximum value that is plant and climate dependent. When the head is somewhere in between the bottom of the root zone and the land surface, the evapotranspiration flux varies between zero and the maximum value. A leaky confining layer can be represented as a mixed type boundary, where the head in the aquifer across the layer is specified and the boundary conductance is represented by the hydraulic conductivity of the layer divided by its thickness. See McDonald and Harbaugh (1988) [71] for more details of the application of these various types of boundary conditions.

## 10.5. TRANSIENT SIMULATIONS

Transient simulations are for situations where the effects of hydraulic stresses need to be followed over time. This corresponds to the situation where  $Q$  and  $h$  in Eq. (10.1) are time dependent  $Q(t)$  and  $h(t)$ . The simulation is then discretized into time steps that follow a given timeline and stresses are defined as to how they change over time. An initial condition of head everywhere in the model domain is required. Extractions from wells are often added to aquifers over time as pumping rates change. Under these conditions, the specific storage (Eq. (10.1)) of the rocks or sediments is also a required hydraulic parameter for the simulations. For water table aquifers, the specific yield is also required. The specific yield is the volume of water that drains from an unconfined aquifer per unit surface area of aquifer per unit decline in the water table. The value will, in general, be somewhat less than the porosity of the aquifer near the water table. In addition, heads at boundary conditions may change over time. Recharge may change over short time periods, such as seasons, or over very long time

periods, as the result of climate change. For regional systems where old groundwater has been dated, the travel times of the groundwater are usually of the order of thousands of years or more. In these cases, simulating steady state conditions as they existed before aquifer development began is frequently the approach taken. It is often more realistic for long time periods if a transient simulation is chosen and recharge is varied to simulate changing climate, during the recent ice age, for example.

## 10.6. MODEL CALIBRATION

The objective of most groundwater modelling studies is to create the best numerical model of the aquifer system possible given the available data on the hydraulic characteristics of the system. Adjusting the hydraulic parameters of the model until a best or satisfying fit to the observed data is achieved is known as the ‘model calibration’ (Hill (1998) [605]; Hill and Tiedeman (2007) [606]). This should not be confused with the terms ‘model verification’, which refers to the testing of the mathematics in the code to solve the equations accurately, and ‘validation’, which refers to the general process of producing a model that is ‘valid’ or represents the system well — although, in a strict sense, groundwater models cannot be validated (Konikow and Bredehoeft (1992) [607]). The hydraulic parameters that need to be adjusted during calibration include the hydraulic conductivity of the hydrogeological units and potentially its distribution within the units, recharge and its distribution, and specific storage for transient problems. Observed data almost always include head measurements and some type of measurements or estimates of flux. Some knowledge of the hydraulic properties of the rocks or sediment is often known a priori, as is some estimate of recharge. This is frequently referred to as prior information. As prior information is usually obtained from small scale or local tests or studies, and a model is most often developed to represent a large scale or regional system, the prior information is not usually assigned directly to the parameters, but rather serves as a guide for reasonable values within which the parameters should be adjusted during the calibration process.

As the model is based on Darcy’s law, using only heads and head gradients as observations will result in a very, if not completely, non-unique calibration. The head gradient is based on the ratio of the flux to the hydraulic conductivity, so using head values alone will only constrain the ratio of flux to hydraulic conductivity, not individual values of either. Thus, some type of flux observation needs to be included in addition to heads. The most common flux observation used is the baseflow to a stream. The baseflow is directly related to the long term recharge in the stream’s watershed. Although recharge is also a flux, it usually cannot be measured directly as an observation, especially in an integrated manner over space and time, and so it is often adjusted as a parameter of the model. Tracer model ages give information on the travel time (flux) within the system, and so can also be used in addition to hydraulic head data, or in addition to both hydraulic-head and base flow data to calibrate a model.

The simplest approach to calibrating a model is by trial and error. It is recommended to start with a simpler model and add complexity over time as the data permit. If there are only a few parameters in a model to adjust, they can be adjusted by hand to create the model that best fits the observed data. For any given set of parameter values, the model is run and the simulated values at the observation locations are compared with the data collected from those observation locations. The goal is to minimize the error difference between the simulated and observed data, most often done by calculating the sum of the squared errors (or some similar quantity). As computers have become faster, they have allowed models to become more complex to the point that they can include dozens or more parameters (usually these are different values of hydraulic conductivity in different units and regions of the model). Automated parameter estimation codes have been developed to greatly accelerate the calibration process (Doherty (2004) [608]; Poeter et al. (2005) [609]). These codes are shell programmes that are able to call any model and keep adjusting the parameters and rerunning the model in a direction that leads to the minimization of the total sum of squared errors. This is done through a continuous cycle of (i) changing the parameter values in the input files, (ii) running the model and (iii) examining the simulated observations. The result is a set of parameters that gives a model with the best fit to the data. However,

the best fit does not always indicate the best model and the calibration process must be guided carefully to avoid erroneous parameter values (Hill (1998) [605]; Reilly and Harbaugh (2004) [610]).

## 10.7. CALCULATION OF FLOW MODEL AGES

In order to use tracer model ages to calibrate a model, the model must be able to simulate a flow model age. Alternatively, a tracer concentration at any given point (usually a well or spring) can be simulated and compared directly with the measured concentrations, an approach discussed in Section 10.8. One simple and straightforward way to obtain an age from a flow model is to calculate it as a hydraulic time of travel. This is done by dividing the distance between two points along a flowline by the interstitial velocity calculated using Darcy's law. In a discretized groundwater model, this is done over regional distances by calculating the advective path line that an imaginary particle of water will travel along through the aquifer from one model cell to the next, and the time required to move along the path line given the hydraulic conditions defined in the model. Solute dispersion within the groundwater system for this type of calculation is neglected, and although this is not reality, and it is known to introduce some error during a calibration process, that error is often small relative to the uncertainties in the hydraulic properties of the system. Finite difference groundwater models are aptly suited for the calculations of such path lines and flow model ages. Velocities at cell boundaries can be calculated from the head values at the cell nodes using Darcy's law and a specified porosity. A particle of water can be followed from cell to cell, either forwards or backwards, from any specified starting point based on the calculated velocity field for the model grid. A post-processing programme (MODPATH; Pollock (1994) [611]), available for use with MODFLOW, calculates such path lines and travel times. To calculate a unique path that a particle of water would follow across a finite-difference cell, the assumption is first made that the velocity along each coordinate direction varies only in that coordinate direction and not along the other directions (Fig. 10.3). This assumption allows the simplification of the calculation of the distance travelled to the far side of a cell as a smooth curved path. The time required to traverse that distance in the  $x$  direction becomes:

$$\Delta t = \left( \frac{\Delta x}{V_{x2} - V_{x1}} \right) \ln \left( \frac{V_{x2}}{V_{xp}} \right) \quad (10.2)$$

where

- $\Delta t$  is the travel time to the far side of the cell;
- $\Delta x$  is the distance to the far side the cell;
- $V_{x2}$  is the velocity at the far cell wall;
- $V_{x1}$  is the velocity at the near side of the cell;
- $V_{xp}$  is the velocity at the  $x$  location of the particle.

The integration of the changing velocity across the cell yields the natural log term in Eq. (10.2). A similar equation is written for the  $y$  direction. Whichever  $\Delta t$  is less ( $x$  or  $y$ ) is the time of travel to the cell wall at the point the particle exits the cell. The exit point can then be calculated and the exit point becomes the entrance point of the neighbouring cell. The particle is, thus, tracked through the cells until a discharge cell is reached (or a recharge cell if backward tracking is being used). Full details on these particle calculations can be found in Pollock (1994) [611]. For finite element models, the velocity is usually regarded as a constant across any given element, and so similar travel times could be calculated for particles to traverse elements. No such software has, however, currently been developed for the widely used finite-element code SUTRA.

Hydraulic path line simulations can be made either in the forwards or backwards direction. Thus, in MODPATH, the time of travel of a particle can be calculated from the water table forwards to its

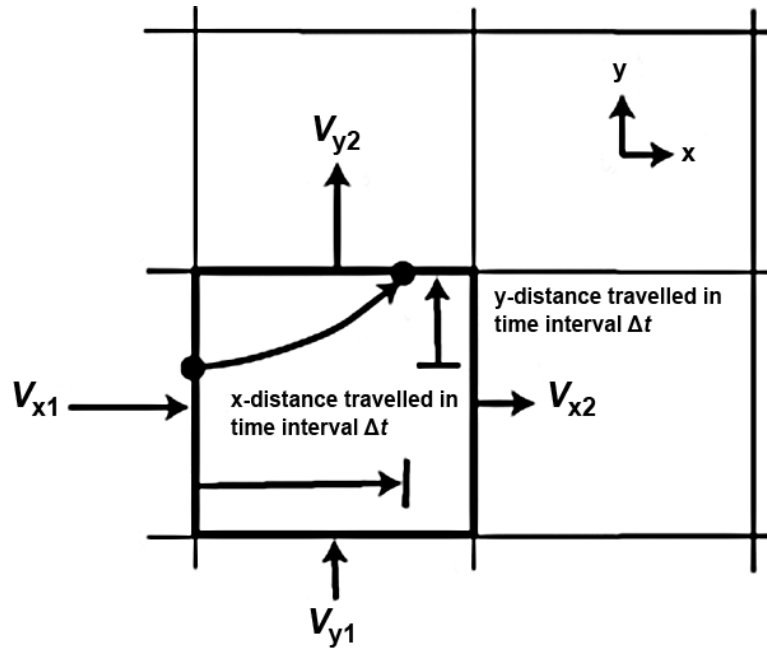


FIG. 10.3. Schematic showing the computation of exit point and travel time for the case of two dimensional flow in the  $x$ - $y$  plane (after Pollock (1994) [611]).

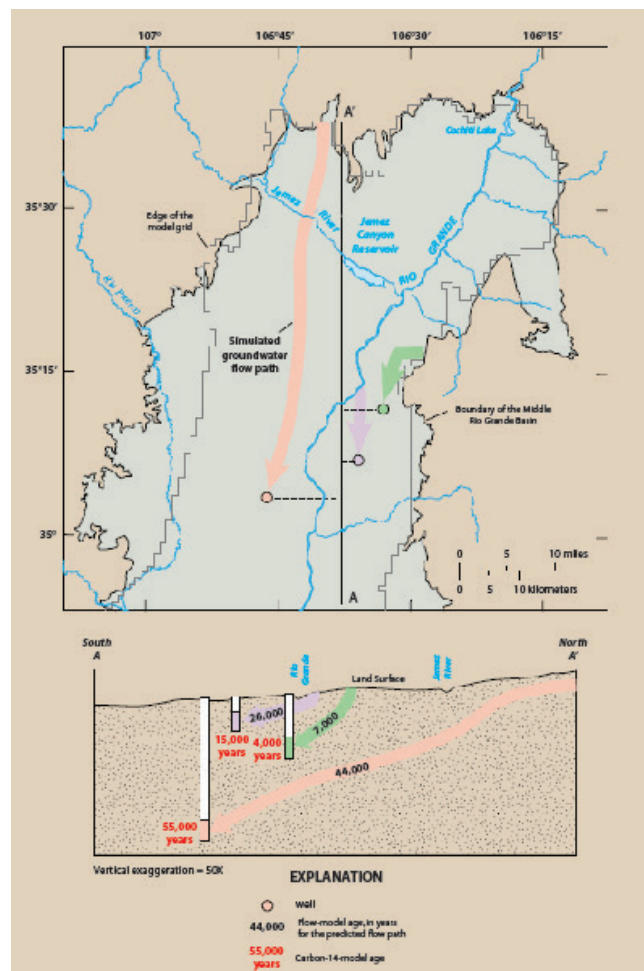


FIG. 10.4. Simulated flow paths and flow model ages in the Middle Rio Grande Basin in comparison with  $^{14}\text{C}$  model ages (after Bartolino and Cole (2002) [612]).

discharge location (e.g. a stream) or the time of travel can be calculated from a well screen backwards to its recharge location (e.g. the water table). The latter can be used to calculate a flow model age at any point within an aquifer system given the set of parameters currently being assigned to the model. For a transient flow model (e.g. with transient recharge), the procedure has the added requirement of storing the flow field at each time step. Flow model ages can be calculated for multiple sites at a time and, therefore, a set of tracer model ages can be compared with the flow model ages (Fig. 10.4) intermittently as parameters are adjusted during the calibration, and the errors can be added to the total sum of squared errors being calculated for the model calibration. For long screen wells, multiple particles can be simulated along the well screen, with the result being a range of different flow model ages assigned to and ‘mixing’ in the well bore. It should be noted, however, that for environmental tracers it is the concentration of the solute species that is actually mixing and not idealized groundwater ages. For tracers where the solute or isotopic concentrations are not linear functions of time, the average of the flow model ages will not give the equivalent result to the more appropriate average of simulated concentrations that are each back calculated from the flow model ages. A useful visualization technique is to start particles at the centre of every cell in the model and track backwards to the origin location. All of the travel times for these paths are then plotted at their starting cell locations. The result is the flow model age distribution throughout the entire system that can be visualized in two dimensions as maps of flow model age across an entire model layer or cross-sections (e.g. Fig. 13 of Sanford et al. (2004) [47]).

## 10.8. SIMULATION OF DISPERSION AND APPARENT GROUNDWATER AGE

Advective path lines and flow model ages are straightforward to calculate following groundwater flow simulations, but environmental tracers are subject to hydrodynamic dispersion as well as advection. Dispersion of a solute occurs because heterogeneity in the hydrogeological framework creates variations in velocities from the pore scale to the field scale. These heterogeneities are inherently present but too small to discretize all into the model domain. A potentially more accurate model calibration can be undertaken if the effect of the dispersion on the tracer is also known and simulated. Such a simulation could produce dispersion model ages, as opposed to the previously discussed flow model ages, which are strictly advection model ages. The advection–dispersion transport equation can be written with concentration as the dependent variable and groundwater velocity as a parameter in cartesian–tensor notation as:

$$\frac{\partial}{\partial x_i} \left( D_{ij} \frac{\partial C}{\partial x_j} \right) - \frac{\partial}{\partial x_i} (C V_i) = \frac{\partial C}{\partial t} + C' Q + R \quad (10.3)$$

where

$C$  is concentration;

$V_i$  is the seepage velocity;

$C'$  is the concentration of a fluid entering the domain at rate  $Q$ ;

$R$  is the chemical reaction rate of the solute or isotopic species;

$D_{ij}$  the hydrodynamic dispersion tensor, which is a function of the velocity components in each direction, the dispersivity and molecular diffusion (Konikow and Grove (1977) [613]).

The velocity field is predetermined from the flow simulation and can vary in space and time. The source term  $Q$  and reaction term  $R$  can also vary in space and time. The dispersivity is a parameter that describes the inherent make-up of the porous or fractured media that causes spreading, and is usually assumed to simplify into two components, a longitudinal dispersivity that is parallel to the direction of flow and a transverse dispersivity that is perpendicular to the direction of flow. In three dimensional flow systems, two different transverse dispersivities can be used that are perpendicular to each other.

Several codes have been developed that solve Eq. (10.3) (Koch and Prickett (1993) [614]; Konikow et al. (1996) [615]; Voss and Provost (2002) [616]; Zheng and Wang (1999) [617]). The numerical methods used are either Eulerian (fixed reference frame) or Lagrangian (moving reference frame), or a combination of the two. Eulerian techniques include finite differences or finite elements, whereas Lagrangian techniques include random walk or the method of characteristics. The nature of Eq. (10.3) is such that in systems with a high ratio of velocities to dispersivities (known as the Peclet number) Eulerian mathematical solutions (e.g. standard finite differences or finite elements) become unstable. Thus, when simulating transport with dispersion, special care must be taken to make the grid fine enough to avoid numerical oscillations or numerical dispersion. The random walk method tracks a large number of particles, most often from a point source, and randomly adds variability to the particle path in directions both longitudinal and transverse to the flow direction (Prickett et al. (1981) [618]). As this method requires large numbers of particles to get repeatable results, it is not often feasible to use in regional transport problems where tracer model ages are measured. The method of characteristics was developed as a particle tracking technique with the advantage of particle tracking, but with a Eulerian dispersion component, but it has its own set of inherent limitations (Konikow and Bredehoeft (1978) [619]). For all of these methods, the fine resolution requirement of the grid often precludes full three dimensional advection–dispersion simulations of an aquifer on a regional scale.

The final term of Eq. (10.3),  $R$ , represents the chemical reactions that the tracer of interest may be involved in that either remove it from or add it to the solution. Radioactive decay is the most common of these that would be included for environmental tracers when the objective is to simulate the concentration field of the tracer directly. Carbon-14 has a number of potential reactions and exchanges that can take place with the mineral phase in the aquifer material (e.g. Kalin (1999) [111]; see Chapter 4), and such reactions could also be included if the  $^{14}\text{C}$  concentration field were to be simulated directly. Geochemical codes are available that solve multiple species reactions with transport in one (PHREEQC; Parkhurst and Appelo (1999) [149]) or more (PHAST; Parkhurst et al. (2004) [200]) dimensions. Each of the tracers that might be used to date old groundwater that are described in this book have their own set of issues to be considered when using their tracer model ages in conjunction with a flow and/or transport model. A list of these tracers and the issues are listed in Table 10.1. A more general table of old age tracers are listed in Table 1.1.

Reviews of field studies by Gelhar (1986) [620] and Schulze-Makuch (2005) [621] have suggested that dispersivity is scale dependent and that the longitudinal dispersivity is roughly about 10% of the distance of travel; however, the most detailed field studies (LeBlanc et al. (1991) [622]) suggest that this may greatly overestimate dispersivity, which can often be closer to 1% of the distance of travel. Transverse dispersivity is typically 1–10% of the longitudinal dispersivity. Dispersivity almost certainly also varies spatially within most formations and is difficult to measure directly without special tracer tests, so although dispersion can be simulated, the uncertainty with respect to the accuracy of simulated concentration fields is usually high. One regional effect is that under steady state conditions

TABLE 10.1. TRACER METHODS AND ISSUES TO CONSIDER FOR JOINT USE WITH NUMERICAL FLOW MODELS

Tracer method	Issues to consider
$^{14}\text{C}$	Long term variable input, definition of initial $^{14}\text{C}$ , often reactive, dispersion, matrix diffusion
He	Generated in situ, uncertain production rate, quantifying basin flux
$^{36}\text{Cl}$	Long term variable input, mixing with other Cl sources, matrix diffusion
$^{81}\text{Kr}$	Input variations only in the very long term, sampling still difficult at the time of the publication of this book
U	Generated in situ, uncertain production rate

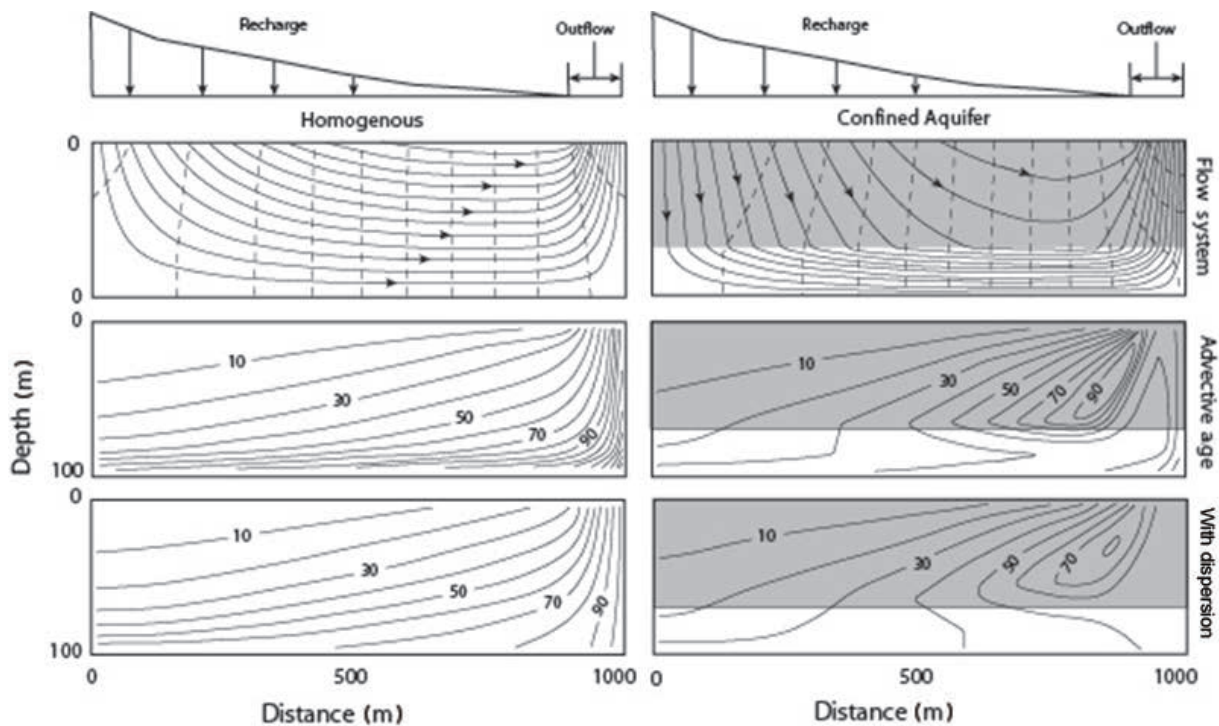


FIG. 10.5. The effect of dispersion on the patterns and magnitudes of flow model ages. Dashed lines are equipotentials. Arrowed lines are flow directions. Solid lines without arrows are contours of equal advection or dispersion model age (in years). Grey regions have lower hydraulic conductivity. (Modified from Goode (1996) [69]).

(not always applicable) the flow model age of groundwater is not a function of the interchange (transverse dispersion) of solutes between aquifers and interbeds, but simply a function of the ratio of the total porosity of the system to the porosity of the aquifer (Bethke and Johnson (2002) [623]; Sanford (1997) [207]). For tracers with long half-lives (e.g.  $^{14}\text{C}$  and  $^{36}\text{Cl}$ ), the relatively constant (or slowly changing) input function through time creates a condition where the longitudinal dispersion of the solute is relatively small (5–10%) relative to its decay rate (Johnson and DePaolo (1996) [624]), indicating that advective path line and flow model age calculations may not be a bad assumption for many old groundwater simulations.

In spite of the uncertainty associated with the simulation of dispersion in groundwater, hypothetical simulations can illustrate well the expected behaviour on environmental tracers. When possible, it is most straightforward to simulate the tracer of interest, as each tracer may have a different input function or reactive behaviour in the subsurface. These individual tracer characteristics can be included directly in the simulation parameters. A more generalized approach is also possible where a dispersion model age can be simulated directly (Goode (1996) [69]) by setting  $R$  in Eq. (10.3) to a value of one, and  $Q$  to zero. This approach is often known in the modelling community as ‘direct age simulation’. The reaction term  $R$  is used to represent the passing of time and the concentration field becomes the dispersion age field. Much discussion has surrounded the simulation of dispersion model ages in this manner (Bethke and Johnson (2008) [84]; Perrochet and Etcheverry (2000) [625]; Varni and Carrera (1998) [83]). The technique for simulating the dispersion model age can also be used to calculate the frequency distribution of groundwater ages expected to be encountered at a sampling site such as a long screened well (Varni and Carrera (1998) [83]). A dispersion model age simulation is useful for visualizing the potential impact of dispersion on advection model age simulations (Fig. 10.5). This approach is also useful for finite element models that do not have advection model age calculation software available. From Fig. 10.5, it can be seen that dispersion spreads out the transport model age

and typically reduces the size and magnitude of pockets of old water that may result from stagnant regions of circulation.

## 10.9. MODEL CALIBRATION USING TRACER BASED AGES

A number of regional modelling studies have used tracer model ages effectively as constraints (e.g. Castro et al. (1998) [96]; Park et al. (2002) [90]; Sanford and Buapeng (1996) [626] and Sanford et al. (2004) [47]). Some of these studies have been described in detail in other chapters of this manual. Tracer model ages can be valuable data with which to help calibrate a model (Sanford (2011) [627]). They provide information directly related to the fluxes in the system, which are often more difficult to obtain than heads. Baseflows to streams, a common measurement of flux in the system, cannot always be easily measured, especially in arid environments, and so tracer model ages can provide another much needed source of flux data. Tracer model age data, however, require one additional type of information, porosity, to be used as model constraints. Flow model ages are based on travel paths that are based on seepage velocities that include porosity in their calculations. Simulated baseflows do not require porosity measurements. This porosity requirement does not necessarily hamper the use of tracer model ages to calibrate a model. In unconsolidated sediments, porosity can often be easily estimated or measured and so can be added to the model as prior information. When both baseflow and tracer model age data are available in hard rock terrains, the tracer model ages can help constrain the porosity, which might otherwise be poorly known.

A number of different hydraulic characteristics of a groundwater flow system can affect the distribution of the flow model age within that system (Fig. 10.6), including the distribution of recharge, the vertical anisotropy and the regional scale heterogeneity. Homogeneous systems with

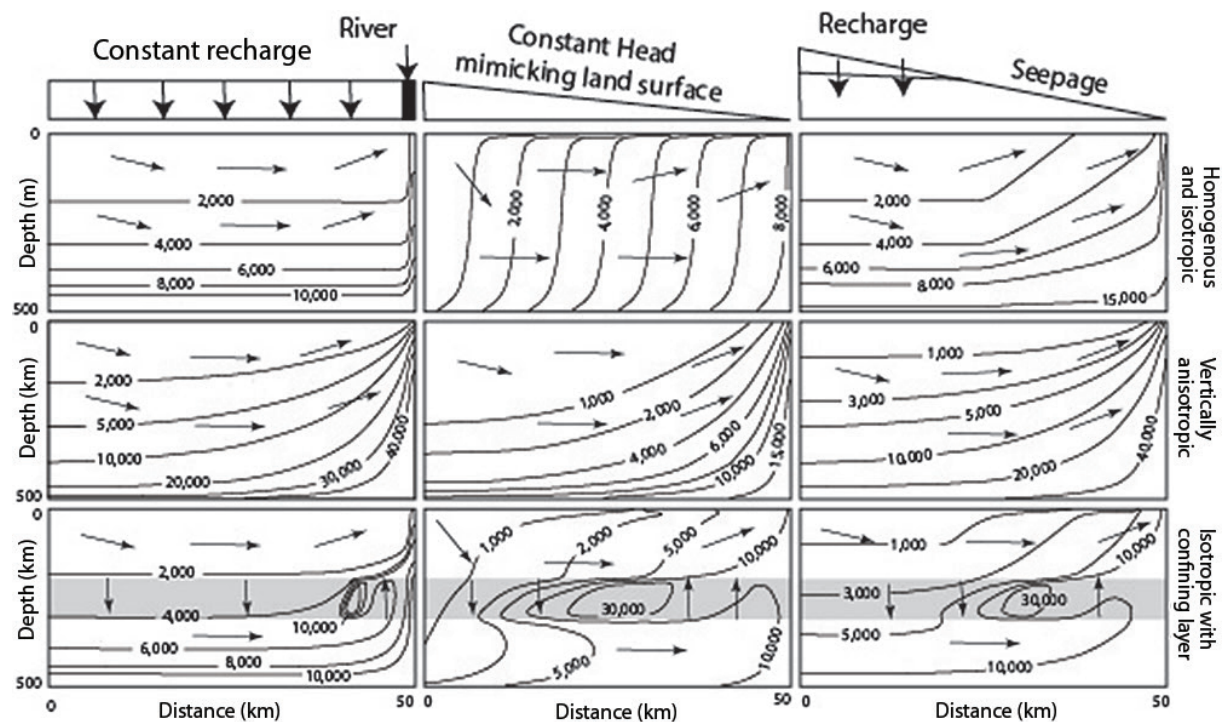


FIG. 10.6. Spatial patterns of groundwater age as a result of various distributions of recharge and hydraulic conductivity ( $K$ ). Contour values are flow model age (in years). Arrows show general direction of flow. The vertical anisotropy ratio in the middle set of simulations is 10 000 horizontal to 1 vertical. The confining layer contrast in  $K$  in the lower set of simulations is 1000 to 1. (After Sanford (2011) [627].)

evenly distributed recharge can be expected to have flow model ages that increase with depth and have lines of equal flow model age that are nearly horizontal. If the recharge is distributed predominantly towards the upper reaches of the flow system, however, as is often the case in arid environments or low lying areas where the water table closely mimics the topography, the lines of equal flow model age can become closer to vertical. Increasing vertical anisotropy in a system nearly always increases the vertical gradient in the flow model age.

Regional heterogeneities such as confining layers can create pockets of older water where substantial vertical hydraulic gradients are not present. In general, the distribution, connectivity and vertical hydraulic conductivity of the confining layers are one of the largest controlling factors on both the flow model ages and the tracer model ages within a groundwater flow system. The conceptual model adopted for the presence of confining layers is important. For example, a system conceptualized as having a large regional vertical anisotropy, but not a discrete heterogeneity, cannot under any conditions yield a depth profile of flow model ages that are overturned (younger beneath older), whereas overturned tracer model ages in regional systems are not uncommon in discharge areas. The fact that hydraulic properties can greatly impact the flow model age distribution is equally an indicator that spatially distributed tracer model age data can provide good information on the nature of the flow system. This equally demonstrates that tracer model age data can be quite valuable in constraining conceptual and numerical models of flow systems. This is additionally supported by the fact that regional scale confining unit properties are often the most difficult to measure directly.

A number of field studies using tracer model ages to calibrate groundwater flow models have demonstrated that matching of individual flow model ages to tracer model ages is more difficult than matching simulated water levels to observed water levels. Water levels represent a potential field of energy within a groundwater system, and as such values vary relatively smoothly within the system as a function of the spatial distribution of the hydraulic property distribution and the boundary conditions. In addition, boundary conditions using specified water levels already partially constrain the simulated water level values. On the other hand, flow model ages are calculated based on the velocity field, which is based on the gradient or first derivative of the water level (potential) field. As the flow field is usually complicated by heterogeneity in the hydraulic properties and recharge distribution, the velocity field is usually relatively complex both in magnitude and direction. It, therefore, becomes very common for the variations that exist within the velocity fields (creating, for example, local flow cells within regional flow cells) to be misrepresented at the very local scale at which the tracer samples were collected and the flow model ages were simulated. A well screen, for example, may be located near the boundary between a local and regional flow subsystem, and the slightest misrepresentation of those systems in the model might cause the equivalent flow model age to be calculated at a very different value because it is located within the wrong flow subsystem. In addition, the first derivatives (velocities) are not continuous across the boundaries of flow subsystems, and this can further complicate automated calibration tools that rely on the parameter sensitivities (first derivatives). The resulting end effect very often appears like a poor match between tracer model ages and flow model ages. Two recent examples of this using  $^{14}\text{C}$  model ages demonstrate this issue (Fig. 10.7). Although this demonstrates the difficulty in using tracer model ages to calibrate flow models at fine scales, it still does not negate the usefulness of tracer model ages in the calibration of flow models at coarser scales.

In spite of the usefulness of tracer model ages in model calibration, a number of caveats should be noted. Steady state model assumptions are often used for regional models with relatively old flow model ages, but these assumptions are not always valid. Climatic changes leading to changing recharge rates over time may need to be considered. Substantial groundwater withdrawals from wells may also need to be included in the model as these can affect the distribution of flow model and tracer model age in the system (Zinn and Konikow (2007) [628]). Use of advection model ages alone will create some degree of error from the lack of considering dispersion. Simulating dispersion with advection can reduce this error, but the uncertainty in the appropriate field dispersivities to assign to the model may offset this benefit. Simulation of dispersion in three dimensions is also computationally very

challenging on a regional scale without introducing numerical dispersion (Sanford and Pope (2010) [629]). Thus, although, in theory, it is possible to simulate dispersion model ages, this is usually not tractable for three dimensional groundwater models. In spite of the assumptions behind advection model age simulation, it is still an efficient and potentially very useful tool for model calibration. This is especially true considering that there is often a lack of other basic flux information in addition to that provided by tracer model ages, and groundwater models lacking in adequate flux information can remain relatively unconstrained.

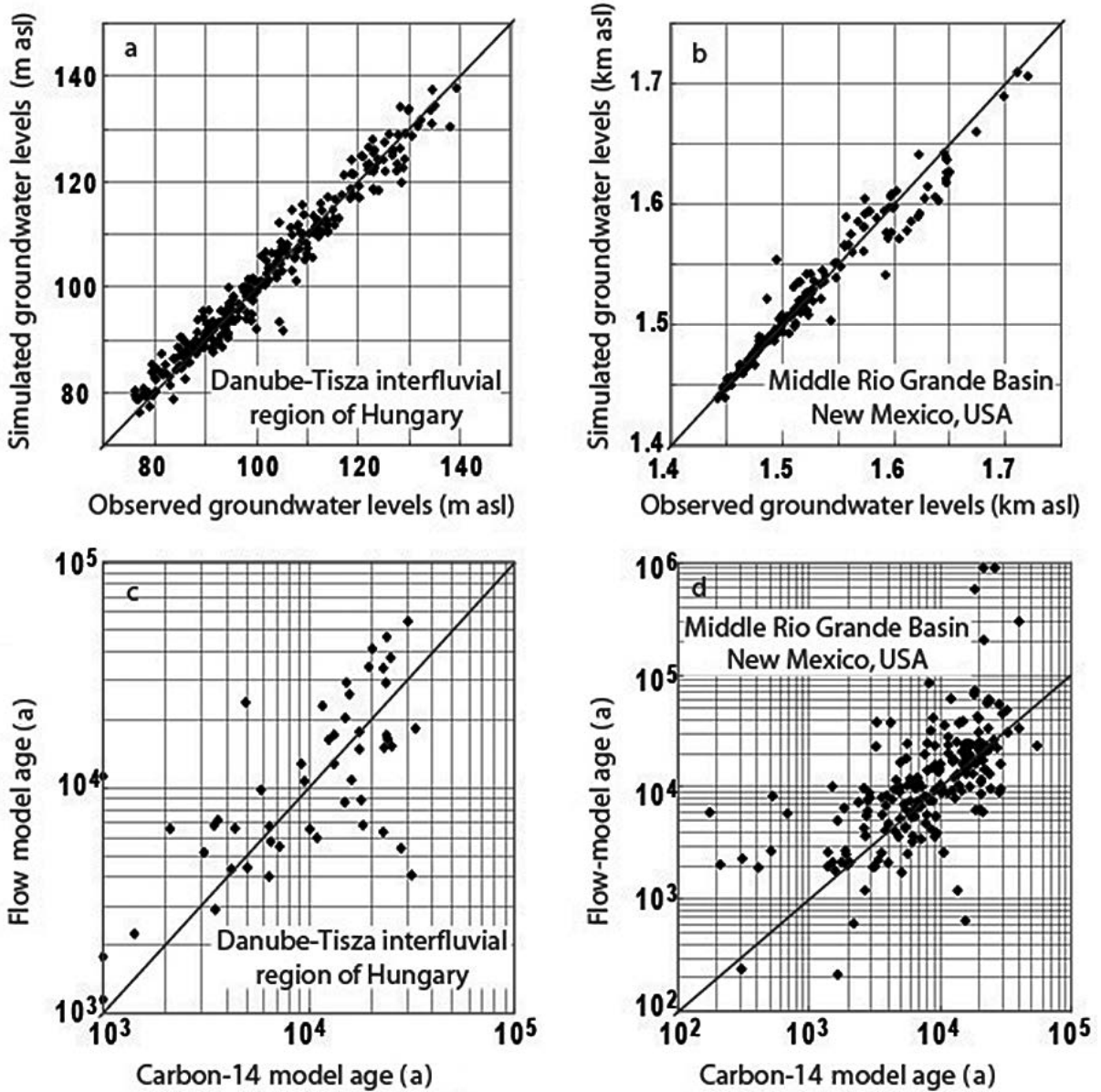


FIG. 10.7. Plots of observed versus simulated water levels in (a) central Hungary and (b) New Mexico, USA; and  $^{14}\text{C}$  model and flow model ages in (c) central Hungary and (d) New Mexico, USA (after Sanford et al. (2004) [47] and Sanford et al. (2001) [630]). It should be noted that the age plots are in log–log scale, yet still have more visual scatter around the perfect match (solid) lines than the water level plots.

## Chapter 11

### MILK RIVER AQUIFER, ALBERTA, CANADA — A CASE STUDY

K. FRÖHLICH  
Vienna, Austria

#### 11.1. INTRODUCTION

The Milk River aquifer is a complex system in terms of origin and evolution of the chemical and isotopic composition of the groundwater. Fortunately, a wealth of physical and chemical data of the groundwater and the bonding shales was collected by numerous authors over a period of about 15 a that allowed applying various complementary approaches in dating the groundwater. Although these Milk River aquifer studies were carried out more than two decades ago, they can still be considered an outstanding example for dating of old groundwater.

The Milk River aquifer fits the definition of an idealized confined aquifer system, and dips gently from its outcrop area (~5 m/km). A short distance from the recharge area, the 'idealized groundwater age'<sup>1</sup> extends beyond the <sup>14</sup>C dating limit and further downstream reaches values up to more than one million years. Owing to this feature, the Milk River aquifer was selected for an IAEA sponsored international project that was aimed at evaluating all isotope techniques available for dating of old groundwater; it finally resulted in the most comprehensive application of isotope and geochemical techniques to an individual aquifer system at that time. Analyses were carried out for halides and other major and minor ions, stable isotopes (<sup>2</sup>H, <sup>3</sup>He, <sup>4</sup>He, <sup>13</sup>C, <sup>18</sup>O) and radioactive isotopes (<sup>222</sup>Rn, <sup>85</sup>Kr, <sup>37</sup>Ar, <sup>39</sup>Ar, <sup>14</sup>C, <sup>81</sup>Kr, <sup>36</sup>Cl, <sup>129</sup>I, <sup>234</sup>U, <sup>238</sup>U). The results of the various isotopic and geochemical studies were published in a special edition of *Applied Geochemistry* (Ivanovich et al. (1991) [631]). The following is a summary and comparative discussion of the results, with particular emphasis on the determination of the groundwater age in the Milk River aquifer system.

#### 11.2. GEOLOGICAL AND HYDROLOGICAL BACKGROUND

The Milk River aquifer underlies 15 000 km<sup>2</sup> of southern Alberta. Most of the area is covered by Pleistocene glacial drift (Hendry et al. (1991) [632]). The aquifer crops out in southern Alberta, Canada, predominantly on the flanks of Sweetgrass Hills, northern Montana, USA, at the southern end of the study area (Fig. 11.1). The Milk River Formation is composed of sandstone (30–75 m in thickness) sandwiched between shales. It is confined above by marine shale of the Pakowki Formation (typically 120 m thick) and below by the Colorado Group that ranges in thickness from 500 to 650 m (Fig. 11.2). The transmissivity of the aquifer decreases from south to north, and from west and east.

This decrease is caused by a general thinning of the sandstone in these directions and a decrease in hydraulic conductivity towards the north due to an increase in the shale content. The groundwater flow is generally towards the north, west and east, following the dip of the aquifer. Two main flow paths were identified by valleys of low Cl<sup>-</sup> concentrations (Fig. 11.3). Since the sandstone pinches out in all directions, the aquifer must discharge by upward and downward leakage. All water that leaves the aquifer must, therefore, pass through the shale/sand interface. Hendry and Schwartz (1988) [633] suggested that about 500 ka ago the outcrop area was uncovered by erosion and meteoric water replaced connate water at that time. In fact, groundwater model ages of this order were found by <sup>36</sup>Cl dating (Phillips et al. (1986) [319]).

<sup>1</sup> The 'idealized groundwater age' is defined in Chapter 3 of this book. For the sake of simplicity, in the following the expression 'groundwater age' is used.

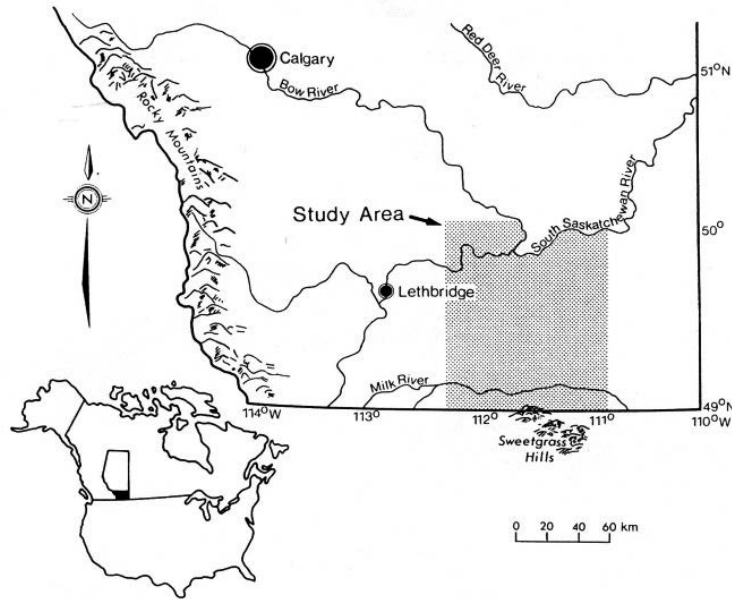


FIG. 11.1. Study area (from Hendry and Schwartz (1988) [633]).

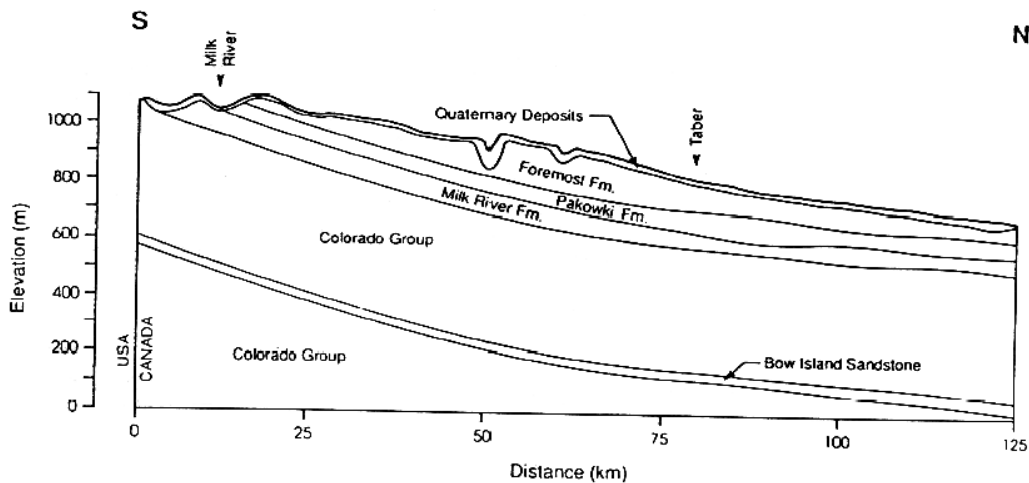


FIG. 11.2. Geology of the Milk River aquifer along the S-N cross-section (from Hendry et al. (1991) [632]).

### 11.3. THE ROLE OF GEOCHEMISTRY IN CONSTRAINING WATER AND SOLUTE TRANSPORT MODELS — THE MILK RIVER AQUIFER EXPERIENCE

The geochemistry of the Milk River aquifer was studied by numerous authors (Hendry and Schwartz (1988) [633]; Hitchcock and Friedman (1969) [634]; Meyboom (1960) [635]; Phillips et al. (1986) [319]; Schwartz and Muehlenbachs (1979) [636]; Schwartz et al. (1981) [637]; Swanick (1982) [638]). It is characterized by significant changes in major ion concentrations along the groundwater flow. Ion exchange of  $\text{Ca}^{2+}$  (and  $\text{Mg}^{2+}$ ) for  $\text{Na}^+$  creates calcite undersaturation that forces calcite dissolution down the flow path and raises the  $\text{HCO}_3^-$  concentration. Concentrations of  $\text{SO}_4^{2-}$  are high in groundwater of the recharge area but due to bacterial reduction virtually disappear in the central part of the aquifer. The concentrations of  $\text{Cl}^-$  and  $\text{I}^-$  strongly increase in the flow direction; near the recharge area, they are less than 0.5 and 0.001 mmol/L, respectively, and increase to more than 100 and 0.15 mmol/L,

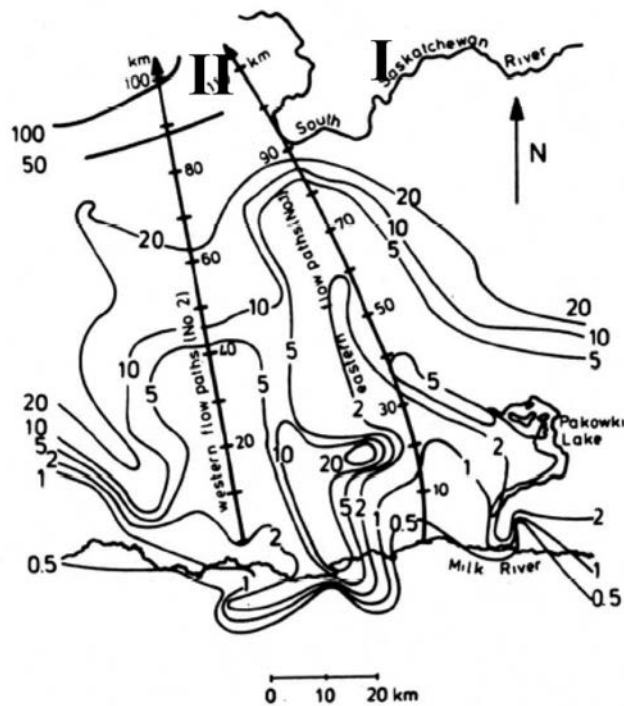


FIG. 11.3. Contour plot of the Cl concentrations with the two main flow paths (I = eastern flow path, II = western flow path) along the valleys of the Cl concentrations. The numbers give the concentration in mmol/L (from Nolte et al. (1991) [291]).

respectively, at the northern edge of the aquifer. Similarly, the  $^{18}\text{O}$  ( $\delta^2\text{H}$ ) values increase from less than  $-21\%$  ( $-167\%$ ) near the recharge area to  $-8\%$  ( $-70\%$ ) in the north. While the  $\delta^{18}\text{O}$  and  $\delta^2\text{H}$  values of the recharge waters plot on the global meteoric water line, further downstream, the data deviate from the meteoric water line and fit a line with a slope of 6.3 instead of 8 (Hendry and Schwartz (1988) [633]). Several alternative mechanisms were proposed to explain the observed distribution of non-reactive species in the Milk River aquifer (Fig. 11.4): (i) introduction of connate formation water through the Colorado shale and subsequent mixing with infiltrating meteoric water (Schwartz and Muehlenbachs (1979) [636]; Schwartz et al. (1981) [637]); (ii) meteoric recharge mixing with more saline water in the aquifer (Domenico and Robbins (1985) [639]); (iii) chemical and isotopic enrichment due to ion filtration (Phillips et al. (1986) [319]); and (iv) aquitard diffusion (Hendry and Schwartz (1988) [633]).

Hendry and Schwartz (1988) [633] reviewed the previously proposed mechanisms (i)–(iii), especially ion filtration, and concluded that these mechanisms are not supported by hydraulic conductivity and hydraulic head data,  $\text{Cl}^-$  concentrations of drill cuttings and isotope values from Colorado shale groundwater. They proposed an alternative mechanism based on diffusion between saline, isotopically enriched water of the Colorado shale and fresher, isotopically depleted water in the aquifer. Using an analytical mass transport model, the authors found that the pattern in  $\text{Cl}^-$ ,  $\text{I}^-$ ,  $\delta^{18}\text{O}$  and  $\delta^2\text{H}$  in the aquifer can be explained by aquitard diffusion. The best model fit to both  $\text{Cl}^-$  and  $\delta^{18}\text{O}$  data yielded an effective aquitard diffusion coefficient (the most critical parameter in the model) of  $6 \times 10^{-12} \text{ m}^2/\text{s}$  for these species. On the basis of this aquitard diffusion mechanism, Hendry and Schwartz (1988) [633] evaluated  $^{36}\text{Cl}$  data published by Phillips et al. (1986) [319]. The derived  $^{36}\text{Cl}$  model ages of the groundwater were found to be consistent with earlier age estimates based on hydraulic modelling (Swanick (1982) [638]). Consequently, Hendry and Schwartz (1988) [633] concluded that aquitard

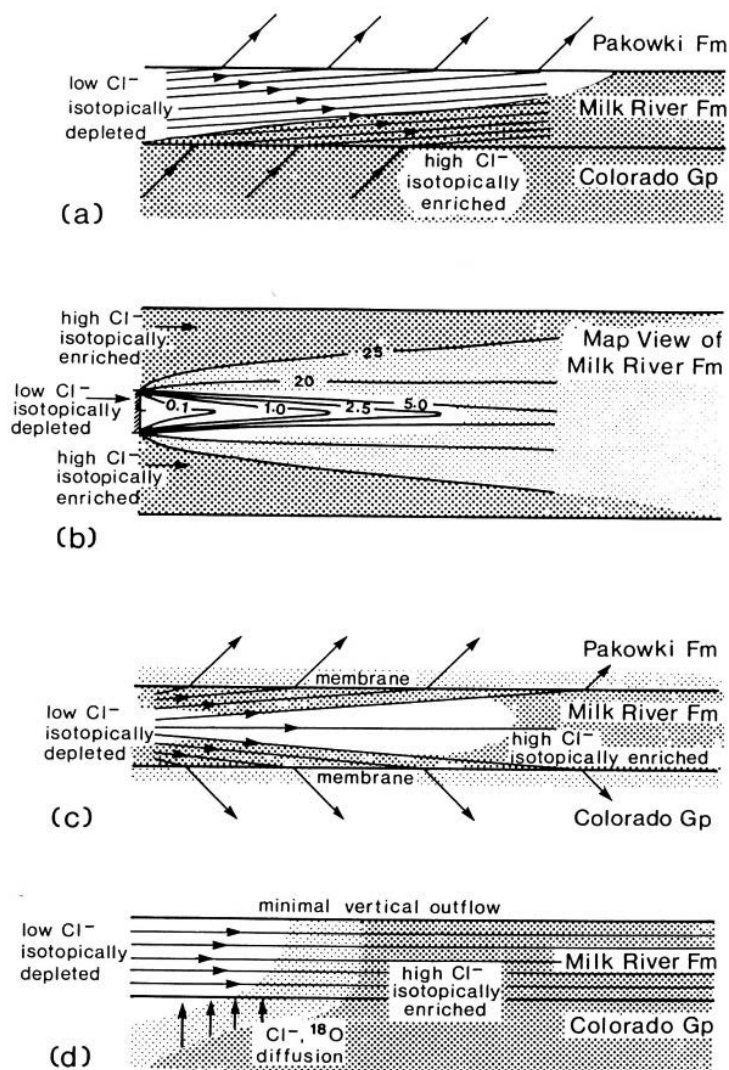


FIG. 11.4. Conceptual models to explain the origin of chemical patterns in the Milk River aquifer: (a) megascopic dispersion; (b) partial area of recharge; (c) membrane filtration; and (d) aquitard diffusion (from Hendry and Schwartz (1988) [633]).

diffusion must be considered when using  $^{36}\text{Cl}$  to date groundwater in aquifer–aquitard systems such as the Milk River aquifer.

In contrast, Phillips et al. (1990) [640] concluded from an in-depth review of Hendry and Schwartz’s arguments, that there was no evidence for aquitard diffusion. On the basis of a Peclet number analysis with parameter values selected from Hendry and Schwartz’s paper, they found that “transport in the aquitard is strongly advection dominated”. However, it should be noted that the Peclet numbers referred to by Phillips et al. (1990) [640] are proportional to the square of the seepage velocity and that this parameter was estimated from the measured hydraulic conductivity. Given that the hydraulic conductivity values of the aquitard ranged from less than  $10^{-11}$  up to about  $10^{-8}$  m/s (Hendry and Schwartz (1988) [633]), it can be concluded that the uncertainty of the Peclet numbers estimated by Phillips et al. (1990) [640] is very high. Thus, the observed ambiguity in the conceptual models on the solute transport appears to be associated with high uncertainty of the field data used in both approaches. Phillips et al. (1990) [640] came to the conclusion that “the reality is that we very seldom possess even a fraction of the field data necessary to constrain such models”. It should, however, be

TABLE 11.1. IODINE-129 IN GROUNDWATER OF THE MILK RIVER AQUIFER (from Fabryka-Martin et al. (1991) [385])

Well	$^{129}\text{I}/\text{I} \times 10^{-15}$	$^{129}\text{I}$ (atoms/mL)
3	—	—
4	$90 \pm 30$	$5200 \pm 1700$
5	$1130 \pm 70$	$850 \pm 53$
9	$135 \pm 40$	$960 \pm 280$
10	$390 \pm 65$	$5700 \pm 950$
11	$165 \pm 50$	$250 \pm 76$
14	$790 \pm 10$	$1240 \pm 20$
16	$190 \pm 80$	$1900 \pm 785$
18	$145 \pm 50$	$3200 \pm 1100$

noted, that additional data became available which provided new insights into the processes operating in the Milk River aquifer.

Fabryka-Martin et al. (1991) [385] measured the  $^{129}\text{I}/\text{I}$  ratio in groundwater samples of the aquifer which turned out to be useful for answering the question of whether ion filtration or diffusion controls the observed increase of halide concentrations. The highest value of the  $^{129}\text{I}/\text{I}$  ratio ( $1.1 \times 10^{-12}$ ) was found in the youngest groundwater of the recharge area (Table 11.1, well 5). This value corresponds to a meteoric input that is undiluted by iodine released from the aquifer matrix or from the confining units. Further down flow, the  $^{129}\text{I}/\text{I}$  ratio decreased remarkably; in the oldest groundwater (well 18), it was about one order of magnitude lower. These lower values cannot be explained with radioactive decay of the meteoric component of  $^{129}\text{I}$  since the half-life of  $^{129}\text{I}$  (16 Ma) is so long that even for groundwater model ages of 2 Ma the radioactive decay of the meteoric component of  $^{129}\text{I}$  would be insignificant. Thus, Fabryka-Martin et al. (1991) [385] concluded that a subsurface source of iodine must be present and that the high iodine concentrations in the water are not a simple result of ion filtration. On the basis of their study of halides, the authors advanced an additional hypothesis. They found that the Cl/I and Cl/Br ratios of groundwater close to the recharge zone are well below those of sea water. This suggests diagenesis of organic matter in the sediments as the source of the halides.

However, moving down flow, the halide ratios reach nearly constant values, suggesting the dominance of a common subsurface source for these ions. Fabryka-Martin et al. (1991) [385] concluded that the observed halide ratios rule out unaltered sea water or leakage and/or diffusion from the underlying Bow Island sandstone as a major source of the halides in the groundwater. They suggested that the primary source of the halides is altered connate sea water diffusing from low permeability units within the Milk River Formation. This is also at variance with the hypothesis offered by Hendry and Schwartz (1988) [633] in which the halides and other dissolved constituents diffuse primarily from the underlying Colorado shales. Fabryka-Martin et al. (1991) [385] emphasized that this (fifth) conceptual model does not require the assumption of mixing with an external water body or complex mechanisms such as ion filtration. Furthermore, they argued that “other saline sources proposed by other authors cannot be ruled out altogether and are probably contributing to the groundwater geochemistry to some extent, but the model, in which the solute source resides mainly within the Milk River Formation, is the simplest one and is able to account for most of the observed data”. Phillips (2000) [306] largely agreed with this explanation admitting that a significant portion of the increase of  $\text{Cl}^-$  concentration observed in the Milk River aquifer is due to diffusion from low permeability units within the aquifer and “the remainder is most likely due either to ion filtration or variable evaporation during recharge”.

Finally, it has to be noted that in the case of the Milk River aquifer a possible glacial ‘squeeze’ effect should be taken into account. It is known that the aquifer experienced massive glacial loading moving from north to south and, thus, potentially squeezing water out of the shale into the aquifer at the initiation of glaciation and reversing the flow at glacial retreat (F. Phillips, personal communication<sup>2</sup>). Recent research on glacial chronology of the area in south-western Alberta, Canada, suggests that there was perhaps only one glacial advance over the study area, the Wisconsin (Jackson and Little (2004) [641]).

Overall, the situation that a number of alternative mechanisms were suggested for the explanation of observed geochemical data points to an ambiguity that seems to be inherent in complex systems such as the Milk River aquifer. In such systems, shale aquitards and interbeds can play a critical role as sources of the chemistry of the groundwater in the aquifer. Tackling this ambiguity is a formidable challenge in connection with dating of old groundwater.

## 11.4. ISOTOPIC STUDIES OF THE MILK RIVER AQUIFER

### 11.4.1. Radiocarbon and stable isotopes

Measurements of <sup>2</sup>H, <sup>3</sup>H and <sup>18</sup>O in groundwater, <sup>2</sup>H and <sup>13</sup>C in methane, <sup>18</sup>O and <sup>34</sup>S in SO<sub>4</sub><sup>-</sup>, <sup>13</sup>C and <sup>14</sup>C in DIC and DOC have been discussed by Drimmie et al. (1991) [168]. Here, focus is put on interpretation of the <sup>18</sup>O and <sup>2</sup>H data and the <sup>14</sup>C results. Plotting  $\delta^{18}\text{O}$  against  $\delta^2\text{H}$ , the authors were able to identify three distinct clusters (Fig. 11.5): cluster A with  $\delta^{18}\text{O}$  values of approximately  $-19\text{‰}$ , cluster B with  $\delta^{18}\text{O}$  of  $-16\text{‰}$ , and cluster C with  $\delta^{18}\text{O}$  of  $-8\text{‰}$ . Cluster A represents groundwater near the recharge area in the southern part of the aquifer (some samples contained measurable levels of bomb tritium). The isotopic signatures are not followed by even more negative  $\delta^{18}\text{O}$  and  $\delta^2\text{H}$  values down flow as might be expected if Pleistocene recharge were present. This absence of a glacial signature suggests that this groundwater was recharged before 15 ka, and that the Pleistocene period of that region is characterized by insignificant recharge over long periods. The uniform  $\delta^{18}\text{O}$  and  $\delta^2\text{H}$  values found in groundwater to about 20 km distance from the recharge zone indicate a minimum flow rate of about 1 to 1.5 m/a in this part of the aquifer. The data in cluster B fall close to the modern meteoric water line for the region. However, this groundwater contains no measurable <sup>14</sup>C and could, thus, have been recharged before the last glaciation.

Assuming constant flow rates beyond the Milk River on the order of 0.1 m/a, Drimmie et al. (1991) [168] suggested groundwater model ages  $>50$  ka BP and possibly as much as 600 ka BP along path I. Cluster C data represent groundwater in the most distant section of the Milk River aquifer. They follow a line that deviates from the meteoric water line. Hendry and Schwartz (1988) [633] suggest that this line represents diffusive mixing between isotopically enriched water in the confining shales and meteoric water recharged during warm climate phases. Alternatively, Phillips et al. (1990) [640] mentioned that the slope of this line is consistent with ion filtration (see Chapter 3).

Radiocarbon was measurable only in groundwater sampled from wells located within 20 km of the recharge zone. Although the DIC <sup>14</sup>C pmc values are much lower than those for DOC in both wells, the age differences between the two wells are quite similar, averaging about 14 ka (Fig. 11.6). The lower DIC values led to the conclusion that the DIC <sup>14</sup>C content when the water entered the aquifer was as low as 30 pmc. From these data, a flow rate of  $\sim 1$  m/a has been estimated for the distance of 12 km between the two wells (Fig. 11.6). This flow rate agrees surprisingly well with the stable isotope data but is an order of magnitude higher than the flow rates estimated for the northern part of the aquifer by hydraulic modelling (Hendry and Schwartz (1988) [633]; Swanick (1982) [638]), <sup>36</sup>Cl data (Nolte et al. (1991) [291]; Phillips et al. (1986) [319]) and uranium isotope measurements (Ivanovich et al. (1991) [422]). Thus, the <sup>14</sup>C derived flow rates for the southern part cannot be adopted for the entire flow

<sup>2</sup> PHILLIPS, F., Department of Earth and Environmental Science, New Mexico Tech, personal communication.

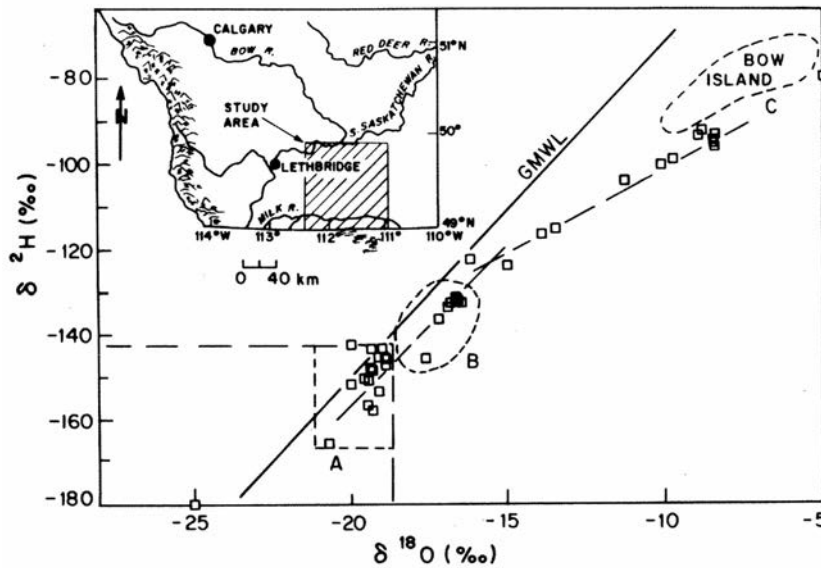


FIG. 11.5. Oxygen-18 versus deuterium plot including the global meteoric water line (GMWL) (from Drimmie et al. (1991) [168]).

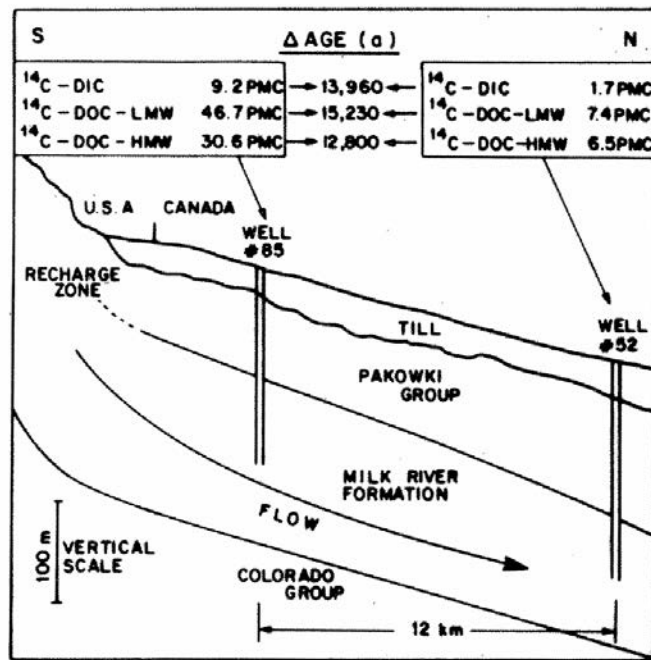


FIG. 11.6. Cross-section from the recharge zone in the Sweetgrass Hills, USA, to well No. 52 (approximately the Milk River). The boxes above give the <sup>14</sup>C results for the three main pools of C and their difference in years (from Drimmie et al. (1991) [168]).

system in which <sup>14</sup>C is, for the most part, absent. It is, therefore, concluded that the fast groundwater movement in the southern part of the aquifer (about 1 m/a) occurs only up to the Milk River. This river, thus, represents a discharge rather than a recharge strip. Consequently, the flow rate north of the river slows down to values of about 0.1 m/a in the northern sections of the aquifer.

#### 11.4.2. Dissolved gases

Andrews et al. (1991) [397] discussed the results obtained from analyses of CH<sub>4</sub> and its isotopic composition, N<sub>2</sub>, noble gases (He, Ne, Ar, Kr and Xe), and isotopic composition of Ar and <sup>222</sup>Rn.

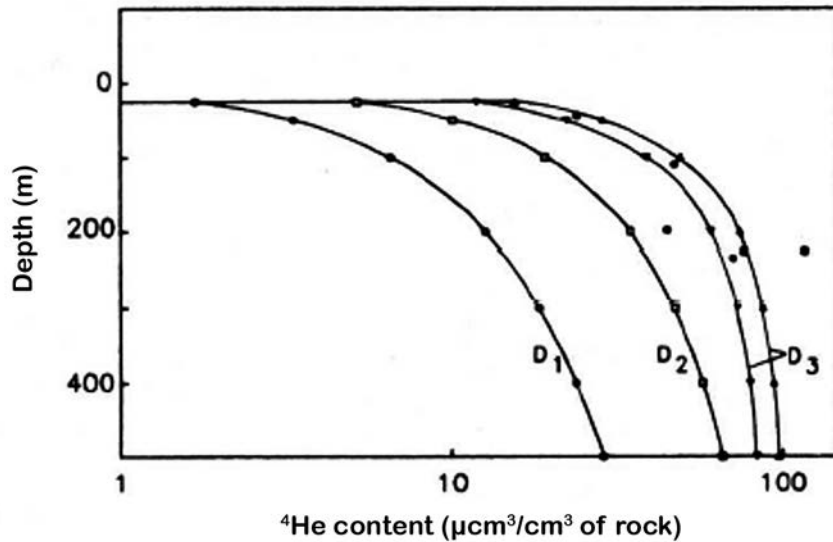


FIG. 11.7. Theoretical stored He contents as a function of depth for the radioelement contents of Milk River sandstone and for the underlying Colorado shale. Milk River sandstone profiles are shown for the diffusion coefficient of water ( $D_1 = 3.2 \times 10^{-2} \text{ m}^2/\text{a}$ , open circles), rock with 10% interstitial water ( $D_2 = 3.2 \times 10^{-3} \text{ m}^2/\text{a}$ ) and to match the observed He/depth profile for groundwater ( $D_3 = 3.2 \times 10^{-4} \text{ m}^2/\text{a}$ , triangles). The calculated profile for the Colorado shale is shown for the diffusion coefficient  $D_4$  (inverted triangles). Helium data for the Milk River groundwater are shown as filled circles (from Andrews et al. (1991) [397]).

The recharge temperatures derived from the noble gases indicated that the youngest groundwater was recharged under cooler climatic conditions than the ones prevailing during earlier recharge episodes. The inferred recharge temperature difference of about 4 to 5°C has been found to be consistent with estimates based on the stable isotope data.

The concentration of  $^4\text{He}$  varies with depth of the aquifer. This result is consistent with radiogenic  $^4\text{He}$  accumulation in the aquifer and adjacent shales. From the  $^4\text{He}$  depth profile of the Milk River sandstone and the Colorado shale, the diffusion constant for  $^4\text{He}$  loss from the formation was estimated to be  $\sim 3.2 \times 10^{-4} \text{ m}^2/\text{a}$  (Fig. 11.7). With this value and the  $^4\text{He}$  generation rate derived from U and Th content and porosity of the Milk River sandstone and Colorado shale, a  $^4\text{He}$  flux from the surface of the Colorado shale of about  $1.2\text{--}1.8 \times 10^8 \text{ atoms} \cdot \text{cm}^{-2} \cdot \text{s}^{-1}$  was obtained. This value corresponds to less than 2% of other continental  $^4\text{He}$  flux estimates and is consistent with the assumption that  $^4\text{He}$  release from continental crust is a discontinuous process controlled by random tectonic events or by aqueous transport (Torgersen (1989) [546]). The  $^4\text{He}$  content tends to increase with the Cl content of the groundwater. Since increasing Cl content is regarded as an index of groundwater ageing, the increase of the  $^4\text{He}$  content appears to be associated with an increase of the groundwater age. However, no reliable age values could be inferred from the available  $^4\text{He}$  data because some of these data are distorted by degassing during groundwater sampling.

The mean  $^{222}\text{Rn}$  activity concentration of the Milk River groundwater was found to be  $1.7 \times 10^4 \text{ Bq/m}^3$  (Andrews et al. (1991) [397]). The  $^{222}\text{Rn}$  content of the groundwater is controlled by the uranium content of the aquifer and by the fractional release,  $E$ , of  $^{222}\text{Rn}$  from the rock matrix into the interstitial fluid:  $E = \varphi N_w / [(1 - \varphi)N_m] = \varphi N_w N_b$ , where  $N_w$ ,  $N_m$  and  $N_b$  is the concentration of  $^{222}\text{Rn}$  atoms in the groundwater, the equilibrium concentration in the rock matrix and in the bulk rock, respectively;  $\varphi$  is the rock porosity. With this equation, Andrews et al. (1991) [397] estimated a value of the fractional release in the Milk River sandstone of 2.7%. They used the measured value of the mean  $^{222}\text{Rn}$  content of  $1.7 \times 10^4 \text{ Bq/m}^3$ , a porosity of 10% and a uranium content of 2.4 ppm for the confined sandstone. The observed fluctuation of the  $^{222}\text{Rn}$  concentration was attributed to the variability of



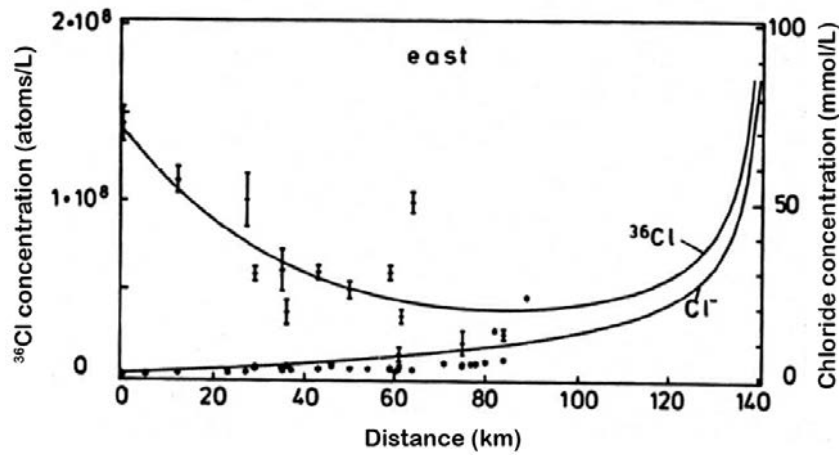


FIG. 11.9. Concentration of Cl and  $^{36}\text{Cl}$  along the eastern flow path calculated by the diffusion model, with in situ  $^{36}\text{Cl}$  production (from Nolte et al. (1991) [291]).

TABLE 11.2. COMPARISON OF FLOW VELOCITIES DETERMINED (after Nolte et al. (1991) [291])

		Eastern flow path		Western flow path	
		Without in situ production	With in situ production	Without in situ production	With in situ production
Flow velocity (m/a)	without diffusion	0.11	0.09	0.08	0.06
	with diffusion	0.14	0.5	0.1	0.07

The groundwater flow velocities were obtained by least square fits of the theoretical curves to the experimental data. Figure 11.9 shows the results of the diffusion model with in situ production for the eastern flow path.

Table 11.2 compiles all values of the groundwater flow velocity obtained with different assumptions. In the first approach (without diffusion), consideration of in situ production yields a value of the flow velocity that is only 75% of the value without in situ production. The flow velocities inferred from the diffusion model (second approach) are about 30% greater than the values deduced without consideration of diffusive losses of  $^{36}\text{Cl}$ . Thus, Nolte et al. (1991) [291] conclude that radioactive decay of  $^{36}\text{Cl}$  rather than diffusive loss controls the  $^{36}\text{Cl}$  concentration in groundwater during advective transport in the aquifer. The flow velocities are in the range 0.09–0.14 m/a (eastern flow path) and 0.06–0.10 m/a (western flow path). The corresponding groundwater model ages at a distance of 80 km from the recharge area are in the range of 0.6–0.9 Ma (east) and 0.8–1.6 Ma (west). For comparison: using ion filtration to describe the evolution of Cl in the Milk River groundwater, Phillips et al. (1986) [319] obtained ages of up to about 2 Ma at the end of the aquifer. On the other hand, the values of the groundwater velocity determined by Hendry and Schwartz (1988) [633] are remarkably larger than the ones deduced by Nolte et al. (1991) [291]. For the eastern flow path, they obtained 0.32 m/a and for the western flow path 0.16 m/a. Comparing the various  $^{36}\text{Cl}$  dating approaches of the Milk River aquifer, Phillips (2000) [306] suggested that the age estimates derived from the  $^{36}\text{Cl}/\text{Cl}$  ratio under assumption of ion filtration ('ion filtration age', Phillips et al. (1990) [640]) may be more accurate for regions close to the recharge zone while further away dating based on the  $^{36}\text{Cl}$  concentration (Nolte et al. (1991) [291]) may be more adequate.

Although in situ production of  $^{36}\text{Cl}$  in aquifer matrices is generally known to be significant, its contribution to the  $^{36}\text{Cl}$  content of Milk River aquifer groundwater appeared to be relatively low in

comparison to the cosmogenic input. Groundwater ages calculated with in situ production of  $^{36}\text{Cl}$  were only between 30% (western flow path) and 25% (eastern flow path) higher than the ages calculated for zero in situ production. However, when the groundwater Cl content reaches very high values (~500 ppm), in situ production may be significant (Figs 11.8 and 11.9).

#### 11.4.4. Uranium isotopes

For uranium isotope analysis, 21 water samples and two rock samples (core samples) were collected from the Milk River aquifer, and one surface water sample from the Milk River (Fig. 11.10). The uranium concentrations were found to decrease along the groundwater flow direction.

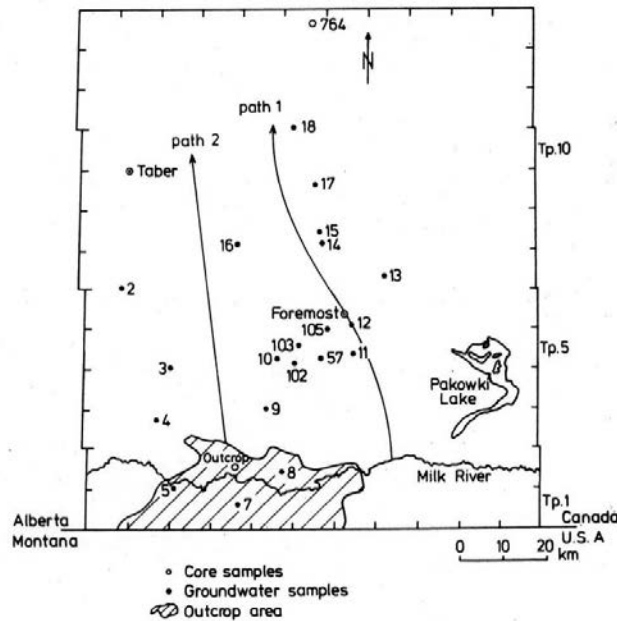


FIG. 11.10. Location of sampling wells and core samples in the Milk River aquifer. Two identified flow paths are indicated by arrows (from Ivanovich et al. (1991) [422]).

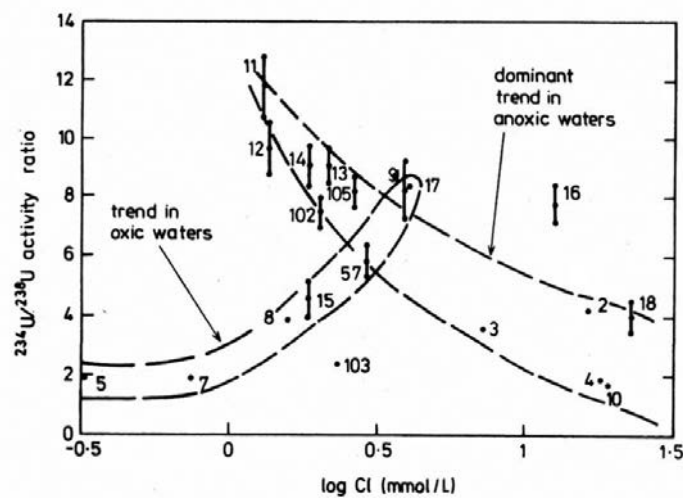


FIG. 11.11.  $^{234}\text{U}/^{238}\text{U}$  ratio against Cl concentration in the groundwater of the Milk River aquifer and delineation of the oxic and anoxic regions (from Ivanovich et al. (1991) [422]).

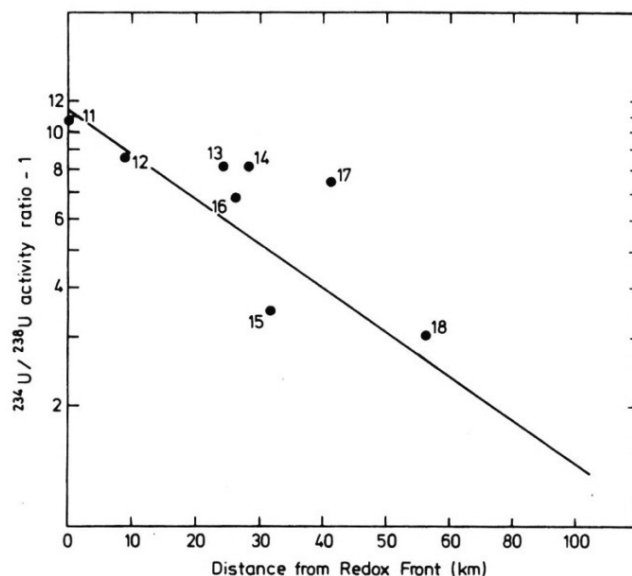


FIG. 11.12. Decrease of the relative  $^{234}\text{U}$  excess ( $^{234}\text{U}/^{238}\text{U}$  activity ratio - 1) along flow path 1 (from Ivanovich et al. (1991) [422]).

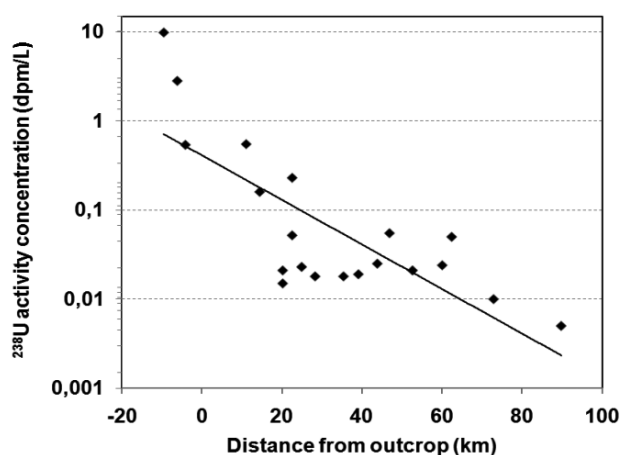


FIG. 11.13(a). Plot of the  $^{238}\text{U}$  activity concentration against the distance along the flow path from the outcrop of the Milk River aquifer. The solid line represents the best-fit line of approach to using the complete data set (after Ivanovich et al. (1991) [422]).

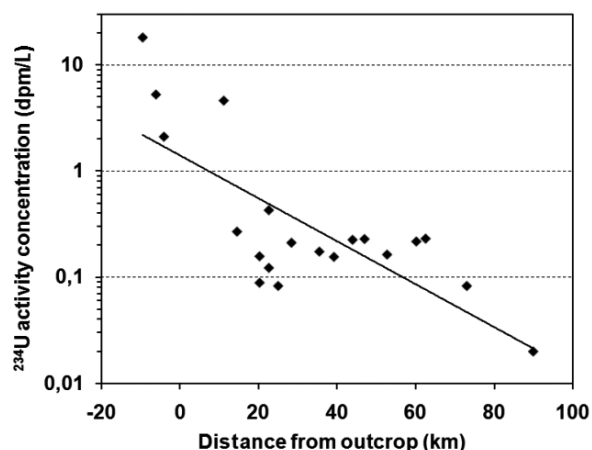


FIG. 11.13(b). Plot of the  $^{234}\text{U}$  activity concentration against the distance along the flow path from the outcrop of the Milk River aquifer. The solid line represents the best-fit line of approach to using the complete data set (after Ivanovich et al. (1991) [422]).

In the oxidizing zone near the recharge area, the uranium concentrations ranged from about 12 to 0.7  $\mu\text{g}/\text{L}$  and under anoxic conditions from 0.07 to 0.007  $\mu\text{g}/\text{L}$ .

Parallel geochemical investigations of dissolved ions in groundwater (Ivanovich et al. (1991) [422]) have shown that all groundwater samples are undersaturated with respect to common uranium minerals, which suggests that uranium minerals do not precipitate. Furthermore, the Cl concentrations were found to increase with the groundwater age. The  $^{234}\text{U}/^{238}\text{U}$  ratios tend to increase with distance down flow of the outcrop in the oxic zone and reach a maximum at well 11 where the redox front is positioned. In the downstream anoxic zone, the  $^{234}\text{U}/^{238}\text{U}$  ratios decrease with increasing Cl concentrations, i.e. increasing groundwater age (Fig. 11.11). The decrease in  $^{234}\text{U}/^{238}\text{U}$  is accompanied

by a constant but low  $^{238}\text{U}$  concentration, and the change in  $^{234}\text{U}/^{238}\text{U}$  ratio could, thus, be attributed to the radioactive decay of  $^{234}\text{U}$  and exchange between the liquid and adsorbed phase (retardation). It should be noted that a similar pattern of the evolution of the uranium isotopes (low and basically constant uranium concentration at decreasing  $^{234}\text{U}/^{238}\text{U}$  ratios down dip the anoxic zone) was also observed in other regional aquifers such as the Hosston aquifer (Kronfeld and Adams (1974) [424]), Carrizo aquifer (Cowart and Osmond (1974) [419]), Lincolnshire limestone (Edmunds (1973) [643]) and Lincolnshire chalk (Cuttell et al. (1986) [644]).

The Milk River uranium isotope data were evaluated by two different approaches. In a first approach, only the data of the anoxic part of the aquifer were evaluated, assuming constant  $^{238}\text{U}$  concentration and exponential decrease of  $^{234}\text{U}$  excess down flow. The model corresponds to Eq. (7.17) assuming that the stationary value of the  $^{234}\text{U}$  excess is zero (no  $^{234}\text{U}$  production by recoil ejection). Figure 11.12 shows the best fit line of the model to the experimental data in a semi-logarithmic plot. According to Eq. (7.17), the slope of this line represents the ratio  $\lambda_{234}/v^*$ , from which the velocity,  $v^*$ , can be calculated. The obtained value is 0.12 m/a (Ivanovich et al. (1991) [422]). Using a hydraulic model, Hendry and Schwartz (1988) [633] determined a groundwater flow velocity  $v$  of 0.3 m/a for the same flow path. Obviously, the velocity  $v^*$  characterizes the uranium migration velocity which is related to the groundwater flow velocity by the expression  $v^* = v/R$ , where  $R$  is the retardation factor. Thus, for the considered anoxic part of the Milk River aquifer, the uranium retardation factor appears to be  $R = 0.3/0.12 = 2.5$ .

In a second approach, all measured  $^{238}\text{U}$  and  $^{234}\text{U}$  concentrations were plotted against distance along a generalized flow path from the Milk River outcrop area (Figs 11.13(a) and 11.13(b)). For the estimation of the distances, the position of each sampled well was projected onto the generalized N-S flow path. The main feature of the semi-logarithmic plots in Figs 11.13(a) and 11.13(b) is an approximately linear decrease of the uranium isotope concentrations with increasing distance along the flow path. However, there are considerable deviations of individual data from the linear trend lines which point to significant local fluctuations of the geochemical and/or hydrological conditions along groundwater flow.

Nevertheless, the absence of any independent evidence for these inhomogeneities in the aquifer was deemed to justify this statistical approach that does not explicitly take into consideration the influence of a redox front. Assuming, as in the first approach, that the stationary values of the uranium isotope concentrations are negligible, the slope,  $s$ , of the best-fit lines in Figs 11.13(a) and 11.13(b) can be derived from Eqs (7.7, 7.8), respectively (see Chapter 7). The following expression is obtained:

$$s_i = K_i/v \tag{11.1}$$

where

$K_i$  is defined by Eq. (7.11);  
*i* stands for  $^{234}\text{U}$  and  $^{238}\text{U}$ , respectively.

The following values have been determined by this approach:  $s_8 = 5.8 \times 10^{-5}/\text{m}$  and  $s_4 = 4.7 \times 10^{-5}/\text{m}$ . Thus, within the accuracy of this estimate, the two lines have the same slope of about  $5 \times 10^{-5}/\text{m}$ . Adopting the value of the parameter  $K$  determined by Fröhlich and Gellermann (1987) [426] for the Hosston aquifer ( $K_8 \approx K_4 \approx (1-3) \times 10^{-5}/\text{a}$ ), Ivanovich et al. (1991) [422] estimated a groundwater flow rate for the Milk River aquifer of between 0.2 and 0.6 m/a. Within the range of the given uncertainties, this result seems to be in good agreement with estimates by other methods (Table 11.3), which indicates “that uranium isotope data are a viable tool for dating very old groundwater provided the local uranium geochemistry is understood adequately” (Ivanovich et al. (1991) [422]).

TABLE 11.3. COMPARISON OF METHODS APPLIED TO DATE GROUNDWATER OF THE MILK RIVER AQUIFER

	Hydraulic method <sup>a</sup>		<sup>36</sup> Cl <sup>b</sup>		U isotopes <sup>c</sup>	
	Path 1	Path 2	Path 1	Path 2	Method 1 Anoxic part	Method 2 Total aquifer
<i>v</i> (m/a)	0.32	0.16	0.09–0.14	0.05–0.10	0.12	0.2–0.6
age(Ma) <sup>d</sup>	0.25	0.51	0.6–0.9	0.8–1.6	0.7	0.13–0.4

<sup>a</sup> Hendry and Schwarz (1988) [633].

<sup>b</sup> Nolte et al. (1991) [291].

<sup>c</sup> Ivanovich et al. (1991) [422].

<sup>d</sup> At a distance of 80 km from the outcrop.

## 11.5. CONCLUSIONS

Examining the hydrochemistry, in particular the distribution of chloride, it was possible to identify major groundwater flow paths through the extended confined aquifer system. The stable isotopes <sup>2</sup>H and <sup>18</sup>O provided information on the groundwater regime under past climate conditions. Radiocarbon has been of use near the recharge zone; after a distance of 20 km down flow, its concentration was below the detection limit. From the <sup>14</sup>C data, a value of about 1 m/a was derived for the flow velocity of the groundwater between the outcrop area and the Milk River. The river acts as a discharge strip which is manifested by a drastic decrease in the groundwater flow velocity further down flow.

The analyses of noble gases provided information on the groundwater recharge temperatures. The <sup>4</sup>He content was found to increase along the flow path but could not be used to date the groundwater because some of the <sup>4</sup>He data appeared to be distorted by degassing during groundwater sampling. Only one <sup>81</sup>Kr measurement could be afforded at this early stage in the development of the <sup>81</sup>Kr method. An upper limit of 140 ka has been calculated for the <sup>81</sup>K based model age of groundwater collected about 20 km from the recharge area. This model age value is consistent with results obtained by other dating tools. Argon isotope measurements could not be interpreted in terms of groundwater age. The observed <sup>39</sup>Ar concentrations were found to be in good agreement with values corresponding to in situ production. Furthermore, the <sup>39</sup>Ar and <sup>37</sup>Ar data indicate that these isotopes are released to groundwater from the sandstone of the aquifer rather than the Colorado shale.

The <sup>36</sup>Cl data indicate that, in comparison to in situ production, the cosmogenic <sup>36</sup>Cl input to this system is high. Thus, radioactive decay of <sup>36</sup>Cl appeared to be the dominant process controlling the decrease of the <sup>36</sup>Cl content with distance down flow. On the contrary, most of the measured <sup>129</sup>I concentrations clearly point to in situ production of <sup>129</sup>I in the aquifer sandstone, with subsequent release to the surrounding groundwater. The groundwater flow velocities estimated from the uranium isotope data were found to be in reasonable agreement with the results obtained by hydraulic modelling and <sup>36</sup>Cl dating. In this context, it should be noted that hydraulic modelling based on present day hydraulic heads may underestimate the groundwater age because of the impact of climatic changes on the groundwater flow regime in the past.

In conclusion, the Milk River aquifer is a complex system in terms of origin and evolution of the chemical and isotopic composition of the groundwater. Fortunately, a wealth of physical and chemical data of the groundwater and the bonding shales was collected by numerous authors over a period of about 15 a that allowed applying various complementary approaches in dating the groundwater. Although the Milk River aquifer studies were carried out more than two decades ago, they can still be considered an outstanding example for dating of old groundwater.

## Chapter 12

### CASE STUDY MIDDLE RIO GRANDE BASIN, NEW MEXICO, USA

L.N. PLUMMER, W. SANFORD  
United States Geological Survey,  
Reston, Virginia,  
United States of America

#### 12.1. INTRODUCTION

Chemical and isotopic patterns in groundwater can record characteristics of water sources, flow directions and groundwater age information. This hydrochemical information can be useful in refining conceptualization of groundwater flow, in calibration of numerical models of groundwater flow and in estimation of palaeo- and modern recharge rates. This case study shows how chemical and isotopic data were used to characterize sources and flow of groundwater in the Middle Rio Grande Basin, New Mexico, USA. The  $^{14}\text{C}$  model ages of the groundwater samples are on the tens of thousands of years timescale. These data changed some of the prevailing ideas about flow in the Middle Rio Grande Basin, and were used to improve a numerical model of the aquifer system.

#### 12.2. BACKGROUND: HYDROGEOLOGICAL SETTING

The Middle Rio Grande Basin covers about 7800 km<sup>2</sup> along the Rio Grande Rift in central New Mexico, USA (Fig. 12.1). The Rio Grande Rift is a zone of faults and sediment filled basins that extends from northern Mexico to southern Colorado, USA. The basin consists of generally unconsolidated Cenozoic basin-fill sediment with a maximum thickness of about 4300 m (Fig. 12.2). The average elevation is about 1500 m, with surrounding mountains approaching 3300 m. The primary aquifer system of the Middle Rio Grande Basin consists of generally unconsolidated to moderately consolidated basin-fill sediment of the Santa Fe Group.

The Santa Fe Group aquifer system is defined by Thorn et al. (1993) [21] as including both the Santa Fe Group deposits, which are of Oligocene to middle Pleistocene age, and the more recent (post-Santa Fe Group) flood plain, channel and basin-fill deposits of Pleistocene to Holocene age that are in hydraulic connection with the Santa Fe Group. The Santa Fe Group deposits range in thickness from about 900 to 4300 m. The lower Santa Fe Group ranges in thickness from about 300 to 1000 m and consists largely of piedmont-slope, eolian sand and silt, and fine to medium grained basin-floor deposits (Fig. 12.2). The middle Santa Fe Group deposits range in thickness from about 75 to 2740 m and consist of piedmont-slope sediments and fluvial deposits (identified mostly as medium sand in Fig. 12.2). The upper Santa Fe Group sediments are generally less than 300 m thick and consist predominantly of piedmont-slope and fluvial basin-floor deposits, and are the most productive part of the aquifer system (denoted axial gravel, blanket sand/gravel, and medium-coarse sand in Fig. 12.2). A red-brown clay separates the upper and middle Santa Fe Group deposits at Albuquerque. Geophysical measurements have recognized three sub-basins within the Middle Rio Grande Basin that are separated by structural highs (Grauch et al. (1999) [645]; Grauch et al. (2001) [646]; see Bartolino and Cole (2002) [612] for further details). Most production wells are completed in the upper and/or middle Santa Fe Group, although wells on the west side of the Rio Grande reach parts of the lower Santa Fe Group.

In the 1980s, there was the perception that Albuquerque was situated over a large and almost unlimited supply of fresh groundwater, and optimism prevailed for seemingly unlimited growth potential. However, as new and detailed geological and hydrological data were gathered (Bartolino

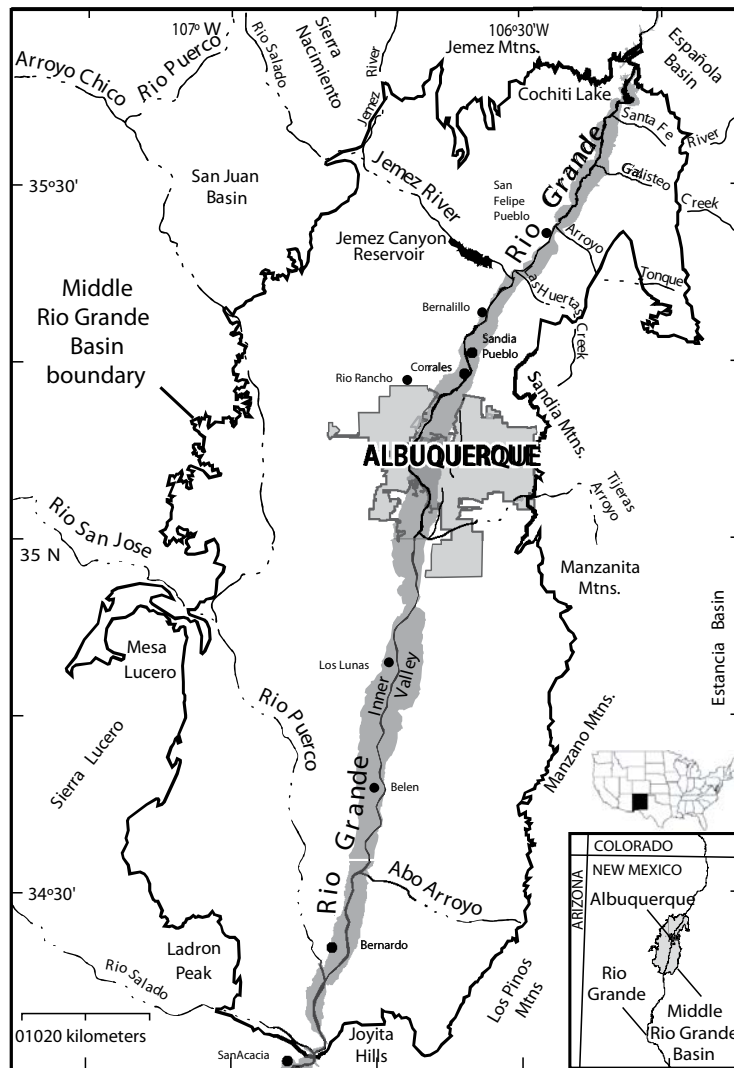


FIG. 12.1. Location of the Middle Rio Grande Basin in west-central New Mexico, USA, and other physiographic features of the region.

and Cole (2002) [612]; Cole (2001) [647]; Connell et al. (1998) [648]; Hawley and Haase (1992) [649]; Thorn et al. 1993) [21]), the conceptualization of the aquifer system greatly changed. The most productive part of the aquifer system was found to be limited to a relatively small area of ancestral Rio Grande sediments under parts of Albuquerque.

Water level declines of as much as 40 m (130 ft) were observed between 1960 and 2002 at Albuquerque (Fig. 12.3). Until recently, groundwater was the sole source of drinking water for Albuquerque. During the 1990s, basin-wide pumping was about 200 Mm<sup>3</sup> annually and about 75% of this water was withdrawn for public supply at Albuquerque. It is now thought that the basin-wide pumping rate amounted to about three times the modern recharge rate for the entire basin.

Recharge occurs along and near the basin margin. This includes mountain front processes, infiltration from arroyos and subsurface groundwater inflow. The other major source of recharge is surface water, particularly from the Rio Grande in central parts of the basin, its tributaries and, more recently, irrigation canals. Today, areal recharge is thought to be negligible across the semi-arid basin.

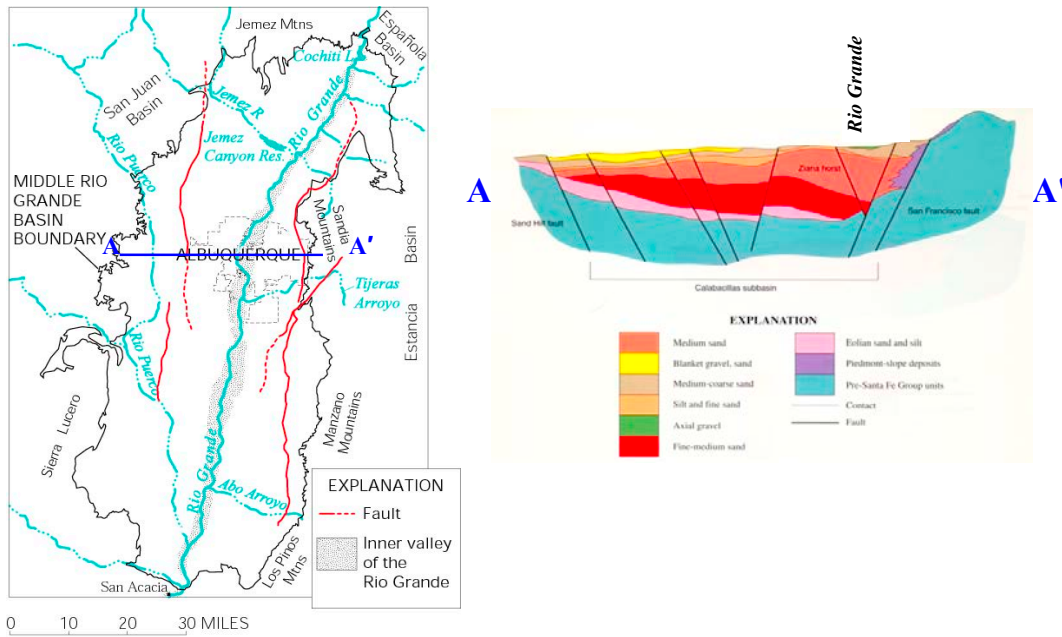


FIG. 12.2. Map and cross-section of the Middle Rio Grande Basin in west-central New Mexico, USA, showing (left) major physiographic features of the region, major faults in the basin, the basin boundary, the lowland inner valley of the Rio Grande and other drainage in the basin. The cross-section, A–A' (right), shows stratigraphic, lithologic and structural features of the basin to depths of more than 3500 m along an east–west cross-section at Albuquerque (from Bartolino and Cole (2002) [612]).

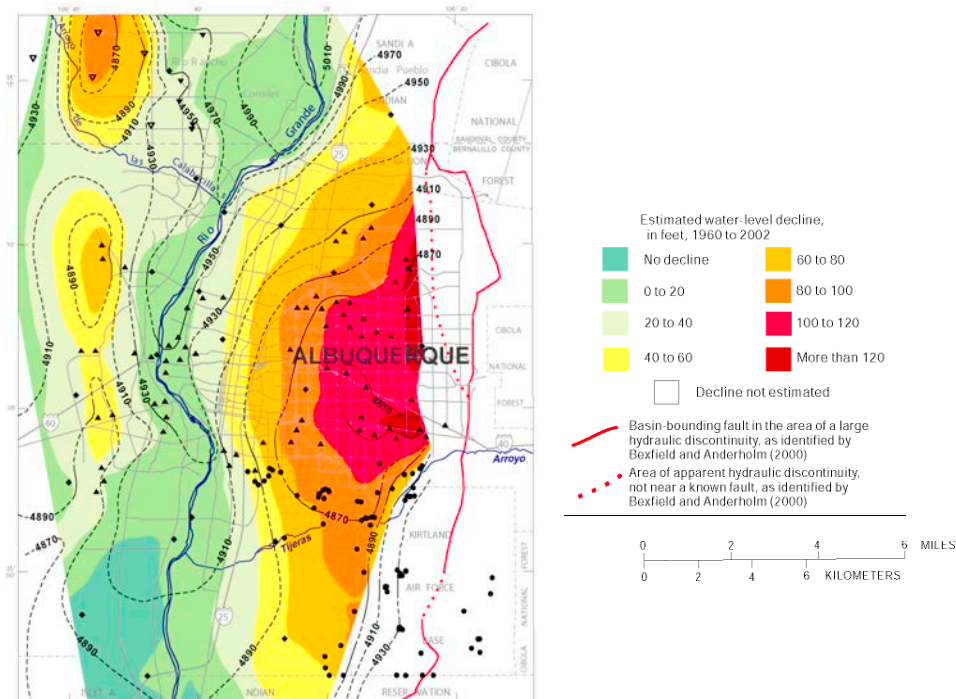


FIG. 12.3. Groundwater levels that represent 2002 conditions in the Santa Fe Group aquifer system in the Albuquerque area showing water level declines of more than 40 m since 1960 (from Bexfield and Anderholm (2002) [650]). Water level contours for the year 2002 (in feet; 1 ft = 0.3048 m) are shown as black lines, dashed where inferred.

### 12.3. THE UNITED STATES GEOLOGICAL SURVEY MIDDLE RIO GRANDE BASIN STUDY

A series of numerical groundwater models have been constructed for the basin by the United States Geological Survey (USGS). The model completed by Kernodle et al. (1995) [651], just before the present hydrochemical study began, included the geological and hydrogeological framework of Hawley and Haase (1992) [649], and the hydrogeological work of the USGS as summarized in Thorn et al. (1993) [21]. However, this model was not based on any hydrochemical data. Due to computational limitations at the time and the large model size, it could not be rigorously calibrated and some model parameters were assumed, such as recharge rate along the eastern mountain front. This model indicated no net recharge from the Rio Grande to the aquifer system — only infiltration to the inner valley of the Rio Grande, which was taken up by evapotranspiration. The basin-scale recharge rate was 5.45 m<sup>3</sup>/s and 62% of this was attributed to mountain block recharge and infiltration from arroyos adjacent to mountains. The relatively high recharge rate along mountain fronts resulted in the model calculating flow of mountain block recharge westward from the Sandia Mountains (on the eastern margin of the basin at Albuquerque) all the way to the Rio Grande at Albuquerque. Thus, the model indicated that water pumped at Albuquerque was recharged along the eastern mountain front. Although some stable isotope data on water from public supply wells at Albuquerque (Yapp (1985) [652]) suggested a Rio Grande source of the water beneath most of Albuquerque, these data were not accounted for in development of the Kernodle et al. (1995) [651] model.

Further studies by the USGS (1995–2001) and other federal and state agencies were conducted to improve the understanding of the hydrology, geology and land surface characteristics of the Middle Rio Grande Basin and to provide the scientific information needed for water resource management. The investigations included:

- (a) Detailed geological mapping and high resolution airborne geophysics to better characterize faults and hydrological properties;
- (b) Use of chemical and environmental tracers to quantify mountain front recharge, characterize river–aquifer interaction and improve knowledge of the flow system;
- (c) Groundwater flow modelling.

A series of 20 deep monitoring well clusters were drilled during the investigation, typically with 3–6 completions at each location. Most of these were in the vicinity of Albuquerque with a maximum depth of 550 m below the land surface and open intervals, typically of 1.5 m at each discrete depth. About 280 groundwater samples from wells and springs were collected throughout the basin and analysed for a wide range of chemical and isotopic constituents, including 30 major and minor elements, stable isotopes of water (<sup>2</sup>H and <sup>18</sup>O), carbon isotopic composition (<sup>13</sup>C and <sup>14</sup>C) of dissolved inorganic carbon (DIC), dissolved nitrogen (N<sub>2</sub>), argon (Ar), helium (He), <sup>3</sup>He/<sup>4</sup>He isotope ratio, neon (Ne), sulphur hexafluoride (SF<sub>6</sub>), CFCs and tritium (<sup>3</sup>H). These and additional chemical and hydrogeological data are tabulated and discussed in Plummer et al. (2004) [49]. Selected observations based on the stable isotope, <sup>14</sup>C, helium and water chemical composition data are discussed below.

### 12.4. STABLE ISOTOPES, <sup>4</sup>He, RADIOCARBON AGES AND HYDROCHEMICAL ZONES

#### 12.4.1. Stable isotopes

Groundwater of the Middle Rio Grande Basin varied widely in stable isotopic composition, due mostly to the source of recharge and age (palaeoclimatic variation). The  $\delta^2\text{H}$  composition of the groundwater varied more than 50‰ throughout the basin (Fig. 12.4). Most of the stable isotope

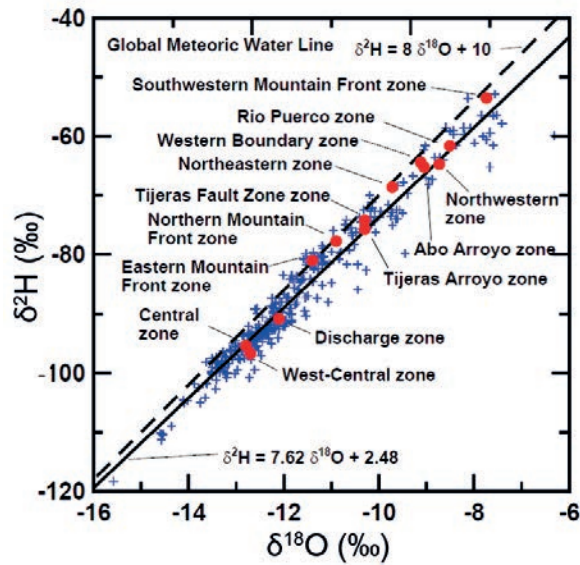


FIG. 12.4. Variations in the stable isotopic composition of groundwater samples (blue + signs) in the Middle Rio Grande Basin. The solid line shows the least squares fit to the values and is compared to the global meteoric water line (dashed line). The red circles show the median isotopic composition of the hydrochemical zones (12 zones of recharge and one of discharge; see Fig. 12.12). The data suggest that discharge from the basin is dominated by water recharged from the Rio Grande (central zone and water from the west-central zone). There is typically more than 50‰ variation in  $\delta^2\text{H}$  of Middle Rio Grande Basin groundwater (Plummer et al. (2004) [49]; Plummer et al. (2004) [50]).

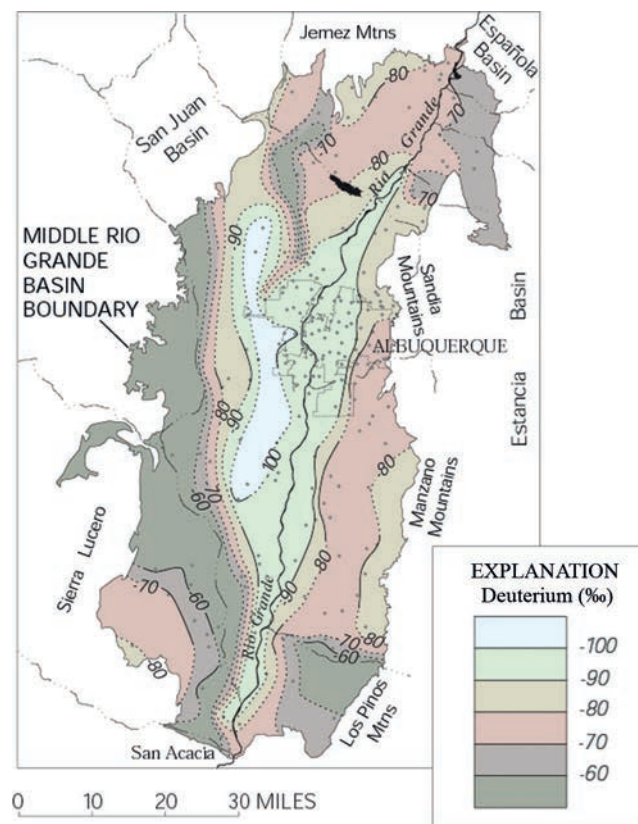


FIG. 12.5. The  $\delta^2\text{H}$  isotopic composition, in per mille, of groundwater was mapped throughout the basin and is indicative of the source of recharge. Contours for deuterium align generally north to south in the central part of the basin, parallel to the regional north to south direction of groundwater flow (from Plummer et al. (2004) [51]).

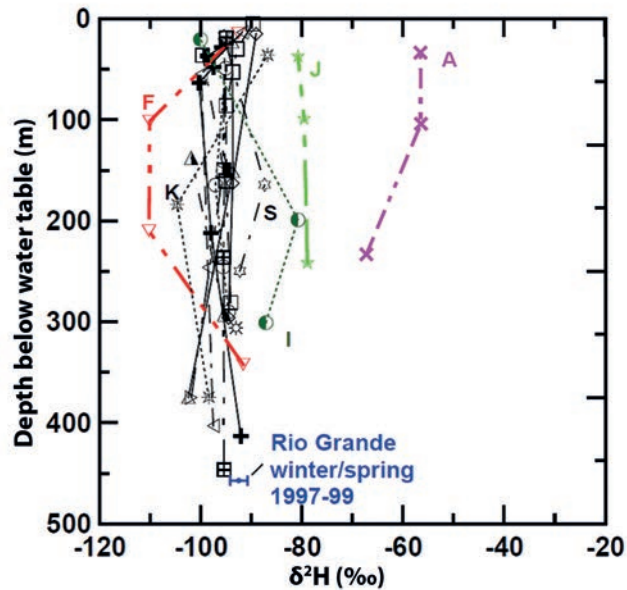


FIG. 12.6.  $\delta^2\text{H}$  composition of groundwater from narrow-screened monitoring wells, mostly in the Albuquerque vicinity, as a function of depth below the water table (Plummer et al. (2004) [49]).

values plotted below the global meteoric water line (Fig. 12.4) and fitted a least squares line of  $\delta^2\text{H} = 7.62 \delta^{18}\text{O} + 2.48$ .

Spatial patterns in the chemical and isotopic composition of groundwater were recognized and mapped basin-wide for approximately the upper 60 m of the aquifer (Plummer et al. (2004) [49]). The contours for deuterium (Fig. 12.5) aligned generally north to south in the central part of the basin, parallel to the regional north to south direction of groundwater flow, and reflected the isotopic composition of the source.

The most depleted water was found throughout the west-central part of the basin. Enriched water was found in the western and south-western parts of the basin,  $-90\text{s}\text{‰}$  values in  $\delta^2\text{H}$  were found along the Rio Grande, and the  $-70\text{s}$  and  $-80\text{s}\text{‰}$  range occurred along the eastern and northern margins of the basin (Fig. 12.5). The  $\delta^2\text{H}$  composition of groundwater from the narrow-screened monitoring wells, mostly in the Albuquerque vicinity, show that  $\delta^2\text{H}$  was nearly constant to depths of more than 400 m below the water table at Albuquerque, and was similar in isotopic composition to that of the Rio Grande measured during the late winter to spring runoff period (Fig. 12.6). The red line in well nest (F) (Fig. 12.6) is in the depleted zone that extends down through the west-central part of the basin. The green line (J) is adjacent to the eastern mountain front. Line A (magenta) appears to be water recharged at low altitude along the northern margin of the basin. Other well nests (K, S, I) appear to contain fractions of either depleted or enriched water at intermediate depths.

#### 12.4.2. Carbon-14 model age

The measured  $^{14}\text{C}$  content of DIC in groundwater from 211 sites ranged from 0.62 to 123.1 pmc. Most of the contours in  $^{14}\text{C}$  align in a north–south direction that roughly parallels the pattern in  $\delta^2\text{H}$  (Fig. 12.7). The unadjusted  $^{14}\text{C}$  model age of DIC in the upper 60 m of the aquifer (Fig. 12.8) is based on the measured non-normalized  $^{14}\text{C}$  pmc value of DIC in groundwater and was calculated using an initial  $^{14}\text{C}$  value of 100 pmc in recharge water (see Fig. 4.1, Chapter 4). Patterns in  $^{14}\text{C}$  model age were similar to the patterns in  $^{14}\text{C}$  content of the DIC. Carbon-14 values were highest along the eastern mountain front, along the northern margin of the basin, and along the inner valley of the Rio Grande

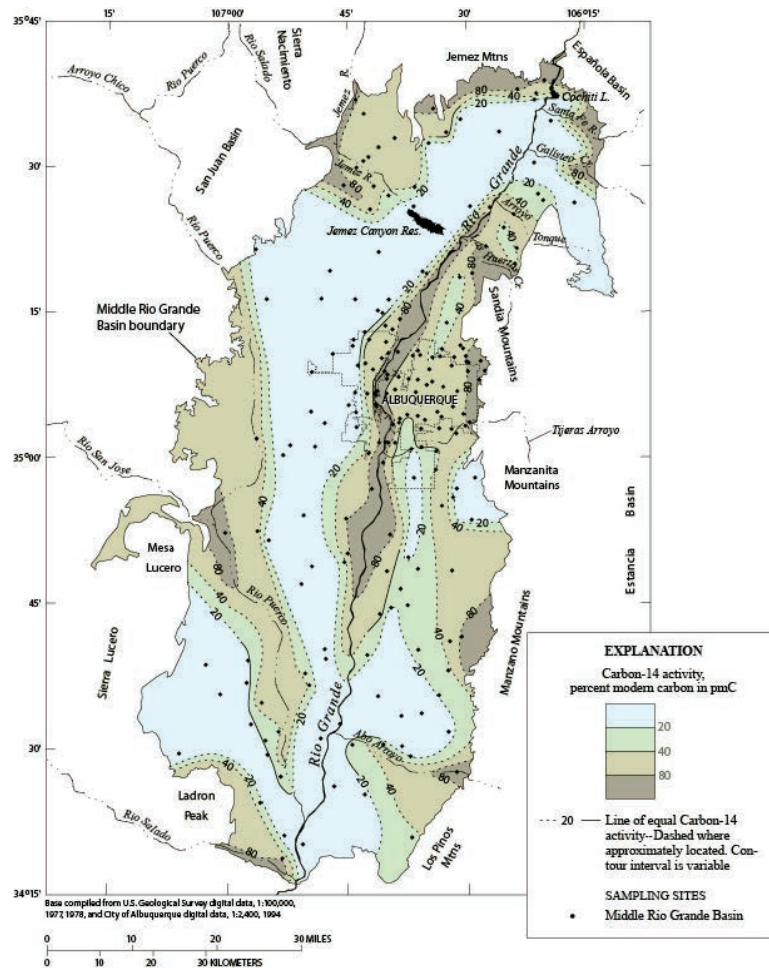


FIG. 12.7. Carbon-14 content in pmc of dissolved inorganic carbon in the upper approximately 60 m of the aquifer throughout the Middle Rio Grande Basin (after Plummer et al. (2004) [51]).

(Fig. 12.7, dark brown pattern,  $>80$  pmc). Relatively high  $^{14}\text{C}$  values also occurred near areas where surface water inflow (from Abo Arroyo, the Rio Puerco and the Jemez River) enters the basin.

Waters with low  $^{14}\text{C}$  values of the DIC were present along the western and south-western basin margins ( $<20$  pmc). Another zone of low  $^{14}\text{C}$  content extended through nearly the entire length of the west-central part of the basin.

Along the eastern mountain front, values of  $^{13}\text{C}$  of DIC tended to be more negative (typically  $-12\%$ ) than those of DIC further down gradient into the aquifer (typically  $-7$  to  $-8\%$ ). The change in  $\delta^{13}\text{C}$  of DIC could indicate dissolution of carbonate rock fragments of marine origin, which may occur in low abundance within the alluvial and fluvial sediments of the basin. If so, it would then be necessary to adjust the  $^{14}\text{C}$  model ages for carbonate rock dissolution. However, geochemical mass balance calculations indicated that water-rock reactions were probably minimal in the primarily siliciclastic basin-fill sediment and that the shift in  $\delta^{13}\text{C}$  must be attributed to other processes. The geochemical modelling supported the unadjusted  $^{14}\text{C}$  model ages that were then well defined in the range from modern to more than 30 ka BP (Plummer et al. (2004) [49]; Plummer et al. (2004) [50]; Plummer et al. (2004) [51]) (Fig. 12.8). The shift in  $\delta^{13}\text{C}$  isotopic composition with distance of flow (and age) into the basin was concluded to be the result of climate change. In the past few thousand years, or less, there appears to have been an increase in  $\text{C}_3$  plant abundance relative to  $\text{C}_4$  plants in the recharge areas of the Middle Rio Grande Basin (Plummer et al. (2004) [49]; Plummer et al. (2004) [50]; Plummer et al. (2004) [51]), resulting in a decrease in  $\delta^{13}\text{C}$  of DIC along the eastern mountain front. The cause is

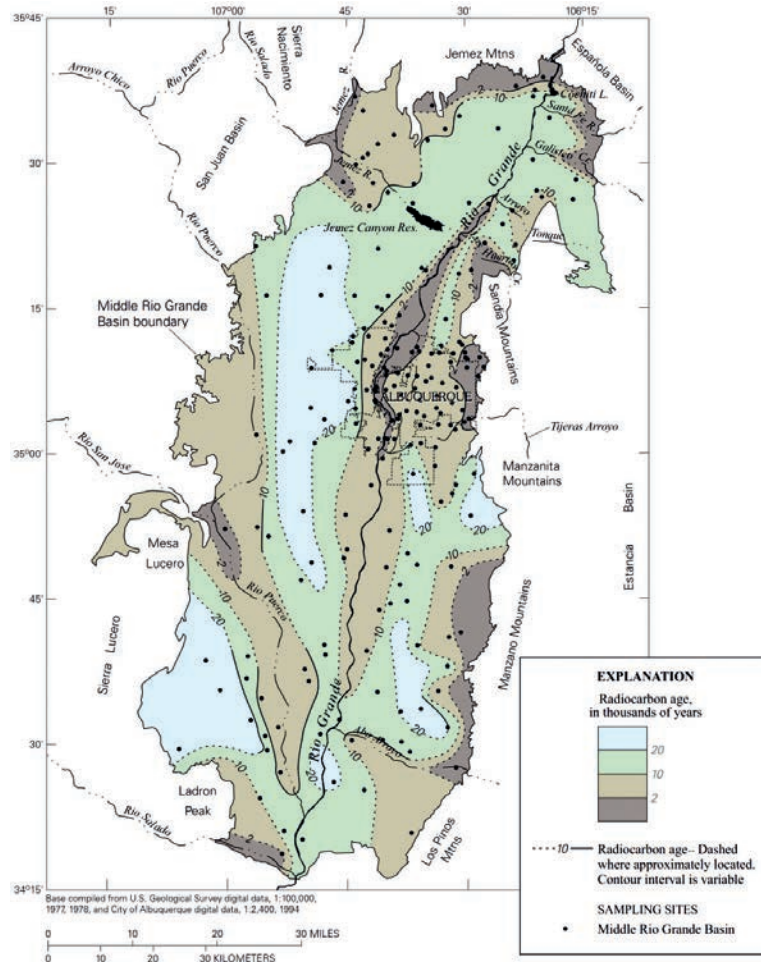


FIG. 12.8. Unadjusted  $^{14}\text{C}$  model age in thousands of years BP in the upper approximately 60 m of the aquifer throughout the Middle Rio Grande Basin (after Plummer et al. (2004) [51]).

not known but possible factors include increased precipitation in recharge areas and, more recently, an increase in the atmospheric mixing ratio of  $\text{CO}_2$  (Plummer et al. (2004) [49]; Plummer et al. (2004) [51]). Geochemical modelling of water–rock reactions and quantification of mixing of waters from adjacent hydrochemical zones were critical in demonstrating that geochemical corrections were negligible in the siliciclastic sediments of the Middle Rio Grande Basin, even though a shift to enriched  $\delta^{13}\text{C}$  of DIC was evident between the recharge area and older waters further down gradient.

### 12.4.3. Helium-4

Helium-4 concentrations in Middle Rio Grande Basin groundwater increased with depth below the water table and with  $^{14}\text{C}$  model age (Fig. 12.9). The  $^4\text{He}$  concentrations ranged from values near air–water equilibrium ( $\sim 5 \times 10^{-8} \text{ cm}^3 \text{ STP/g}$ ) to about  $1.2 \times 10^{-4} \text{ cm}^3 \text{ STP/g}$ .

The isotopic composition of dissolved helium, along with amounts of dissolved He and Ne, were determined by mass spectrometry in a relatively small subset of the Middle Rio Grande Basin samples — basically a subset that was thought to contain a fraction of young water that might possibly be dated by the  $^3\text{H}$ – $^3\text{He}$  method. Unfortunately, relatively few of the samples could be dated by this method due to large excesses of (predominantly) mantle-derived helium.

A log–log plot of the  $^3\text{He}/^4\text{He}$  isotope ratio as a function of the Ne/He ratio for these samples indicates two sources of He in the Middle Rio Grande Basin waters: (i) a crustal source with a  $^3\text{He}/^4\text{He}$

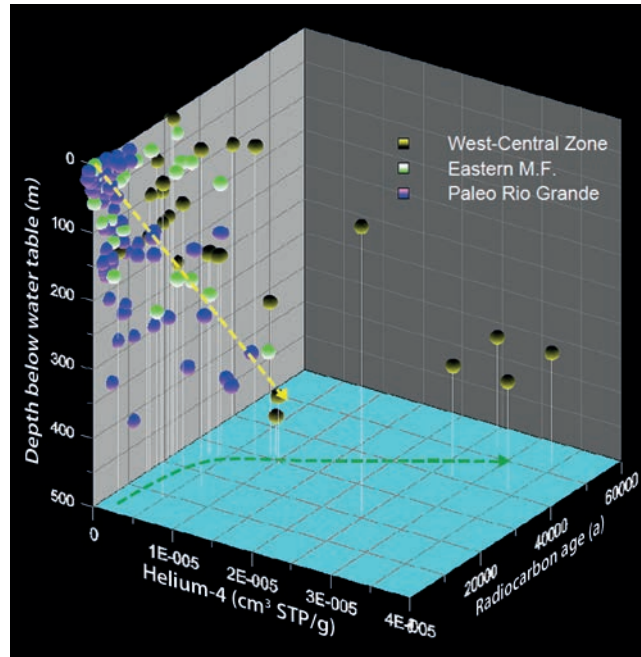


FIG. 12.9. Three dimensional plot showing  $^4\text{He}$  concentration as a function of depth below the water table and  $^{14}\text{C}$  model age for waters from the eastern mountain front, central zone (palaeo-Rio Grande water) and the west-central hydrochemical zones (hydrochemical zones are defined in Section 12.4.4).

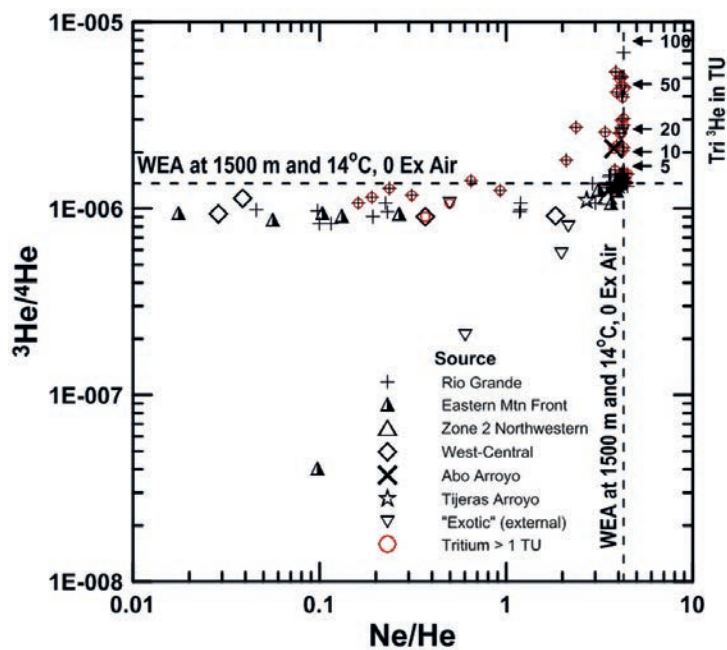


FIG. 12.10. Plot showing variations in the  $^3\text{He}/^4\text{He}$  ratio of dissolved He as a function of  $\text{Ne}/\text{He}$  for various hydrochemical zones of the Middle Rio Grande Basin (the hydrochemical zones are defined in Section 12.4.4). The red circles denote samples containing tritium of more than 1 TU. Most of the groundwater samples of the Middle Rio Grande Basin contain a mantle signature of  $^3\text{He}/^4\text{He}$  ratio near  $1 \times 10^{-6}$ . Samples with a  $^3\text{He}/^4\text{He}$  ratio greater than  $1 \times 10^{-6}$  have  $\text{Ne}/\text{He}$  ratios near those of water in equilibrium with air and probably are bomb era waters infiltrated from the Rio Grande; some of these samples contain more than 50 TU of tritiogenic  $^3\text{He}$ .

ratio of approximately  $1 \times 10^{-8}$ , and (ii) a mantle source, which predominates most of the samples, with a  $^3\text{He}/^4\text{He}$  ratio near  $1 \times 10^{-6}$  (Fig. 12.10).

The red circles in Fig. 12.10 denote those samples that contain more than 1 TU of tritium. Many of the tritiated samples plot along the Ne/He line for water in equilibrium with air (at 1500 m, 14°C) and were identified as samples of Rio Grande water that has infiltrated the Middle Rio Grande Basin. The  $^3\text{He}/^4\text{He}$  ratio of these samples indicates some of them originally contained more than 50 TU of tritogenic  $^3\text{He}$ , and are likely representative of Rio Grande water from the bomb era. The largest amount of tritium in any of the samples was 28 TU when sampled in 1996–1998. A few samples probably contain a crustal He signature near  $1 \times 10^{-8}$ , and are derived from water sourced outside the eastern basin margin.

The samples containing more than 1 TU (red-circled samples in Fig. 12.10) and having a Ne/He ratio less than that of water in equilibrium with air are mixtures of young and old water pumped from wells open to both the shallow aquifer and considerable depth (several hundred metres). Excluding the samples with a crustal  $^3\text{He}/^4\text{He}$  signature, there are 23 samples with Ne/He < 1.0. The average  $^3\text{He}/^4\text{He}$  ratio of these samples was  $1.02 \pm 0.15 \times 10^{-6}$ . No trend was recognized in He isotope ratio with regard to source or location in the basin for those samples with a mantle signature (Fig. 12.10).

It appears that the samples with the crustal signature represent relatively shallow water, with a recharge source outside the eastern margin of the basin. The one sample originally identified as being from the eastern mountain front zone with the lowest  $^3\text{H}/^4\text{He}$  ratio (Fig. 12.10) was obtained down gradient from where the other ‘exotic’ samples were obtained and the water could have originated along with that of the other ‘exotic’ samples just outside the eastern margin of the basin. All of the samples with the mantle signature were obtained within the Middle Rio Grande Rift zone (Fig. 12.11).

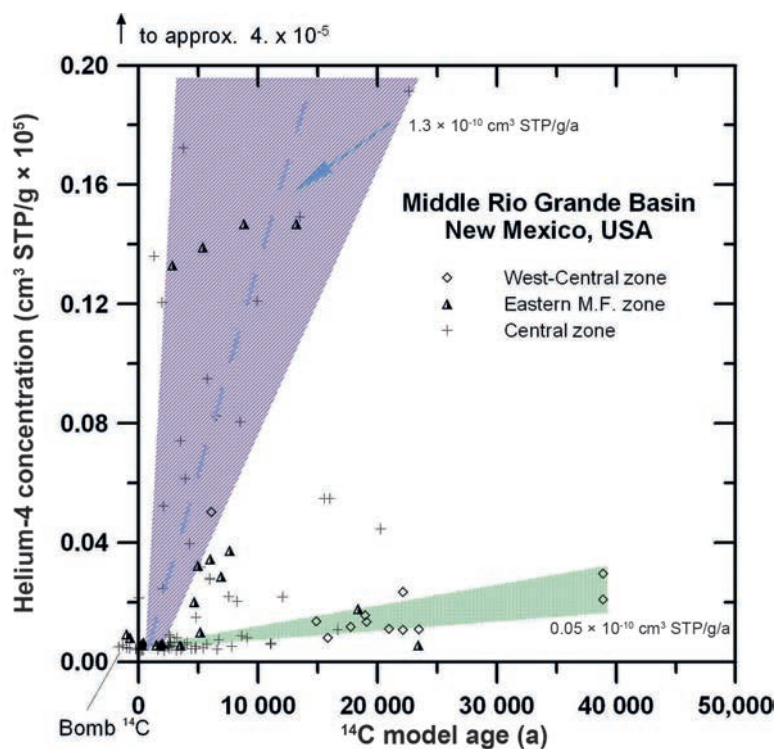


FIG. 12.11. Helium-4 accumulation in the Middle Rio Grande Basin plots in two groups with average accumulation rates of about  $1.3 \times 10^{-10} \text{ cm}^3 \text{ STP} \cdot \text{g}^{-1} \cdot \text{a}^{-1}$  and  $0.05 \times 10^{-10} \text{ cm}^3 \text{ STP} \cdot \text{g}^{-1} \cdot \text{a}^{-1}$ . Many of the samples with the lowest  $^4\text{He}$  accumulation rates are from the west-central zone, beneath deep unsaturated zones.

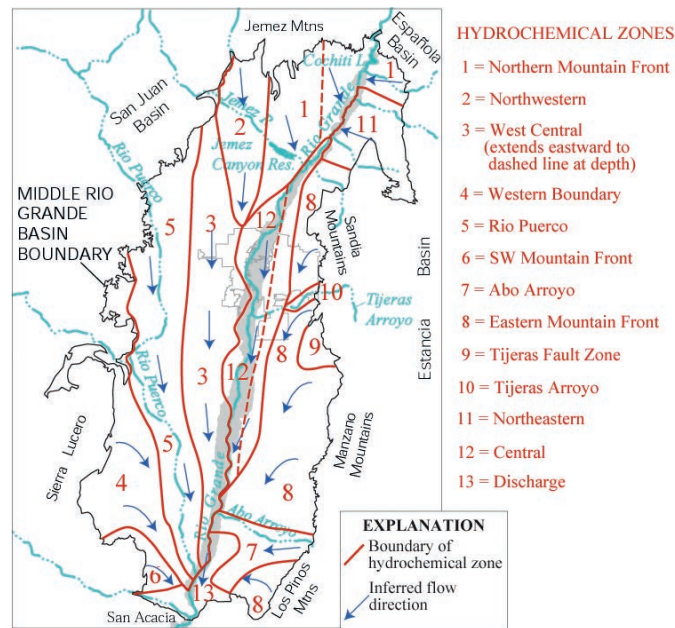


FIG. 12.12. Location of 12 sources of water to the Middle Rio Grande Basin identified based on chemical and isotopic characteristics (after Plummer et al. (2004) [49]). The arrows show the inferred directions of groundwater flow based on the chemical and isotopic data.

The rate of He accumulation varied more than two orders of magnitude in the Middle Rio Grande Basin samples (Fig. 12.11). Using the unadjusted  $^{14}\text{C}$  model ages that were more than 1 ka, and calculating the He accumulation rates for samples from monitoring wells (and other narrow-screened wells), the He accumulation rates varied from 0.044 to  $7.7 \times 10^{-10} \text{ cm}^3 \text{ STP} \cdot \text{g}^{-1} \cdot \text{a}^{-1}$ . This rate can be compared to an average value of  $1.3 \times 10^{-10}$  reported by Solomon et al. (1996) [295] for a variety of sedimentary environments. Some of the samples, particularly from the west-central and central zones have very low  $^4\text{He}$  accumulation rates (Fig. 12.11) and may be in sediment that is particularly low in U and Th content (see Chapter 8). Given the observed wide variations in He accumulation rate, additional data on U and Th abundance in sediment of the Middle Rio Grande Basin, and data on He flux in the basin would be needed for application of He accumulation as a reliable age indicator in this complex hydrogeological environment.

#### 12.4.4. Hydrochemical zones

Using much of the available chemical and isotopic data, including the deuterium,  $^{14}\text{C}$  and major and minor element composition, 12 separate zones of recharge to the basin and a zone of groundwater discharge (zone 13) were recognized (Plummer et al. (2004) [49]). The hydrochemical zones (Fig. 12.12) provided insight into likely recharge sources, flow paths and aquifer properties. Zone 12 (Fig. 12.12) was determined to be water sourced from the Rio Grande. Mountain front recharge waters were identified along the northern, eastern and southern margins of the basin (zones 1, 8 and 6; Fig. 12.12). Palaeowater that entered the basin along the northern margin either as underflow (subsurface inflow) or recharge from the Jemez Mountains north of the basin margin, extends down the west-central part of the basin. It flows beneath zone 2 in the north, and beneath parts of zones 1 and 12 in the northern and central parts of the basin, as denoted by the dashed line on Fig. 12.12. The arrows (Fig. 12.12) show the inferred directions of flow based on identified source and location of hydrochemical zones. Most of the flow in the basin appears to be from north to south.

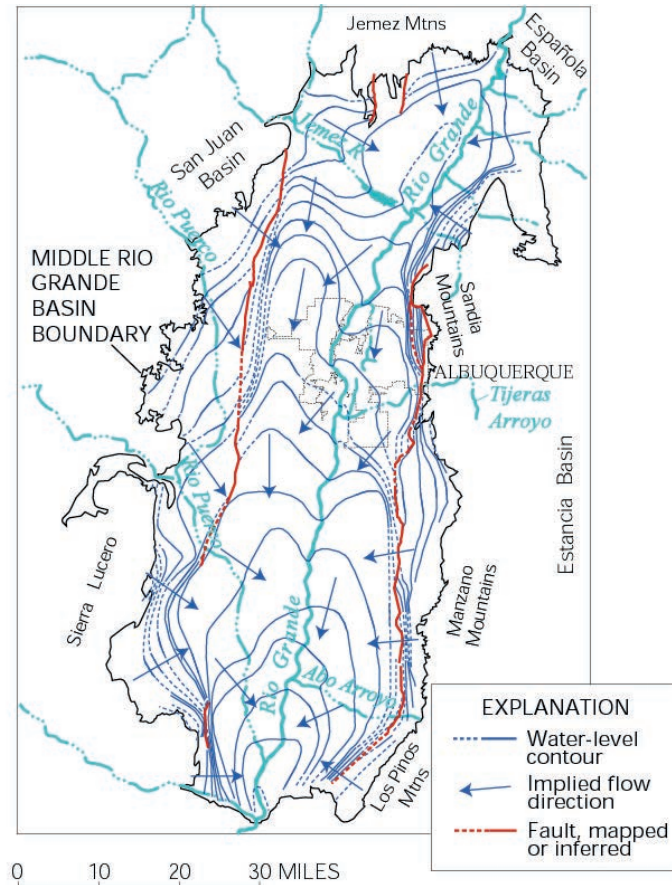


FIG. 12.13. Map showing pre-development water levels in the Middle Rio Grande Basin, inferred directions of flow based on the pre-development potentiometric surface and location of major faults (Bexfield and Anderholm (2000) [653]; Plummer et al. (2004) [49]; Plummer et al. (2004) [50]).

#### 12.4.5. Pre-development water levels

The pre-development water levels (Fig. 12.13) were constructed from water level measurements from the mid-1930s in the vicinity of Albuquerque, NM that predate groundwater production, and other sources of data throughout the basin that are representative of pre-development conditions (Bexfield and Anderholm (2000) [653]). An interesting feature of the water table surface is a groundwater trough that extends through much of the west-central part of the basin. The trough was originally observed in the early 1960s (Titus (1963) [654]). The arrows show the implied directions of groundwater flow based on the pre-development water levels.

The pre-development hydraulic-head map (Bexfield and Anderholm (2000) [653]; Bjorklund and Maxwell (1961) [655]; Titus (1961) [656]) is broadly consistent with the primary direction of groundwater flow indicated by geochemical data, but there are some apparent inconsistencies. In particular, the pre-development hydraulic heads indicate greater east–west components of flow through the centre of the basin into the groundwater trough than are suggested by the orientation of the hydrochemical zones. The differences in flow direction indicated by hydraulic heads compared with geochemical tracers are likely associated with different time horizons — the chemistry being on the 10 ka timescale and the pre-development water levels on a more recent timescale.

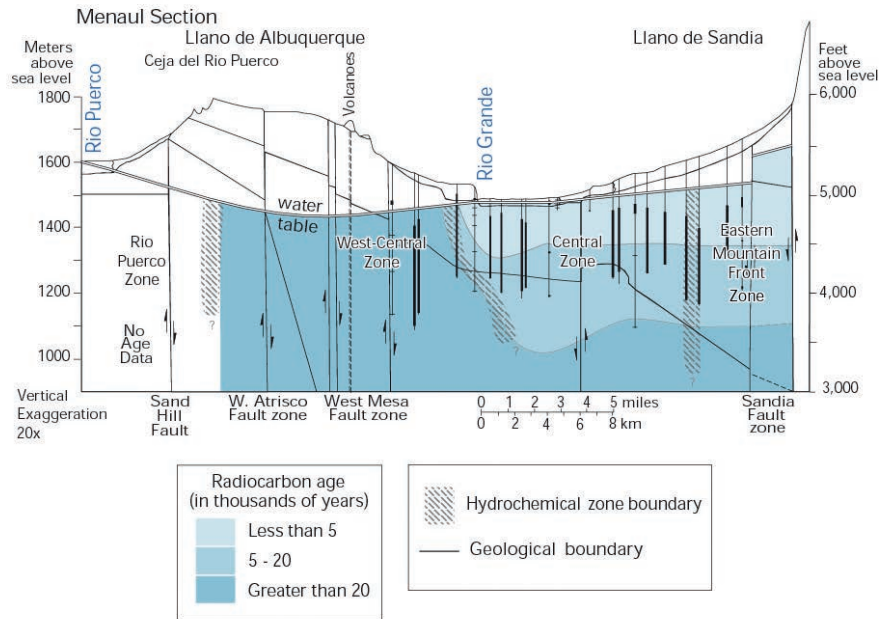


FIG. 12.14. Cross-section of the Upper Santa Fe aquifer system at Albuquerque showing ranges of  $^{14}\text{C}$  model age as a function of depth and water sources. The slanted grey patterns denote approximate locations of hydrochemical zone boundaries. The direction of groundwater flow is generally north to south, that is, out of the plane of the cross-section (see Fig. 12.2 for approximate location of cross-section; after Plummer et al. (2004) [49]).

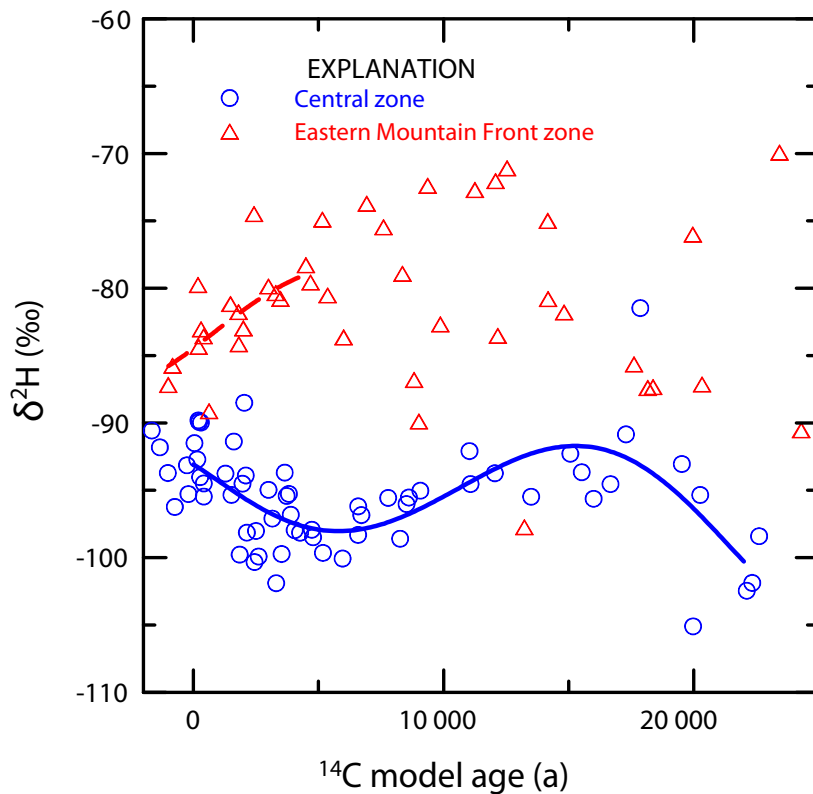


FIG. 12.15. Comparison of  $\delta^2\text{H}$  in groundwater recharged along the eastern mountain front of the Middle Rio Grande Basin and infiltration from the Rio Grande (central zone) as a function of  $^{14}\text{C}$  model age (Plummer et al. (2004) [49]; Plummer et al. (2004) [51]).

#### 12.4.6. Variations in $^{14}\text{C}$ model age with depth

A cross-section of the Middle Rio Grande Basin aquifer system through central Albuquerque, NM (Fig. 12.14; at approximately the same location as cross-section A–A' in Fig. 12.2), shows ranges of  $^{14}\text{C}$  model ages (less than 5 ka, 5–20 ka and >20 ka) in relation to water sources (hydrochemical zones).

There is a large central core of palaeo-Rio Grande water beneath Albuquerque, the base of which was not located. The boundary between water recharged along the eastern mountain front and infiltration from the Rio Grande is nearly vertical. Palaeowater of the west-central zone flows beneath palaeo-Rio Grande water under the river. Palaeowater of more than 20 ka was at the water table beneath deep unsaturated zones west of Albuquerque.

#### 12.4.7. Stable isotopes, deuterium excess and radiocarbon age

During the past 5 ka,  $\delta^2\text{H}$  of water from the central zone (Rio Grande origin) increased by nearly 6‰ from a minimum near  $-98\text{‰}$ ; and  $\delta^2\text{H}$  of moisture recharged along the eastern mountain front became more depleted in  $^2\text{H}$ , by about 7‰ (Fig. 12.15).

Most groundwater samples from the eastern mountain front zone, with radiocarbon ages greater than 5 ka BP, ranged in  $^2\text{H}$  isotopic composition from about  $-90$  to  $-70\text{‰}$  with little evidence of temporal variability (Fig. 12.15). Water recharged from the Rio Grande to the central zone apparently had a minimum  $\delta^2\text{H}$  isotopic composition at approximately 5 ka BP, reached a maximum at about 15 ka BP, but was relatively depleted in  $^2\text{H}$  at about 22 ka BP (Fig. 12.15). The changes in  $\delta^2\text{H}$  of water from the central and eastern mountain front zones during the past 20 ka were interpreted in terms of changes in palaeoclimatic conditions (Plummer et al. (2004) [49]; Plummer et al. (2004) [51]), i.e. (i) changes in temperature; (ii) changes in the balance between the amount of precipitation falling within

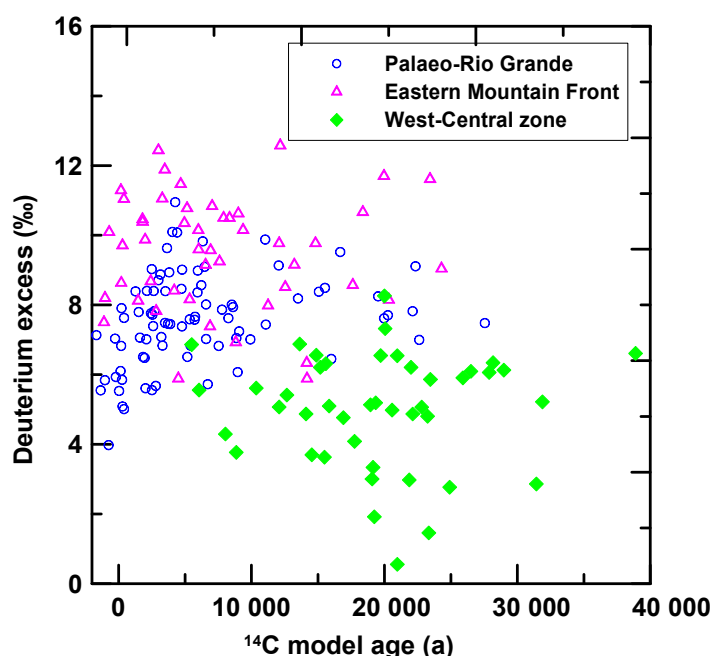


FIG. 12.16. Comparison of the deuterium excess in groundwater recharged from the palaeo-Rio Grande, water recharged along the eastern mountain front, and palaeowater from the west-central part of the Middle Rio Grande Basin as a function of  $^{14}\text{C}$  model age. Water recharged to the west-central zone during the last glacial maximum had the lowest deuterium excess and that recharged 3–5 ka BP during the mid-Holocene warm period has relatively high deuterium excess.

the basin and that falling within the mountain watershed source areas to the Rio Grande; and (iii) shifts in season of predominant runoff (snowmelt) affecting discharge within the Rio Grande. Although affected by many climatic variables, the most depleted waters in the Middle Rio Grande Basin had  $^{14}\text{C}$  model ages of about 20 ka. Similarly, the waters with the lowest recharge temperatures, based on dissolved  $\text{N}_2$  and Ar measurements, also had  $^{14}\text{C}$  model ages of about 20 ka (Plummer et al. (2004) [51]), consistent with cooling during the LGM. Therefore, the stable isotope and dissolved gas data helped to corroborate the  $^{14}\text{C}$  model ages. During the past 5 ka, the  $\delta^2\text{H}$  isotopic composition of recharge along the eastern mountain front decreased about 7‰ (Fig. 12.15), suggesting an average cooling of about 1.5°C following the mid-Holocene warm period (Plummer et al. (2004) [49]; Plummer et al. (2004) [51]). Over the same time span, the  $\delta^2\text{H}$  isotopic composition of Rio Grande water increased 5–10‰, consistent with a shift in season of peak snowmelt into the beginning of the summer monsoon season, which is again, likely a result of cooling during the past 5 ka.

In Fig. 12.16, the deuterium excess as a function of  $^{14}\text{C}$  model age for waters from three hydrochemical zones is examined: (i) the central zone, which represents palaeo-infiltration from the Rio Grande; (ii) the eastern mountain front zone, which represents mountain recharge along the eastern margin of the basin; and (iii) the palaeowaters that fill the west-central part of the basin, which may represent recharge from the Jemez Mountains north of the basin or subsurface inflow from north of the Middle Rio Grande Basin.

The deuterium excess,  $d_{\text{excess}}$  in per mille, is defined as  $d_{\text{excess}} = \delta^2\text{H} - 8 \times \delta^{18}\text{O}$ , and can be related to relative humidity (and, thus, sea surface temperature) for the oceanic source water (Jouzel et al. (1982) [657]; Merlivat and Jouzel (1979) [658]; Straaten and Mook (1983) [59]). The highest values of  $d_{\text{excess}}$  were found in waters of the eastern mountain front zone (12.6‰), and the lowest values were in waters from the west-central zone (0.6‰). The median values of  $d_{\text{excess}}$  for water from the west-central, eastern mountain front and central zones were 5.0, 9.3 and 7.2, respectively during the past 40 000 radiocarbon years. Values of  $d_{\text{excess}}$  are expected to be low during the last glacial minimum (LGM) due to lower sea surface temperature, resulting in elevated relative humidity over the oceanic source relative to today (Jouzel et al. (1982) [657]; Merlivat and Jouzel (1979) [658]; Straaten and Mook (1983) [59]), and elevated during warm periods due to lower relative humidity at the source in response to the elevated sea surface temperature. The data of Fig. 12.16 at least partially support this expectation, showing a peak in  $d_{\text{excess}}$  approximately 3–5 ka during the time of the mid-Holocene warm period, and low values of  $d_{\text{excess}}$  at approximately 20–25 ka during the LGM. This, at least qualitatively, provides further evidence in support of the  $^{14}\text{C}$  model ages.

A strong El Niño was observed in the Pacific Ocean during the period 1997–1998 (Oceanic ENSO Index of 2.5, <http://ggweather.com/enso/oni.htm>). Monthly samples of Rio Grande water collected just north of Albuquerque from December 1996 through May 1999 were analysed for stable isotope composition (Plummer et al. (2004) [49]). Values of  $d_{\text{excess}}$  increased from about 5‰ in late 1996 to 8‰ in January 1998, then fell again to about 4–5‰ in late 1998 to early 1999. Although a number of factors, including moisture source, can affect the values of  $d_{\text{excess}}$ , this correlation suggests there may be, at least in part, a connection today between  $d_{\text{excess}}$  of precipitation reaching the Middle Rio Grande Basin and sea surface temperatures in the Pacific Ocean.

#### 12.4.8. Carbon-14 model age profiles and recharge rates

In addition to providing information on spatial variations in  $^{14}\text{C}$  model age throughout the basin, the radiocarbon data help to constrain recharge-rate estimates. Along the eastern mountain front, there appear to be two different age–depth relations (Fig. 12.17). Water from the eastern mountain front zone found north of Albuquerque, or south of Tijeras Arroyo, just south of Albuquerque (red symbols), had a relatively high age gradient (approximately 6.6 a/cm) in relation to waters from the eastern mountain front zone at Albuquerque (approximately 0.4 a/cm) (blue symbols; Fig. 12.17). Apparently, over at least the past 10 ka, there was appreciably more recharge along the eastern mountain front at

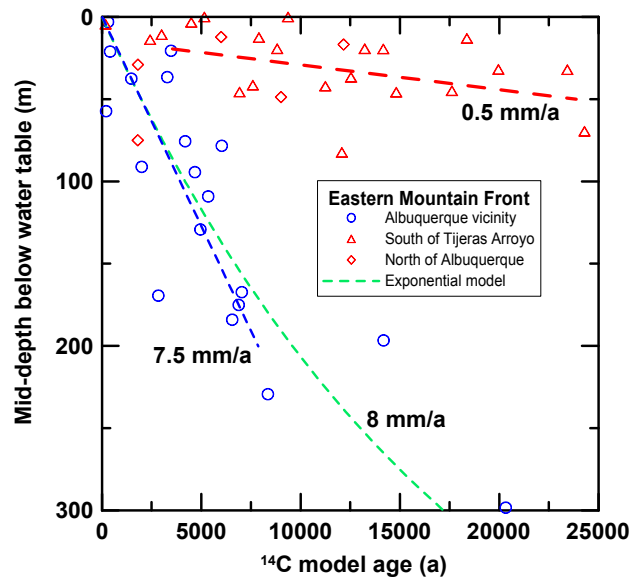


FIG. 12.17. Carbon-14 model ages of dissolved inorganic carbon in groundwater of the Middle Rio Grande Basin at Albuquerque and in areas just north and south of Albuquerque (south of Tijeras Arroyo) as a function of depth below the water table. Two depth–age gradients imply recharge rates, assuming 30% porosity, of 7.5 mm/a at Albuquerque compared to 0.5 mm/a north and south of Albuquerque. The fit to the exponential model suggests a slightly higher recharge rate, 8 mm/a, at Albuquerque. The depth–age relations can be related to lithologic and structural features along the eastern margin of the basin (Plummer et al. (2004) [49]; Plummer et al. (2004) [50]).

Albuquerque than either to the north or south of Albuquerque. Assuming a porosity of 30%, a recharge rate of 7.5 mm/a is found at Albuquerque from the linear depth–age relation (blue line) compared to 0.5 mm/a for recharge north and south of Albuquerque from the linear depth–age relation (red line). If an exponential model is fitted to the data at Albuquerque, assuming an aquifer thickness of 500 m, the recharge rate is 8 mm/a (green line). Factors that may contribute to this difference are: (i) a greater thickness of ancestral Rio Grande sands and gravels at Albuquerque than elsewhere along the eastern mountain front (Hawley and Haase (1992) [649]); (ii) the presence of structural features, including the Hubble Bench and Tijeras and Hubble Springs fault zones to the south, which place low permeability rocks at shallow depths; and (iii) higher precipitation rates along the Sandia Mountains at Albuquerque than along lower altitude portions of the eastern mountain front.

## 12.5. SUMMARY OF CHEMICAL AND ENVIRONMENTAL TRACER CONSTRAINTS ON THE FLOW SYSTEM

This study demonstrates some of the benefits of obtaining a diverse and extensive chemical and isotopic dataset when characterizing hydrological processes and tracer model age in groundwater systems and when there is a need to refine the conceptual model of the groundwater flow system. A wide range of chemical and isotopic constituents were identified in groundwater from the Middle Rio Grande Basin (Plummer et al. (2004) [49]; Plummer et al. (2004) [50]; Plummer et al. (2004) [51]). Selected results from stable isotope,  $^{14}\text{C}$ , helium and major element chemistry are summarized below.

The  $\delta^2\text{H}$  composition of groundwater in the Middle Rio Grande Basin varied regionally more than 50‰, and in combination with other chemical and isotopic constraints, allowed recognition and mapping of flow from 12 separate recharge sources to the basin, and a zone of discharge.

The boundaries between waters of different recharge sources align parallel to the general north to south direction of groundwater flow, a property of inert tracers in groundwater systems (Glynn and Plummer (2005) [15]), and are generally in agreement with regional north to south flow directions indicated by the pre-development water levels.

The chemical and isotopic patterns trace groundwater flow regionally on the timescale of the aquifer system (tens of thousands of years), but locally are inconsistent with flow directions implied by a trough in the pre-development surface through the central part of the basin. The trough in the pre-development surface is thought to be the response of the water levels to a recent lowering of recharge rate along the basin margin (see modelling section).

The stable isotope data showed that groundwater at Albuquerque is mostly derived from the Rio Grande and not from the eastern mountain front, as early groundwater models had predicted.

Carbon-14 content was highest along the eastern mountain front, along the northern margin of the basin, along the inner valley of the Rio Grande, and along other surface water sources, indicating areas of recent recharge (past several thousands of years).

In this semi-arid region, the initial  $^{14}\text{C}$  content in recharge areas was found to be near 100 pmc in pre-bomb waters (open system conditions). Geochemical mass balance calculations showed that water-rock interactions were negligible in the primarily siliciclastic sediments of the Middle Rio Grande Basin, justifying use of the unadjusted  $^{14}\text{C}$  model age. Shifts in the stable isotope composition of mountain front recharge over the past 5 ka, and of palaeo-Rio Grande water over the past 20 ka were consistent with known climate variation and support the unadjusted  $^{14}\text{C}$  model ages. Other evidence helping to corroborate the  $^{14}\text{C}$  model ages was found in recharge temperatures calculated from dissolved  $\text{N}_2$  and Ar data, and in the deuterium excess as a function of  $^{14}\text{C}$  model age.

Gradients in  $^{14}\text{C}$  model age (and inferred recharge rates) varied by more than an order of magnitude in the vicinity of Albuquerque, resulting mostly from geological factors.

The waters sampled as a part of the investigation were representative of only relatively shallow parts of the aquifer system (typically, the upper 60 m of the aquifer, though some samples were from as deep as 500 m below the water table). The lowest  $^{14}\text{C}$  content measured was 0.6 pmc and beyond the usefulness of radiocarbon as an age indicator.

Excess helium in the Middle Rio Grande Basin is dominated by a mantle source and has a remarkably uniform  $^3\text{He}/^4\text{He}$  ratio of  $1.02 \pm 0.15 \times 10^{-6}$ . Helium accumulation rates in groundwater from the Middle Rio Grande Rift vary more than two orders of magnitude and could be used only as a quasi-age indicator in the Middle Rio Grande Basin.

## 12.6. GROUNDWATER MODEL DEVELOPMENT

A groundwater flow model developed with MODFLOW (McDonald and Harbaugh (1988) [71]) was used to estimate recharge to the Middle Rio Grande Basin. Travel times to observation wells were calculated using MODPATH (Pollock (1994) [611]). The MODFLOW and MODPATH representations of the basin were calibrated using UCODE (Poeter and Hill (1998) [659]). The model domain was divided into a rectilinear grid comprised of 156 rows and 80 columns of equally spaced 1 km sized cells (Sanford et al. (2004) [47]; Sanford et al. (2004) [48]). The eastern and western model boundaries mostly were coincident with faults that either act as barriers to horizontal groundwater movement or separate areas with different thickness of permeable sediment (Kernodle et al. (1995) [651]). The vertical extent of the aquifer system was represented by nine model layers of variable thickness down to the base of the Santa Fe Group sediments at 2400 m below sea level at the deepest point.

River-cell boundaries were implemented over the width of the inner valley of the Rio Grande, and along the Jemez River and Rio Puerco to represent the groundwater/surface water interaction along those waterways. The recharge was divided into segments along the eastern and southern mountain fronts and arroyos. Several underflow segments were specified, extending the length of the northern and western model boundaries. The hydraulic conductivity zones for the basin were based on the three

dimensional geological model of Cole (2001) [647] (see also Bartolino and Cole (2002) [612]). A total of 18 hydraulic conductivity zones were defined within the groundwater flow model (Sanford et al. (2004) [47]; Sanford et al. (2004) [48]). Vertical conductances in the groundwater flow model were divided into 12 zones — the associated parameters were represented as values of vertical anisotropy. Two fault zones, representative of the Cat Mesa fault zone in the south-western part of the basin and the Sandia Fault zone along the eastern mountain front at Albuquerque, were added to the groundwater flow model as discrete (low), hydraulic conductivity zones (Fig. 12.13).

Porosity for the unconsolidated sediment of the basin was estimated from field measurements (Haneberg (1995) [660]; Stone et al. (1998) [661]) and assigned separately for the model layers, beginning with 36% for model layer 1 and decreasing 2% per layer down to 20% for layer 9.

Hydrochemical tracer data were used as a part of the calibration of the groundwater flow model. Groundwater ages obtained from  $^{14}\text{C}$  measurements were one set of these data. Simulated ages were obtained by using MODPATH to track the line of travel of a parcel of water from the observation well backwards to its recharge location. Hydrodynamic dispersion in these calculations was neglected, as the effect of dispersion on the concentrations from a nearly invariant source over a 100 km basin would be negligible for values of longitudinal dispersivity less than 1 km (Johnson and DePaolo (1996) [624]; Phillips et al. (1989) [39]).

Another source of tracer information that was used for model calibration was the delineation of the hydrochemical zones (Fig. 12.12), representing different water sources. MODPATH was used to simulate the locations of the boundaries between hydrochemical zones, which were compared to the observed locations (Fig. 12.12).

The groundwater model was calibrated using a combination of a non-linear least squares regression method as it is implemented in the computer code UCODE (Poeter and Hill (1998) [659]), and manual adjustment of individual parameters. A total of 200 hydraulic heads, 200  $^{14}\text{C}$  measurements, and the locations of two of the river water hydrochemical zones within nine hydrochemical target regions were used as observations, making a grand total of 409 observations (Sanford et al. (2004) [47]; Sanford et al. (2004) [48]). The groundwater model was first set up to simulate steady state groundwater flow prior to the development of groundwater as a resource within the basin. The head data were compiled by Bexfield and Anderholm (2000) [653] from many sources (Fig. 12.13), and the hydraulic heads from the final simulation matched relatively well with the observed heads (Sanford et al. (2004) [47]; Sanford et al. (2004) [48]).

Values for hydraulic conductivities were calibrated to values mostly between  $3 \times 10^{-6}$  and  $3 \times 10^{-5}$  m/s, and were similar to estimates from previous models (Kernodle et al. (1995) [651]; McAda and Barroll (2002) [662]; Tiedeman et al. (1998) [663]) and prior field measurements concerning the basin-fill material (Thorn et al. (1993) [21]). The anisotropy ( $K_v/K_h$ ) was calibrated for 12 individual zones within the basin, and the calibrated values all ranged between  $1 \times 10^{-4}$  and  $1 \times 10^{-2}$ . These values are consistent with what might be expected for a layered aquifer system where the individual layers are isotropic and have hydraulic conductivity values that vary by two to four orders of magnitude.

During each of the time steps, all recharge and underflow boundary cells were multiplied by a single coefficient. These coefficients, or multipliers, were all given an initial value of 1.0 to reproduce the conditions in the steady state simulation. The multiplier for each time step was then adjusted until an optimum fit was obtained between the measured and simulated observations. The non-linear regression routine in UCODE was initially used to reduce the total sum of the squared errors, but eventually the individual recharge multipliers were adjusted manually to obtain the ‘best-fit’ multiplier values.

The observed hydraulic heads are strongly correlated with the simulated heads along the 1:1 line (Fig. 12.18(a)), but the observed  $^{14}\text{C}$  pmc values show a substantially greater amount of scatter about the 1:1 line compared to the simulated values (Fig. 12.18(b)). This poorer fit to the  $^{14}\text{C}$  data than to the head data results from the fact that the heads represent a smoothly varying potential field that can be fitted without much difficulty to the solution of the flow equation, but the groundwater ages are

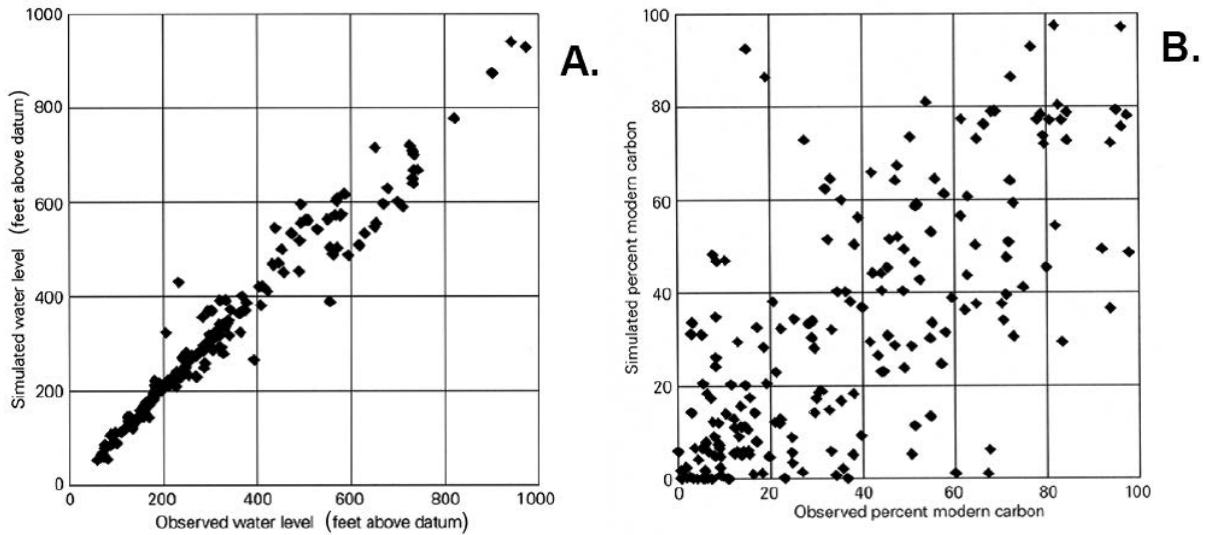


FIG. 12.18. Comparison of (a) observed and simulated hydraulic heads, and (b) observed and simulated  $^{14}\text{C}$  values in per cent modern carbon (Sanford et al. (2004) [47]; Sanford et al. (2004) [48]).

a function of velocities that are, in turn, a function of the first derivatives of the groundwater potential field and, thus, are more difficult to fit.

This difficulty in matching observed and simulated  $^{14}\text{C}$  values exists because, although the travel time to a point in the aquifer is an integration of the upstream velocity field, errors in calculated velocities can accumulate down a flow path. In addition, multiple source areas in the Middle Rio Grande Basin (Fig. 12.12) create age patterns within the basin that are discontinuous (Fig. 12.19), increasing further the complexity and difficulty in fitting the age related simulations to observations. The multiple sources of water in the Middle Rio Grande Basin create numerous flow divides. These divides often have very sharp gradients in age across them and are difficult to match exactly, increasing the scatter in simulated versus observed  $^{14}\text{C}$  model ages.

The final model configuration reproduced the groundwater trough that extends north to south through the west-central part of the basin, although not as far north as some of the measured water levels indicate (Fig. 12.13). Earlier models (e.g. Kernodle et al. (1995) [651]) did not manage to reproduce this feature. Attempts were also made by Tiedeman et al. (1998) [663] to investigate different conceptual models of what was creating the trough, including a high permeability zone or a north–south trending fault. Sanford et al. (2004) [48], however, demonstrated that by lowering the basin boundary recharge in the model, the aquifer system changed from one dominated by the movement of water from the boundaries towards the Rio Grande to one dominated by water leaking from and back into the Rio Grande. The latter conceptual system results in heads to the west of the Rio Grande that are lower than the river, and is consistent with the presence of the trough and the relatively low recharge values estimated with the model. The final model configuration also reproduces the section of the Rio Grande that loses water into the aquifer, just north of Albuquerque (Fig. 12.13). Additional details of the groundwater flow model and calibration procedure are given in Sanford et al. (2004) [47], Sanford et al. (2004) [48] and Plummer et al. (2004) [51].

From the water level contours (Fig. 12.13), one can see that groundwater moves away from the Rio Grande, both to the west towards the trough, and to the south beneath Albuquerque, as is also shown by the pre-development water table map (Fig. 12.13). This zone of Rio Grande water beneath the city of Albuquerque is also corroborated by the hydrochemical zone delineation (Figs 12.12 and 12.14).

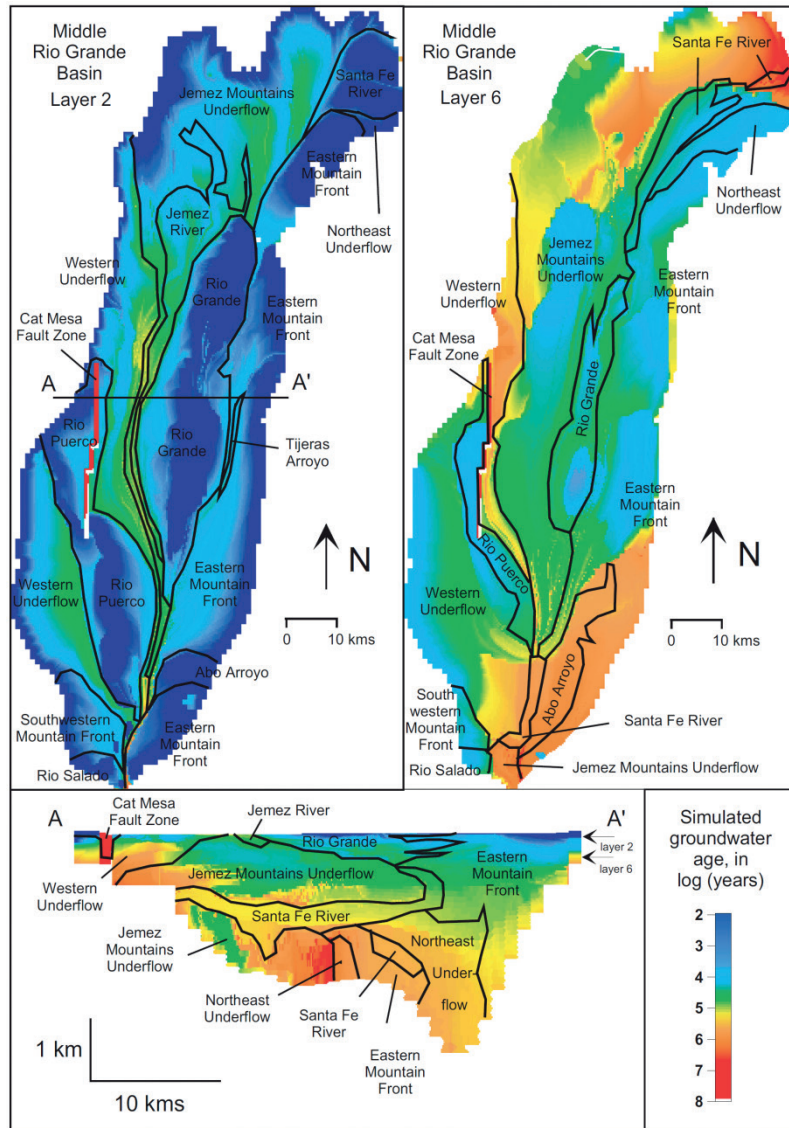


FIG. 12.19. Simulated groundwater flow model ages at relatively shallow depths (50–100 m, model layer 2) and deeper depths (300–500 m, model layer 6). Simulated hydrochemical zones (source areas) are delineated by black lines and labelled (Plummer et al. (2004) [51]; Sanford et al. (2004) [47]; Sanford et al. (2004) [48]).

Simulated groundwater flow model ages are shown in Fig. 12.19 for two of the model layers. Young water (<math>< 3000</math> a), represented by the dark blue areas in layer 2, is present near the mountain fronts where recharge occurs at the land surface, and along the Rio Grande and Rio Puerco near where the rivers are losing water to the aquifer system. Flow model ages in layer 6 at depths of 300–500 m below the water table are shown in the right panel of Fig. 12.19. A cross-section of the simulated ages reveals a general pattern of increasing simulated age with depth, but the heterogeneity of the system in some places creates local inversions where old water is simulated above younger water moving through a more permeable zone. The hydrochemical zones were also simulated with MODPATH, using source area delineation of path lines, as shown in Fig. 12.19.

Recharge was not specified directly for the Rio Puerco and the Jemez River in the model, but was calculated through their riverbed conductance values. The calculated recharge rates were  $0.14 \text{ m}^3/\text{s}$  for the Rio Puerco and  $0.01 \text{ m}^3/\text{s}$  for the Jemez River (Plummer et al. (2004) [51]; Sanford et al. (2004)

[47]; Sanford et al. (2004) [48]). The recharge for the Rio Puerco was similar to values used in earlier models, but the Jemez River recharge value was much lower. Recharge from the eastern mountain front was estimated to be 0.33 m<sup>3</sup>/s, with 0.04 m<sup>3</sup>/s of additional recharge from Abo Arroyo. These numbers are appreciably lower than previous estimates that were based on rainfall–runoff equations (Kernodle et al. (1995) [651]), but are similar to estimates of recharge of 0.35 and 0.05 m<sup>3</sup>/s along the eastern mountain front and Abo Arroyo and vicinity, respectively, made from a field study of chloride mass balance (Anderholm (2001) [664]). McAda and Barroll (2002) [662] created a groundwater flow model of the basin partially incorporating preliminary results from this study. They used a combination of some higher recharge values used in the earlier studies, and lower values estimated by Anderholm (2001) [664], Sanford et al. (2004) [47] and Sanford et al. (2004) [48].

Total recharge to the basin was estimated by Sanford et al. (2004) [47] and Sanford et al. (2004) [48] to be 2.14 m<sup>3</sup>/s, with 0.78 m<sup>3</sup>/s of the total attributed to infiltration from the Rio Grande. The basin-margin recharge estimated from the model, 1.37 m<sup>3</sup>/s, is one fourth of the 5.45 m<sup>3</sup>/s estimate used in the Kernodle et al. (1995) [651] model and one half of that used by McAda and Barroll (2002) [662]. Overall, the lower recharge values are consistent with the presence of the groundwater trough and zone of Rio Grande water in the central basin. McAda and Barroll (2002) [662] partially reproduced these features by adding N–S trending fault barriers in the centre of the basin.

## 12.7. REFINING CONCEPTUALIZATION OF GROUNDWATER FLOW IN THE BASIN

Some of the results of Plummer et al. (2004) [49], Plummer et al. (2004) [50], Plummer et al. (2004) [51], Sanford et al. (2004) [47] and Sanford et al. (2004) [48] helped change conceptualization of groundwater flow in the Middle Rio Grande Basin.

The Kernodle et al. (1995) [651] model obtained a modern basin-scale recharge rate of 5.45 m<sup>3</sup>/s, which was mostly derived from mountain front and arroyo recharge, with no net recharge from the Rio Grande. In comparison, the Sanford et al. (2004) [47] and Sanford et al. (2004) [48] model found a basin-scale recharge rate of 2.14 m<sup>3</sup>/s, which is only about 39% of the previous model, with mountain front recharge at Albuquerque only about 20% of the previous model. Further, the Sanford et al. model shows that there is much more recharge from the Rio Grande than previously thought (36% of the basin recharge is from the Rio Grande). From a water management perspective, the results show that there is even less modern recharge to the aquifer in the vicinity of Albuquerque than previously thought (Fig. 12.20). The Sanford model benefited from the revised hydrogeological data for the basin, and was calibrated using water levels, the determined <sup>14</sup>C model ages and locations of hydrochemical zone boundaries. The pie areas in Fig. 12.20 are in proportion to the modelled modern basin-wide recharge rate: (a) 5.45 m<sup>3</sup>/s; (b) 2.14 m<sup>3</sup>/s.

The Sanford et al. model and hydrochemical data show that groundwater flow paths are generally parallel to the Rio Grande, rather than perpendicular, near the eastern mountain front, and especially beneath Albuquerque.

Most of the locations of the hydrochemical zones are consistent with the pre-development surface, but the groundwater trough is not, and may represent a recent lowering of recharge along the basin margins.

Steep gradients in <sup>14</sup>C model age with depth indicate most flow occurs in upper parts of the aquifer (large vertical anisotropy); spatial differences in <sup>14</sup>C model age gradients indicate differences in geological and hydrological conditions. A recharge rate of 3 cm/a was found along the mountain front at Albuquerque and beneath the Rio Grande at Albuquerque.

There appear to be relatively large amounts of groundwater inflow into the northern part of the basin, either under or from the Jemez Mountains.

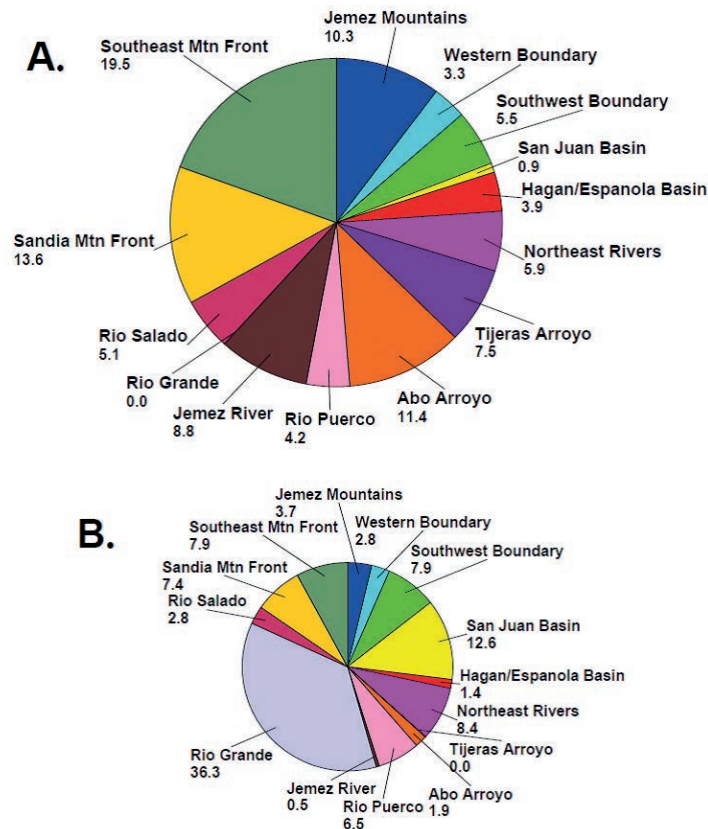


FIG. 12.20. Pie diagrams showing modelled quantities of recharge to the Middle Rio Grande Basin, in per cent of each source to the total modelled basin recharge. (a) Kernodle et al. (1995) [651] show a MODFLOW model using an earlier hydrogeological framework, pre-development water levels and assumed mountain front recharge rates that did not account for evapotranspiration. (b) Sanford et al. (2004) [47] and Sanford et al. (2004) [48] is based on a MODFLOW–MODPATH calibration procedure using inverse modelling with UCODE.

## 12.8. PALAEORECHARGE RATES

Finally, a transient groundwater flow simulation was performed using twelve 2500 a time steps (Plummer et al. (2004) [51]; Sanford et al. (2004) [47]; Sanford et al. (2004) [48]) to investigate the effect of time-varying recharge rates over the past 30 ka. Results from the transient simulation indicate that recharge was greater before 15 ka ago than today. The optimal values for the recharge multipliers are greater than ten for the period between 20 ka and 25 ka BP. Evidence for a wetter climate during this period is present in the Estancia Basin, just east of the Sandia Mountains, in the form of playa lake deposits (Allen and Anderson (2000) [665]; Bachhuber (1992) [666]). Although precipitation may have increased by a factor of approximately 2.5 during the LGM relative to today (Thompson et al. (1999) [667]), a small percentage increase in rainfall in arid regions can easily lead to a much larger percentage increase in recharge. The palaeorecharge rates from the transient simulation were accompanied by high degrees of uncertainty. Underflows ten times modern rates would also require hydraulic gradients ten times greater, and this rate is highly unlikely, if not physically impossible in some regions. In addition, vertical transverse dispersivity likely contributes additional  $^{14}\text{C}$  to some older waters of the basin, leading to ages that are younger than advective travel times and, in turn, higher palaeorecharge rates. The highest values of palaeorecharge predicted should, therefore, be seen as maximum rates, and likely greater than the actual rates. The results consistently point to an amount of recharge just before or at the beginning of the Holocene that was lower than modern values.

## 12.9. CONCLUDING REMARKS

The overall lesson from the Middle Rio Grande Basin study is that geochemical and isotopic data were of considerable value in refining the conceptual model of groundwater flow and improving the calibration of numerical models of groundwater flow in the basin. The model was improved by new hydrogeological data collected as a part of this study. The modelling exercise is viewed as an iterative process of data gathering and model refinement (as discussed in Chapter 2).

### **Acknowledgements**

This chapter was improved by technical reviews from A. Suckow, P. Aggarwal and R. Purtschert. Any use of trade, product or firm names is for descriptive purposes only and does not imply endorsement by the US Government.



## Chapter 13

### METHODS FOR DATING VERY OLD GROUNDWATER: EASTERN AND CENTRAL GREAT ARTESIAN BASIN CASE STUDY

T. TORGERSEN  
Department of Marine Sciences,  
University of Connecticut,  
Groton, Connecticut,  
United States of America

#### 13.1. INTRODUCTION

The Great Artesian Basin extends across  $1.7 \times 10^6$  km<sup>2</sup> or one fifth of the Australian continent. Annual rainfall ranges from 100 mm in the arid western parts to a maximum of 600 mm near the main recharge areas along the eastern basin margin. Average annual runoff is less than 10 mm and generally less than 5 mm. Ephemeral rivers dominate the land surface of the basin, except for a few perennial rivers in the most northern, tropical parts of the region. Most interior rivers drain into Lake Eyre (a dry salt pan at 12 m below sea level); however, the river waters often evaporate or infiltrate before reaching Lake Eyre because of the long distances. With little or no surface water present in the dry, hot and harsh climate of Australia's interior, the ability of the early settlers to explore and exploit the resources of this region were limited.

Artesian water was discovered in this vast interior region in the late 1870s and eventually most of the 4700 flowing artesian waterbores were drilled into the artesian aquifers in the Cadna-owie Formation and Hooray Sandstone aquifers, the main exploited confined aquifers in the Lower Cretaceous–Jurassic sedimentary sequence (Habermehl (1980) [668]; Habermehl (2001) [669]). In addition, the overlying Cretaceous aquifers are tapped by 20 000 pumped waterbores. This degree of exploitation led to a significant drawdown of the artesian groundwater levels and by 1970–2000, only 3100 wells remained flowing under artesian pressure and many of the artesian bores which ceased flowing were pumped, usually by windmills (Habermehl (1980) [668]; Radke et al. (2000) [670]). Recent estimates of the artesian groundwater in storage in the Great Artesian Basin ( $8.70 \times 10^{12}$ – $1.0 \times 10^{15}$  m<sup>3</sup>) make it one of the largest artesian aquifers in the world (Radke et al. (2000) [670]). Investigations including the geology, groundwater hydrology and borehole measurements have been conducted since the early 1900s, but a significantly increased scientific effort has been in effect beginning in the early 1970s to understand the hydrogeology, hydrodynamics, hydrochemistry and isotope hydrology characteristics of this system, as well as its recharge, discharge and groundwater movement.

In the following sections, a case study is developed to demonstrate how the Eastern and Central Great Artesian Basin was studied, quantified and evaluated. This case study deals predominantly with the structure and components of the scientific study of very old groundwater and places this in a logical framework, so that the knowledge, precedents and the lessons of the Great Artesian Basin can be applied to other systems.

The Great Artesian Basin comprises multiple subsystems or three sedimentary basins which are hydraulically connected, the Eromanga, Surat and Carpentaria Basins (Fig. 13.1), with each system subject to differing developmental pressures as well as unique recharge flow and discharge conditions. Jack (1923) [671] recognized the convergence of two separate flow systems near longitude 138°E characterized by high alkalinity waters from the east and high sulphate waters from the west. In this case study, the focus will be on the primary, long timescale flow within the Central Eromanga Basin portion of the Great Artesian Basin. The primary groundwater use in the Central Eromanga Basin is the pastoral industry, with an emphasis on cattle for beef and sheep for wool. Additionally, the artesian

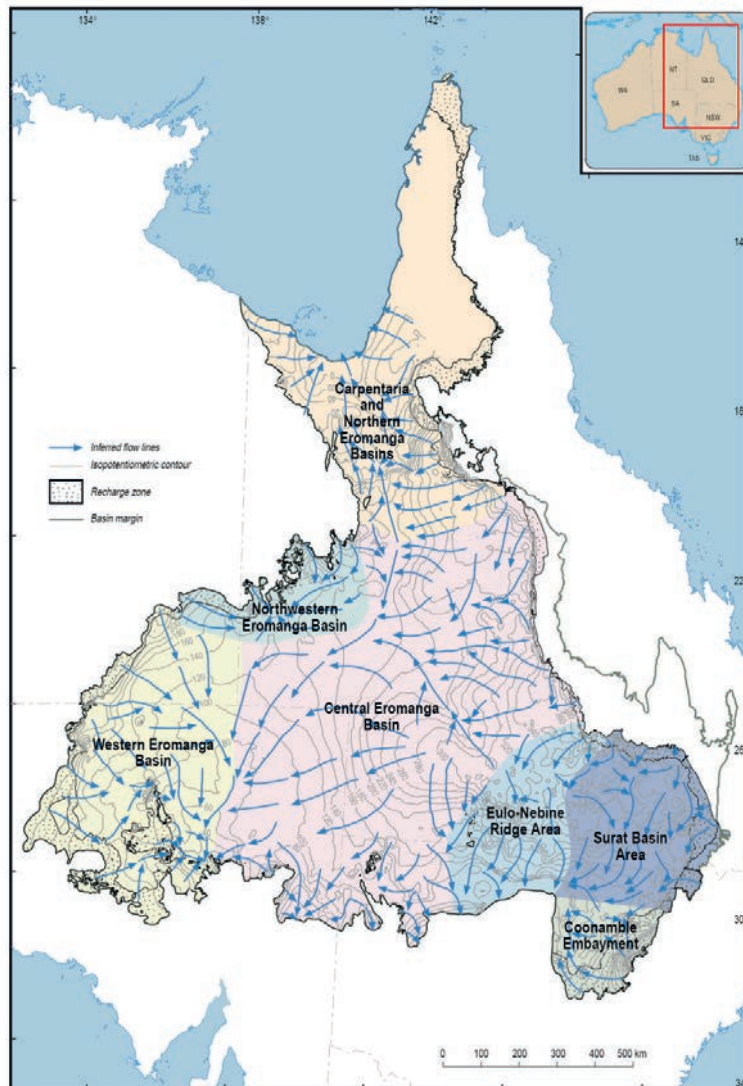


FIG. 13.1. The Great Artesian Basin of Australia (from Radke et al. (2000) [670]). The basin is composed of several sub-basins that are both hydrologically and structurally identifiable. The recharge areas, the reconstructed 1880 potentiometric surface and the inferred flow directions are also shown.

groundwater is also the vital supply for town water and homesteads, and for the petroleum (since the 1960s) and mining (since the 1980s) industries. The driving economics of the Basin are utilization of a sustainable resource, with conservation, rehabilitation and/or removal of some waterbores. As the artesian groundwater in this part of the Great Artesian Basin has some of the longest flowlines and some of the slowest flow rates, it provides an end member for the application, analysis and evaluation of methods for dating very old groundwater.

Habermehl (1980) [668], Habermehl (2001) [669], and Habermehl and Lau (1997) [672] set the stage for detailed scientific investigations of the Great Artesian Basin system and the individual studies discussed below. The discussion in the following sections is largely an overview of the information contained within the individual studies with a historical context to elucidate how dating methods and field sampling were guided by existing information. The reader is referred to these primary literature sources for greater detail. Radke et al. (2000) [670] provide details about the field sampling and detailed interpretations of the combined geological, hydrogeological, hydrodynamics, hydrochemical, radiochemical and isotopic analyses, and is an example of how information can be combined, integrated and utilized for the fullest understanding of very old groundwater basins.

### 13.2. DEPOSITION, STRUCTURE AND HYDROGEOLOGY OF THE EASTERN GREAT ARTESIAN BASIN

The primary deposition of the sediments comprising the aquifers and the aquitards of the Great Artesian Basin began with an intracratonic downwarp (Shaw (1990) [673]; Veevers (1984) [674]) of the eastern Australian continent. During Jurassic–Cretaceous (200–100 Ma) time, fluvial and fluvio-lacustrine sediments were deposited in the three constituent sedimentary basins of the Great Artesian Basin (the Eromanga, Surat and Carpentaria Basins; Senior et al. (1978) [675]), as a result of drainage from the east, west and south. Rising sea levels in the early Cretaceous deposited shallow marine sediments over much of the previous fluvio-lacustrine sequences from the north with maximum marine inundation around 120–110 Ma (Struckmeyer and Brown (1990) [676]). Major uplift of the continent commenced around 95 Ma ago and reached 200 m over a time span of 110–60 Ma (Gurnis et al. (1998) [677]). These fluvio-lacustrine and marine sediments were converted to a hydrogeological groundwater system by regional uplift along the eastern margins of the continent between 10–15 Ma (Senior and Habermehl (1980) [678]) and 5 Ma ago (Toupin et al. (1997) [679]). The eastern margin of the present Great Artesian Basin was marked by Jurassic and Cenozoic volcanism (Duncan and McDougall (1989) [680]). The present hydrogeological structure of the Great Artesian Basin is shown in Fig. 13.2.

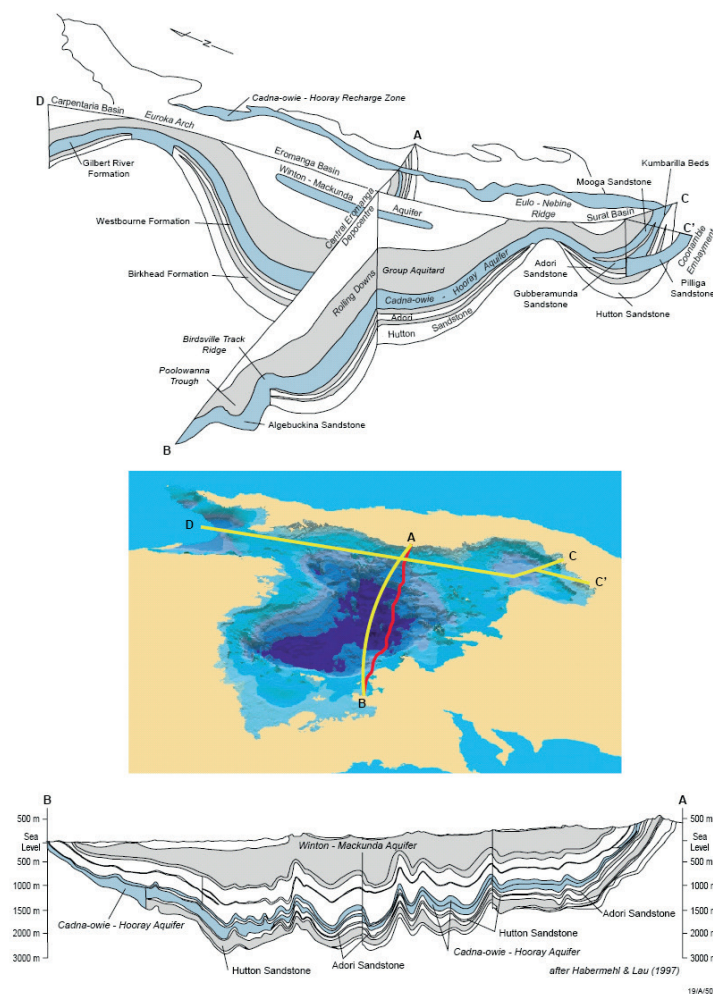


FIG. 13.2. The regional geological and hydrogeological structure of the Great Artesian Basin of Australia (from Radke et al. (2000) [670]). It should be noted that north is to the left.

This hydrogeological history is important in the subsequent evaluation because the residence times of groundwaters in the Great Artesian Basin (of the order of 1 Ma) may or may not have had time to flush connate waters from the aquifers in the Cadna-owie Formation and Hooray Sandstone, and/or from the overlying marine and continental connate waters in the Cretaceous aquifers. Secondly, because Cenozoic volcanism was common along the eastern margin of the Great Artesian Basin, specific locales have been ‘spiked’ with components representing contact with the volcanic centres including low  $^{87}\text{Sr}/^{86}\text{Sr}$  groundwater (Collerson et al. (1988) [681]) and high  $^3\text{He}/^4\text{He}$  ratios (Torgersen et al. (1987) [682]).

After the uplift of the eastern margins, it is likely that Australia was latitudinally positioned to benefit from coastal rains in summer along the north-east slopes of the Great Dividing Range that include parts of the eastern recharge zone as well as monsoon rains that provide precipitation for the main recharge areas on the western slopes of the Great Dividing Range and that can penetrate deeper into the arid continental interior. The palaeoclimatic records of Lake Eyre (Magee et al. (2004) [683]) and the fluvial records of the interior (Nanson and Price (1999) [684]; Nanson et al. (1992) [685]) suggest a clear trend towards aridity from 130 ka to the present. The analysis of Torgersen et al. (1985) [686] and Torgersen et al. (1988) [687] suggests that Pleistocene–Holocene climates in the Gulf of Carpentaria region (northern parts of the Great Artesian Basin) were similar to the present.

### 13.3. SETTING THE STAGE

The synthesis of Habermehl (1980) [668] summarized the geology and hydrogeology of the Great Artesian Basin, its primary aquifers and its fundamental chemical characteristics. Hydraulic conductivities of the aquifers are found to be generally in the range of 0.1–10 m/d with transmissivities

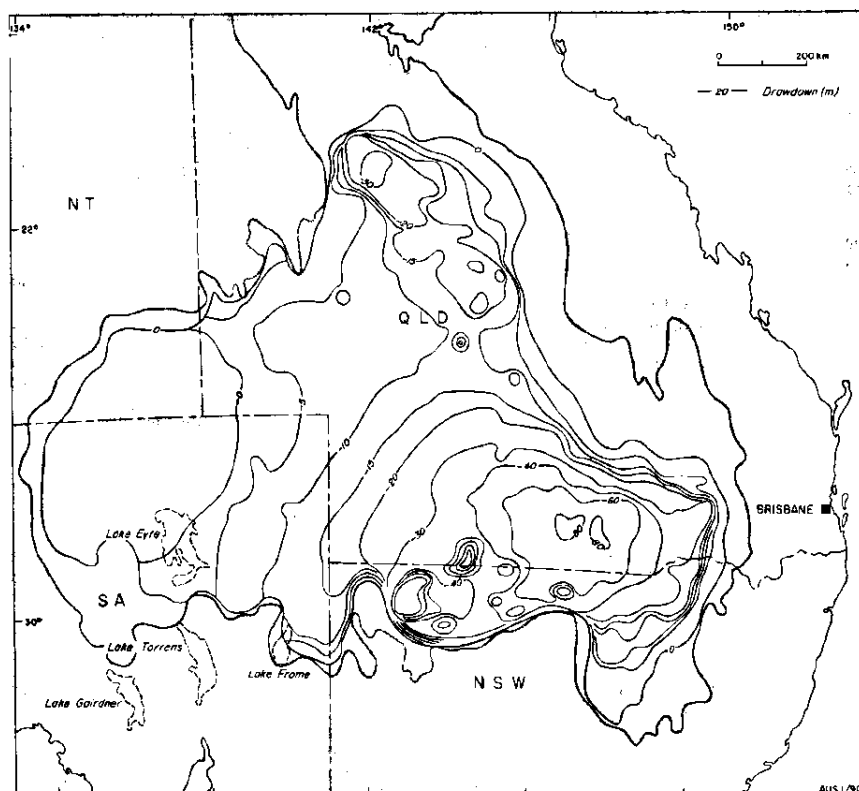


FIG. 13.3. Regional drawdown (m) of the potentiometric surface of the Cadna-owie–Hooray aquifer following development during the period 1880–1970 (from Habermehl (1980) [668]; copyright Commonwealth of Australia).

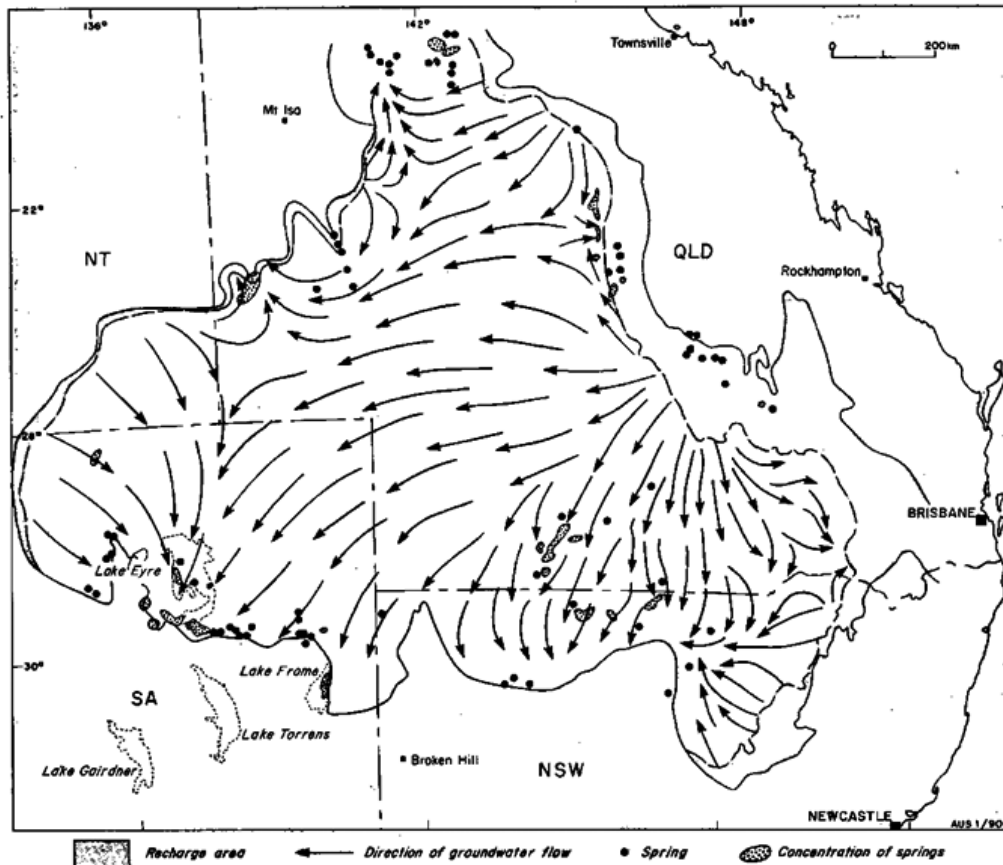


FIG. 13.4. Recharge, natural spring discharge areas and directions of regional groundwater flow in the primary Cadna-owie–Hooray aquifer of the Great Artesian Basin based on 1980 data sources (from Habermehl (1980) [668]; copyright Commonwealth of Australia). These inferred flowlines were used to guide the sampling locations for the 1982 and 1985 fieldwork (should be compared with Fig. 13.1).

on the order of 1–2000 m<sup>2</sup>/d. Artesian pressure heads had been mapped and the 1970 potentiometric contours defined the drawdown of potentiometric head and the loss of storage relative to the reconstructed 1880 (pre-development) potentiometric head (Fig. 13.3). This reconstruction and the bore-measured hydraulic conductivities enabled the numerical groundwater flow model of Seidel (1980) [688]; and the interpretation and definition of artesian groundwater flow directions (Fig. 13.4) and estimates of flow velocities for broad sections of the Great Artesian Basin. Regional scale applications of the model were developed (Habermehl and Seidel (1979) [689]), and model application and calibration were reported in Seidel (1980) [688]. Subsequent updates of artesian groundwater flow models have preserved these basic characteristics while defining details. The basic bidirectional artesian groundwater flow pattern that defines the eastern and central Great Artesian Basin from the western Great Artesian Basin was confirmed by the distribution of water chemistry types and confirmed the preliminary analysis of Jack (1923) [671] and in more detail by Habermehl (1986) [690]. The original hydrodynamic model of Seidel (1980) [688] was subsequently replaced by (steady state and transient) MODFLOW models described by Welsh (2000) [691], Welsh and Doherty (2005) [692], and Welsh (2006) [693].

#### 13.4. STABLE ISOTOPE AND <sup>14</sup>C MEASUREMENTS

Airey et al. (1979) [578] reported stable isotope (<sup>2</sup>H, <sup>18</sup>O) measurements from bores within the eastern part of the Great Artesian Basin and showed that the composition was consistent with

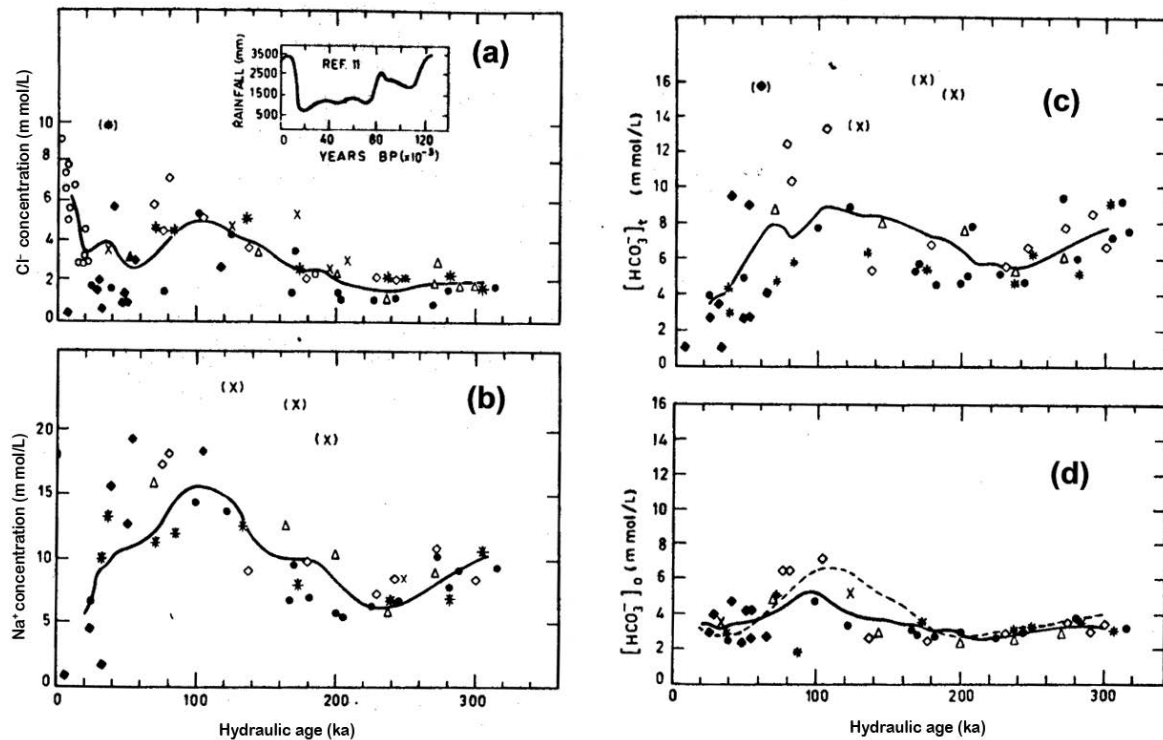


FIG. 13.5. Chemical profiles along multiple flowlines within the Central Eromanga Basin of the eastern Great Artesian Basin. (a) Chloride, (b) sodium, (c) bicarbonate, (d) initial bicarbonate based on a <sup>13</sup>C balance. The solid lines indicate 8-point moving averages of all wells except those in parentheses. Differing symbols represent various flowlines within the central Eromanga Basin. The insert in part (a) shows the variation of rainfall for the region over the past 120 ka. These data (from Airey et al. (1979) [578]) provided guidance for 1982 fieldwork.

a rainwater source and minimal interaction with the host rock. The minimal variation in the stable isotope ratios along apparent flowlines indicated a minimal climate signal over the timescale represented by the transect and the time interval allowed by the bore spacing. Transects of Na, Cl and HCO<sub>3</sub> indicated some co-variation down flowlines (Fig. 13.5) that may or may not have resulted from rainfall variations (Kershaw (1978) [694]; Kershaw (1994) [695]; Kershaw and Nanson (1993) [696]). Carbon-13 ratios were shown to co-vary with HCO<sub>3</sub> (Calf and Habermehl (1984) [697]). This variation was interpreted as a two-component system where HCO<sub>3</sub> introduced during recharge increasingly reacts with and is diluted by dissolved CaCO<sub>3</sub> of marine origin along the flow path.

### 13.5. THE 1982 FIELDWORK: STANNUM TO INNAMINCKA AND BONNA VISTA TO THARGOMINDAH

The above studies set the stage for the fieldwork in the Great Artesian Basin in 1982 which focused on sampling bores located along artesian groundwater flowlines (Fig. 13.6) identified by the potentiometric head and previous chemistry and stable isotope profiles. This field effort included sampling for <sup>14</sup>C, <sup>36</sup>Cl and <sup>4</sup>He that had the potential to quantify groundwater ages and flow rates within the eastern and central Great Artesian Basin in addition to chemistry and stable isotopes.

Stable isotope measurements from the 1982 fieldwork (Airey et al. (1983) [363]; Calf and Habermehl (1984) [697]) confirmed flowlines inferred from potentiometric heads (Habermehl (1980) [668]) (Fig. 13.7). Specifically, the deuterium contours show tongues of isotopically heavier water (Airey et al. (1983) [363]) that are consistent with those flow directions. Numerous <sup>14</sup>C samples collected

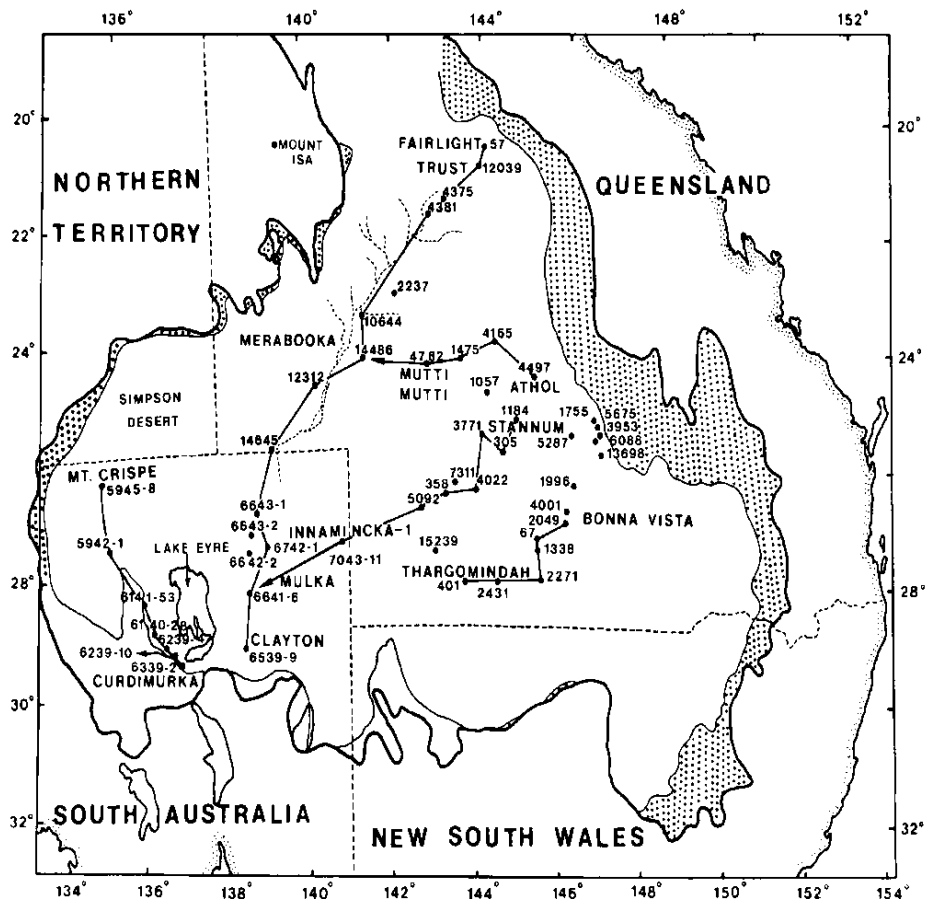


FIG. 13.6. Sampling locations and bore numbers for both the 1982 and the 1985 fieldwork. Discussion of flowline evolution is typically discussed in terms of first and last waterbore (from Torgersen et al. (1992) [698]).

along the flowlines near the recharge areas confirmed the presence of relatively young groundwaters (for the Great Artesian Basin) that contained measurable modern carbon (>1%; Calf and Habermehl (1984) [697]). The transects of  $^{13}\text{C}$  generally confirmed flow directions inferred from the reconstructed potentiometric surface when the effects of increasing down gradient dissolution of marine carbonates identified in earlier work (Airey et al. (1979) [578]) were included. Bentley et al. (1986) [301] tested the  $^{36}\text{Cl}$  groundwater dating method and developed its potential. Extensive  $^{14}\text{C}$  samples taken in and near the recharge area were used to define the initial condition for  $^{36}\text{Cl}$  within the confined portion of the basin. Hydrological ages were used to select bores to define the recharge condition for  $^{36}\text{Cl}$ ;  $^{14}\text{C}$  was used to confirm the appropriateness of those bores.

The evaluation by Bentley et al. (1986) [301] of the  $^{36}\text{Cl}$  samples taken in 1982 identified dissolution of 'dead' Cl (presumably from ancient marine deposits) and/or addition of Cl from other sources to be a significant diluent for  $^{36}\text{Cl}$ . Consequently,  $^{36}\text{Cl}$  ages are calculated by one of three end member equations. The comparison in Fig. 13.8 generally confirms the validity of the hydraulically calculated groundwater ages through the calculation of the isotope tracer ages. It is noted, however, that the interpreted  $^{36}\text{Cl}$  tracer ages do not account for mixing of waters via flow convergences and it is noted that the artesian groundwater flowlines used for the 1982 expedition were specifically selected to minimize flow convergence.

The helium isotope collection of 1982 sought to verify the potential for  $^4\text{He}$  dating of groundwater as proposed by, for example, Davis and De Wiest (1966) [699] and within the background of work that had already been conducted (Andrews (1977) [536]; Andrews and Lee (1979) [577]; Heaton and Vogel (1979) [700]; Marine (1976); Marine (1976) [701]; Torgersen (1980) [535]). Torgersen and Clarke

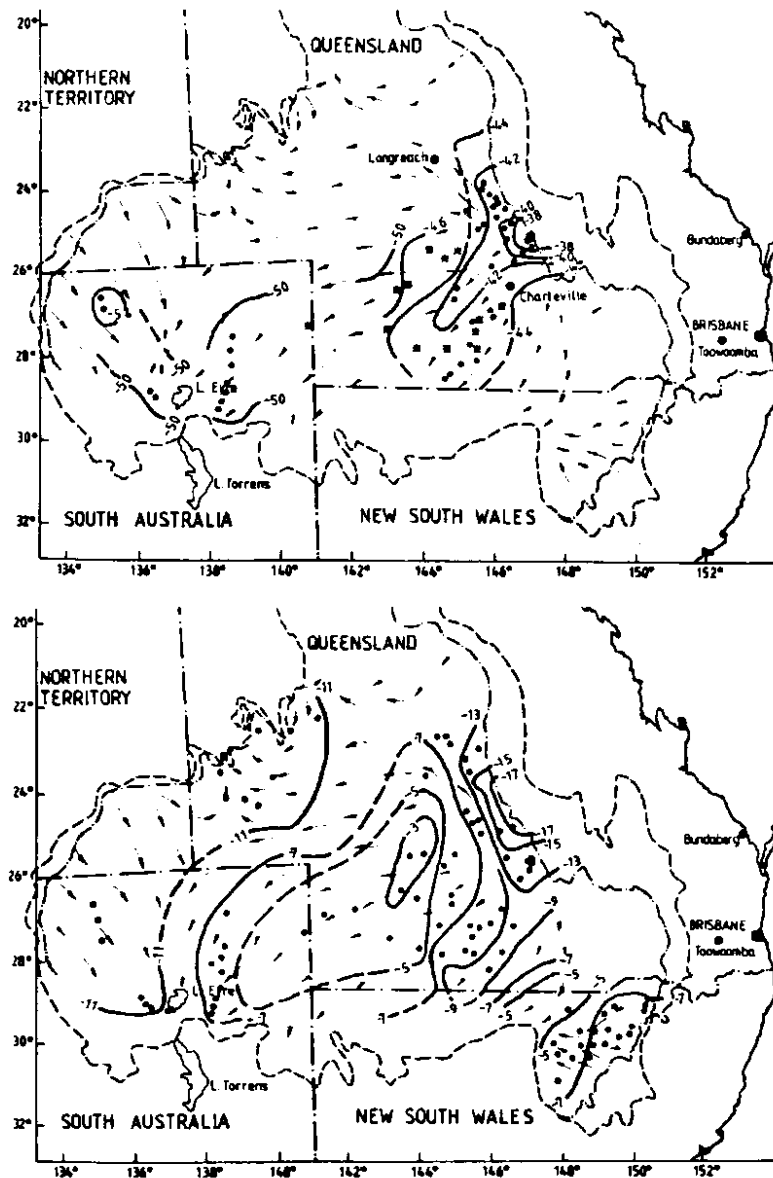


FIG. 13.7. Contours of deuterium isotopes (top) show a tongue of isotopically heavy water following the trends in flow directions seen in Fig. 13.4. Contours of  $^{13}\text{C}$  isotopes (bottom) reflect the trend in flow directions and the dissolution of marine carbonates (from Airey et al. (1983) [363]).

(1985) [293], working with knowledge that the apparent hydraulic groundwater ages had been confirmed by  $^{36}\text{Cl}$  measures, showed that (relatively) 'young' groundwaters of the Great Artesian Basin increased their  $^4\text{He}$  concentration at a rate that was consistent with a  $^4\text{He}$  source derived from local sources within the aquifer sandstones. However, further along flowlines in 'older' groundwaters, the rate at which  $^4\text{He}$  increased was up to 74 times the rate of in situ production (Fig. 13.9). Measurements of  $^{222}\text{Rn}$  in the 1982 groundwater samples showed no significant increase in the  $^{222}\text{Rn}$  activity in the older portion (high  $^4\text{He}$  flux region) of the flowline and, thus, no evidence that a stronger, local, in situ source of  $^4\text{He}$  was acting to increase the rate of  $^4\text{He}$  introduction. These helium results indicated the predominance of an external source of  $^4\text{He}$  that was consistent with a basal flux derived from U–Th series decay in the Earth's crust beneath the Great Artesian Basin. Most importantly, the inference of a large basal flux of  $^4\text{He}$  was supported by the simple hydraulic flow model of Torgersen and Ivey (1985) [93] that accounted for the delay time (see Fig. 13.9) before the enhanced rate of  $^4\text{He}$  accumulation (the basal

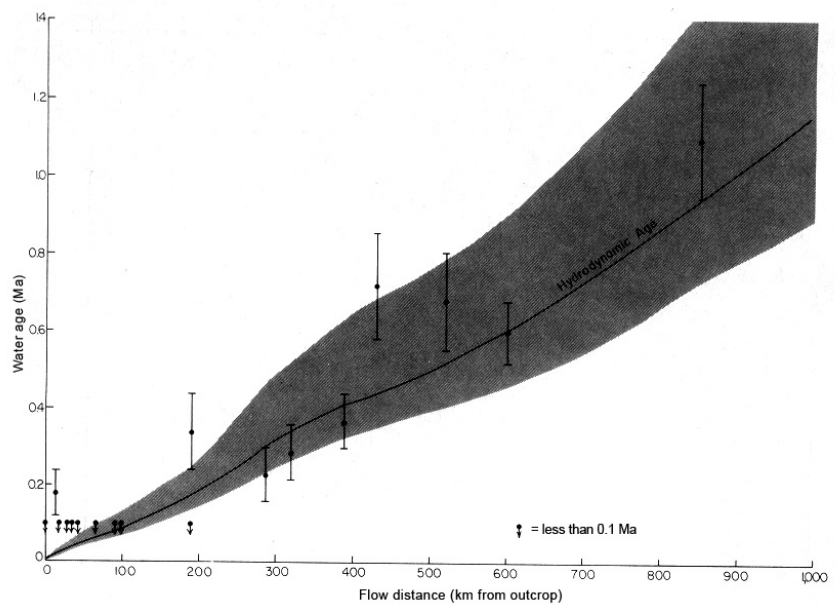
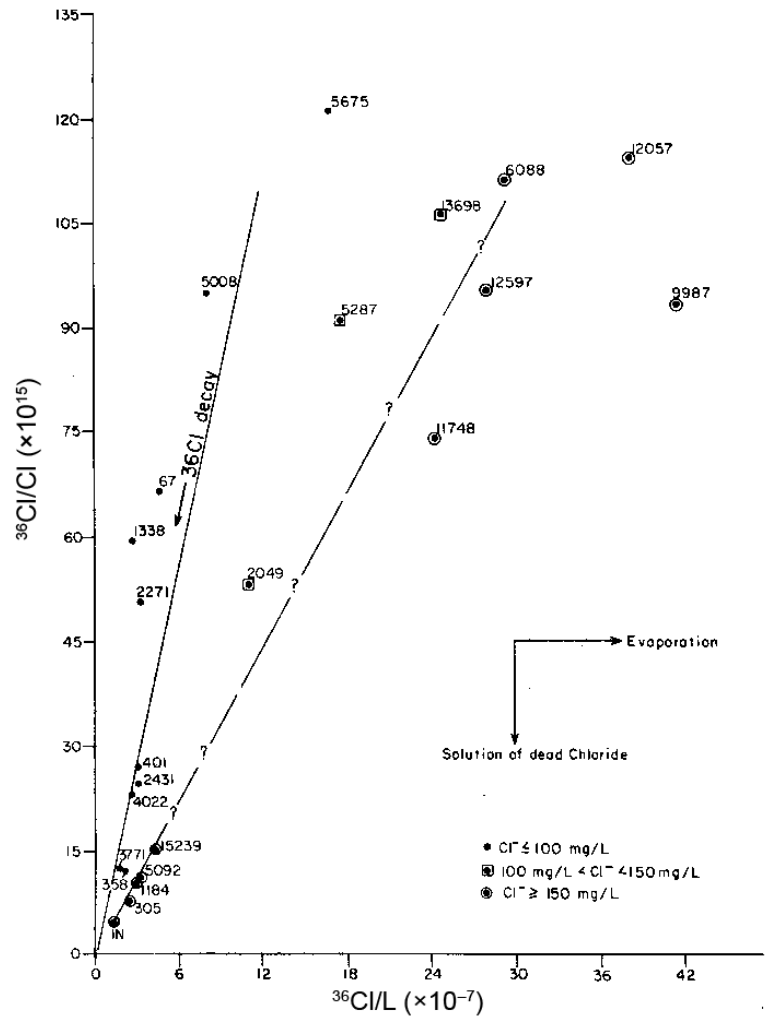


FIG. 13.8.  $^{36}\text{Cl}/\text{Cl}$  versus  $^{36}\text{Cl}$  concentration for the Great Artesian Basin (top) and the comparison (bottom) of apparent  $^{36}\text{Cl}$  tracer ages to apparent groundwater ages calculated from hydraulic properties (from Bentley et al. (1986) [310]; reproduced with permission of the American Geophysical Union).

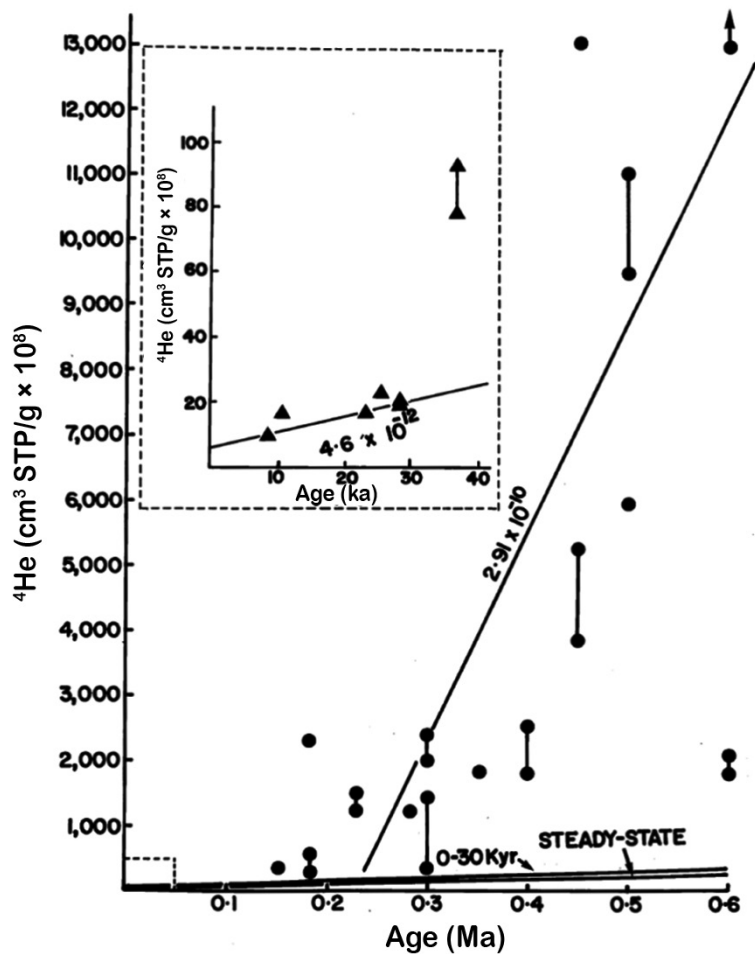


FIG. 13.9. Helium concentrations versus groundwater hydraulic age (as supported by  $^{36}\text{Cl}$  dates (Bentley et al. (1986) [310])) for the Great Artesian Basin, Australia as deduced from the 1982 fieldwork. For groundwaters younger than 40 ka, the accumulation rate is  $4.6 \times 10^{-12} \text{ cm}^3 \text{ STP } ^4\text{He} \cdot \text{cm}^{-3} \text{H}_2\text{O} \cdot \text{a}^{-1}$  which agrees with the calculated rate ( $A_{\text{He}} = 1$ ) of  $3.95 \times 10^{-12} \text{ cm}^3 \text{ STP } ^4\text{He} \cdot \text{cm}^{-3} \text{H}_2\text{O} \cdot \text{a}^{-1}$ . For groundwaters greater than 100 ka, the rate of accumulation is  $2.91 \times 10^{-10} \text{ cm}^3 \text{ STP } ^4\text{He} \cdot \text{cm}^{-3} \text{H}_2\text{O} \cdot \text{a}^{-1}$  or 74 times in situ production. An external bottom boundary flux provides the best explanation for the source and the timescale over which it can be seen (Torgersen and Clarke (1985) [293]).

flux) was observed. Owing to the predominance of this external  $^4\text{He}$  source, the  $^4\text{He}$  tracer ages were never calculated from the Great Artesian Basin  $^4\text{He}$  measurements.

Helium isotope measurements from the 1982 and 1985 expeditions (Torgersen et al. (1987) [682]) showed that the isotope ratio of helium accumulating along most flow paths was consistent with the calculated in situ production ratio and was, additionally, indistinguishable from an expected deep crustal production ratio (both order  $10^{-8}$ ; Fig. 13.10). However, some paths showed  $^3\text{He}/^4\text{He}$  ratios that were significantly elevated (Fig. 13.10) and suggested a mantle source of helium ( $^3\text{He}/^4\text{He}$  ratios of the order of  $10^{-5}$ ). These data suggest a point source input of a  $^3\text{He}$ -rich component that is diluted along the groundwater flow path by mixing and addition of helium from the basal fluxes to the in situ production. This stable helium tracer, thus, defines a unique source region within the recharge area that can be tracked downstream to define a flow path. This  $^3\text{He}$ -rich tracer, thus, further defines and supports the flow paths inferred by Habermehl (1980) [668] from the potentiometric surface. In addition, Collerson et al. (1988) [681] showed that recharge area groundwaters were 'spiked' with low  $^{87}\text{Sr}/^{86}\text{Sr}$  ratios (and a higher Ca/Sr ratio) as a result of Cenozoic volcanic intrusions, and Jurassic and

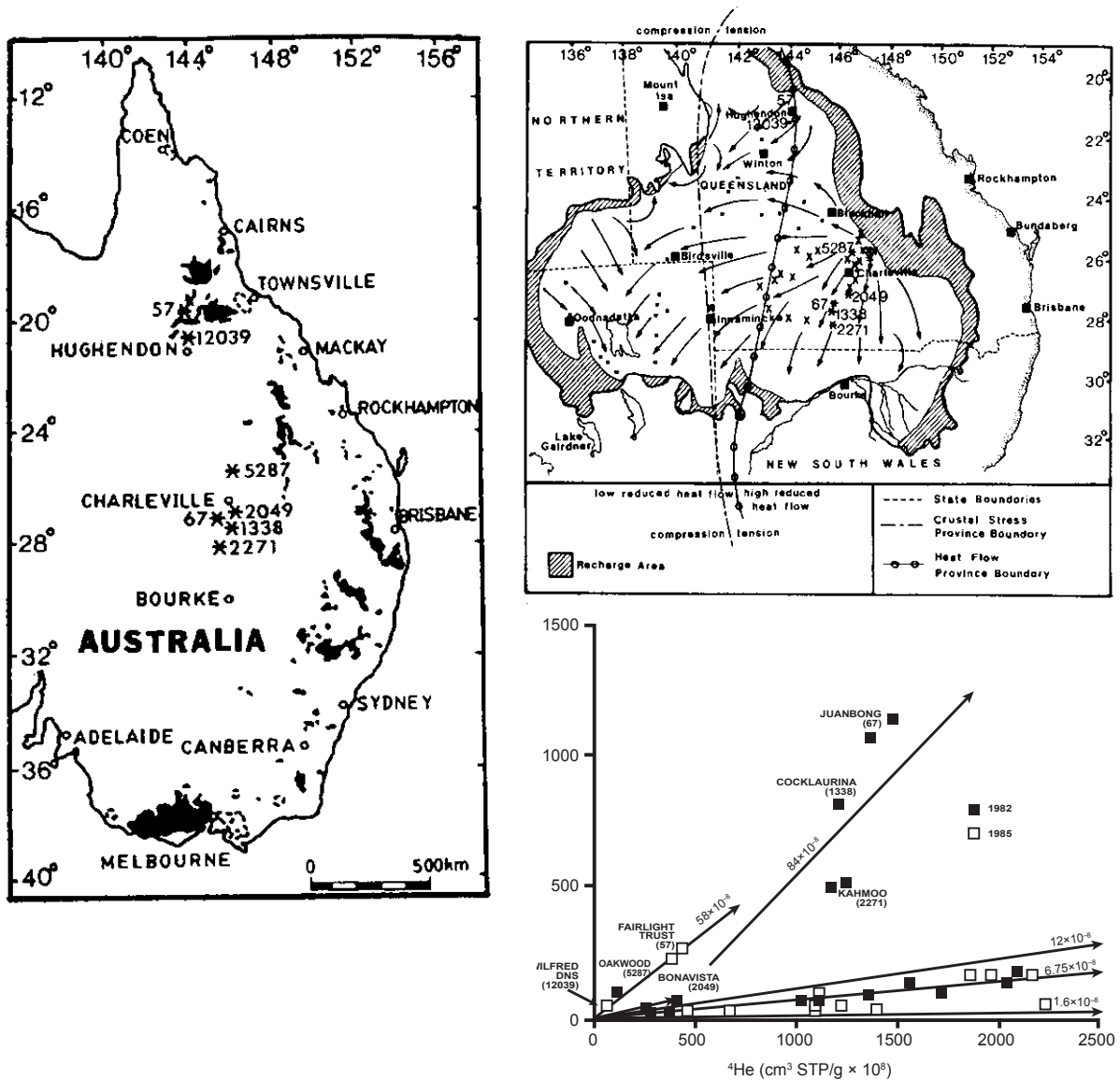


FIG. 13.10. Mantle  $^3\text{He}$  is identified in portions of the two flowlines of the Great Artesian Basin (Fairlight Trust to Wilfred Downs and Juanbong to Bonna Vista; lower right numbers in parentheses indicate bore number for cross-referencing with the top two figures) based on the occurrence of the high ratio in  $^3\text{He}/^4\text{He}$  as seen by the slope of the line. The occurrence of Cenozoic volcanism (left) in the area of recharge and the groundwater flowlines (top right) show how this signal is carried into the interior of the Great Artesian Basin (from Torgersen et al. (1987) [682]; reproduced with permission of the American Geophysical Union).

younger volcanic activity that was active in and along the eastern margin of the sedimentary basin of what would become the Great Artesian Basin (Fig. 13.11). The downstream dilution of this recharge area  $^{87}\text{Sr}/^{86}\text{Sr}$  'spike' again serves to strongly support the validity of the flowlines identified from potentiometric surfaces.

Torgersen et al. (1989) [573] show that  $^{40}\text{Ar}$  results appear to follow the same dynamics as  $^4\text{He}$  in the Great Artesian Basin and are also consistent with in situ production followed by input from an external basal flux. The  $^4\text{He}$  and  $^{40}\text{Ar}$  data are generally explained by similar processes but the  $^4\text{He}/^{40}\text{Ar}$  ratio remains quite variable. This suggests that these deep crustal noble gas fluxes are decoupled. Decoupling of  $^4\text{He}$  and  $^{40}\text{Ar}$  from their U–Th series and K sources is likely accomplished by processes at the grain scale including recoil, diffusive release and dissolution as well as large scale fracturing that

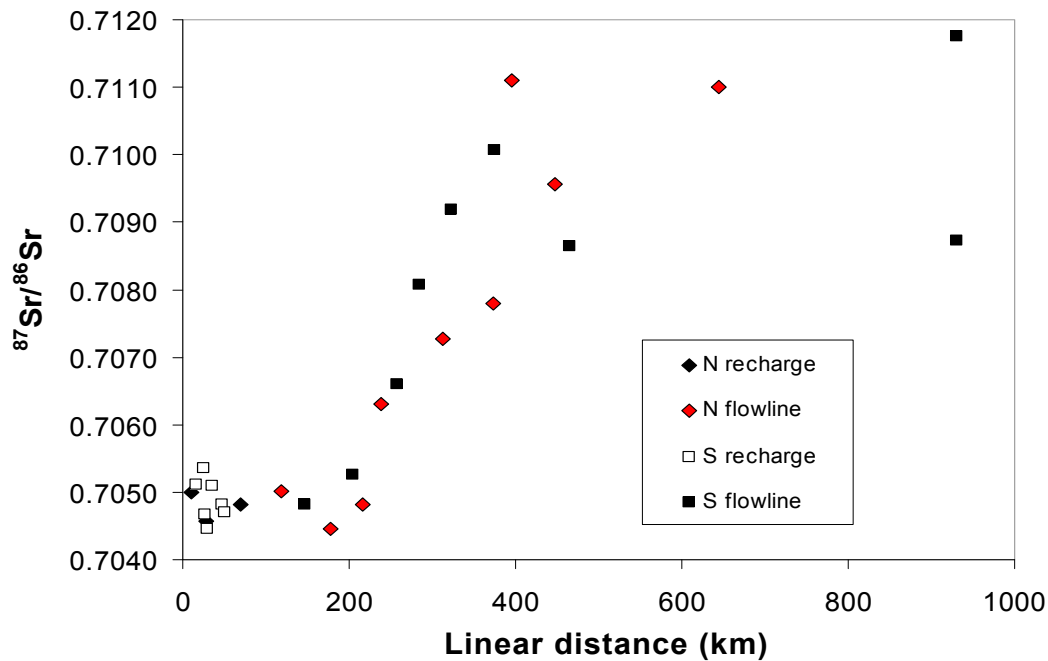


FIG. 13.11. The evolution of dissolved  $^{87}\text{Sr}/^{86}\text{Sr}$  within two flowlines of the Great Artesian Basin (north is Stannum to Innamincka and south is Bonna Vista to Thargomindah). The low  $^{87}\text{Sr}/^{86}\text{Sr}$  ratio is acquired in the recharge zone, likely via contact with Cenozoic volcanics (see Fig. 13.9 and note also the acquired  $^3\text{He}$  signature). As the flowing groundwaters dissolve the host rock ( $^{87}\text{Sr}/^{86}\text{Sr} \sim 0.7111$ ) and marine carbonates ( $^{87}\text{Sr}/^{86}\text{Sr} \sim 0.709234$ ) in situ, that end member is steadily acquired in the dissolved phase (after the measurements of Collerson et al. (1988) [681]).

will additionally separate  $^4\text{He}$  and  $^{40}\text{Ar}$  (Torgersen and O'Donnell (1991) [543]). Given the relative signal strengths, the  $^{40}\text{Ar}$  results suggest that  $^4\text{He}$  is more useful for basins with very old groundwater.

### 13.6. THE 1985 FIELDWORK: FAIRLIGHT TRUST TO CLAYTON, ATHOL TO MUTTI MUTTI AND MT. CRISPE TO CURDIMURKA

In continuing to build a knowledge base of the flow paths and flow rates of the eastern Great Artesian Basin, fieldwork in 1985 addressed additional flowlines in the eastern and central Great Artesian Basin as well as a flowline in the western Great Artesian Basin that is not included in this discussion. The flowlines sampled explore the northern area of the basin and the role of converging flowlines as a complication in the application and use of tracer age calculations.

Torgersen et al. (1991) [300] identified an increase in Cl and  $\text{SO}_4$  down the flowline for the Athol to Mutti Mutti group which also showed  $^{36}\text{Cl}$  ages on the high side of hydraulic ages (see Fig. 13.12). A discontinuous  $^{36}\text{Cl}$  evolution is distinct near Meerabooka where the east–west transect possibly intersects the north–south transect. Distinct addition of Cl is also evident near the end of the north–south transect at Clayton bore, as flowing groundwater rises from depth and is subject to convergent mixing. The impact of such mixing on the calculated tracer age was estimated based on linear mixing along an exponential decay curve. For this flowline, convergent mixing was suspected to cause minimal offset of the apparent tracer age.

Torgersen et al. (1992) [698] combine the helium isotope data of 1982 and 1985 fieldwork, and show the area of highest He concentration to be coincident with the oldest water and the lowest

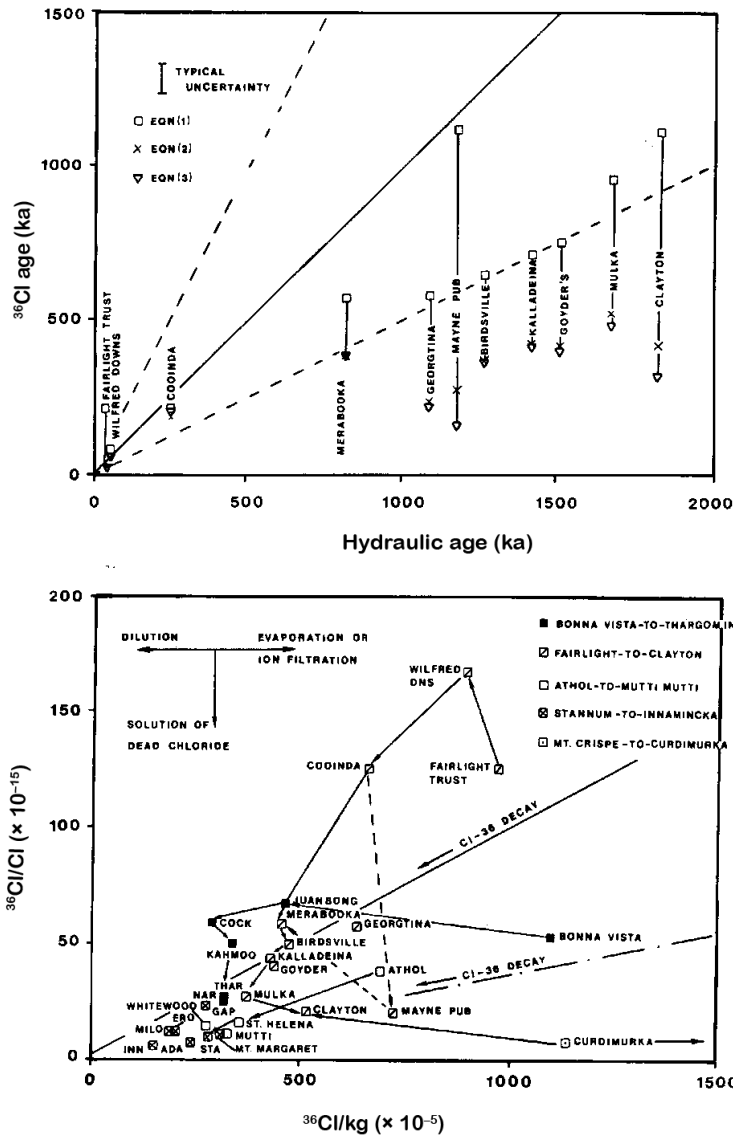


FIG. 13.12. Chlorine-36 measures along the Fairlight Trust to Clayton flowline show a distinct discontinuity at Meerabooka, possibly indicating flowline mixing as deduced by both the <sup>36</sup>Cl/Cl versus the <sup>36</sup>Cl plot (bottom) and the tracer <sup>36</sup>Cl age versus the hydraulic groundwater age (top) (from Torgersen et al. (1991) [300]; reproduced with permission of the American Geophysical Union).

(and near radioequilibrium) <sup>36</sup>Cl concentration (compare Figs 13.13 and 13.14). The helium data also show the impact of the western recharge area and the limited recharge along the north-western recharge margin.

### 13.7. MODELLING <sup>36</sup>Cl AND <sup>4</sup>He

The results of the 1982 and 1985 fieldwork for both <sup>36</sup>Cl and <sup>4</sup>He presented new data and new methods for the evaluation of very old groundwater. Discussion in the literature regarding the approach, assumptions and necessary conditions for the application of new methods (Bentley et al. (1986) [310]) is common. Andrews and Fontes (1991) [702], Andrews and Fontes (1993) [703], Fontes and Andrews (1993) [704], and Mazor (1992) [705] presented an evaluation of Great Artesian Basin <sup>36</sup>Cl data that explained spatial variations in <sup>36</sup>Cl as the result of mixing between groundwaters along flowlines and



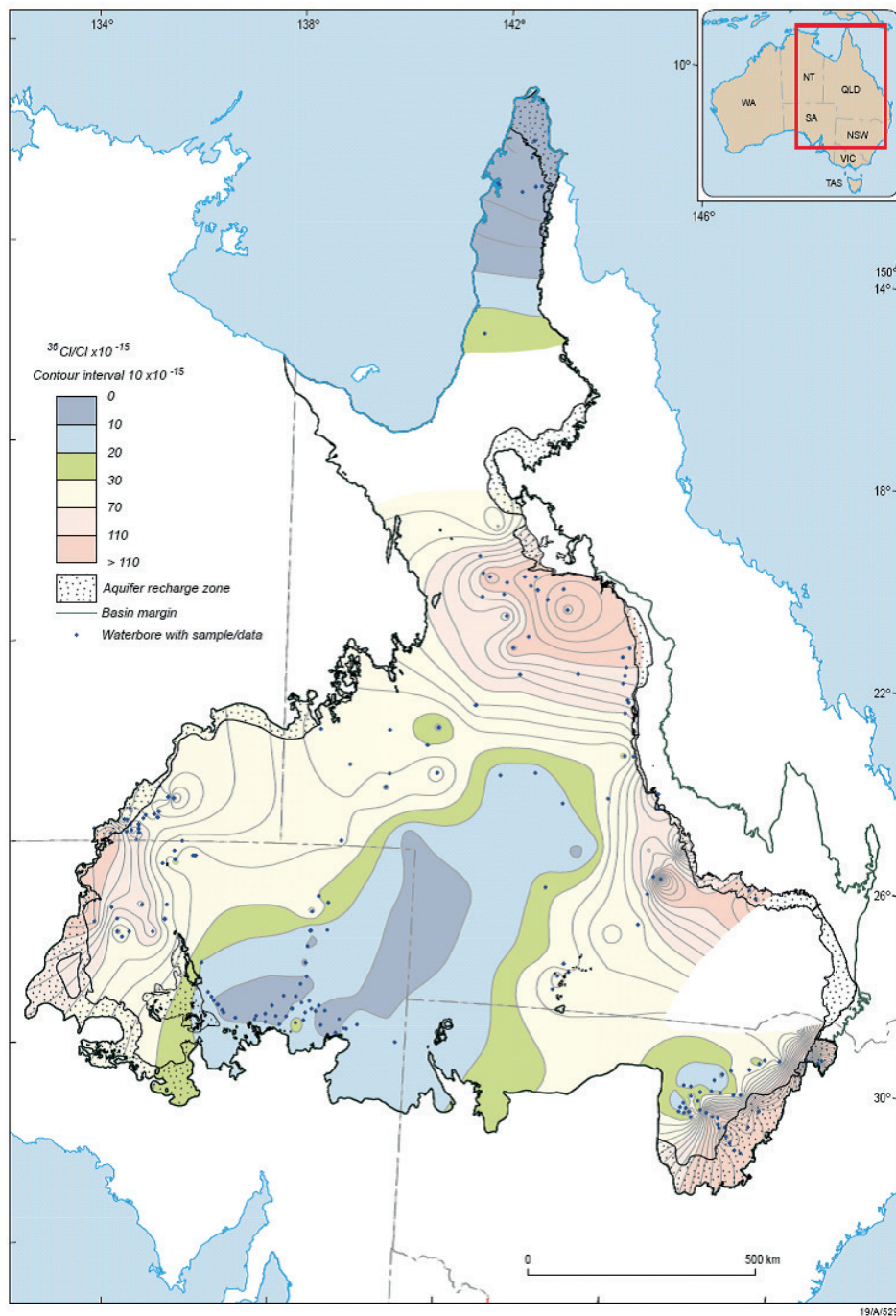


FIG. 13.14. Contours of  $^{36}\text{Cl}$  from Radke et al. (2000) [670]. The primary recharge areas (high  $^{36}\text{Cl}$ ) are clearly delineated as is the locale for very old groundwater (low  $^{36}\text{Cl}$ ). The agreement between the areas of low  $^{36}\text{Cl}$  and high  $^4\text{He}$  (older) and between high  $^{36}\text{Cl}$  and low  $^4\text{He}$  (younger) (Fig. 13.13) is clear.

the Great Artesian Basin groundwater flow system, including the  $^4\text{He}$  accumulation and concluded that the distribution of  $^4\text{He}$  is controlled not only by lateral flow but also by upflow and downflow regions that develop in response to basin topography and structure. This modelling effort showed that the spatial distribution of  $^4\text{He}$  can be quantitatively reconciled with groundwater flow patterns using a 3-D modelling framework. Similar modelling of the  $^{36}\text{Cl}$  dynamics (Park et al. (2002) [90]) again confirmed the need to consider 3-D flow in aquifer systems and the role of upflow, downflow and

convergent flow in the reconciliation of hydraulic ages with tracer based ages. The summary manuscript (Bethke and Johnson (2008) [84]) reiterates these principles.

### 13.8. GEOCHEMICAL MODELLING OF GROUNDWATER REACTION PATHS

Herczeg et al. (1991) [711] conducted a detailed analysis of the groundwater geochemistry from the 1985 fieldwork using PHREEQE (Parkhurst et al. (1980) [160]). That study explained the increase in total dissolved solids (TDS) along flowlines and distinct chemical differences between the eastern Great Artesian Basin (Na–HCO<sub>3</sub> type) and the western Great Artesian Basin (Na–SO<sub>4</sub>–Cl type) waters. Figures 13.15 and 13.16 show clearly the strong increase in alkalinity, DIC and  $\delta^{13}\text{C}$  along eastern Great Artesian Basin groundwater flowlines as well as the slowly increasing Na, Cl and TDS, and the decreasing Ca and Mg. Herczeg et al. (1991) [711] discussed the increase in TDS as a result of: (i) mixing of flowline groundwaters with saline waters within the deeper portions of the basin; (2) ion filtration through mudstone membranes; and (3) dissolution of evaporates, carbonate minerals or other minerals in situ. They inferred that saline waters most likely originated from the overlying Cretaceous marine sediments and were introduced by downward diffusion into the aquifers of the Cadna-owie Formation and Hooray Sandstone. However, given the upward leakage of artesian groundwater from

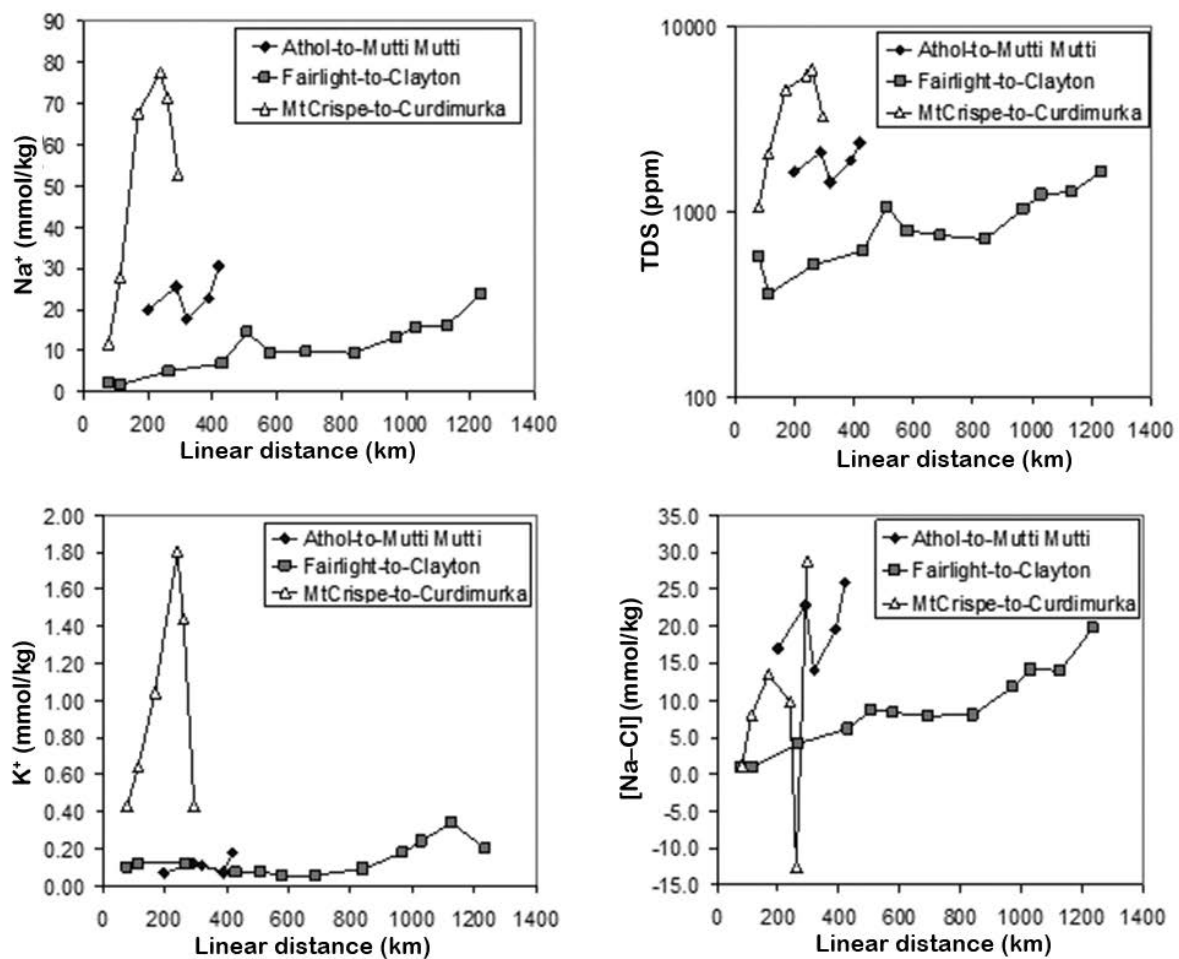


FIG. 13.15. Evolution of Na and K chemistry and TDS along the 1985 sampling lines as reported by Herczeg et al. (1991) [711]. It should be noted that the western Great Artesian Basin (Mt. Crispe-o-Curdimurka) is distinct from the eastern Great Artesian Basin and that mixing with the eastern Great Artesian Basin flow is apparent at the end of the western flowline.

the deeper, stratigraphically lower aquifers to the stratigraphically higher Cretaceous aquifers, mixing is likely to be slight. Herczeg et al. (1991) [711] further inferred that ion filtration is likely to be minimal based on the  $^{36}\text{Cl}$  studies of Bentley et al. (1986) [301], and concluded that variable evapotranspiration in the recharge areas in combination with mineral dissolution along flowlines represented the most plausible mechanism for the chemical evolution observed in Figs 13.15 and 13.16.

The eastern Great Artesian Basin flowline trends of increasing Na alkalinity and DIC together with the decreasing Ca and Mg were evaluated (Herczeg et al. (1991) [711]) in terms of a model proposed by Blake (1989) [712] which includes: (i) dissolution of carbonate minerals resulting in increased Ca, Mg and  $\text{HCO}_3^-$ ; (ii) cation exchange of Ca and Mg for Na in clay minerals, followed by; (iii) a reaction of Na with kaolinite to produce Na-smectite. Reasoning that the down gradient flow increase in alkalinity can only be accomplished by carbonate dissolution in the presence of high  $\text{pCO}_2$ , they concluded that  $\text{CO}_2$  respiration by plants in the recharge zone can drive the  $\delta^{13}\text{C}$  of DIC resulting from these reactions from an initial  $-15\text{‰}$  to approximately  $-12\text{‰}$ . However, to enable the reactions to continue requires the addition of  $\text{CO}_2$  as a result of anaerobic fermentation and reduction of  $\text{CO}_2$  to methane.

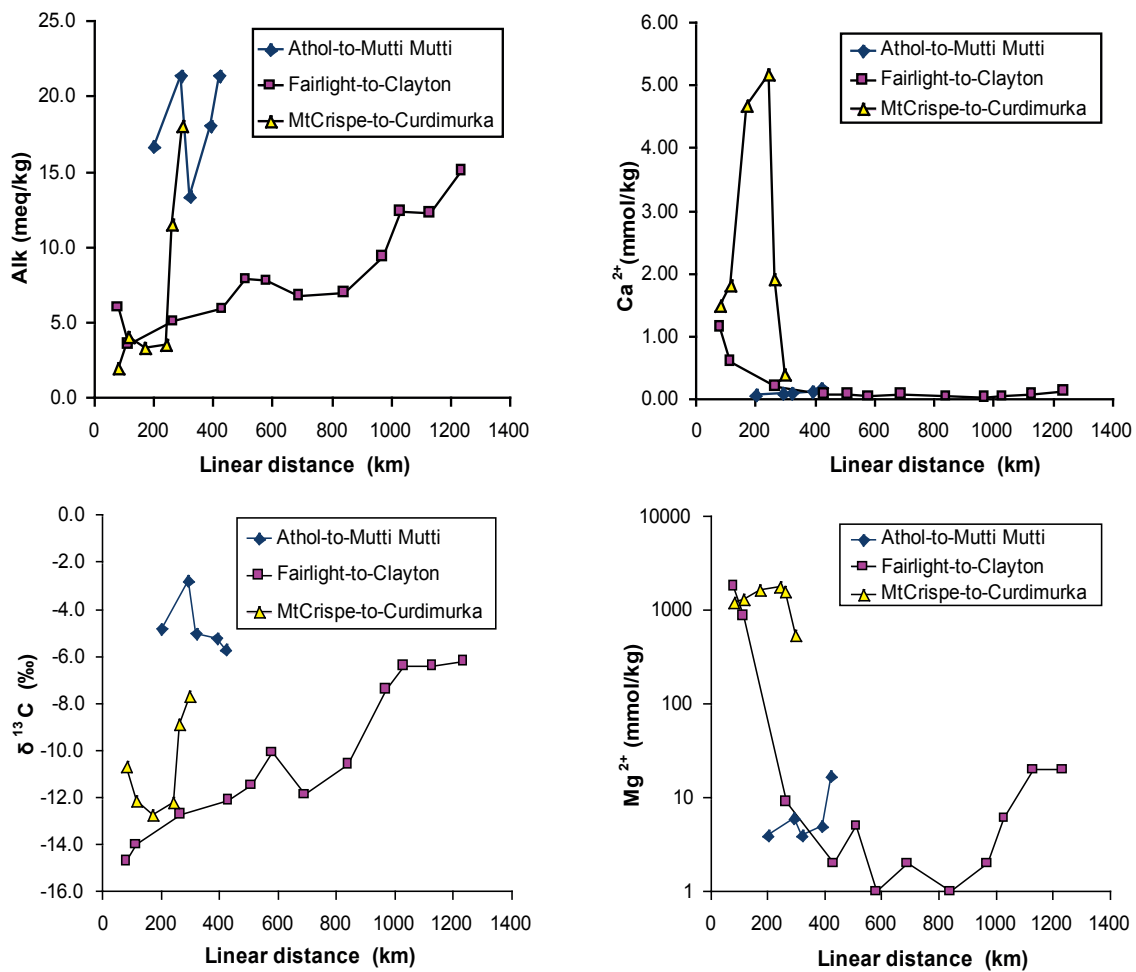


FIG. 13.16. Evolution of alkalinity,  $^{13}\text{C}$ ,  $\text{Ca}^{+2}$  and  $\text{Mg}^{+2}$  chemistry along the 1985 sampling lines as reported by Herczeg et al. (1991) [711]. It should be noted that the western Great Artesian Basin (Mt. Crispe-to-Curdimurka) is distinct from the eastern Great Artesian Basin and that mixing with the eastern Great Artesian Basin flow is apparent at the end of the western flowline.

### 13.9. THE 2000 BENCHMARK AND SYNTHESIS

Following the seminal paper of Habermehl (1980) [668], the publication by Radke et al. (2000) [670] is a compilation and synthesis of the hydrogeology, hydrochemistry and isotope hydrology of the Great Artesian Basin. It is based largely on samples and laboratory results of the fieldwork by Habermehl and others during the 1970s, 1980s and 1990s, with some additions of analyses and results from Queensland and South Australia. This benchmark paper synthesized groundwater flow models, geochemical reaction and transport models, and the dating of the artesian groundwater in the aquifers of the Cadna-owie Formation and Hooray Sandstone to infer the timescale of recharge and the in situ flow rates. It further utilized distinctive hydrogeochemical anomalies to infer details of groundwater flow in these aquifers. In the few paragraphs that follow, these findings are summarized, especially as they relate to this case study and the additional detail deduced through the use of modern hydrodynamic and hydrogeochemical codes.

The mapped (Radke et al. (2000) [670]) spatial distributions of modern  $^{14}\text{C}$  (Fig. 13.17) and  $^{36}\text{Cl}$  (Fig. 13.14) are consistent with previous work. The location of very old groundwater (near equilibrium values of  $^{36}\text{Cl}$ ) is consistent with the mapped regions of very high  $^4\text{He}$  (Fig. 13.13). Recharge, flow direction and discharge zones (Figs 13.18 and 13.19) reported by Radke et al. (2000) [670] were similar to the original diagrams of Habermehl (1980) [668]. Recharge is estimated to be on the order of  $10^{12}$  L/a with an unknown proportion distributed between rainfall and river infiltration. This current recharge rate may be enhanced as a result of the previous century of drawdown. Natural discharge is of the order of  $0.5 \times 10^{12}$  L/a with most discharge via upward leakage and minimal discharge via outlet springs (see Table 13.1). The range of estimates for Great Artesian Basin storage of water is significant (Table 13.1), leading to vastly different simple estimates of groundwater residence times (storage volume divided by input rate (or output rate)). The climate reconstructions of, for example, Magee et al. (2004) [683] suggest a decline in rainfall over Pleistocene time and discharge springs have experienced a significantly reduced head over the past century. Thus, it is not anticipated that discharge rates contribute significantly to this residence time discrepancy. Using the Habermehl and Seidel (1979) [689] estimated storage ( $10^{18}$  L) would yield recharge-based and discharge-based residence times of 1 and 2 Ma which are in general agreement with estimates from  $^{36}\text{Cl}$  and hydraulic estimates. The precision and the precise meanings of these differences in storage are not clear but it may be the difference between in situ storage and recoverable storage.

The eastern Great Artesian Basin is characterized by increasing TDS and alkalinity along flowlines. Chemical anomalies are noted along the Birdsville-Diamantina Track with additional high Cl anomalies along the Eulo-Nebine Ridge area. Groundwater temperatures increase with depth of the aquifers and anomalous geothermal gradients throughout the basin (Habermehl and Pestov (2002) [713]; Habermehl et al. (2002) [714]) and the Central Eromanga Basin shows a distinct increase in Na especially when expressed as sodium excess (e.g.  $[\text{Na}] - [\text{Cl}]$ ). High fluoride concentrations occur over basement highs where the aquifer is possibly in contact with igneous and metamorphic basement rocks. The stable isotopic signature of the groundwater suggests that heavy monsoon rainfall in the eastern recharge zone is responsible for the majority of recharge although evapotranspiration before recharge may be significant. Stable isotopes throughout the basin (Radke et al. (2000) [670]) show little variation. This apparent lack of any palaeoclimatic signature may be the result of minimal climatic variation and/or attenuation by dispersive mixing. Hydrodynamic models of groundwater flow calibrated against  $^{14}\text{C}$  in and near the recharge areas suggest flow rates range from 1.4 to 2.9 m/a (Radke et al. (2000) [670]). Flow rates calculated by hydrodynamic models and estimates of the  $^{36}\text{Cl}$  controls indicate several areas with artesian groundwater flow rates as low as 0.03–0.3 m/a (see Fig. 13.18). Very slow flow regions are areas of predominant water loss via upward leakage although the hydrochemical signatures in low flow areas also indicate the possibility of downward diffusion of some ions from overlying Lower Cretaceous aquitards into the Lower Cretaceous–Jurassic aquifers (Fig. 13.19). It would appear that discharge from artesian springs (11%) is small compared to discharge via upward leakage (89%) for

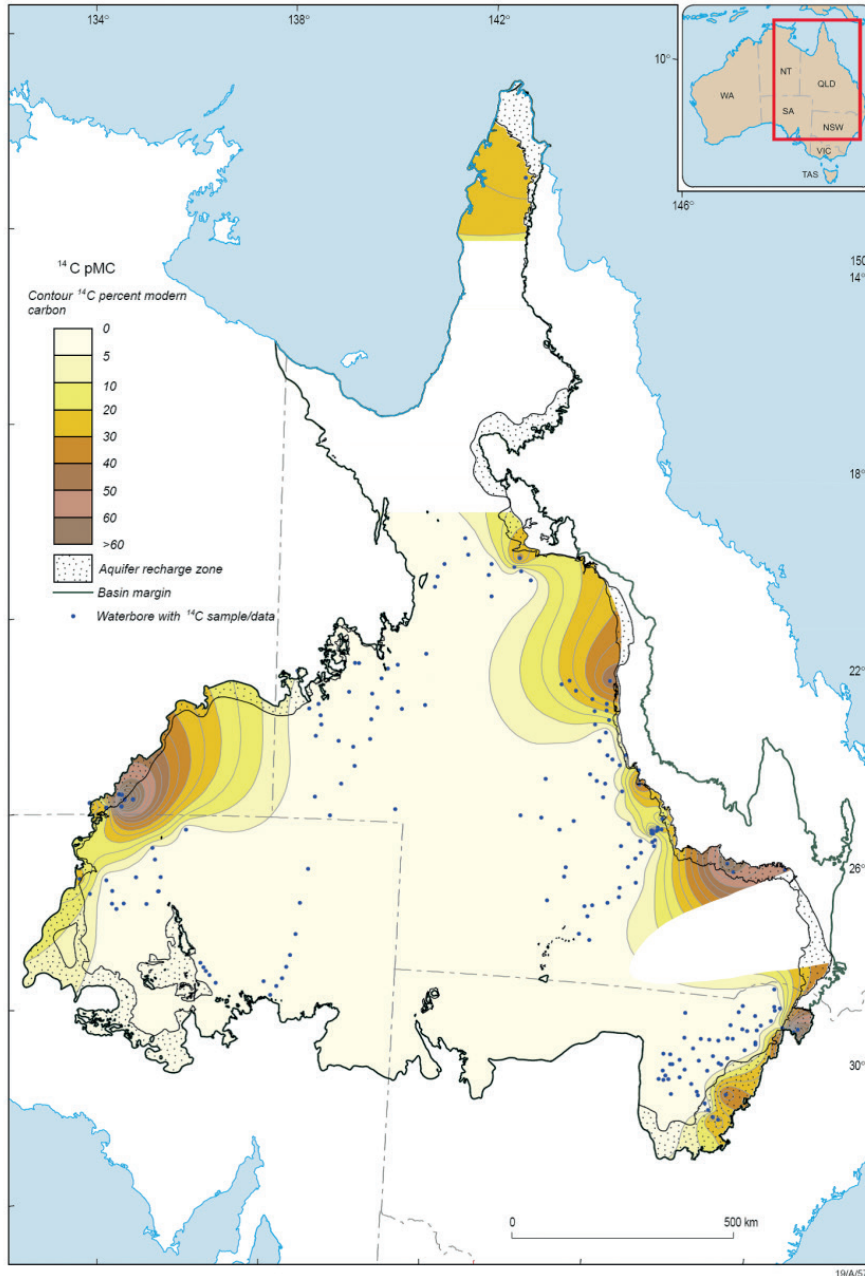


FIG. 13.17. Contours of  $^{14}\text{C}$  (in per cent modern) from Radke et al. (2000) [670]. The primary recharge areas are clearly delineated and the loss of  $^{14}\text{C}$  in the older regions of the Great Artesian Basin is clear.

a total natural discharge of  $0.5 \times 10^9$  L/a. However, spring discharges might have been much larger in past geological times (Prescott and Habermehl (2008) [715]). Anthropogenic discharge ( $0.57 \times 10^9$  L/a) is estimated to currently be slightly in excess of natural discharge.

Overall, the benchmark paper of Radke et al. (2000) [670] is in general agreement with earlier studies including the flow rate and age of groundwater inferred from  $^{14}\text{C}$ ,  $^{36}\text{Cl}$  and  $^4\text{He}$  studies. However, their detailed analysis appears to identify high flow regimes with lower salinities in the shallow depth of burial regions. NETPATH (Plummer et al. (1994) [120]) modelling of Great Artesian Basin geochemistry produced results in agreement with the overall net reactions postulated by Herczeg et al. (1991) [711] but suggested that carbonate dissolution reactions are the primary driving mechanism rather than smectite–kaolinite transformations. Thermal convection (Pestov (2000) [716]) has not been substantiated.

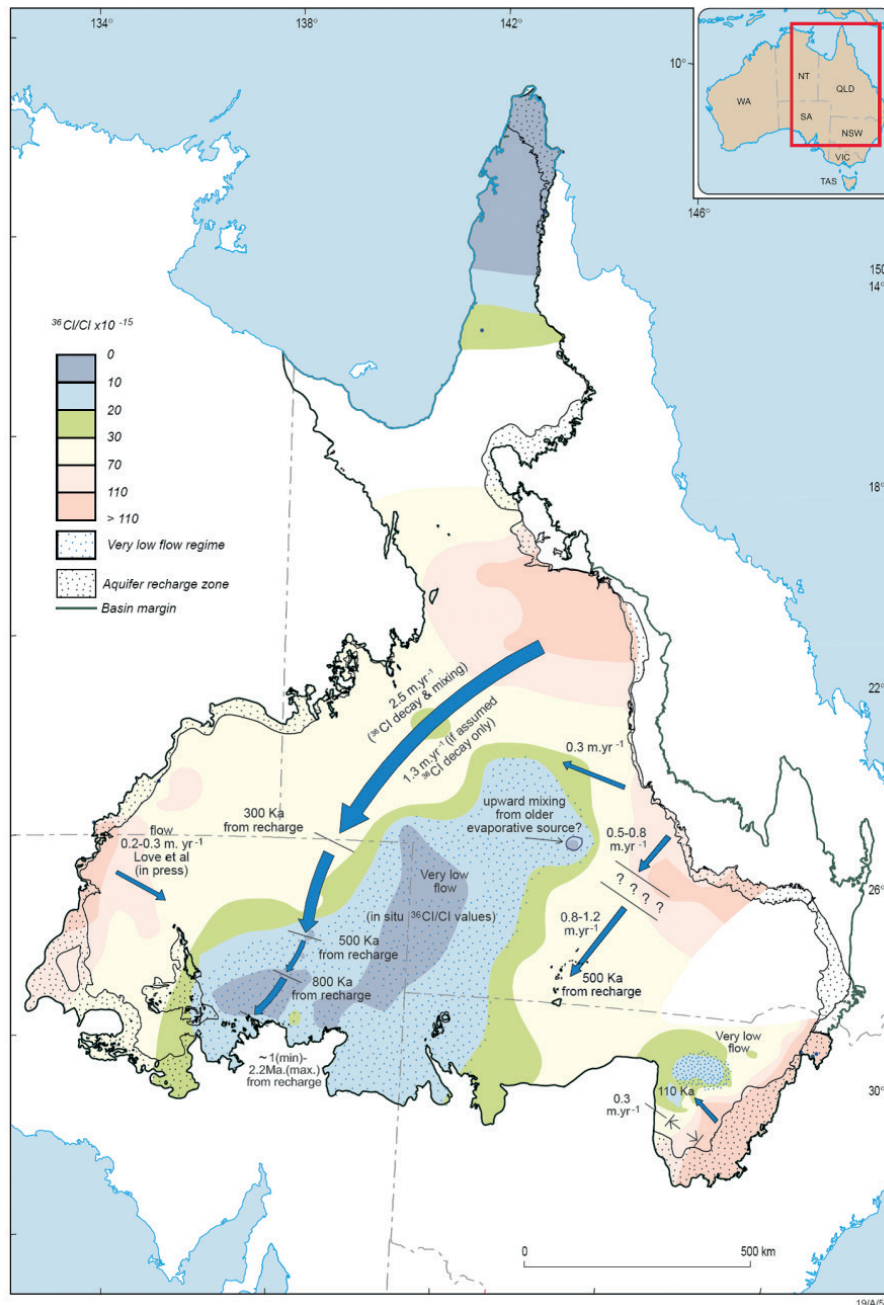


FIG. 13.18. Benchmark synthesis of flow rates and chemical evolution of the Great Artesian Basin (Radke et al. (2000) [670]).

### 13.10. CONTINUING WORK IN THE GREAT ARTESIAN BASIN

As a result of the large data base available for the Great Artesian Basin, several anomalies have been identified within the recharge areas (Collerson et al. (1988) [681]; Torgersen et al. (1987) [682]). The TACEM anomalies are found near wellbores named Tambo, Augathella, Charleville, Eddystone and Mitchell (Radke et al. (2000) [670]). Other anomalies are found along artesian groundwater flow paths. The groundwaters in the central and western Queensland and northern South Australia portions of the Great Artesian Basin (and, in particular, along the Birdsville Track) are characterized by higher temperatures than anticipated (Habermehl and Pestov (2002) [713]). TDS are low along the Birdsville Track compared to central and western Queensland and South Australia. This trend is inferred to be the result of mixing induced by the rapid rise in elevation of the crystalline bedrock

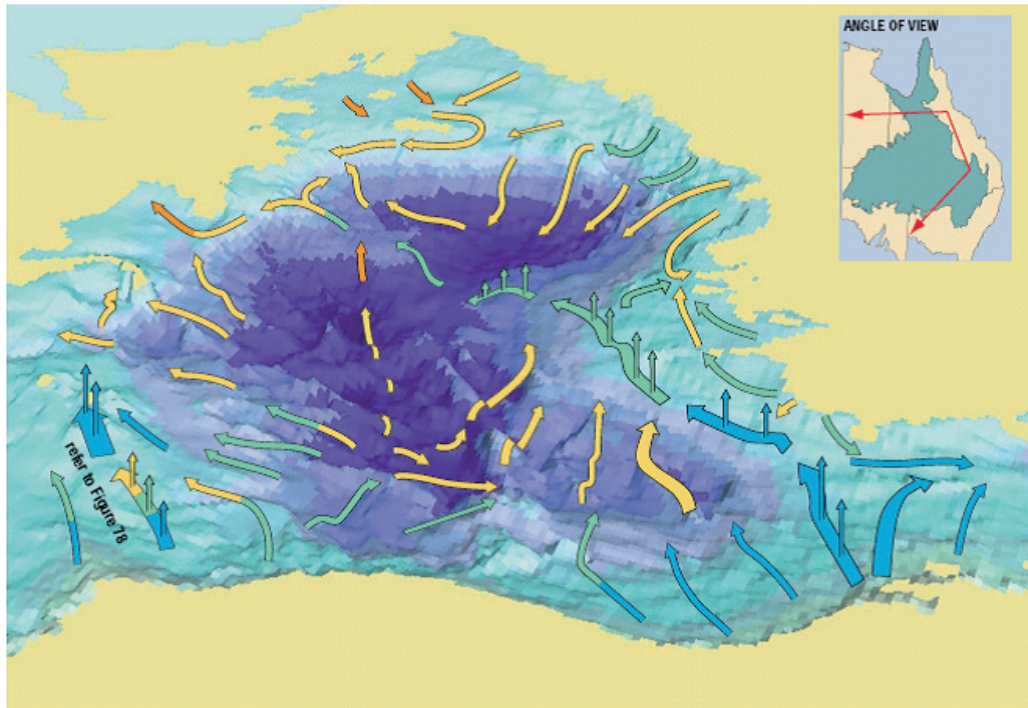


FIG. 13.19. Benchmark synthesis of the Great Artesian Basin showing flow rates, upward leakage and chemical evolution (increasing salinity; blue to orange) displayed over the basal structure of the Cadna-owie–Hooray aquifer (from Radke et al. (2000) [670]).

TABLE 13.1. WATER BALANCE FOR THE GREAT ARTESIAN BASIN, AUSTRALIA: FLUXES, STORAGE AND RESIDENCE TIMES

			Storage	Residence time: storage /rate
Natural recharge	Rainfall plus rivers	$10^{12}$ L/a	(1)	8.7 ka
			(2)	1 Ma
			(3)	65 ka
Natural discharge	Upward leakage	$0.45 \times 10^{12}$ L/a		
	Springs	$0.05 \times 10^{12}$ L/a		
Natural discharge	Sum	$0.5 \times 10^{12}$ L/a	(1)	17.4 ka
			(2)	2 Ma
			(3)	130 ka
Anthropogenic discharge	Waterbores	$0.5 \times 10^{12}$ L/a		
Storage (1)	Radke et al. (2000)			$8.7 \times 10^{15}$ L
Storage (2)	Habermehl and Senior (1979)			$1 \times 10^{18}$ L
Storage (3)	QDNRW (2007)			$6.5 \times 10^{16}$ L

based on geothermometry studies of Pirlo (2004) [717]. Evidence for this mixing of waters is provided by the discord among silica geothermometers and cation geothermometers. As silica geothermometers re-equilibrate relatively quickly compared to cation geothermometers, the low Si temperatures and the high cation temperatures indicate mixing from deeper, hotter (faster reactions) regions and shallow regions.

O'Shea and Jankowski (2006) [718] have performed hierarchical cluster analysis on the chemical compositions in the Coonamble Embayment (south-eastern Great Artesian Basin and an area in New South Wales not discussed above) and compared them with traditional Piper diagrams (Piper (1944) [719]), Durov diagrams (Chiligar (1956) [720]) and a modification of Piper analysis (Chada (1999) [721]). This cluster analysis indicates three main geochemical water types that can be associated with processes of ion exchange, precipitation and mixing from different sources. They were also able to identify an anomalous sample that is suspected to be influenced by magmatic sources of CO<sub>2</sub>. This indication of magmatic CO<sub>2</sub> is consistent with the location of other anomalies observed in <sup>87</sup>Sr/<sup>86</sup>Sr (Collerson et al. (1988) [681]) and <sup>3</sup>He/<sup>4</sup>He (Torgersen et al. (1987) [682]) that are geographically associated with the eastern recharge zone that was subject to considerable Cenozoic and pre-Cenozoic volcanism (Duncan and McDougall (1989) [680]).

Recharge, recharge processes and rates, detailed hydrochemistry and isotope studies, including stable ( $\delta^2\text{H}$ ,  $\delta^{18}\text{O}$  and  $\delta^{13}\text{C}$ ) and radioactive (<sup>14</sup>C, <sup>36</sup>Cl) isotopes have been carried out in the Queensland (Kellett et al. (2003) [722]) and New South Wales (Habermehl et al. (2009) [723]) parts of the Great Artesian Basin and recharge rates range from 0.5 to 10 mm/a, with some higher values. A detailed study of recharge along the western margin and discharge in the south western region of the Great Artesian Basin commenced in 2009.

Shimada et al. (1998) [724], Shimada et al. (1999) [725] and Shimada et al. (1997) [726] sampled several transects in the Coonamble Embayment in 1996 and interpreted the hydrochemistry, and stable ( $\delta^2\text{H}$ ,  $\delta^{18}\text{O}$  and  $\delta^{13}\text{C}$ ) and radioactive (<sup>14</sup>C, <sup>36</sup>Cl) isotope results for this south-eastern part of the Great Artesian Basin, which has its own recharge area.

Extensive sampling of flowing artesian waterbores tapping the aquifers in the Cadna-owie Formation and Hooray Sandstone was carried out in 2002 and 2003 along transects similar to the 1982 and 1985 transects, with additional transects in the Queensland, South Australia and Northern Territory parts of the Great Artesian Basin. This was followed in 2004 and 2005 by the construction of fully cored drill-holes through the Lower Cretaceous aquitards into the aquifers near the north-eastern recharge area and the south-western discharge area. Laboratory results on hydrochemistry, stable isotopes ( $\delta^2\text{H}$ ,  $\delta^{18}\text{O}$  and  $\delta^{13}\text{C}$ ), radioactive isotopes (<sup>14</sup>C, <sup>36</sup>Cl) and noble gases (<sup>4</sup>He, <sup>3</sup>He/<sup>4</sup>He, Ne) were analysed and interpreted and confirm the results of earlier studies. Additional <sup>36</sup>Cl and <sup>4</sup>He measures continue to show they remain useful indicators for groundwater residence times of very old groundwater (Hasegawa et al. (2009) [727]; Mahara et al. (2009) [728]).

## Chapter 14

### KRYPTON-81 CASE STUDY: THE NUBIAN AQUIFER, EGYPT

N. STURCHIO

Department of Earth and Environmental Sciences,  
Chicago, Illinois,  
United States of America

R. PURTSCHERT

Physics Institute,  
University of Bern,  
Bern, Switzerland

#### 14.1. NUBIAN AQUIFER

The Nubian aquifer of north-east Africa is one of the world's largest fresh groundwater resources (~150 000 km<sup>3</sup>). An area in the Western Desert of Egypt, for which a number of earlier studies provided sufficient background data on the Nubian aquifer, was selected for the first application of the atom trap trace analysis (ATTA) method (Section 5.4.3) for measurement of <sup>81</sup>Kr in groundwater. This area has relatively simple geology, potential for containing very old groundwater, and favourable characteristics for comparison of the <sup>81</sup>Kr and <sup>36</sup>Cl methods (Sturchio et al. (2004) [5]). Before this work, little evidence regarding absolute groundwater residence time in the Nubian aquifer was available. Estimates of groundwater age in the range of  $0.54 \times 10^6$ – $1.58 \times 10^6$  a had been obtained from He/Ar ratios (Himida (1967) [729]). A large number of <sup>14</sup>C data had been obtained for the Nubian aquifer waters in Egypt (Fröhlich et al. (2007) [730]; Sonntag et al. (1979) [731]). Chlorine-36 data indicated possible residence times of up to  $\sim 9 \times 10^5$  a (unpublished data<sup>1</sup>).

#### 14.2. METHODS

Nubian aquifer groundwater was sampled in May 2002 from six irrigation wells in major oasis areas of the Western Desert of Egypt for measurements of <sup>81</sup>Kr, <sup>36</sup>Cl, <sup>14</sup>C, <sup>4</sup>He and other chemical and isotopic constituents. Dissolved gas was extracted from several 10<sup>3</sup> kg of water at the field sites using the Bern vacuum-stripping method described above (Section 5.4.1). Krypton was separated from the extracted gas samples at Bern by molecular sieve absorption and gas chromatographic methods; LLC was used to confirm that the abundances of <sup>85</sup>Kr in these samples were indeed low (<sup>85</sup>Kr/Kr < 3% of modern air) as expected for old groundwaters, verifying minimal air contamination during sampling. For normalization in ATTA analyses, a calibrated amount of <sup>85</sup>Kr was mixed with each Kr sample. The <sup>81</sup>Kr/<sup>85</sup>Kr ratios in the spiked Kr samples were then measured using ATTA at Argonne National Laboratory (Du et al. (2003) [249]). Chloride concentrations in water samples were measured by ion chromatography and Cl was then precipitated as AgCl for measurements of <sup>36</sup>Cl that were performed by AMS at the PRIME Lab of Purdue University. Noble gas samples were collected in copper tubes and measurements were performed on separate sets of samples at both ETH Zurich and Lawrence Berkeley National Laboratory. Aliquots of purified CO<sub>2</sub> were measured for <sup>14</sup>C abundance at the University of Arizona accelerator mass spectrometry facility; these samples were obtained from a portion of the gas used for Kr extraction.

<sup>1</sup> STURCHIO, N., University of Illinois, PURTSCHERT, R., University of Bern, unpublished data.

### 14.3. KRYPTON-81 DATA

Results of the Nubian aquifer groundwater analyses for  $^{81}\text{Kr}$  are shown in Fig. 14.1 and Table 14.1. Krypton-81 is expressed in terms of the air-normalized ratio,  $R/R_{\text{air}} = (^{81}\text{Kr}/\text{Kr})_{\text{sample}} / (^{81}\text{Kr}/\text{Kr})_{\text{air}}$ , where  $R_{\text{air}}$  is the modern atmospheric ratio  $(^{81}\text{Kr}/\text{Kr})_{\text{air}} = 1.10 (\pm 0.05) \times 10^{-12}$  as measured by ATTA (Du et al. (2003) [249]). Measured  $R/R_{\text{air}}$  values in Nubian aquifer groundwater samples range from 4.8% to 52.6% modern. Using the simple expression for radioactive decay, and the  $^{81}\text{Kr}$  decay constant  $\lambda_{\text{Kr}} = 3.03 (\pm 0.14) \times 10^{-6}/\text{a}$ , the  $^{81}\text{Kr}$  tracer age  $t_{\text{Kr}}$  of a groundwater sample is given by:

$$t_{\text{Kr}} = -\frac{1}{\lambda} \ln\left(\frac{R}{R_{\text{air}}}\right) \quad (14.1)$$

The range of ages thus derived is  $0.2\text{--}1.0 \times 10^6$  a (Fig. 14.1). These are apparent piston flow ages because the extent of age mixing within the sampled wells is unknown.

Ages increase progressively along flow vectors predicted by numerical hydrodynamic models (Brinkman et al. (1987) [732]), verifying distant lateral flow of deep groundwater towards the north-east from a recharge area south-west of Dakhla. The correspondence of  $^{81}\text{Kr}$  age with predicted hydrodynamic age indicates negligible input of  $^{81}\text{Kr}$  from subsurface sources, in agreement with theoretical calculations and conclusions reached from  $^{81}\text{Kr}$  measurements of groundwater from the Milk River Aquifer in Canada (Lehmann et al. (1991) [282]) and the Great Artesian Basin in Australia (Collon et al. (2000) [281]). The estimated diffusive loss of  $^{81}\text{Kr}$  to aquitards was limited to  $\leq 20\%$  for the Great Artesian Basin (Lehmann et al. (2003) [256]), and is expected to be even lower within

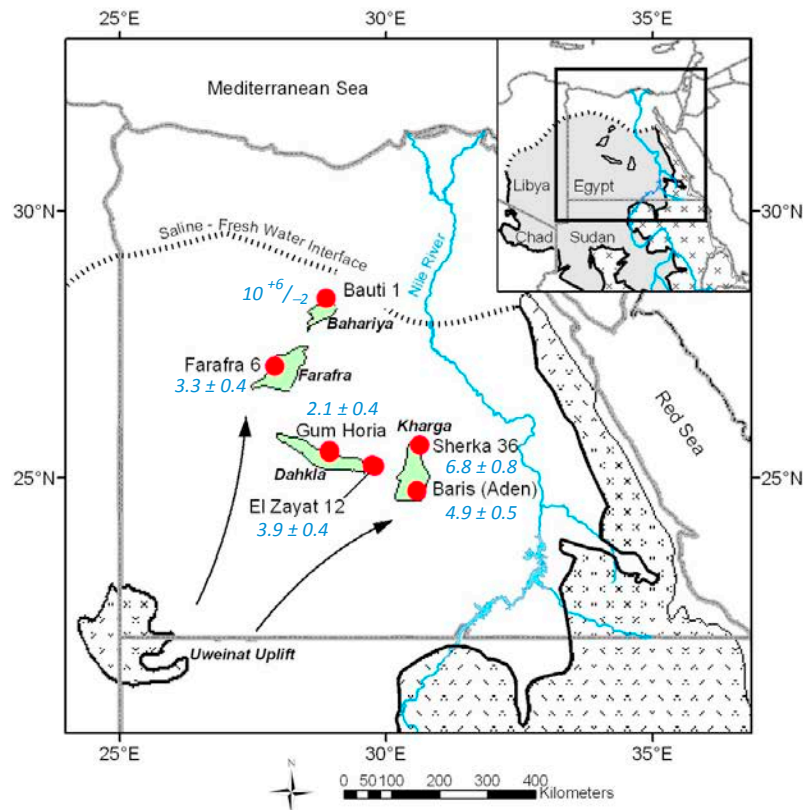


FIG. 14.1. Map showing sample locations (red circles) in relation to oasis areas (shaded green), Precambrian basement areas (patterned) and other regional features. Groundwater flow in the Nubian aquifer is generally towards the north-east, but diverges towards the north and east as shown by arrows (Brinkman et al. (1987) [732]; Hesse et al. (1987) [733]). Krypton-81 ages are shown in blue numbers (in units of  $10^5$  a).

TABLE 14.1. ISOTOPIC DATA FOR NUBIAN AQUIFER WATER SAMPLES

Well name (depth)*	Cl (mg/L)	<sup>36</sup> Cl/Cl (10 <sup>-15</sup> )	<sup>81</sup> Kr/Kr (R/R <sub>air</sub> %)	<sup>4</sup> He (10 <sup>-6</sup> cm <sup>3</sup> STP/g)	<sup>14</sup> C (pmC)	δ <sup>2</sup> H (‰)	<sup>40</sup> Ar (10 <sup>-5</sup> cm <sup>3</sup> STP/g)
Dakhla Oasis							
Gum Horia (1200 m)	20	76.5 (±3.4)	52.6 (±6.1)	3.0 (±0.3)	n.a.	-81	57 (±6)
El Zayat 12 (720 m)	59	72.7 (±1.7)	30.6 (±3.6)	3.3 (±0.3)	<1.6	-82	33 (±3)
Kharga Oasis							
Sherka 36 (750 m)	95	12.2 (±5.1)	12.8 (±3.0)	43 (±4)	0.28 (±0.11)	-82	67 (±7)
Baris-Aden (600 m)	92	45.6 (±2.1)	22.8 (±3.0)	32 (±3)	3.26 (±0.21)	-81	50 (±5)
Farafra Oasis							
Farafra 6 (800 m)	24	65.0 (±3.0)	36.5 (±4.2)	3.7 (±0.4)	0.96 (±0.11)	-79	50 (±5)
Bahariya Oasis							
Bauti 1 (1200 m)	52	20.2 (±1.6)	4.8 (±3.8)	5.1 (±0.5)	n.a.	-81	40 (±4)

Note: n.a. = not analysed; \*sample locations shown in Fig. 14.1; 1σ errors in parentheses.

the Nubian aquifer because of the lower porosity and smaller proportion of aquitard formations within this aquifer system (see Figs 5.3 and 5.4).

Krypton-81 ages increase progressively with distance to the north and east of Dakhla; their areal distribution indicates a flow velocity of ~2 m/a from Dakhla towards Farafra, and a lower velocity towards Kharga and Baris and from Farafra to Bahariya. These observations are consistent with the distribution of hydraulically conductive sandstone within the aquifer and they provide support to some of the early hydrodynamic models (Brinkman et al. (1987) [732]; Hesse et al. (1987) [733]). South-westward extrapolation of the ~2 m/a flow rate inferred from the difference in <sup>81</sup>Kr ages for Dakhla and Farafra is consistent with recharge in the area of the Uweinat uplift near the Egypt–Sudan border. In this area, the Nubian sandstone is exposed (or buried beneath sand sheets or dunes) at elevations between 200 and 600 m above sea level over a wide area, forming a broad catchment for recharge of the Nubian aquifer.

#### 14.4. CHLORINE-36 DATA

Patterson et al. (2005) [43] presented <sup>36</sup>Cl data for 22 groundwater samples from the Nubian aquifer in the Western Desert of Egypt, including the six samples also measured for <sup>81</sup>Kr. The areal distribution of groundwater ages derived from this data set is shown in comparison with Basin 2 hydrodynamic model ages in Fig. 14.2. The best estimates of groundwater ages from <sup>36</sup>Cl data range from about 2 × 10<sup>5</sup> to 7 × 10<sup>5</sup> a, and the distribution of these ages indicates flow from south to north, in agreement with <sup>81</sup>Kr ages and hydrodynamic models. The <sup>36</sup>Cl ages agree with hydrodynamic model ages within ±30%.

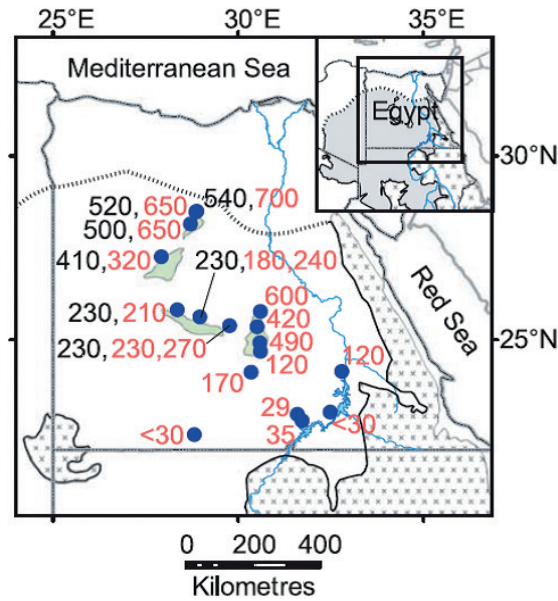


FIG. 14.2. Map of the Western Desert of Egypt showing hydrodynamic ages (black numbers) and  $^{36}\text{Cl}$  ages (red numbers) in the Nubian aquifer calculated from  $^{36}\text{Cl}/\text{Cl}$  ratios and assuming  $R_i = 130 \times 10^{-15}$ ,  $R_{se}^{\text{sandstone}} = 5 \times 10^{-15}$  and  $R_{se}^{\text{shale}} = 15 \times 10^{-15}$  (from Patterson et al. (2005) [43]). Age units are  $10^3$  a.

#### 14.5. CORRELATION OF $^{36}\text{Cl}$ AND $^{81}\text{Kr}$ DATA

There is a good correlation between  $^{36}\text{Cl}/\text{Cl}$  ratios and  $^{81}\text{Kr}$  ages (Fig. 14.3), in samples for which both measurements were made, providing a firm basis for calibrating apparent  $^{36}\text{Cl}$  ages to an apparent value of  $(^{36}\text{Cl}/\text{Cl})_{\text{initial}} = R_i$  for the Nubian aquifer. A best-fit curve through the data using the function:

$$R_{\text{meas}} = R_{\text{se}} + (R_i - R_{\text{se}}) \exp(-t_{\text{Kr}} \lambda_{\text{Cl}}) \quad (14.2)$$

where  $t_{\text{Kr}}$  is the  $^{81}\text{Kr}$  age in years,  $\lambda_{\text{Cl}} = 2.30(\pm 0.02) \times 10^{-6}/\text{a}$  is the  $^{36}\text{Cl}$  decay constant and  $R_{\text{se}} = 8(\pm 3) \times 10^{-15}$  is the secular equilibrium in situ production value for the aquifer (assuming constant Cl concentration in water) gives  $R_i = 131(\pm 11) \times 10^{-15}$ , which coincidentally agrees with the initial value of  $125(\pm 10) \times 10^{-15}$  estimated for the Great Artesian Basin (Love et al. (2000) [292]). Krypton-81 and  $^{36}\text{Cl}$  ages for most of these samples agree within error, but two samples exhibit significant age discordance that may be explained by deviations from assumptions used for calculating the best-fit curve (i.e. different values of  $R_{\text{se}}$  and/or  $R_i$ , or addition of subsurface Cl). Stable Cl isotope ratios and Cl concentrations for these and other Nubian aquifer groundwater samples measured for  $^{36}\text{Cl}$  (Patterson et al. (2005) [43]) indicate subsurface Cl addition for some samples and, in fact, age calculations taking into account added Cl using Eq. (14.2) (Section 5.5 and Chapter 6) yield  $^{36}\text{Cl}$  ages in excellent agreement with  $^{81}\text{Kr}$  ages. These results demonstrate that the integrity of the  $^{36}\text{Cl}$  chronometer is vulnerable to additions of Cl at any point along a flow path, whereas, in contrast, the potential for open system behaviour of Kr is minimal after water has reached the aquifer. Nonetheless, methods for correcting  $^{36}\text{Cl}$  ages for subsurface additions of Cl and  $^{36}\text{Cl}$  are well established (Section 5.5 and Chapter 6). The main uncertainty in  $^{81}\text{Kr}$  ages is diffusional exchange of Kr between different water masses (Section 5.1.2.2).

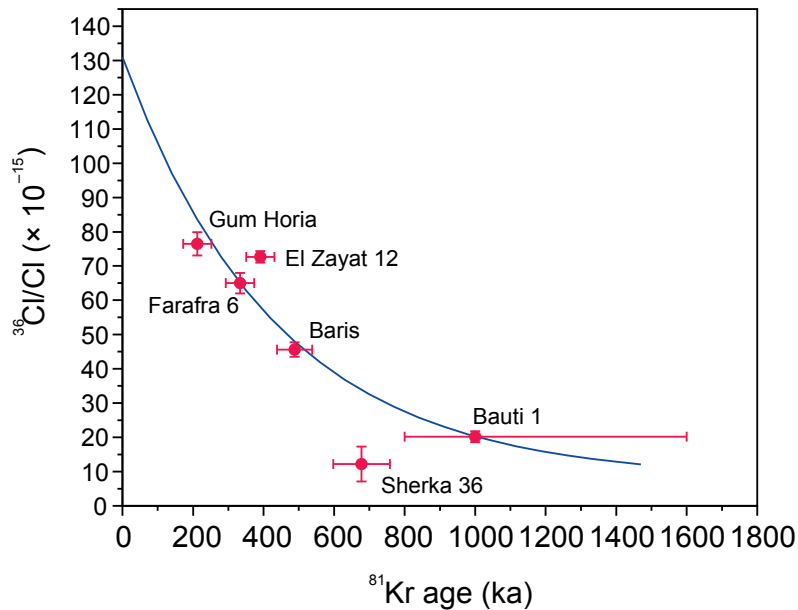


FIG. 14.3. Correlation of  $^{36}\text{Cl}/\text{Cl}$  ratio with  $^{81}\text{Kr}$  age. The blue line is an exponential best fit assuming a secular equilibrium  $^{36}\text{Cl}/\text{Cl}$  ratio of  $8 \times 10^{-15}$  (with the input ratio  $R_i$  as a free fitting parameter).

#### 14.6. HELIUM-4 DATA

Measured  $^4\text{He}$  and  $^{40}\text{Ar}$  concentrations in the Nubian aquifer samples are provided in Table 14.1. Concentrations of  $^{40}\text{Ar}$  range from  $33\text{--}67 \times 10^{-5} \text{ cm}^3 \text{ STP/g}$  and indicate excess air incorporation at recharge. Ratios of  $^{40}\text{Ar}/^{36}\text{Ar}$  were not measurably different from the atmospheric ratio of  $295.5 \pm 0.5$ , so it appears that  $^{40}\text{Ar}$  production and accumulation within the sandstone aquifer is minimal. However,  $^4\text{He}$  concentrations ( $3.0\text{--}43 \times 10^{-6} \text{ cm}^3 \text{ STP/g}$ ) are two to three orders of magnitude greater than the air-saturated water concentration of  $^4\text{He}$  at  $20^\circ\text{C}$ , indicating subsurface addition of  $^4\text{He}$  that could reflect groundwater age.  $^4\text{He}_{\text{ter}}$  concentrations show apparently linear accumulation along the Dakhla-Bahariya flow path (Table 14.1), suggesting qualitatively that groundwater age increases by nearly a factor of two between Dakhla and Bahariya. Using rock compositions that gave the best fit of the measured  $^{36}\text{Cl}/\text{Cl}$  data in the Basin 2 model, and by assuming that the aquifer is composed of 80% sandstone and 20% shale, the flux of  $^4\text{He}$  produced in situ,  $J_{\text{He}}$ , then equals  $3.3 \times 10^{-12} \text{ cm}^3 \text{ STP} \cdot \text{g}^{-1} \cdot \text{a}^{-1}$  and the corresponding  $^4\text{He}$  residence times (assuming zero external flux of  $^4\text{He}$  into the aquifer) range from 870 to 1500 ka. These apparent  $^4\text{He}$  ages are two to four times greater than either the hydrodynamic ages or the  $^{36}\text{Cl}$  ages, which indicates that the assumed  $^4\text{He}$  production rate or the assumption of zero external He flux is inaccurate. Thus, 50–80% of the  $^4\text{He}$  in these four samples may be from a source external to the aquifer. An external source of  $^4\text{He}$  is apparent in the Sherka-36 and Baris samples, for which  $^4\text{He}$  concentrations are much higher and  $^4\text{He}$  was not used to estimate residence time.

#### 14.7. CARBON-14 DATA

Radiocarbon data for four of the  $^{81}\text{Kr}$  samples is given in Table 14.1. The  $\text{CO}_2$  samples for which these measurements were made were purified from aliquots of the dissolved gas extracted for  $^{81}\text{Kr}$  measurements. Unfortunately, aliquots from two other samples were lost during shipping between laboratories because of damage to the package containing them. The fraction of modern carbon in these samples is uniformly low and ranges from about 0.01 to 0.03. These data constrain the upper limits of atmospheric contamination of the Kr samples as well as possible mixing fractions of young

groundwater, and are in good agreement with the constraints from  $^{85}\text{Kr}$  data. The measured  $^{14}\text{C}$  activities of these samples are at the low end of the range for Nubian aquifer waters (Fröhlich et al. (2007) [730]), indicating minimal contributions from young groundwater.

#### 14.8. HYDROGEOLOGICAL AND PALAEOCLIMATIC IMPLICATIONS OF GROUNDWATER AGE DATA

The concordance of the  $^{36}\text{Cl}$  and  $^{81}\text{Kr}$  data supports mean groundwater residence times approaching  $10^6$  a in the Western Desert of Egypt. A steady state, two dimensional hydrodynamic model incorporating constraints from  $^{36}\text{Cl}$  and available measurements of aquifer hydraulic parameters yields groundwater velocities in the range of 0.5 to 3.5 m/a, consistent with residence times estimated from  $^{81}\text{Kr}$  (Patterson et al. (2005) [43]). A model proposed by Fröhlich et al. (2007) [730] estimates a recharge rate of 0.4 mm/a and a discharge rate of 0.65 mm/a for water in the deep portion of the aquifer. Further progress in understanding the aquifer hydrodynamics will require extensive, depth dependent sampling and measurement of multiple stable and radioactive isotopic tracers.

Stable isotope ratios of hydrogen and oxygen in the Nubian aquifer (and equivalent) groundwaters from across Saharan North Africa indicate a clearly defined continental isotope effect involving precipitation from air masses having an Atlantic moisture source;  $\delta^2\text{H}$  values decrease gradually from west to east with a geographic pattern resembling that observed in modern European groundwaters (Sonntag et al. (1979) [731]). In the deep Nubian aquifer samples, nearly constant  $\delta^2\text{H}$  values (from  $-82$  to  $-79$ ) as a function of  $^{81}\text{Kr}$  age reveal that this Atlantic moisture source was recurrent during all major pre-Holocene pluvial periods throughout the past  $1 \times 10^6$  a. In contrast, the isotopic composition of modern precipitation in the study area, which mostly delivers moisture from the Mediterranean, is much less depleted in  $^2\text{H}$  ( $\delta^2\text{H}$  ranges from  $-28$  to  $+14\text{‰}$ ) (El Bakri et al. (1992) [734]). These observations indicate that Nubian aquifer groundwaters were recharged under a climatic regime in which there had been a persistent southward shift of the intertropical convergence zone relative to modern climate in the region.

#### Acknowledgements

This work was supported by the United States National Science Foundation and the United States Department of Energy.

## REFERENCES

- [1] SHIKLOMANOV, I., RODDA, J.C., World Water Resources at the Beginning of the Twenty-First Century, UNESCO, International Hydrology Series, Cambridge University Press, Paris (2004).
- [2] ANDERSON, M., Groundwater, IAHS Benchmark Papers in Hydrology No. 3, International Association of Hydrological Sciences, Wallingford, UK (2008).
- [3] AGGARWAL, P., et al., Isotope Hydrology, IAHS Benchmark Papers in Hydrology No. 8, International Association of Hydrological Sciences, Wallingford, UK (2012).
- [4] INTERNATIONAL ATOMIC ENERGY AGENCY, Atlas of Isotope Hydrology: Africa, IAEA, Vienna (2007).
- [5] STURCHIO, N.C., et al., One million year old groundwater in the Sahara revealed by krypton-81 and chlorine-36, *Geophys. Res. Lett.* **31** (2004).
- [6] BEAR, J., *Hydraulics of Groundwater*, McGraw-Hill, New York (1979).
- [7] de MARSILY, G., *Quantitative hydrogeology — Groundwater Hydrology for Engineers*, Academic Press, Orlando, FL (1986).
- [8] DOMENICO, P.A., SCHWARTZ, F.W., *Physical and Chemical Hydrogeology*, John Wiley and Sons, New York (1998).
- [9] DRISCOLL, F.G., *Groundwater and Wells* (1986).
- [10] FETTER, C.W., *Applied Hydrogeology*, Prentice-Hall, Inc., Englewood Cliffs, NJ (2000).
- [11] FREEZE, R.A., CHERRY, J.A., *Groundwater*, Prentice-Hall, Englewood Cliffs, NJ (1979).
- [12] MAZOR, E., *Chemical and Isotopic Groundwater Hydrology*, Marcel Dekker, New York, Basel (2004).
- [13] TODD, D.K., MAYS, L.W., *Ground-water Hydrology*, John Wiley and Sons, New York (2005).
- [14] BACK, W., ROSENSHEIN, J.S., SEABER, P.R., “Hydrogeology”, *The Geology of North America*, The Geological Society of America, Boulder, CO (1988).
- [15] GLYNN, P.D., PLUMMER, L.N., Geochemistry and the understanding of ground-water systems, *Hydrogeol. J.* **13** (2005) 263–287.
- [16] GLYNN, P.D., VOSS, C.I., Geochemical Characterization of Simpevarp Ground Waters near the Äspö Hard Rock Laboratory, Swedish Nuclear Power Inspectorate (SKI) Report (1999).
- [17] HEATH, R.C., *Ground-Water Regions of the United States*, U.S. Geological Survey Water-Supply Paper **2242** 78 (1984).
- [18] MILLER, J.A., *Ground Water Atlas of the United States*, U.S. Geological Survey Hydrologic Atlas, U.S. Geological Survey (2000).
- [19] REILLY, T.E., DENNEHY, K.F., ALLEY, W.M., CUNNINGHAM, W.L., Ground-water availability in the United States, U.S. Geological Survey Circular **1323** (2008) 70.
- [20] SANFORD, W.E., CAINE, J.S., WILCOX, D.A., McWREATH, H.C., NICHOLAS, J.R., Research opportunities in interdisciplinary ground-water science in the U.S. Geological Survey, U.S. Geological Survey Circular **1293** (2006) 21.
- [21] THORN, C.R., MCADA, D.P., KERNODLE, J.M., Geohydrologic framework and hydrologic conditions in the Albuquerque Basin, central New Mexico, U.S. Geological Survey Water-Resources Investigations Report **93-4149** (1993) 106.
- [22] FRANKE, O.L., REILLY, T.E., BUXTON, H.T., SIMMONS, D.L., Study guide for a beginning course in ground-water hydrology: Part 2 — instructor’s guide, Open-File Report **92-637**, U.S. Geological Survey (1993) 128.
- [23] FRANKE, O.L., REILLY, T.E., HAEFNER, R.J., SIMMONS, D.L., Study guide for a beginning course in ground-water hydrology: Part 1 — course participants, Open-File Report **90-183**, U.S. Geological Survey (1990) 184.
- [24] HEATH, R.C., *Basic ground-water hydrology*, U.S. Geological Survey Water-Supply Paper **2220** (1983) 84.
- [25] REILLY, T.E., FRANKE, O.L., BUXTON, H.T., BENNETT, G.D., A conceptualization for ground-water solute-transport studies with emphasis on physical mechanisms of solute movement, U.S. Geological Survey Water-Resources Investigations Report **87-4191** (1987) 44.

- [26] MOOK, W.G., *Environmental Isotopes in the Hydrological Cycle, Principles and Applications, Vol. I: Introduction. Theory, Methods, Review*, UNESCO International Hydrological Programme (IHP-V), Paris, Vienna (2000).
- [27] HEALY, R.W., WINTER, T.C., LABAUGH, J.W., FRANKE, O.L., *Water budgets: Foundations for effective water-resources and environmental management*, U.S. Geological Survey Circular **1308** (2007) 90.
- [28] TÓTH, J., *A theoretical analysis of groundwater flow in small drainage basins*, *J. Geophys. Res.* **68** (1963) 4795–4812.
- [29] HELY, A.G., MOWER, R.W., HAN, C.A., *Water resources of Salt Lake County, Utah*, Utah Department of Natural Resources Technical Publication **21** (1971) 244.
- [30] THIROS, S.A., *Quality of shallow ground water in areas of recent residential and commercial development in Salt Lake Valley, Utah, 1999*, USGS Fact Sheet, U.S. Geological Survey (2000).
- [31] BETHKE, C.M., *A numerical model of compaction-driven groundwater flow and heat transfer and its application to the palaeohydrology of intracratonic sedimentary basins*, *J. Geophys. Res.* **90** (1985) 6817–6828.
- [32] BEXFIELD, L.M., *Ground-water-level maps and how they are used to understand the aquifer*, U.S. Geological Survey Circular **1222** (2002) 47–48.
- [33] FERRIS, J.G., KNOWLES, D.B., BROWN, R.H., STALLMAN, R.W., *Theory of aquifer tests*, U.S. Geological Survey Water-Supply Paper **1536-E** (1962) 174.
- [34] KRUSEMAN, G.P., de RIDDER, N.A., *Analysis and evaluation of pumping test data*, International Institute for Land Reclamation and Improvement, Wageningen, The Netherlands (1990).
- [35] SHUTER, E., TEASDALE, W.E., *Application of drilling, coring, and sampling techniques to test holes and wells*, *Techniques of Water-Resources Investigations of the United States Geological Survey* (1989).
- [36] de VRIES, J.J., SIMMERS, I., *Groundwater recharge: an overview of processes and challenges*, *Hydrogeol. J.* **20** (2002) 5–17.
- [37] SCANLON, B.R., HEALY, R.W., COOK, P.G., *Choosing appropriate techniques for quantifying groundwater recharge*, *Hydrogeol. J.* **10** (2002) 18–39.
- [38] WOOD, W.W., SANFORD, W.E., *Chemical and isotopic methods for quantifying ground-water recharge in a regional, semiarid environment*, *Ground Water* **33** (1995) 458–468.
- [39] PHILLIPS, F.M., TANSEY, M.K., PEETERS, L.A., CHENG, S., LONG, A., *An isotopic investigation of groundwater in the central San Juan Basin, New Mexico: Carbon-14 dating as a basis for numerical flow modeling*, *Water Resour. Res.* **25** (1989) 2259–2273.
- [40] AESCHBACH-HERTIG, W., CLARK, J.F., STUTE, M., REUTER, R.F., SCHLOSSER, P., *Apalaeotemperature record derived from dissolved noble gases in groundwater of the Aquia Aquifer (Maryland, USA)*, *Geochim. Cosmochim. Acta* **66** (2002) 797–817.
- [41] CASTRO, M.C., HALL, C.M., PATRIARCHE, D., GOBLET, P., ELLIS, B.R., *A new noble gas palaeoclimate record in Texas — Basic assumptions revisited*, *Earth Planet. Sci. Lett.* **257** (2007) 170–187.
- [42] STUTE, M., SCHLOSSER, P., CLARK, J.F., BROECKER, W.S., *Palaeotemperatures in the southwestern United States derived from noble gas measurements in groundwater*, *Science* **256** (1992) 1000–1003.
- [43] PATTERSON, L.J., et al., *Cosmogenic, radiogenic, and stable isotopic constraints on groundwater residence time in the Nubian Aquifer, Western Desert of Egypt*, *Geochim. Geophys. Geosystems* **6** (2005) 1–19.
- [44] WALVOORD, M., PHILLIPS, F.M., TYLER, S.W., HARTSOUGH, P.C., *Deep arid system hydrodynamics, Part 2: Application to palaeohydrologic reconstruction using vadose-zone profiles from the northern Mojave Desert*, *Water Resour. Res.* **38** (2002) 1291.
- [45] BACK, W., *Origin or hydrochemical facies of ground water in the Atlantic Coastal Plain*, 21st Int. Geol. Congr., Copenhagen (1960).
- [46] BACK, W., *Hydrochemical facies and ground-water flow patterns in northern part of Atlantic Coastal Plain*, U.S. Geol. Surv. Prof. Pap. **498-A** (1966).
- [47] SANFORD, W.E., PLUMMER, L.N., McADA, D.P., BEXFIELD, L.M., ANDERHOLM, S.K., *Hydrochemical tracers in the Middle Rio Grande Basin, USA: 2. Calibration of a Ground-water Flow Model*, *Hydrogeol. J.* **12** (2004) 389–407.

- [48] SANFORD, W.E., PLUMMER, L.N., McADA, D.P., BEXFIELD, L.M., ANDERHOLM, S.K., Use of environmental tracers to estimate parameters for a predevelopment-ground-water-flow model of the Middle Rio Grande Basin, New Mexico, U.S. Geological Survey Water-Resources Investigations Report **03-4286** (2004) 102.
- [49] PLUMMER, L.N., BEXFIELD, L.M., ANDERHOLM, S.K., SANFORD, W.E., BUSENBERG, E., Geochemical characterization of ground-water flow in the Santa Fe Group aquifer system, Middle Rio Grande Basin, New Mexico, U.S. Geological Survey Water-Resources Investigations Report **03-4131** (2004) 395.
- [50] PLUMMER, L.N., BEXFIELD, L.M., ANDERHOLM, S.K., SANFORD, W.E., BUSENBERG, E., Hydrochemical tracers in the Middle Rio Grande Basin, USA: 1. Conceptualization of groundwater flow, *Hydrogeol. J.* **12** (2004) 359–388.
- [51] PLUMMER, L.N., SANFORD, W.E., BEXFIELD, L.M., ANDERHOLM, S.K., BUSENBERG, E., “Using geochemical data and aquifer simulation to characterize recharge and groundwater flow in the Middle Rio Grande Basin, New Mexico”, *Groundwater Recharge in a Desert Environment: The Southwestern United States* (HOGAN, J.F., PHILLIPS, F.M., SCANLON, B.R., Eds), American Geophysical Union, Washington, DC (2004).
- [52] CLARK, I.D., FRITZ, P., *Environmental Isotopes in Hydrogeology*, Springer Verlag, Berlin, Heidelberg, New York (1997).
- [53] COOK, P.G., HERCZEG, A.L., *Environmental Tracers in Subsurface Hydrology*, Kluwer Academic Press, Boston, MA (1999).
- [54] STUTE, M., SCHLOSSER, P., “Principles and applications of the Noble Gas Palaeothermometer”, *Climate Change in Continental Isotopic Records* (SWART, P.K., LOHMANN, K.C., McKENZIE, J., SVIN, S., Eds), Geophysical Monograph, American Geophysical Union (1993).
- [55] AESCHBACH-HERTIG, W., PEETERS, F., BEYERLE, U., KIPFER, R., Palaeotemperature reconstruction from noble gases in ground water taking into account equilibration with entrapped air, *Nature* **405** (2000) 1040–1044.
- [56] HEATON, T.H.E., TALMA, A.S., VOGEL, J.C., Origin and history of nitrate in confined groundwater in the western Kalahari, *J. Hydrol.* **62** (1983) 243–262.
- [57] DANSGAARD, W., Stable isotopes in precipitation, *Tellus* **16** (1964) 436–468.
- [58] ROZANSKI, K., ARAGUÁS-ARAGUÁS, L., GONFIANTINI, R., “Isotopic patterns in modern global precipitation”, *Climate Change in Continental Isotopic Records* (SWART, P.K., LOHMANN, K.C., McKENZIE, J., SVIN, S., Eds), American Geophysical Union (1993).
- [59] STRAATEN, C.M.V.D., MOOK, W.G., “Stable isotopic composition of precipitation and climatic variability”, *Palaeoclimates and Palaeowaters: A Collection of Environmental Isotope Studies, Panel Proceedings Series No. 146*, IAEA, Vienna (1983).
- [60] PLUMMER, L.N., Stable isotope enrichment in palaeowaters of the southeast Atlantic Coastal Plain, United States, *Science* **262** (1993) 2016–2020.
- [61] ALLEY, W.M., REILLY, T.E., FRANKE, O.L., Sustainability of ground-water resources, U.S. Geological Survey Circular **1186** (1999) 79.
- [62] PLUMMER, L.N., et al., Low-level detections of halogenated volatile organic compounds in groundwater: Use in vulnerability assessments, *J. Hydrol. Eng.* **13** (2008) 1049–1068.
- [63] GENUCHTEN, M.T.V., ALVES, W.J., Analytical solutions of the one-dimensional convective-dispersion solute transport equation, *Tech. Bull.* **1661** (1982) 151.
- [64] MAŁOSZEWSKI, P., RAUERT, W., STICHLER, W., HERRMANN, A., Application of flow models in an alpine catchment area using tritium and deuterium data, *J. Hydrol.* **66** (1983) 319–330.
- [65] MAŁOSZEWSKI, P., ZUBER, A., “Lumped parameter models for interpretation of environmental tracer data”, *Manual on the Mathematical Models in Isotope Hydrogeology* **910** (1996) 9–59.
- [66] HUYAKORN, P.S., PINDER, G.F., *Computational Methods in Subsurface Flow*, Academic Press (1983).
- [67] KONIKOW, L.F., GLYNN, P.D., “Modeling ground-water flow and quality”, *Essentials of Medical Geology* (SELINUS, O., Ed.), Academic Press (2005).
- [68] WANG, J.F., ANDERSON, M.P., *Introduction to Groundwater Modeling*, Freeman, San Francisco, CA (1982).
- [69] GOODE, D.J., Direct simulation of groundwater age, *Water Resour. Res.* **32** (1996) 289–296.

- [70] HARBAUGH, A.W., BANTA, E.R., HILL, M.C., McDONALD, M.G., MODFLOW-2000, The U.S. Geological Survey Modular Groundwater Model-User Guide to Modularization Concepts and the Groundwater Flow Process, Open-File Report, U.S. Geological Survey (2000).
- [71] McDONALD, M.G., HARBAUGH, A.W., A modular three-dimensional finite-difference ground-water flow model, Techniques of Water-Resources Investigations of the United States Geological Survey (1988).
- [72] REILLY, T.E., System and boundary conceptualization in ground-water flow simulation, U.S. Geological Survey Techniques of Water-Resources Investigations (2001).
- [73] POLLOCK, D.W., Documentation of a computer program to compute and display pathlines using results from the U.S. Geological Survey modular three-dimensional finite-difference ground-water flow model, U.S. Geological Survey, Open File Report **89-381** (1989).
- [74] POETER, E.P., HILL, M.C., Documentation of UCODE, a computer code for universal inverse modeling, U.S. Geological Survey Water-Resources Investigations Report (1998).
- [75] MÜNNICH, K.-O., Messung des  $^{14}\text{C}$ -Gehaltes von hartem Grundwasser, *Naturwissenschaften* **34** (1957) 32–33.
- [76] DAVIS, S.N., BENTLEY, H.W., “Dating groundwater: A short review”, Nuclear and Chemical Dating Techniques, Interpreting the Environmental Record (CURRIE, L.A., Ed.), American Chemical Society, Washington, DC (1982).
- [77] PHILLIPS, F.M., CASTRO, M.C., Groundwater dating and residence time measurements, *Treatise on Geochemistry* **5** (2003) 51–497.
- [78] DANCKWERTS, P.V., Continuous flow systems: Distribution of residence times, *Chem. Eng. Sci.* **2** (1953) 1–13.
- [79] HOOPER, R.P., Diagnostic tools for mixing models of stream water chemistry, *Water Resour. Res.* **39** (2003).
- [80] LOAICIGA, H.A., Residence time, groundwater age, and solute output in steady-state groundwater systems, *Advances in Water Resources* **27** (2004) 681–688.
- [81] MCGUIRE, K.J., McDONNELL, J.J., A review and evaluation of catchment transit time modeling, *J. Hydrol.* **330** (2006) 543–563.
- [82] MAŁOSZEWSKI, P., ZUBER, A., Determining the turnover time of groundwater systems with the aid of environmental tracers, I. Models and their applicability, *J. Hydrol.* **57** (1982) 207–231.
- [83] VARNI, M., CARRERA, J., Simulation of groundwater age distributions, *Water Resour. Res.* **34** (1998) 3271–3281.
- [84] BETHKE, C.M., JOHNSON, T.M., Groundwater age and groundwater age dating, *Annu. Rev. Earth Planetary Sci.* **36** (2008) 121–152.
- [85] INTERNATIONAL ATOMIC ENERGY AGENCY, Use of Chlorofluorocarbons in Hydrology: A Guidebook, IAEA, Vienna (2006).
- [86] KIRCHNER, J.W., FENG, X.H., NEAL, C., Fractal stream chemistry and its implications for contaminant transport in catchments, *Nature* **403** (2000) 524–527.
- [87] MCGUIRE, K.J., et al., The role of topography on catchment-scale water residence time, *Water Resour. Res.* **41** (2005).
- [88] CASTRO, M.C., STUTE, M., SCHLOSSER, P., Comparison of  $^4\text{He}$  ages and  $^{14}\text{C}$  ages in simple aquifer systems: implications for groundwater flow and chronologies, *Appl. Geochem.* **15** (2000) 1137–1167.
- [89] CASTRO, M.C., GOBLET, P., Calibration of regional groundwater flow models: working toward a better understanding of site-specific systems, *Water Resour. Res.* **39** (2003).
- [90] PARK, J., BETHKE, C.M., TORGERSEN, T., JOHNSON, T.M., Transport modeling applied to the interpretation of groundwater  $^{36}\text{Cl}$  age, *Water Resour. Res.* **38** (2002) 1043.
- [91] WEISSMANN, G.S., ZHANG, Y., LABOLLE, E.M., FOGG, G.E., Dispersion of groundwater age in an alluvial aquifer system, *Water Resour. Res.* **38** (2002).
- [92] BERGER, P. M., An optimization approach to groundwater age dating: how old is water in the Paris Basin? MSc Thesis, University of Illinois (2008).
- [93] TORGERSEN, T., IVEY, G.N., Helium accumulation in groundwater: II, A model for the accumulation of the crustal  $^4\text{He}$  degassing flux, *Geochim. Cosmochim. Acta* **49** (1985) 2445–2452.

- [94] BETHKE, C.M., TORGERSEN, T., PARK, J., The 'age' of very old groundwater: insights from reactive transport models, *J. Geochem. Explor.* **69–70** (2000) 1–4.
- [95] BETHKE, C.M., ZHAO, X., TORGERSEN, T., Groundwater flow and the  $^4\text{He}$  distribution in the Great Artesian Basin of Australia, *J. Geophys. Res.* **104** (1999) 12 999–13 011.
- [96] CASTRO, M.C., GOBLET, P., LEDOUX, E., VIOLETTE, S., MARSILY, G.D., Noble gases as natural tracers of water circulation in the Paris Basin 2, Calibration of a groundwater flow model using noble gas isotope data, *Water Resour. Res.* **34** (1998) 2467–2483.
- [97] CASTRO, M.C., JAMBON, A., MARSILY, G. D., SCHLOSSER, P., Noble gases as natural tracers of water circulation in the Paris Basin 1, Measurements and discussion of their origin and mechanisms of vertical transport in the basin, *Water Resour. Res.* **34** (1998) 2443–2466.
- [98] ZHAO, X., FRITZEL, T.L.B., QUINODOZ, H.A.M., BETHKE, C.M., TORGERSEN, T., Controls on the distribution and isotopic composition of helium in deep groundwater flows, *Geology* **26** (1998) 291–294.
- [99] GOMEZ-HERNANDEZ, J.J., GORELICK, S.M., Effective groundwater model parameter values: Influence of spatial variability of hydraulic conductivity, leakance, and recharge, *Water Resour. Res.* **25** (1989) 405.
- [100] MOOK, W.G., "Preface to hydrology section", *Radiocarbon after Four Decades: An Interdisciplinary Perspective*, Springer (1992) 241.
- [101] KAMEN, M.D., Early history of carbon-14, *Science* **140** (1963) 584–590.
- [102] RUBEN, S., KAMEN, M.D., Long-lived radioactive carbon: C14, *Phys. Rev.* **59** (1941) 349–354.
- [103] ANDERSON, E.C., et al., Natural radiocarbon from cosmic radiation, *Phys. Rev.* **72** (1947) 931–936.
- [104] LIBBY, W.F., ANDERSON, E.C., ARNOLD, J.R., Age determination by radiocarbon content: World-wide assay of natural radiocarbon, *Science* **109** (1949) 227–228.
- [105] MACKAY, C., The elementary chemistry of atomic carbon, *Chemical Effects of Nuclear Transformations 2* (1961) 17–26.
- [106] MAK, J.E., BRENNINKMEIJER, C.A.M., SOUTHON, J.R., Direct measurement of the production rate of  $^{14}\text{C}$  near Earth's surface, *Geophys. Res. Lett.* **26** (1999) 3381–3384.
- [107] GODWIN, H., Half life of radiocarbon, *Nature* **195** (1962) 984.
- [108] CHIU, T.C., FAIRBANKS, R.G., CAO, L., MORTLOCK, R.A., Analysis of the atmospheric  $^{14}\text{C}$  record spanning the past 50,000 years derived from high-precision  $^{230}\text{Th}/^{234}\text{U}/^{238}\text{U}$ ,  $^{231}\text{Pa}/^{235}\text{U}$  and  $^{14}\text{C}$  dates on fossil corals, *J. Radioanal. Nucl. Chem. Quaternary Sci. Rev.* **26** (2007) 18–36.
- [109] MOOK, W.G., Carbon-14 in hydrological studies, *The Terrestrial Environment A1*, Elsevier (1980) 49–74.
- [110] STUIVER, M., POLACH, H.A., Discussion of reporting of  $^{14}\text{C}$  data, *Radiocarbon* **19** (1977) 355–363.
- [111] KALIN, R.M., "Radiocarbon dating of groundwater systems", *Environmental Tracers in Subsurface Hydrology* (COOK, P.G., HERCZEG, A.L., Eds), Kluwer Academic Press, Boston, MA (1999).
- [112] BARD, E., HAMELIN, B., FAIRBANKS, R.G., ZINDLER, A., Calibration of the  $^{14}\text{C}$  timescale over the past 30,000 years using mass spectrometric U–Th ages from Barbados corals, *Nature* **345** (1990) 405–410.
- [113] PELTIER, W.R., FAIRBANKS, R.G., Global glacial ice volume and Last Glacial Maximum duration from an extended Barbados sea level record, *J. Radioanal. Nucl. Chem. Quaternary Sci. Rev.* **25** (2006) 3322–3337.
- [114] MÜNNICH, K.-O., Isotopen-Datierung von Grundwasser, *Naturwissenschaften* **55** (1968) 158–163.
- [115] FONTES, J.-C., Dating of groundwater, *Guidebook on Nuclear Techniques in Hydrology*, Tech. Rep. Ser. **91** (1983) 285–317.
- [116] FONTES, J.-C., GARNIER, J.-M., Determination of the initial  $^{14}\text{C}$  activity of the total dissolved carbon: A review of the existing models and a new approach, *Water Resour. Res.* **15** (1979) 399–413.
- [117] FONTES, J.C., Chemical and isotopic constraints on C-14 dating of groundwater, *Radiocarbon after Four Decades* (1992) 242–261.
- [118] GEYH, M.A., "Dating of old groundwater — History, potential, limits and future", *Isotopes in the Water Cycle: Past, Present and Future of a Developing Science* (AGGARWAL, P.K., GAT, J.R., FRÖHLICH, K., Eds), Springer, The Netherlands (2005).
- [119] MOOK, W.G., *Introduction to Isotope Hydrology*, IAH Series, Taylor & Francis (2005).

- [120] PLUMMER, L.N., PRESTEMON, E.C., PARKHURST, D.L., An interactive code (NETPATH) for modelling net geochemical reactions along a flow path, Version 2.0, Water Resources Investigations Report, U.S. Geological Survey (1994).
- [121] BROOK, G.A., FOLKOFF, M.E., BOX, E.O., A world model of soil carbon dioxide, *Earth Surface Processes and Landforms* **8** (1983) 79–88.
- [122] DEINES, P., LANGMUIR, D., HARMON, R.S., Stable carbon isotope ratios and the existence of a gas phase in the evolution of carbonate groundwaters, *Geochim. Cosmochim. Acta* **38** (1974) 1147–1164.
- [123] VERHAGEN, B.T., “Environmental isotope study of a groundwater supply project in the Kalahari of Gordonia”, *Isotope Hydrology 1983*, IAEA, Vienna (1984).
- [124] VERHAGEN, B.T., MAZOR, E., SELLSHOP, G.P.F., Radiocarbon and tritium evidence for direct rain recharge to ground waters in the northern Kalahari, *Nature* **249** (1974) 643–644.
- [125] PLUMMER, L.N., BUSENBERG, E., “Chlorofluorocarbons”, *Environmental Tracers in Subsurface Hydrology* (COOK, P.G., HERCZEG, A.L., Eds), Kluwer Academic Press, Boston, MA (2000).
- [126] GEYH, M.A., An overview of  $^{14}\text{C}$  analysis in the study of groundwater, *Radiocarbon* **42** (2000) 99–114.
- [127] VOGEL, J.C., GROOTES, P.M., MOOK, W.G., Isotopic fractionation between gaseous and dissolved carbon dioxide, *Zeitschrift für Physik* **230** (1970) 225–238.
- [128] LEVIN, I., KROMER, B., Twenty years of atmospheric  $^{14}\text{CO}_2$  observations Schauinsland station, Germany, *Radiocarbon* **39** (1997) 205–218.
- [129] LEVIN, I., et al., “ $^{14}\text{CO}_2$  record from sites in Central Europe”, *Trends ‘93: A Compendium of Data on Global Change* (1994) 203–222.
- [130] EICHINGER, L., A contribution to the interpretation of  $^{14}\text{C}$  groundwater ages considering the example of a partially confined sandstone aquifer, *Radiocarbon* **25** (1983) 347–356.
- [131] EVANS, G.V., OTLET, R.L., DOWNING, A., MONKHOUSE, R.A., RAE, G., “Some problems in the interpretation of isotope measurements in United Kingdom Aquifers”, *Isotopes in Hydrology II*, IAEA, Vienna (1979).
- [132] INGERSON, E., PEARSON F.R., Jr., “Estimation of age and rate of motion of groundwater by the  $^{14}\text{C}$ -method”, *Recent Researches in the Fields of Atmosphere, Hydrosphere, and Nuclear Geochemistry*, Sugara Festival Volume (MIYAKE, Y., KOYAMA, T., Eds), Maruzen, Tokyo (1964).
- [133] MOOK, W.G., “On the reconstruction of the initial  $^{14}\text{C}$  content of groundwater from the chemical and isotopic composition”, *8th Int. Conf. on Radiocarbon Dating* **1** (1972) 342–352.
- [134] TAMERS, M.A., Validity of radiocarbon dates on groundwater, *Geophys. Surveys* **2** (1975) 217–239.
- [135] PLUMMER, L.N., SPRINKLE, C.L., Radiocarbon dating of dissolved inorganic carbon in groundwater from confined parts of the Upper Floridan aquifer, Florida, USA, *Hydrogeol. J.* **9** (2001) 127–150.
- [136] WIGLEY, T.M.L., PLUMMER, L.N., PEARSON F.J., JR., Mass transfer and carbon isotope evolution in natural water systems, *Geochim. Cosmochim. Acta* **42** (1978) 1117–1139.
- [137] VOGEL, J.C., “Investigation of groundwater flow with radiocarbon”, *Isotopes in Hydrology*, Vienna (1967).
- [138] VOGEL, J.C., “ $^{14}\text{C}$ -dating of groundwater”, *Isotope Hydrology 1970*, Proceedings Series No. 131, IAEA, Vienna (1970).
- [139] VOGEL, J.C., EHHALT, D., “The use of carbon isotopes in groundwater studies”, *Radioisotopes in Hydrology*, Proceedings Series No. 38, IAEA, Vienna (1963).
- [140] TAMERS, M.A., “Surface-water infiltration and groundwater movement in arid zones in Venezuela”, *Isotopes in Hydrology*, Proceedings Series No. 80, IAEA, Vienna (1967).
- [141] SALEM, O., VISSER, J.H., DRAY, M., GONFIANTINI, R., “Environmental isotopes used in a hydrogeological study of north-eastern Brazil”, *Arid-zone Hydrology: Investigations with Isotope Techniques*, Panel Proceedings Series No. 134, IAEA, Vienna (1980).
- [142] MOOK, W.G., “The dissolution-exchange model for dating groundwater with  $^{14}\text{C}$ ”, *Interpretation of Environmental Isotope and Hydrochemical Data in Groundwater Hydrology*, Panel Proceedings Series No. 108, IAEA, Vienna (1976).
- [143] CRAIG, H., Carbon-13 in plants and their relationships between carbon-13 and carbon-14 variations in nature, *J. Geol.* **62** (1954) 115–149.

- [144] McMAHON, P.B., CHAPELLE, F.H., Redox processes and water quality of selected principal aquifer systems, *Ground Water* **46** (2008) 259–271.
- [145] PLUMMER, L.N., BUSBY, J.F., LEE, R.M., HANSHAW, B.B., Geochemical modeling of the Madison aquifer in parts of Montana, Wyoming, and South Dakota, *Water Resour. Res.* **26** (1990) 1981–2014.
- [146] APPELO, C.A.J., Cation and proton exchange, pH variations, and carbonate reactions in a freshening aquifer, *Water Resour. Res.* **30** (1994) 2793–2805.
- [147] WIGLEY, T.M.L., PLUMMER, L.N., PEARSON, F.J., Errata, *Geochim. Cosmochim. Acta* **43** (1979) 1395.
- [148] PLUMMER, L.N., PARKHURST, D.L., THORSTENSON, D.C., Development of reaction models for ground-water systems, *Geochim. Cosmochim. Acta* **47** (1983) 665–686.
- [149] PARKHURST, D.L., APPELO, C.A.J., User's guide to PHREEQC — A computer program for speciation, batch-reaction, one-dimensional transport, and inverse geochemical calculations, U.S. Geological Survey Water-Resources Investigations Report, U.S. Geological Survey (1999).
- [150] PARKHURST, D.L., PLUMMER, L.N., Geochemical models, Regional Ground-Water Quality (1993) 199–225.
- [151] PEARSON, F.J., “Effects of parameter uncertainty in modeling  $^{14}\text{C}$  in groundwater”, *Radiocarbon after Four Decades, An Interdisciplinary Perspective* (1992) 262–275.
- [152] PARKHURST, D.L., User's guide to PHREEQC — A computer program for speciation, reaction-path, advective-transport, and inverse geochemical calculations, U.S. Geological Survey Water-Resources Investigations Report **95-4227** (1995) 143.
- [153] PARKHURST, D.L., Geochemical mole-balance modeling with uncertain data, *Water Resour. Res.* **33** (1997) 1957–1970.
- [154] GLYNN, P.D., BROWN, J.G., “Integrating field observations and inverse and forward modeling: Application at a site with acidic, heavy-metal-contaminated groundwater”, *Geochemical Modeling of Groundwater, Vadose and Geothermal Systems* (BUNDSCHUH, J., ZILBERBRAND, M., Eds), CRC Press (2012) 181–234.
- [155] THORSTENSON, D.C., PARKHURST, D.L., Calculation of individual isotope equilibrium constants for geochemical reactions, *Geochim. Cosmochim. Acta* **68** (2004) 2449–2465.
- [156] PARKHURST, D.L., CHARLTON, S.R., NetpathXL — An Excel® interface to the program NETPATH, U.S. Geological Survey Techniques and Methods (2008) 11.
- [157] EL-KADI, A.I., PLUMMER, L.N., AGGARWAL, P.K., NETPATH-WIN: An interactive user version of the mass-balance model, NETPATH, *Ground Water* **49** (2011) 593–599.
- [158] PARKHURST, D.L., PLUMMER, L.N., THORSTENSON, D.C., BALANCE — A computer program for calculating mass transfer for geochemical reactions in ground water, Water-Resources Investigations Report, U.S. Geological Survey (1982).
- [159] CHENG, S.L., LONG, A., “Implementation of a carbon isotope subroutine to the computer program PHREEQE and the application to  $^{14}\text{C}$  ground-water dating”, *Hydrology and Water Resources in Arizona and the Southwest, 1984 Meeting of the Arizona Section of the American Water Resources Association and the Hydrogeology Section of the Arizona–Nevada Academy of Sciences* (1984) 121–135.
- [160] PARKHURST, D.L., THORSTENSON, D.C., PLUMMER, L.N., PHREEQE — a computer program for geochemical calculations, Water Resources Investigations Report, U.S. Geological Survey (1980).
- [161] PLUMMER, L.N., “Geochemical modeling: A comparison of forward and inverse methods”, *First Canadian/American Conference on Hydrogeology* (HITCHON, B., WALLICK, E.I., Eds), National Water Well Assoc., Banff, Alberta (1985).
- [162] HELGESON, H.C., Evaluation of irreversible reactions in geochemical processes involving minerals and aqueous solutions, I. Thermodynamic relations, *Geochim. Cosmochim. Acta* **32** (1968) 853–877.
- [163] BUDDEMEIER, R.W., OKAMOTO, H.S., HURD, D.C., HUFEN, T.H., “Effects of solution and exchange on the radiocarbon dating of sediments and natural waters”, *8th Int. Conf. on Radiocarbon Dating* (1972) C73–C86.
- [164] GARNIER, J.-M., Retardation of dissolved radiocarbon through a carbonated matrix, *Geochim. Cosmochim. Acta* **49** (1985) 683–693.
- [165] MOZETO, A.A., FRITZ, P., REARDON, E.J., Experimental observations on carbon isotope exchange in carbonate-water systems, *Geochim. Cosmochim. Acta* **48** (1984) 495–504.

- [166] ARAVENA, R., WASSENAAR, L.I., PLUMMER, L.N., Estimating  $^{14}\text{C}$  groundwater ages in a methanogenic aquifer, *Water Resour. Res.* **31** (1995) 2307–2317.
- [167] ARAVENA, R., WASSENAAR, L.I., Dissolved organic carbon and methane in a regional confined aquifer, southern Ontario, Canada: Carbon isotope evidence for associated subsurface sources, *Appl. Geochem.* **8** (1993) 483–493.
- [168] DRIMMIE, R.J., et al., Radiocarbon and stable isotopes in water and dissolved constituents, Milk River aquifer, Alberta, Canada, *Appl. Geochem.* **6** (1991) 381–392.
- [169] HENDRY, M.J., WASSENAAR, L.I., Origin and migration of dissolved organic carbon fractions in a clay-rich aquitard:  $^{14}\text{C}$  and  $\delta^{13}\text{C}$  evidence, *Water Resour. Res.* **41** (2005) W02021.
- [170] LONG, A., MURPHY, E.M., DAVIS, S.N., KALIN, R.M., “Natural radiocarbon in dissolved organic carbon in groundwater”, *Radiocarbon after Four Decades: An Interdisciplinary Perspective* (1992) 288–308.
- [171] MURPHY, E.M., DAVIS, S.N., LONG, A., DONAHUE, D., JULL, A.J.T.,  $^{14}\text{C}$  in fractions of dissolved organic carbon in groundwater, *Nature* **337** (1989) 153–155.
- [172] MURPHY, E.M., DAVIS, S.N., LONG, A., DONAHUE, D., JULL, A.J.T., Characterization and isotopic composition of organic and inorganic carbon in the Milk River aquifer, *Water Resour. Res.* **25** (1989) 1893–1905.
- [173] PURDY, C.B., BURR, G.S., RUBIN, M., HELZ, G.R., MIGNEREY, A.C., Dissolved organic and inorganic  $^{14}\text{C}$  concentrations and ages for Coastal Plain aquifers in southern Maryland, *Radiocarbon* **34** (1992) 654–663.
- [174] TULLBORG, E.L., GUSTAFSSON, E.,  $^{14}\text{C}$  in bicarbonate and dissolved organics — a useful tracer? *Appl. Geochem.* **14** (1999) 927–938.
- [175] WASSENAAR, L.I., ARAVENA, R., FRITZ, P., The geochemistry and evolution of natural organic solutes in groundwater, *Radiocarbon* **31** (1989) 865–876.
- [176] WASSENAAR, L.I., ARAVENA, R., HENDRY, M.J., FRITZ, P., BARKER, J.F., Radiocarbon in dissolved organic carbon, a possible groundwater dating method: Case studies from western Canada, *Water Resour. Res.* **27** (1991) 1975–1986.
- [177] DREVER, J.I., *The Geochemistry of Natural Waters: Surface and Groundwater Environment*, 2nd edn, Prentice Hall (1997).
- [178] LEENHEER, J.A., MALCOLM, R.L., MCKINLEY, P.W., ECCLES, L.A., Occurrence of dissolved organic carbon in selected groundwater samples in the United States, *U.S. Geological Survey, J. Res.* **2** (1974) 361–369.
- [179] PABICH, W.J., VALIELA, I., HEMOND, H.F., Relationship between DOC concentration and vadose zone thickness and depth below water table in groundwater of Cape Cod, U.S.A., *Biogeochemistry* **55** (2001) 247–268.
- [180] THURMAN, E.M., MALCOLM, R.L., Preparative isolation of aquatic humic substances, *Environ. Sci. Technol.* **15** (1981) 463–466.
- [181] MURPHY, E.M., Carbon-14 Analyses and Characterization of Dissolved Organic Carbon in Ground Water, PhD Thesis (1987).
- [182] AIKEN, G.R., MALCOLM, R.L., Molecular weight of aquatic fulvic acids by vapor pressure osmometry, *Geochim. Cosmochim. Acta* **51** (1987) 2177–2184.
- [183] BUCKAU, G., et al.,  $^{14}\text{C}$  dating of Gorleben groundwater, *Appl. Geochem.* **15** (2000) 583–507.
- [184] BURR, G.S., et al., Sample preparation of dissolved organic carbon in groundwater for AMS  $^{14}\text{C}$  analysis, *Radiocarbon* **43** (2001) 183–190.
- [185] PETTERSSON, C., ALLARD, B., Dating of groundwaters by  $^{14}\text{C}$ -analysis of dissolved humic substances, *Humic Substances in the Aquatic and Terrestrial Environment* **33** (1991) 135–141.
- [186] THOMAS, J.M., MORSE, B.S., BURR, G.S., Reines, D.L., “Age dating groundwater using dissolved organic carbon — an example from southern Nevada, USA”, *Tenth Int. Symp. WRI-10* (CIDU, R., Ed.), A.A. Balkema, Villasimius, Italy (2001).
- [187] BUCKAU, G., et al., Groundwater in-situ generation of aquatic humic and fulvic acids and the mineralization of sedimentary organic carbon, *Appl. Geochem.* **15** (2000) 819–832.
- [188] INGALLS, A.E., PEARSON, A., Ten years of compound-specific radiocarbon analysis, *Oceanography* **18** (2005) 18–31.
- [189] KONIKOW, L.F., NEUZIL, C.E., A method to estimate groundwater depletion from confining layers, *Water Resour. Res.* **43** (2007).

- [190] ATTEIA, O., ANDRE, L., DUPUY, A., FRANCESCHI, M., Contributions of diffusion, dissolution, ion exchange, and leakage from low-permeability layers to confined aquifers, *Water Resour. Res.* **41** (2005).
- [191] MAŁOSZEWSKI, P., ZUBER, A., Influence of matrix diffusion and exchange reactions on radiocarbon ages in fissured carbonate aquifers, *Water Resour. Res.* **27** (1991) 1937–1945.
- [192] PLUMMER, L.N., MICHEL, R.L., THURMAN, E.M., GLYNN, P.D., “Environmental tracers for age dating young ground water”, *Regional Ground-Water Quality* (ALLEY, W.M., Ed.), Van Nostrand Reinhold, New York (1993).
- [193] LaBOLLE, E.M., FOGG, E.G., EWEIS, J.B., Diffusive fractionation of  $^3\text{H}$  and  $^3\text{He}$  in groundwater and its impact on groundwater age estimates, *Water Resour. Res.* **42** (2006) W07202.
- [194] NEUZIL, C.E., Groundwater flow in low-permeability environments, *Water Resour. Res.* **22** (1986) 1163–1195.
- [195] NEUZIL, C.E., PROVOST, A.M., Recent experimental data may point to a greater role for osmotic pressure in the subsurface, *Water Resour. Res.* **45** (2009) W03410.
- [196] DePAOLO, D.J., Isotopic effects in fracture-dominated reactive fluid-rock systems, *Geochim. Cosmochim. Acta* **70** (2006) 1077–1096.
- [197] ZITO, R., DONAHUE, D.J., DAVIS, S.N., BENTLEY, H.W., FRITZ, P., Possible subsurface production of carbon-14, *Geophys. Res. Lett.* **7** (1980) 235–238.
- [198] ANDREWS, J.N., et al., The in-situ production of radioisotopes in rock matrices with particular reference to the Stripa granite, *Geochim. Cosmochim. Acta* **53** (1989) 1803–1815.
- [199] HELFFERICH, F., *Ion Exchange*, Dover Publications (1995).
- [200] PARKHURST, D.L., KIPP, K.L., ENGESGAARD, P., CHARLTON, S.R., PHAST — A program for simulating ground-water flow, solute transport, and multicomponent geochemical reactions, *U.S. Geological Survey Techniques and Methods* (2004) 154.
- [201] NERETNIEKS, I., Diffusion in the rock matrix: An important factor in radionuclide retardation, *J. Geophys. Res.* **85** (1980) 4379–4397.
- [202] NERETNIEKS, I., Age dating of groundwater in fissured rocks: Influence of water volume in micropores, *Water Resour. Res.* **17** (1981) 421–422.
- [203] TANG, D.H., FRIND, E.O., SUDICKY, E.A., Contaminant transport in fractured porous media: Analytical solution for a single fracture, *Water Resour. Res.* **17** (1981) 555–564.
- [204] SUDICKY, E.A., FRIND, E.O., Contaminant transport in fractured porous media: Analytical solutions for a system of parallel fractures, *Water Resour. Res.* **18** (1982) 1634–1642.
- [205] SUDICKY, E.A., FRIND, E.O., Contaminant transport in fractured porous media: Analytical solution for a two-member decay chain in a single fracture, *Water Resour. Res.* **20** (1984) 1021–1029.
- [206] THERRIEN, R., SUDICKY, E.A., Three-dimensional analysis of variably-saturated flow and solute transport in discretely-fractured porous media, *J. Contam. Hydrol.* **23** (1996) 1–44.
- [207] SANFORD, W.E., Correcting for diffusion in carbon-14 dating of groundwater, *Groundwater* **35** (1997) 357–361.
- [208] COOK, P.G., LOVE, A.J., ROBINSON, N.I., SIMMONS, C.T., Groundwater ages in fractured rock aquifers, *J. Hydrol.* **308** (2005) 284–301.
- [209] ROZANSKI, K., Deuterium and oxygen-18 in European groundwaters — Links to atmospheric circulation in the past, *Chem. Geol.* **52** (1985) 349–363.
- [210] HEATON, T.H.E., Dissolved gases: Some applications to groundwater research, *Trans. Geol. Soc. South Afr.* **84** (1981) 91–97.
- [211] HEATON, T.H.E., VOGEL, J.C., ‘Excess air’ in groundwater, *J. Hydrol.* **50** (1981) 201–216.
- [212] HERZBERG, O., MAZOR, E., Hydrological applications of noble gases and temperature measurements in underground water systems: Examples from Israel, *J. Hydrol.* **41** (1979) 217–231.
- [213] STUTE, M., CLARK, J.F., SCHLOSSER, P., BROECKER, W.S., BONANI, G., A 30,000 yr continental palaeotemperature record derived from noble gases dissolved in groundwater from the San Juan Basin, New Mexico, *Quaternary Res.* **43** (1995) 209–220.

- [214] STUTE, M., et al., Cooling of tropical Brazil (5°C) during the Last Glacial Maximum, *Science* **269** (1995) 379–383.
- [215] STUTE, M., SCHLOSSER, P., “Atmospheric noble gases”, *Environmental Tracers in Subsurface Hydrology* (COOK, P.G., HERCZEG, A.L., Eds), Kluwer Academic Press, Boston, MA (2000).
- [216] MOOK, W.G., VAN DER PLICHT, J., Reporting  $^{14}\text{C}$  activities and concentrations, *Radiocarbon* **41** (1999) 227–239.
- [217] LINICK, T.W., HYLL, A.J.T., ROOLIN, L.J., DONAHUE, D.J., Operation of the NSF-Arizona accelerator facility for radio-isotope analysis and results from selected collaborative research projects, *Radiocarbon* **28** (1986) 522–533.
- [218] DONAHUE, D.J., LINICK, T.W., JULL, A.J.T., Isotope-ratio and background corrections for accelerator mass spectrometry radiocarbon measurements, *Radiocarbon* **32** (1990) 135–142.
- [219] STUIVER, M., ROBINSON, S.W., University of Washington Geosecs North Atlantic carbon-14 results, *Earth Planet. Sci. Lett.* **23** (1974) 87–90.
- [220] MOOK, W.G., BOMMERSON, J.C., STAVERMAN, W.H., Carbon isotope fractionation between dissolved bicarbonate and gaseous carbon dioxide, *Earth Planet. Sci. Lett.* **22** (1974) 169–176.
- [221] THODE, H.G., SHIMA, M., REES, C.E., KRISHNAMURTY, K.V., Carbon-13 isotope effects in systems containing carbon dioxide, bicarbonate, carbonate, and metal ions, *Can. J. Chem.* **43** (1965) 582–595.
- [222] RUBINSON, M., CLAYTON, R.N., Carbon-13 fractionation between aragonite and calcite, *Geochim. Cosmochim. Acta* **33** (1969) 997–1002.
- [223] EMRICH, K., EHHALT, D.H., VOGEL, J.C., Carbon isotope fractionation during the precipitation of calcium carbonate, *Earth Planet. Sci. Lett.* **8** (1970) 363–371.
- [224] SALIEGE, J.F., FONTES, J.C., Essai de détermination expérimentale du fractionnement des isotopes  $^{13}\text{C}$  et  $^{14}\text{C}$  du carbone au cours de processus naturels, *Int. J. Appl. Radiat. Isot.* **35** (1984) 55–62.
- [225] WIGLEY, T.M.L., MULLER, A.B., Fractionation corrections in radiocarbon dating, *Radiocarbon* **23** (1981) 173–190.
- [226] STUIVER, M., et al., INTCAL98 radiocarbon age calibration, 24,000–0 cal BP, *Radiocarbon* **40** (1998) 1041–1083.
- [227] STUIVER, M., REIMER, P.J., BRAZIUNAS, T.F., High-precision radiocarbon age calibration for terrestrial and marine samples, *Radiocarbon* **40** (1998) 1127–1151.
- [228] BARD, E., ARNOLD, M., FAIRBANKS, R.G., HAMELIN, B.,  $^{230}\text{Th}$ - $^{234}\text{U}$  and  $^{14}\text{C}$  ages obtained by mass spectrometry on corals, *Radiocarbon* **35** (1993) 191–199.
- [229] BARTLEIN, P.J., EDWARDS, M.E., SHAFER, S.L., BARKER, E.D.J., Calibration of radiocarbon ages and the interpretation of palaeoenvironmental records, *Quaternary Res.* **44** (1995) 417–424.
- [230] STUIVER, M., KROMER, B., BECKER, B., FERGUSON, C.W., Radiocarbon age calibration back to 13,300 years B.P. and the  $^{14}\text{C}$  age matching of the German oak and US Bristlecone pine chronologies, *Radiocarbon* **28** (1986) 980–1021.
- [231] STUIVER, M., REIMER, P.J., Extended  $^{14}\text{C}$  data base and revised CALIB 3.0  $^{14}\text{C}$  age calibration program, *Radiocarbon* **8** (1993) 534–540.
- [232] FAIRBANKS, R.G., et al., Radiocarbon calibration curve spanning 0 to 50,000 years BP based on paired  $^{230}\text{Th}/^{234}\text{U}/^{238}\text{U}$ ,  $^{231}\text{Pa}/^{235}\text{U}$  and  $^{14}\text{C}$  dates on pristine corals, *Quaternary Sci. Rev.* **24** (2005) 1781–1796.
- [233] KITAGAWA, H., VAN DER PLICHT, J., A 40 000 years varved chronology from Lake Suigetsu, Japan: Extension of the  $^{14}\text{C}$  calibration curve, *Radiocarbon* **40** (1998) 505–515.
- [234] KITAGAWA, H., VAN DER PLICHT, J., Atmospheric radiocarbon calibration to 45,000 yr B.P.: Late glacial fluctuations and cosmogenic production, *Science* **279** (1998) 1187–1190.
- [235] KITAGAWA, H., PLICHT, J.V.D., Atmospheric radiocarbon calibration beyond 11,900 cal BP from Lake Suigetsu laminated sediments, *Radiocarbon* **42** (2000) 369–380.
- [236] BARD, E., ARNOLD, M., HAMELIN, B., TISNERAT-LABORDE, N., CABIOCH, G., Radiocarbon calibration by means of mass spectrometric  $^{230}\text{Th}/^{234}\text{U}$  and  $^{14}\text{C}$  ages of corals: An updated database including samples from Barbados, Mururoa and Tahiti, *Radiocarbon* **40** (1998) 1085–1092.
- [237] BARD, E., Extending the calibrated radiocarbon record, *Science* **292** (2001) 2443–2444.

- [238] BECK, J.W., et al., Extremely large variations of atmospheric  $^{14}\text{C}$  concentration during the last glacial period, *Science* **292** (2001) 2453–2458.
- [239] CHIU, T.C., FAIRBANKS, R.G., MORTLOCK, R.A., BLOOM, A.L., Extending the radiocarbon calibration beyond 26,000 years before present using fossil corals, *Quaternary Sci. Rev.* **24** (2005) 1797–1808.
- [240] CHIU, T.C., et al., Redundant  $^{230}\text{Th}/^{234}\text{U}/^{238}\text{U}$ ,  $^{231}\text{Pa}/^{235}\text{U}$  and  $^{14}\text{C}$  dating of fossil corals for accurate radiocarbon age calibration, *J. Radioanal. Nucl. Chem. Quaternary Sci. Rev.* **25** (2006) 2431–2440.
- [241] BAYER, R., et al., Performance and blank components of a mass spectrometric system for routine measurement of helium isotopes and tritium by the  $^3\text{He}$  ingrowth method, *Sitzungsberichte der Heidelberger Akademie der Wissenschaften, Mathematisch-naturwissenschaftliche Klasse* **5** (1989) 241–279.
- [242] CLARKE, W.B., JENKINS, W.J., TOP, Z., Determination of tritium by mass spectrometric measurement of  $^3\text{He}$ , *Int. J. Appl. Radiat. Isot.* **27** (1976) 515–522.
- [243] VERNIANI, F., The total mass of the earth's atmosphere, *J. Geophys. Res.* **71** (1966) 385–391.
- [244] AOKI, N., MAKIDE, Y., The concentration of krypton in the atmosphere — its revision after half a century, *Chem. Lett.* **34** (2005) 1396.
- [245] COLLON, P.B., et al., Measurement of  $^{81}\text{Kr}$  in the atmosphere, *Nucl. Instrum. Meth. B* **123** (1997) 122–127.
- [246] KUZMINOV, V.V., POMANSKY, A.A., “ $^{81}\text{Kr}$  production rate in the atmosphere”, 18th Int. Cosmic Ray Conf. (DURGAPRASAD, N., Ed.), Int. Union of Pure and Appl. Physics, Bangalore, India (1983).
- [247] LOOSLI, H.H., OESCHGER, H.,  $^{37}\text{Ar}$  and  $^{81}\text{Kr}$  in the atmosphere, *Earth Planet. Sci. Lett.* **7** (1969) 67–71.
- [248] PLUMMER, M.A., et al., Chlorine-36 in fossil rat urine: An archive of cosmogenic nuclide deposition during the past 40,000 years, *Science* **277** (1997) 538–541.
- [249] DU, X., et al., A new method of measuring  $^{81}\text{Kr}$  and  $^{85}\text{Kr}$  abundances in environmental samples, *Geophys. Res. Lett.* **30** (2003) 2068.
- [250] LEHMANN, B.E., DAVIS, S.N., FABRYKA-MARTIN, J., Atmospheric and subsurface sources of stable and radioactive nuclides used for groundwater dating, *Water Resour. Res.* **29** (1993) 2027–2040.
- [251] OZIMA, M., PODOSEK, F.A., *Noble Gas Geochemistry*, Cambridge University Press (2002) 367.
- [252] WINGER, K., FEICHTER, M.B., KALINOWSKI, M., SARTORIUS, H., SCHLOSSER, P., A new compilation of the atmospheric  $^{85}\text{Kr}$  inventories from 1945 to 2000 and its evaluation in a global transport model, *J. Environ. Radioact.* **80** (2005) 183–215.
- [253] FIRESTONE, R.B., SHIRLEY, V.S., *Table of Isotopes*, John Wiley, New York (1996).
- [254] WEISS, R.F., KYSER, T.K., Solubility of krypton in water and seawater, *J. Chem. Eng. Data* **23** (1978) 69–72.
- [255] WEAST, R.C., *Handbook of Chemistry and Physics*, CRC Press, Cleveland, OH (1981).
- [256] LEHMANN, B.E., et al., A comparison of groundwater dating with  $^{81}\text{Kr}$ ,  $^{36}\text{Cl}$  and  $^4\text{He}$  in four wells of the Great Artesian Basin, Australia, *Earth Planet. Sci. Lett.* **211** (2003) 237–250.
- [257] MAŁOSZEWSKI, P., ZUBER, A., On the theory of tracer experiments in fissured rocks with a porous matrix, *J. Hydrol.* **79** (1985) 333–358.
- [258] EINSTEIN, A., Über die von der molekularkinetischen Theorie der Wärme geforderte Bewegung von in ruhenden Flüssigkeiten suspendierten Teilchen, *Annalen der Physik* **17** (1905) 549–560.
- [259] LEHMANN, B.E., LOOSLI, H.H., Use of noble gas radioisotopes for environmental research RIS 1984, Knoxville, TN (1984).
- [260] ALTHAUS, R., et al., “Cross-border groundwater management: The contribution of deep groundwater to quaternary basins deduced from isotope data”, *Advances in Isotope Hydrology and its Role in Sustainable Water Resource Management (HIS-2007)* (Proc. Symp. Vienna, 2007), 2 vols, IAEA, Vienna (2007).
- [261] LOOSLI, H.H., LEHMANN, B.E., SMETHIE, W.M.J., “Noble gas radioisotopes:  $^{37}\text{Ar}$ ,  $^{85}\text{Kr}$ ,  $^{39}\text{Ar}$ ,  $^{81}\text{Kr}$ ”, *Environmental Tracers in Subsurface Hydrology* (COOK, P.G., HERCZEG, A.L., Eds), Kluwer Academic Press, Boston, MA (2000).
- [262] LOOSLI, H.H., A dating method with  $^{39}\text{Ar}$ , *Earth Planet. Sci. Lett.* **63** (1983) 51–62.
- [263] CORCHO, A., et al., European climate variations over the past half-millennium reconstructed from groundwater, *Geoph. Res. Lett.* **36** (2009) 5.

- [264] CORCHO, J.A., et al., Constraining groundwater age distribution using  $^{39}\text{Ar}$ : a multiple environmental tracer ( $^3\text{H}$ ,  $^3\text{He}$ ,  $^{85}\text{Kr}$ ,  $^{39}\text{Ar}$  and  $^{14}\text{C}$ ) study in the semi-confined Fontainebleau Sands aquifer (France), *Water Resour. Res.* **43** (2007).
- [265] COLLON, P., et al., Developing an AMS method to trace the oceans with  $^{39}\text{Ar}$ , *Nucl. Instrum. Meth. B* **223–224** (2004) 428–434.
- [266] WILLIAMS, W., et al., Towards laser trapping of argon-39 — A spectroscopic study of the metastable cycling transition at 811.8 nm, *Bull. Am. Phys. Soc.* **55** (2010) W5/1.
- [267] LOOSLI, H.H., LEHMANN, B.E., BALDERER, W., Argon-39, argon-37, and krypton-85 isotopes in Stripa groundwaters, *Geochim. Cosmochim. Acta* **53** (1989) 1825–1829.
- [268] PURTSCHERT, R., LEHMANN, B.E., LOOSLI, H.H., “Groundwater dating and subsurface processes investigated by noble gas isotopes ( $^{37}\text{Ar}$ ,  $^{39}\text{Ar}$ ,  $^{85}\text{Kr}$ ,  $^{222}\text{Rn}$ ,  $^4\text{He}$ )”, *Water Rock Interaction* (CIDU, R., Ed.), WRI-10, Villasimus, Italy (2001).
- [269] SMETHIE, W.M.J., MATHIEU, G., Measurement of krypton-85 in the ocean, *Marine Chem.* **18** (1986) 17–33.
- [270] SIDLE, W.C., FISCHER, R.A., Detection of  $^3\text{H}$  and  $^{85}\text{Kr}$  in groundwater from arsenic-bearing crystalline bedrock of the Goose River basin, Maine, *Environ. Geol.* **44** (2003) 781–789.
- [271] WIESLER, F., Membrane Contactors: An Introduction to the Technology, *Ultrapure Water* **13** 4 (1996) 27–33.
- [272] KROPF, S., Bestimmung der Altersverteilung junger Grundwässer mit Hilfe des Edelgasisotops  $^{85}\text{Kr}$  und Tritium, unpublished Diploma Thesis, Univ. Bern (1996).
- [273] OHTA, T., et al., Separation of dissolved Kr from a water sample by means of a hollow fiber membrane, *J. Hydrol.* **376** (2009) 152–158.
- [274] PROBST, P.C., YOKOCHI, R., STURCHIO, N.C., “Method for extraction of dissolved gases from groundwater for radiokrypton analysis”, 4th Mini Conf. on Noble Gases in the Hydrosphere and in Natural Gas Reservoirs, GFZ, Potsdam, Germany (2007).
- [275] KLASS, D.L., Methane from aerobic fermentation, *Science* **223** (1984) 1021–1028.
- [276] BEYERLE, U., et al., A mass spectrometric system for the analysis of noble gases and tritium from water samples, *Environ. Sci. Technol.* **34** (2000) 2042–2050.
- [277] LOOSLI, H.H., PURTSCHERT, R., “Rare gases”, *Isotopes in the Water Cycle: Past, Present and Future of a Developing Science* (AGGARWAL, P., GAT, J.R., FROEHLICH, K., Eds), IAEA/Springer (2005).
- [278] YOKOCHI, R., HERATY, L.J., STURCHIO, N.C., Method for purification of krypton from environmental samples for analysis of radiokrypton isotopes, *Anal. Chem.* **80** (2008) 8688–8693.
- [279] LOOSLI, H.H., MOELL, M., OESCHGER, H., SCHOTTERER, U., Ten years of low level counting in the underground laboratory in Bern, Switzerland, *Nucl. Instrum. Meth. B* **17** (1986) 402–405.
- [280] PURTSCHERT, R., “Timescales and tracers”, *The Natural Baseline Quality of Groundwater* (EDMUNDS, W.M., SHAND, P., Eds), Blackwell Publishing, Oxford (2008).
- [281] COLLON, P., et al.,  $^{81}\text{Kr}$  in the Great Artesian Basin, Australia: a new method for dating very old groundwater, *Earth Planet. Sci. Lett.* **182** (2000) 103–113.
- [282] LEHMANN, B.E., LOOSLI, H.H., RAUBER, D., THONNARD, N., WILLIS, R.D.,  $^{81}\text{Kr}$  and  $^{85}\text{Kr}$  in groundwater, Milk River aquifer, Alberta, Canada, *Appl. Geochem.* **6** (1991) 419–424.
- [283] CHEN, C.Y., et al., Ultrasensitive isotope analysis with a magneto-optical trap, *Science* **286** (1999) 1139–1141.
- [284] ACOSTA-KANE, D., et al., Discovery of underground argon with low level of radioactive  $^{39}\text{Ar}$  and possible applications to WIMP dark matter detectors, *Nucl. Instrum. Meth. B* **587** (2007) 46–51.
- [285] PEARSON F.J., Jr., et al., “Applied isotope hydrogeology: A case study in Northern Switzerland”, *Studies in Environmental Science*, Elsevier, Amsterdam (1991).
- [286] COLLON, P., et al., Measurement of the long-lived radionuclide  $^{81}\text{Kr}$  in pre-nuclear and present day atmospheric krypton, *Radiochim. Acta* **85** (1999) 13–19.
- [287] LU, Z.-T., MUELLER, P., “Atom trap trace analysis of rare noble gas isotopes”, *Advances in Atomic, Molecular, and Optical Physics* (BERMAN, P., ARIMONDO, E., LIN, C., Eds), Elsevier (2010).
- [288] LEHMANN, B.E., *Counting Radioactive Noble Gas Atoms: Lasers, Accelerators or Decay Counters Resonance Ionization Spectroscopy and Its Applications*, Knoxville, TN (2000).

- [289] LEHMANN, B.E., et al., Counting  $^{81}\text{Kr}$  atoms for analysis of groundwater, *J. Geophys. Res.* **90** (1985) 11 547–11 551.
- [290] THONNARD, N., WILLIS, R.D., WRIGHT, M.C., DAVIS, W.A., LEHMANN, B.E., Resonance ionization spectroscopy and the detection of  $^{81}\text{Kr}$ , *Nucl. Instrum. Meth. B* **29** (1987) 398–406.
- [291] NOLTE, E., et al., Measurements and interpretations of  $^{36}\text{Cl}$  in groundwater, Milk River aquifer, Alberta, Canada, *Appl. Geochem.* **6** (1991) 435–445.
- [292] LOVE, A.J., HERCZEG, A.J., SAMPSON, L., CRESSWELL, R.G., FIFIELD, L.K., Sources of chloride and implications for  $^{36}\text{Cl}$  dating of old groundwater, southwestern Great Artesian Basin, *Water Resour. Res.* **36** (2000) 1561–1574.
- [293] TORGERSEN, T., CLARKE, W.B., Helium accumulation in groundwater, I: An evaluation of sources and the continental flux of crustal  $^4\text{He}$  in the Great Artesian Basin, Australia, *Geochim. Cosmochim. Acta* **49** (1985) 1211–1218.
- [294] TORGERSEN, T., CLARKE, W.B., Geochemical constraints on formation fluid ages, hydrothermal heat flux and crustal mass transport mechanisms at Cajon Pass, *J. Geophys. Res.* **97** (1992) 5031–5038.
- [295] SOLOMON, D.K., HUNT, A., POREDA, R.J., Source of radiogenic helium-4 in shallow aquifers: Implications for dating young groundwater, *Water Resour. Res.* **32** (1996) 1805–1813.
- [296] DAVIS, S.N., DEWAYNE, C., ZREDA, M., SHARMA, P., Chlorine-36 and the initial value problem, *Hydrogeol. J.* **6** (1998) 104–114.
- [297] GELHAR, L.W., WELTY, C., REHFELDT, K.R., A critical review of data on field-scale dispersion in aquifers, *Water Resour. Res.* **28** (1992) 1955–1974.
- [298] LEHMANN, B.E., PURTSCHERT, R., Radioisotope dynamics — the origin and fate of nuclides in groundwater, *Appl. Geochem.* **12** (1997) 727–738.
- [299] SUDICKY, E.A., FRIND, E.O., Carbon-14 dating of groundwater in confined aquifers: Implications of aquitard diffusion, *Water Resour. Res.* **17** (1981) 1060–1064.
- [300] TORGERSEN, T., et al., Chlorine-36 dating of very old groundwater: Further studies in the Great Artesian Basin, Australia, *Water Resour. Res.* **27** (1991) 3201–3213.
- [301] BENTLEY, H.W., et al., Chlorine-36 dating of very old groundwater, 1. The Great Artesian Basin, Australia, *Water Resour. Res.* **22** (1986) 1991–2001.
- [302] AESCHBACH-HERTIG, W., PEETERS, F., BEYERLE, U., KIPFER, R., Interpretation of dissolved atmospheric noble gases in natural waters, *Water Resour. Res.* **35** (1999) 2779–2792.
- [303] MAZOR, E., Palaeotemperatures and other hydrological parameters deduced from noble gases dissolved in groundwaters: Jordan Rift Valley, Israel, *Geochim. Cosmochim. Acta* **36** (1972) 1321–1336.
- [304] ZHANG, M., et al., Chlorine stable isotope studies of old groundwater, southwestern Great Artesian Basin, Australia, *Appl. Geochem.* **22** (2007) 557–574.
- [305] LEHMANN, B.E., LOOSLI, H.H., PURTSCHERT, R., ANDREWS, J.N., “A comparison of chloride and helium concentrations in deep groundwaters”, *Isotopes in Water Resources Management*, IAEA, Vienna (1996).
- [306] PHILLIPS, F.M., “Chlorine-36”, *Environmental Tracers in Subsurface Hydrology* (COOK, P.G., HERCZEG, A.L., Eds), Kluwer Academic Press, Boston, MA (2000).
- [307] ROBERTS, P.V., VALOCHI, A.J., *Principles of organic contaminant behaviour during artificial recharge, Quality of groundwater*, Elsevier, Amsterdam (1981).
- [308] LÜTHI, D., et al., High-resolution carbon dioxide concentration record 650,000–800,000 years before present, *Nature* **453** (2008) 379–382.
- [309] LAL, D., PETERS, B., “Cosmic ray produced radioactivity on the earth”, *Handbuch der Physik* (SITTE, K., Ed.), Springer-Verlag, Berlin (1967).
- [310] BENTLEY, H.W., PHILLIPS, F.M., DAVIS, S.N., “Chlorine-36 in the terrestrial environment”, *Handbook of Environmental Isotope Geochemistry* (FRITZ, P., FONTES, J.-C., Eds), Elsevier, Amsterdam (1986).
- [311] DAVIS, S.N., MOYSEY, S., CECIL, L.D., ZREDA, M., Chlorine-36 in groundwater of the United States: empirical data, *Hydrogeol. J.* **11** (2003) 217–227.
- [312] KEYWOOD, M.D., CHIVAS, A.R., FIFIELD, L.K., CRESSWELL, R.G., AYERS, G.P., The accession of chloride to the western half of the Australian continent, *Aust. J. Soil Res.* **35** (1997) 1177–1189.

- [313] MOYSEY, S., DAVIS, S.N., ZREDA, M., CECIL, L.D., The distribution of meteoric  $^{36}\text{Cl}/\text{Cl}$  in the United States: A comparison of models, *Hydrogeol. J.* **11** (2003) 615–627.
- [314] DAVIS, R.J., SCHAEFFER, O.A., Chlorine-36 in nature, *Ann. NY Acad. Sci.* **62** (1955) 105–122.
- [315] RONZANI, C., TAMERS, M.A., Low-level chlorine-36 detection with liquid scintillation techniques, *Radiochem. Acta* **6** (1966) 206–210.
- [316] TAMERS, M.A., RONZANI, C., SCHARPENSEEL, H.W., Naturally occurring chlorine-36, *Atompraxis* **15** (1969) 433–437.
- [317] ELMORE, D., et al., Analysis of  $^{36}\text{Cl}$  in environmental water samples using an electrostatic accelerator, *Nature* **277** (1979) 22–25.
- [318] DAVIS, S.N., BENTLEY, H.W., PHILLIPS, F.M., ELMORE, D., Use of cosmic-ray produced radionuclides in hydrogeology, *EOS* **64** (1983) 283.
- [319] PHILLIPS, F.M., BENTLEY, H.W., DAVIS, S.N., ELMORE, D., SWANICK, G.B., Chlorine-36 dating of very old groundwater, 2. Milk River aquifer, Alberta, Canada, *Water Resour. Res.* **22** (1986) 2003–2016.
- [320] JANNIK, N.O., Lake history in the palaeo-Owens River system, California, for the past 2.0 Myr based on  $^{36}\text{Cl}$  dating of evaporites from Searles Lake (1989) 190.
- [321] DESILETS, D., ZREDA, M., ALMASI, P.F., ELMORE, D., Determination of cosmogenic Cl-36 in rocks by isotope dilution: innovations, validation and error propagation, *Chem. Geol.* **233** (2006) 185–195.
- [322] ELMORE, D., PHILLIPS, F.M., Accelerator mass spectrometry for measurement of long-lived radioisotopes, *Science* **236** (1987) 543–550.
- [323] GOVE, H.E., “The history of AMS, its advantages over decay counting: Applications and prospects”, *Radiocarbon after Four Decades* (TAYLOR, R.E., LONG, A., KRA, R.J., Eds), Springer-Verlag, New York (1992).
- [324] MUZIKAR, P., ELMORE, D., GRANGER, D.E., Accelerator mass spectrometry in geologic research, *Geol. Soc. Am. Bull.* **115** (2003) 643–654.
- [325] SUTER, M., 25 years of AMS — a review of recent developments, *Nucl. Instrum. Meth. B* **223–224** (2004) 139–148.
- [326] JIANG, S., LIN, Y., ZHANG, H., Improvement of the sample preparation method for AMS measurement of  $^{36}\text{Cl}$  in natural environment, *Nucl. Instrum. Meth. B* **223–224** (2004) 318–322.
- [327] MAHARA, Y., ITO, Y., NAKAMURA, T., KUDO, A., Comparison of Cl-36 measurements at three laboratories around the world, *Nucl. Instrum. Meth. B* **223–24** (2004) 479–482.
- [328] ROBERTS, M.L., et al., The LLNL AMS facility, *Nucl. Instrum. Meth. B* **123** (1996) 57–61.
- [329] ELMORE, D., et al., Status and plans for the PRIME Lab AMS facility, *Nucl. Instrum. Meth. B* **123** (1996) 69–72.
- [330] SYNAL, H.-A., BEER, J., BONANI, G., LUKASCZYK, C., SUTER, M.,  $^{36}\text{Cl}$  measurements at the Zurich AMS facility, *Nucl. Instrum. Meth. B* **92** (1994) 79–84.
- [331] FIFIELD, L.K., Advances in accelerator mass spectrometry, *Nucl. Instrum. Meth. B* **172** (2000) 1223–1274.
- [332] FREEMAN, S., et al., Initial measurements with the SUERC accelerator mass spectrometer, *Nucl. Instrum. Meth. B* **223–24** (2004) 195–198.
- [333] AZE, T., et al., Improvement of the  $^{36}\text{Cl}$ -AMS system at MALT using a Monte Carlo ion-trajectory simulation in a gas-filled magnet, *Nucl. Instrum. Meth. B* **259** (2007) 144–148.
- [334] SASA, K., et al.,  $^{26}\text{Al}$  and  $^{36}\text{Cl}$  AMS system at the University of Tsukuba: A progress report, *Nucl. Instrum. Meth. B* **259** (2007) 41–46.
- [335] ALFIMOV, V., POSSNERT, G., ALDAHAN, A., Measurements of  $^{36}\text{Cl}$  with a gas-filled magnet at the Uppsala tandem laboratory, *Nucl. Instrum. Meth. B* **259** (2007) 199–203.
- [336] GALINDO-URIBARRI, A., et al., Pushing the limits of accelerator mass spectrometry, *Nucl. Instrum. Meth. B* **259** (2007) 123–130.
- [337] FABRYKA-MARTIN, J., et al., Iodine-129 and chlorine-36 in uranium ores: 2. Discussion of AMS measurements, *Chem. Geol.* **72** (1988) 7–16.

- [338] WAGNER, G., et al., Reconstruction of the palaeoaccumulation rate of central Greenland during the last 75 kyr using the cosmogenic radionuclides  $^{36}\text{Cl}$  and  $^{10}\text{Be}$  and geomagnetic field intensity data, *Earth Planet. Sci. Lett.* **193** (2001) 515–521.
- [339] PURDY, C.B., et al., Aquia aquifer dissolved  $\text{Cl}^-$  and  $^{36}\text{Cl}/\text{Cl}$ : Implications for flow velocities, *Water Resour. Res.* **32** (1996) 1163–1172.
- [340] ZHU, C., WINTERLE, J.R., LOVE, E.I., Late Pleistocene and Holocene groundwater recharge from the chloride mass balance method and chlorine-36 data, *Water Resour. Res.* **39** (2003) 1182.
- [341] WISCHUSEN, J.D.H., FIFIELD, L.K., CRESSWELL, R.G., Hydrogeology of Palm Valley, central Australia: a Pleistocene flora refuge? *J. Hydrol.* **293** (2004) 20–46.
- [342] CRESSWELL, R.G., JACOBSON, G., WISCHUSEN, J., FIFIELD, L.K., Ancient groundwaters in the Amadeus Basin, Central Australia: evidence from the radio-isotope  $^{36}\text{Cl}$ , *J. Hydrol.* **223** (1999) 212–220.
- [343] KULONGOSKI, J.T., HILTON, D.R., CRESSWELL, R.G., HOSTETTER, S., JACOBSON, G., Helium-4 characteristics of groundwaters from Central Australia: Comparative chronology with chlorine-36 and carbon-14 dating techniques, *J. Hydrol.* **348** (2008) 176–194.
- [344] MAHARA, Y., HABERMEHL, M.A., MIYAKAWA, K., SHIMADA, J., MIZUOCHI, Y., Can the  $^4\text{He}$  clock be calibrated by  $^{36}\text{Cl}$  for groundwater dating? *Nucl. Instrum. Meth. B* **259** (2007) 536–546.
- [345] DESILETS, D., ZREDA, M., Spatial and temporal distribution of secondary cosmic-ray nucleon intensities and applications to in situ cosmogenic dating, *Earth Planet. Sci. Lett.* **206** (2003) 21–42.
- [346] POWELL, C.F., The primary cosmic radiation, *Observatory* **75** (1955) 14–27.
- [347] SIMPSON, J.A., URETZ, R.B., Cosmic-ray neutron production in elements as a function of latitude and altitude, *Phys. Rev.* **90** (1953) 44–50.
- [348] BUSECK, P.R., SCHWARTZ, S.E., “Tropospheric aerosols”, *The Atmosphere* (KEELING, R.F., Ed.), Oxford University Press, Oxford (2003).
- [349] PARRAT, Y., et al., Atmospheric production rates of  $^{36}\text{Cl}$ , Paul Scherrer Institute, Annual Report 1996, Annex IIIA (1996).
- [350] KNIES, D.L., Cosmogenic Radionuclides in Precipitation, PhD Thesis, Purdue Univ. (1994).
- [351] HAINSWORTH, L.J., MIGNEREY, A.C., HELZ, G.R., SHARMA, P., KUBIK, P.W., Modern chlorine-36 deposition in southern Maryland, USA, *Nucl. Instrum. Meth. B* **92** (1994) 345–349.
- [352] ELSASSER, W., NEY, E.P., WINCKLER, J.R., Cosmic-ray intensity and geomagnetism, *Nature* **178** (1956) 1226–1227.
- [353] KORTE, M., CONSTABLE, C.G., Centennial to millennial geomagnetic secular variation, *Geophys. J. Int.* **167** (2006) 43–52.
- [354] VALET, J.-P., MEYNADIER, L., GUYODO, Y., Geomagnetic dipole strength and reversal rate over the past two million years, *Nature* **435** (2005) 802–805.
- [355] BAUMGARTNER, S., et al., Geomagnetic modulation of the  $^{36}\text{Cl}$  flux in the GRIP ice core, Greenland, *Science* **279** (1998) 1330–1332.
- [356] PLUMMER, M.A., Secular variation of cosmogenic nuclide production from chlorine-36 in fossil pack rat middens, MSc Thesis, New Mexico Institute of Mining and Technology (1996).
- [357] TYLER, S.W., et al., Soil–water flux in the southern Great Basin, United States: Temporal and spatial variations over the last 120,000 years, *Water Resour. Res.* **32** (1996) 1481–1499.
- [358] ZERLE, L., FAESTERMANN, T., KNIE, K., KORSCHINEK, G., NOLTE, E., The  $^{41}\text{Ca}$  bomb pulse and atmospheric transport of radionuclides, *J. Geophys. Res.* **102** (1997) 19 517–19 527.
- [359] SCHEFFEL, C., et al.,  $^{36}\text{Cl}$  in modern atmospheric precipitation, *Geophys. Res. Lett.* **26** (1999) 1401–1404.
- [360] BERNER, E.K., BERNER, R.A., *The Global Water Cycle: Geochemistry and Environment*, Prentice-Hall, Englewood Cliffs, NJ (1987).
- [361] LERNER, D.N., ISSAR, A.S., SIMMERS, I., *Groundwater Recharge — A Guide to Understanding and Estimating Natural Recharge*, Verlag Heinz Heise, Hannover (1990).
- [362] SCANLON, B.R., et al., Global synthesis of groundwater recharge in semiarid and arid regions, *Hydrol. Proc.* **20** (2006) 3335–3370.

- [363] AIREY, P.L., et al., "Isotope hydrology of the Great Artesian Basin" Groundwater and Man (Proc. Int. Conf.), Australian Government Publishing Service, Sydney (1983).
- [364] SHEPPARD, S.C., EVENDON, W.G., MACDONALD, C.R., Variation among chlorine concentration ratios for native and agronomic plants, *J. Environ. Radioact.* **43** (1999) 65–76.
- [365] JOBBAGY, E.G., JACKSON, R.B., The distribution of soil nutrients with depth: Global patterns and the imprint of plants, *Biogeochemistry* **53** (2001) 51–77.
- [366] KASHPAROV, V., COLLE, C., LEVCHUK, S., YOSCHENKO, V., SVYDYNUK, N., Transfer of chlorine from the environment to agricultural foodstuffs, *J. Environ. Radioact.* **94** (2007) 1–15.
- [367] LATURNUS, F., MATUCHA, M., Chloride — a precursor in the formation of volatile organochlorines by forest plants? *J. Environ. Radioact.* **99** (2008) 119–125.
- [368] MYNENI, S.C.B., Formation of stable chlorinated hydrocarbons in weathering plant material, *Science* **295** (2002) 1039–1041.
- [369] LEE, R.T., SHAW, G., WADEY, P., WANG, X., Specific association of  $^{36}\text{Cl}$  with low molecular weight humic substances in soils, *Chemosphere* **43** (2001) 1063–1070.
- [370] ELMORE, D., et al., The  $^{36}\text{Cl}$  bomb pulse measured in a shallow ice core from Dye 3, Greenland, *Nature* **300** (1982) 735–737.
- [371] ALVARADO, J.A.C., et al., Cl-36 in modern groundwater dated by a multi-tracer approach (H-3/He-3, SF<sub>6</sub>, CFC-12 and Kr-85): a case study in quaternary sand aquifers in the Odense Pilot River Basin, Denmark, *Appl. Geochem.* **20** (2005) 599–609.
- [372] HOGAN, J.F., et al., Geological origins of salinization in a semiarid river: The role of sedimentary brines, *Geology* **35** (2007) 1063–1066.
- [373] MILTON, G.C.D., et al., A new interpretation of the distribution of bomb-produced chlorine-36 in the environment, with special reference to the Laurentian Great Lakes, *Nucl. Instrum. Meth. B* **123** (1997) 382–386.
- [374] VAN VALKENBURGH, J., Chlorine-36 in southern Maryland soil, MSc Thesis, University of Maryland (1996).
- [375] MILTON, G.M., et al.,  $^{36}\text{Cl}$  — A potential palaeodating tool, *Nucl. Instrum. Meth. B* **123** (1997) 371–377.
- [376] CORNETT, R.J., et al., Is  $^{36}\text{Cl}$  from weapons' test fallout still cycling in the atmosphere? *Nucl. Instrum. Meth. B* **123** (1997) 378–381.
- [377] FOSTER, S.S.D., SMITH-CARRINGTON, A., The interpretation of tritium in the chalk unsaturated zone, *J. Hydrol.* **46** (1980) 343–364.
- [378] CAMPBELL, K., WOLFSBERG, A., FABRYKA-MARTIN, J., SWEETKIND, D., Chlorine-36 data at Yucca Mountain: Statistical tests of conceptual models for unsaturated-zone flow, *J. Contam. Hydrol.* **62–3** (2003) 43–61.
- [379] CIZDZIEL, J.V., et al., Recent measurements of  $^{36}\text{Cl}$  in Yucca Mountain rock, soil and seepage, *J. Radioanal. Nucl. Chem.* **275** (2008) 133–144.
- [380] GOSSE, J.C., PHILLIPS, F.M., Terrestrial in-situ cosmogenic nuclides: Theory and application, *Quaternary Sci. Rev.* **20** (2001) 1475–1560.
- [381] FEIGE, Y., OLTMAN, B.G., KASTNER, J., Production rates of neutrons in soils due to natural radioactivity, *J. Geophys. Res.* **73** (1968) 3135–3142.
- [382] FABRYKA-MARTIN, J.T., Production of Radionuclides in the Earth and Their Hydrogeologic Significance, with Emphasis on Chlorine-36 and Iodine-129, PhD Thesis, Univ. Arizona (1988).
- [383] MICHELOT, J.-L., Hydrologie isotopique des circulations lentes en milieu cristallin fracturé: Essai méthodologique, PhD Thesis, Univ. Paris-Sud (1988).
- [384] FABRYKA-MARTIN, J., DAVIS, S.N., ELMORE, D., Applications of  $^{129}\text{I}$  and  $^{36}\text{Cl}$  to hydrology, *Nucl. Instrum. Meth. B* **29** (1987) 361–371.
- [385] FABRYKA-MARTIN, J., WHITTEMORE, D.O., DAVIS, S.N., KUBIK, P.W., SHARMA, P., Geochemistry of halogens in the Milk River aquifer, Alberta, Canada, *Appl. Geochem.* **6** (1991) 447–464.
- [386] DAVIS, S.N., FABRYKA-MARTIN, J.T., WOLFSBERG, L.E., Variations in bromide in potable ground water in the United States, *Ground Water* **42** (2004) 902–909.

- [387] WHITTEMORE, D.O., Geochemical differentiation of oil and gas brine from other saltwater sources contaminating water resources: Case studies from Kansas and Oklahoma, *Environ. Geosci.* **2** (1995) 15–31.
- [388] RAO, U., et al., The use of Cl-36 and chloride/bromide ratios in discerning salinity sources and fluid mixing patterns: A case study at Saratoga Springs, *Chem. Geol.* **222** (2005) 94–111.
- [389] STEWART, M.A., SPIVACK, A.J., The stable-chlorine isotope composition of natural and anthropogenic materials, *Rev. Mineral. Geochem.* **55** (2004) 231–254.
- [390] EASTOE, C.J., PERYT, T.M., PETRYCHENKO, O.Y., GEISLER-CUSSEY, D., Stable chlorine isotopes in Phanerozoic evaporites, *Appl. Geochem.* **22** (2007) 575–588.
- [391] WEAVER, T.R., “Stable isotopes of chlorine”, *Environmental Tracers in Subsurface Hydrology* (COOK, P., HERCZEC, A.L., Eds), Kluwer Academic, Boston, MA (2000).
- [392] VOLPE, C., SPIVACK, A.J., Stable chlorine isotopic composition of marine aerosol particles in the western Atlantic Ocean, *Geophys. Res. Lett.* **21** (1994) 1161–1164.
- [393] SNYDER, G.T., FABRYKA-MARTIN, J.T., I-129 and Cl-36 in dilute hydrocarbon waters: Marine-cosmogenic, in situ, and anthropogenic sources, *Appl. Geochem.* **22** (2007) 692–714.
- [394] DAVIS, S.N., FABRYKA-MARTIN, J., WOLFSBERG, L., MOYSEY, S., Chlorine-36 in ground water containing low chloride concentrations, *Ground Water* **38** (2000) 912–922.
- [395] HURWITZ, S., MARINER, R.H., FEHN, U., SNYDER, G.T., Systematics of halogen elements and their radioisotopes in thermal springs of the Cascade Range, Central Oregon, Western USA, *Earth Planet. Sci. Lett.* **235** (2005) 700–714.
- [396] METCALFE, R., et al., Characteristics of deep groundwater flow in a basin marginal setting at Sellafield, Northwest England: Cl-36 and halide evidence, *Appl. Geochem.* **22** (2007) 128–151.
- [397] ANDREWS, J.N., DRIMMIE, R.J., LOOSLI, H.H., HENDRY, M.J., Dissolved gases in the Milk River aquifer, Alberta, Canada, *Appl. Geochem.* **6** (1991) 393–404.
- [398] CHERDYNTSEV, V.V., CHALOV, P.I., KHASDAROV, G.Z., “On isotopic composition of radioelements in natural objects, and problems of geochronology”, 2012 Trans. 3rd Session of the Commission on Determination of Absolute Age of Geological Formations, *Izv. Acad. Nauk SSR* (1955).
- [399] CHALOW, P.I., MERKULOVA, K.I., Comparative oxidation rates of  $^{234}\text{U}/^{238}\text{U}$  atoms in certain minerals, *Dokl. AN SSR* **167** (1966) 669–671.
- [400] CHERDYNTSEV, V.V., Uranium-234, *Atomisdat*, Moscow (1969).
- [401] OSMOND, J.K., COWART, J.B., The theory and uses of natural uranium isotopic variations in hydrology, *Atom. Energy Rev.* **14** (1976) 621–679.
- [402] OSMOND, J.K., COWART, J.B., “Groundwater”, *Uranium Series Disequilibrium: Applications to Environmental Problems* (IVANOVIC, M., HARMON, R.S., Eds), Oxford University Press, Oxford (1982).
- [403] PLATER, A.J., IVANOVICH, M., DUGDALE, R.E., Uranium series disequilibrium in river sediments and waters: the significance of anomalous activity ratios, *Appl. Geochem.* **7** (1992) 101–110.
- [404] PORCELLI, D., SWARZENSKI, P.W., The behavior of U- and Th-series nuclides in groundwater, *Rev. Mineral. Geochem.* **52** (2003) 317–361.
- [405] SARIN, M.M., KRISHNASWAMI, S., SOMAYAJULU, B.L.K., MOORE, W.S., Chemistry of uranium, thorium, and radium isotopes in the Ganga-Brahmaputra river system: Weathering processes and fluxes to the Bay of Bengal, *Geochim. Cosmochim. Acta* **54** (1990) 1387–1396.
- [406] TUZOVA, T.V., Study of the runoff distribution and estimation of water resources of the Sarydzhas River basin from uranium isotopic composition data, *Translation of Vodnye Resursy* **12** (1986) 99–105.
- [407] TUZOVA, T.V., NOVIKOV, V.N., Uranium isotope-related features of streamflow formation for Pyandzh River, *Translation of Vodnye Resursy* **18** (1991) 59–65.
- [408] ANDERSEN, M.B., EREL, Y., BOURDON, B., Experimental evidence for  $^{234}\text{U}$ – $^{238}\text{U}$  fractionation during granite weathering with implications for  $^{234}\text{U}/^{238}\text{U}$  in natural waters, *Geochim. Cosmochim. Acta* **73** (2009) 4124–4141.
- [409] DOSSETO, A., BOURDON, B., TURNER, S.P., Uranium-series isotopes in river materials: insights into the timescales of erosion and sediment transport, *Earth Planet. Sci. Lett.* **265** (2008) 1–17.

- [410] VIGIER, N., et al., The relationship between riverine U-series disequilibria and erosion rates in a basaltic terrain, *Earth Planet. Sci. Lett.* **249** (2006) 258–273.
- [411] BRIEL, L.I., An Investigation of the  $^{234}\text{U}/^{238}\text{U}$  Disequilibrium in the Natural Waters of the Santa Fe River Basin of North-central Florida, PhD Thesis, Florida State Univ. (1976).
- [412] DURAND, S., CHABAUX, F., RIHS, S., DURINGER, P., ELSASS, P., U isotope ratios as tracers of groundwater inputs into surface waters: Example of the Upper Rhine River hydrosystem, *Chem. Geol.* **220** (2005) 1–19.
- [413] OSMOND, J.K., RYDELL, H.S., KAUFMAN, M.I., Uranium disequilibrium in groundwater: An isotope dilution approach in hydrologic investigations, *Science* **162** (1968) 997–999.
- [414] CHALOV, P.I., TUZOVA, T.V., TIKHONOV, A.I., MERKULOVA, K.I., SVETLITCHNAYA, N.A., Uranium disequilibrium as indicator in studies of recharge and circulation processes of groundwater, *Geochimica* **10** (1979) 1499–1507.
- [415] OSMOND, J.K., COWART, J.B., IVANOVIC, M., Uranium isotopic disequilibrium in ground water as an indicator of anomalies, *Int. J. Appl. Radiat. Isot.* **34** (1983) 283–308.
- [416] ANDREWS, J.N., et al., Radioelements, radiogenic helium and age relationships for groundwaters from the granites at Stripa, Sweden, *Geochim. Cosmochim. Acta* **46** (1982) 1533–1543.
- [417] ANDREWS, J.N., KAY, R.L.F., The U contents and  $^{234}\text{U}/^{238}\text{U}$  activity ratios of dissolved uranium in groundwaters from some Triassic Sandstones in England, *Isot. Geosci.* **1** (1983) 101–117.
- [418] BARR, G.E., LAMBERT, S.J., CARTER, J.A., “Uranium isotope disequilibrium in groundwaters of Southeastern New Mexico and implications regarding age dating of waters”, *Isotope Hydrology 1978* (Proc. Neuherberg, 1978), IAEA, Vienna (1979).
- [419] COWART, J.B., OSMOND, J.K., “ $^{234}\text{U}$  and  $^{238}\text{U}$  in the Carrizo Sandstone aquifer of South Texas”, *Isotope Techniques in Groundwater Hydrology 1974*, Proceedings Series No. 186, IAEA, Vienna (1974).
- [420] ESHOVA, M.P., “Use of uranium isotopes in investigations of the formation of mineral waters”, *Investigations of Natural Water with Isotope Methods* (FERRONSKIJ, V.I., Ed.), Nauka, Moscow (1981).
- [421] FRÖHLICH, K., GELLERMANN, R., HEBERT, D., “Uranium isotopes in a Sandstone Aquifer. Interpretation of data and implications for groundwater dating”, *Isotope Hydrology 1983* (Proc. Vienna, 1983), IAEA, Vienna (1984).
- [422] IVANOVICH, M., FRÖHLICH, K., HENDRY, M.J., Uranium-series radionuclides in fluids and solids, Milk River Aquifer, Alberta, Canada, *Appl. Geochem.* **6** (1991) 405–418.
- [423] KIGOSHI, K., Uranium 234/238 disequilibrium and age of underground water, IAEA Panel on Interpretation of Uranium Isotope Disequilibrium as a Hydrological Tracer, IAEA, Vienna (1973).
- [424] KRONFELD, J., ADAMS, J.A.S., Hydrologic investigations of the groundwaters of Central Texas using  $^{234}\text{U}/^{238}\text{U}$  disequilibrium, *J. Hydrol.* **22** (1974) 77–88.
- [425] PEARSON, F.J., NOROWHA, C.J., ANDREWS, R.W., Mathematical modelling of the distribution of natural  $^{14}\text{C}$ ,  $^{234}\text{U}$ , and  $^{238}\text{U}$  in a regional groundwater system, *Radiocarbon* **25** (1983) 291–300.
- [426] FRÖHLICH, K., GELLERMANN, R., On the potential use of uranium isotopes for groundwater dating, *Chem. Geol.* **65** (1987) 67–77.
- [427] BONOTTO, D.M., “Some constraints on the modelling using the uranium isotopes  $^{238}\text{U}$  and  $^{234}\text{U}$  for dating groundwaters from Guarany aquifer, South America”, *Risk Analysis II* (BREBBIA, C.A., Ed.), WIT Press, Southampton (2000).
- [428] BONOTTO, D.M., Hydro(radio)chemical relationships in the giant Guarani aquifer, Brazil, *J. Hydrol.* **323** (2006) 353–386.
- [429] DESCHAMPS, P., et al.,  $^{234}\text{U}/^{238}\text{U}$  disequilibrium along stylolitic discontinuities in deep Mesozoic limestone formations of the Eastern Paris basin: evidence for discrete uranium mobility over the last 1–2 million years, *Hydrol. Earth Syst. Sci.* **8** (2004) 35–46.
- [430] LUO, S., KU, T.-L., ROBACK, R., MURELL, M., McLING, T.L., In-situ radionuclide transport and preferential groundwater flows at INEEL (Idaho): Decay-series disequilibrium studies, *Geochim. Cosmochim. Acta* **64** (2000) 867–881.
- [431] ROGOJIN, V., CARMÍ, I., KRONFELD, J.,  $^{14}\text{C}$  and  $^{234}\text{U}$ -excess dating of groundwater in the Haifa Bay region, Israel, *Radiocarbon* **40** (1998) 945–951.

- [432] TRICCA, A., WASSERBURG, G.J., PORCELLI, D., BASKARAN, M., The transport of U- and Th-series nuclides in a sandy unconfined aquifer, *Geochim. Cosmochim. Acta* **65** (2001) 1187–1210.
- [433] CHEN, J.H., EDWARDS, R.L., WASSERBURG, G.J., <sup>238</sup>U, <sup>234</sup>U, and <sup>230</sup>Th in seawater, *Earth Planet. Sci. Lett.* **80** (1986) 241–251.
- [434] GOLDSTEIN, S.J., STIRLING, C.H., Techniques for measuring uranium-series nuclides 1992–2002, *Rev. Mineral. Geochem.* **52** (2003) 23–57.
- [435] RADEMACHER, L.K., LUNDSTROM, C., JOHNSON, T.C., High Precision Measurements of <sup>235</sup>U/<sup>238</sup>U Isotopic Fractionations Resulting From Uranium Reduction Induced by Zero Valent Iron, Fall Meeting 2003, American Geophysical Union (2003).
- [436] CHERDYNTSEV, V.V., Uranium-234, Keter Press, Jerusalem (1971).
- [437] OSMOND, J.K., “Uranium disequilibrium in hydrologic studies”, *Handbook of environmental Isotope Geochemistry* (FRITZ, P., FONTES, J.C., Eds), Elsevier, Amsterdam (1980).
- [438] OSMOND, J.K., COWART, J.B., “Ground water”, *Applications to Earth, Marine and Environmental Sciences, Uranium Series Disequilibrium* (IVANOVIC, M., HARMON, R.S., Eds), Clarendon Press, Oxford (1992).
- [439] OSMOND, J.K., COWART, J.B., “U-series nuclides as tracers in groundwater hydrology”, *Environmental Tracers in Subsurface Hydrology* (COOK, P.G., HERCZEG, A.L., Eds), Kluwer Academic Press, Boston, MA (2000).
- [440] IVANOVICH, M., HARMON, R.S., *Uranium Series Disequilibrium: Applications to Environmental Problems*, Oxford University Press, Oxford (1982).
- [441] IVANOVICH, M., HARMON, R.S., *Uranium Series Disequilibrium: Applications to Earth, Marine and Environmental Sciences*, Clarendon Press, Oxford (1992).
- [442] BOURDON, B., HENDERSON, G.M., LUNDSTROM, C.C., TURNER, S.P., *Uranium-Series Geochemistry. Reviews in Mineralogy & Geochemistry*, Geochemical Society, Mineralogical Society of America (2003).
- [443] ANDERSEN, M.B., et al., The tracing of riverine U in Arctic seawater with very precise <sup>234</sup>U/<sup>238</sup>U measurements, *Earth Planet. Sci. Lett.* **259** (2007) 171–185.
- [444] ROBINSON, L.F., BELSHAW, N.S., HENDERSON, G.M., U and Th concentrations and isotope ratios in modern carbonates and waters from the Bahamas, *Geochim. Cosmochim. Acta* **68** (2004) 1777–1789.
- [445] CHABAUX, F., RIOTTE, J., DEQUINCEY, O., U-Th-Ra fractionation during weathering and river transport (2003).
- [446] FERRONSKY, V.I., POLYAKOV, V.A., *Environmental Isotopes in the Hydrosphere*, John Wiley and Sons (1982).
- [447] GELLERMANN, R., FRÖHLICH, K., Nutzung der Uranisotope <sup>234</sup>U und <sup>238</sup>U in der Hydrologie und Hydrogeologie, *Freiberger Forschungshefte* **C397** (1984) 48–57.
- [448] BONDARENKO, G.N., On the formation of the isotopic composition of uranium in groundwater, *Isotopes in the Hydrosphere, Symposium, Tallin* (1981).
- [449] SYROMYATNIKOV, N.G., *Uranium, Thorium and Radium Isotope Migration and Interpretation of Radioactive Anomalies*, Izd. AN KazSSR, Alma-Ata (1961).
- [450] LANGMUIR, D., Uranium solution-mineral equilibria at low temperatures with applications to sedimentary ore deposits, *Geochim. Cosmochim. Acta* **42** (1978) 547–569.
- [451] ROSE, A.W., WRIGHT, R.J., Geochemical exploration models for sedimentary uranium deposits, *J. Geochem. Explor.* **13** (1980).
- [452] GASCOYNE, M., “Geochemistry of the actinides and their daughters”, *Uranium-Series Equilibrium: Applications to Earth, Marine and Environmental Sciences* (IVANOVIC, M., HARMON, R.S., Eds), Clarendon Press, Oxford (1992).
- [453] LENHART, J.J., HONEYMAN, B.D., Uranium (VI) sorption to haematite in the presence of humic acid, *Geochim. Cosmochim. Acta* **63** (1999) 2891–2901.
- [454] AMES, L.L., MCGARRAH, J.E., WALKER, B.A., SALTER, P.F., Uranium and radium sorption on amorphous ferric oxyhydroxide, *Chem. Geol.* **40** (1983) 135–148.
- [455] ARNOLD, T., ZORN, T., BERNHARD, G., NITSCHKE, H., Sorption of uranium (VI) onto phyllite, *Chem. Geol.* **151** (1998) 129–141.

- [456] DUFF, M.C., COUGHLIN, J.U., HUNTER, D.B., Uranium co-precipitation with iron oxide minerals, *Geochim. Cosmochim. Acta* **66** (2002) 3533–3547.
- [457] HSI, C.D., LANGMUIR, D., Adsorption of uranyl onto ferric oxyhydroxides, Application of the surface complexation site-binding model, *Geochim. Cosmochim. Acta* **49** (1985) 1931–1941.
- [458] LIGER, E., CHARLET, L., CAPPELLEN, P.V., Surface catalysis of uranium (VI) reduction by iron (II), *Geochim. Cosmochim. Acta* **63** (1999) 2939–2955.
- [459] KRAWCZYK-BARSCH, E., et al., Formation of secondary Fe-oxyhydroxide phases during the dissolution of chlorite effects on uranium sorption, *Appl. Geochem.* **19** (2004) 1403–1412.
- [460] OHNUKI, T., et al., Change in sorption characteristics of uranium during crystallization of amorphous iron minerals, *J. Nucl. Sci. Technol.* **34** (1997) 1153–1158.
- [461] PAYNE, T.E., DAVIS, J.A., WAITE, T.D., Uranium retention by weathered schists — the role of iron minerals, *Radiochim. Acta* **66** (1994) 297–303.
- [462] GIAMMAR, D.E., HERING, J.G., Time scales for sorption-desorption and surface precipitation of uranyl on goethite, *Environ. Sci. Technol.* **35** (2001) 3332–3337.
- [463] ANDREWS, J.N., KAY, R.L.F., Natural production of tritium in permeable rocks, *Nature* **298** (1982) 361–363.
- [464] FLEISCHER, R.L., Isotopic disequilibrium of uranium: Alpha-recoil damage and preferential solution effects, *Science* **208** (1980) 979–981.
- [465] FLEISCHER, R.L., Alpha-recoil damage and solution effects in minerals: uranium isotopic disequilibrium and radon release, *Geochim. Cosmochim. Acta* **46** (1982) 2191–2201.
- [466] HUSSAIN, N., LAL, D., “Preferential solution of  $^{234}\text{U}$  from recoil tracks and  $^{234}\text{U}/^{238}\text{U}$  radioactive disequilibrium in natural waters”, *Proc. Indian Acad. Sci., Earth Planet. Sci.* **95** (1986) 245–263.
- [467] ROSHOLT, J.N., SHIELDS, W.R., GARNER, E.L., Isotope fractionation of uranium in sandstone, *Science* **139** (1963) 224–226.
- [468] ZIELINSKI, R.A., PETERMAN, Z.E., STUCKLESS, J.S., ROSHOLT, J.N., NKOMO, I.T., The chemical and isotopic record of rock-water interaction in the Sherman granite, Wyoming and Colorado, *Contrib. Mineral. Petrol.* **78** (1981) 209–219.
- [469] DOOLEY, J.R., GRANGER, H.C., ROSHOLT, J.N., Uranium-234 fractionation in the sandstone-type uranium deposits of the Ambrosia Lake District, New Mexico, *Econ. Geol.* **61** (1966) 1362–1382.
- [470] ADLOFF, J.P., ROESSLER, K., Recoil and transmutation effects in the migration behaviour of actinides, *Radiochim. Acta* **52/53** (1991) 269.
- [471] EYAL, Y., FLEISCHER, R.L., Preferential leaching and the age of radiation-damage from alpha-decay in minerals, *Geochim. Cosmochim. Acta* **49** (1985) 1155–1164.
- [472] CHAUMONT, J., SOULET, S., KRUPA, J.C., CARPENA, J., Competition between disorder creation and annealing in fluoroapatite nuclear waste forms, *J. Nucl. Mater.* **301** (2002) 122–128.
- [473] EYAL, Y., OLANDER, D.R., Leaching of uranium and thorium from monazite, 1. Initial leaching, *Geochim. Cosmochim. Acta* **54** (1990) 1867–1877.
- [474] HENDRIKS, B.W.H., REDFIELD, T.F., Apatite fission track and (U–Th)/He data from Fennoscandia: an example of underestimation of fission track annealing in apatite, *Earth Planet. Sci. Lett.* **236** (2005) 443–458.
- [475] KIGOSHI, K., Alpha-recoil thorium-234: Dissolution into water and the uranium-234/uranium-238 disequilibrium in nature, *Science* **173** (1971) 47–48.
- [476] HUSSAIN, N., KRISHNASWAMI, S., U-238 series radioactive disequilibrium in groundwaters: implications to the origin of excess U-234 and fate of reactive pollutants, *Geochim. Cosmochim. Acta* **44** (1980) 1287–1291.
- [477] RAMA, MOORE, W.S., Mechanism of transport of U-Th series radioisotopes from solids into groundwater, *Geochim. Cosmochim. Acta* **48** (1984) 395–399.
- [478] DePAOLO, D.J., MAHER, K., CHRISTENSEN, J.N., MCMANUS, J., Sediment transport time measured with U-series isotopes: results from ODP North Atlantic drift site 984, *Earth Planet. Sci. Lett.* **248** (2006) 394–410.
- [479] LANGMUIR, D., HERMAN, J.S., The mobility of thorium in natural waters at low temperatures, *Geochim. Cosmochim. Acta* **44** (1980) 1753–1766.

- [480] LALLY, A.E., “Chemical procedures”, Uranium-series Disequilibrium: Applications to Earth, Marine, and Environmental Sciences (IVANOVICH, M., HARMON, R.S., Eds), Clarendon Press, Oxford (1992).
- [481] CHEN, J.H., EDWARDS, R.L., WASSERBURG, G.J., “Mass spectrometry and applications to uranium-series disequilibrium”, Uranium-series Disequilibrium: Applications to Earth, Marine, and Environmental Sciences (IVANOVICH, M., HARMON, R., Eds), Clarendon Press, Oxford (1992).
- [482] EDWARDS, R.L., CHEN, J.H., WASSERBURG, G.J.,  $^{238}\text{U}$ – $^{234}\text{U}$ – $^{230}\text{Th}$ – $^{232}\text{Th}$  systematics and the precise measurement of time over the past 500,000 years, *Earth Planet. Sci. Lett.* **81** (1987) 175–192.
- [483] GOLDSTEIN, S.J., MURRELL, M.T., JANECKY, D.R., Th and U isotopic systematics of basalts from the Juan de Fuca and Gorda Ridges by mass spectrometry, *Earth Planet. Sci. Lett.* **96** (1989) 134–146.
- [484] KU, L.-T., LUO, S., LESLIE, B.W., HAMMOND, D.E., “Decay-series disequilibria applied to the study of rock-water interaction and geothermal systems”, Uranium-series Disequilibrium: Applications to Earth, Marine, and Environmental Sciences (IVANOVICH, M., HARMON, R.S., Eds), Clarendon Press, Oxford (1992).
- [485] FRÖHLICH, K., BATTAGLIA, A., CECCARELLI, A., RIDOLFI, A., PANICHI, C., Radium isotopes contribution to geothermal exploration in Central Italy, *World Geothermal Congr. Florence* (1995).
- [486] KRONFELD, J., Hydrologic Investigations and the Significance of  $^{234}\text{U}/^{238}\text{U}$  Disequilibrium in the Groundwaters of Central Texas, PhD Thesis, Rice Univ. (1971).
- [487] COWART, J.B., OSMOND, J.K., Uranium isotopes in groundwater: their use in prospecting for sandstone-type uranium deposits, *J. Geochem. Expl.* **8** (1977) 365–379.
- [488] FRITZ, P., et al., “Geochemical and isotopic investigations at the Stripa test site (Sweden)”, *Underground Disposal of Radioactive Wastes (Proc. Otaniemi, 1979)*, IAEA, Vienna (1980).
- [489] ANDREWS, J.N., et al., “Environmental isotope studies in two aquifer systems: A comparison of groundwater dating methods”, *Isotope Hydrology 1983 (Proc. Vienna, 1983)*, IAEA, Vienna (1984).
- [490] FJELD, R.A., et al., Characterization of the mobilities of selected actinides and fission/activation products in laboratory columns containing subsurface material from the Snake River Plain, *Nuclear Technology* **135** (2001) 92–108.
- [491] INTERNATIONAL ATOMIC ENERGY AGENCY, Natural Analogues in Performance Assessments for the Disposal of Long Lived Radioactive Wastes, Technical Reports Series No. 304, IAEA, Vienna (1989).
- [492] PEARSON, F.J.J., WHITE, D.E., Carbon-14 ages and flow rates of water in Carrizo Sand, Atacosa County, Texas, *Water Resour. Res.* **3** (1967) 251–261.
- [493] ALEXANDER, W.H., WHITE, D.E., Ground-water Resources of Atacosa and Frio Counties, Texas, Texas Water Development Board Rep. 32 (1966).
- [494] EDMUNDS, W.M., et al., Groundwater evolution in the Continental Intercalaire aquifer of southern Algeria and Tunisia: trace element and isotopic indicators, *Appl. Geochem.* **18** (2003) 805–822.
- [495] EDMUNDS, W.M., et al., Recharge characteristics and groundwater quality of the Grand Erg Oriental Basin, *Hydrogeology Series*, BGS, Wallingford (1997).
- [496] GONFIANTINI, R., CONRAD, G., FONTES, J.C., SAUZAY, G., PAYNE, B., “Etude isotopique de la nappe du Continental Intercalaire et ses relations avec les autres nappes du Sahara septentrional”, *Isotope Techniques in Groundwater Hydrology 1974*, Proceedings Series No. 186, IAEA, Vienna (1974).
- [497] UNITED NATIONS EDUCATIONAL, SCIENTIFIC AND CULTURAL ORGANIZATION, *Projet ERESS, Etude des ressources en eau du Sahara septentrional*, UNESCO, Paris (1972).
- [498] MICHELOT, J.-L., et al., “Chlorine-36 in deep groundwaters and hostrocks of northern Switzerland: sources, evolution and hydrological implications”, *Water-Rock Interaction (MILES, D.L., Ed.)*, Balkema, Rotterdam (1989).
- [499] GUENDOOUZ, A., MICHELOT, J.-L., Chlorine-36 dating of deep groundwater from northern Sahara. *J. Hydrol.* **328** (2006) 572–580.
- [500] CHKIR, N., GUENDOOUZ, Z.A., ZOUARI, K., HADJ AMMAR, F., MOULLA, A.S., Uranium isotopes in groundwater from the continental intercalaire aquifer in Algerian Tunisian Sahara (Northern Africa), *J. Environ. Radioact.* **100** (2009) 649–656.
- [501] MATSUDA, J., Noble Gas Geochemistry and Cosmochemistry, Terra Scientific Publishing, Tokyo (1994).

- [502] PORCELLI, D., BALLENTINE, C.J., WIELER, R., “An overview of noble gas in geochemistry and cosmochemistry”, *Noble Gases in Geochemistry and Cosmochemistry*, *Rev. Mineral. Geochem.* **47** 1 (2002) 1–19.
- [503] SUCKOW, A., SCHLOSSER, P., RUPP, H., BAYER, R., Diffusion and permeation constants of helium in various glasses, *Glass Technology* **31** (1990) 160–164.
- [504] WEISS, R.F., Piggyback samplers for dissolved gas studies on sealed water samples, *Deep Sea Res.* **15** (1968) 659–699.
- [505] SOLBAU, R., WERES, O., HANSEN, L., DUDAK, B., Description of a high temperature downhole fluid sampler, Lawrence Berkeley Lab, Berkeley, CA (1986).
- [506] SANFORD, W.E., SHROPSHIRE, R.G., SOLOMON, D.K., Dissolved gas tracers in groundwater: Simplified injection, Sampling and analysis, *Water Resour. Res.* **32** (1996) 1635–1642.
- [507] SHELDON, A.L., Diffusion of Radiogenic Helium in Shallow Groundwater: Implications for Crustal Degassing, PhD Thesis, Univ. Utah (2002).
- [508] LOOSE, B., STUTE, M., ALEXANDER, P., SMETHIE, W.M., Design and deployment of a portable membrane equilibrator for sampling aqueous dissolved gases, *Water Resour. Res.* **45** (2009) W00D34.
- [509] DYCK, W., DA SILVA, F.G., The use of ping-pong balls and latex tubing for sampling of the helium content of lake sediments, *J. Geochem. Explor.* **14** (1981) 41–48.
- [510] GASCOYNE, M. SHEPPARD, M.I., Evidence of terrestrial discharge of deep groundwater on the Canadian Shield from helium in soil gases, *Environ. Sci. Technol.* **27** (1993) 2420–2426.
- [511] SPALDING, B., WATSON, D., Measurement of dissolved H<sub>2</sub>, O<sub>2</sub>, and CO<sub>2</sub> in groundwater using passive samplers for gas chromatographic analyses, *Environ. Sci. Technol.* **40** (2006) 7861–7867.
- [512] GARDNER, P., SOLOMON, D.K., An advanced passive diffusion sampler for the determination of dissolved gas concentrations, *Water Resour. Res.* (2009) W06423.
- [513] ALI, S., STUTE, M., TORGERSEN, T., WINCKLER, G., KENNEDY, B.M., Helium measurements of pore-fluids obtained from SAFOD drillcore, *Hydrogeol. J.* **19** 1 (2010) 237–247.
- [514] OSENBRÜCK, K., Alter und Dynamik tiefer Grundwässer: eine neue Methode zur Analyse der Edelgase im Porenwasser von Gesteinen, PhD Thesis, Univ. Heidelberg (1996).
- [515] OSENBRÜCK, K., LIPPMANN, J., SONNTAG, C., Dating very old pore waters in impermeable rocks by noble gas isotopes, *Geochim. Cosmochim. Acta* **62** (1998) 3041–3045.
- [516] RUDOLPH, J., Edelgase, Paläotemperaturen und Heliumalter <sup>14</sup>C-datierter Paläowässer, PhD Thesis, Univ. Heidelberg (1981).
- [517] TORGERSEN, T., Limnologic Studies Using the Tritium-helium-3 Tracer Pair: A Survey Evaluation of the Method, PhD Thesis, Columbia Univ. (1977).
- [518] SMITH, S.P., KENNEDY, B.M., The solubility of noble gases in water and in NaCl brine, *Geochim. Cosmochim. Acta* **47** (1983) 503–515.
- [519] SMITH, S.P., KENNEDY, B.M., Noble gas evidence for two fluids in the Baca (Vales Caldera) geothermal reservoir, *Geochim. Cosmochim. Acta* **49** (1985) 893–902.
- [520] LUDIN, A., WEPPEMING, R., BÖNISCH, G., SCHLOSSER, P., Mass spectrometric measurement of helium isotopes and tritium in water samples, Lamont-Doherty Technical Report, Lamont-Doherty Earth Observatory (1998).
- [521] MAMYRIN, B.A., TOLSTIKHIN, I.N., *Helium Isotopes in Nature*, Elsevier, New York (1984).
- [522] STUTE, M., Edelgase im Grundwasser — Bestimmung von Paläotemperaturen und Untersuchung der Dynamik von Grundwasserfließsystemen, PhD Thesis, Univ. Heidelberg (1989).
- [523] WEISS, R.F., The solubility of nitrogen, oxygen and argon in water and seawater, *Deep Sea Res.* **17** (1970) 721–735.
- [524] WEISS, R.F., Solubility of helium and neon in water and seawater, *J. Chem. Eng. Data* **16** (1971) 235–241.
- [525] CLEVER, H.L., Argon, International Union for Pure and Applied Chemistry Solubility Data Series, Pergamon Press, New York (1979).

- [526] CLEVER, H.L., Helium–Neon — Gas Solubilities, International Union for Pure and Applied Chemistry Solubility Data Series, Pergamon Press, New York (1979).
- [527] CLEVER, H.L., Krypton, Xenon and Radon Solubilities, International Union for Pure and Applied Chemistry Solubility Data Series, Pergamon Press, New York (1979).
- [528] KIPFER, R., AESCHBACH-HERTIG, W., PEETERS, F., STUTE, M., “Noble gases in lakes and groundwaters”, Noble Gases in Geochemistry and Cosmochemistry, *Rev. Mineral. Geochem.* **47** 1 (2002) 615–700.
- [529] SUCKOW, A., SONNTAG, C., “The influence of salt on the noble gas thermometer”, Isotope Techniques in the Study of Past and Current Environmental Changes in the Hydrosphere and Atmosphere (Proc. Int. Conf. Vienna, 1993), IAEA, Vienna (1993).
- [530] BALLENTINE, C.J., BURGESS, R., MARTY, B., “Tracing fluid origin, transport and interaction in the crust”, Noble Gases in Geochemistry and Cosmochemistry, *Rev. Mineral. Geochem.* **47** 1 (2002) 539–614.
- [531] PEETERS, F., et al., Improving noble gas based palaeoclimate reconstruction and groundwater dating using  $^{20}\text{Ne}/^{22}\text{Ne}$  ratios, *Geochim. Cosmochim. Acta* **67** (2002) 587–600.
- [532] AESCHBACH-HERTIG, W., BEYERLE, U., HOLOCHER, J., PEETERS, F., KIPFER, R., “Excess air in groundwater as a potential indicator of past environmental changes”, Study of Environmental Change Using Isotope Techniques (Proc. Int. Conf. Vienna, 2001), IAEA, Vienna (2001).
- [533] HOLOCHER, J., et al., Experimental investigations on the formation of excess air in quasi-saturated porous media, *Geochim. Cosmochim. Acta* **66** (2002) 4103–4117.
- [534] CRAIG, H., LUPTON, J.E., Primordial neon, helium and hydrogen in oceanic basalts, *Earth Planet. Sci. Lett.* **31** (1976) 369–385.
- [535] TORGERSEN, T., Controls on porefluid concentration of  $^4\text{He}$  and  $^{222}\text{Rn}$  and the calculation of  $^4\text{He}/^{222}\text{Rn}$  ages, *J. Geochem. Explor.* **13** (1980) 57–75.
- [536] ANDREWS, J.N., “Radiogenic and inert gases in groundwater”, Second Int. Symp. on Water Rock Interaction (PAQUET, H., TARDY, Y., Eds), Institut de Géologie, Université Louis Pasteur, Strasbourg (1977).
- [537] FLÜGGE, S., ZIMENS, K.E., Die Bestimmung von Korngrößen und von Diffusionskonstanten aus dem Emaniervermögen, *Z. Phys. Chem.* **B343** (1939) 179–200.
- [538] HEATON, T.H.E., Rates and sources of  $^4\text{He}$  accumulation in groundwater, *Hydrolog. Sci. J.* **29** (1984) 29–47.
- [539] CARSLAW, H.S., JAEGER, J.C., Conduction of Heat in Solids, Clarendon Press, Oxford (1959).
- [540] LIPPOLT, H.J., WEIGEL, E.,  $^4\text{He}$  diffusion in  $^{40}\text{Ar}$ -retentive minerals, *Geochim. Cosmochim. Acta* **52** (1988) 1449–1458.
- [541] TRULL, T.W., KURZ, M.D., JENKINS, W.J., Diffusion of cosmogenic  $^3\text{He}$  in olivine and quartz: Implications for surface exposure dating, *Earth Planet. Sci. Lett.* **103** (1991) 241–256.
- [542] HONDA, M., KURITA, K., HAMANO, Y., OZIMA, M., Experimental studies of He and Ar degassing during rock fracturing, *Earth Planet. Sci. Lett.* **59** (1982) 429–436.
- [543] TORGERSEN, T., O’DONNELL, J., The degassing flux from the solid earth: Release by fracturing, *Geophys. Res. Lett.* **18** (1991) 951–954.
- [544] KNAPP, R.B., KNIGHT, J.E., Differential expansion of porefluids: fracture propagation and microearthquake production in hot pluton environments, *J. Geophys. Res.* **82** (1977).
- [545] SAVAGE, W.Z., The development of residual stress in cooling rock bodies, *Geophys. Res. Lett.* **5** (1978) 633–636.
- [546] TORGERSEN, T., Terrestrial helium degassing fluxes and the atmospheric helium budget: Implications with respect to the degassing processes of continental crust, *Chem. Geol.* **79** (1989) 1–14.
- [547] TORGERSEN, T., Continental degassing flux of  $^4\text{He}$  and its variability, *Geochem. Geophys. Geosys.* **11** (2010) Q06002.
- [548] CLARKE, W.B., TOP, Z., BEAVAN, A.P., GANDHI, S.S., Dissolved helium in lakes; uranium prospecting in the Precambrian terrain of Central Labrador, *Econ. Geol.* **72** (1977) 233–242.
- [549] CLARKE, W.B., TOP, Z., EISMONT, W.C., “Helium isotope and tritium content of lakes and uranium exploration in the NEA/IAEA Athabasca test area”, Uranium Exploration in Athabasca Basin, Saskatchewan, Canada (CAMERON, E., Ed.), Geol. Survey Canada (1983).

- [550] TOP, Z., CLARKE, W.B., Dissolved helium isotopes and tritium in lakes: further results for uranium prospecting in Central Labrador, *Econ. Geol.* **76** (1981) 2018–2031.
- [551] ETHERIDGE, M., WALL, V.J., COX, S.F., VERNON, R.H., High fluid pressures during regional metamorphism: implications for mass transport and deformation mechanisms. *J. Geophys. Res.* **89** (1984).
- [552] ETHERIDGE, M., WALL, V.J., VERNON, R.H., The role of the fluid phase during regional metamorphism and deformation, *J. Metamorph. Geol.* **1** (1983) 205–226.
- [553] BALLENTINE, C.J., BURNARD, P.G., “Production release and transport of noble gases in the continental crust”, *Noble Gases in Geochemistry and Cosmochemistry, Rev. Mineral. Geochem.* **47** 1 (2002) 481–538.
- [554] MORRISON, P., PINE, J., Radiogenic origin of the helium isotopes in rocks, *Ann. N.Y. Acad. Sci.* **62** (1955) 69–92.
- [555] FIEGGE, Y., OTTMAN, B.G., KASTNER, J., Production rates of neutrons in soils due to natural radioactivity, *J. Geophys. Res.* **73** (1968) 3135–3142.
- [556] ANDREWS, J.N., The isotopic composition of radiogenic helium and its use to study groundwater movement in confined aquifers, *Chem. Geol.* **49** (1985) 339–351.
- [557] MARTEL, D.J., O’NIONS, R.K., HILTON, D.R., OXBURGH, E.R., The role of element distribution in production and release of radiogenic helium; The Carnmenellis Granite, Southwest England, *Chem. Geol.* **88** (1990) 207–221.
- [558] CHAZAL, V., et al., Neutron background measurements in the underground laboratory of Modane, *Astroparticle Phys.* **9** (1998) 163–172.
- [559] TOLSTIKHIN, I., LEHMANN, B.E., LOOSLI, H.H., GAUTSCHI, A., Helium and argon isotopes in rocks, minerals, and related groundwaters: A case study in northern Switzerland, *Geochim. Cosmochim. Acta* **60** (1996) 1497–1514.
- [560] WEISE, S.M., Heliumisotopen-Gehalte im Grundwasser, Messung und Interpretation, PhD Thesis, Univ. Munich (1986).
- [561] STUTE, M., SONNTAG, C., DEAK, J., SCHLOSSER, P., Helium in deep circulating groundwater in the Great Hungarian Plain: Flow dynamics and crustal and mantle helium fluxes, *Geochim. Cosmochim. Acta* **56** (1992) 2051–2067.
- [562] WEISE, S.M., MOSER, H., “Groundwater dating with helium isotopes”, *Int. Symp. on Isotope Techniques in Water Resources Development*, Vienna (1987).
- [563] CRAIG, H., LUPTON, J.E., “Helium-3 and mantle volatiles in the ocean and the oceanic crust”, *The Sea* (EMILIANI, C., Ed.), Wiley, New York (1981).
- [564] STUTE, M., DEAK, J., Environmental isotope study ( $^{14}\text{C}$ ,  $^{13}\text{C}$ ,  $^{18}\text{O}$ , D, noble gases) on deep groundwater circulation systems in Hungary with reference to palaeoclimate, *Radiocarbon* **31** (1989) 902–918.
- [565] ROETHER, W., “Estimating the tritium input to groundwater from wine samples: groundwater and direct run-off contribution to central European surface waters”, *Isotopes in Hydrology (Proc. Vienna, 1966)*, IAEA, Vienna (1967) 73–91.
- [566] SCHLOSSER, P., STUTE, M., SONNTAG, C., MÜNNICH, K.-O., Tritiogenic  $^3\text{He}$  in shallow groundwater, *Earth Planet. Sci. Lett.* **94** (1989) 245–256.
- [567] KENNEDY, B.M., TORGERSEN, T., VAN SOEST, M., Multiple atmospheric noble gas components in hydrocarbon reservoirs: a study of the northwest shelf, Delaware Basin, SE New Mexico, *Geochim. Cosmochim. Acta* **66** (2002) 2807–2822.
- [568] LIPPMANN, J., et al., Dating ultra-deep mine waters with noble gases and  $^{36}\text{Cl}$ , Witwatersrand Basin, South Africa, *Geochim. Cosmochim. Acta* **67** (2003) 4597–4619.
- [569] DRESCHER, J., KIRSTEN, T., SCHAFER, K., The rare gas inventory of the continental crust, recovered by the KTB continental Deep Drilling Project, *Earth Planet. Sci. Lett.* **154** (1998) 247–263.
- [570] TORGERSEN, T., Defining the role of magmatism in extensional tectonics: helium-3 fluxes in extensional basins, *J. Geophys. Res.* **98** (1993) 16 257–16 269.
- [571] TORGERSEN, T., DRENKARD, S., FARLEY, K., SCHLOSSER, P., SHAPIRO, A., “Mantle helium in the groundwater of the Mirror Lake Basin, New Hampshire, U.S.A.”, *Noble Gas in Geochemistry and Cosmochemistry* (MATSUDA, J., Ed.), Terra Scientific Publishing Company (TERRAPUB), Tokyo (1994).

- [572] KRISHNASWAMI, S., SEIDEMANN, D.E., Comparative study of  $^{222}\text{Rn}$ ,  $^{40}\text{Ar}$ ,  $^{39}\text{Ar}$  and  $^{37}\text{Ar}$  leakage from rocks and minerals: Implications for the role of nanopores in gas transport through natural silicates, *Geochim. Cosmochim. Acta* **52** (1988) 655–658.
- [573] TORGERSEN, T., et al., Argon accumulation and the crustal degassing flux of  $^{40}\text{Ar}$  in the Great Artesian Basin, Australia, *Earth Planet. Sci. Lett.* **92** (1989) 43–56.
- [574] BETHKE, C.M., LEE, M., PARK, J., Basin Modelling with Basin2, Release 5, *Hydrogeol. Prog. Univ. Illinois, Urbana-Champaign* (2002).
- [575] FRITZEL, T.L.B., Numerical modeling of the distribution of  $^3\text{He}$  and  $^4\text{He}$  in groundwater flow systems with applications in determining the residence times of very old groundwaters, MSc Thesis, Univ. Illinois (1996).
- [576] MARINE, I.W., The use of naturally occurring helium to estimate groundwater velocities for studies of geologic storage of radioactive waste, *Water Resour. Res.* **15** (1979) 1130–1136.
- [577] ANDREWS, J.N., LEE, D.J., Inert gases in groundwater from the Bunter Sandstone of England as indicators of age and palaeoclimatic trends, *J. Hydrol.* **41** (1979) 233–252.
- [578] AIREY, P.L., et al., “Aspects of the isotope hydrology of the Great Artesian Basin, Australia”, *Isotope Hydrology 1978 (Proc. Neuherberg, 1978)*, IAEA, Vienna (1979).
- [579] BETHKE, C.M., LEE, M., QUINODOZ, H.A.M., KREILING, W.N., Basin modeling with Basin2 and Basin2view, University of Illinois, Urbana-Champaign (1993).
- [580] MAZOR, E., Stagnant aquifer concept Part 1. Large-scale artesian systems — Great Artesian Basin, Australia, *J. Hydrol.* **173** (1995) 219–240.
- [581] WEI, H.F., LEDOUX, E., MARSILY, G.D., Regional modelling of groundwater flow and salt and environmental tracer transport in deep aquifers in the Paris Basin, *J. Hydrol.* **120** (1990) 341–358.
- [582] EKWURZEL, B., et al., Dating of shallow groundwater: Comparison of the transient tracers  $^3\text{H}/^3\text{He}$ , chlorofluorocarbons, and  $^{85}\text{Kr}$ , *Water Resour. Res.* **30** (1994) 1693–1708.
- [583] SANO, Y., WAKITA, H., HUANG, C.W., Helium flux in a continental land area estimated from  $^3\text{He}/^4\text{He}$  ratio in northern Taiwan, *Nature* **323** (1986) 55–57.
- [584] NUR, A., WALDER, J., “Time dependent hydraulics of the Earth’s crust”, *The role of Fluids in Crustal Processes*, Geophysics Study Committee, National Academy of Science Press, Washington, DC (1990).
- [585] COYLE, B.J., ZOBACK, M.D., In situ permeability and fluid pressure measurements at ~2km depth in the Cajon Pass research well, *Geophys. Res. Lett.* **15** (1988) 1029–1032.
- [586] ALI, S., STUTE, M., TORGERSEN, T., WINCKLER, G., “SAFOD helium isotope study on pore fluids obtained from drill core samples”, *AGU Abstract, San Francisco, CA* (2008).
- [587] STUTE, M., TORGERSEN, T., WINCKLER, G., SCHLOSSER, P., Helium Isotope Measurements on Matrix Fluids from the SAFOD Drillcore Earthscope National Mtg, Monterey, CA (2007).
- [588] STUMPP, C., STICHLER, W., MALOSZEWSKI, P., Application of the environmental isotope  $^{18}\text{O}$  to study water flow in unsaturated soils planted with different crops: Case study of a weighable lysimeter from the research field in Neuherberg, Germany, *J. Hydrol.* **368** (2009) 68–78.
- [589] VITVAR, T., BALDERER, W., Estimation of mean water residence time and runoff generation by  $^{18}\text{O}$  measurements in a Pre-Alpine catchment (Rietholzbach Eastern Switzerland), *Appl. Geochem.* **12** (1997) 787–796.
- [590] LIN, R., WEI, K., Tritium profiles of pore water in the Chinese loess unsaturated zone: Implications for estimation of groundwater recharge, *J. Hydrol.* **328** (2006) 192–199.
- [591] RAPP, M.C., et al., The dual pumping technique (DPT) for level-determined sampling in fully screened groundwater wells, *J. Hydrol.* **207** (1998) 220–235.
- [592] BENSON, B.B., KRAUSE, D.J., Isotopic fractionation of helium during solution: a probe for the liquid state, *J. Solution Chem.* **9** (1980) 895–909.
- [593] SCHWARTZ, F.W., ZHANG, H., *Fundamentals of Ground Water*, John Wiley & Sons, New York (2003).
- [594] COOK, P.G., BÖHLKE, J.-K., “Determining timescales for groundwater flow and solute transport”, *Environmental Tracers in Subsurface Hydrology (COOK, P.G., HERCZEG, A.L., Eds)*, Kluwer Academic Press, Boston, MA (1999).

- [595] HARBAUGH, A.W., MODFLOW-2005, The U.S. Geological Survey Modular Ground-water Model — The Ground-water Flow Process, Survey Techniques and Methods, U.S. Geological Survey (2005).
- [596] MEHL, S.W., HILL, M.C., MODFLOW-2005, the U.S. Geological Survey Modular Ground-water Model — Documentation of Shared Node Local Grid Refinement (LGR) and the Boundary Flow and Head (BFH) Package, Techniques and Methods, U.S. Geological Survey (2005).
- [597] MEHL, S.W., HILL, M.C., MODFLOW-2005, the U.S. Geological Survey Modular Ground-water Model — Documentation of Multiple Refined-areas of Local Grid Refinement (LGR) and the Boundary Flow and Head (BFH) Package, Techniques and Methods, U.S. Geological Survey (2007).
- [598] WINSTON, R.B., ModelMuse — A Graphical User Interface for MODFLOW-2005 and PHAST, Techniques and Methods, U.S. Geological Survey (2009).
- [599] HSIEH, P.A., WINSTON, R.B., User's Guide to Model Viewer, a Program for Three-dimensional Visualization of Ground-water Model Results, Open-File Report, U.S. Geological Survey (2002).
- [600] ANDERSON, M.P., WOESSNER, W.W., Applied Groundwater Modeling: Simulation of Flow and Advective Transport, Academic Press, San Diego, CA (1992).
- [601] HAITJEMA, H.M., Analytic Element Modeling of Groundwater Flow, Academic Press (1995).
- [602] ANDERMAN, E.R., HILL, M.C., MODFLOW-2000, the U.S. Geological Survey Modular Ground-water Model — Documentation of the Hydrogeologic-Unit Flow (HUF) Package, Open-File Report, U.S. Geological Survey (2000).
- [603] ANDERMAN, E.R., HILL, M.C., MODFLOW-2000, the U.S. Geological Survey Modular Ground-water Model — Three Additions to the Hydrogeologic Unit Flow (HUF) Package: Alternate Storage for the Uppermost Active Cells, Flows in Hydrogeologic Units, and the Hydraulic-conductivity Depth-dependence (KDEP) Capability, Open-File Report, U.S. Geological Survey (2003).
- [604] YAGER, R.M., SOUTHWORTH, S., VOSS, C.I., Simulation of Ground-water Flow in the Shenandoah Valley, Virginia and West Virginia, Using Variable-direction Anisotropy in Hydraulic Conductivity to Represent Bedrock Structure, Scientific Investigations Report, U.S. Geological Survey (2008).
- [605] HILL, M.C., Methods and Guidelines for Effective Model Calibration, Water-Resources Investigations Report, U.S. Geological Survey (1998).
- [606] HILL, M.C., TIEDEMAN, C.R., Effective Groundwater Model Calibration, Wiley-Interscience, New Jersey (2007).
- [607] KONIKOW, L.F., BREDEHOEFT, J.D., Ground-water models cannot be validated, *Adv. Water Resour.* **15** (1992) 75–83.
- [608] DOHERTY, J., PEST: Model Independent Parameter Estimation, Watermark Computing, Brisbane (2004).
- [609] POETER, E.P., HILL, M.C., BANTA, E.R., MEHL, S.W., CHRISTENSEN, S., UCODE-2005 and Six Other Computer Codes for Universal Sensitivity Analysis, Calibration, and Uncertainty Evaluation, Techniques and Methods, U.S. Geological Survey (2005).
- [610] REILLY, T.E., HARBAUGH, A.W., Guidelines for Evaluating Ground-water Flow Models, Scientific Investigations Report, U.S. Geological Survey (2004).
- [611] POLLOCK, D.W., User's Guide for MODPATH/MODPATH-PLOT, Version 3: A Particle Post-processing Package for MODFLOW, the U.S. Geological Survey Finite-difference Ground-water Flow Model, Open-File Report, U.S. Geological Survey (1994).
- [612] BARTOLINO, J.R., COLE, J.C., Ground-water resources of the Middle Rio Grande Basin, U.S. Geological Survey Circular (2002).
- [613] KONIKOW, L.F., GROVE, D.B., Derivation of Equations Describing Solute Transport in Ground Water, Water-Resources Investigations Report, U.S. Geological Survey (1977).
- [614] KOCH, D.H., PRICKETT, T.A., "RAN3D, a three-dimensional ground-water solute transport model, user's manual", Engineering Technologies Associates, Ellicott City, MD (1993).
- [615] KONIKOW, L.F., GOODE, D.J., HORNBERGER, G.Z., A Three-dimensional Method-of-characteristics Solute-transport Model (MOC3D), Water-Resources Investigations Report, U.S. Geological Survey (1996).
- [616] VOSS, C.I., PROVOST, A.M., SUTRA - A Model for Saturated-unsaturated Variable Density Ground-water Flow with Solute or Energy Transport, Water-Resources Investigations Report, U.S. Geological Survey (2002).

- [617] ZHENG, C., WANG, P.K., MT3DMS: A Modular Three-dimensional Multispecies Transport Model for Simulation of Advection, Dispersion, and Chemical Reactions of Contaminants in Groundwater Systems; Documentation and User's Guide, U.S. Army Corp of Engineers (1999).
- [618] PRICKETT, T.A., NAYMIK, T.G., LONNQUIST, C.G., A 'random walk' solute transport model for selected groundwater quality evaluations, Bull. Illinois State Water Survey, Champaign, IL (1981).
- [619] KONIKOW, L.F., BREDEHOEFT, J.D., "Computer model of two-dimensional solute transport and dispersion in ground water", Techniques of Water Resources Investigations of the U.S. Government Printing Office, Washington, DC (1978).
- [620] GELHAR, L.W., Stochastic subsurface hydrology from theory to applications, Water Resour. Res. **22** (1986) 135S–145S.
- [621] SCHULZE-MAKUCH, D., Longitudinal dispersivity data and implications for scaling behaviour, Ground Water **43** (2005) 443–456.
- [622] LEBLANC, D.R., et al., Large-scale natural gradient tracer test in sand and gravel, Cape Cod, Massachusetts, I, Experimental design and observed tracer movement, Water Resour. Res. **27** (1991) 895–910.
- [623] BETHKE, C.M., JOHNSON, T.M., Paradox of groundwater age, Geology **30** (2002) 107–110.
- [624] JOHNSON, T.M., DePAOLO, D.J., Reaction-transport models for radiocarbon in groundwater: the effect of longitudinal dispersion and the use of Sr isotope ratios to correct for water-rock interaction, Water Resour. Res. **32** (1996) 2203–2212.
- [625] PERROCHET, P., ETCHEVERRY, D., Direct simulation of groundwater transit-time distributions using the reservoir theory, Hydrogeol. J. **8** (2000) 200–208.
- [626] SANFORD, W.E., BUAPENG, S., Assessment of a groundwater flow model of the Bangkok Basin, Thailand, using carbon-14-based ages and palaeohydrology, Hydrogeol. J. **4** (1996) 26–40.
- [627] SANFORD, W.E., Calibration of models using groundwater age, Hydrogeol. J. **19** (2011) 13–16.
- [628] ZINN, B.A., KONIKOW, L.F., Potential effects of regional pumpage on groundwater age distribution, Water Resour. Res. **43** (2007) W06418.
- [629] SANFORD, W.E., POPE, J.P., Current challenges in forecasting seawater intrusion: Lessons from the Eastern Shore of Virginia, USA, Hydrogeol. J. **18** (2010) 73–93.
- [630] SANFORD, W.E., REVESZ, K., DEAK, J., "Inverse modeling using <sup>14</sup>C ages: Application to groundwater in the Danube-Tisza interfluvial region of Hungary", New Approaches to Characterizing Groundwater Flow (Seiler, K.-P., Wohnlich, S., Eds), A.A. Balkema, Lisse (2001).
- [631] IVANOVICH, M., FRÖHLICH, K., HENDRY, M.J., Dating very old groundwater, Milk River aquifer, Alberta, Canada, Appl. Geochem. **6** (1991) 367–475.
- [632] HENDRY, M.J., SCHWARTZ, F.W., ROBERTSON, C., Hydrogeology and hydrochemistry of the Milk River aquifer system, Alberta, Canada: a review, Appl. Geochem. **6** (1991) 369–380.
- [633] HENDRY, M.J., SCHWARTZ, F.W., An alternative view on the origin of chemical and isotopic patterns in groundwater from the Milk River aquifer, Canada, Water Resour. Res. **24** (1988) 1747–1763.
- [634] HITCHEON, B., FRIEDMAN, I., Geochemistry and origin of formation waters in the western Canada sedimentary basin, I. Stable isotopes of hydrogen and oxygen, Geochim. Cosmochim. Acta **33** (1969) 1321–1349.
- [635] MEYBOOM, P., Geology and groundwater resources of the Milk River sandstone in southern Alberta, Mem. 2, Alberta Res. Council, Edmonton, Alberta **2** (1960) 89.
- [636] SCHWARTZ, F.W., MUEHLENBACHS, K., Isotope and ion geochemistry of groundwaters in the Milk River aquifer, Alberta, Water Resour. Res. **15** (1979) 259–268.
- [637] SCHWARTZ, F.W., MUEHLENBACHS, K., CHORLEY, D.E., Flow-system controls of the chemical evolution of groundwater, J. Hydrol. **54** (1981) 225–243.
- [638] SWANICK, G.B., The Hydrochemistry and Age of the Water in the Milk River Aquifer, Alberta, Canada, MSc Thesis, Univ. Arizona (1982).
- [639] DOMENICO, P.A., ROBBINS, G.A., The displacement of connate water from aquifers, Bull. Geologic. Soc. Amer. **96** (1985) 328–335.

- [640] PHILLIPS, F.M., KNOWLTON, R.G., BENTLEY, H.W., Comment on 'An alternative view on the origin of chemical and isotopic patterns in groundwater from the Milk River aquifer, Canada' by M.J. Hendry and F.W. Schwartz, *Water Resour. Res.* **26** (1990) 1693–1698.
- [641] JACKSON, L.E.J., LITTLE, E.C., "A single continental glaciation of Rocky Mountain Foothills, south-western Alberta, Canada", *Quaternary Glaciations — Extent and Chronology, Part II: North America* (EHLERS, J., GIBBARD, P.L., Eds) (2004).
- [642] ANDREWS, J.N., FLORKOWSKI, T., LEHMANN, B.E., LOOSLI, H.H., Underground production of radionuclides in the Milk River aquifer, Alberta, Canada, *Appl. Geochem.* **6** (1991) 425–434.
- [643] EDMUNDS, W.M., "Trace element variations across an oxidation-reduction barrier in a limestone aquifer", *Symp. Hydrogeochemistry and Biogeochemistry, Clarke Co, Tokyo* (1973).
- [644] CUTTELL, J.C., LLOYD, J.W., IVANOVICH, M., A study of uranium and thorium series isotopes in chalk groundwaters of Lincolnshire, U.K., *J. Hydrol.* **86** (1986) 343–365.
- [645] GRAUCH, V.J.S., GILLESPIE, C.L., KELLER, G.R., "Discussion of new gravity maps for the Albuquerque Basin area", *Albuquerque Geology, New Mexico Geological Society Fiftieth Annual Field Conf.* (PAZZAGLIA, F.J., LUCAS, S.G., Eds), New Mexico Geological Society (1999).
- [646] GRAUCH, V.J.S., SAWYER, D.A., KELLER, G.R., GILLESPIE, C.L., "Contributions of gravity and aeromagnetic studies to improving the understanding of subsurface hydrogeology, Middle Rio Grande Basin, New Mexico", *U.S. Geological Survey Middle Rio Grande Basin Study (Proc. Fourth Annual Workshop Albuquerque, NM, 2000)* (COLE, J.C., Ed.), Open-File Report, U.S. Geological Survey (2001) 00-488.
- [647] COLE, J.C., "3-D geologic modeling of regional hydrostratigraphic units in the Albuquerque segment of the Rio Grande rift", *Fourth Annual Workshop* (COLE, J.C., Ed.), U.S. Geological Survey, Albuquerque, NM (2001).
- [648] CONNELL, S.D., ALLEN, B.D., HAWLEY, J.W., Subsurface stratigraphy of the Santa Fe Group from borehole geophysical logs, Albuquerque area, New Mexico, *New Mexico Geology* **17** (1998) 79–87.
- [649] HAWLEY, J.W., HAASE, C.S., *Hydrogeologic Framework of the Northern Albuquerque Basin*, Open-File Report New Mexico Bureau Mines and Mineral Resour., Socorro, NM (1992).
- [650] BEXFIELD, L.M., ANDERHOLM, S.K., *Estimated Water-level Declines in the Santa Fe Group Aquifer System in the Albuquerque Area, Central New Mexico, Predevelopment to 2002*, Water-Resources Investigations Report, U.S. Geological Survey (2002).
- [651] KERNODLE, J.M.M., McADA, D.P., THORN, C.R., *Simulation of Ground-water Flow in the Albuquerque Basin, Central New Mexico, 1901–1994, with Projections to 2020*, Water-Resources Investigations Report, U.S. Geological Survey (1995).
- [652] YAPP, C.J., D/H variations of meteoric waters in Albuquerque, New Mexico, USA, *J. Hydrol.* **76** (1985) 63–84.
- [653] BEXFIELD, L.M., ANDERHOLM, S.K., *Predevelopment Water-level Map of the Santa Fe Group Aquifer System in the Middle Rio Grande Basin Between Cochiti Lake and San Acacia, New Mexico*, Water-Resources Investigations Report, U.S. Geological Survey (2000).
- [654] TITUS, F.B., *Geology and Ground-water Conditions in Eastern Valencia County, New Mexico*, Ground-Water Report, New Mexico Bureau of Mines and Mineral Resources Socorro, NM (1963).
- [655] BJORKLUND, L.J., MAXWELL, B.W., *Availability of Groundwater in the Albuquerque Area, Bernalillo and Sandoval Counties, New Mexico*, Engineer Tech. Rep., New Mexico State (1961).
- [656] TITUS, F.B., "Ground-water geology of the Rio Grande trough in north-central New Mexico, with sections on the Jemez Caldera and Lucero Uplift", *Guidebook of the Albuquerque Country* (NORTHROP, S.A., Ed.), New Mexico Geol. Soc. (1961).
- [657] JOUZEL, J., MERLIVAT, L., LORIUS, C., Deuterium excess in an East Antarctic ice core suggests higher relative humidity at the oceanic surface during the last glacial maximum, *Nature* **299** (1982) 688–691.
- [658] MERLIVAT, L., JOUZEL, J., Global climatic interpretation of the deuterium-oxygen-18 relationship for precipitation, *J. Geophys. Res.* **84** (1979) 5029–5033.
- [659] POETER, E.P., HILL, M.C., *Documentation of UCODE, a Computer Code for Universal Inverse Modeling*, Water-Resources Investigations Report, U.S. Geological Survey (1998).
- [660] HANEBERG, W.C., *Depth-porosity relationships and virgin specific storage estimates for the upper Santa Fe Group aquifer system, central Albuquerque Basin, New Mexico*, *New Mexico Geology* **17** (1995) 62–71.

- [661] STONE, B.D., et al., Preliminary Lithostratigraphy, Interpreted Geophysical Logs, and Hydrogeologic Characteristics of the 98th Street Core Hole, Albuquerque, New Mexico, Open-File Report, U.S. Geological Survey (1998).
- [662] McADA, D.P., BARROLL, P., Simulation of Ground-water Flow in the Middle Rio Grande Basin between Cochiti and San Acacia, New Mexico, Water-Resources Investigations Report, U.S. Geological Survey (2002).
- [663] TIEDEMAN, C.R., KERNODLE, J.M., McADA, D.P., Application of Nonlinear-regression Methods to a Ground-water Flow Model of the Albuquerque Basin, New Mexico, Water-Resources Investigations Report, U.S. Geological Survey (1998).
- [664] ANDERHOLM, S.K., Mountain-front Recharge along the East Side of the Albuquerque Basin, Central New Mexico (revised), Water-Resources Investigations Report, U.S. Geological Survey (2001).
- [665] ALLEN, B.D., ANDERSON, R.Y., A continuous, high-resolution record of late Pleistocene climate variability from the Estancia basin, New Mexico, *Geol. Soc. Am. Bull.* **112** (2000) 1444–1458.
- [666] BACHHUBER, F.W., “A pre-late Wisconsin palaeolimnologic record from the Estancia Valley, central New Mexico”, *The Last Interglacial-Glacial Transition in North America* (CLARK, P.U., LEA, P.D., Eds) (1992).
- [667] THOMPSON, R.S., ANDERSON, K.H., BARTLEIN, P.J., Quantitative Palaeoclimatic Reconstructions from Late Pleistocene Plant Macrofossils of the Yucca Mountain Region, Open-File Report, U.S. Geological Survey (1999).
- [668] HABERMEHL, M.A., The Great Artesian Basin, Australia, *BMR J. Aust. Geol. Geophys.* **5** (1980) 9–38.
- [669] HABERMEHL, M.A., “Hydrogeology and environmental geology of the Great Artesian Basin, Australia”, *Gondwana to Greenhouse — Australian Environmental Geoscience* (GOSTIN, V.A., Ed.), Geological Society of Australia (2001).
- [670] RADKE, B.M., FERGUSON, J., CRESSWELL, R.G., RANSLEY, T.R., HABERMEHL, M.A., Hydrochemistry and Implied Hydrodynamics of the Cada-owie-Hooray Aquifer Great Artesian Basin, Bureau of Rural Sciences, Australia (2000).
- [671] JACK, R.L., “The composition of the waters of the Great Australian Artesian Basin in South Australia and its significance”, *Trans. Proc. Royal Soc. South Australia* **47** (1923) 316–321.
- [672] HABERMEHL, M.A., LAU, J.E., Hydrogeology of the Great Artesian Basin, Australian Geological Survey Organisation, Canberra (1997).
- [673] SHAW, R.D., “The seismo-tectonics of southeastern Queensland”, *The Eromanga-Brisbane Transect: A Guide to Basin Development across Phanerozoic Australia in Southern Queensland* (FINLAYSON, D.M., Ed.), Bureau of Mineral Resources, Geology and Geophysics, Australia (1990).
- [674] VEEVERS, J.J.E., *Phanerozoic Earth History of Australia*, Oxford University Press, New York (1984).
- [675] SENIOR, B.R., MOND, A., HARRISON, P.L., *Geology of the Eromanga Basin*, Bureau of Mineral Resources, Geology and Geophysics, Canberra, *Bull.* **167** (1978).
- [676] STRUCKMEYER, H.I.M., BROWN, P.J., *Australian Sealevel Curves, Part 1, Australian Inundation Curves*, Bureau of Mineral Resources, Australia (1990).
- [677] GURNIS, M., MULLER, R.D., MORESI, L., Cretaceous vertical motion of Australia and the Australian–Antarctic discordance, *Science* **279** (1998) 1499–1504.
- [678] SENIOR, B.R., HABERMEHL, M.A., Structure, hydrodynamics and hydrocarbon potential of the Central Eromanga Basin, Queensland, Australia, *BMR J. Aust. Geol. Geophys.* **5** (1980) 47–55.
- [679] TOUPIN, D., et al., Petroleum hydrogeology of the Cooper and Eromanga Basins, Australia: some insights from mathematical modeling and fluid inclusion data, *AAPG Bull.* **81** (1997) 577–603.
- [680] DUNCAN, R.A., McDOUGALL, I., “Time-space relationships for Cainozoic intraplate volcanism in Eastern Australia, the Tasman Sea and New Zealand”, *Intraplate Volcanic Activity in Australia and New Zealand* (JOHNSON, J.W., Ed.), Cambridge University Press, Cambridge (1989).
- [681] COLLERSON, K.D., ULLMAN, W.J., TORGERSEN, T., Ground waters with unradiogenic  $^{87}\text{Sr}/^{86}\text{Sr}$  ratios in the Great Artesian Basin, Australia, *Geology* **16** (1988).
- [682] TORGERSEN, T., HABERMEHL, M.A., CLARKE, W.B., Helium isotopic evidence for recent subcrustal volcanism in eastern Australia, *Geophys. Res. Lett.* **14** (1987) 1215–1218.

- [683] MAGEE, J., MILLER, G.H., SPOONER, N.A., QUESTIAUX, D., Continuous 150 kyr monsoon record from Lake Eyre, Australia: insolation forcing implications and unexpected Holocene failure, *Geology* **32** (2004) 885–888.
- [684] NANSON, G.C., PRICE, D.M., The drying of Australia during the Middle and Late Quaternary Long Records Workshop, Geology Department, Australian National University, Canberra (1999).
- [685] NANSON, G.C., PRICE, D.M., SHORT, S.A., Wetting and drying of Australia over the past 300 Ka, *Geology* **20** (1992) 791–794.
- [686] TORGERSEN, T., JONES, M.R., STEPHENS, A.W., SEARLE, D.E., ULLMAN, W.J., Late Quaternary hydrologic changes in the Gulf of Carpentaria, *Nature* **313** (1985) 785–787.
- [687] TORGERSEN, T., et al., Late Quaternary environments of the Carpentaria Basin, Australia, *Palaeogeogr. Palaeoclimatol. Palaeoecol.* **67** (1988) 285–261.
- [688] SEIDEL, G.E., Application of the GABHYD groundwater model of the Great Artesian Basin, Australia, *BMR J. Aust. Geol. Geophys.* **5** (1980) 39–45.
- [689] HABERMEHL, M.A., SEIDEL, G.E., “Groundwater resources of the Great Artesian Basin”, Second Invitation Symposium Land and Water Resources of Australia — Dynamics of Utilisation (HALLSWORTH, E.G., WOODCOCK, J.T., Eds), Australian Academy of Technological Sciences, Sydney (1979).
- [690] HABERMEHL, M.A., “Regional groundwater movement, hydrochemistry and hydrocarbon migration in the Eromanga Basin”, Contributions to the Geology and Hydrocarbon Potential of the Eromanga Basin (GRAVESTOCK, D.I., MOORE, P.S., PITT, G.M., Eds), Geological Society of Australia (1986).
- [691] WELSH, W.D., GABFLOW: A steady state groundwater flow model of the Great Artesian Basin, Bureau of Rural Sciences, Canberra (2000).
- [692] WELSH, W.D., DOHERTY, J., ”Great Artesian Basin groundwater modelling”, 29th Hydrology and Water Resources Symp., Engineers Australia, Canberra (2005).
- [693] WELSH, W.D., Great Artesian Basin Transient Groundwater Model, Australia, Bureau of Rural Sciences, Canberra (2006).
- [694] KERSHAW, A.P., Record of the last interglacial-glacial cycle from northeastern Queensland, *Nature* **272** (1978).
- [695] KERSHAW, A.P., Pleistocene vegetation of the humid tropics of northeastern Queensland, Australia, *Palaeogeogr. Palaeoclimatol. Palaeoecol.* **109** (1994) 399–412.
- [696] KERSHAW, A.P., NANSON, G.C., The last full glacial cycle in the Australian region, *Global Planet. Change* **7** (1993) 1–9.
- [697] CALF, G.E., HABERMEHL, M.A., “Isotope hydrology and hydrochemistry of the Great Artesian Basin, Australia”, Isotope Hydrology 1983 (Proc. Vienna, 1983), IAEA, Vienna (1984).
- [698] TORGERSEN, T., HABERMEHL, M.A., CLARKE, W.B., Crustal helium fluxes and heat flow in the Great Artesian Basin, Australia, *Chem. Geol.* **102** (1992) 139–152.
- [699] DAVIS, S.N., DE WIEST, R.J.M., Hydrogeology, John Wiley, New York (1966).
- [700] HEATON, T.H.E., VOGEL, J.C., Gas concentrations and ages of groundwaters in Beaufort Group Sediments, South Africa, *Water South Africa* **5** (1979) 160–170.
- [701] MARINE, I.W., Geochemistry of Groundwater at the Savannah River Plant, E.I. DuPont de Nemours Co. Savannah River Laboratory NTIS (1976).
- [702] ANDREWS, J.N., FONTES, J.-C., “Importance of in situ production of chlorine-36, argon-36 and carbon-14 in hydrology and hydrochemistry”, Isotope Techniques in Water Resources Development (Proc. Vienna, 1991), IAEA, Vienna (1991).
- [703] ANDREWS, J.N., FONTES, J.-C., Comment on ‘Chlorine-36 dating of very old groundwater: Further studies in the Great Artesian Basin, Australia’ by Torgersen et al., *Water Resour. Res.* **27** (1991), *Water Resour. Res.* **29** (1993) 1871–1874.
- [704] FONTES, J.-C., ANDREWS, J.N., Comment on ‘Reinterpretation of <sup>36</sup>Cl data: physical processes, hydraulic interconnections and age estimations in groundwater systems’ by E. Mazor, *Appl. Geochem.* **8** (1993) 663–666.
- [705] MAZOR, E., Reinterpretation of Cl-36 data: physical processes, hydraulic interconnections, and age estimates in groundwater systems, *Appl. Geochem.* **7** (1992) 351–360.

- [706] TORGERSEN, T., PHILLIPS, F.M., Reply to comment on ‘Chlorine-36 dating of very old groundwater: Further studies in the Great Artesian Basin, Australia’, *Water Resour. Res.* **29** (1993) 1875–1877.
- [707] PHILLIPS, F.M., Comment on ‘Reinterpretation of  $^{36}\text{Cl}$  data: physical processes, hydraulic interconnections and age estimations in groundwater systems’ by E. Mazor, *Appl. Geochem.* **8** (1993) 643–647.
- [708] MAZOR, E., NATIV, R., Hydraulic calculation of groundwater flow velocity and age: Examination of the basic premises, *J. Hydrol.* **138** (1992) 211–222.
- [709] MAZOR, E., NATIV, R., Stagnant groundwater stored in isolated aquifers: implications related to hydraulic calculations and isotope dating, Reply, *J. Hydrol.* **154** (1994) 409–418.
- [710] TORGERSEN, T., Hydraulic calculation of groundwater flow velocity and age: Examination of the basic premises — Comment, *J. Hydrol.* **154** (1994) 403–408.
- [711] HERCZEG, A.L., TORGERSEN, T., CHIVAS, A.R., HABERMEHL, M.A., Geochemistry of ground waters from the Great Artesian Basin, Australia, *J. Hydrol.* **126** (1991) 225–245.
- [712] BLAKE, R., “The origin of high sodium bicarbonate waters in the Otway Basin, Victoria, Australia”, *Water-Rock Interactions* (MILES, D.L., Ed.), Balkema, Rotterdam (1989).
- [713] HABERMEHL, M.A., PESTOV, I., Geothermal resources of the Great Artesian Basin, Australia, *Geo-Heat Center Quarterly Bull.* **23** (2002) 20–26.
- [714] HABERMEHL, M.A., PESTOV, I., RANSLEY, T., “Sustainable development of geothermal resources in the Great Artesian Basin, Australia”, *Balancing the Groundwater Budget* (Proc. Int. Groundwater Conf. Darwin, 2002).
- [715] PRESCOTT, J.R., HABERMEHL, M.A., Luminescence dating of spring mound deposits in the southwestern Great Artesian Basin, northern South Australia, *Aust. J. Earth Sci.* **55** (2008) 167–181.
- [716] PESTOV, I., Thermal convection in the Great Artesian Basin, Australia, *Water Resour. Manag.* **14** (2000) 391–403.
- [717] PIRLO, M.C., Hydrogeochemistry and geothermometry of thermal groundwaters from the Birdsville Track Ridge, Great Artesian Basin, South Australia, *Geothermics* **33** (2004).
- [718] O’SHEA, B., JANKOWSKI, J., Detecting subtle hydrochemical anomalies with multivariate statistics: an example from ‘homogeneous’ groundwaters in the Great Artesian Basin, Australia, *Hydrol. Proc.* **20** (2006) 4317–4333.
- [719] PIPER, A.M., A graphical procedure in the geochemical interpretation of water analyses, *Trans. Amer. Geophys. Union* **25** (1944) 914–923.
- [720] CHILIGAR, G.V., Durov’s classification of natural waters and chemical composition of atmospheric precipitation in USSR, a review, *Trans. Amer. Geophys. Union* **37** (1956) 193–196.
- [721] CHADA, D.K., A proposed new diagram for geochemical classification of natural waters and interpretation of chemical data, *Hydrogeol. J.* **7** (1999) 431–439.
- [722] KELLETT, J.R., et al., Groundwater recharge in the Great Artesian Basin intake beds, Queensland, Queensland Department of Natural Resources and Mines (2003).
- [723] HABERMEHL, M.A., DEVONSHIRE, J., MAGEE, J.W., Sustainable groundwater allocations in the intake beds of the Great Artesian Basin in New South Wales: Final Report, Bureau of Rural Sciences, Canberra (2009).
- [724] SHIMADA, J., HABERMEHL, M.A., MAHARA, Y., KAYANE, I., 100 000 Year Palaeohydrological Information from Artesian Groundwater in the Great Artesian Basin, Australia GLOCOPH ’98, Third Int. Mtg on Global Continental Palaeohydrology — Palaeohydrology with an Emphasis on Humid, Temperate, and Tectonically Active Zones, Risho University, Kumagaya, Japan (1998).
- [725] SHIMADA, J., HABERMEHL, M.A., MAHARA, Y., KAYANE, I., “Use of  $^{36}\text{Cl}$  to compile the recent 200 K year palaeohydrological information from artesian groundwater in Great Artesian Basin, Australia”, *Groundwater in Environmental Problems* (Proc. Int. Symp.), Chiba University, Japan (1999).
- [726] SHIMADA, J., et al., A 100 000 Year Palaeohydrological Information from Artesian Groundwater in the Great Artesian Basin, Australia International Workshop on Global Change and Terrestrial Environment in Monsoon, Asia, Tsukuba, Japan (1997).
- [727] HASEGAWA, T., MAHARA, Y., NAKATA, K., HABERMEHL, M.A., “Verification of  $^4\text{He}$  and  $^{36}\text{Cl}$  dating of very old groundwater in the Great Artesian Basin, Australia”, *Integrating Groundwater Science and Human Well-Being* (36th IAH Congress), Toyama, Japan (2009).

- [728] MAHARA, Y., et al., Groundwater dating by estimation of groundwater flow velocity and dissolved  $^4\text{He}$  accumulation rate calibrated by  $^{36}\text{Cl}$  in the Great Artesian Basin, Australia, *Earth Planet. Sci. Lett.* **287** (2009) 43–56.
- [729] HIMIDA, I.H., Remarks on the absolute age determination of the artesian water of the oases of the Western Desert with a special reference to Kharga oasis, *Bulletin de l'Institut du Désert d'Égypte* **XII** (1967) 61–124.
- [730] FRÖHLICH, K., AGGARWAL, P.K., GARNER, W.A., “An integrated approach in evaluating isotope data of the Nubian Sandstone Aquifer System (NSAS) in Egypt”, *Advances in Isotope Hydrology and its Role in Sustainable Water Resources Management (Proc. Symp. Vienna, 2007)*, 2 vols, IAEA, Vienna (2007).
- [731] SONNTAG, C., et al., “Palaeoclimatic information from deuterium and oxygen-18 in carbon-14-dated north Saharian groundwater formation in the past”, *Isotope Hydrology 1978 (Proc. Neuherberg, 1978)* IAEA, Vienna (1979).
- [732] BRINKMAN, P.J., HEINDL, R., HOLLANDER, R., REICH, G., Retrospective simulation of groundwater flow and transport in the Nubian Aquifer system, *Berliner Geowiss. Abh.* **75** (1987) 465–516.
- [733] HESSE, K.H., et al., Hydrogeological investigations in the Nubian Aquifer System, Eastern Sahara, *Berliner Geowissenschaftliche Abhandlungen A* **75** 2 (1987) 397–464.
- [734] EL BAKRI, A., BLAVOUX, B., DRAY, M., “Sources of water recharge identified by isotopes in El Minya Governate (Nile valley, Middle Egypt)”, *Isotope Techniques in Water Resources Development 1991 (Proc. Vienna, 1991)*, IAEA, Vienna (1992).

## CONTRIBUTORS TO DRAFTING AND REVIEW

Aggarwal, P.K.	International Atomic Energy Agency
Fröhlich, K.	Vienna, Austria
Glynn, P.D.	United States Survey, United States of America
Phillips, F.M.	Department of Earth and Environmental Science, United States of America
Plummer, L.N.	United States Geological Survey, United States of America
Purtschert, R.	University of Bern, Switzerland
Reilly, T.E.	United States Geological Survey, United States of America
Sanford, W.E.	United States Geological Survey, United States of America
Sturchio, N.C.	University of Illinois, United States of America
Stute, M.	Barnard College and Lamont Doherty Earth, United States of America
Suckow, A.	Leibniz-Institut für Angewandte Geophysik, Germany
Torgersen, T.	University of Connecticut, United States of America
Yokochi, R.	University of Illinois, United States of America





# Where to order IAEA publications

In the following countries IAEA publications may be purchased from the sources listed below, or from major local booksellers. Payment may be made in local currency or with UNESCO coupons.

## AUSTRALIA

DA Information Services, 648 Whitehorse Road, MITCHAM 3132  
Telephone: +61 3 9210 7777 • Fax: +61 3 9210 7788  
Email: [service@dadirect.com.au](mailto:service@dadirect.com.au) • Web site: <http://www.dadirect.com.au>

## BELGIUM

Jean de Lannoy, avenue du Roi 202, B-1190 Brussels  
Telephone: +32 2 538 43 08 • Fax: +32 2 538 08 41  
Email: [jean.de.lannoy@infoboard.be](mailto:jean.de.lannoy@infoboard.be) • Web site: <http://www.jean-de-lannoy.be>

## CANADA

Bernan Associates, 4501 Forbes Blvd, Suite 200, Lanham, MD 20706-4346, USA  
Telephone: 1-800-865-3457 • Fax: 1-800-865-3450  
Email: [customercare@bernan.com](mailto:customercare@bernan.com) • Web site: <http://www.bernan.com>

Renouf Publishing Company Ltd., 1-5369 Canotek Rd., Ottawa, Ontario, K1J 9J3  
Telephone: +613 745 2665 • Fax: +613 745 7660  
Email: [order.dept@renoufbooks.com](mailto:order.dept@renoufbooks.com) • Web site: <http://www.renoufbooks.com>

## CHINA

IAEA Publications in Chinese: China Nuclear Energy Industry Corporation, Translation Section, P.O. Box 2103, Beijing

## CZECH REPUBLIC

Suweco CZ, S.R.O., Klecakova 347, 180 21 Praha 9  
Telephone: +420 26603 5364 • Fax: +420 28482 1646  
Email: [nakup@suweco.cz](mailto:nakup@suweco.cz) • Web site: <http://www.suweco.cz>

## FINLAND

Akateeminen Kirjakauppa, PO BOX 128 (Keskuskatu 1), FIN-00101 Helsinki  
Telephone: +358 9 121 41 • Fax: +358 9 121 4450  
Email: [akatilaus@akateeminen.com](mailto:akatilaus@akateeminen.com) • Web site: <http://www.akateeminen.com>

## FRANCE

Form-Edit, 5, rue Janssen, P.O. Box 25, F-75921 Paris Cedex 19  
Telephone: +33 1 42 01 49 49 • Fax: +33 1 42 01 90 90  
Email: [formedit@formedit.fr](mailto:formedit@formedit.fr) • Web site: <http://www.formedit.fr>

Lavoisier SAS, 145 rue de Provigny, 94236 Cachan Cedex  
Telephone: + 33 1 47 40 67 02 • Fax +33 1 47 40 67 02  
Email: [romuald.verrier@lavoisier.fr](mailto:romuald.verrier@lavoisier.fr) • Web site: <http://www.lavoisier.fr>

## GERMANY

UNO-Verlag, Vertriebs- und Verlags GmbH, Am Hofgarten 10, D-53113 Bonn  
Telephone: + 49 228 94 90 20 • Fax: +49 228 94 90 20 or +49 228 94 90 222  
Email: [bestellung@uno-verlag.de](mailto:bestellung@uno-verlag.de) • Web site: <http://www.uno-verlag.de>

## HUNGARY

Librotrade Ltd., Book Import, P.O. Box 126, H-1656 Budapest  
Telephone: +36 1 257 7777 • Fax: +36 1 257 7472 • Email: [books@librotrade.hu](mailto:books@librotrade.hu)

## INDIA

Allied Publishers Group, 1st Floor, Dubash House, 15, J. N. Heredia Marg, Ballard Estate, Mumbai 400 001,  
Telephone: +91 22 22617926/27 • Fax: +91 22 22617928  
Email: [alliedpl@vsnl.com](mailto:alliedpl@vsnl.com) • Web site: <http://www.alliedpublishers.com>

Bookwell, 2/72, Nirankari Colony, Delhi 110009  
Telephone: +91 11 23268786, +91 11 23257264 • Fax: +91 11 23281315  
Email: [bookwell@vsnl.net](mailto:bookwell@vsnl.net)

## ITALY

Libreria Scientifica Dott. Lucio di Biasio "AEIOU", Via Coronelli 6, I-20146 Milan  
Telephone: +39 02 48 95 45 52 or 48 95 45 62 • Fax: +39 02 48 95 45 48  
Email: [info@libreriaaeiou.eu](mailto:info@libreriaaeiou.eu) • Website: [www.libreriaaeiou.eu](http://www.libreriaaeiou.eu)

## **JAPAN**

Maruzen Company Ltd, 1-9-18, Kaigan, Minato-ku, Tokyo, 105-0022  
Telephone: +81 3 6367 6079 • Fax: +81 3 6367 6207  
Email: journal@maruzen.co.jp • Web site: <http://www.maruzen.co.jp>

## **REPUBLIC OF KOREA**

KINS Inc., Information Business Dept. Samho Bldg. 2nd Floor, 275-1 Yang Jae-dong SeoCho-G, Seoul 137-130  
Telephone: +02 589 1740 • Fax: +02 589 1746 • Web site: <http://www.kins.re.kr>

## **NETHERLANDS**

De Lindeboom Internationale Publicaties B.V., M.A. de Ruyterstraat 20A, NL-7482 BZ Haaksbergen  
Telephone: +31 (0) 53 5740004 • Fax: +31 (0) 53 5729296  
Email: books@delindeboom.com • Web site: <http://www.delindeboom.com>

Martinus Nijhoff International, Koraaalrood 50, P.O. Box 1853, 2700 CZ Zoetermeer  
Telephone: +31 793 684 400 • Fax: +31 793 615 698  
Email: info@nijhoff.nl • Web site: <http://www.nijhoff.nl>

Swets and Zeitlinger b.v., P.O. Box 830, 2160 SZ Lisse  
Telephone: +31 252 435 111 • Fax: +31 252 415 888  
Email: info@swets.nl • Web site: <http://www.swets.nl>

## **NEW ZEALAND**

DA Information Services, 648 Whitehorse Road, MITCHAM 3132, Australia  
Telephone: +61 3 9210 7777 • Fax: +61 3 9210 7788  
Email: service@dadirect.com.au • Web site: <http://www.dadirect.com.au>

## **SLOVENIA**

Cankarjeva Zalozba d.d., Kopitarjeva 2, SI-1512 Ljubljana  
Telephone: +386 1 432 31 44 • Fax: +386 1 230 14 35  
Email: import.books@cankarjeva-z.si • Web site: <http://www.cankarjeva-z.si/uvoz>

## **SPAIN**

Díaz de Santos, S.A., c/ Juan Bravo, 3A, E-28006 Madrid  
Telephone: +34 91 781 94 80 • Fax: +34 91 575 55 63  
Email: compras@diazdesantos.es, carmela@diazdesantos.es, barcelona@diazdesantos.es, julio@diazdesantos.es  
Web site: <http://www.diazdesantos.es>

## **UNITED KINGDOM**

The Stationery Office Ltd, International Sales Agency, PO Box 29, Norwich, NR3 1 GN  
Telephone (orders): +44 870 600 5552 • (enquiries): +44 207 873 8372 • Fax: +44 207 873 8203  
Email (orders): book.orders@tso.co.uk • (enquiries): book.enquiries@tso.co.uk • Web site: <http://www.tso.co.uk>

### **On-line orders**

DELTA Int. Book Wholesalers Ltd., 39 Alexandra Road, Addlestone, Surrey, KT15 2PQ  
Email: info@profbooks.com • Web site: <http://www.profbooks.com>

### **Books on the Environment**

Earthprint Ltd., P.O. Box 119, Stevenage SG1 4TP  
Telephone: +44 1438748111 • Fax: +44 1438748844  
Email: orders@earthprint.com • Web site: <http://www.earthprint.com>

## **UNITED NATIONS**

Dept. 1004, Room DC2-0853, First Avenue at 46th Street, New York, N.Y. 10017, USA  
(UN) Telephone: +800 253-9646 or +212 963-8302 • Fax: +212 963-3489  
Email: publications@un.org • Web site: <http://www.un.org>

## **UNITED STATES OF AMERICA**

Bernan Associates, 4501 Forbes Blvd., Suite 200, Lanham, MD 20706-4346  
Telephone: 1-800-865-3457 • Fax: 1-800-865-3450  
Email: customercare@bernan.com • Web site: <http://www.bernan.com>

Renouf Publishing Company Ltd., 812 Proctor Ave., Ogdensburg, NY, 13669  
Telephone: +888 551 7470 (toll-free) • Fax: +888 568 8546 (toll-free)  
Email: order.dept@renoufbooks.com • Web site: <http://www.renoufbooks.com>

**Orders and requests for information may also be addressed directly to:**

### **Marketing and Sales Unit, International Atomic Energy Agency**

Vienna International Centre, PO Box 100, 1400 Vienna, Austria  
Telephone: +43 1 2600 22529 (or 22530) • Fax: +43 1 2600 29302  
Email: sales.publications@iaea.org • Web site: <http://www.iaea.org/books>

This book provides theoretical and practical information for using a variety of isotope tracers for dating 'old' groundwater, that is water stored in geological formations for periods ranging from about a thousand to a million years. Theoretical underpinnings of the methods and guidelines for using isotope tracers in different hydrogeological environments are described. The book also presents a number of case studies providing insight into how various isotopes have been used in aquifers around the world. The methods, findings and conclusions presented in this publication will enable students and practising groundwater scientists to evaluate the use of isotope dating tools for specific issues related to the assessment and management of groundwater resources.

INTERNATIONAL ATOMIC ENERGY AGENCY  
VIENNA  
ISBN 978-92-0-137210-9